A Spectroscopic and Diagnostic Study of Laser Plasma Generation and Evolution under Multi-variable Target Conditioning

Thesis Submitted to the Faculty of Science for the Degree of Doctor of Philosophy

By

Patrick Yeates B.Sc.

Dublin City University

School of Physical Sciences
Centre for Laser Plasma Research
Dublin City University

Research Supervisor
Professor Eugene T. Kennedy, B.Sc. PH.D. C.Phys. F.Inst.P.

July 2004

Declaration

I hereby certify that this material, which I now submit for assessment on the programme of study leading to the award of the degree of Doctor of Philosophy is entirely my own work and has not been taken from the work of others save and to the extent that such work has been cited and acknowledged within the text of my work.

Signed: P Yeates ID No: 99145189

(Candidate)

Date: 8th July 2004

This thesis is dedicated to my parents,

'With care and watering and fertile ground from which to spring, the little sapling becomes the great oak'

Acknowledgments

I would like to thank firstly my supervisor, Prof Eugene Kennedy For the past four and a half years he has been a constant source of unbiased, professional and critical advice and guidance, who has continuously bestowed upon all of his students (my self included) the trust, freedom, intellectual and financial support necessary for a young scientist to mature in to a professional researcher Despite difficulties and uncertainties, Professor Kennedy always helpful to the point of being critical, ensuring focus but never harsh, and always willing to assist me in the numerous problems which I encountered during the course of this work

However despite his seniority and busy schedule, Eugene remained always light hearted and approachable to every one vying for his attention Thus one understands why his colleagues call him 'The great K'

I would also like to extend my thanks to the other members of CLPR, especially the senior staff members Dr John Costello whose advice on issues involving electronics, lasers and my over enthusiastic interest in high voltages was life saving (literally) Dr J P Mosnier, for advice on issues involving laser plasmas, and for use of his lab in the later stages of the project Dr P V Kampen, for many hours of advice and guidance during the difficult first few months of my project, and for allowing me the chance to inflict my German on him

For Alan and Mark, who decided to inflict the experience of PhDs upon themselves at the same time as myself, I wish you both all the best in your future careers and personal lives To the gang of young researchers currently inflicting themselves upon the physics department , Eoin, Kevin, Adrian, Jonathan, Nelly, recently departed John Hirsch and Jaoine, and newly arrived Deirdre and Jean-rene, I hope all goes well in the future To my friend and former student of Eugenes, Dr Mohamed Khater, may all be well in Egypt and with your family in the future Finally for former researchers and my good friends Dr Amit Neogi and his lovely wife Dr Chatalli Roy, many thanks for displaying a generosity and kindness few can comprehend. A special thanks is reserved for Des and Keane of the workshop, who labored hard and long to finish the vacuum chamber which was so critical to this work Also Patrick Wogan deserves a particular mention for the many months (and some hairy moments) in designing building and testing the magnetic pulse generator, which represents an enormous engineering achievement To every one at the physics department, postgrads, secretaries (especially Shelia-NCPST), my sincere thanks

Abstract

The spectroscopic and electrostatic properties of laser generated plasmas under the influence of different target configurations have been investigated Three main diagnostic techniques have been employed Firstly, time and space resolved EUV(7-45nm) emission spectroscopy was used for timescales during and up to 35nsec after the laser pulse Secondly, space and time resolved visible (273-620nm) emission spectroscopy and fast frame visible imaging, was used for timescales during and up to 600nsec after the laser pulse Finally, ion and electron probes, sampled the temporal range from 800nsec onwards after the laser pulse

These three techniques, distinct in the space-time envelope in which they are applicable, divided the work into three regimes of the plasma lifetime under study, these were termed, 'near field', 'intermediate field' and finally, 'far field'

For EUV(near field) studies, laser plasma generation and evolution within rectangular cavities was studied and compared to plasma undergoing free expansion from a flat target Substantial enhancement of intensities of the lines studied was demonstrated, while extended lifetimes of contained EUV plasma was observed Space and time resolved line widths, ionization (line ratio) and electron (Boltzmann) temperatures were calculated to characterize plasma behavior

For visible (intermediate field) studies, laser plasma generation and evolution within rectangular cavities, capillaries, and between vertical parallel plates and flat targets was undertaken Space and time resolved electron densities, ionization temperatures (line ratio) and electron temperatures (line-to-continuum) were calculated to characterize plasma behavior Gated ICCD images were used to study plasma dynamics with each of the target configurations studied Large increases in plasma electron and ionization temperature, electron density, and forward expansion velocities were observed, for the three targets studied when compared to flat targets Enhanced plume 'splitting', was also demonstrated for confined plasma

For probe (far field) studies, arrays of ion and electron probes were used to study plume dynamics from various target configurations Ion and electron densities, electron temperature and velocities were calculated, and plume collimation and superior time of flight velocities were observed for plasma generated within a confining target, when compared to plasma plumes from flat targets

Contents:

Introduction

Laser ablation of solids with pulsed laser beams of high intensity results in complicated interactions of the laser beam with both the solid target and the ablated mass. Transfer of laser energy leads to a rapid rise in surface temperature on the target surface, which drives evaporation of particles from the solid. The threshold for evaporation for nanosecond lasers range is typically of the order of 0.2-1.0GWcm^{-2} to 1.0GWcm^{-2}. The evaporated particles are highly charged with energies up to several hundred eV. Depending on the pulse width, laser wavelength, and the atomic properties of the target amongst other variables, varying proportions of the beam energy will be absorbed by the evaporated highly ionized plume. The transition from heating, evaporation of particles, and temperature rise through laser energy absorption is a gradual process. The rapid heating of the evaporated particles by the laser leads to a high velocity, 1dimensional isothermal expansion of the plasma. The plasma plume moves away from the target surface rapidly, expanding and cooling. Under such conditions, a highly energetic plume exists, the ions are structured spatially throughout the plumes, with the more highly ionized localized at the center. The spatial distribution of the ions as they decay was studied by Boland et al 1968 in figure I. The trends were seen through space and time resolved spectroscopic analysis of the ions from a copper laser generated plasma expanding in vacuum. The trends seen were the creation of highly ionized species first which by virtue of higher kinetic energy expanded at a higher velocity, followed later, as the average temperature within the plume drops, by the appearance of lower charged states further out from the target surface.

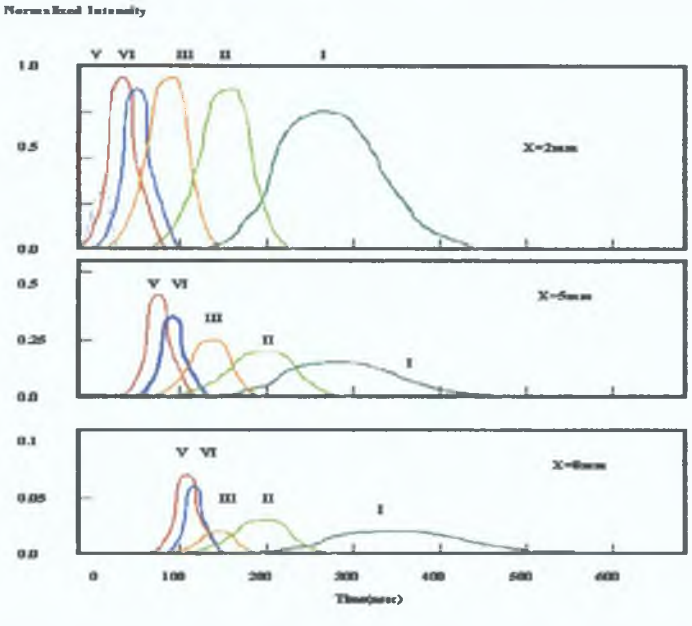

Figure I: Space-time distribution of copper ions in a laser generated plasma plume. This was one of the first bodies of work to study laser plasma plumes and their unique properties. (Boland et al 1968)

The earliest studies found that the energy density of a laser plasma is usually very high, given the high density and radiation trapping. It is this which fuels the expansion of the plasma long after the laser pulse

has terminated. The emission lifetime is heavily dependent on the wavelength and pulse width of the laser used. Higher ion stages, heated to higher temperatures and traveling at greater velocities than neutrals and lower charged ions, lead the expanding plume, showing a narrow angular distribution about the normal, back along the laser path. This was studied by Irons, shown in figure II (Irons et al 1972 [21]) who demonstrated the radial distribution of particles about the laser axis. More recently this aspect of laser generated plasma plumes has also been investigated with plasma probes and the results are displayed in figure III. (Lunney et al 2003[20]). Such studies have given experimentalists an overall picture of the particle distributions within the plumes, and have allowed theoretical studies to compare the experimental trends with those modeled.

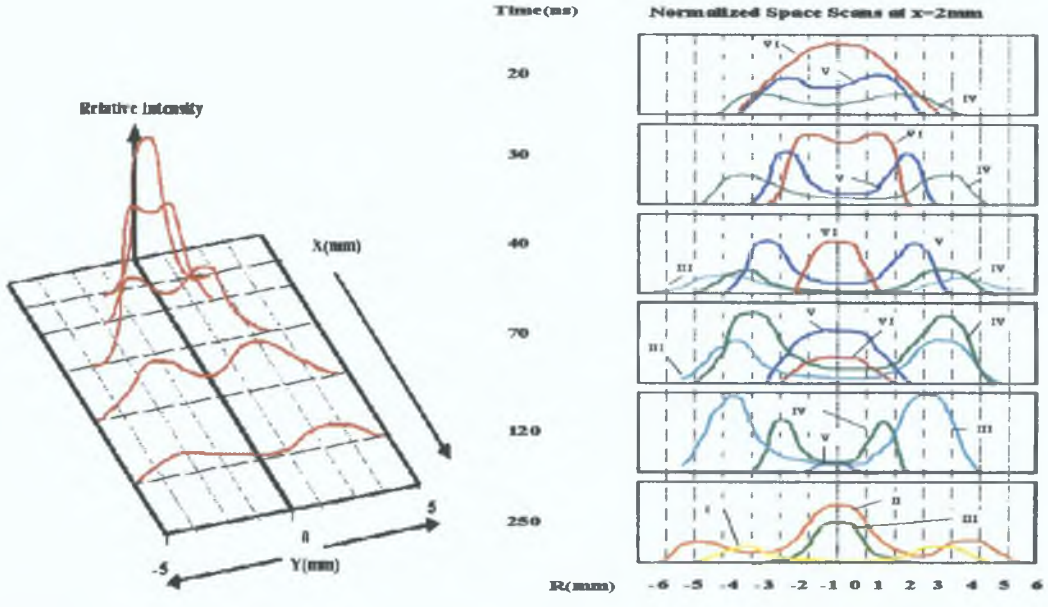

Fig II: Irons [21] work on studying the ion distributions about the axis normal to the target surface. This demonstrated strong collimation of the plumes constituents about the laser axis. This trend was especially pronounced early on in the plume's history.

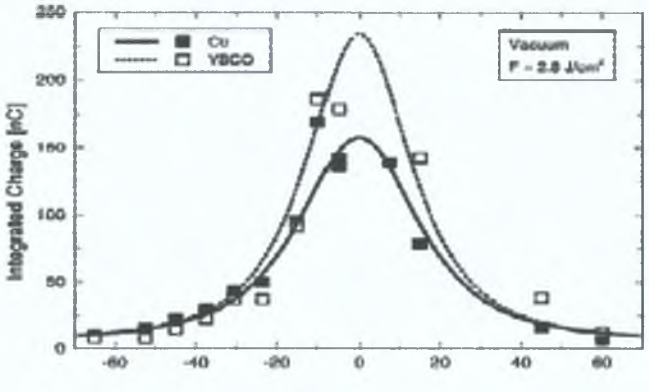

Figure III: The angular distribution of ions at a fixed time delay after the laser (1200nsec) in the horizontal plane from a $Yba_2CU_3O_7$ (YBCO) and copper plasma, showing strong particle collimation about the normal studied using ion probes, the horizontal axis is angle in degress. (Lunney et al 2003[20])

Over the last fifteen to twenty years a huge body of work involving the variation in laser generated plasma properties with various experimental conditions has been undertaken The study of laser plasma generation and evolution has generally involved experimental studies and theoretical analysis of the plasma properties under the influence of simple target shapes [1], gas pressure, fluence [2], wavelength of the laser used [3], and the atomic number of the ablated species[4] Other studies involve magnetic fields, electric fields [4] and other 'non-contact' influences Some of the simplest techniques have been the most successful in increasing x-ray conversion efficiencies and peak brightness In [1], the authors studied enhanced XUV emission, both in emission spectra, and XUV pin hole images Here the authors used femtosecond laser pulses and studied the enhanced emission properties of plasma emerging from aluminum capillaries Large increases in AL IX and AL VIII intensities were observed from plasma plumes emerging from the capillaries when compared to planar targets (figure IV, V) In [5] the authors doped a glass target with neodymium of various concentrations, this resulted in a 150 fold increase in the conversion efficiency of laser energy to x-ray emission In [6] the authors collided two plasmas, in order to study collisionally driven ionization enhancement Other target modifications include doping one target with another material Studies in the XUV have demonstrated clearly that not only are the spectroscopic properties of doped targets different, but the bulk dynamics of the XUV plume are different [7] Here the authors also used temperature diagnostics to determine that boron nitride plumes were appreciably hotter than a plume of either boron, or boron carbide (fig VI) They also attempted to employ spectroscopic diagnostics to early times during the plasma's history Using time integrated spectra from the XUV (2-15nm) they utilized line intensity ratios to calculate the plasma temperature as a function of distance from the target surface (fig VII) The value calculated indicated that peak plasma temperatures for boron were approximately 30eV, and 50eV for boron nitride

Figure IV XUV images (pin hole camera gate time, 2nsec) from Z Andreic et al[1] The first image (far left) is taken at 10nsec, the second (middle) is after 18nsec the third 58nsc (right) after the laser pulse In all cases the laser came from the left

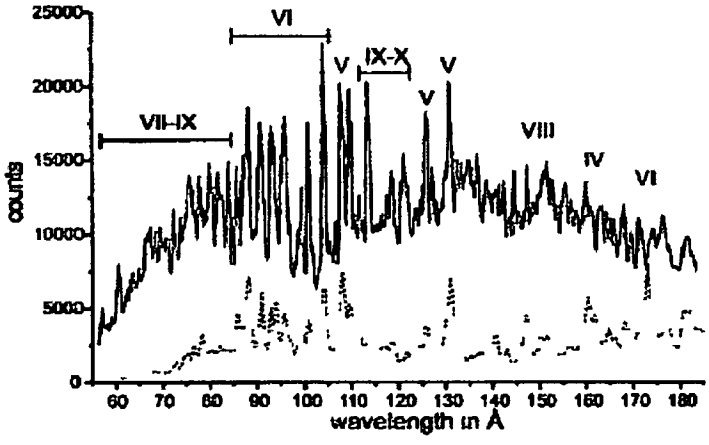

Figure V Emission spectra from plasma outside of the capillary (solid line) 1mm from the target surface, and inside the capillary (dashed line) The main difference seen here is the large increase in the continuum, for the plasma outside the capillary This is likely to be recombination continuum occurring as the plume undergoes rapid expansion (Z Andreic et al [1])

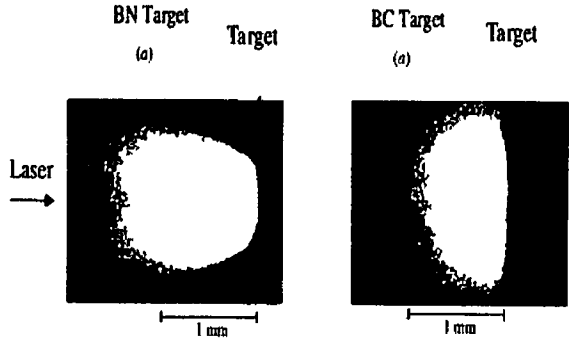

Figure VI Plume expansion differences for XUV pinhole images, 'BN target -boron nitride, 'BC target'-boron carbide from H-J Kunze et al [6] Not only is the emission spectrum different but the plume dynamics are different

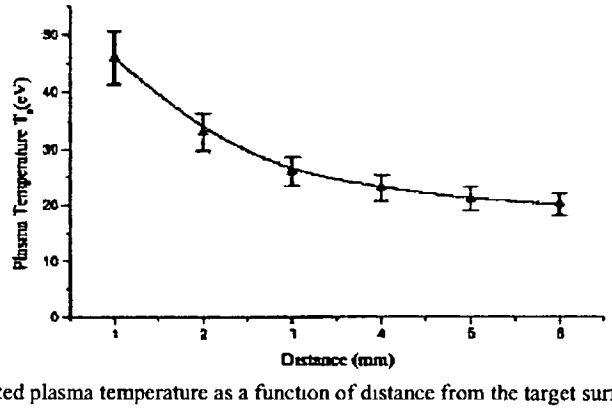

Figure VII Time integrated plasma temperature as a function of distance from the target surface (80GW cm ^{2}) Peak temperature for boron did not exceed 30eV yet for boron nitride they were 50eV (S S Harilal et al [6])

An important aspect of short wavelength plasma diagnostic studies such as those reported by Harilal [6], is the clear peaking of the plasma density and temperature at a specific point in space and time, which is not

the target surface, but a short distance from the targets surface (figure VII), and after the termination of the laser pulse (figure VIII). These temperature curves display a steep riding edge of the temperature which peaks, and then displays a gradual decay.

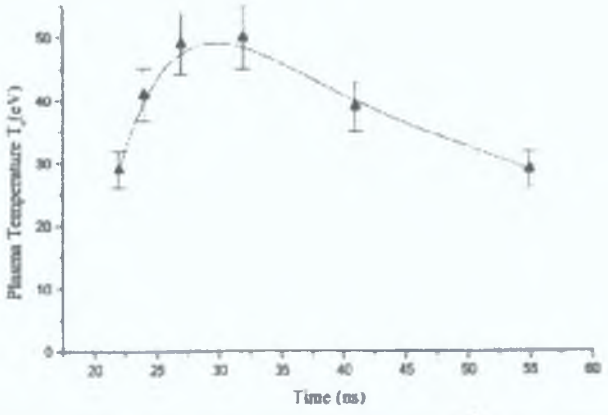

Figure VIII: Plasma temperature of the expanding boron nitride plasma as a function of time (distance from target surface=1mm, at 80GWcm^{-2}).The curve displays a clearly defined rising edge in the temperature profile. (S. S. Harilal et al [6])

Another scheme used was borosilicate glass doped with cerium, and ablated with a pre-pulse laser beam [8], giving enhanced soft x-ray emission in the EUV range. More recently isochoric heating driven by ultra short laser pulses with durations in the sub-pico second range have allowed temperatures in laser plasma generation to reach 500eV for short periods by burying a second layer of material below the surface of the main target material (figure IX). This has led to studies of the influence of fast electrons in collision driven processes at high densities. Substantial line broadening, center-of-mass line shifts to the red, and significant high-order satellite line emission have been observed for aluminum layers buried in carbon seen in figure X. (Eidmann et al[9])

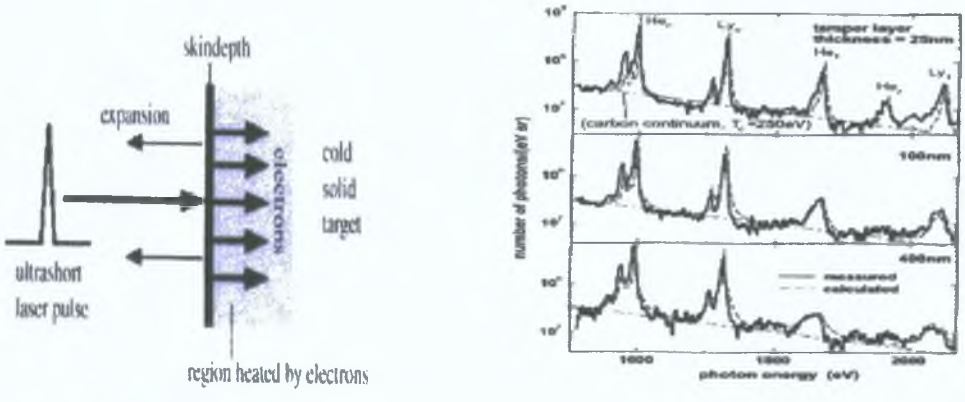

Figure IX (left): Schematic of isochoric heating via fast electrons. A short laser pulse, which must have a very low pre-pulse to avoid low-density pre-plasma formation, deposits its energy within the skin depth layer of thickness 5-10nm. This thin layer expands rapidly during the irradiation by the laser pulse. In order to achieve isochoric heating the energetic electrons in the absorption zone are crucial. These energetic electrons penetrate deep into the target and heat a region whose thickness is determined by their mean free path. The main effect of this is substantial broadening of emitted lines. Figure X(right), Line shape shifts in emitted lines, as secondary target (Carbon) layer thickness increases. (Eidmann et al[9])

The use of multi-composite targets along with the use of foils [10] is a direct attempt to configure the generation of a laser plasma by configuring the conditions under which energy from the laser is coupled to the target medium A second means of achieving this is to bypass the bulk target altogether, and instead to couple the laser pulse to a pre-existing plasma [11, 12, 13, 14] Here, the bulk of the laser energy is used to heat the pre-plasma to very high temperatures, dramatically increasing the particle collision rate and hence the ionization level [3, 4, 6, 8, 10]

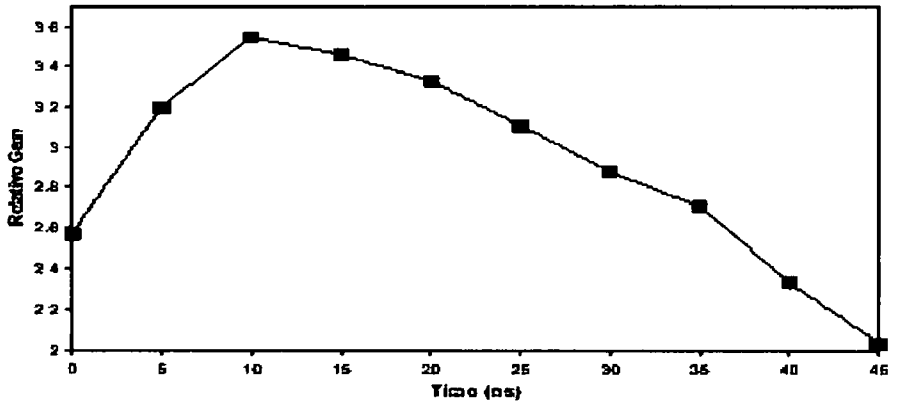

Figure XI Influence of pre-plasma to plasma time interval on plasma VUV output, Murphy et al[14]

Murphy et al [14], utilized a 0 8J, 8nsec duration laser to generate a pre plasma on a copper target This pre-plasma was then re-heated by a 150psec laser, and the time delay between the two lasers was varied Intensity enhancement factors up to 3 6 were observed at a specific delay between the two lasers(figure XI) The enhancement factor was optimized at a particular time delay, this inter-laser time delay dependency is a general trend of laser interaction with a preformed plume

Uesug et al [15], studied the effect of target geometry on laser plasma formation with femotsecond pulses

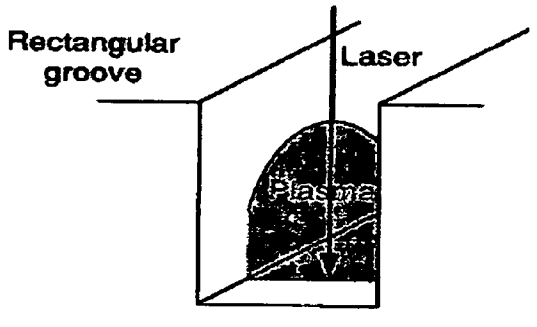

Figure XII Target geometry employed by Nishikawa et al[15]

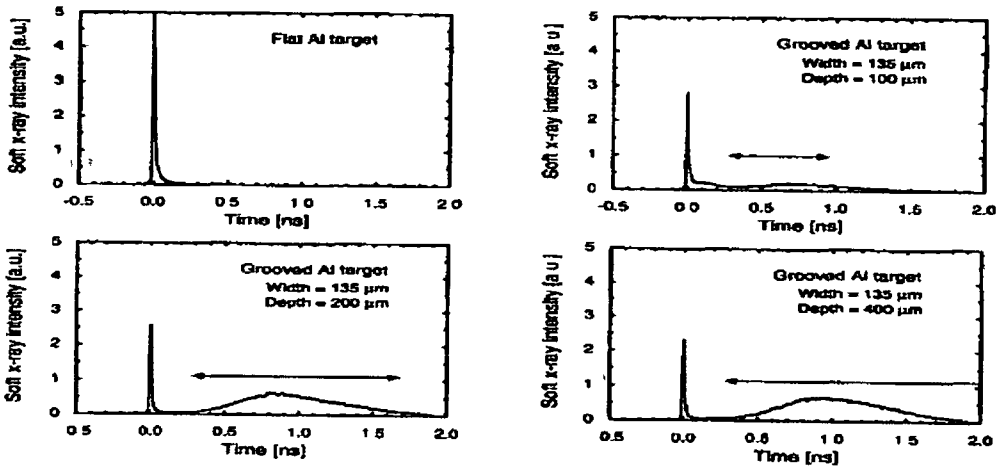

Figure XIII Influence of target containment on plasma XUV temporal output profile measured with a XUV photodiode, Nishikawa et al[15]

Here the authors studied the XUV temporal output from a 100fsec laser generated aluminum plasma from rectangular cavities of varying dimensions (figure XII and XIII) Their work was both spatially limited to one point within the cavity, and their spectra were temporally integrated However large enhancements in XUV photodiode signal after the laser pulse were observed The degree of enhancement was heavily dependent upon the cavity size This work indicates that target effects are important not only in plume dynamics but also for potential light source development Studies of plasma variables involving plasma interactions are not limited to emission studies Anisimov et al [16], studied the changing in the velocity distribution of copper particles, as they stream through a grid Using a Faraday cup, the measured velocity distribution of the laser ablated copper particles before plume interaction with the grid and afterwards displayed a non-linear transformation of particle velocities and the formation of a two component plasma (figure XIV)

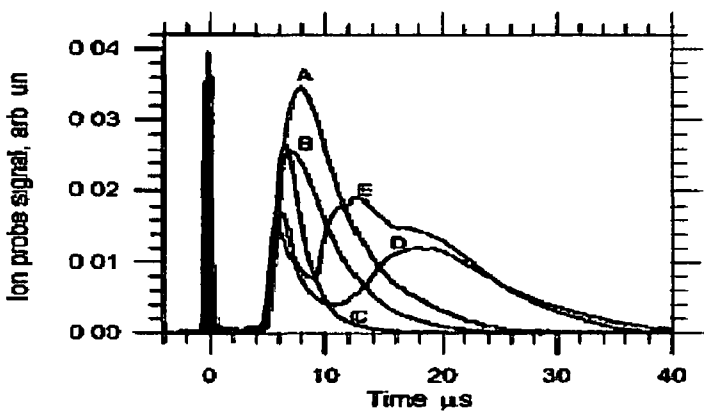

Figure XIV Velocity distribution shift, as a consequence of plasma interaction with a grid. Here a streaming plasma plume is forced through a grid placed a distance z from the target surface a)without grid b) z=32mm, c) z=8mm, d) z=4mm, e) z=2mm As the grid is moved closer to the target, the plume which interacts with it, does so at increasing temperature and density (the grid being closer to the generation point, and with the plume having less distance to travel and hence undergoing less of a decay in temperature and density), Anisimov et al[16]

Similar studies of plasma grid interaction were undertaken by Williamson [17]. The chief difference to Anisimov's work was the presence of a floating voltage on the grid, relative to a grounded target. The techniques used were optical absorption spectroscopy and laser induced fluorescence. The author studied the spatial distribution of selected ions for various fluences, grid voltages and gas pressures. Similar shifts in the velocity distribution were observed by Williamson, with the plasma-grid interaction increasing the velocity difference between the groups of ions within the plume,

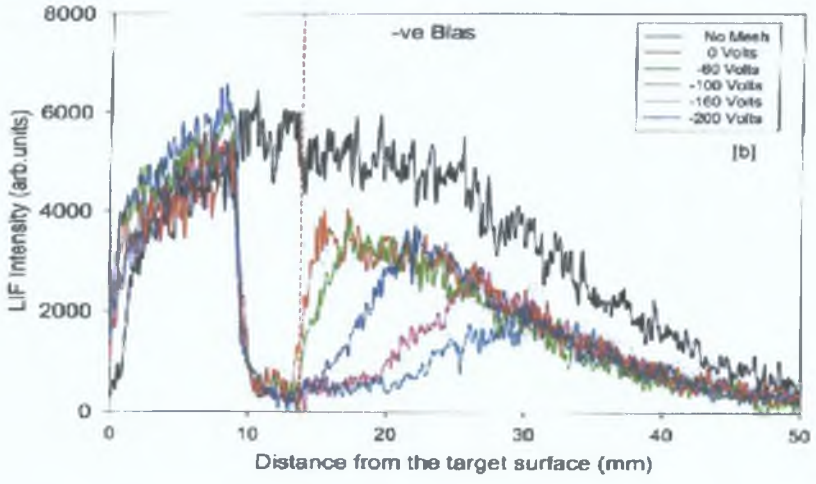

Figure XV: LIF intensity distribution along the z-direction (normal to the target surface). Not only is the distribution shifted for the grid compared to a freely expanding plume, but the electric influence provides a secondary influence by retarding same polarity charged ions and accelerating oppositely charged ions, Williamson [17].

as well as increasing the emission intensities of the ions as the grid voltages were increased (figure XV). Williamson's work involves both a physical influence i.e. the grid itself and the resulting interaction of the plume with the grid, but also the influence of the electric field on charged particle.

Another body of work using electric fields as a 'non-standard' influence was carried out by Varro et al [22]. The configuration of the target and bias plate was similar to that used by Williamson. The target was however made of gold, and the bias voltages used much larger (±20KV), and the laser beam was focused on to the target at a grazing angle (figure XVI).

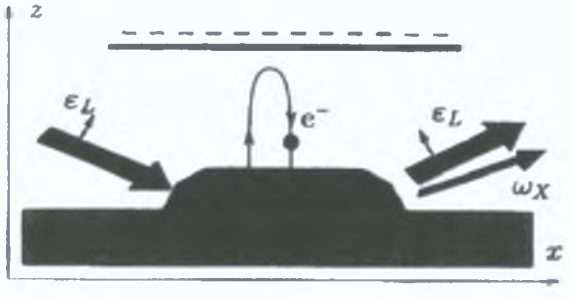

Figure XVI: Configuration of field and target for the study of enhanced XUV emission from bias gold targets, Varro et al [22].

The generation of short X-ray pulses was observed by Varro, for negative bias voltages at 20KV The duration of these pulses was identical to that of the ps laser ($I \sim 10^{12} Wcm^{2}$) used to generate the gold plasma No X-ray signal was observed for zero or positive bias voltages This simple experiment demonstrated the viability of enhancing short wavelength emission from plasma by means other then increased laser intensity, and motivates the study of non-standard or unusual influences on plasma behaviour

Regarding target effects, some work has been done on plume parameters from capillaries in the visible by Zeng et al [18] Here a 266nm, 3nsec Nd Yag laser was used to generate fused silica laser plasmas in capillaries of varying diameter and fixed length Emission spectra in the range 284-492nm were studied and electron temperatures and densities determined from the line widths and intensities of the lines The limiting factor in this work was the cavities themselves were formed via laser ablation, and were not perfectly smooth or exactly cylindrical(figure XVII, and XVIII) However the clear conclusion is that physical interaction of a plasma with surfaces has a substantial and complex set of effects on plume properties

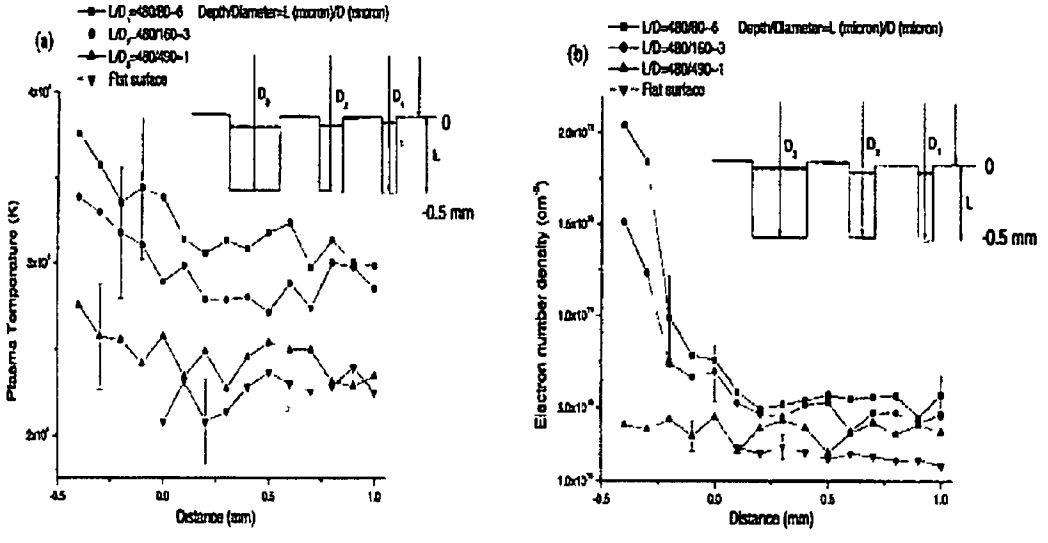

Figure XVII (left), XVIII (right) Space plots of electron density and temperature from capillaries from Zeng et al [18] The trend is of lower peak electron temperature and density as the capillary diameter decreases The length (or depth) of the capillary is ~0 5mm

Conclusion

One can definitely state that changes in a variable's profile (spatially or temporally) due to external influences are not completely characterized by a single diagnostic tool Since the range of variables in any experiment are many and diverse, a multi diagnostic approach is needed A good example of this multi-pronged data acquisition approach is that reported by Geohegan et al[19] Using ion probes, fast frame imaging in the visible range, optical absorption and emission spectroscopy, studies of yttrium laser plasma

plumes were performed in argon gas (200mTorr) Geohegan was able to overlap data trends from different diagnostic devices in order to build up a complete overview of 'plume splitting' of the plasma as it propagated through the gas This approach not only helps to build up a more coherent picture of the plume dynamics, but also lends more credibility to unusual findings in such work, when multiple diagnostics confirm unexpected trends in the plasma behaviour

At this time, despite the work on target conditioning discussed above, there is an absence of data on the systematic effects of various target geometries on plasma behaviour It is this imbalance which is addressed in this work Trends which seem clear during a certain space time range for a specific diagnostic device or detector, may not however be maintained at other time scales/wavelengths which are not sampled by a particular diagnostic tool Thus to truly understand the effects of a particular variable, one must probe the space-time envelope over as large a range as is feasible Thus in this body of work, the plasma was studied with multiple diagnostic tools, and in each case, a particular diagnostic device was applicable to a different space-time region of plasma history In all data presented, analysis is grounded in attempting to compare the plasma properties from different targets via physical parameters such as ion and electron density, ionization and electron temperatures (or velocities) Where spectroscopic constants (atomic data) are not available for this, emission spectra are compared and the space-time profile of various ions are used to study the effects of target geometries, electric field influence, and plasma re-heating via a second laser pulse on the plasma behavior Attempts are made to correlate trends seen in one space-time regime with the other two employed, in order to build up a coherent overview of target containment affects on laser generated plasmas, over as large a space-time envelope as possible The chief variable, target configuration, was varied in a systematic manner, with an intention to 'restrain' or 'prevent' plasma expansion along different expansion vectors Thus a plume generated within a rectangular cut in a block as seen in figure VII (Uesug et al) , orientated horizontally, would prevent plume expansion into the vertical plane, while plasma generated between two parallel plates, where the plates lie in the vertical plane, would retard the forward expansion of the plume from the target surface For each diagnostic tool, where possible, more than one theory was applied to convert raw data to meaningful physical parameters This was done both as a precaution to guard against errors in theory's applicability, but also for scientific validity

References

[1] Z Andreic, L Aschket, H-J Kunze, Inst Phys Conf Ser no 159, X-Ray Laser Conf 31'st Aug, 1998

[2] M Khater Ph D Thesis, Dec 2001 Ch6, pg175, Dublin City University

[3] A P McKiernan, J -P Mosnier Appl Surf Sci 197-198(2002) 325-330

[4] S Suckewer, C H Skinner, H Milchberg Physical Rev Lett vol55 no 17, 1753 (1995)

[5] T Nishikawa, H Nakano, N Uesugi, Applied Phys Letts, Vol 72, No 18, 2208-2210 (1998)

[6] S S Harilal, C V Bindhu, H J Kunze, Journal of Applied Physics, Vol 89, No 9 (2001)

[7] T Atwee, S S Harilal, H J Kunze, Journal of Physics D, 34, (2001) 1213-1218

[8] P Dunne, G O'Sullivan D O'Reilly, Appl Phys Letts, Vol 76, No 1, 34-36

[9] K Eidmann, K Witte, Journal of Quantitative Spectroscopy and Radiative Transfer, Elsevier Science

[10] O Renner , E Forster, J of Quantitative Spectroscopy and Radiative Transfer 81, (2003) 385-394

[11] L St-Onge, M Sabsabi, P Cielo, Spectrochimca Acta Part B 53 (1998) 40-415

[12] F Loewenthal, R. Tommasini, J E Balmer, Optics Communications 154 (1998) 325-328

[13] A G MacPhee, C L S Lewis, J Krishnan, Optics Communications 133 (1997) 525-533

[14] A Murphy et al, SPIE proceedings vol 1, pp 4876, 2003

[15] T Nishikawa, H Nakano, N Uesugi, Inst Phys Conf Proc No 159, 539-542, 1998

[16] V N Anisimov, V Yu Baranov, M A Stepanova, Appl Phys Letts, 67, (20) 13, Nov 1995

[17] T Williamson, PhD Thesis September 2001, Queens University Belfast

[18] X Zeng, S S Mao, R E Russo, Spectrochima Acta Part B 58 (2003) 867-877

[19] D B Geohegan, A A Puretzky, Appl Phys Lett 67 (2) July 1995

[20] B Thestrup, B Toftmann, J Schou, B Doggitt, J G Lunney, Appl Surf Sci, 208-209 (2003) 33-38

[21] F E Irons, N J Peacock, R S Pease (Soviet Journal of Quantum Electronics 1972)

[22] S Varro, Gy Farkas, F Ehlotzky, Optics Comm 172 (1999) 47-53

Chapter One: Plasma Theory and Review

Introduction

This chapter introduces the basic principles which govern the interaction of a high powered Q-switched laser with a material. The resulting generation of a high temperature, high density plasma, and the processes which define its behaviour are studied. The different atomic processes which occur in plasmas, both during and after the laser pulse are discussed. An overview of heating, melting and vaporization processes is presented. Plasma expansion in vacuum is also studied.

Plasmas theory and overview

1.0: Defining Characteristics.

Plasma is generally stated as being the fourth state of matter in the universe. Since it is an extreme state, it is not dominant in the terrestrial environment, but does predominate in the astrophysical environment. There exists a substantial range of conditions under which matter can become energetic enough to be considered an ionized gas or plasma. However generally the temperature must lie in the range of 1eV and upwards (1eV=11600K). In experimental nuclear fusion systems, or Tokamaks, the plasma density is approximately on the order of 10^{12}-10^{15} electrons per cubic centimeter. In laser generated plasmas, the densities easily exceed 10^{16} per cm^3, with the laser generated plasma showing heavy dependence on the pressure of the surrounding environment. The range of densities found in stars can vary from a few particles per cm^3 in the outer regions of the stars corona, to 10^{25} particles per cm^3 in the stars interior. Figure 1.0 shows the range of temperature and densities which exist within plasma, both natural and man made.

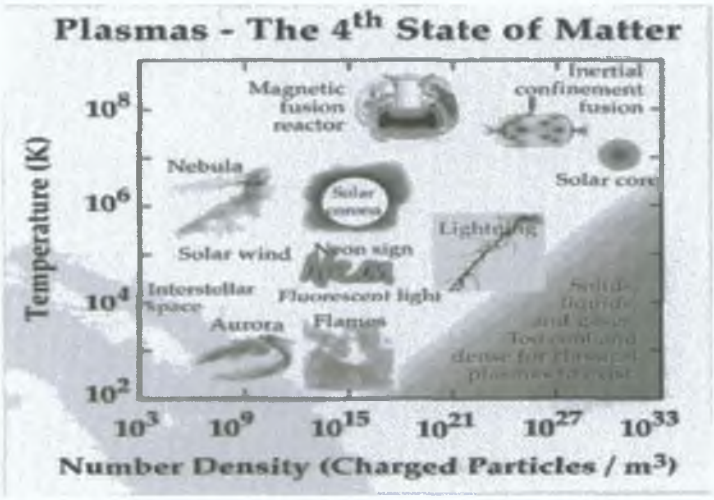

Fig 1.0: Density and temperature relations for plasma. (http://www.plasmas.org/powers.htm).

The importance of the temperature and density of a plasma is underlined by the dependence on existing theories and models in understanding the spectroscopic emission and absorption of light from plasmas. In the case of stars this is the only means we have of studying such phenomena. The most important relation between a plasma's internal state and its observed emission or absorption spectrum is the energy balance between energy lost via emission and cooling, and the energy gained to sustain the plasma, either acquired externally from heating, or internally from collisions and self heating. For example, electron-ion collisions limit electron thermal conduction, which affects the cooling rate, the expansion rate and thus ultimately the observed spectra, while photon-ion interactions, limit the radiative heat conduction. These then affect the radiative decay rate of the plasma, and consequently its internal temperature, lifetime, and the intensity of

the emitted radiation Such systems are complicated by the fact that they rarely exist in thermal equilibrium, in the sense that across their volume, large thermal and pressure gradients may exist In laser plasma systems, or indeed any highly energetic plasma systems, the large densities usually lead to a high electron collision rate (collisions between electrons and electrons with ions) This leads to plasmas which are populated by highly charged particles, whose emission behavior is dependent upon their local population which is itself dependent upon the bulk number density of the sample and the extent to which it is ionized

Ionization is the most profoundly important physical mechanism m plasma generation and dynamics When radiation of sufficient energy impinges upon neutral matter, the resulting absorption of energy allows electrons to be promoted to more extended orbits about the nucleus If the absorbed energy is sufficiently high then the electron is excited to a level beyond which the columbic force of attraction can bind the negatively charged electron to the positively charged nucleus Thus the escape of an electron leaves the atom in a state of electrostatic imbalance, giving it a bulk positive charge, a secondary result is a rearrangement of the internal structure of the electron orbits that remain This process is termed photo ionization The advent of the laser and its wide spread deployment in generating plasmas of high temperature and density saw a huge explosion in the understanding of plasma dynamics from 1960 onwards When matter undergoes the transition to plasma, the removal of electrons from atoms leaves an assembly of ions and electrons Although separate, a simplifying assumption is that the total collective volume retains overall charge neutrality such that

$$\text{Equ 1} \quad N_e = \Sigma N_z \bullet z \qquad \text{(Amusia et al [1])}$$

where N_e is the electron density, and N_z is the density of ions of charged state z Generally in neutral matter interactions the distance over which such interactions occur are limited to the nearest neighbor influence However in plasmas, where Coulombic forces can be both large in magnitude and long ranged, the term 'collective response' of a plasma to outside influences can be applied To characterize this aspect of plasma behaviour the Debye Length λ_D, is defined as the range in metres over which the electric field of any charged particle is extended before its influence is counterbalanced by the fields of the other charged particles

$$\text{Equ 2} \quad \lambda_D = \left(\frac{\varepsilon_0 k T_e}{n_e e} \right)^{1/2} = 0\,69 \left(\frac{T_e}{n_e} \right)^{1/2} \qquad \text{(Anderson et al [2])}$$

where $T_e(eV)$ is the electron temperature and $n_e(m^{-3})$ is the electron density Only beyond the Debye length are collective effects of importance and dominating, but these are small in a laser plasma whose behaviour is usually close to that of an ideal gas Thus by extension of the above, the

linear extent of a plasma of width L, relative to the Debye length must be such that $L >> \lambda_D$ Such a condition can be used to distinguish between a true plasma and a highly energetic medium

A second condition for plasma behaviour is the assumption that the number of particles within a sphere of radius equal to a Debye length must be far greater than unity

$$\text{Equ 3} \quad N_D = \frac{4}{3}\pi n_e \lambda_D^{\ 3} = 1.72 \times \left[\frac{T_e(eV)^{3/2}}{n_e(m^{-3})^{1/2}} \right] >> 1 \quad \text{(Baier and Sonntag [3])}$$

Another aspect of plasma behavior is the oscillation of charged particles in the plasma The *natural* frequency of oscillations, is termed, the plasma frequency, w_p For the case of electron oscillation

$$\text{Equ 4} \quad w_p = \left(\frac{n_e e^2}{m_e \varepsilon_0} \right)^{1/2} = 56.4 n_e^{\ 1/2} \quad \text{(Lochte-Holtgreven [4])}$$

The above relation is also valid for ions, with the electron mass m_e being replaced by the ionic mass m_i

The plasma frequency is the chief variable which determines the response of the plasma to external radiation The optimum condition for transfer of energy from impinging radiation is that its frequency matches that of the natural frequency of the plasma For radiation whose frequency is greater then the natural frequency of the plasma, the radiation will propagate through the plasma with very little absorption occurring, while for radiation frequencies lower than that of the plasma frequency the radiation will be reflected The critical plasma density N_c where the electromagnetic wave frequency equals that of the plasma and for which radiation absorption occurs can be expressed as,

$$\text{Equ 5} \quad N_c = \frac{\varepsilon_0 m_e w_p^2}{e^2} = 3.14 \times 10^{-4} w_p^{\ 2} \quad \text{(Balmer et al [5])}$$

This parameter is very important in determining the kinetics of plasma generation and the plasma lifetime, when the radiation is of a very short duration, such as a high powered, Q-switched laser pulse

1.1 Laser Ablation

Since the plasmas studied in this work are laser generated, an overview of the ablation mechanisms and stages of expansion should be considered

The stages of laser plasma generation and evolution can be broken down into three stages

1 Laser surface interaction

2 Laser plasma interaction and subsequent 1Dimensional expansion

3 After termination of the laser pulse, the 3Dimensional expansion of the plume

1 1 1 Laser-surface interaction

The initial stages of the beam-target interaction are mostly dependent upon the bulk properties of the sample, such as the thermo-physical and optical properties, and this interaction occurs within a limited volume, dictated by the beam characteristics The free electron collisions within the target material lattice, which occur as a result of the absorption of radiation are the first in a series of interactions of varying duration The number of collisions is large and typically exists over a region of many several mean free path lengths This causes a highly localized temperature gradient to form within the material The fall off in the intensity of the incoming radiation is governed by Beer's law, where the electromagnetic radiation of intensity I_s falls to 1/e of I_s over a depth α^{-1} (the absorption length)

$$\text{Equ 6} \quad I_d = I_s e^{-\alpha d} \quad \text{(Bernath [6])}$$

where I_d is the intensity at a depth d The absorption coefficient of the material (α) is dependent on the wavelength λ and the complex component of the refractive index n_I, thus

$$\text{Equ 7} \quad \alpha = \frac{4\pi n_I}{\lambda} \qquad \text{(Hecht [6 1])}$$

The temperature at any depth in the target material T(z,t) during the laser pulse duration can be expressed by the heat flow equation, where z is a vector perpendicular to the target surface

$$\text{Equ 8} \quad C_v(T)\frac{\partial T(z,t)}{\partial t} = \frac{\partial}{\partial z}\left[K(T)\frac{\partial T(z,t)}{\partial z}\right] + (1-R)I_s(z,t)\alpha e^{-\alpha z} \quad \text{(Singh et al [7])}$$

where C_v is the specific heat capacity, K(T) is the thermal heat conductivity of the material and R is the reflectivity The rapid rise in temperature following the onset of the laser, conducts heat to a depth L_{th} below the target surface This is defined as the diffusion length

$$\text{Equ 9} \quad L_{th} = \left(\frac{2K\tau}{\rho C_v}\right)^{1/2} = (2D_{th}\tau)^{1/2} \quad \text{(Cheung et al [8])}$$

where τ is the duration of the laser pulse and D_{th} is the material's thermal diffusivity Under such conditions the energy from the laser pulse propagates into the target and is located in a volume, represented approximately by a cylinder of diameter equal to the ablation spot size, and of length equal to the diffusion length For aluminum irradiated by a 16nsec Nd YAG, the diffusion length, L_{th}= 163μm (constants from table 1, page 18) Returning to the 1dimensional heat flow equation, the surface temperature T_s(eV) after irradiation by a laser pulse of duration τ/nsec, and assuming a top hat temporal beam profile is given by

Equ.10 $$T_s = \frac{2I(1-R)t^{1/2}}{(\pi K C_v \rho)^{1/2}} + T_0$$ (Kelly et al [9])

In the above equation, I is the laser power density, R is the material reflectivity at the ablation wavelength and T_0 is the material temperature before the laser pulse. The above assumes that the thermo-physical properties of the material and laser beam intensity over the pulse duration remain constant during the pulse lifetime. Of course this is a simplification, the interaction of the laser pulse with the pre-plume is highly complex with many competing processes. For the above equation, re-arranging, the time taken for the plasma to reach a particular temperature is given by:

Equ.11 $$T_p = \frac{\pi \rho K C_v (T_s - T_p)^2}{(2I_0(1=R))^2}$$ (Kelly et al [9])

The extent of the temperature increase which occurs is determined by the skin depth of the target material in question. This is the depth to which the EM radiation of the incoming laser light can permeate into the solid and is given by:

Equ.12 $\delta=(\pi\nu\sigma\mu_0)^{-1/2}$ (Lochte-Holtgreven [4]).

Here μ_0 is the permeability of free space, σ is the electrical conductivity in Mhos m^{-1} or $(\Omega m)^{-1}$ and ν is the frequency of laser radiation. Thus for aluminum irradiated by a Nd:YAG pulse at 1.064μm, δ~5nm. The variation in skin depth with temperature was plotted by Ready (1965), in figure 1.1.

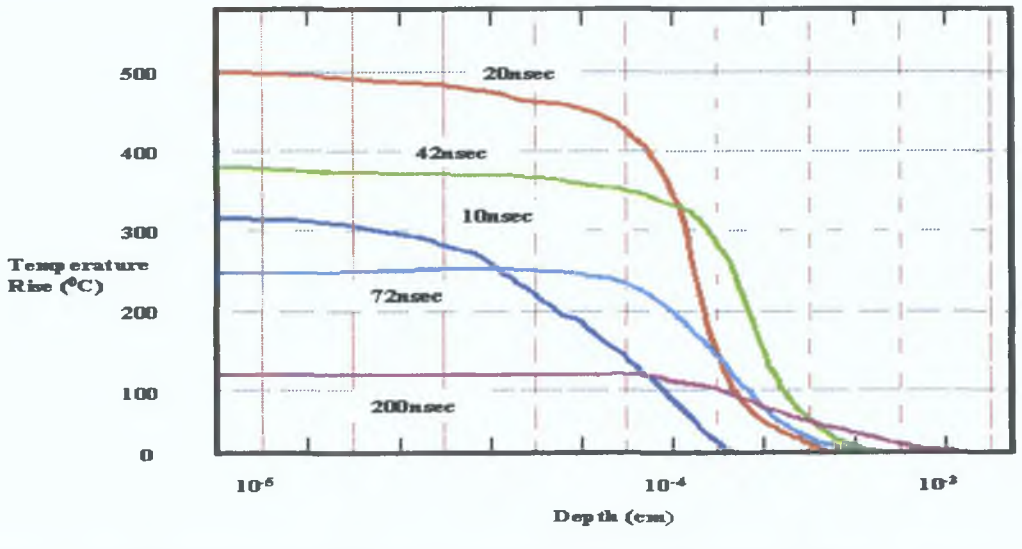

Figure 1.1: Temperature rise as a function of depth caused by absorption of a Q-switched laser pulse in copper. Note how rapid the rate of cooling is with a reduction in temperature of 75% after 200nsec (Ready 1965).

Material; Aluminum	T/K	Tp
Melting point	933	3.4nsec
Boiling point ($I\sim8\times10^9 W/cm^2$)	2792	5.3nsec
Critical Temperature ($I\sim8\times10^9 W/cm^2$)	2867	5.6nsec
Density (kgm^{-3}), ρ	2700	
Reflectivity, R	0.973	
Thermal Conductivity, K ($Wm^{-1}K^{-1}$)	205	
Specific Heat Capacity, C_v ($Jk^{-1}kg^{-1}$)	910	
Absorption coefficient, $\alpha(T_s)$	$0.075+4.53\times10^{-5}T_s+.04\times\theta(T_s-T_m)$	
All values assume $I\sim8\times10^9 W/cm^2$)		

Table 1: Material and atomic constants for aluminum.(http://www.allmeasures.com/Formulae)

Using equation 11, and the constants given in table1 the time taken for the plasma to reach its melting, boiling and critical temperature were calculated and are also given in table one (right hand side). For the absorption coefficient α, T_s is the initial surface temperature (assumed to be 300K), and θ is the Heaviside function.

The above are however all thermal processes and are of greatest importance in plasma initiation for low level irradiation and early timescales. In reality, the high frequency of laser light and the focusing of such beams leads to large electric fields at the beam-target interface. It is this process that is of importance for material vaporization. The laser's EM field penetrates the target by less than one laser wavelength, causing rapid vaporization of the condensed matter into gases/vapour. Thus for the work reported here, with aluminum $\sigma=3.54\times10^7$ mhos m^{-1} and a Nd:Yag laser of frequency 2.81×10^{14}Hz, the depth of penetration is 5nm approximately. The magnitude of the electric field is such that it can strip electrons from the surface of the target. The r.m.s electric field E, is related to the irradiance ϕ (Wm^{-2}) by

$$\text{Equ.13} \qquad \overline{E}_{rms} = 19.4\phi^{1/2} \ (\text{V cm}^{-1})$$

In this work the irradiance used was of the order 10^{15} Wm^{-2} , thus $\overline{E}_{rms}$ has a corresponding value of $\sim6\times10^8 Vcm^{-1}$.

1.1.2: Knudsen layer formation.

One effect of importance during the plasma generation and subsequent expansion, both during the laser pulse and after, is the formation of a Knudsen layer. This is defined as a region within the plasma which exhibits a pronounced change in the velocity distribution of particles. This shift is most pronounced at high

densities where the collisional rate is high The velocity distribution is no longer Maxwellian but conforms to the function formulated by Kelly and Dreyfus [9]

Equ 14 $$f_K^{\pm}(v_2, E_1) = \left[\frac{n_K E_I^{(J/2-1)}}{(2\pi T_K / m)^{J/2}} \frac{1}{\Gamma(J/2)(kT_K)^{1/2}}\right] \exp\left[-\frac{2E_I + m[v_z - u_K]^2}{2kT_K}\right]$$ [9, 10]

In the above, v_z is the velocity component normal to the target surface, E_1 is the total internal energy, n_K the number density of the Knudsen layer, T_K is the Knudsen temperature, m is the particle mass, while Γ is the gamma function and j the degrees of freedom and u_K is the center of mass velocity Effectively the above equation modifies the Maxwellian distribution The particle velocity is mapped onto a positive flow velocity, analogous to electron drift velocity for conductors This then accounts for negative velocity components back towards the target, which typically occur within the Knudsen layer The behaviour of particles emitted from the target surface has been summarized by Dreyfus and Kelly [11]

Case 1 Particles emitted from the target's hot layer, do not have enough energy to form a Knudsen layer, and thus have velocity vectors which are all positive In the above equation this corresponds to the case where $n_K = n_S$, the gas number density near the surface, and $T_K = T_S$ the surface temperature and $u_K = 0$ (i e f_+) This set of parameters describes the system before the onset of a Knudsen layer

Case 2 As the layer starts to form, the velocity components of the particles depend on whether they permeate the layer or *not* Thus velocity components are usually towards or away from the target

In this case $f = f_-^+$

Case 3 The last case is usually described by a lower temperature range than the above, where particles re-condense on the target surface with a probability of value unity Here $v_z \leq 0$, and $f = f^-$ As reported by Song et al [12], species that traverse the Knudsen layer no longer undergo one dimensional expansion, but expand iso-thermally in three dimensions

1 2 Atom-light interactions in plasmas.

The low density vapour formed on the target surface occurs during the very early stages of the pulse-target interaction However this thermally driven process cannot account for the highly ionized plasma state that emerges after the laser pulse has terminated For absorption of a beam in a vapour/plasma the beam intensity at a depth z, within the plasma can be stated as

Equ 15 $$I(z) = I_0 \exp\left(-\int_0^z \alpha(z)\, dz\right)$$

where $\alpha(z)$ is the length dependent absorption coefficient

Although scattering of the beam does occur, absorption within the vapour is the most dominant and important process The processes that control laser beam absorption and the resulting range of particle-photon interactions are classified by the mechanism which defines the initial and final state of the electron involved in the absorption/emission of photons

These can be defined as

Bound-bound interactions (B-B)	the initial and final states of the electron are bound within the shells of the atom or ion	Collisional Excitation/De-Excitation Or Photo-Excitation/De-Excitation
Bound-free interactions (B-F)	the initial state is bound within the atom or ion, and the final state is a free-electron	Collisional Ionization/Recombination Or Photo-Ionization/Recombination
Free-Free interactions (F-F)	are interactions where the electron is free throughout the interaction	Bremsstrahlung Or Inverse Bremsstrahlung

Electrons lose energy by elastic and inelastic collisions with particles through excitation of the electronic states of atoms and ions in a plasma Some electrons will be lost by attachment, but new electrons will be generated by ionizing collisions If the laser irradiance is high enough, then a few electrons will gain energy larger than the ionization potential, despite all loss mechanisms The free electrons will undergo collisions with ions, further enhancing the free electron density, resulting in a cascade growth of the plasma For each excitation process an opposite decay process exists

1 2 1 Bound-Bound transitions

A bound-bound transition occurs when an electron bound within the orbital of an ion or atom undergoes transitions within the allowed energy levels Absorption of a photon raises the electron to a more excited state, while emission of a photon from an electron results in the electron decaying to a lower energy level The absorption process requires that the photon energy exactly matches the transition energy between the two levels under consideration Equally possible is collisional excitation, between two particles, which transfers energy to or away from an electron Collisional excitation is extremely important in high temperature plasmas due to the higher kinetic energy of the particles, which thus impart greater energy to the excited system during the collision The emitted line spectrum from collisions is temperature dependent The higher the temperature the greater the number and energy of the collisions Thus increasing temperature leads to shorter wavelength emission, depending on the material Above a certain temperature the bulk of the atoms will be ionized, thus leading to multiple ionization of many electron atoms The reduction in the electrostatic screening of the nucleus leads to very large transition energies, thus emission in the VUV and XUV (also called EUV) is possible

$N+h\nu(\text{or collision}) \Leftrightarrow N^*$ (Photo-excitation/De-excitation)

$N+e(E_1) \Leftrightarrow N^*+e(E_2)$ where $E_2<E_1$ (Collision excitation/De-excitation, E_2, E_1 are electron kinetic energies before and after the collision)

1.2 2 Free-Bound transitions (Photoionization)

If a photon has sufficient energy it may be absorbed by an electron, and assuming the photon energy is greater then the binding energy of the electron, the latter is free to leave the atomic system, leading to ion formation Equally if an n times ionized ion captures a free electron then the captured electron decays to a bound state within the ion (whose charge state deceases to n-1) and the resulting surplus energy is emitted as a photon

Equ 15 1 $N^n + h\nu \Leftrightarrow N^{n+1} + e(\text{free})$ or $N^{n+1} + e(\text{free}) \Leftrightarrow h\nu + N^n$

The emission process is called recombination or free-bound, while photon capture and electron escape is called photoionization (bound-free) Both *continuum* and line photons can be produced in such a recombination event as the electron passes from the continuum (i e free) levels into the upper bound levels of the ion and then cascades down to form a ground state ion

1 2 3 Free-Free transitions

Free-Free radiation or Bremsstrahlung occurs when an electron collides with other particles The electron collision leaves one particle in a lower state, the difference appearing as the emission of a photon The emission spectrum associated with this scattering process is a continuum The predominance of this process increases with plasma temperature and target atomic number

Inverse Bremsstrahlung occurs when a photon interacts with an electron within the electric field surrounding an atom/ion Under such a condition the electron can gain kinetic energy via the photon by absorbing the latter while the presence of the ion/atom provides the reaction mass to accommodate the change in momentum In order for inverse Bremsstrahlung to be significant there must exist sufficient numbers of free electrons in the plasma Thus since photo-ionization is an important process in free electron generation, the two processes go hand in hand Both Bremsstrahlung and inverse Bremsstrahlung are very important processes in plasma kinetics

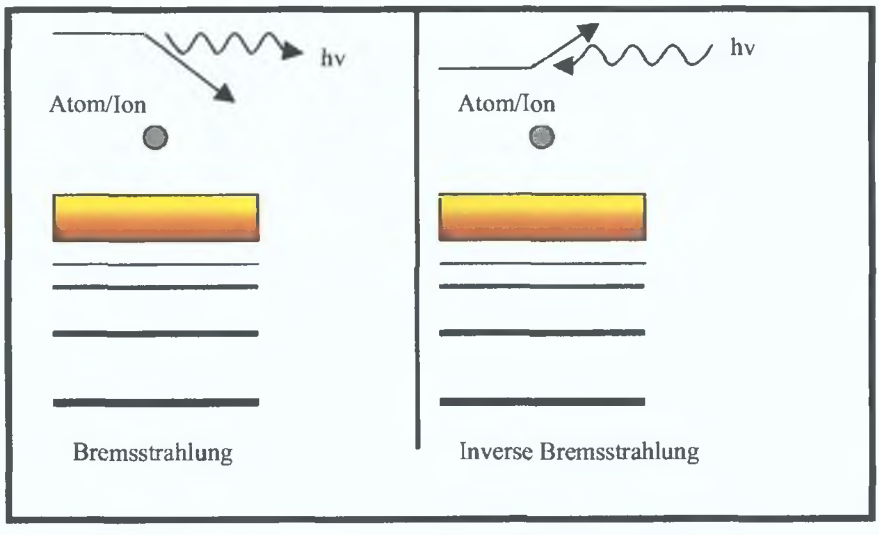

Figure 1.2: excitation mechanisms for Bremsstrahlung and inverse Bremsstrahlung.

One can see from the above, that for each excitation mechanism there is an inverse decay mechanism. This counter balancing influence is fundamental in plasma modeling, given the assumption of equilibrium. Analysis (Song et al [12]) indicates that photo-ionization is the most dominant form of radiation absorption for laser produced plasmas at irradiances less then 400MWcm^{-2}, while ionic inverse Bremsstrahlung is more dominant at irradiances beyond 500MWcm^{-2} [13, 14].

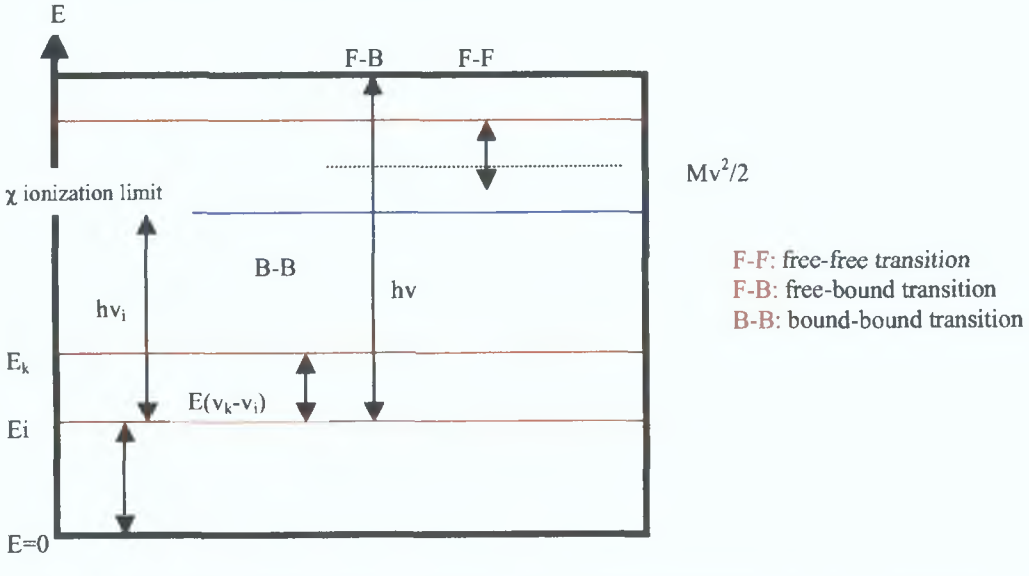

Figure 1.3: Schematic diagram illustrating the transition energy relation for free-free, free-bound and bound-bound transitions.

1 2 4 Three Body Recombination

The plasma plume is subject to a loss mechanism that is non-radiative, involving three body recombination Here no photon is emitted, as two electrons collide with an ion simultaneously One electron is captured by the ion, while its surplus energy is transferred to the second electron which rebounds with greater kinetic energy Both continuum and line photons can be produced following a recombination event as the electron passes from the continuum (i e free) levels into the upper bound levels of the ion and then cascades down to form a ground state ion

Equ 15 2 $2e+N^{+} \Rightarrow N+e$

For singly ionised species the rate of three body recombination is given by

Equ 16 $\Gamma = \frac{8.78 \times 10^{-27} N_e^2}{T_e^{9/2}}$ (Zel'dovich et al [15])

In the initial stages of plasma formation above the target surface, the electron number density will be small Thus three-body recombination processes will not play a dominant role However with increases in electron density, three body recombination will increase in importance The process is maximised by low temperatures and high densities Such conditions can exist later in the plasma's expansion phase However rapid expansion drives a rapid drop in density Thus in later stages loss mechanisms are dominated by other two body processes, such as radiative capture and electron impact de-excitation

1 2 5 Opacity

Radiation emitted from a plasma may undergo re-absorption, while transiting to the plasmas edge, via other ions The optical depth of a plasma is defined as

Equ 17 $\tau(\nu) = \int \alpha(\nu) dx$ (Locke-Holtgreven 1995, [4])

with $\alpha(\nu)$ as the linear absorption coefficient and x the coordinate along the line of sight For a homogeneous plasma the above reduces to $\tau(\nu)=\kappa(\nu)\times l$ where l is the length of the absorber In the case of an optically thin plasma the absorption is negligible In this case the vast bulk of the photons emitted within the plasma contribute to the intensity observed

1.3 Plasma Plume expansion

1.3 1 Plasma Models

The number of variables that can be given by plasma models are large, such as ionization rates, plasma potential, electron velocity, temperature (plasma, electron or ionization), populations and plasma density However despite the large range of variables available, most rely on the electron temperature and density as the chief parameters defining the plasma's generation and evolution envelope The vast bulk of plasma models treat the plasma either as a gas [16-19] or a thermal system (Amoruso et al [20]), or a fluid (Sheno et al [21])

A common assumption is that the equilibrium velocity distribution of particles is Maxwellian, thus allowing a temperature to be calculated A condition for the statistical approach to be valid is that the mean free path between collisions must be much smaller then the maximum extension of the plasma, and the time between these collisions must be short compared to other heating mechanisms Laser plasmas usually fulfill these criteria, for electrons but not for ions, thus ion temperature calculations are usually not reliable and generally crude approximations (Chen et al [22])

Although the particle collisions and dynamics are of great importance in plume behavior, radiation fields are also of great importance When radiation cannot escape from the plasma volume due to re-absorption within its volume, the plasma is said to be optically thick and a state of complete thermodynamic equilibrium is said to exist For this simplified state the following set of conditions exist

1 As stated above, for each radiative mechanism the transition rate is the same for both the decay and the excitation processes (Hughes and McWhirter 1965 [23])

2 The ion distribution is given by the Saha equation (Hughes and McWhirter 1965 [23]),

$$\text{Equ 18} \quad \frac{N_z N_e}{N_{z-1}} = 2\left(\frac{2\pi m_e kT_e}{h^2}\right)^{3/2} \times \frac{w_z}{w_{z-1}} \times \exp\left(\frac{\chi_{z-1\,g}}{kT_e}\right)$$

N_z and $N_{z\,1}$ are the ion stage populations, and w_z and $w_{z\,1}$ are the statistical weights associated with levels within these ion stages and $\chi_{z\,1\,g}$ is ionization potential of the ion charge z-1 in its ground level g

3 The population densities of bound levels within the atomic system are given by the Boltzmann formula,

Equ 19 $$\frac{n(p)}{n(q)} = \frac{w(p)}{w(q)} \times \exp\left(-\frac{\chi(p,q)}{kT_e}\right)$$

where n(p), n(q), w(p) and w(q) are the populations and statistical weights of states labeled p and q respectively and χ(p,q) is the energy difference between levels p and q which could equally be represented by $\omega\hbar$

4 As stated above the free electron velocity distribution is Maxwellian Then the number of electrons with velocities between v and v+dv is given by (Hughes and McWhirter 1965 [23])

Equ 20 $$dN_e(v) = 4\pi n_e \left(\frac{m_e}{2\pi kT_e}\right)^{3/2} \times \exp\left(\frac{-m_e v^2}{2kT_e}\right) \times v^2 \partial v$$

5 The intensity distribution as a function of frequency and plasma temperature is described by Planck's law In reality the assumption of complete thermodynamic equilibrium throughout the plasma volume is not valid, as such a system is highly dynamic, and in a constant state of flux The radiation emitted and velocity distributions are clear evidence of this Thus all models of plasma dynamics and radiation emission are based on approximations The chief difference between each model is the density range it is applicable to

1 3 2 Local Thermodynamic Equilibrium (LTE)

As the plasma density increases to very large values ($>10^{15}$ cm^3), the rate of collisions between particles increases dramatically, and begins to override the effect of radiative processes The rate of collisions is such that the changes in the parameters of the plasma system allow the electron population densities to respond almost immediately Thus the system is a good approximation to a system in thermodynamic equilibrium However the radiation spectrum is no longer described by Planck's Law Because of the mass differences the electrons have larger velocities than the ions, and thus undergo the most collisions They are therefore responsible for the bulk of the collisional transitions, and the electron collision rate is the most important factor in determining the relative temperature McWhirter derived the relationship between electron temperature and electron density for which LTE is said to hold

Equ 21 $$N_e \geq 1.6\times10^{12} T_e^{1/2} \gamma(p,q)^3 \text{cm}^{-3}$$

where T_e is measured in K and χ(p,q) in eV

1.3 3 Coronal Equilibrium (CE)

LTE applies generally to high density plasmas However not all plasmas are high density The solar corona, while existing at high temperature (~10^6K) is usually of low density (10^8 cm^3) The development of the

Coronal-equilibrium model is based upon the balance of collisional ionization and radiative recombination, instead of the LTE assumption of collisional processes being balanced by their inverse processes The plasma must be optically thin, i e radiation emitted within the volume of the plasma, is not significantly absorbed as its passes through the plume to the outer edge Thus by extension radiation escapes from the plume in a manner such that equal rates of photon absorption and radiative de-excitation are not obtained Another defining boundary of coronal equilibrium theory is the electron density dependency of both collisional ionization (N_e dependency) and the inverse mechanism, three body recombination (Ne_e^2 dependency) Given the N_e dependency of radiative recombination, it becomes more important as the electron density decreases The various ion populations are independent of N_e This was summarized by McWhirter (McWhirter et al [30])

Equ 22 $$\frac{n_{z-1}}{n_z} \cong 8\times10^{-9}\,\chi_{z-1\,g}{}^{11/4}\times(kT_e)^{-3/4}\exp\left[\frac{\chi_{z-1\,g}}{kT_e}\right]$$

One defining limitation in this model is the need for the collisional transition from an exited state to be slower than radiative decay Since increases in n, the principal quantum number, lead to increases in the probability of spontaneous radiation emission, but decreases the collisional transition probabilities this then limits n to an upper limit of 6 Using this in the McWhirter formula, leads to an expression for N_e for hydrogen like ions Here z is the ion charge state

Equ 23 $$N_e < 5\,6\times10^{8}\times(z+1)^{6}T_e^{1/2}\times\exp\left(\frac{1\,162\times10^{3}(z+1)^{2}}{T_e}\right)\ \mathrm{cm}^{3}$$

where T_e is in Kelvin

1.3 4 Collisional Radiative Model (CR)

In reality no one model is suitable for all ranges of density and temperature Thus with LTE ranging from 10^{15} cm^3 and CE theory ranging for densities from 10^8 cm^3 and lower, there is thus a middle range of values for which the above two approaches are not suitable However if CE theory is modified to include collisional transitions from higher bound levels, and also three body recombination, then greater convergence of experimental data and theory is seen This was done by Bates and McWhirter in 1962 [30] The important difference here is the acceptance of collisional processes between upper levels This was not taken into account in CE theory, as it assumes that all atoms and ions are in their ground states, thus collisional excitation can only be considered from those states However like the other two theories, CR theory begins to fail the validity test as the electron density increases Graphically each model is displayed in figure 1 4

Figure 1.4 also displays how a Nd and a CO_2 laser generated plasma are described approximately by this system. For a Nd:YAG laser plasma the following approximations can be stated:

1: LTE model applies to ionization stages z<10.

2:The Coronal model applies for high z stages (z>30).

3: The CR model generally applies to z stages in both of the above.

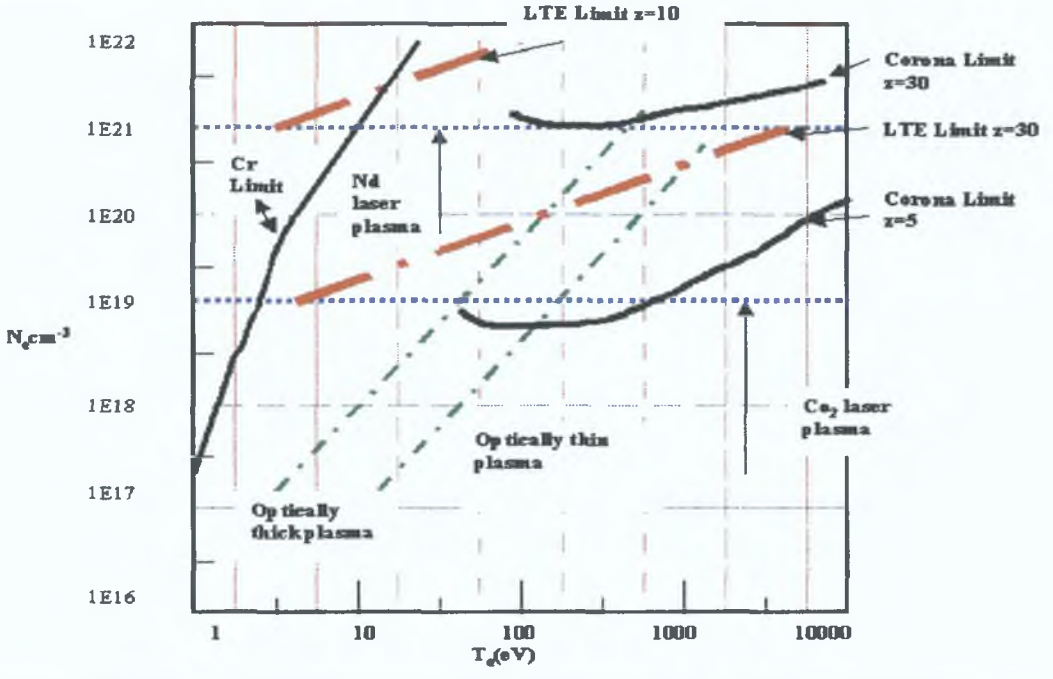

Figure 1.4: Electron density and temperature ranges for applicability of LTE, CE, and CR models. (Colombant and Tonon 1973).

The criteria set out by Colombant and Tonon (1973) define the conditions under which CR model applies

1: The efficiency of collisions, i.e. between electrons or electrons and ions, defines what processes are considered, the process of autoionization and its inverse mechanism are also considered.

2: A Maxwellian velocity distribution must predominate. Such a distribution is satisfied when the relaxation time is smaller than the electron heating time, and at very high densities. The electron relaxation time is the smallest time resolved event in the plasma.

3:The plasma must be optically thin, with minimum self absorption of the emitted radiation.

1.3.5: Plasma Expansion and Ion dynamics.

Although there have many attempts to successfully model plume generation and expansion [24-29], our discussion will be limited to those that are of most relevance to laser plasma conditions seen in this work. These are the modeling of laser-solid-plasma interaction by Amoruso [20], laser plasma expansion in gas

(low pressure) by Wood (Wood and Chen [33]), and subsequent explanation for observed 'plume splitting'[32] seen by many authors The cavity analysis presented by Shannon [29] is also of interest, in attempting to model the effects of target geometry on laser beam coupling to the target surface Lastly a comparison is made between the most recent and successful model of plume expansion by Narayan and Singh [27] Although each model is complex and detailed, we present a brief overview of the main aspects of each analysis and their main conclusions

1.3 5 1 Laser-solid-plasma interaction model

The first model to be presented is Amoruso's analysis of laser-plasma-target interaction Amoruso limited his analysis to high intensities, where laser generated vapour becomes significantly ionized absorbing part of the incident laser radiation and leading to vapour breakdown and plasma formation A simplifying aspect of the model is the assumption that the laser beam uniformly irradiates the surface over its area This allows for the use of a 1dimensional model An exponential temperature distribution in the target is assumed

$$\text{Equ 24} \quad T(z,t)=T_0+\Delta T_s \exp\left(-\frac{z}{z_0(t)}\right)$$

where T_0 is the target initial temperature and $z_0(t)$ is the thermal penetration depth at a time t, approximated by (Amoruso's version of equation 9)

$$\text{Equ 24} \quad Z_0(t)\approx\sqrt{\frac{\pi}{4}Dt}$$

where D is the thermal diffusivity ($D=k/\rho C_v$) of the target The model is of heat conduction and evaporation with a time integrated model by considering an energy balance analysis of the various processes as taking place in the laser-solid interaction (fusion, evaporation, heat conduction) When this process is done, the following relations are derived for the time evolution of the surface temperature ΔT_s for time scales less than and greater than the laser pulse duration (τ)

$$\text{Equ 25} \quad \Delta T_s(t)=\frac{1}{\rho C_v z_0(t)}\int_0^{\tau}\left\{I_T(t')-\left[C_v\Delta T_s(t')+L_f+L_v\right]\mu(t')dt'\right\} \qquad (t\le\tau)$$

$$\text{Equ26} \quad \Delta T_s(t)=\frac{1}{\rho C_v z_0(t)}\left(\Delta T_s(\tau)z_0(\tau)\rho c-\int_{\tau}^{t}\left\{\left[C_v\Delta T_s(t')+L_f+L_v\right]\mu(t')dt'\right\}\right) \qquad (t\ge\tau)$$

The above two equations can be iteratively solved to give spatial and temporal distributions inside the target I_T is the laser intensity absorbed by the target, ρ is the target density, C_v is the specific heat capacity , L_f and L_v are the latent heat of fusion and vaporization and μ is the mass removal rate The laser intensity absorbed by the target is strongly dependent upon the vapour formed in front of the target surface In

particular at high mass removal rate the vapour formed by the leading edge of the laser pulse can strongly absorb the incoming beam, leading to vapour breakdown and plasma formation The absorbed laser intensity I_T is given by

$$\text{Equ 27} \qquad I_T(t) = A(t) I_0 \exp[-(\alpha_{IB} + \sigma_{PI} n_x) H]$$

where A(t) is the time dependent absorption coefficient, α_{IB} is the IB inverse absorption length, and σ_{PI} is the photo ionization cross section, n_x is the number density of the excited neutrals and H is the vapour height The vapour excitation and ionization kinetics are based on a two stage process of electron impact excitation from the ground state to the first excited state, and then subsequent singly charged ion production by electron impact ionization and photo ionization Results calculated by Amoruso are given in figure 1 5

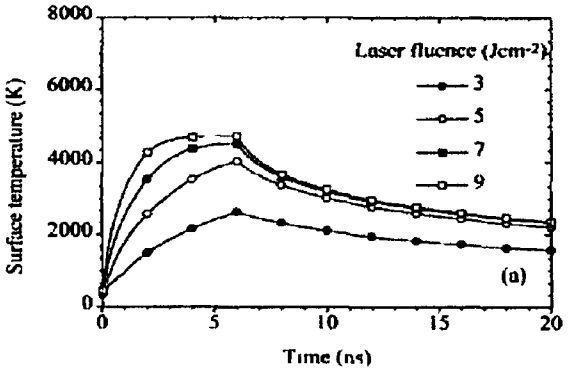

Fig 1 5 Amoruso's modeled values for the time evolution of target temperature during and after the laser pulse for various values of fluence, power density ~10^9Wcm^{-2}

Considering figure 1 5, at fluences (up to 3Jcm^{-2}) the laser intensity reaching the targets follows that of the incident laser pulse, but at higher fluences it decreases indicating the presence of vapour/plasma absorption process The onset of plasma absorption occurs earlier in the pulse at higher fluences, and is well correlated to the target surface temperature time history The model proves the importance of laser-plasma interaction processes and plasma kinetics are of great importance during the nanosecond laser ablation of metallic targets for power densities higher then 10^9 Wcm^{-2} It also highlights the strong influence pre-plasma or vapors play in full formation of laser plasmas

1.3 5 2 Plasma plume and 'plume splitting' model

Wood, Chen and Geohegan [33] attempted to model plasma plume expansion based on a combination of multiple elastic scattering and hydrodynamics formulations The model provided new solutions to the observed plume splitting aspect of plume expansion under certain conditions (i e in gaseous medium) The model uses plume expansion in Argon and Helium Wood suggested that plume splitting occurs because the mean free path in the expanding plume is initially comparable to the target-detector distance No other plume expansion model has predicted plume splitting The assumptions made in the model include that of quasi-two dimensional (2D) formulation Secondly Wood et al considered only elastic collisions, for both head-on and non-head-on so that the transfer of translational energy into internal energy is minimal under the conditions used The model is based on breaking the plume into orders corresponding to the number of

collisions with the background gas The first order reaches the detector without any scattering collisions with the background gas The second order undergoes one scattering event, this pattern is extended for all orders $\rho_p(t,x,k)$ is stated to be the density of the k'th order plume at time t and distance x The differential equations for the ablated plume including the scattering term are

Equ 28 $$\partial_t\rho_p=-\partial_x(\rho_p v_p)+\partial_t\rho^s_p$$

Equ 29 $$\partial_t(\rho_p v_p)= -\partial_x(\rho_p v^2_p+P_p)+\delta_t(\rho^s_p v^s_p)$$

Here the terms with the superscript 's' represent the rate of change of the scattered density and momentum, while v and P are the velocity and pressure The plume was laser generated Si and Si^+ plasma, the background gas is always entirely neutral Hence only neutral-neutral, ion-neutral, and Si^+-Si^+ collisions occur The last of these were neglected by Wood for the following reasons The Si plume is collisionless in vacuum beyond the Knudsen layer and Si Si collisions may occur after one of the ions has been scattered by the background gas Also, the collision of two Si ions will have little effect on the mass and momentum transport of the plume itself (none at all for truly head-on collisions) and no direct effect on the transfer of momentum from the background plume Consequently all Si-Si collisions are of secondary importance The most important collisions are those between the plume and the neutral background gas The general trends to emerge from Wood's analysis is that the kinetics of propagation and scattering processes are virtually the same for ions and neutrals Calculations which removed the influence of the background pressure effects on the scattering process showed that the background quickly becomes "snowplowed" into a peak that is much greater than that of the plume

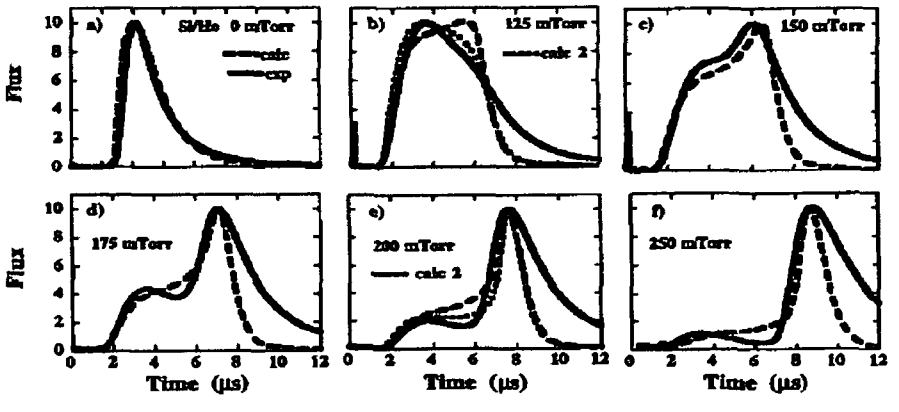

Figure 1 6 Comparison of the experimental data taken by Geohegan et al versus Wood and Chens model Here the plume background scattering cross section was varied to fit the raw data from experiment [33]

By comparing experimental data with the predicted output from the model Wood and Chen were able to demonstrate plume splitting in the temporal profile on the ion signal from the plume (figure 1 6)
The importance of this model is the fact that no other plume dynamical model has been able to correctly take into account the observed aspect of plume splitting It demonstrates the important role ambient media

play in influencing the velocity distributions of ions and the importance of scattering processes on the plume's behavior

1.3 5.3 Laser-target interaction model

Another important model relative to the study of target geometry is the role that the geometry of the target surface plays in laser matter interactions The importance of this model is that to the author's knowledge no other analysis exists at this time to attempt to understand the effect of target geometry on laser-solid interactions and subsequent generation of a laser plasma Shannon [29] approached that problem from the viewpoint of heat transfer from the laser beam to the target Since such a process is very complex and highly non-linear, Shannon stated that this approach meant that results were "reasonable analytical estimates of laser energy coupling due to the formation of a cavity using easily obtained observables, without resorting to a full numerical analysis" The first assumption is that if net energy absorbed by a flat target can be estimated using the material's optical and thermal properties, plus the emission from the target, then the energy absorbed by a cavity can be estimated Shannon formulated a function, which he termed the departure function 'f', defined as the ratio of the net laser energy absorbed in a cavity over the net energy absorbed on a flat target The variables required to calculate f are the incident power, the thermal emission from the surface, the material reflectivity, and the size and shape of the cavity The departure function for a flat surface, with energy input 'q' is defined as

$$\text{Equ 30} \qquad f \equiv \frac{q_{net} / q_{in}}{q_{net} / q_{in}\,|_{flat}}$$

The basis of this analysis is the heat transfer equation, modified for laser irradiation Consider figure 1 7 The heat transfer in the solid at the k'th surface, Q_k is equal to the amount of absorbed radiation, $Q_{a,k}$ such that

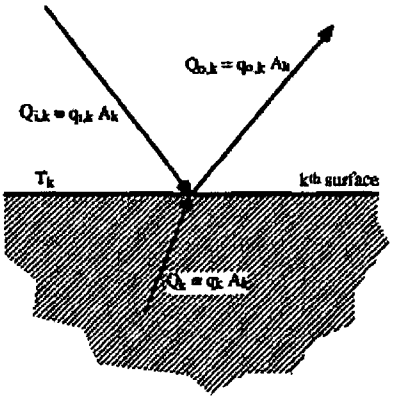

Figure 1 7 Heats balance at an isothermal surface of an opaque solid modeled by Shannon (k^{th} surface refers to a non-planar target geometry)

Equ 30 $Q_k=Q_{o\,k}-Q_{i\,k}$ and Equ 31 $q_kA_k=A_kq_{o\,k}-A_kq_{i,k}$ which simplifies to Equ 32 $q_{0\,k}=q_{i,k}+q_k$

where $q_{i,k}$ is the incident radiative power per unit area, and $q_{o,k}$ is the radiosity The latter can be defined as the sum of the heat emitted from the surface, $q_{e\,k}$, and the amount of incident heat reflected $\rho_k q_{i,k}$ from the diffuse surface, or

Equ 33 $Q_{o,k}=q_{e\,k}+\rho_k q_{i,k}$

where ρ_k is the total hemispherical reflectivity Using this approach, the incident flux comes from the radiation emitted from all other objects or surfaces, and that irradiated in from other surfaces, $q_{in,k}$ For this model, $q_{in,k}$ comes from the heat radiated from the surroundings and from the incident laser light For a cavity which is composed of many diffuse, isothermal surfaces (figure 1 8)

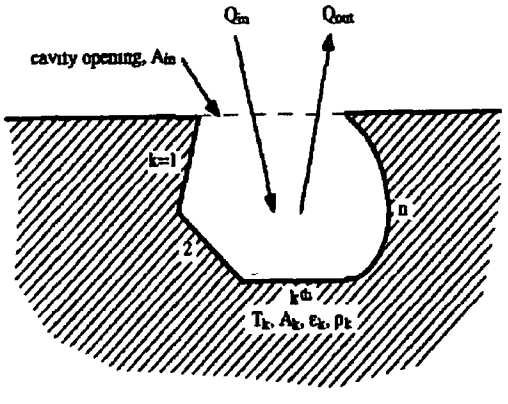

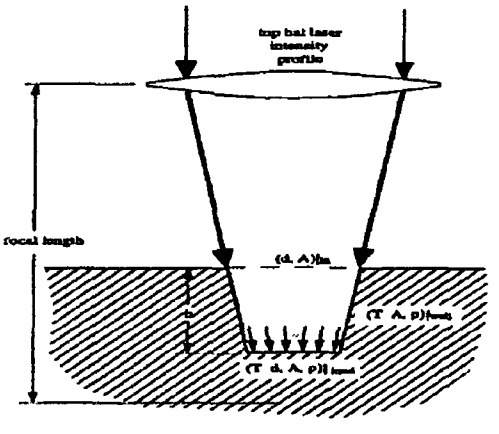

Fig 1 8 (left) Concept of an arbitrarily shaped cavity of n isothermal opaque surfaces
Fig 1 9 (right) Model of top-hat laser profile ablating a truncated conical cavity The irradiated surface is assumed to be the base of the cavity, Shannon [19]

Shannon's analysis is complex and so it is not completely presented here It is sufficient to state that the method used is to sum the total heat flux, Q_{in} (into a surface), and Q_{out} (out of a surface) for each surface in a target For a flat target, k=1, and there is only one surface When this analysis is performed for the two cavity types displayed in figure 1 8 and 1 9, Shannon derived the departure function for both target types

Equ 34 $$f=\frac{1}{1-v}\left[1-\sum_{k=1}^{n} A_k / A_{in} F_{k\to in} \times\left(\frac{1}{1-\rho_k}\frac{q_{e\,k}}{q_{in}}\right)-\frac{\rho_k}{1-\rho_k}\frac{q_k}{q_{in}}\right]$$

(for the irregular cavity, figure 1 8)

Equ 35 $$f=\frac{1=a}{1-v}+a$$ where a is a purely geometric factor $$a=\sum_{k=irrad}^{m} A_k / A_{in} F_{k\to in}$$

(for the conical cavity, figure 1 9)

In both of the above equations v, the dimensionless heat transfer parameter, may take values only from 0 to 1

Equ 36 $$v=\frac{1}{1-\rho}\frac{q_e}{q_{in}}-\frac{\rho}{1-\rho}\frac{q}{q_{in}}$$

Even without discussing the above two relations, one can see that due to irregular surfaces, equation 34 has an extra term inside the summation The major result of this analysis, is that not only is geometry important in energy absorption by a cavity, but the heat transfer that occurs at a surface is also important in determining the net absorption One important conclusion is that the more heat which is thermally radiated and transferred non-radiatively, the greater the effect that a cavity has on laser energy coupling to the target This increase is due to the recapturing of heat that would usually be lost to the surroundings

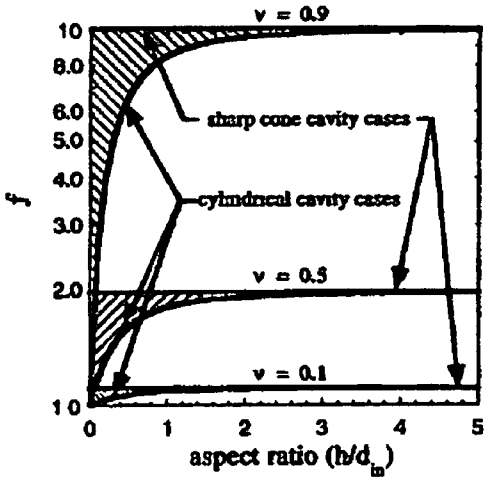

Figure 1 10 The departure function f plotted as a function of the aspect ratio of the cavity for three different heat transfer parameters v The two limits are the truncated cone, the sharp cone and the cylindrical case

A broader set of conclusions by Shannon is that an infinitely deep cone will give the maximum possible value for irradiation for a given value of v (the dimensionless heat transfer parameter) Figure 1 10 displays Shannon's graphical analysis on the value of the departure function 'f' with the aspect ratio h/d_{in}, where d is the diameter of the cone/cavity and h is its depth The trend is of increasing values of 'f' for increasing aspect ratio (as the cavity becomes deeper and narrower) The greatest rate of changing of laser energy coupling from the flat case occurs just as the cavity is formed This analysis should help to explain some well-known instabilities of laser material interactions near the physical ablation threshold, if a cavity begins to form due to cratering Shannon and Li have recently extended the model and compared its predicted values with experimental work [34] and found good agreement between experimental and theoretical results

13 5 5 Laser plasma generation and plume expansion model

The simplest parameter characterization of the plasma conditions at the termination of the laser pulse is the temperature dependence on the radial distance from the laser-target interaction region

Equ 37 $T(x,y,z)=T_0\left(\frac{x_o y_o z_o}{xyz}\right)^{\gamma-1}$ (Dawson [24])

This is for an isothermal system, where T(x,y,z) is the plasma temperature as a function of the coordinate z, normal to the target surface and T_o is the initial temperature This simplified approach is best suited to very high irradiance, where the assumption of a linear velocity model is valid

A more realistic approach is taken by Narayan and Singh [18] In their analysis Narayan and Singh treated the plasma as an ideal gas at high pressure and temperature, which is initially confined in small dimensions and then is allowed to expand rapidly in vacuum In their model, the plasma processes are divided into three distinct phases Firstly, the interaction of the laser beam with the bulk target, secondly the plasma formation, heating and initial three-dimensional isothermal expansion, and finally the adiabatic expansion Narayan and Singh set up the equations of compressible gas dynamics to simulate the expansion of the plasma in the last two phases The interaction of the laser with the target surface essentially involves solving the one-dimensional heat flow equation with appropriate boundary conditions taking into account the phase changes in the material Using simple energy balance equations the amount of material evaporated per pulse is calculated The energy deposited by the laser beam on the target is equal to the energy needed to vaporize the surface layers plus the conduction losses by the substrate and the absorption losses by the plasma This is given by the energy threshold E_{th} which represents the minimum energy above which appreciable evaporation is observed The heat balance equation yields

Equ 38 $\Delta x_t = (1-R)(E-E_{th})/(\Delta H+C_v\Delta T)$

where Δx_t, ΔH, C_v and ΔT are the evaporated thickness, latent heat, volume heat capacity, and the maximum temperature rise Secondly, high temperatures induced by laser irradiation leads to emission of positive ion and electrons from the surface The primary absorption mechanism for a plasma is the electron-ion collisions The absorption primarily occurs by an inverse bremsstrahlung process, which involves the absorption of a photon by a free electron The absorption coefficient α_p of the plasma can be expressed as

Equ 39 $\alpha_p = 3\,69\times10^8(Z^3n_i^2/T^{1/2}v^3)[1-\exp(-hv/kT)]$,

where Z, n_i and T are the average charge, the ion density, and the temperature of the plasma respectively The laser energy is highly absorbed if $\alpha_p X$ is large (X is the dimension perpendicular to the target surface) The heating of the evaporated material depends on many variables by virtue of the plasma absorption coefficient Thus the concentration of the ionized species, the laser pulse duration, and laser frequency are all important Also the particle density within the plasma plays a role However, it depends on the degree of ionization, the evaporation rate and the plasma expansion velocities The rapid expansion of the plasma leads to a steep decay in the electron density and temperature In the expansion profiles Narayan and Singh assumed that the density profiles would display an exponential decay profile with increasing distance from

the target surface The assumption is that initially the plasma is a high temperature, high density isothermal plume expanding rapidly after the laser pulse has ended, with initial edge position given by X_0, Y_0, Z_0

$$\text{Equ 40} \quad X(t)\frac{d^2X}{dt^2} = Y(t)\frac{d^2Y}{dt^2} = Z(t)\frac{d^2Z}{dt^2} = \frac{k_B T_0}{M}\left[\frac{X_0 Y_0 Z_0}{X(t)Y(t)Z(t)}\right]^{\bar{\gamma}-1}$$

for $t>\tau$ (where τ is the laser pulse duration)

Here γ is the ratio of specific heat capacities at constant pressure and volume, k_B is the Boltzmann constant, T_0 is the plasma temperature at the termination of the laser pulse, M is the particle mass while X,Y,Z at time t, is the extent of the plume in three dimensional space The laser energy absorbed after the initial generation is thus converted directly to kinetic energy within the expanding plume The latter is driven by massive pressure and density gradients which are most pronounced parallel to the laser axis

$$\text{Equ 40} \quad P(x,y,z,t)=\frac{N_T t k T_0}{2^{0.5}\pi^{1.5}\tau X(t)Y(t)Z(t)} \times \exp\left(-\frac{x^2}{2X(t)^2}-\frac{y^2}{2Y(t)^2}-\frac{z^2}{2Z(t)^2}\right) \quad \text{for } t<\tau$$

Eventually the plasma enters a phase of free-expansion, where collisions are negligible (such a state is called 'self similar , by Hora [35])

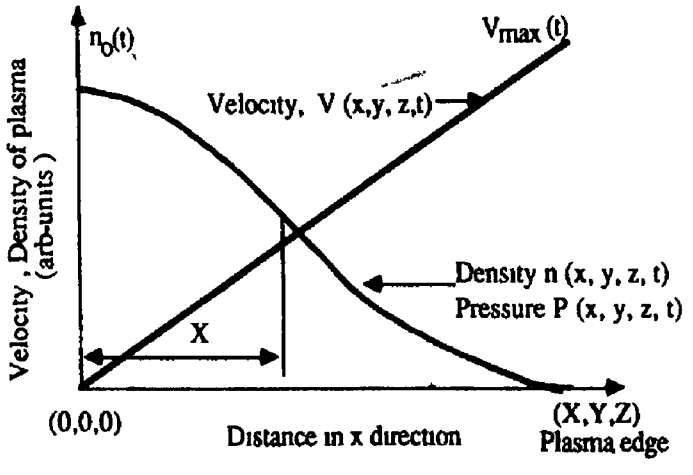

Figure 1 11 Schematic profile showing the density (n), pressure (P) and velocity (v) gradients in the plasma in the x-direction, which is perpendicular to the target surface The density and plasma gradients are monotonically decreasing from the target surface with a linear increase in the velocity (Narayan and Singh [18])

The modeled behaviour assumes isothermal expansion from the initiation of the laser pulse until its termination However, upon termination of the pulse the expansion becomes adiabatic The latter refers to the relation between the plasma volume and its temperature defined by the adiabatic thermodynamic equation

$$\text{Equ 41} \quad T[X(t)Y(t)Z(t)]^{\gamma-1}=\text{const},$$

Figure 1 12, displays a schematic overview of the main processes modeled by Narayan and Singh, in their model Its also displays the profile for temperature, density, and laser intensity

The maximum obtainable velocity from the conversion of thermal energy to rapid expansion is given by $2a/(\gamma-1)$ where a is the velocity of sound $[a=(\gamma RT/M)^{0.5}]$ By inputting the variables of interest (laser XECL excimer laser, λ=308nm, τ_{pulse}=45nsec) the model was able to map density and temperature trends for various configurations of a virtual experiment Generally the authors reported plume velocities ranging from 10^5-10^7 cm/sec, the latter being heavily dependent on the surrounding pressure of the environment, the atomic mass of the sample and the fluence of the beam. The pressure gradients that drive plasma expansion are greatest along the laser axis, this is what gives the laser plasma its characteristic shape, elongated normal to the target surface Typically expansion lengths at the end of the isothermal phase give the forward expansion a length of 4mm, while the expansion parallel to the target surface peaked at approximately 150μm The high densities near the target surface tend to shield the target from the latter half of the laser pulse, thus allowing the beam to heat the frontal regions of the plume, thus enhancing the already large difference in the pressure gradient along the different axis Generally after the first 400-500nsec of plasma adiabatic expansion, temperature within the plume drops rapidly, due to expansion However Narayan and Singh noted that the rate of decay is lower than that modeled This is most likely due to recombination within the plume offsetting the decay, as ionized species within the plume release energy from recombination

The earlier analysis of Boland in the late sixties led to temperature measurements from line ratios and densities from line widths The edge propagation velocity was also measured The temperature was found to decay rapidly away from the target surface (90-12eV) over a range of approximately 2mm Velocities of 3.3×10^7 cm/sec for C^{6+}, and 0.7×10^6 cm/sec for C^+ were measured Utilizing the Saha equation densities of the order of 10^{17} cm^{-3} were calculated Thus approximately 60% of the incident energy was converted into kinetic energy of ions and only 6% of all carbon atoms vaporized by the laser were ionized Irons (1972)[18 1] later extended this work by measuring the radial distribution of particles The overall picture to emerge is the inherent separation of ions within the plume With more highly energetic ions nearest the laser axis, where the temperature is at a maximum, the maximum charge state allowed decreases with the decrease in the average plasma temperature, as predicted by Narayan and Singh

1.3.5.6: Over view of plasma generation and evolution.

Laser-target interaction schematic (upper diagram), and main processes modeled by Narayan and Singh (lower diagrams).

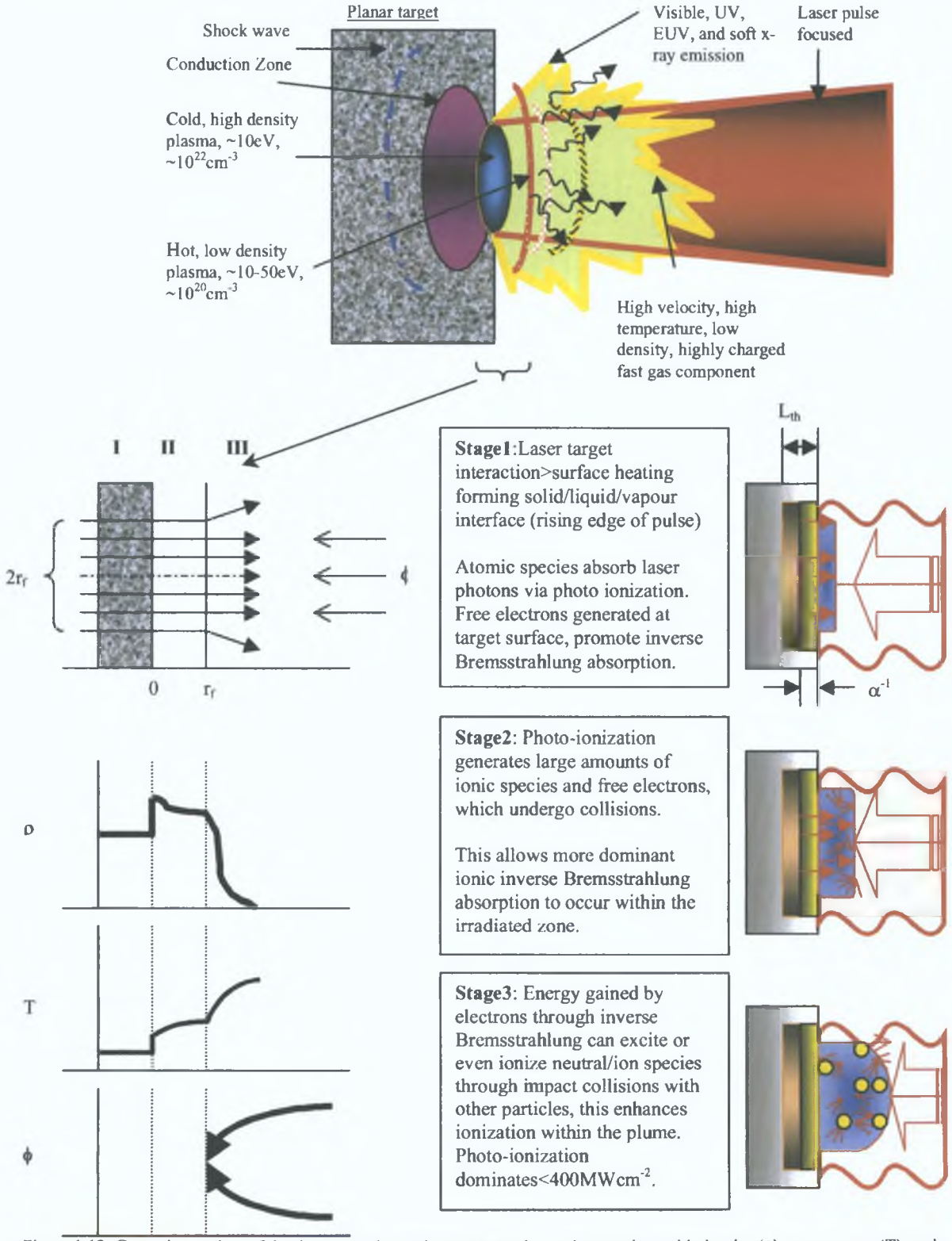

Figure 1.12: General overview of the three stage laser plasma generation and expansion, with density (ρ), temperature (T), and laser power (ϕ) displayed in relation to the target and layering due to beam penetration and heating of the material.

Figure 1.13 displays the a schematic representing the four distinct processes seen in vacuum laser-surface interaction at high irradiance, studied by Phipps and Dreyfus [36]. In their analysis Phipps and Dreyfus assumed a 100μm diameter beam irradiating aluminum in vacuum at energies between 5-10 J/cm^2 from a pulse of duration between 10-100nsec.

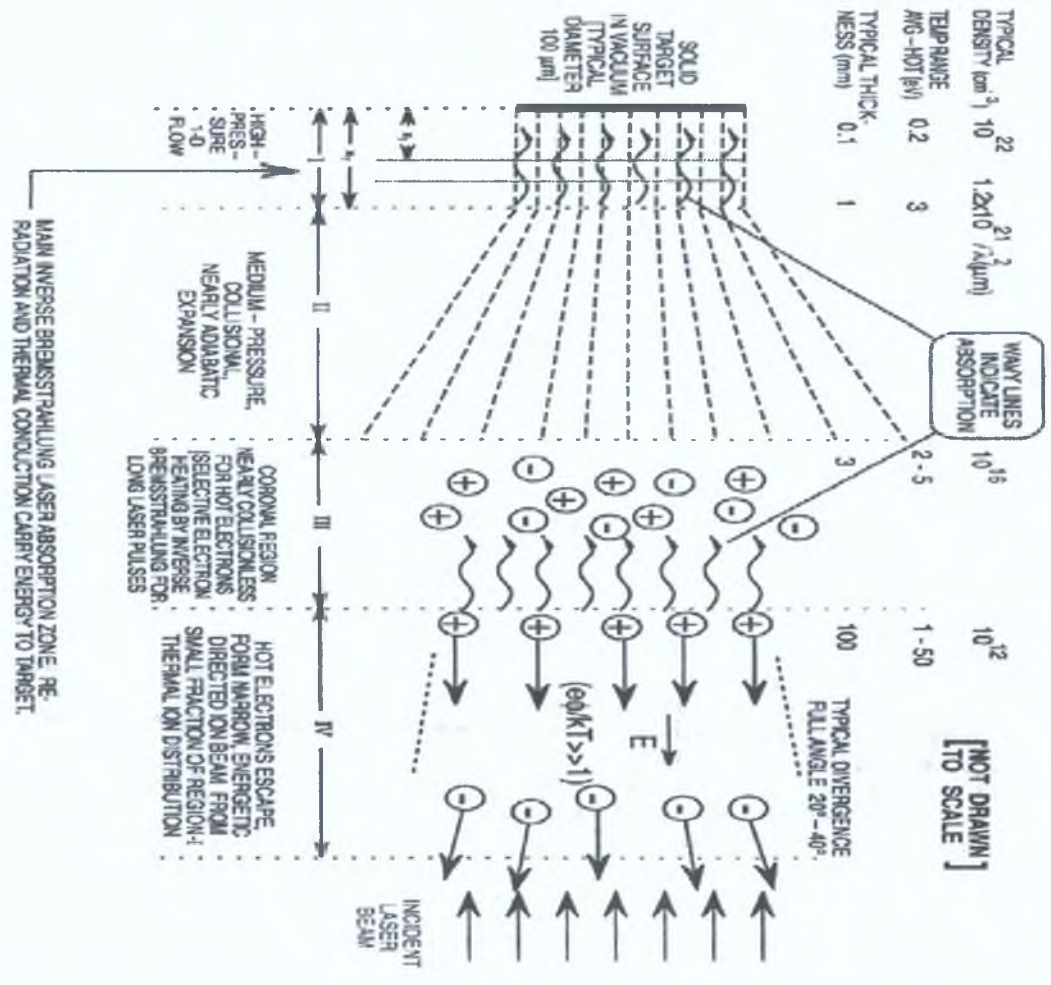

Figure 1.13: General overview of laser plasma generation and expansion, with numerical values of density, temperature, and typical thickness of the plasma normal to the target surface (Phipps & Dreyfus [36]).

The four regions characterized involve:

Region I: Laser energy absorption at a thin layer of pre-plasma on the target surface, with a dynamic and continuous change in the plasma density such that the rate of laser ablation of the target surface varies as the density profile in this thin plasma plume varies, leading to absorption of the beam and heating of the plume during the laser pulse duration, driving rapid expansion. Expansion is treated as one dimensional.

Region II: Knudsen layer formation. Here the expansion becomes three dimensional, and due to a high collisional rate a Knudsen layer will form. This is a region where an explicit centre of mass velocity develops, leading to a beam like expansion and deviations from a typical Maxwellian velocity distribution.

Region III Also called a coronal region, due to the low rate of collisions between thermal electrons and the absence of collisions between energetic electrons Highly energetic electrons from regions I and II, now begin to decouple from the main body of the plume and exhibit a velocity distribution which strongly differs from that exhibited by the main plume Here three body recombination ceases to be a factor Any inverse bremsstrahlung heating which may still exist in this region is offset by strong adiabatic cooling due to rapid expansion

Region IV Here a minority of hot-highly energetic electrons completely escape the plume having undergone relatively few collisions As a consequence of this, a large potential difference develops across the length of the plasma normal to the target surface This then accelerates some ions electro statically, and given sufficient lengths some ions will reach the same average velocity as the hot electrons Generally increasing the power density of the laser beam will lead to a even greater disparity in velocity distributions between the main plume and that component which moves away at a higher velocity This phenomena has been termed 'plasma splitting'

1.3 5 7 Concluding remarks

Since the early days of Boland and Irons, much work has been done to extend the understanding of both the generation mechanism of laser plasma formation, but also the expansion parameters and processes which control the interaction of particles, targets, laser light and plume components with ambient gas environments Models have increased in complexity considerably, while experimental work continues to probe plume dynamics with greater spatial and temporal resolution Anisimov and Luk'yanchuk [26] have developed an expansion model for laser plasma plumes in both vacuum and background gases, which is formulated using gas dynamic equations As stated previously Shannon and Li have extended their model for laser interaction with irregularly shaped cavities[34] while more recently Hirsch et al (Hirsch et al [31]) have mapped the intensities of selected calcium ions in two dimensions with a tunable backlighting VUV source, and later used this technique to map plasma densities within the plasma plume (Hirsch and et al) [32]) Thus the conclusion at this time, is that although each model and analysis approach is valid for the boundary conditions and assumptions upon which they are based, they are however deliberately based upon ignoring secondary effects such as target configuration which Shannon has shown played an important role in laser target coupling Secondly as Chen and Wood has shown, complex processes such as scattering must be included in expansion models if phenomena such as plume splitting are to be included in expansion models, while it is not feasible to simply continue to ignore geometric effects in laser-melt-evaporation models such as that by Amoruso

Thus future models will have to incorporate all approaches adopted by the above authors if a complete picture of laser plasma generation and evolution is to be understood

References

[1] Amusia M Ya, Cherepkov N A and Chernysheva, ZH Eksp Toer, 60, 160 (Sov Phys-JETP, 33, p90, 1971)

[2] Anderson J , Ap J ,59, 76, (1924)

[3] Baier S , Sonntag B J Phys At Mol Opt Phys, 25, 923-930 (1992)

[4] W Lochte-Holtgreven, 1995, AIP, Plasma Diagnostics

[5] Balmer J , Lewis C L S , Lee R W , Phys Rev A, 40, 1, pp 330-340, 1989

[6] P F Bernath, Spectra of Atoms and Molecules, ISBN 0-19-507598-6 (1995), Oxford Univ Press

[6 1] E Hecht, 'Optics', 3rd Edition, Addison-Wesley, (1998) ISBN 0-201-30425-2, pp 127

[7] R K Singh, D Bhattacharya, J Naryan Mat Res Soc Symp Proc 201, 427 (1991)

[8] J T Cheung, H Sankur, C R C Reviews of in Solid State and Material Science, 15, 163 (1988)

[9] R Kelly, R W Dreyfus Surface Science 198, pp 263 (1988)

[10] A Miotello, R Kelly, Appl Surf Sci, 138-139, pp 44 (1999)

[11] R Kelly, R W Dreyfus Nucl Instr Methods B 32, pp 341,(1988)

[12] K H Song, X Xiu Appli Phys, A 65, pp 447, (1995)

[13] R W Dreyfus J Appl Phys 69, pp 1721, (1991)

[14] A L Thomann, C Boulmer-Lebourge, B Dubriel Plasma Sources Sci Tech, 6, pp 298 (1997)

[15] Y Zel'dovich, Y Raiser, 'physics of Shock Waves and High Temperature Hyrdodynamic Phenomena', Academic press , NewYork and London (1996)

[16] I V I Mazhukin, I Smuro, G Flamant,Appl Sur Sci, 96-98 (1996) 89-96

[17] S I Anisimov, B S Luk'yanchuk, A Luches, Appl Surf Sci, 96-98(1996) 24-32

[18] R Singh, J Naranyan, Phys Rev B, vol41, no13, 1990

[18 1] F E Irons, R W P McWhirter, N J Peacock, J> Phys B At Mol Phys , 5, 1975-1987 (1972)

[19] R L Williamson, D C Haggard, International Journal of Heat and Mass Transfer, Vol 46, Iss 22 (2003), pp 4215-4228 2003

[20] S Amoruso, Appli Surf Sci, 138-139 (1999) 292-298

[21] Z H Shen, S Y Zhang, J Lu, X W Ni Optics and Laser Technology 33 (2001) 533-537

[22] Chen, F F , J Appl Phys 36(1965) 675

[23] Hughes 1975, McWhirter 1965

[24] J M Dawson, "Laser Interaction and Related Plasma Phenomena", Seminar, June 9-13 (1969)

[25] V I Mazhukin, I Smuro, G Flamant Appl Surf Sci 96-98 (1996) 89-96

[26] S I Anisimov, B S Luk'yanchuk, A Luches Appli Surf Sci 96-98 (1996) 24-32

[27] R K Singh, J Narayan Phys Rev B, vol41, no 13, 1990 AIP press

[28] Z H Shen, S Y Zhang, J Lu, X W Ni Optics and Laser Technology 33 (2001) 533-537

[29] M Shannon, Appl Surf Sci 127-129 (1998), 218-225

[30] R P McWhirter, Spectral Intensities, in Plasma Diagnostic Techniques, 1965, NY Press

[31] J S Hirsch, J T Costello, Rev of Sci Instr, vol 74, No 6 (2003), pp 2992-2998

[32] J S Hirsch, O Meighan, J T Costello, J Appl Phys, vol 88, No 9, No 2000, pp 4953-4960

[33] R F Wood, K R Chen, D B Geohegan, Phys Rev Letts, 25 August 1997, 1571-1574

[34] Chuandong Li, M Shannon, 150 (1999), 211-226, Appl Surf Sci

[35] PLASMAS AT HIGH TEMPERATURE AND DENSITY, H Hora (S Roderer, Regensburg 2000)

[36] C R Phipps, R W Dreyfus, 'Laser Ionization Mass Analysis', 1993 J Wiley & Sons

Chapter Two: Spectroscopic Diagnostics

Introduction

This chapter introduces the most important aspects of spectral emission interpretation. Theories of line broadening and line profiles, and their use in density determination are presented. The main spectroscopic techniques used to calculate temperatures and densities within the plasma are also presented. The equations and assumptions required, for data analysis transformation to meaningful physical quantities are discussed. Finally, the three temperature techniques used here are compared in terms of the space-time limits of each technique. The limitations encountered in this work are also discussed.

Spectroscopic Diagnostics

2 0 Introduction

Spectroscopic diagnostics offer a unique means to sample the plasma conditions and relate a change in the environment variables to a response in the plasma While ion and electron probes offer measurements of plasma parameters directly, they can however represent a dramatic perturbation of the plume They also are limited in the extent of scale Very early timescales, and also distances close to the target are effectively non-accessible due to the inherent assumptions in probe theories about plasma behaviour The latter break down under the extreme conditions found early on in the plasma lifetime

Spectroscopic theories used to relate the emission spectrum and physical parameters are both varied and detailed All rely on exact knowledge of the atomic properties of the transition responsible for the emission Atoms which undergo transitions from one bound state to another of lower energy, emit radiation of well defined energy and line shape The line shape is related to the lifetime of the upper state of the transition and is also influenced by perturbations due to external influences as well as the velocity distribution of the emitting species Thus if one is to use line profiles to diagnose the plasma conditions, one must consider the factors affecting the emission profiles of lines

2 1 Natural Broadening

From the Heisenberg uncertainty principle, $\Delta E \approx \frac{\hbar}{\tau}$, and effective spreading of the quantum states in an atom leads to line broadening in the emission of a photon from such a system The lifetime is given by

$$\text{Equ 1} \quad \frac{1}{\tau} = \sum_i A_{Ki} \quad (s^{-1}) \qquad \text{(Lochte-Holtgreven [1])}$$

The range of values for τ in the optical region of the EM spectrum are of the order 10^{-8} s, thus for example in the visible for AL III (463nm) 4p-4d($2P^0$-2D), $\tau = 0.391 \times 10^{-8}$s The general profile for emission lines is Lorentzian Such broadening is negligible for visible and infrared lines, but may be significant in the EUV range

2 1 1 Doppler Broadening

Doppler broadening is interpreted in terms of atom or ion thermal motions within the plume If the velocities of the particles are described by a Maxwellian distribution with temperature T, then this gives rise to a Gaussian line profile of full width half maximum (FWHM)

$$\text{Equ 2} \quad \Delta\lambda_{D1/2} = 2\sqrt{Ln2}\sqrt{\frac{2k_B T\lambda_0}{Mc^2}} \quad \text{(Lochte-Holtgreven [1])}$$

This can be simplified to

$$\text{Equ 3} \quad \Delta\lambda_{D1/2} = 7.16\times10^{-10}\lambda_0\sqrt{\frac{T}{M_A}} \quad \text{(Lochte-Holtgreven [1])}$$

Here M is the particle mass (kg), and M_A is the atomic mass number, λ_0 is the center wavelength in nanometers and T is the temperature in Kelvin Thermal broadening is most important for very high temperatures in light elements

2.1.2 Stark Broadening Electron density

The main influence in Stark broadening is the presence of other particles and their electric fields upon the emitting particle Such electric fields are within a Debye length squared of the emitting particle Thus as one would expect, where densities are high and there is the presence of many free electrons within the plasma, Stark Broadening pre-dominates in terms of broadening mechanisms At high densities, the mean time between collisions are less than the time needed for photon emission The contribution of other broadening mechanisms, i e Van der Waals, Doppler, and resonance, can be neglected here in this work because of the relatively low temperatures (~2 eV max) and high densities (10^{16} -10^{18} cm^{-3}) The emitted profile of a line broadened by Stark influences is given by

$$\text{Equ 4} \quad \Delta\lambda_{1/2} = 2W\left(\frac{N_e}{10^{16}}\right) + 3.5A\left(\frac{N_e}{10^{16}}\right)^{1/4} \times [1-1.2N_d^{-1/3}] \times W\left(\frac{N_e}{10^{16}}\right) \quad \text{(Zeng et al [2])}$$

$\Delta\lambda_{1/2}$ is the FWHM (Angstroms) due to Stark broadening, N_e (cm^{-3}) is the electron density W and A are the electron and ion broadening parameters which are independent of the electron density and only weakly dependent on the electron temperature N_d is the number of particles in a Debye sphere, The first term on the right is the electron broadening The second is broadening due to ion collisions For non-hydrogenic ions Stark broadening is predominantly due to electron impact, thus one can ignore the effect of the second term which is negligible

2.1.3 Line profiles

In reality the line broadened profile is usually due to a combination of influences, and depends greatly on local conditions Thus the multiple factors usually lead to a Voigt profile

The normalized Gaussian profile is given by

$$\text{Equ 5} \quad \phi_{\text{Gaussian}} = \left(\frac{Ln2}{\pi}\right)^{1/2}\frac{1}{\Delta_G}\exp\left[-Ln2\left(\frac{\nu-\nu_o}{\Delta_G}\right)^2\right] \quad \text{(Whitty [3])}$$

Here Δ_G is the half width at half max Such profiles can be obtained by taking into account Doppler shifts due to a Maxwellian (thermal) distribution of velocities, thus relating Δ_G to the kinetic temperature of the emitting particles The normalized Lorentzian profile is given by

$$\text{Equ 6} \quad \phi_{\text{Lorentzian}} = \frac{1}{\pi\Delta_L} \frac{1}{\left[1+\left(\frac{\nu-\nu_0}{\Delta_L}\right)^2\right]} \qquad \text{(Whitty [3])}$$

Here Δ_L is the half width at half max, and ν_0 is the resonant frequency between two levels involved in the transition Lorentzian profiles are normally associated with natural and Stark widths of a spectral line
The Voigt Profile is given by

$$\text{Equ 7} \quad \phi_{\text{Voigt}} = \left(\frac{Ln2}{\pi}\right)^{1/2} \frac{1}{\Delta_G} \frac{1}{\pi\Delta_L} \int_{-\infty}^{\infty} \exp\left[-Ln2\left(\frac{\nu}{\Delta_G}\right)\right]^2 \frac{1}{\left[1+\left(\frac{\nu-\nu}{\Delta_L}\right)^2\right]} d\nu' \qquad \text{(Whitty [3])}$$

Such a function results from folding a Gaussian profile (due to Doppler broadening) and a Lorentzian type profile (due to radiation and/or impact damping) In all work reported here the line shape function fitted was Lorentzian assuming Doppler broadening is negligible and broadening is assumed to be due to particle collisions within the plasma The line widths were used to evaluate the plasma electron density for different targets Despite a large volume of work on both electron collisions and density measurements, the main deciding factor in the use of line broadening for density measurements is the accessibility of electron impact parameters (W) for that particular transition of interest The electron impact parameters were taken from Dimitrijevic [14], who has calculated W values for various ions in the EUV, UV, and visible wavelengths In using spectrometers an important issue is the role of the instrument function This can add to the measured line width, and since this latter quantity is directly used in the determination of the electron density, it is important to subtract its contribution to the measured line with In the event that the instrument function is determined to be Lorentzian and the line function used to determine the width of the emitted line is also Lorentzian, then one can effectively deconvolute the instrument function by subtracting the FWHM of the instrument function from the FWHM of the measured line However in the event of either line shape being Gaussian, full deconvolution must be applied to remove the instrument function FWHM from the measured line

2 1 4 Ionization Temperature Ion-to-Atom line Intensity ratio

One of the simplest and most widely used means to diagnose plasma temperature is to consider the peak intensities of lines from two successively ionized ion stages When lines are of the same ionization stage, as they are in the Boltzmann plot method, the small energy differences between the line's upper levels makes this method unreliable However when two successive ion stages are used, the energy difference is now

enhanced by the ionization energy which is usually much larger than kT. It is important for accuracy that the spectral lines be located in the same spectral window, with no overlapping lines present. Equation 8 gives the required equation. The left hand side represents the line intensity ratio of the ion to the atom. Here, N_e (cm^{-3}) is the electron density, gA is the product of the statistical weight and the Einstein coefficient for spontaneous emission of the upper level (s^{-1}). λ is the wavelength of the line (nm), T_{ion} is the ionization temperature (eV), E_{ion} and E_{atom} are the excitation energies of the upper and lower stage. ΔE_∞ in equation 9 is the correction to the ionization energy E_∞ of the lower ionization stage due to plasma interactions.

$$\text{Equ 8: } \frac{I_{ion}}{I_{atom}} = 4.83 \times 10^{15} \left(\frac{gA}{\lambda}\right)_{ion} \cdot \left(\frac{\lambda}{gA}\right)_{atom} \cdot \left(\frac{1}{Ne}\right) \times$$

$$T_{ion}^{3/2} \exp\left[\frac{E_\infty + E_{ion} - E_{atom} - \Delta E_\infty}{-kT_{ion}}\right] \text{ (Gordillo-Vazquez [5])}$$

$$\text{Equ 9: } \Delta E\infty \text{ (eV)} = 3zb\frac{e^2}{4\pi\varepsilon_o}\left[\frac{4\pi \times 10^{16}}{3}\right]^{1/3} \text{ (Gordillo-Vazquez [5])}$$

z=2 for the lowest ionization stage, e is the electron charge (C), ε_0 is the permittivity of free space (F m^{-1}), N_e is the electron density (cm^{-3}), and b = 6.24×10^{18} is the energy conversion factor from joules to eV. Details of the spectral constants for work reported here were taken from [4, 6, 7].

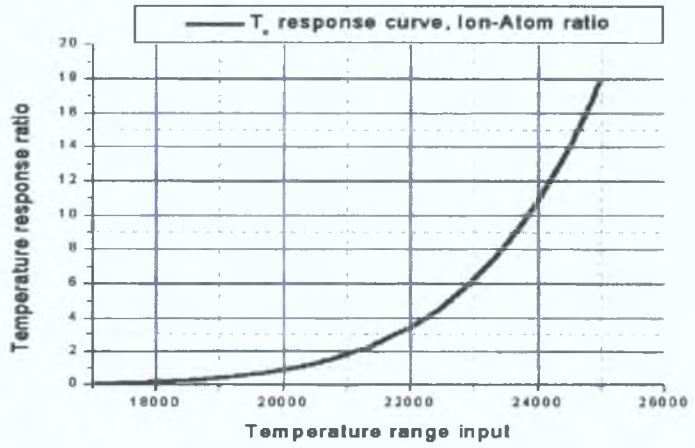

Figure 2.1: Typical temperature calibration curve for ion-atom line ratios, calculated from equation 8. This curve is the output from the right hand side of equation 8. Here one enters the spectroscopic constants and a value for the electron density. Then using Origin 6.0, a large range of temperature values are entered. This generates the curve seen above. One must then compare this curve to the actual values of line intensity ratio (value on the vertical axis), which can then be related to a temperature value (on the horizontal axis).

The main constraint here is the presence of the continuum. Only when the lines are clearly visible can one safely apply the above procedure. For our system the earliest time delay was 70nsec after the laser pulse.

All spectra before this time were continuum dominated The main limitation of this technique is that ions of different stages will inherently have different expansion velocities, and thus will cover different regions of a spatially resolved detector

2 1 5 Electron temperature Line-to-Continuum

Ionization temperatures from atom to ion ratios are not feasible for early timescales where continuum emission is pronounced, and line peaks can be difficult to distinguish Also line ratios can be insensitive to temperature changes under extreme, early phase timescales For early timescales, broadening due to the relative motion of the particles can be important for calculations involving the ratio of areas because the Doppler broadening is dependent upon the wavelength of the transition, the atomic mass of the species and the temperature The broadening can be calculated from

Equ 10 $W_{1/2}=7\ 16\times10^{-7}\lambda(T/M_A)^{1/2}$ (Liu et al [8])

where T is the temperature in Kelvin, M_A is the atomic mass and λ is the line wavelength in nanometers From the experimental data and the extrapolated temperatures (discussed later) the temperatures do not exceed 250000K If λ=453nm (discussed in chapter five), and M_A=26 98 (aluminum) then equation 10 gives $W_{1/2}$ =0 0339nm, thus the contributions of Doppler shifts are negligible with respect to the line widths calculated from Stark broadening These widths are measured from 80nsec onwards, thus widths at early timescales should be even larger as densities increase Although atom to ion ratios are used here, they are only presented for timescales after 80nsec, thus to study temperatures before 80nsec the line-to continuum ratio method is employed Under the assumption of LTE in the plasma, the electron temperature, T_e can be assumed equal to the excitation temperature T_{exc} Thus $T_e=T_{exc}=T$ Therefore the plasma temperature (T/K) can be determined by the relative line-to-continuum intensity ratio using the following equation

Equ 11
$$\frac{\varepsilon_l}{\varepsilon_c} = C_r \frac{A_{21} g}{U_l} \frac{\lambda_c^{\,2}}{\lambda_l T_e} \exp\left(\frac{E_1 - E_2 - \Delta E_l}{kT_e}\right) \times \left[\xi\left(1-\exp(\frac{-hc}{\lambda kT_e})\right) + G\left(\exp(\frac{-hc}{kT_e})\right)\right]^{-1}$$
(Liu et al [8])

where C_r = 2 005×10^{5} (s K) and ε_c is the continuum emission coefficient, with units of energy per unit time per unit volume per wavelength interval ε_l is the integrated spectral profile of the line used and has units of energy per unit volume per unit time In the above statements, per unit time refers to the gate time or sampling time on a time resolved detector, per unit energy simply refers to photon energy Finally per unit

volume, refers to the area under the curve representing a line profile This is only considered if the volume of the plasma under study is physically large Laser plasmas, are however physically small, and the continuum emission is localized to regions of high density The $\varepsilon_l / \varepsilon_c$ ratio can be calculated from the integrated line intensity and continuum intensity at certain adjacent wavelength positions λ_l and λ_c are the line and continuum center wavelength positions By taking the center wavelength positions to be the same in the both cases i e $\lambda_l=\lambda_c$ equation 11 is simplified A_{21} is the Einstein transition probability of spontaneous emission, and E_i is the ionization potential E_2 and g_2 are the upper level energy and degeneracy of the line ΔE_i is the lowering of the ionization potential of atoms in a field of ions and is insignificant in magnitude U_i is the partition function for the ion , which is a weak function of temperature G is the Gaunt free-free factor, which is assumed to be unity by Kramer's rule ξ is the free-bound continuum factor

The partition function is given by

$$\text{Equ 12} \quad U(T)=\sum_i g_i \exp\left(-\frac{E_i}{kT}\right) \quad \text{(Griem [9])}$$

where g_i is the degeneracy or statistical weight of the i'th energy level E_i $g_i=2J_i+1$,
J_i is the angular momentum quantum number of the level E_i and J_i values were obtained from the NIST database

The main limitation and advantage of this technique is the requirement that the peak magnitudes of the line being used and the continuum are of the same order of magnitude Large differences in magnitude, such as later timescales when the continuum falls away rapidly lead to highly unstable continuum coefficients, thus causing the calculated temperature T, to fluctuate widely Thus useful measurements are limited to time delays well after the initiation of the laser pulse, and for aluminum laser plasma in the visible, the earliest sample time was 40nsec after the laser pulse initiation However since the ionization temperatures calculated from line ratios are only valid when the peak of the line is well defined, then both techniques allow a large range of space-time plasma behaviour to be studied, with one technique covering a range of time and space that the other does not, and vice versa.

As the relative magnitude of the continuum decreases relative to the line, the ratio of the area under the line to that of the continuum coefficient becomes unstable As time progresses, and the plasma decays, the ratio becomes more unstable over a larger spatial range, eventually the ratio becomes unusable after a time delay for which the continuum emission is weak The calibration curve, must be matched to the actual ratio, hence this is analogous to trying different values for T_e in the right hand side of equation 8 in trying to match the actual ratio on the left hand side of equation 8 The same procedure is used for ion-atom ratios

2 1 6 Electron Temperature Boltzmann plot

A third method of diagnosing the plasma temperature (in this case excitation temperature) is the Boltzmann plot method Here one determines the area under a number of lines of the same ionization stage over a large energy range to indicate the thermal conditions in the region of the plasma being sampled
The excitation temperature involving the emission from two lines is given by

$$\text{Equ 13} \quad T_{exc}=\frac{E_j-E_i}{k}\ln\left(\frac{I_j g_i A_i \lambda_j}{I_i g_j A_j \lambda_i}\right) \quad \text{(Boumans 1996[10])}$$

where I is the relative integrated intensity recorded for each spectral line in question, E is the excitation energy of the upper level for each line, g_i and g_j is the statistical weight of the upper and lower levels, A is the transition probability of the upper and lower levels for each line One disadvantage of the two line technique is the relatively small difference in the upper level energies (typically ~2eV) Secondly the values of A, the transition probability, for each line must be known One way around this problem is to study the emission from a large number of lines Considering the relation between oscillator strength and transition probability

$$\text{Equ 14} \quad I=\frac{2\pi he^2}{m\lambda^3}\left(\frac{N_T(gf)}{Q(T_e)}\right)\exp\left[-\frac{E}{kT_{exc}}\right] \quad \text{(Boumans 1987[11])}$$

If the log of both sides is now taken we get the relation

$$\text{Equ 15} \quad Ln\left(\frac{I\lambda^3}{gf}\right)=Ln\left(\frac{2\pi N_T he^2}{Q(T_e)m}\right)-\frac{E}{kT_{exc}} \quad \text{(Boumans 1987[11])}$$

where Q is the partition function, and N_T is the total number of particles If the population of the excited states follows a Boltzmann distribution law, then the plot of $Ln(I\lambda^3/gf)$ versus the excitation energy should give a straight line with a slope equal to $(-1/kT_{exc})$ In the above, I is the integrated intensity of the line, and gf is the product of the degeneracy of the upper level and the oscillator strength Requirements for good Boltzmann plots are lines in close proximity, which are reasonably intense and of known transition probability Also, good upper level energy separation stabilizes the plot, making measurements less vulnerable to shifts in the log value of one particular point In order to ensure the stability of the plots, one should use as many lines as is feasible and these lines should have a large upper level energy separation in their transition This will ensure that the plots are not too dependent on a particular point, and are also

stable to changes, avoiding sudden changes to the slope of the line fitted Physically this ensures smooth space and time resolved temperature plots, with fewer discontinuities

2 1 7 Electron density Density sensitive line ratios

Electron density values in laser plasmas are an important parameter in understanding the plasma response to different experimental conditions However the applicability of using Stark broadening as a means to diagnose the plasma electron density depends on the availability of an impact parameter W Due to the complexity of the calculations involved in determining W, it has been estimated for only a few ions, with the majority being in the VUV and Visible In fact only two values for W have been calculated for aluminum in the EUV by Dimitrijevic [4], and these were for AL X, which is too weak and too short lived at the power densities employed in this work Thus some other means of determining the electron density at such short wavelengths is required Tijerina et al [12] have produced calibration curves for aluminum over various wavelengths for a number of different ion stages in the visible, using the CHIANTI 2 0 code developed by the US Naval Observatory This code solves the equations of statistical equilibrium, assuming that the only active processes are radiative decay and collisional excitation and de-excitation , and determines the emission spectrum of an optically thin plasma in a very wide wavelength range (50-11000A) Contact with Tijerina has led to the running of the CHIANTI 2 0 code, for EUV and Visible lines of interest in this work, thus allowing this density determination technique to be employed here Inputting a range of plasma densities, leads to the expected spectrum from a plasma, which can then be used to calculate the ratio of two ion stages of moderate wavelength separation (figure 2 2)

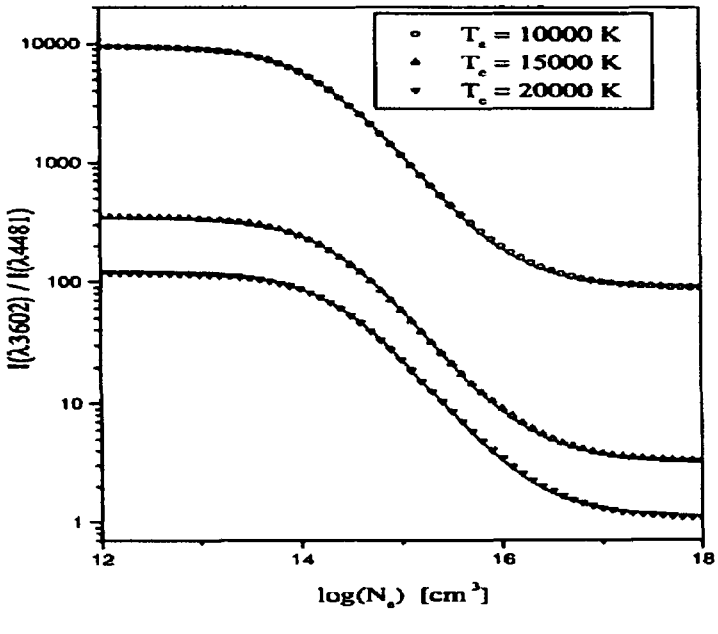

Figure 2 2 Calibration curve from Tijerina et al [12](via private communications) This curve is the ratio of two AL III (360 2nm and 448 1nm) ion stages, whose emission spectrum came from the CHIANTI code

The response of the line ratio to a range of densities can be represented as a sigmoid curve The curve itself or rather the line ratio has a strong temperature dependence, as can be seen above The equation of this curve is given by equation 16 Thus if one knows the parameters required to plot the curve for a particular pair of ion stages over a discrete density range for a precise temperature, then the ratio of the peak intensity for the raw data in an experiment can be translated into values of electron density within the plasma

$$\text{Equ 16} \quad R(X)=A+\frac{B-A}{1+\exp[-(X-C/D)]}$$

where $X=\log(N_e)$, and the parameters A,B,C and D are determined from a sigmoid fit to the calibration curve which is the outputted data from the CHIANTI code

Clearly this technique has much in common with that of ionization temperature calculations, thus it also suffers from the same limitations For very early or very late stages in the plasma history, weak or unstable peaks in the spectrum will manifest as a noisy line ratio, and upon translation to electron density, an unstable N_e profile Secondly, in most cases, the parameters required for the calibration curves are available at only a few discrete temperatures If a plasma displays rapid temperature changes in time, then one should use a new calibration curve for each time resolved measurement, fitted for the temperature at that time However in reality, this is not feasible One may be forced to use the same calibration curve, fitted at a precise temperature for a range of time resolved measurements, even though the temperature at each time resolved event is different This can lead to insensitivity in the line ratio in time, and significant changes in the density via line ratio may only be seen when a significant drop in temperature occurs However despite these limitations, the main strength of this technique is its ability to give approximate values of N_e on time scales where clean, stable line profiles may not be feasible or reliable This frequently happens at the late stage of plasma history, or spatially far from the plasma generation point Lastly given the absence of electron impact parameters at short wavelengths, density sensitive line ratios allow for approximate values of the electron density at very early phases in the plasma history to be calculated

2 1 8 Conclusions

Obviously one must take care to consider the stability of the Boltzmann plots for very early timescales and very late timescales, in both cases the signals are weak and a stable baseline may not exist The line ratio technique does not suffer from this problem Once a peak of a line can be resolved then one can calculate the line ratio However as stated before, under extreme conditions line ratios can be insensitive to changes in temperatures and unless clear differences in signal strength from the two lines selected exists from one space/space resolved measurement to the next If measurable changes in the ratio do not occur then one will see only incremental changes in temperatures from one space/space resolved measurement to the next This may result in a plasma temperature which is nearly constant over a large range of space and time These

problems can be avoided or minimized if one performs time resolved measurements. Given the different expansion velocities, leading to a different spatial distribution of emitted light from one ion stage relative to the other, a continuous change in the measure intensity ratio will be ensured over the spatial region under study.

The line to continuum approach has both of the above technique's strengths and weaknesses. It requires good parity between the strength of the lines and the continuum, a difficult requirement as the atomic number of the sample increases, where at short wavelengths, emission is dominated by continuum. However even with weak continuum or line signal, the relative relation between the two is good. However continuum emission is closely linked to electron density and collisions, both of which are important at very early stages, thus limiting this approach to this regime.

In conclusion, each technique is applicable over different regimes of the plasma's emission lifetime, and thus the best way to fully diagnose the plume is to apply as many as is feasible. However the defining limitation is the availability of spectroscopic constants from data bases for the lines under study.

References:

[1]: W. Lochte-Holtgreven, Plasma Diagnostics, American Vacuum Society Classics (ISBN 1-56396-388-4).

[2]: X. Zeng, S.S. Mao, E. Russo. Spectrochima Acta Part B 58 (2003) 867-877.

[3]: W. Whitty, PhD thesis, (1998), Dublin City University.

[4]: MS Dimitrijevic, Z Djuric, AA Mihajlov. J Phys D: AppL Physics 27(1994) 247-252.

[5]: F.J. Gordillo-Vazquez, Appl Phys Letts, Vol 78, No 1, Jan 2001.

[6]: http://physics.nist.gov/cgi-bin/AtData/main_asd (Nist).

[7]: http://physics.nist.gov/PhysRefData/ASD1/archive/GS_IE/Al_gs_ie.html.

[8]: H. C. Liu, X. L. Mao, J. H. Yoo, Spectrochima Acta Part : 54, 1999, 1607-1624.

[9]: H.R. Griem, Plasma Spectroscopy, McGraw-Hill, NewYork, 1964.

[10]: Boumans P W J M(1996). Theory of Spectrochemical Excitation, Plenum Press, New York.

[11]: Boumans P W J M (1987). Inductively coupled plasma emission Spectroscopy.

[12]: E. Perez-Tijerina, J. Bohigas, R. Machorro, J. Appl. Phys. Vol 90, No 7, October 2001.

Chapter Three: Diagnostic Equipment and Experimental Apparatus

Introduction

This chapter introduces the main devices and their operation, used in this work to study plasma generation and evolution. In order to carry out the research reported here in this thesis, a number of different system and hardware developments had to be implemented and new diagnostic techniques had to be effected for the first time. This chapter introduces the main experimental systems (including EUV and visible spectrometers, electron and ion probes, ICCD camera systems, vacuum chamber, prototype magnetic pulse system) and provides an overview of the space and time limitations for each diagnostic technique. The electronic synchronization required for each diagnostic is also introduced and a detailed description of the design and performance aspects is presented.

Diagnostic equipment and experimental apparatus

3 0 Diagnostic performance overview

In studying any system, drawing reliable conclusions about that system's behaviour relies on complete and accurate information about the system's performance and response to stimuli and probing A laser plasma by definition is a highly dynamic system and transient system Studying such a system without both space and time resolved data would be at best an approximation and at worst a gross approximation The influence of any variable on the response of the plasma will have effects which will appear negligible in certain space regions, and large where plasma conditions allow that variable to exert a large influence For example, confining a target within a cavity of certain dimensions, can lead to higher temperatures in the visible, and moderately higher temperatures as determined with probe diagnostics One might then assume that enhanced temperatures should exist during the EUV lifetime of the plasma However this not the case, if the cavity volume is not of the order of the continuum plasma or less Thus in discussing the influence of target geometry and secondary influences such as electric and magnetic field interactions with a plasma, it is important to ensure the convergence of different diagnostic techniques and to understand the limits of their use in space and time sampling Each diagnostic technique has inherent limitations, namely how early in time it can deliver reliable signals and its ability to measure physical parameters that are meaningful There is no hard and fast rule that would allow one to say explicitly where a technique fails, and an important variable in deciding the applicability of a technique is laser fluence or power density

During the course of various experiments, the limits of the three primary diagnostic techniques employed here became apparent from experiments In considering the limit of a diagnostic tool's performance, the experimental parameters must be optimized to ensure that the design of an experiment which, although limited by the diagnostics performance, is still viable Where one technique fails, attempts were made to utilize another and to overlap trends in space and time (where possible) seen in both, so as to provide a more complete overview of the plasma's response to certain variables Where a certain theory began to fail, others were applied, and in general the trend in this work is characterized by 'earlier-further-later-and more of' approach to data acquisition and the space time limits of each experiment Figure 3 1 gives a illustration of the space time limits for each diagnostic tool Each device has four limits, the earliest and latest temporal measurement, and the smallest and greatest distance Z, normal from the target surface Generally it is a well established fact that as the plasma density and temperature increases (generally pushing back to the laser pulse arrival on the target surface), in order to study line emission from the plasma, one must move to shorter and shorter wavelengths Thus for power densities used in this work ($\sim 10^{11} Wcm^{2}$), beginning at the space time origin from figure 3 1, is the EUV grazing incidence spectrometer, the temporal limits of which are bounded by the arrival of the laser pulse (at Z=0mm) and ~40-50nsec after the laser pulse (at Z=~2mm) Generally after the EUV range would be VUV emission, however no VUV studies were performed in this work Beginning ~50-60nsec after the laser pulse (Z~0 5-1 5mm) useful visible line emission begins This lasts no later then 350nsec after the laser pulse (at Z=7-9mm)and visible imaging of

the plume can however remain viable until ~450-500nsec, and with high gain on the ICCD can be extended to ~1600nsec. Finally, ion probes, were used for which the earliest temporal measurement was ~700-850nsec (at Z=5-8mm), and electron probes which could not measure signals reliably before 900-1000nsec after the laser pulse (at Z≈2-6cm depending on the fluence). In fact the space time limits of the probes (both ion and electron probes) is completely dependent on the fluence, or more precisely the presence of high energy ions, which may undermine the analysis.

3.1: Diagnostics performance range.

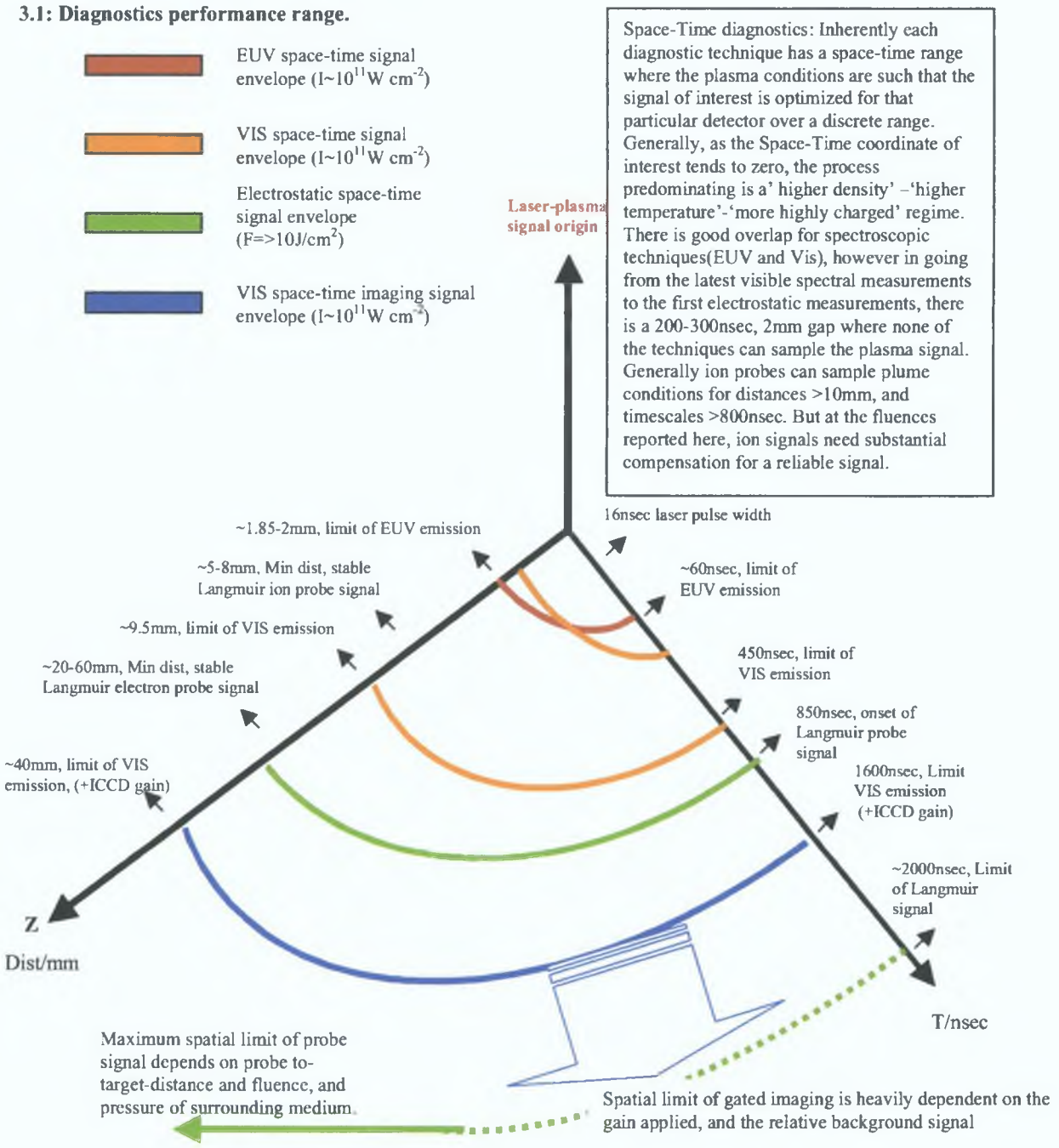

Figure 3.1: Space-time envelope of plasma diagnostics, including EUV emission spectra, Visible emission spectra and imaging, and electrostatic probe signals.

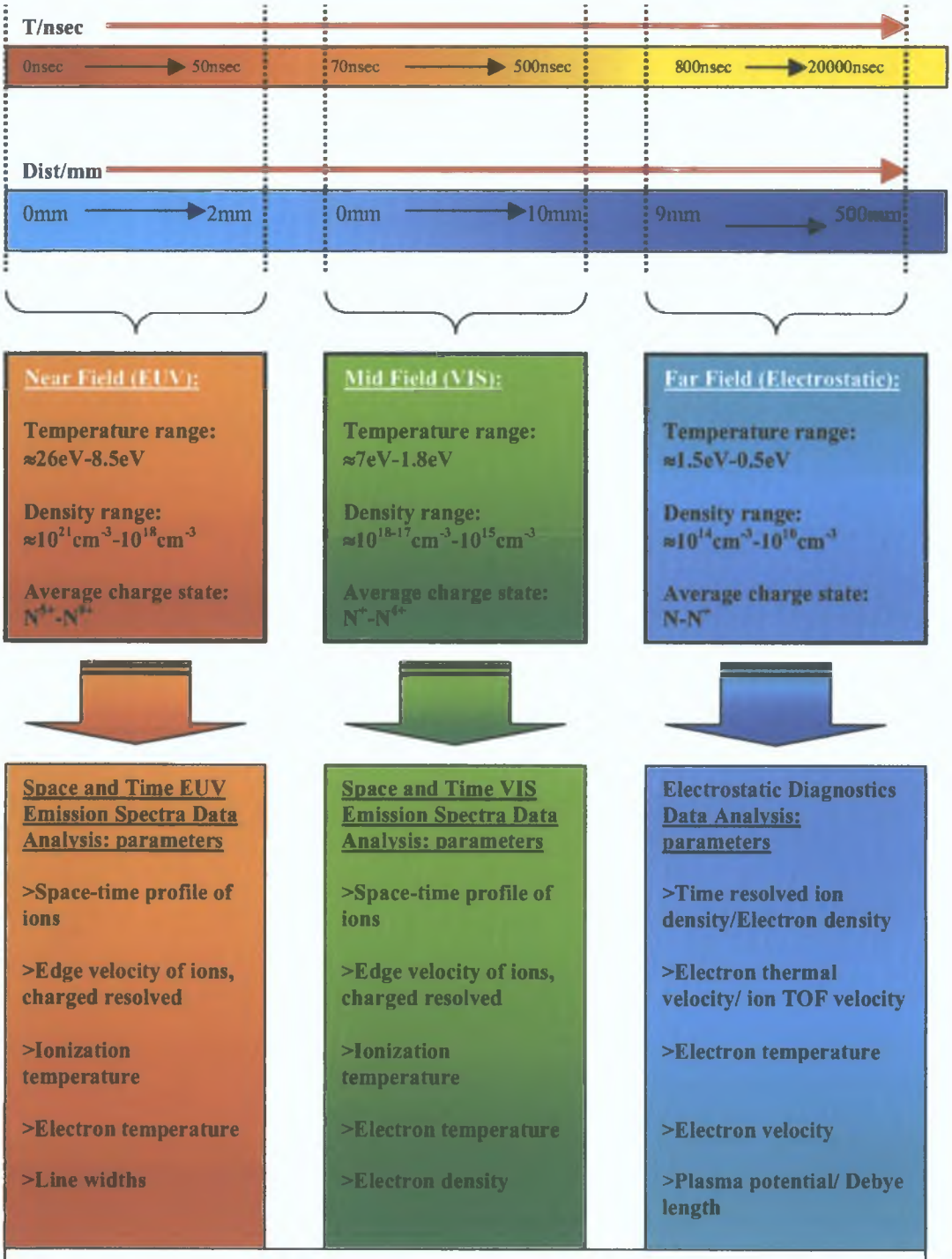

Figure 3.1.1: Diagrammatical overview of each of the diagnostic tools used to study plasma generation and evolution. The applicability of each technique is dependent on the fulfilling of criteria that each technique requires. For example, electron densities in the EUV near-field range were not possible because no electron impact parameters (W) for aluminum in that wavelength range were available. Equally, Boltzmann plots at very short time scales are impractical in the visible given the level of continuum yet are useful in the EUV. Probe diagnostics are also bound by assumptions in their interpretation of signal. Probe theory assumes that the plume consists of neutrals and singly charged ions, and thus is unable to take account of signals arising from multiply charged ions. Langmuir probe theory assumes a Maxwellian distribution of velocities in the plume. A consequence of this is the need to have a stable 'plasma current versus probe voltage' response curve. Without this, interpretation of probe signals is impossible.

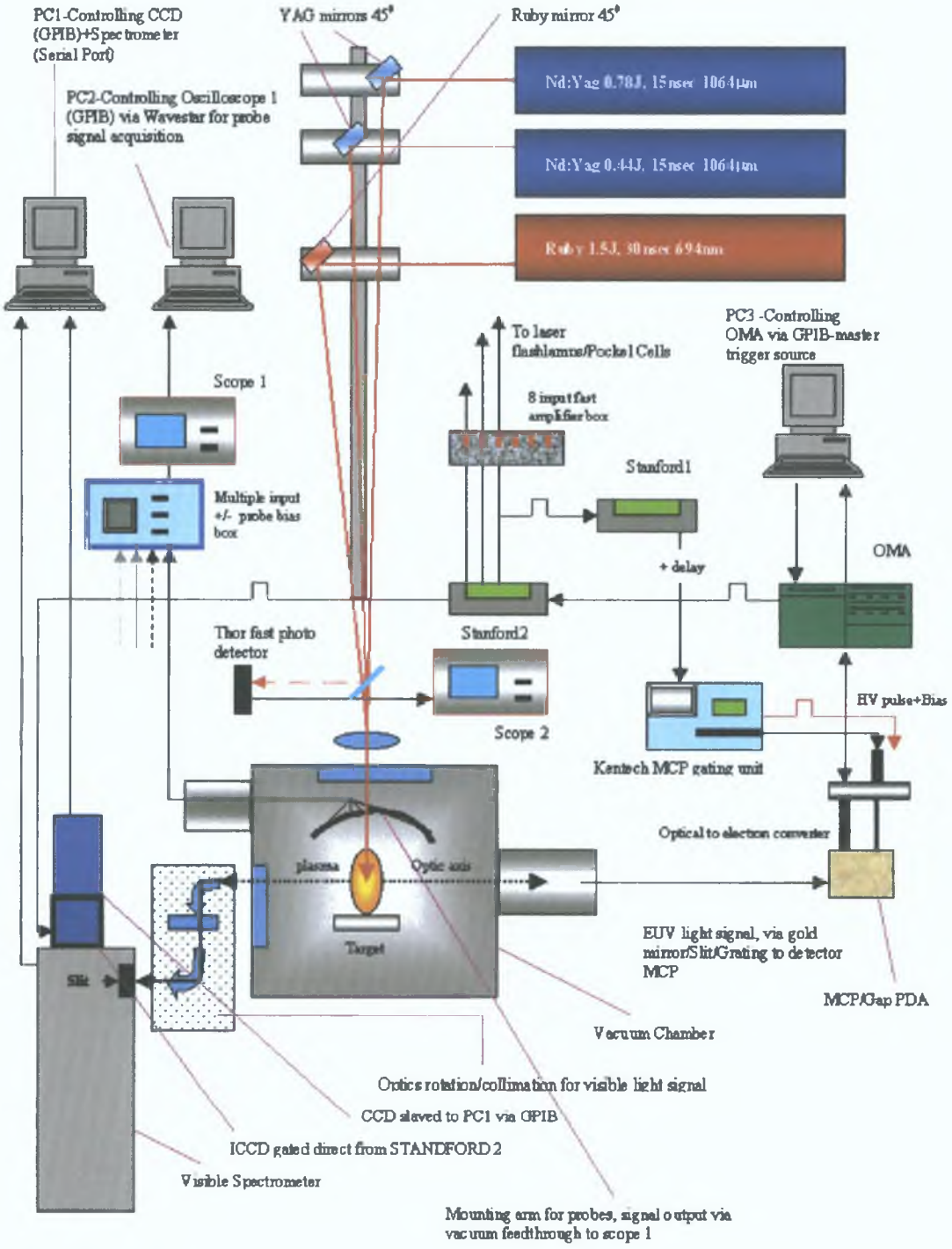

Figure 3.1.2: Overview of the experimental laser laboratory. The chief components are the three lasers, the EUV grazing incidence spectrometer, the visible spectrometer and ICCD, the OMA interface, three PC's for controlling devices, two Tektronix oscilloscopes, amplifier box, Kentech gating unit for the MCP detector head, probe bias box, optical rail with YAG and Ruby steering mirrors, vacuum chamber, two Stanford delay generators, and mounted optics (lens, prisms, optical breadboard, Thor photo detector and glass slide).

3.2: Timing and Synchronization.

3.2.1: EUV Spectrometer timing setup.

The three different type of experiments reported in this thesis, required three types of synchronization and timing. In EUV experiments the first point of control is the Dell PC, which slaves the OMA (optical multi-channel analyzer). The OMA is a Stanford Research converter, which controls the readout process of the detector's EUV signal, allowing the detector head to be PC controlled. The OMA then sends a TTL pulse to the Stanford delay generator. The Stanford triggers the flash lamps and later the Pockel cell of the lasers, for firing of laser pulses. The absolute delay is monitored via Thor fast photo detectors, which receive a few percent of the unfocused laser via reflection of glass slides. The Stanford also sends a TTL pulse to a second Stanford, which triggers the Kentech fast pulsar. This device allows the MCP detector to see a transient pulse superimposed on its DC bias voltage, thus allowing the EUV detector to be gated. Since the flash lamps and Pockel cells of the lasers require >12V pulses to fire, an amplifier box, with eight channels (six non-inverting variable gain, and two inverting variable gain) was constructed by the author. The latter uses Texas TC4428 CPA amplifier chips, which have a rise time of under 3nsec, and can be used to deliver fast pulses up to 25V

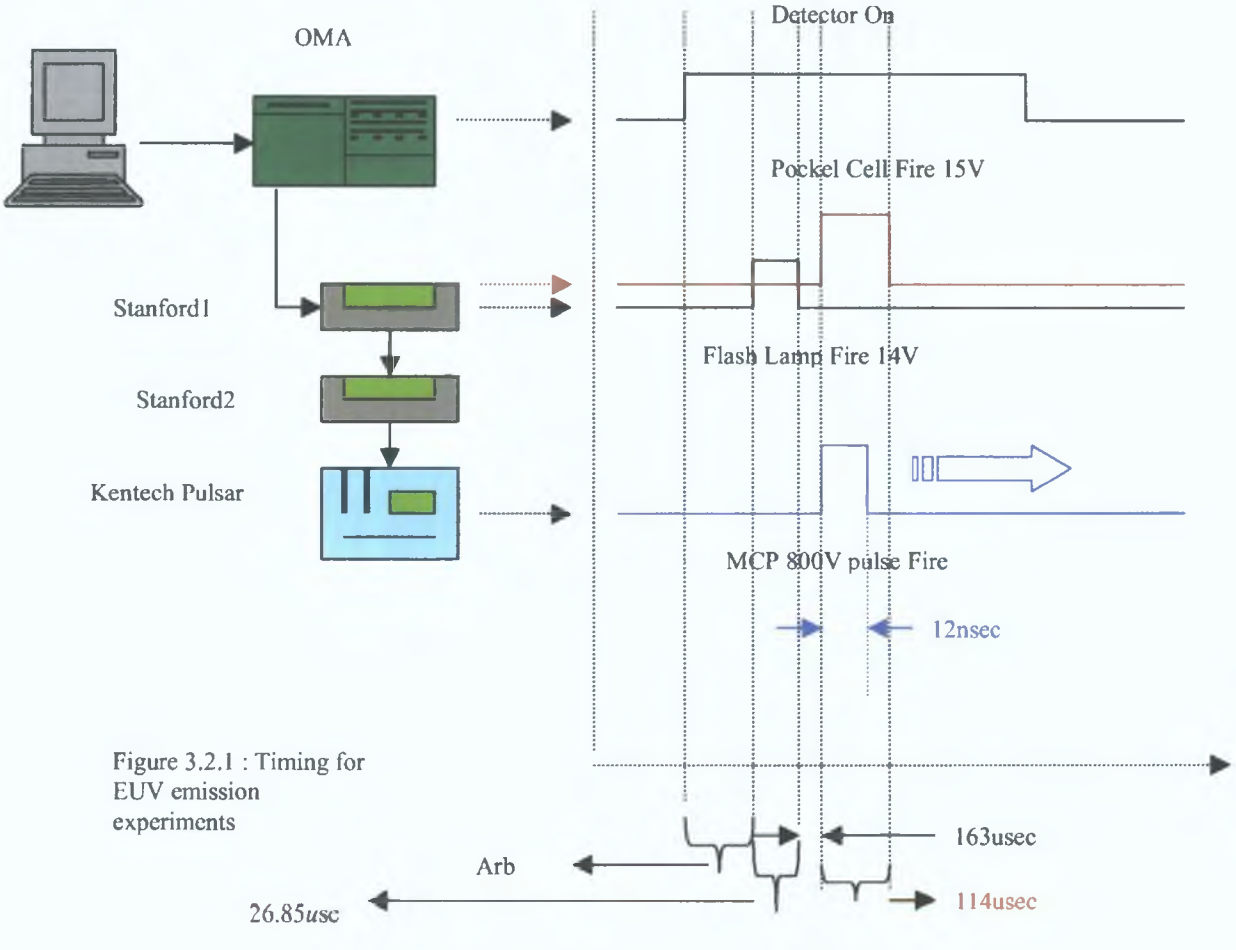

Figure 3.2.1 : Timing for EUV emission experiments

3.2.2: ICCD visible Spectrometer setup timing.

The second setup used, was that involving the ICCD and visible spectrometer. Here the master pulse was sent from the Stanford to the input trigger connection on the acquisition card of the ICCD. This then triggered the read out command on the CCD chip. The intensifier on the ICCD was controlled directly with the Stanford, via a TTL pulse of variable width directly to the ICCD head, while gain control for the intensifier was software controlled. Lastly the lasers were triggered via a Stanford pulse through the amplifier box. The total delay between triggering the laser with the Stanford and the arrival of plasma light to the ICCD is approximately 180-200nsec. This delay is due to the total transit time of the electronic trigger to the lasers, and the response time of the CCD head. The minimum gate that can be applied to the intensifier is 5nsec, and is governed by the response of the voltage driver to the intensifier head.

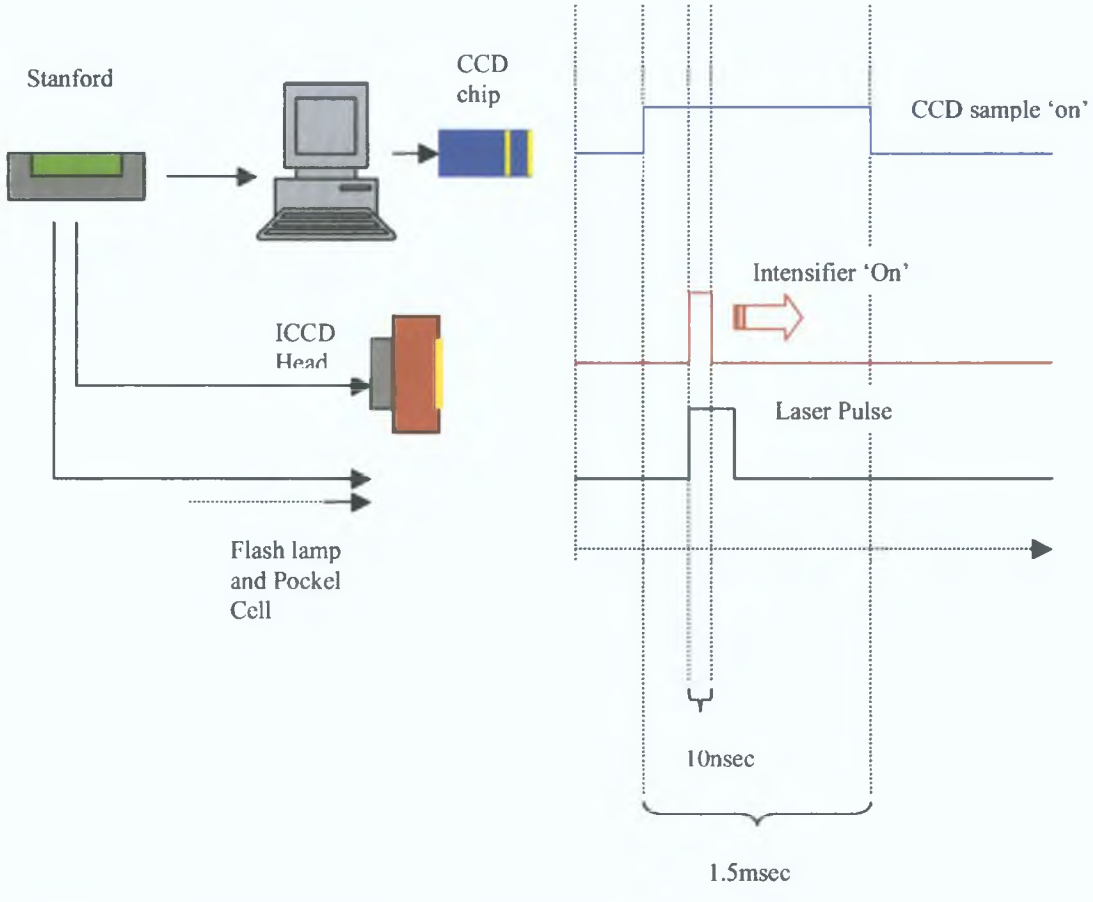

Figure 3.2.2 : Timing overview for visible emission experiments.

3 2 3 Probe timing setup

The final timing setup, involving probes, was a relatively simple arrangement The Stanford triggered the laser as above, and also triggered the oscilloscope, which was synchronized with the Pockel Cell trigger, The oscilloscope (here a HP54010A, and a TektronixTDS2400) were used to calculate the TOF velocity of the plume by observing the delay between the laser firing and the arrival of the probe plasma signal Signal acquisition and remote oscilloscope was achieved by writing a software routine in LABVIEW 5 0a to control the HP545010A, while the Tektronix oscilloscope was controlled using WAVESTAR software from Tektronix In taking plasma images with the ICCD, the above setup in section 3 2 2 was used, the only difference being the absence of the spectrometer

3 2 4 Laser systems

Two types of lasers were used in this work, a single Ruby laser and two Nd YAG lasers, giving a total of three lasers The Ruby laser, was a standard JK laser model QSR2/6 system 2000, which can be operated in free running mode or Q-switched mode The total output of the system is ~1J in 30nsec at 694nm One of the problems with this laser is the relatively large jitter on the firing of the Pockel cells and the relatively low repetition rate of this laser in comparison with other models As a consequence this laser was not suitable for time resolved visible or EUV spectroscopy

The Nd YAG lasers used here were SL800 and SL400 oscillator/amplifier systems made by Spectron Laser Systems Both lasers can be operated in free running mode or Q-switched mode In pulsed mode the laser energy from the SL800 used here was 0 75J at 16nsec at the fundamental (1064nm), while the SL400 gave 0 45J at the same pulse width and wavelength

3.3: EUV diagnostic.

Construction and operational details of the 2.2m grazing incidence spectrometer are described by (Kiernan (1994) [1]). Two major changes to this system were made during this project, namely the design and commissioning of a new target chamber, and the installation of a high speed, high voltage gating unit for the detector. The first enhancement made possible the large range of experiments reported in this work, where requirements for one type of experiment (i.e. plasma probes) were generally in conflict with requirements for others (i.e. precision emission spectroscopy in both the visible and EUV). The second enhancement allowed the response of the MCP unit, responsible for gain in the signal sensor (PDA) to be controlled, and ultimately gated for time resolved measurements. We will present an overview of the spectrometer itself first:

3.3.1: 2.2m EUV grazing incidence spectrometer.

There are five main components in the McPherson model 247M8, 2.217m grazing incidence EUV spectrometer. These are the variable entrance slit and isolation valve, the grating chamber housing the grating, the Turbo/ion pumping system, the flexible bellows and guide rail system for moving the detector head along the Rowland circle, and finally the detector chamber, detector head and supporting components.

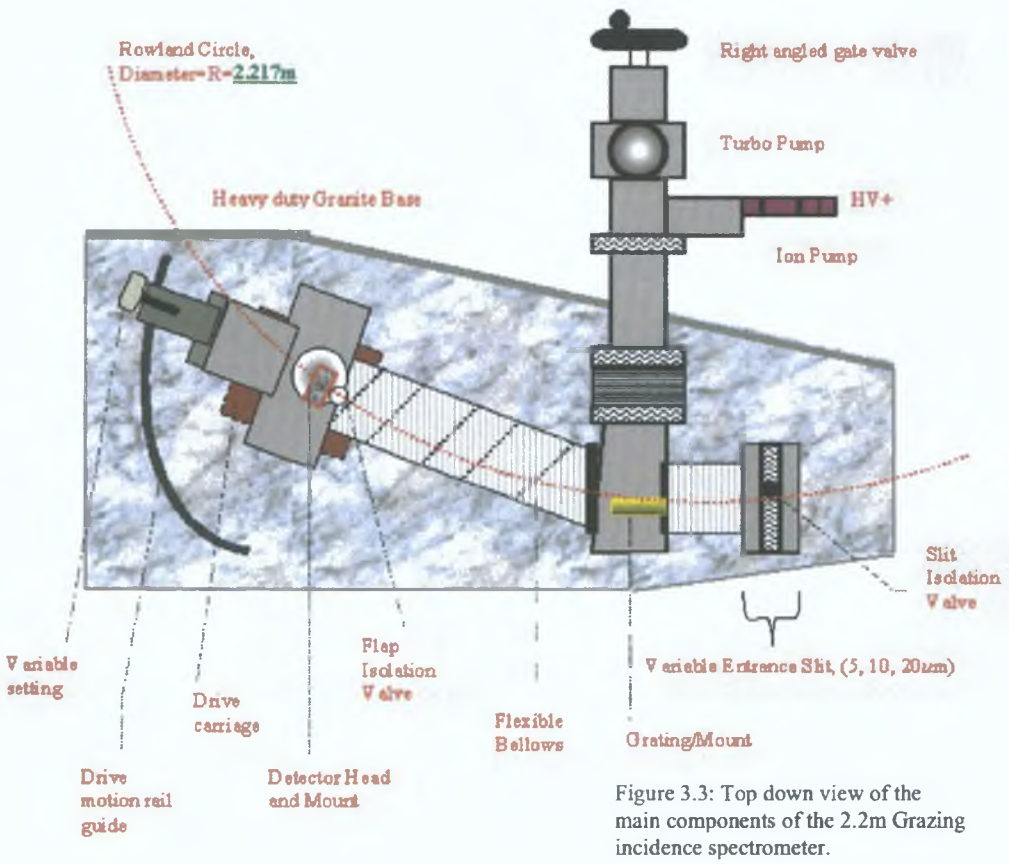

Figure 3.3: Top down view of the main components of the 2.2m Grazing incidence spectrometer.

3.3 2 Toroidal Mirror Chamber

The grazing incidence toroidal mirror chamber, is mounted in an aluminum cube in front of the isolation valve and slit It is separated from the target chamber via a gas powered DN 40 gate valve The electrically powered valve ensures that in the event of power failure, the valve will close automatically, while the absence of manual pressure from the operator opening and closing the valve, insures that no cumulative misalignment occurs over time from experimenters closing a large valve manually, as the valve is coupled to the target chamber via a flexible rubber seal To minimize contamination on the gold mirror from plasma debris and to lesson the effect of pressure differentials during laser plasma generation, a GCA (glass capillary array) is placed between the gate valve and the mirror chamber The GCA used here is a Galileo Electro-Optics Corporation device, of diameter 25mm and pore size 50μm The use of grazing incidence becomes necessary at short wavelengths (300A) due to very low levels of reflectivity at normal incidence for short wavelengths The mirror has two distinct radii of curvature, R (major radius) and r (minor radius), in the Y and X planes, a longitudinal focus at the spectrometer's entrance slit in order to maximize light throughput and parallel light in the vertical in order to obtain spectral lines of uniform height at the different detector settings along the Rowland circle

Lines focused at the detector are 10mm in height and 0 03mm in width The mirror is gold coated with the major and minor radii at 2100mm and 111mm, and the source is at 485mm from the mirror The incident flux angle onto the mirror is 82^0 The focus distance from the mirror is 230mm, at this point the light enters the entrance slit to the diffraction grating With the latter located on the Rowland circle the other components, the concave grating and detector must also be on the Rowland circle

3.3 3 Diffraction grating

Having travelled through the slit the flux now enters the grating chamber and impinges on the grating at an angle of 16^0 At this angle the blazing angle of the grating is equal to 84 34A The grating is fixed at a distance of 231mm from the slit Once the flux is diffracted off the grating the wavelengths are dispersed according to the standard relation

$$\text{Equ 1} \qquad \pm m\lambda=(\sin\alpha+\sin\beta)d,$$

where m is the spectral order, d is the groove separation and α and β are the angles of incidence and diffraction After dispersion the flux travels down the bellows that connect the grating chamber to the detector chamber and is received by the MCP/PDA detector If the detector is moved along the Rowland circle via the hand driven mechanism, a display indicates the inch setting that the detector is set at Figure 3 4 shows a schematic of the grazing incidence system in both the vertical and longitudinal planes

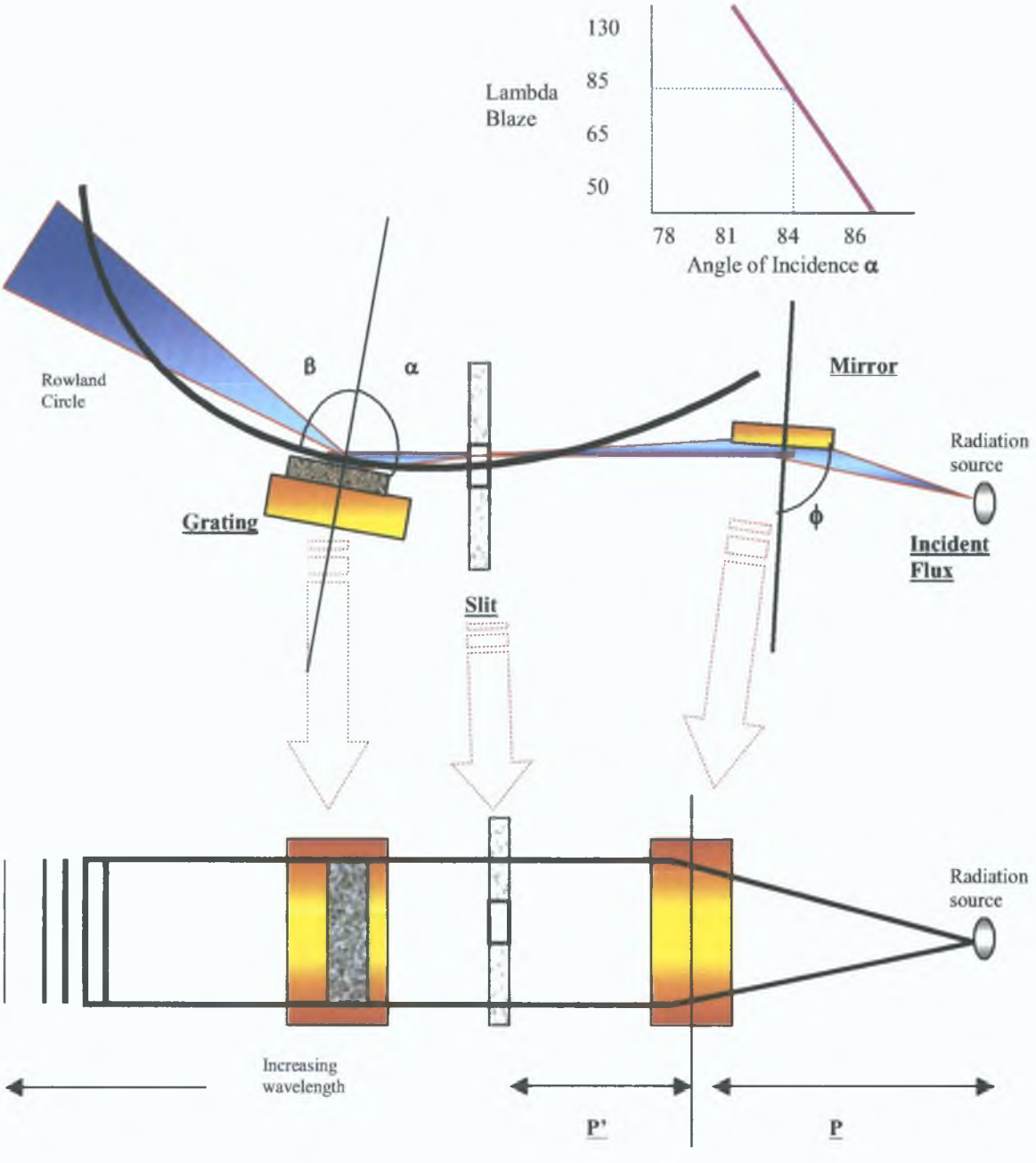

Figure 3.4: Illustration of the optical properties and setup of the system. (Kiernan [1])

Equation 2.2, 2.3: Optical properties of the grazing incidence mirror focus for object distance p, and image distance p'.

Equ 2.2: $[p]^{-1}+[p']^{-1}=2[R\cos\phi]^{-1}$ Equ 2.3: $[p]^{-1}+[p']^{-1}=2[\cos\phi][r]^{-1}$

Here r' is the cordial distance in meters, R is the diameter of the Rowland circle (2 217m) and ϕ is the angle Thus with the angle of incidence fixed at 84^0 and the grating at 1200lines/mm, the wavelength range allowed is 60 to 460A (27 to 207eV), this corresponds to an inch range of 14 5" to 30 5"

3.3 4 MCP/PDA detector

The MCP is a collection of channels over which a large bias voltage is placed (-1kV) The EUV photons impinge on the front surface of the MCP which converts the photons to electrons with a quantum efficiency of ~20% The channels are 12μm in diameter and separated by 15μm at their centers The active area of the matrix is 12 5cm^2 and covers approximately 40mm of spectral coverage at the Rowland circle The channel axes are biased at an angle of 8^0 to the incident photons with energies above 15eV

The electrons are then accelerated down the channels and collide with the secondary emitters (walls) where a gain of 10^4 occurs by the time the electron bunch reaches the exit point The OAR, or 'open area ratio' of the MCP can be increased by increasing the area of the open channels, increasing the detection efficiency Standard MCP's have OAR's typically of about 50% [4], however chemical funneling can produce OAR's of 70% Such increases in response can be important in the grazing incidence regime, where geometric shadowing can prevent incident photons from entering the channels The chemical matrix is manufactured from lead glass and treated in such a way so as to increase the secondary emission characteristics of each channel and to render the walls semi-conducting so as to allow charge replenishment from an external power supply

The emerging output electron bunch is accelerated across a gap, with a +4kV bias across it, and proximity focused upon a visible photon generating phosphor coated fibre optic bundle The bundle reduces in diameter from 40mm to 25mm, this results in a demagnification actor of 1 6 This is required to match the length of the linear PDA

The most influential parameters in defining the response of the system are the MCP bias and Gap bias The first controls the gain of the system, while the latter controls the resolution of the MCP Once incident on the PDA, the accumulated charge on each pixel is read out by a TTL signal sent from the Princeton Applied Research 1461 detector interface device The device is slaved via a GPIB connection to a PC and allows direct user control of the detector functions, such as the number of shots, shot averaging, and delay between shots The 1461 box, sends a TTL output upon triggering, allowing a delay generator to trigger multiple devices such as lasers, magnetic coils and fast discharge systems

3.3 5 MCP Gating unit

The acquisition of a Kentech fast gating unit for the MCP unit allowed the MCP to be used in gating mode The device is a fast gating high voltage pulsar, which sends a TTL pulse of variable bias and amplitude to the MCP head The device has three outputs, a DC bias (0>4 5Kv) which can bias the gap, a DC bias (0>1kV) of variable polarity which can bias the MCP, allowing integration of all signals in time Lastly a

MCP transient output is superimposed on top of the MCP DC bias. Since the MCP pulse bias is fixed at –750v, then by varying the MCP DC bias level, the full transient bias on the MCP can be varied from DC bias to -1.750kV. Secondly since from the Paschen curve for voltage breakdown per mm per mbar, the breakdown voltage for 10^{-7}mbars (detector chamber pressure) over the length of the MCP (~8-10mm) for the duration of a transient bias (16nsec min, to 100μsec safe max) is approximately 10-12Kv. Thus one can bias the MCP 'high' for the duration of the EUV emission from the plasma. Since the gain of the system is dependent upon the MCP bias voltage then the sensitivity of the detector to low flux can be enhanced considerably.

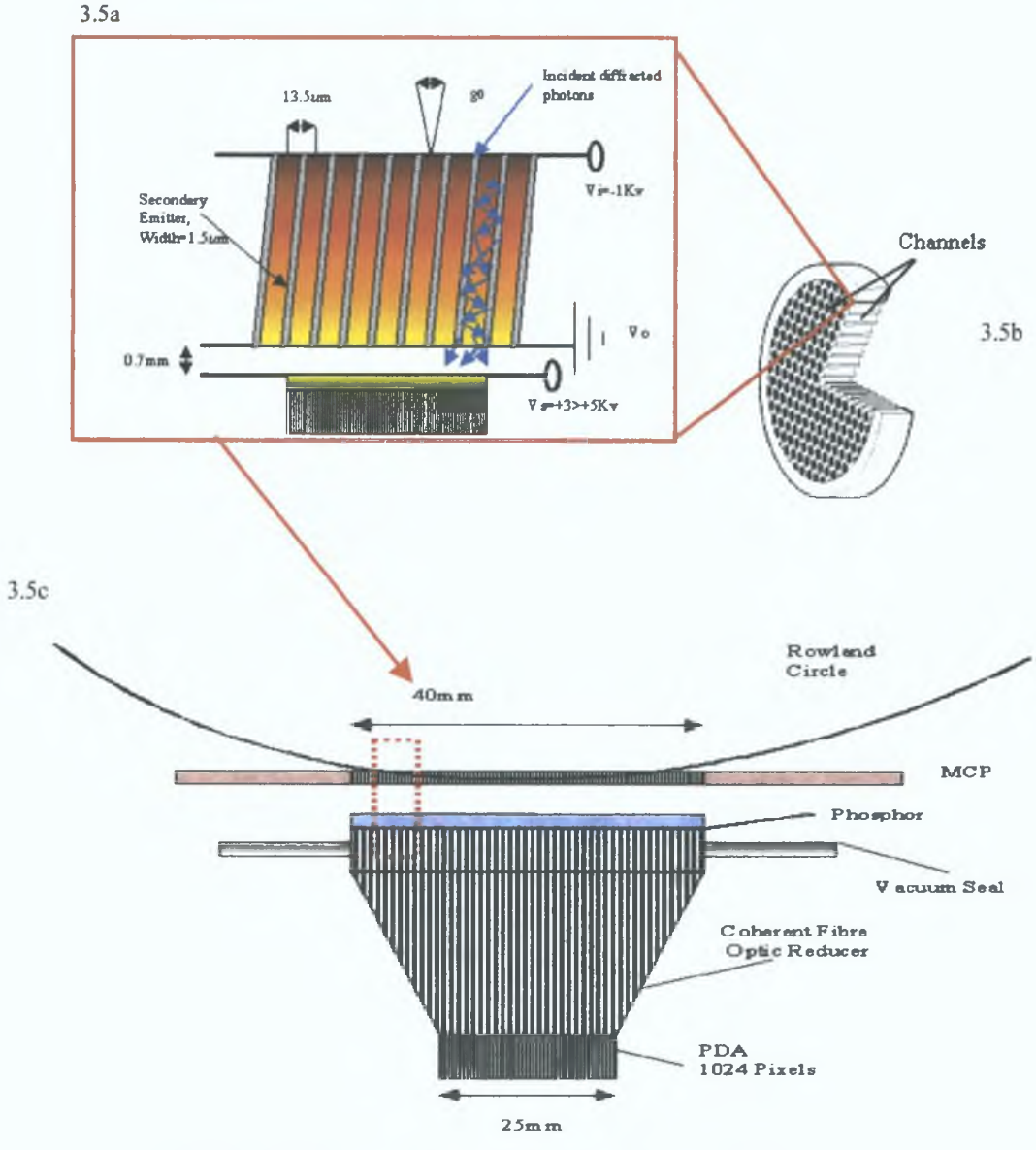

Figure 3.5a,b,c: Main components of the MCP detector system installed in the grazing incidence spectrometer.

3.3 6 Resolving power

Detailed discussions on the resolving power of the instrument are given in other references (Gray 1999 [1], and Kiernan 1994 [2]), thus only a brief over view of the resolving power of the instrument is given Resolving power and reciprocal dispersion are the two defining performance variables in a system The dispersion determines the separation of two wavelengths, while the resolving power determines the separation that can be resolved The resolving power is defined by $\lambda/\Delta\lambda=mN$, where m is the order number of the spectra, and N is the number of ruled lines Here $\Delta\lambda$ is the minimum wavelength separation which can be resolved For a slit width W, an image width on the focal curve of a concave grating on a Rowland mount will correspond to a wavelength separation of Wd/R, where d is the inter groove spacing and R is the radius of curvature of the grating A slit width of 20μm, combined with a 1200 lines/mm grating were used in this work thus giving a instrumental line width of 0 075A This corresponds to approximately 4 pixels on the PDA output By increasing the positive bias across the MCP/phosphor coat gap, the resolution of the system can be increased (Kiernan 1994) The spectra taken from any spectrometer is in fact a convolution of the recorded spectral lines and the instrument's broadening function

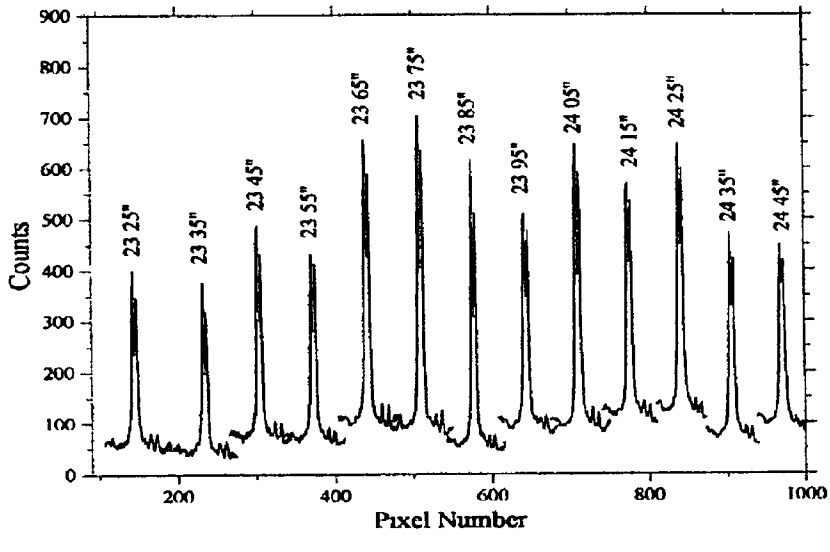

Figure 3 6 Al VII spectra at different detector settings, 13 values displayed in inch s corresponding to different cordial distances (Whitty[3])

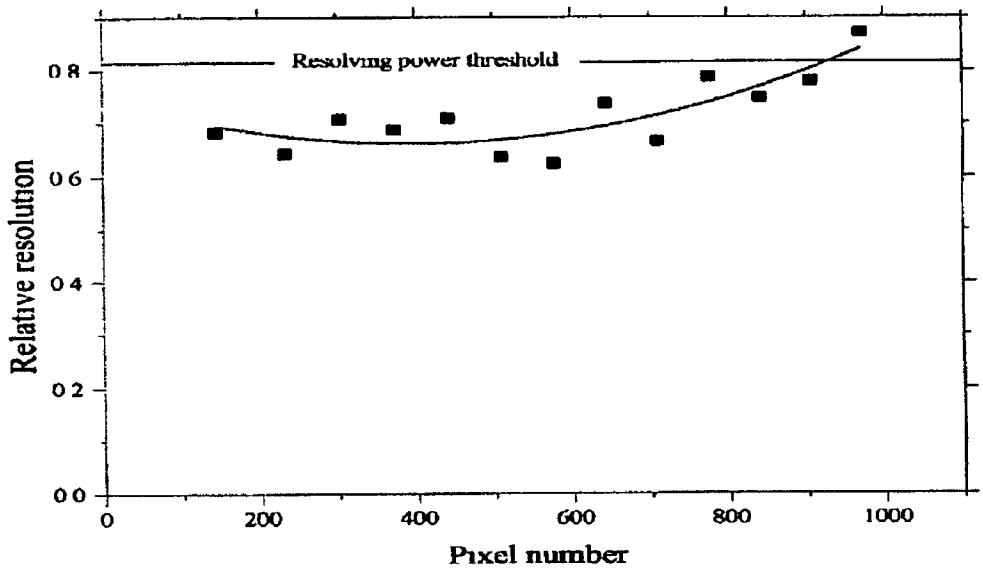

Figure 3 7 Whitty's [3] data on the variation in the resolving power of the instrument for different detector settings on the spectrometer for AL VII at 260A The points display the relative resolution of the Al VII doublet at 260A, for 13 different pixel positions

The latter depends on the width of the entrance slit, the width of one pixel in a multi-channel detector, the quality of the system components and their alignment and diffraction phenomena Measurements by Gray (1999) [2] involving the transition B^{2+} 2s-5p, gave a instrument function of 4 2meV per pixel, which translates to 4 5 pixels taken from a Lorentzian fit, which gives a wavelength broadening of 0 01 Angstroms (FWHM)

A second issue is the use of a flat detector on a curved Rowland circle Whitty (1998) [3] studied the variation in FWHM of the Aluminum line $2s^2p^6$-$2s^22p^53s$ transition at 160 074 Angstroms as a function of the detector setting Whitty [3] has shown that a spectral line is stretched for all pixel positions which are not tangential to the detector The conclusion from this was that the detector is tangential to the Rowland circle between pixels 500 and 600, thus a line imaged there is narrower then if image elsewhere on the Rowland circle via moving the detector head along the circle but keeping the line within the latter's range

3.3 7 Spatial gain across the detector

One important issue for emission studies, is the spatial variation of the response of the detector (Whitty 1998 [3]) In studying the relative shape of continuum emission from tungsten, one can see that the detector shows poor sensitivity at the higher energy end This issue is of importance in considering the intensities of emitted lines For time integrated studies, summation of plasma light over its complete lifetime can give good signal to noise ratios However for time resolved studies, one must consider which wavelength range to study with care Plasma EUV emission for work reported here did not exceed 40nsec in duration (after the termination of the laser pulse) In sampling the plasma EUV emission for durations not exceeding

10nsec (the minimum gate width for the Kentech pulsar), a preference for studying for longer wavelengths will increase the temporal duration of the plasma which one can study, by virtue of a greater sensitivity of the detector to lower energies

3.3 8 Gating issues on time resolved EUV spectroscopy

A number of problems were encountered when the Kentech gating unit was first employed in taking time resolved EUV signals Firstly, jitter from the Stanford 'hat' output at 50Ω when the pulse width is below 15nsec is not large, but on the scale of a laser plasma Here the laser pulse width is no greater then 15nsec, and this jitter creates large jumps in the registered EUV signal This is especially pronounced during the laser pulse where continuum emission changes in peak value rapidly with time The Stanford outputs are much more stable when the output impedance is set at 1MΩ However the Kentech unit will not accept a 1MΩ input To circumvent this problem the hat output from the Stanford unit was taken at 1MΩ, into a fast amplifier chip, whose output impedance was 50Ω The output from the TC4428CPA chip, whose rise time is 1 2nsec, can be varied from 6V to 18V Not only does this stabilize the output from the Stanford, but allows the non-rectangular hat from the Stanford to be better controlled in turning on the MCP pulse from the Kentech unit As a consequence, the Kentech unit can be reliably gated to its hardware minimum of 10nsec, and the turn on jitter-time can be reduced to less than 2nsec

When this approach is combined with shot averaging in the OMA software this then removes signal variation through statistical summation of differences in the peak EUV signal Another important issue for gatable studies is the problem of cratering on the target surface In the absence of drivable target mounts, crating becomes a pressing problem, especially at short wavelengths and under short sampling times The only solution available at this time was to superimpose the decay curve due to cratering onto the time dependent single The total signal fall due to cratering was seen to be 10-15% of the peak EUV signal over a range of 50 shots per surface Thus when studying the space-time emission of targets, the complete temporal range was studied at each spatial point (i e for the time range of 0-45nsec's of EUV emission, involving 9-12 time delays, the target surface was not moved, thus the decay in signal due to cratering was superimposed on the temporal profile of a signal at that spatial point This was then repeated for each spatial point studied, at a clean surface (un-cratered) Although not an ideal solution it is a viable one, given the technical constraints imposed

3 4 Visible Diagnostics

3 4 1 Chromex Visible Spectrometer

The acquisition by the CLPR of a 0 5m visible spectrometer coupled to an Andor ICCD, allowed for the possibility to add a further diagnostic tool in studying plasma generation and evolution under varying target conditions The main advantage of this system is the ability to use the CCD chip in a two dimensional mode, allowing effectively the mapping of an entire spatial region, for each time resolved event, via gating of the image intensifier

An overview of the spectrometer parameters and the ICCD operation in this work is now presented

3 4 2 Spectrometer specifications

Model Chromex 500is/sm ('500'=focal length (mm), 'is'=imaging spectrometer, 'sm'=scanning monochrometer

Grating/mm	RLD/mm	Resolution/nm	Range/nm
3600	0 53	0 0277	13 2
2400	0 80	0 04	20 0
1800	1 07	0 053	26 75
1200	1 6	0 08	40
600	3 2	0 16	80
300	6 4	0 32	160
150	12 8	0 64	320

Table 2 Spectral variables for the 0 5m visible spectrometer per grating design

Specifications

- Focal length 500mm
- Grating type Czeny-Turner with proprietary optics toroidal collimating and focusing mirrors providing aberration-corrected flat field stigmatic imaging performance
- Aperture ratio f/8 0 Spectral range 170nm to 10μm Active area 16mmx30mm focal filed area
- Reciprocal linear dispersion (RLD) 1 6nm/mm
- Slit type straight bilaterally adjustable from 10um to 2mm, computer controlled with stepper motor drive Slit height 10mm
- Wavelength accuracy ± 015nm Wavelength precision reproducibility ± 05nm

- Resolution: 0.07nm FWHM.

The spectrometer's central wavelength and slit width were controlled via a RS-232 serial connection from the spectrometer's control port direct to the computer's Andor controlled card, which slaves both the ICCD and the spectrometer to the PC. Balancing the spectrometer and ensuring that the light enters level and normal to the slit is crucial. The main components of the device are the slit, whose range of widths is 2mm to 10μm. Second is the plane mirror, which sits at 45^0 to deflect the light along the spectrometer's axis, where it propagates, impinging on the first collimating mirror. It then reflects back along the spectrometer to the grating, where the light is dispersed and directed onto a second collimating mirror, which focuses the light into the focal plane, exactly at the adaptor port where the ICCD is coupled to the spectrometer housing. If the alignment is not optimized then as the light source moves away from the target (i.e. the plasma) the emission lines on the CCD curve strongly to one side (left or right) as the second collimating mirror enhances any error in the alignment when the dispersed light is focused onto the focal plane of the spectrometer. In the setup used in this work, the slit width was varied from 50μm to 1mm and the spectral resolution was observed. Too small a slit width gave insufficient light flux, the flux being already low, given the two dimensional dispersion used here (wavelength and space). Thus for the optical system used for light source rotation, the optimum slit width was from 300-450μm.

The sensitivity of the ICCD to stray light was such that all experiments had to be performed in darkness, while scattered light from the plasma, which was not collimated by the first lens in the optical setup was 'blacked' out via a large non-transparent matt black plate, between the three prism rotation system and the chamber port (figure 3.8.2).

Figure 3.8: Chromex 0.5m Visible spectrometer, mated to the Andor ICCD camera. Direct connection to the ICCD head allowed the head to be gated directly from a Stanford delay generator.

3.4.3: Experimental System Configuration and optics

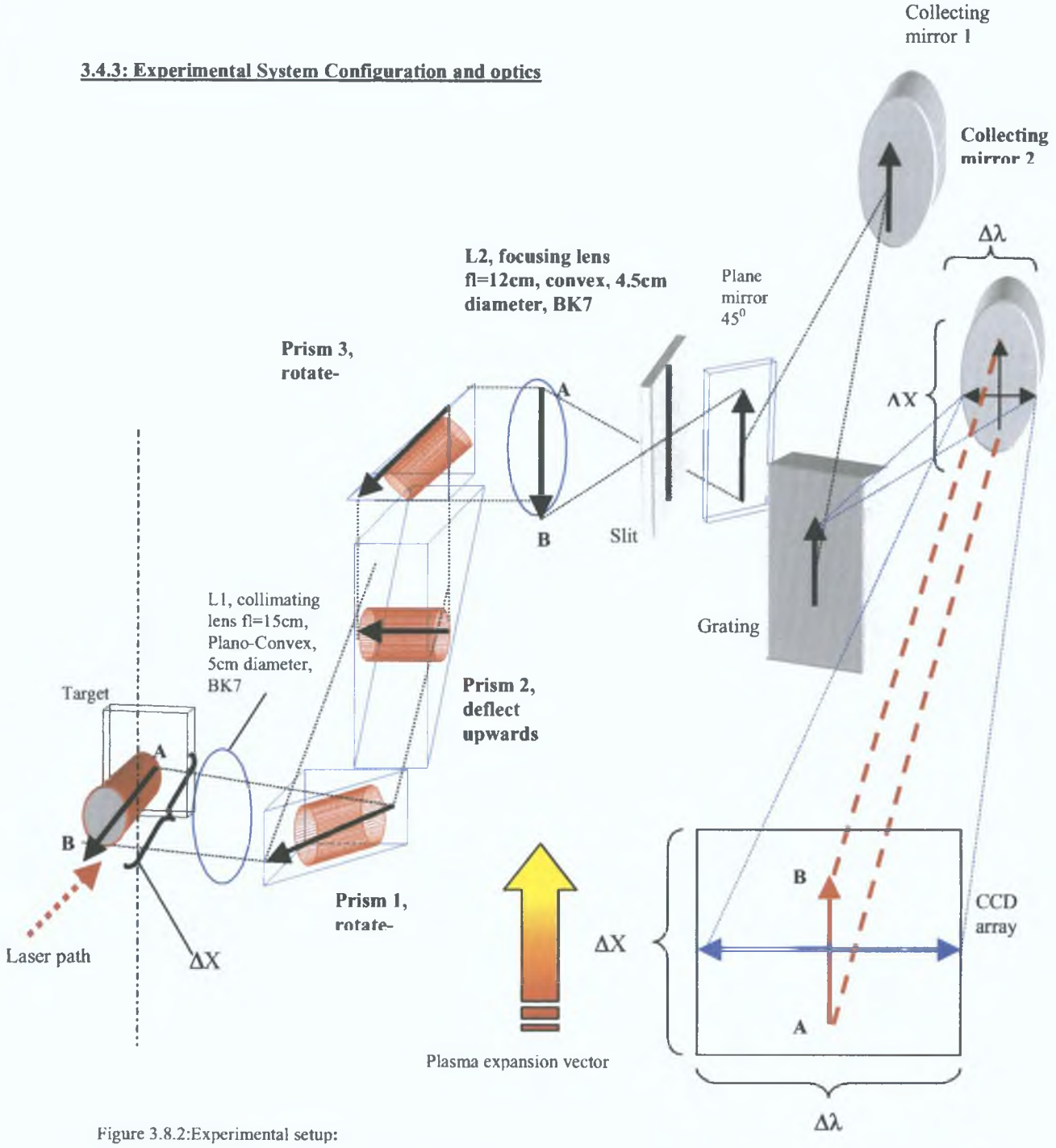

Figure 3.8.2:Experimental setup:

Optical Setup for beam rotation and collimation. The three prism system facilitates beam rotation through 90^0 to allow full spatial acquisition of the plume over its volume. The two lens system, required to collimate and then focus the plasma light gives a magnification of 1.25, spreading the plasma over the entire extent of the CCD at the longest time delay (450nsec), at which point the plasma emission for the selected ions decays below useful levels. For direct imaging, the same two lens system was used to image the plume onto the CCD directly, using a magnification of 1.5, and employing a neutral density filter for the first 100nsec (1.5%transmission).

3.4.4: CCD.

A **Charged Coupled Device,** or CCD is a silicon based semiconductor chip bearing a two-dimensional matrix of photo-sensors or pixels. This matrix is usually referred to as the image area. The pixels are often described as being arranged in rows and columns. The typical CCD-chip usually has between 256 to 1024 rows and columns, depending on the design. When light falls on an element, electrons (photoelectrons) are produced and, in normal operation these electrons are confined to their respective elements. Thus CCDs are essentially metal-oxide-semi conducting (MOS) capacitors (see figure 3.9). The capacitor is formed by growing a layer of silicon dioxide on a silicon substrate (usually p-type). A metal electrode is then evaporated on the oxide layer. The metal electrode is known as the gate and is biased with a positive voltage relative to the silicon substrate. The impinging of light in the cell, leads to the generation of positive hole, negative electron pairs within the silicon. The bias voltage potential between the substrate and the gate, pulls the negative electrons to the surface of the silicon, under the gate. They will remain there so long as the potential is maintained. The total charge held at the surface will depend directly upon the light flux upon the silicon. If the light flux is too high then the CCD cell will saturate, and the readout time, fixed by the device will only partially discharge the cell. If continuous use of the CCD chip with saturated signal occurs, permanent damage to the device will result. Namely the quantum efficiency of the device will suffer. Thus in this work, although the flux from a laser plasma is high, that flux is evenly distributed over the CCD chip, and thus saturation on a particular pixel cannot occur. However when in imaging mode, the camera is exposed directly to the plasma light. Secondly plasma light has a very high divergence rate per unit transit of space. Thus a two lens system was required to collimate and refocus the plasma light. This produced very high flux on the CCD chip, thus it was necessary to lower the flux via a neutral density filter for each timescale (<100nsec). Later camera models allow the readout time to be set by the user, thus changing the response of the device to impinging light.

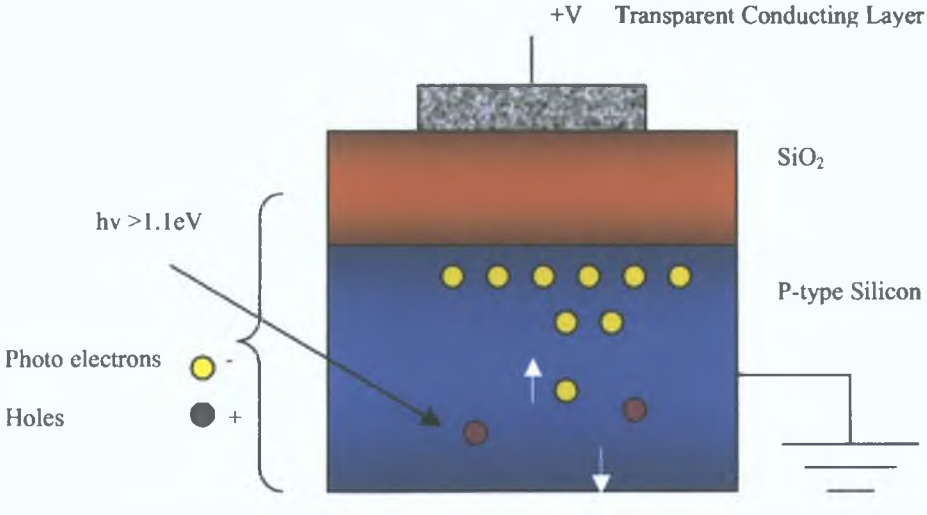

Figure 3.9: MOS capacitor structure. When a positive bias is placed on the gate, photo generated electron-hole pairs are separated. The electrons are pulled to the SiO_2 gate interface.

If an image (or any light pattern) is projected onto the array, a corresponding charge pattern will be produced To capture the image into computer memory, the charge pattern must be transferred off the chip, and this is accomplished by using a series of horizontal and vertical transparent electrodes that cover the array By suitable clocking of the electrodes, the latter can be used to shift or transfer the entire pattern of charge in one row, down into the shift register (extended electronic memory for read out)

The shift register also has a series of electrodes which can be used to move the electronic pattern on to an 'on-chip' amplifier The output of the amplifier feeds the analog-to-digital converter (A/D), which in turn converts each charge packet into 16-bit binary In the course of readout, charge is moved vertically into the shift register, and then horizontally from the shift register into the output mode of the amplifier Thus the charge accumulated by each pixel, is read out One can 'bin' the pixels, i e add the pixels in a particular area to register as a single pixel, thus increasing the measured signal This is chiefly done when the signal to noise ratio is not good, and thus enhancing the signal via binning can help to overcome this However, in binning one is effectively lowering the spatial resolution, and the extent to which the device can resolve spatial detail

3 4 4 ICCD

An image intensifier is a device that amplifies the intensity of an image, not the size of the image The device is small, typically 1 to 2 inch's in diameter by about 1 inch thick An image is projected on to the input window of the device and an intensified image appears on its exit window (usually fiber optic plate) As well as amplifying the image, the intensifier can be rapidly switched on and off, allowing it to be used as a very fast shutter The intensifier used in this system is known as a second generation tube This is a proximity focused device which is compact and, more importantly is easily gated to 5nsec time-scales There are three major elements in an image intensifier The photo cathode, the micro channel plate, and the phosphor screen The input image impinges on the photo cathode, and when a photon strikes the photo cathode, an electron is emitted and this electron is drawn across a small gap (~0 2mm) towards the micro channel plate by an electric field The MCP plate honeycomb channels (~10microns) has a resistive coating A high voltage is placed across the MCP (500-1000V), so that the photoelectron will cascade down the channel producing secondary electrons and exiting as a cloud of electrons The resultant amplification can be as high as 10^4 The cloud is then accelerated across another gap (~0 5mm) by a potential of several hundred volts and strikes a phosphor coating Since the primary amplification of an image intensifier is due to electron cascade in the MCP plate, varying the voltage across the MCP plate can be used to control the gain The enhanced photon signal is then coupled to the CCD chip either via a fiber bundle or a lens system The ICCD used in this work uses a lens system Figure 3 10 displays the spectral response of the intensifier The Andor ICCD camera used here had an active area of 1 77cm^2 The CCD array was composed of 1024 by 1024 Pixels each 13μm square The camera had variable gain (1 50) and was fitted with an image intensifier which when gated could allow for time resolved measurements The minimum gate time was 1 2nsec (Andor specifications), with a spectral range of 180nm-850nm When the

intensifier was coupled to the Chromex visible spectrometer in a specific configuration (discussed later) the plasma could be spectrally dispersed over the entire spatial expansion of the plume, allowing space resolved spectroscopy at each time delay after the laser.

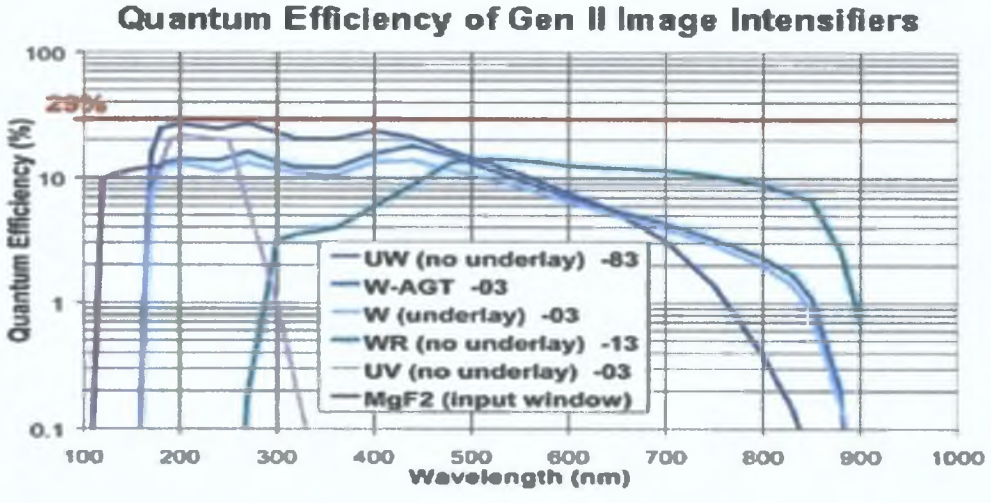

Figure 3.10: Wavelength dependence of the quantum efficiency of image intensifiers. (Andor technology)

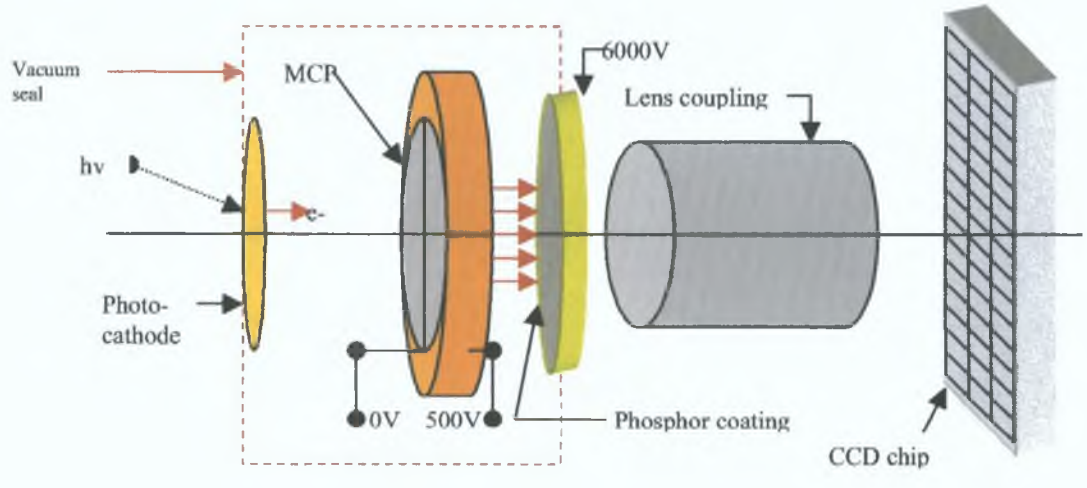

Figure 3.11: ICCD unit overview. The main components are the 2D CCD matrix, the photo-cathode, the MCP and the phosphor coated fibre-optic window.

In the work reported here, imaging and spectral analysis was done over two distinct time domains. First, the early emission from the plasma (<500nsc) was studied. For taking spectra here the intensifier was gated for 25nsec, while no gain was required. For imaging the plume dynamics for this time period, the gate was reduced to 11nsec (depending on the target and laser). The readout time was kept constant

3.4.5: Data acquisition parameters and issues.

Time delayed images of a laser plasma from a flat aluminum target. For the power densities used in this work ($I>10^9 Wcm^{-2}$), the first 50-60nsec of visible emission is continuum dominated and no lines can be properly resolved. As the continuum decays, line emission becomes more pronounced, and with increased time delay, ions are observed to more rapidly away from the target surface. The 2dimensional nature of the CCD allows one to study this process in real-time.

T_d=40nsec

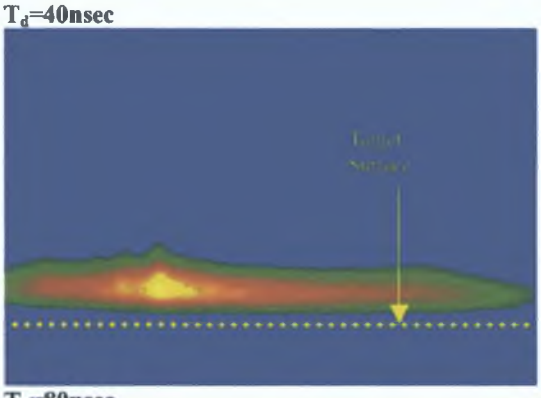

T_d=80nsec

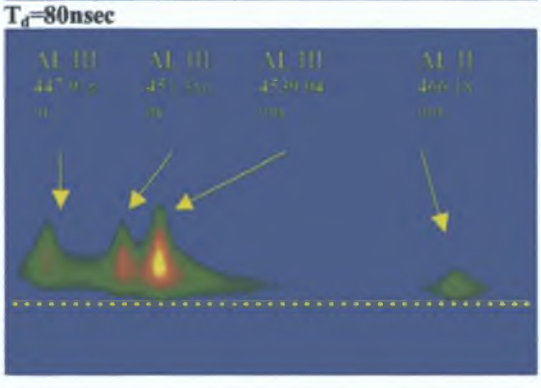

Figures 3.12.1-3.12.5: A sample of space resolved visible emission over the spectral range 447-467nm, for various time delays. Here the continuum is clearly visible at 40nsec. As the time delay after the laser pulse increases the lines emerge from the continuum as the plume expands and cools. Clear differences can be seen in the extent of the expansion of the three AL III lines, in comparison to the single AL II line.

T_d=120nsec

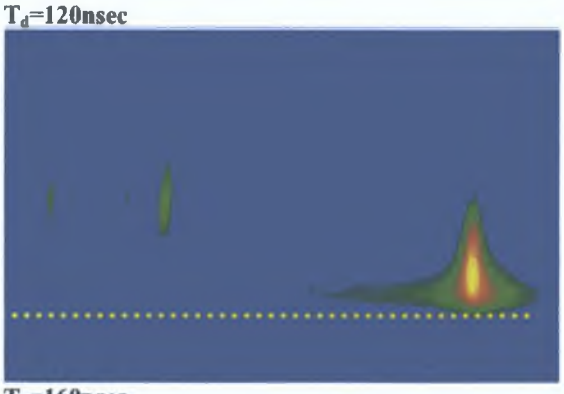

T_d=160nsec

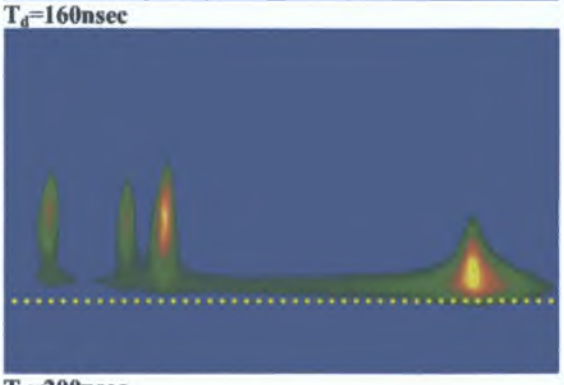

T_d=200nsec

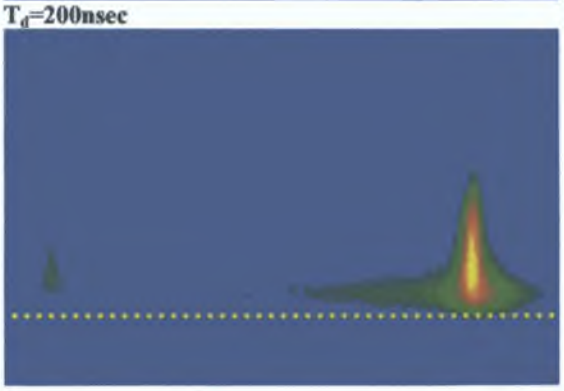

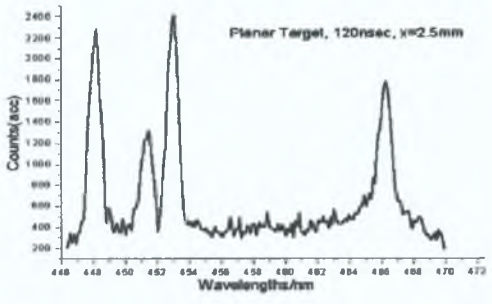

Figure 3.12.6: Sample emission spectrum.

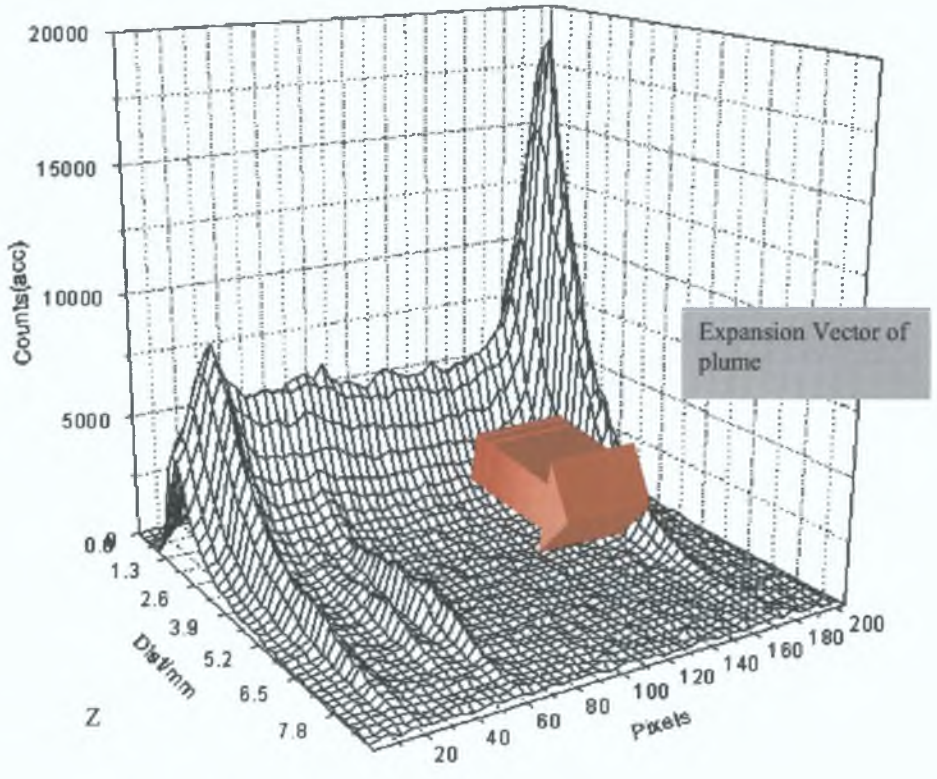

Figure 3.13: 3D Space-wavelength profile at 160nsec after the arrival of the laser pulse onto a flat target. Long lived recombination continuum near the target surface, while the difference in the spatial extension of the three AL III lines compared to the lower stage AL II is clear.

at 16μsec for all experiments, while binning of pixels was set at 4×4 for spectra and 2×2 for images. The second domain was with very long timescales when visible emission from the plume was not intense. In this phase the gain was set high (gain=100, depending on the experimental conditions) while the gate was increased to 20nsec. The total 'capture' (distances from the target surface) of the images and visible spectra was approximately 11mm for the telescope system used in spectra studies, while in imaging mode, the range seen was 4-5cm from the target, thus for the 3D plot in figure 3.13, continuum is placed at the origin (Z=0mm), and as the plasma expands away from the target surface (indicated by the red arrow), it moves along the Z axis. Obviously as the plasma decays and dims, greater gain on the intensifier was required.

Given the difficulty in moving a target and lens in a standard 1D spectrometer, the 2D nature of the CCD and the use of rotating optics allows for exceptional versatility. One aspect of using such a system is the careful balancing of gate width, binning values, gain and the system magnification of the optics used to couple plasma light to the spectrometer slit. Generally one uses space and time resolved line intensity profiles, however these are especially vulnerable to misinterpretation if certain criteria are not followed.

For example, one should always minimize the gate width in order to properly characterize time resolved spatial intensity distributions This may lower the peak photon count considerably, especially if the plasma light is being directed and reflected by multiple optical components, as was used here Thus to off set this, and to give good signal to noise levels, many shots were summed (>15) Increasing the ICCD gain is also a viable option to off set photon loss in systems, but this has the undesirable effect of also amplifying the signal noise This balance between signal-noise and short sampling times was found to be very important for reliable diagnostics in the visible (line widths, intensity ratios etc)

3.5 Electrostatic Diagnostics

3.5 1 Probe Diagnostics

A probe is usually a small metallic electrode which is immersed in the plasma Generally the probe is connected across a voltage potential and referenced to some grounding connection The general procedure is to measure the current flowing from the plasma to the probe Under suitable conditions the charge carrier concentration, the potential and the velocity distribution of electrons of the undisturbed plasma in the vicinity of the probe tip can be calculated from the plasma response to the applied voltages The range of applicability of probe methods varies over a large range of pressures (several orders of magnitude) However despite this the use of probes is subject to many restrictions The advantage of a highly localized measurement and good temporal response is offset by the difficulty for data interpretation requiring proper correction for factors which come about as a consequence of the probe's placement in a highly energetic medium Although probes were used at the turn of the century by Crookes in gas discharges it was not until the early twenties that Langmuir and his co-workers formulated a method of analysis which became one of the most important means of plasma diagnostics Langmuir confined his analysis to low pressure plasma, where collisions are negligible Despite the limitations placed on the analysis by this approach, it still forms the backbone of today's approach to diagnosing the plasma parameters The analysis of plasma parameters is restricted to those which show a Maxwellian velocity distribution of the charge carriers The development of double probes, and more advanced forms of analysis have consistently improved the reliability of probe measurements Still there are a number of important assumptions made during the use of probes (Lochte-Holtgreven[5])

1 The plasma is infinite in extent, homogeneous and quasi-neutral in the absence of the probe

2 Electrons and ions have Maxwellian velocity distributions with temperatures T_e, and T_i respectively with $T_e >> T_i$

3 The mean free paths of electrons λ_e and ions λ_i, are large compared to all other relevant lengths

4 Each charged particle hitting the probe is absorbed by the probe and no reaction with the probe material occurs

5 The region in front of the probe surface, where the plasma parameters deviate from their values in the undisturbed plasma is confined to a space charge sheath with a well defined boundary Outside this layer the space potential is assumed to be constant

6 The sheath thickness d, is small compared to the lateral dimensions of the plane probe, hence edge effects can be ignored

In reality this analysis is confined to large volume, steady state plasmas. Thus the expected behaviou deviates from that seen in reality, where laser plasma plumes are studied, due to their highly energetic and transient nature. Not only is the plasma transient, but the plume is in motion, flowing over the probe surface and undergoing hydrodynamic expansion, and deflection from all solid surfaces, the probe tip included.

The source itself, the highly energetic, highly charged plasma plume, is created by ablation of a solid body, thus cratering, and the resulting variation in the generation conditions is a large cause of signal variation at high fluence. As a consequence of this one must average many shots, and usually after the IV curves (voltage response curves) have been formed, one must employ smoothing and filtering to properly interpret the signals). This is especially so for laser plasmas, at high fluence. Probe theory assumes that the plasma is homogeneous and that the electrons and ions are in separate thermal equilibrium, with the electron temperature being larger then the ion temperature. Analysis of the I/V curve characteristics of the plasma were studied using both the accelerating and the retarding regions by applying both Langmuir theory and Orbital theory (W. Lochte-Holtgreven [5]). In a collision-less, thin sheath theory it is assumed that all charge carriers that enter the sheath edge fall on to the probe and register a signal. The collected probe current should reach a saturated value I_e(sat) when probe bias voltages (V_B) greater then the plasma potential (V_p) are applied. Thus a time trace of probe signal will cross the zero axis (positive ion signal to negative electron signal) at a different bias voltage for each time event (figure.3.14).

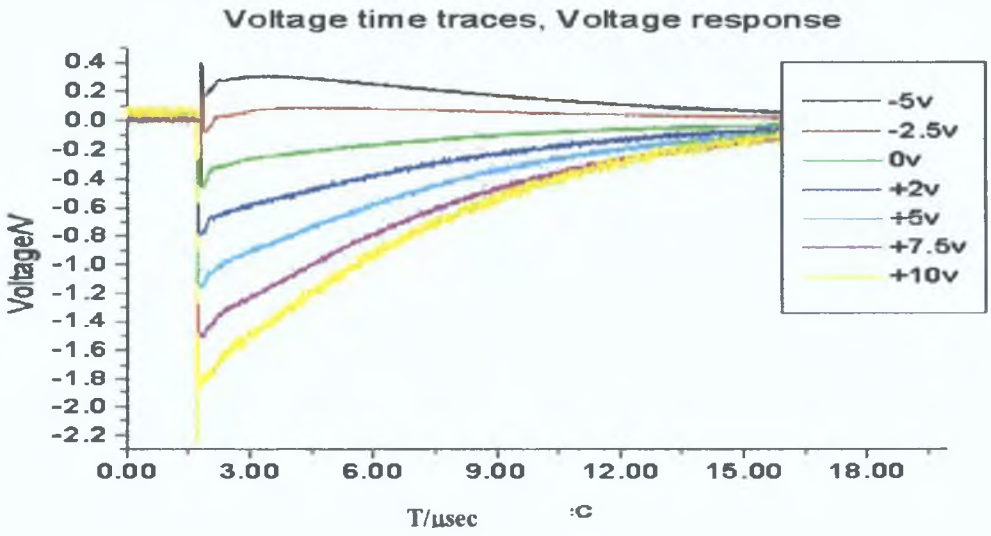

Figure 3.14: Characteristic time trace for the electron probe for different bias voltages.

In this work, the minimum voltage step found to yield reliable IV curves was 0.1V while the maximum did not exceed 0.4v. The voltage range over which the probe was biased varied with the fluence, target type, individual target dimensions and pressure. However the usual range of bias voltages were –5v to +12v. This was sufficient in most cases to acquire both the saturated ion and electron signals. Typically in our

work, the target surface was cleaned with 5 pre-shots, and then a further 3 shots were averaged In this way we could build up the IV curves at every time resolved event for analysis

When the IV curves have been built up, then one must chose a single time resolved event, and plot the natural log of the current versus the bias voltage One must take care to subtract the ion saturation current from the total probe signal In most studies of probe use with laser plasmas or other transient plumes, the electron saturation signal is seen not to saturate, but instead to increase linearly with probe bias voltage (Weaver et al [7) This is due to the growth in the sheath radius around the tip The increasing bias creates a space charge layer, which is localized around the probe The larger the bias voltage, the greater the electric field strength, and the greater the radial influence of this field Thus the charge layer region attracts more charge to its vicinity, and thus the sheath radius grows Thus as a consequence the probe registers an increasing signal, instead of saturation

From the analysis given by (W Lochte-Holtgreven [5]), and applied by (J M Hendron et al [6]) we now present the mathematical analysis of raw data traces for interpretation of plasma parameters

3 5 2 Electron Probe Theory

From (J M Hendron et al [6]), the electron density can be calculated as

$$\text{Equ 1} \qquad I_e(sat)=0\ 25\times N_e V_e A_p \times e$$

where A_p is the probe area, $I_e(sat)$ is the electron saturation current, and V_e is the average thermal speed from

$$\text{Equ 2} \qquad V_e=\left(\frac{8kT_e}{\pi M_e}\right)^{1/2}$$

where M_e is the electron mass, and k is Boltzmann's constant As the voltage on the probe tip is made more negative relative to the plasma potential, only those electrons whose kinetic energy is high enough to allow them to overcome the electrostatic potential on the biased probe tip can register as signal Thus for a Maxwellian electron energy distribution the collected electron current I_e in this region is given by (J M Hendron et al [6])

$$\text{Equ 3} \qquad I_e=0\ 25\times N_e V_e A_p \times \exp\left(\frac{-eV_B}{kT_e}\right)$$

Thus kT_e can be calculated from a plot of $Ln(I_e)$ versus probe voltage The slope of the linear region just before the knee of the curve for positive voltages gives the electron temperature in Kelvin The plasma

potential V_p can be obtained from the voltage position of the knee of the curve where the probe voltage changes from electron retarding to electron accelerating In most fast transient plasmas it is found that the electron and ion saturation currents do not in fact saturate, but show a corresponding increase in signal as the probe voltage is increased

The sheath thickness is given by (J M Hendron et al [6]) as

$$\text{Equ 4} \qquad S=\frac{\sqrt{2}}{3}\lambda_D\left(\frac{2e|V_p-V_B|}{kT_e}\right)^{3/4}$$

where V_B is the bias voltage In our work this did not exceed +12V Under such conditions the sheath size can therefore increase from 100-255μm Thus with sheath expansion, and again assuming a Maxwellian electron energy distribution, then during the incoming trajectory of electrons, an I_e^2 dependence on probe bias voltage can be expected (Weaver et al[7], Lochte-Holtgreven [4]) Then using orbital motion theory, the relationship between electron current and voltage in the accelerating region can be deduced, as demonstrated by Weaver et al [7]

Orbital motion theory predicts that the current on a cylindrical probe operating in saturation (electron accelerating region) is given by

$$\text{Equ 5} \qquad I_e=N_e\times e\times A_p\times\left[\frac{kT_e}{2\pi M_e}\right]^{1/2}\frac{2}{\sqrt{\pi}}\left[1+\frac{e(V-V_p)}{kT_e}\right]^{1/2}$$

assuming a Maxwellian electron distribution Here N_e is the electron density, e is the electron charge, and A_p is the surface area of the probe, kT_e is the Boltzmann temperature, M_e is the electron mass, V is the applied voltage on the probe, and V_p, the plasma potential A physical condition of applying orbital motion theory is that the plasma sheath dimension must be greater then the probe radius The electron number density under these conditions is then taken from the slope of the square of the electron current versus the applied voltage

$$\text{Equ 6 1} \qquad N_e=\left[\frac{M_e\pi^2(dI_e^2/dV)}{2A_p^2e^3}\right]^{1/2} \quad \text{(Weaver et al [7])}$$

In this work, we interpolated the raw data This was necessary to ensure smooth slope evolution from one time resolved curve to the next Otherwise the temporal profile of the electron temperature became unstable due to the influence of large negative log values, themselves stemming from very small negative signals The latter was a consistent problem as the signal changes from ion (positive) signal to negative (electron) signal In order to process these IV curves for data calculation at as many time resolved points as possible, a software package was written in MATLAB 6 0 (this is described in greater detail in appendix A) This

imported the 50-60 current traces over the bias range, and formed the IV curves over all temporal values (ignoring very earlier times where the traces are very unstable, due mostly to fast transient plasma, where the stable low velocity plasma has yet to reach the probe). Automatic linear fitting of both the retarding region and the saturation region allowed electron temperature/ density/ velocity, and plasma potential to be automatically calculated. IV curves are unstable at both very earlier timescales, where stable sheath growth has yet to develop, but also at very late stages in the plumes lifetime. This is primarily due again to small signals.

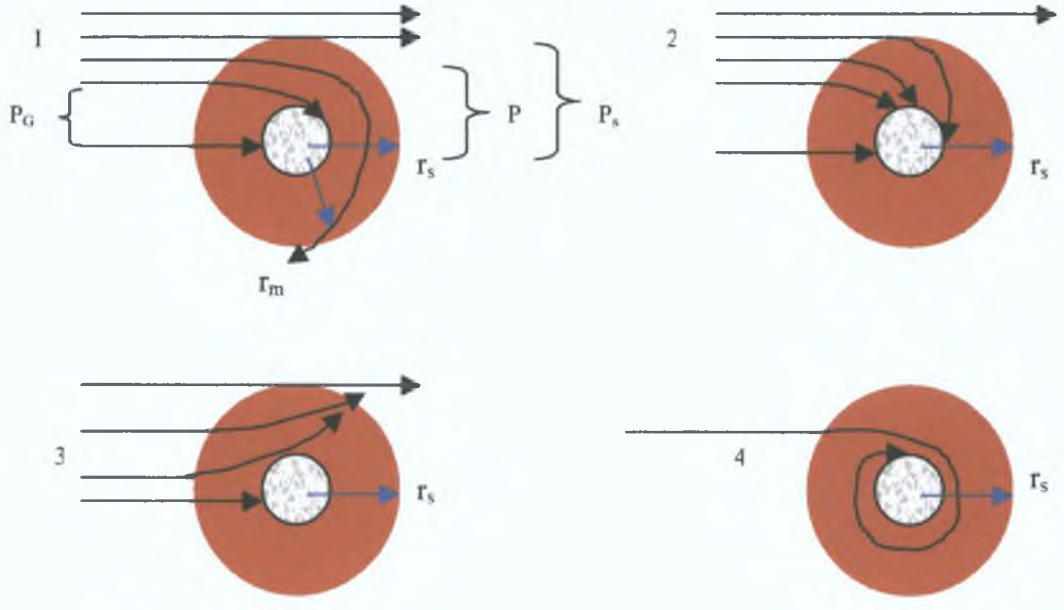

1: qV_p <0; orbital motion limited current.
2: qV_p >0;
3: qV_p <0; Sheath limited current.
4: qV_p <0; particle motion to a probe in a dense plasma (r_p>>h).
Figure 3.15: Orbital relation for charge capture. Schematic cross-section of a cylindrical/spherical probe and particle orbits (Lochte-Holtgreven [5]).

The central difference between Orbital and Langmuir theory is shown above (figure 3.15). Essentially here the two theories differ in the interpretation of the particle cross sections and velocity distributions. From T. N. Hansen et al [8], we can subdivide a streaming body of particles (represented by current I, consisting of either electrons or ions) into infinitesimal streams of particles with uniform initial velocities v, thus giving:

Equ 6.2: $dI=\pi p^2_g \times qvdn$.

Here πp_g^2 is the collisional cross section of the probe tip (spherical or cylindrical) for particles with velocities v, p_g is the impact parameter of the particle that grazes the probe. All particles of the infinitesimal stream (dI) with impact parameters larger than the sheath radius r_s move along a straight orbits outside the sheath. f(u) is the velocity distribution of the particles with u defined by $u=v/c$ where c is the most probable velocity of the distribution, thus giving:

Equ 7: $dn=n_0 f(u)du$ (W. Lochte-Holtgreven [5])

(from an assumed Maxwellian distribution of $f(u)du=\frac{4u^2}{\sqrt{\pi}}e^{-u^2}du$ where $u^2=\frac{mv^2}{2kT}$)

The current to the probe can now be obtained by integration of equation 6 and 7 for the limits of V(r) and v. The limits of integration is the key difference in the two theories, where Langmuir assumes that all particles which fall within the sheath radius are captured irrespective of their particle velocity. Orbital theory integrates over the sheath radius, and the allowed velocity distributions. This is a more accurate means of analysis, because as one can see from figure 3.15, depending on the particle radius and velocity, not all particles are captured by the probe's electrostatic field. Figure 3.16 and 3.17 show IV characteristics for the electron probe. The electron retarding region is the linear region to the left of the 'knee' of the curve at the plasma potential (~0.8V), while the electron saturation region is the linear region at the right hand side of the curve.

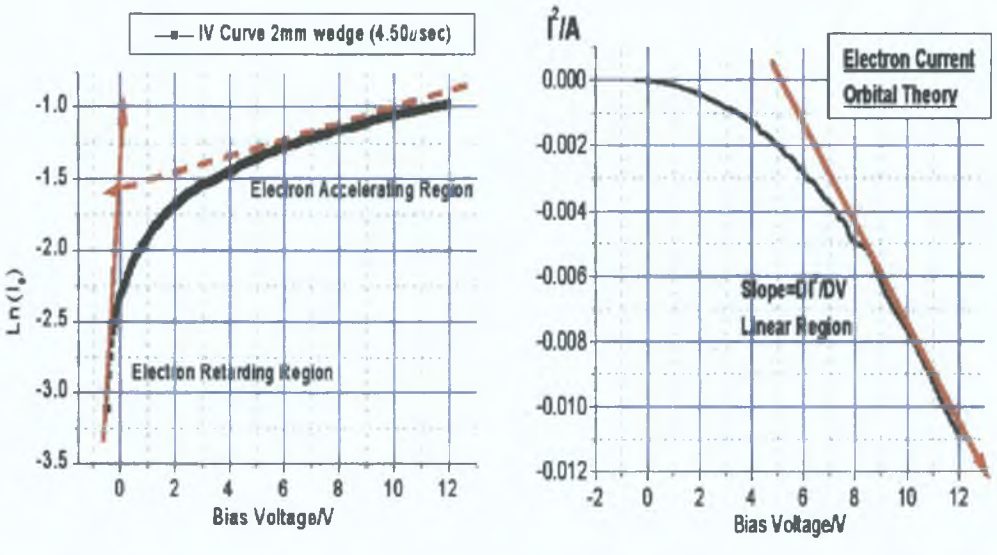

Figure 3.16, 3.17: IV characteristic for the electron probe. This a sample of the IV curves for one of the targets used in this work (2mm wedge at 4.50μsec after the laser pulse for Langmuir theory and Orbital theory). The electron retarding region is the linear region to the left of the 'knee' of the curve at the plasma potential (~0.8V), while the electron saturation region is the linear region at the right hand side of the curve. For orbital theory calculations, the square of the electron current versus the bias voltage is plotted, and a straight line fit to the saturated region relates the electron density to equation 6.1

3 5 3 Ion Probe Theory

In order to study the ion density within the plume, and to compare this with the electron density, ion probe traces were used The ion signal can be acquired by biasing the probe with a negative bias voltage sufficient to repel all electron signals (negative going signals) If the ion signal is given by $I_T(t)$, the ion density is (T N Hansen [8])

$$\text{Equ 8} \qquad N_i(R,t) = \frac{I_T(t)}{eA_p V_0}$$

where $A=2rl$ is the area of the probe projected normal to the plasma flow, V_0 is the time-of-flight velocity of the transmitted peak, and $N_i(R,t)$ is the ion density in the transmitted peak

The assumption is that the ions are single ionization ions Here, $A=2rl$ is the area of the probe projected normal to the plasma flow, V_0 is the TOF velocity of the transmitted peak, and $N_i(R,t)$ is the ion density in the transmitted peak

3 5 4 Discussion

By combining the data from both electron and ion probes, the plasma electron temperature, electron thermal velocity, plasma potential, electron density (Langmuir and orbital theory) and ion density could be ascertained for the full lifetime of the plasma probe signal at whatever point the probe was place in the plume Finally one must mention, that the most important difference between the use of Langmuir and Orbital theory is the difference in the extent of charge capture by the electrostatic field of the probe tip Langmuir theory assumes that all charge which falls within the sheath radius is captured by the probe, irrespective of its velocity and approach angle, and radius from the probe tip center However Orbital theory takes into account particle velocity, and radius from probe center Thus a capture probability based on the distributions of particle velocities is integrated into the analysis Usually this difference in theory results in Orbital theory giving a smaller signal to the probe, and resulting smaller electron densities The difference usually did not exceed one half order of magnitude However in high fluence work it may not be totally accurate to assume singly ionized species for the ion probe signals Disparities in the ion and electron densities measured are seen by other authors, but such work refers to low fluence experiments Here at fluences exceeding 50J/cm2, the difference between ion and electron densities exceed a full order of magnitude, thus inferring some deficiency in the theory as fluences increases The most likely cause of this difference is the true extent of charge capture, and hence registered signal Where ions have time-of-flight velocities of approximately 10^6 cm/sec, such differences in the theoretical approach to signal interpretation will give substantial differences in calculated particle densities

3.5.5: Probe setup and electronics.

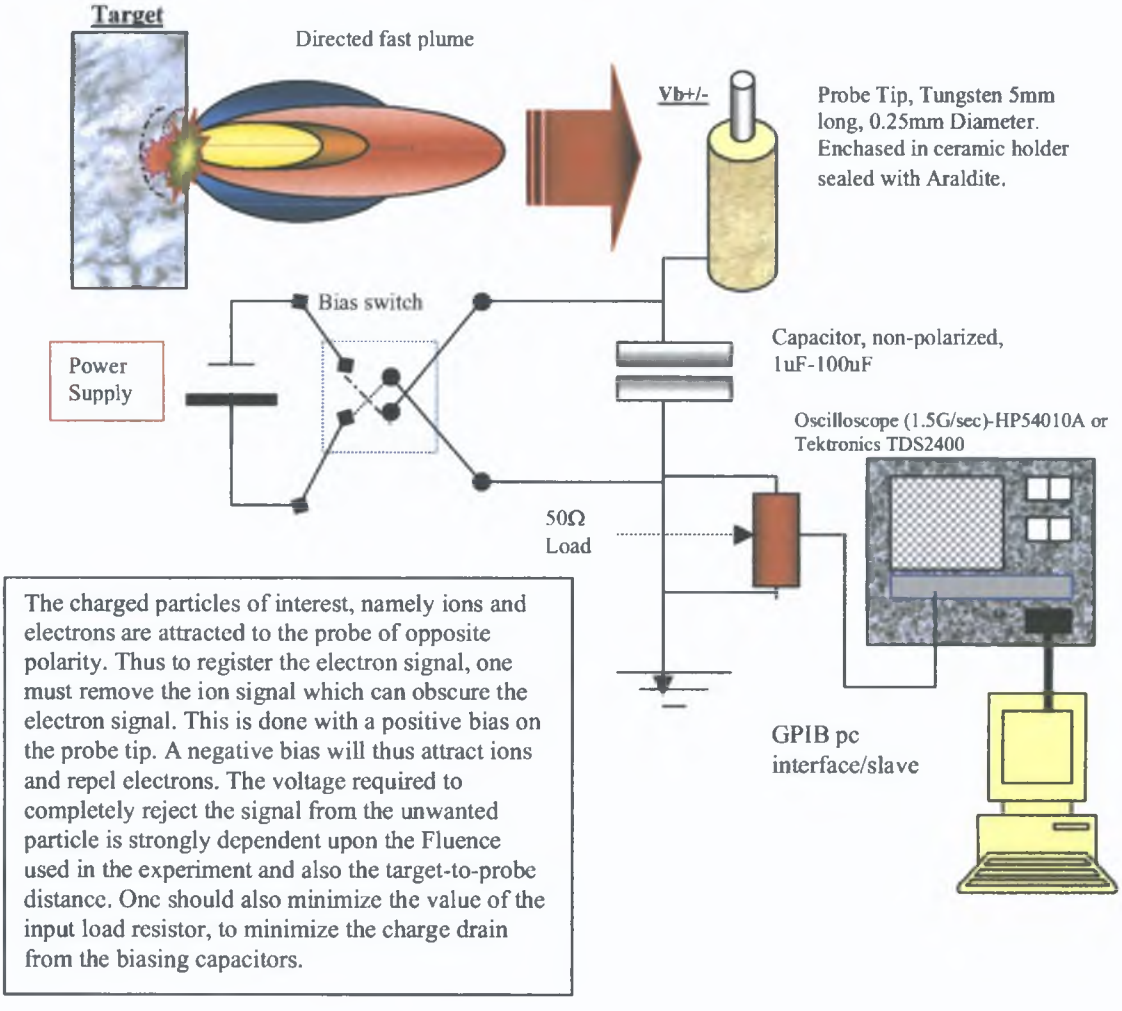

Figure 3.18: Electronic circuit for bias probes and trace capture via software slaved oscilloscope and PC.

3.5.6: Time response of probes.

In many probe experiments the plasma electrostatic signal is of short duration or has very fast fluctuations in its signal. A simplistic measurement of the response time of a probe, related to the redistribution of ions within the sheath, is

Equ 9: $$\tau = \frac{\lambda_D}{v_+} = 4.8\times10^{-4} n_0^{-1/2} \left(\frac{T_e}{T_+}\right)^{1/2} M^{1/2} \quad \text{/sec.}$$ (W. Lochte-Holtgreven [5])

Here λ_D is the Debye length, and v_+ thermal velocity of the ions [9, 10] The assumption here is that the transient behavior of the negative sheath (i e the electron sheath of a probe, positive with respect to the space potential) is determined essentially by the ion velocity, because in any case, the distribution of the ions adjacent to the probe is changed when the probe potential is varied Equation 9 leads to a signal response time within the nanoseconds limit for moderate charge densities In laser generated plasma plumes, depending on the fluence and pressure used, average signal lifetimes are from 1-100μsec Thus given the complicated nature of streaming plumes, and transient nature of the source, probes are a useful and simple tool for plasma diagnostics

3.6: Multi-purpose Target Chamber.

3.6.1: Overview.

From the inception of this project, the need for an exceptionally flexible, large volume vacuum chamber was clear. The large range of experiments performed during this work were generally in conflict regarding the requirements for precision spectroscopy in both the visible and the EUV, relative to the need to position plasma probes, and large heavy, magnetic coils and both internally and externally mounted optics. Given the constraints on aligning the plasma correctly with the detector's optical axis, both the internal optics and the target holder(s) would have to allow precision positioning, driven externally. The chamber would have to be capable of holding a large array of Langmuir probes in a fashion such that one could map the plasma properties, with high resolution over its volume. A many probe array would also require a chamber with multiple electrical signal feed-through capability. The desire to use high voltage, high Tesla solenoids in magnetic studies, required a chamber capable of holding such coils. These solenoids would be heavy, large in volume, and required very high voltage feed-through. The coils would have to be movable over a useful volume within the chamber. One would also have to consider the effect on the internal components of the force from the Magnetic field, both upon the coils themselves but also the internal mounts. On top of all of the above, the chamber would have to have sufficient viewing ports for the placement of visible imaging cameras for studying the plasma expansion.

Figure 3.19: EUV/VIS/probe vacuum chamber mated to EUV spectrometer (left hand side of photograph). The chamber is made from aluminum, a cube of side 24.5cm and internal volume of approximately 5440cm^3. It is equipped with six flanges, each configured for different experiments.

What follows is a technical and schematic overview of the vacuum chambers internal layout, optical and electrical design, and the alignment criteria. The chamber specifications are described in the next section.

3.6.2: Langmuir probe feed-through coupling.

This consists of 15 50Ω electrical feed-throughs, low inductance, vacuum copper pin connections. These are mounted on a single 13cm diameter brass, ceramic insulated flange, which is coupled to the target chambers flange via a custom machined circular reducer (see figures 3.20, 3.21). The maximum DC voltage that each pin can hold off at 10^{-6}mbarrs, is approximately 4200v, while at atmospheric pressure this is reduced to 1000-1400v depending on the humidity. The chief weakness of this flange is the lack of insulation on the vacuum side where the pins emerge from the ceramic sheath, thus if electrical breakdown occurs, it will do so here, due to the small separation between the exposed pin and the flange base. The inductance of this flange is low enough for fast signal transmission (the fastest signal acquired was in the range of 400-560MHz frequency distribution from ion probe signals), however for GHz signals such as those from x-ray diodes (~nsec duration) the flange is not suitable, as the signal attenuation is high.

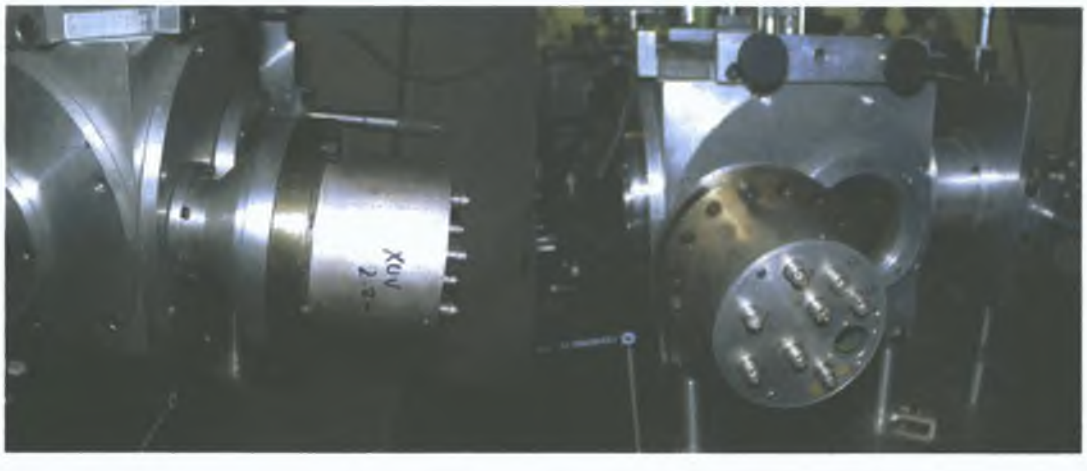

Figure 3.20 (left): Side-on view showing BNC connections. Figure 3.21 (right): Multi-pin feed-through and reducer.

3.6.3: Single pin, BNC-BNC feed-though.

Purchased from Kurt J. Lesker vacuum company, this feed-though has the advantage of having BNC connections on both air and vacuum side. Mounted through a 50cm KF flange, and rated to 300v DC, the feed-through is self grounding and of low inductance, thus it is ideal for fast signal transmission.

3.6.4: 4 Pin high power feed-through.

This was purchased from Kurt J. Lesker vacuum company, with 4 high voltage copper feed-through rods of wide diameter (6mm). The max rated DC current is 150Amps, and maximum rated voltage is 12kV (these were later insulated to hold off 30kV, via glass rods araldite sealed along the copper feed-through with only their ends exposed for connection). The feed-through, mounted on a KF60 flange, was fitted to the chamber flange via a custom machined 14cm long, cylindrical mount, which mated to the same flange

point as the multi-pinned feed-through (above). This ensured that the copper rods were 'self housed' under vacuum outside the internal volume of the chamber. Thus any failure of the flange/insulation under high voltage was localized inside this mounting and not inside the chamber itself.

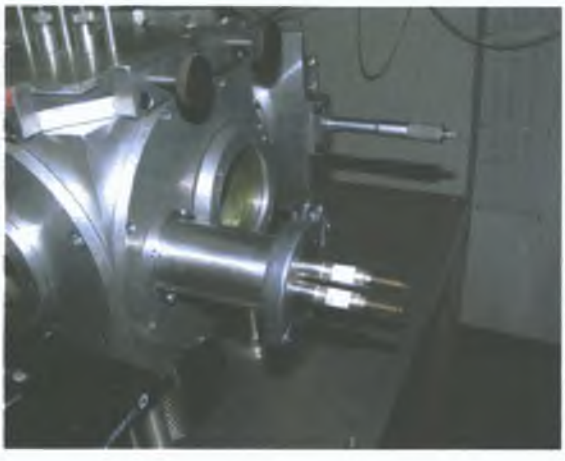

Figure 3.22: High voltage feed-through in self-housing mount.

3.6.5: Internal mounts:.

The chamber has three independent mounts, adjustable under vacuum and a fourth non-adjustable mount.

Vacuum mount 1: (left hand side of chamber)

Degrees of freedom: 3.
Vertical drive, micrometer = ±4.5cm.
Horizontal drive, micrometer = ±4.5cm.
Horizontal rotation, manual = 360deg.

Mounting: 1×45deg YAG mirror.
1×4.5cm plano-convex lens.
2×1mm thick mica plates.

Supported from the floor of the chamber, this precision mount is driven vertically via a micrometer screw underneath the chamber, which counter drives the two vertical rods, moving through two Wilson seals. Horizontal motion is achieved via micrometer drive pushing on the vertical aluminum plate in the background, which traverses the upper portion of the mount along its ball bearing supported rails. A high tension spring mounted on the far side of the table pulls the upper table portion back when the micrometer is withdrawn.

Figure 3.23: Mount 1, for EUV studies, this mount would be used to position baffles, to 'catch' debris from the laser-plasma, and also to lesson the pressure wave which is generated during ablation, which travels down the length of the spectrometer. This can cause arcing of the EUV detector when the laser is firing at a high repetition rate.

Vacuum mount 2: (right hand side of chamber)

Degrees of freedom: 3.
Vertical drive, manual = ±9.5cm.

Mounting: 1×45deg YAG mirror, 1×4.5cm plano-convex. Lense. 2×1mm thick mica plates.

Horizontal drive, manual = ±2.5cm.
Horizontal rotation, manual = 270deg.

Supported from the floor of the chamber, this mount is driven vertically manually and locked in place with a clamp screw. Horizontal motion is achieved via manual drive, locked in place with a clamp screw. The entire mount can be rotated through 270^0, to face any direction.

Figure 3.24: Mount 2. Used to position the probe array arm, independent of the main target table, but also capable of mounting internal optics.

Main target table:

Degrees of freedom: 5. **Mounting:** Various targets.
Vertical drive, micrometer = ±4cm.
Horizontal drive X, micrometer = ±4.5cm.
Horizontal drive Y, micrometer = ±4.5cm.
Horizontal rotation, manual = 360deg.
Differential Vertical drive, micrometer = ±3.5cm, = ±45deg.

Supported from the roof of the chamber, this precision mount is the main target mount. It is driven vertically via two micrometer screws on the chamber roof, which drive the two vertical rods, moving through two Wilson seals. Horizontal motion is achieved via a micrometer drive pushing the main roof piece over the chamber roof which has a rectangle of dimensions 6cm×8cm cut out. The target itself can be fixed at any angle via rotating the circular base mount , while differentially driving the vertical supports can rotate the entire table through 45^0 in the vertical.

Figure 3.25: Mount 3.

Vacuum mount 4: (right hand side of chamber, from rear of chamber)

Degrees of freedom: 4. **Mounting**: Various targets.
Vertical drive, manual = ±8.5cm.
Horizontal drive, manual = ±6.5cm.
Horizontal rotation, manual = 360deg.

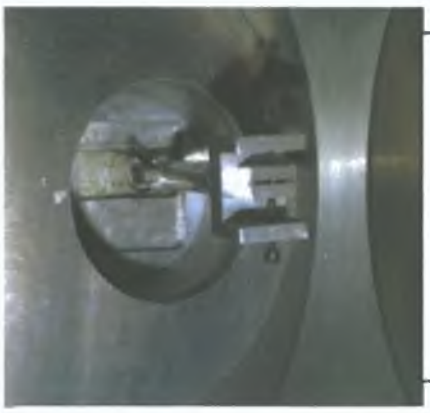

Supported through a two stage Wilson feed-through, this precision mount is driven vertically and horizontally via a micrometer screw driving two plates over each other, separated by a o-ring. The main support rod is driven horizontally from the rear by another micrometer and can also be rotated.

Figure 3.26: Mount 4 (internal image, enlarged). This mount was used to position a continuum EUV source for absorption experiments (not reported in this work) but also for positioning a ion probe for 3D mapping of plume properties.

Figure 3.27: Mount 4 (External)

3.6.6: Probe array mount.

The vacuum chamber was designed to mount a large number of ion and Langmuir probes simultaneously for plume studies. The first mount is a semicircular (radius 6.5cm) 'horseshoe' holder, onto which the probes are clamped using the machined rectangular pinch blocks, which themselves are screwed onto the horseshoe mount and placed radially around the ring. This allows the probes to be positioned radially about the plume, at a constant radius from the laser-target interaction point. The second mount is a rectangular block, also utilizing the pinch blocks to secure the probes, however here the probes sit in a horizontal line parallel to the target surface. There are two ways to support both mounts. Firstly from the base of the main target table, which ensures that even if the target table moves, the probes remain in the same position relative to the plasma generation point. The second method is to support the probe array from the extended arm mount, which is clamped to the vertical support rode on the right hand side of the chamber. This mount is usually used when one requires the probe to target distance to be large, or for the latter quantity to vary throughout the course of an experiment.

Figures 3.28(left)-3.29(middle)-3.30(right): Various mounts for placing Langmuir probe array. (radial via 3D arm, horizontal via 3D arm, radial, bolted to target table).

3.6.7: Rail system/magnetic coil support.

In order to support the large and heavy magnetic coils, the chamber was fitted with a variable rail system, which allowed the distance between the coils to be varied. The two rails, made of aluminum rods of diameter 8mm, and length 24cm, are such that they traverse the length of the chamber, intercepting both flanges on either side of the chamber, where they sit in bored cavities for support. The coils are clamped inside rail carriages, which are then secured on the guide rails, the carriages can be position by sliding them along the guide rails.

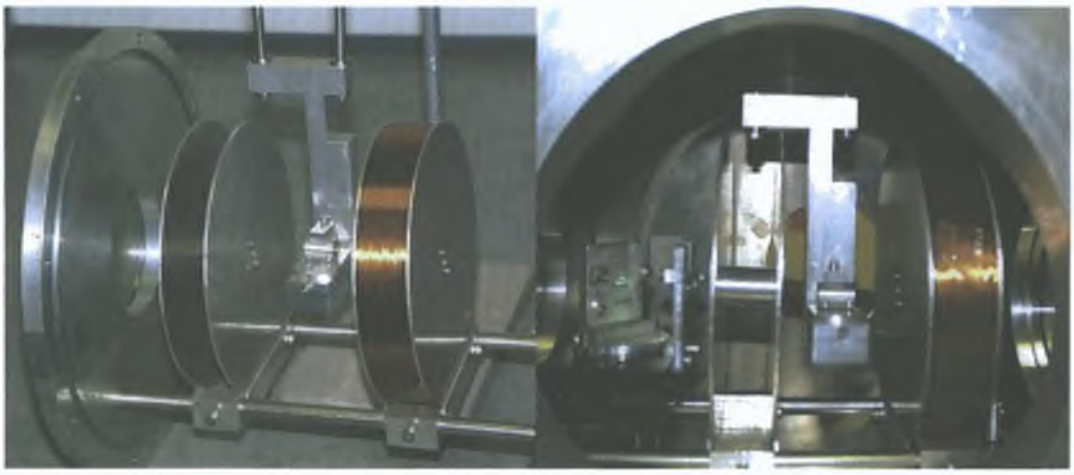

Figure 3.31, 3.32: Rail mounting system, outside chamber, mounted inside vacuum chamber (left hand coil unwound, right hand coil wound).

3.6.8: Pumping system.

The vacuum chamber is evacuated via a Leybold PT361 turbo molecular pump backed by a Leybold TRIVAC-B rotary vane backing pump. The ultimate operating pressure under vacuum of the backing pump is 10^{-4}mbars, however given the size of the chamber and the large number of ports and feed-throughs on the chamber, the best vacuum via the backing pump is ~3×10^{-3}mbar. The best vacuum achieved with both pumps operating together on this chamber is approximately 5×10^{-5}mbars within four minutes of pump down from atmospheric pressure. Operating pressures are monitored via a Leybold PENNINGVAC for pressures below 10^{-2}mbars, and a Leybold THERMOVAC gauge for pressures in the range 10^{3}-10^{-3}mbars. The mating point for the turbo pump was placed on the chamber floor, through which a 80mm diameter hole was machined, this allowed a vacuum bellows to be attached to the base of the chamber which then connected the turbo pump to the chamber, this also had the effect of not 'using up' valuable flange area. This approach was also used in connecting gauges and vent values. These were placed on the flange face which couples the chamber to the EUV spectrometer.

3 6 10 Performance aspects

Figures 3 33 and 3 34 provide a simplified plan of the chamber layout for the experiments performed here Generally for EUV and visible emission studies the layout was exactly the same, with visible light from the plasma viewed from the right hand side of the chamber, through a glass port and coupled via rotational optics to the slit of the visible spectrometer All glass ports are standard glass, of thickness 6 5mm, and of average diameter 10cm Given the high fluence used in all experiments, and the use of collimating targets which produce a high speed plasma plume, coating of glass ports was an issue and would steadily reduce power densities onto the target, thus these were changed after 5hours, of regular use To prevent large debris and loose fittings falling into the bellows connecting the turbo to the chamber, a large circular (11cm diameter) steel gauze mesh was sealed to the chamber floor with Araldite over the aperture where the bellow is connected

When the chamber was used with the EUV detector system, pressure differentials created when the laser ablates the target were not observed in the detector chamber at the other end of the spectrometer this is due to the large size of the chamber and the larger turbo pump used The earlier vacuum chamber employed on the EUV spectrometer was 1/8 the size, and thus pressure differentials created during plasma formation would travel down the spectrometer and register as a pressure fluctuations in the detector chamber This would, at high operating bias voltages cause the detector to arc, a detrimental scenario for detector efficiency However pressure differentials here were greatly reduced and could be removed completely by placing a moderately sized piece of flat mica on mount one, parallel to the mounts alignment, and with a small (5mm) diameter hole for EUV light to travel to the mirror chamber Not only would this completely remove the pressure differential upon firing, it allowed a high rep rate for firing and would also 'catch' plasma debris from the plume, which would otherwise collect on the GCA, and eventually reduce the transmission of radiation through the latter

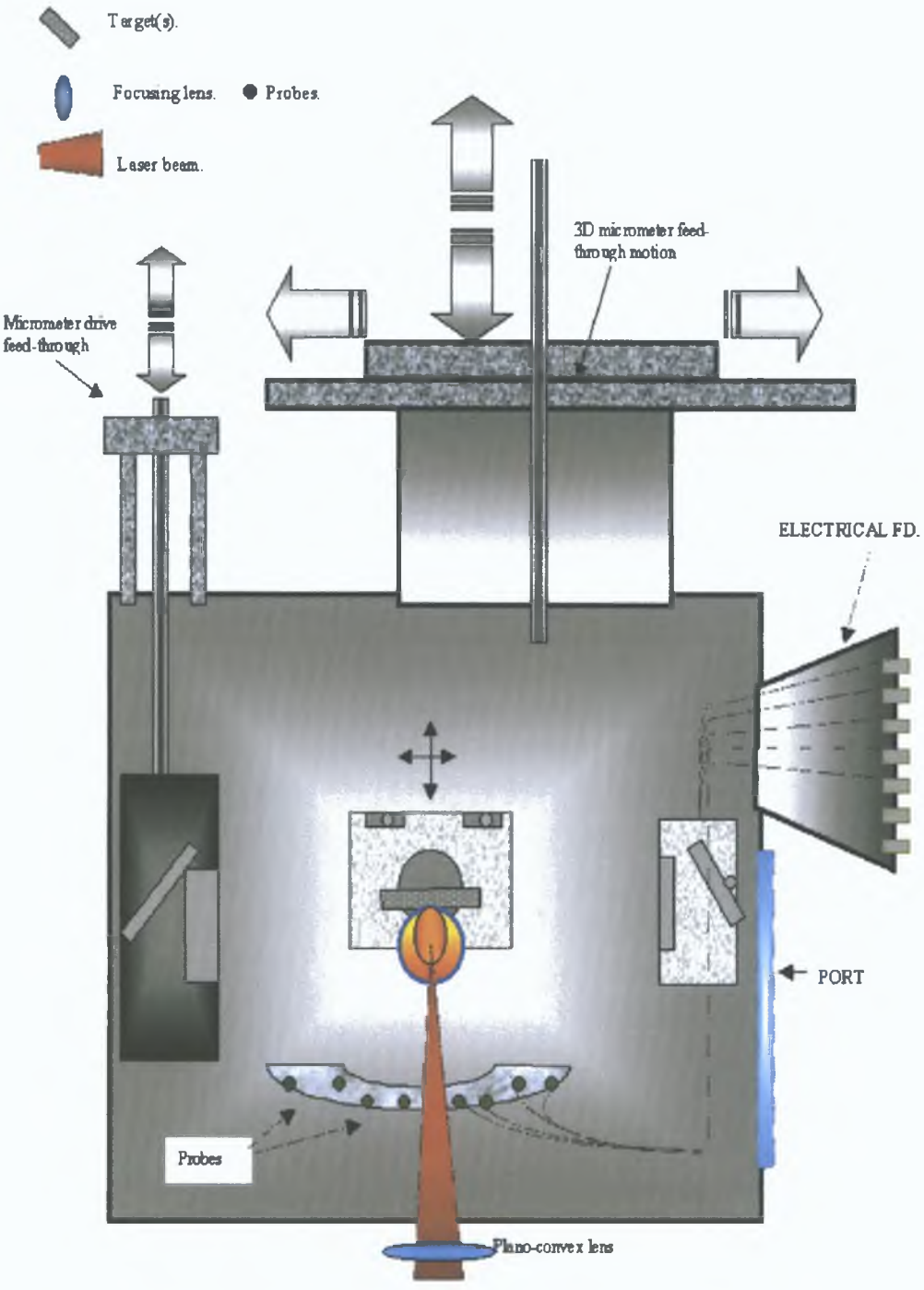

Figure 3.33: Chamber configuration for probe experiments. The probes where mounted in one of the three mounts available (figures 3.28-3.30), with each probe connected to the multi-pin feedthrough for signal transmission to the bias box and then onto the Oscilloscope for capture.

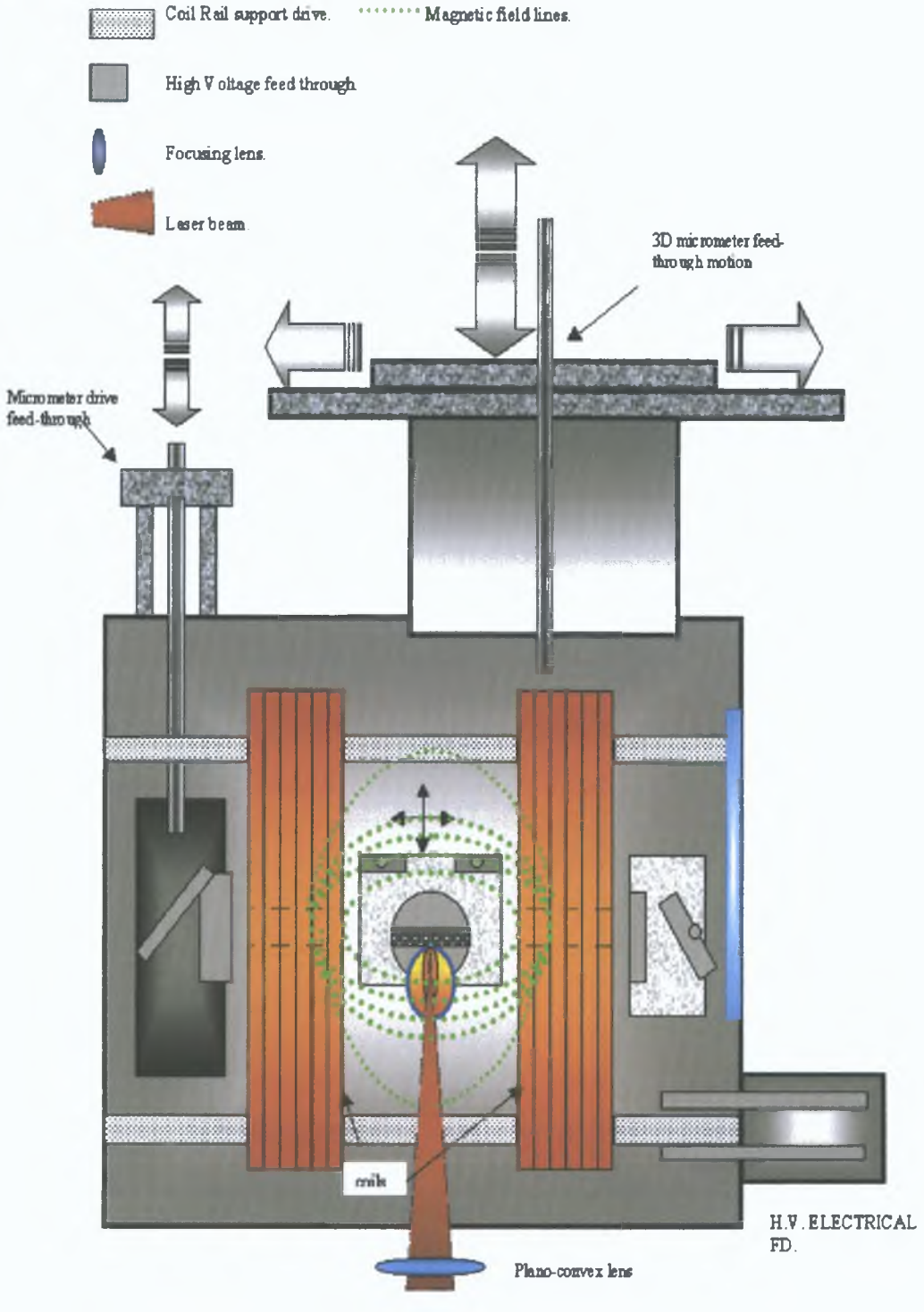

Figure 3.34: Chamber configuration for magnetic pulse experiments. The coils are mounted in movable carriages which slid along horizontal support rods (figure 3.31, 3.32). This allows them to be positioned at various distances from the plasma.

3 7 Magnetic Pulse system and devices

3 7 1 Introduction

There is a large body of work involving the study of enhanced plasma behaviour under the confining influence of magnetic fields [11, 12, 13, 14, 15, 16] where laser plasma generation occurs in the presence of a pulsed or DC magnetic field, of intensity varying from an average minimum of 1Tesla up to 18T

Enhanced plasma temperatures, lifetime, and ionization are all a consequence of the plasma particles responding to the compression of the plume under sufficient field intensity The vast bulk of these pulsed systems are triggered either via gas breakdown under the influence of high voltages, or using high voltage switching using Triacs or Thyristors The latter are problematic in that the jitter in the 'on time'(the duration of the short circuit condition) and the jitter on the actual trigger point mean, that not only are these devices very unstable in reproducing a peak current pulse, but also suffer from problems of synchronization with lasers and detectors

3 7 2 High Power devices

A small but growing body of work has been done on high voltage triggering with MOS devices without the use of a coupling transformer [17, 18, 19, 20] Their chief attributes are speed, turn-off capability, cost, and voltage-based gating However these devices have definite limits on the voltage they can support For example, the on-resistance of the MOSFET is proportional to a factor greater than the square of the breakdown voltage Current ratings are typically greater for 'n' devices in series than for a single MOSFET rated at n times the breakdown voltage There are also limits on the duration of the current pulse that the MOSFET's devices can handle, although generally the shorter the on time of the device, the higher the ratings on voltage and current In order to create a pulsed magnetic field which could be gated to the laser, we attempted to build a pulsed system by stacking high voltage MOSFET's in series Unfortunately while this allows one to operate such a system above the voltage rated value of the device by spreading the applied voltage across the FET array, minute variations in the switching time can lead to large inequities in the voltage 'seen' by each device This leads to instantaneous sequential failure of the array, and can severely compromise the viability of the system However, MOSFET technology has advanced considerably in the past decade, driven by the need to increase the performance of switch mode power supplies Santamaria and Ness [19] constructed a 2400 component FET array in the late eighties The total voltage rating of the array was 6KV at 700 amps, switching at 60KHz width 3μsec pulses The high number of components needed was due to the voltage limits for devices at that time Advances in manufacturing and fabrication have allowed others to produce similar systems with far fewer component parts Baker and Johnson [18] stacked less then five MOSFET devices to switch 1 6KV with a 2nsec rise time and demonstrated that the response time and reproducibility of the pulses in time was far superior to those produced with spark gap, thyristors or other solid state high voltage switches/triggers Other authors (Chokhawala and Sobhani [17]) have developed low voltage high current pulse generators The latter can pulse a load at 400A with a 100nsec square wave pulse Thus the key to pulsed magnetic field generation of

meaningful intensity (>1T) is pulsed current delivery The ability to generate a pulsed magnetic field of varying intensity and duration would be an impressive variable to add to any experiment, and given the highly charged nature of laser plasmas, such a variable would substantially enrich the study of non-typical influences on laser plasma generation We now present a detailed overview of the major components and design/behavior aspects of a high intensity (>1T), triggerable, gatable, precision magnetic pulse generator Design, testing and construction was undertaken by the author and Mr Patrick Wogan (School of Physical sciences, DCU), while systems analysis and calibration, presented in the following sections was undertaken by the author

3 7 3 Power supply

The charging power supply was taken from a Candela dye laser system and is of switch-mode, capacitor charging design The HVD-500A is a 500J/sec pulsed device The maximum rated driving voltage is 50KV, and maximum deliverable current is 50mA (DC) The main advantage of this design is the built in regulator, which constantly monitors the voltage across the capacitor load, and maintains a constant voltage by 'topping up ' the capacitor charge to counteract charge leakage from the capacitor bank There is also an automatic 'shunt' to ground in the event of a short circuit (if the voltage across the internal capacitor in the power supply suddenly drops) This prevents a full scale discharge to ground, limiting damage to components, in the event that some problem arises One can also discharge the capacitive load manually from the front panel of the supply

3 7 4 Magnetic diagnostics

The average peak magnetic field can be measured using a B-dot probe A B-dot probe usually consists of a pickup coil and some sort of electronic integrator The voltage induced between the leads is proportional to the rate of change of the magnetic flux through the coil

$$\text{Equ 1 1} \quad E(t) = -d\phi/dt \quad \text{(R Serov et al [21])}$$

Thus by integrating the voltage in time, the magnetic flux through the coil and the average magnetic field at the probe location can be deduced

The temporal response of an n-turn coil having a loop radius r(cm) is calculated from

$$\text{Equ 1 2} \quad \tau = L/R_0 = Fn^2r/R_0 \quad \text{(R Serov et al [21])}$$

here L is the inductance of the coil, R_0 is the load resistance and F is a constant depending on the ratio of the coil length l, to its radius (for $r/l = 2$, and F=0 029) The sensitivity of the probe can be defined as

$$\text{Equ 1 4} \quad V = 10n(\pi r^2)dB/dt \quad \text{(R Serov et al [21])}$$

where V is the coil voltage before integration and dB/dt is the rate of field change in units of Gauss/nsec.It is clear from the above that the sensitivity of the coil can be increased by increasing the number of turns or the radius of the coil. However this is achieved only at the expense of the temporal response and its spatial resolution. It is important to remember that probe response times are more critically dependent upon the value of n than is the improvement in sensitivity. One can also increase the load resistance R_0, to obtain maximum temporal resolution. However the amplitude of the recorded background noise scales with R_0, so there are limits to how far one can increase the responsiveness of a probe. However given their flexibility, simplicity and the relative ease of data analysis, magnetic flux probes are valuable diagnostic tools in characterizing magnetic signals which are transient in nature. Thus they formed the backbone of the analysis in characterizing the magnetic pulse system constructed.

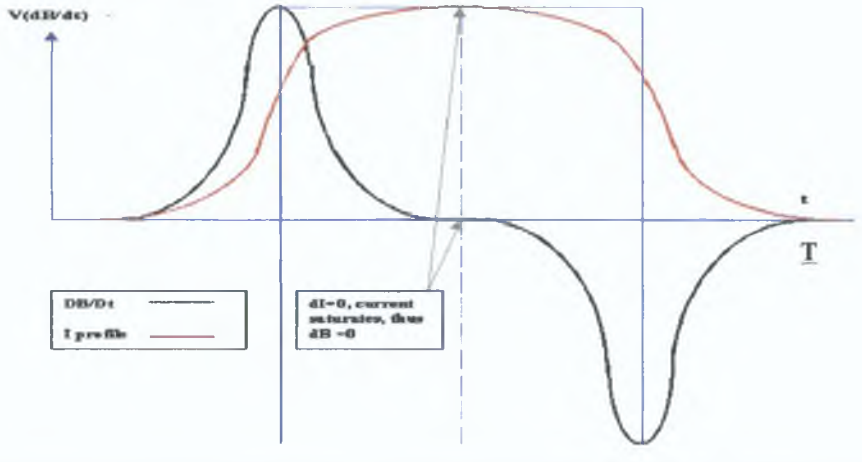

Figure 3.35: Typical dB/dt trace for a current profile which rises rapidly, saturates for a limited period and then falls rapidly.

3.7.5: Magnetic coil analysis and performance specifications.

As it exists, the complete system can be modeled as an RCL circuit. (Figure 3.36). In this case the resistive component is the ohmic resistance of the coils themselves

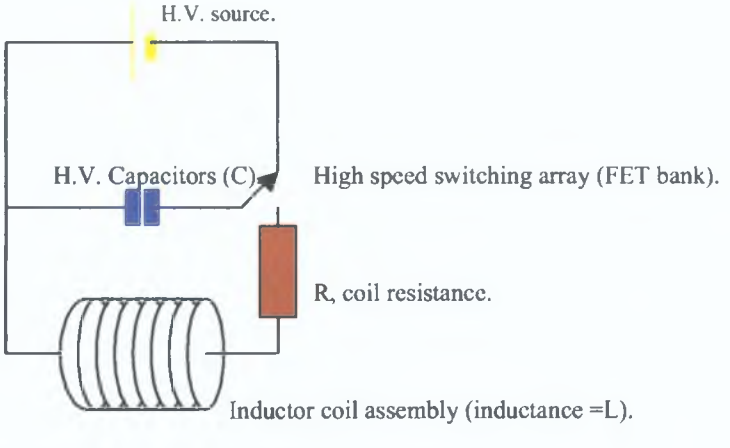

Fig 3.36: Simplified schematic diagram of the system as an RCL oscillator.

Following the analysis of Young [22], applying Kirchoff's loop rule, the second order differential equation

which describes the behaviour of this system is

$$\text{Equ 1} \quad iR+L\frac{\partial i}{\partial t}+\frac{q}{C}=0 \qquad \text{(Young [22])}$$

Replacing 'i' with $\partial q / \partial t$ and rearranging we get

$$\text{Equ 2} \quad \frac{\partial^2 q}{\partial t^2}+\frac{R}{L}\frac{\partial q}{\partial t}+\frac{1}{LC}q=0 \quad \text{(Young [22])}$$

For various values of R the system behaves as either 'underdamped', 'overdamped', or 'critically damped' The way to test this is to consider the relation between the square of the resistance and the relation 4L/C

$$\text{Equ 3} \quad R^2 \Leftrightarrow 4L/C, \qquad \text{(Young [12])}$$

thus given that each coil's resistance is approximately 65Ω, then for the system configuration used here (coils in parallel with the driver system) the total load resistance is ~32Ω For operational purposes we used only one capacitor, thus C=20μF, while the coil's inductance was measured with an inductance meter The values for $L_1$and L_2 are thus 178mH, and 189mH In parallel, the total inductance of the system was thus ~90mH Inputting these values into equation 3 gives R^2~900Ω, for the left hand side and $4L/C=18\times10^3$ for the right hand side Thus this system was heavily underdamped Solving equation 2 we get equation 4, giving the time dependence of the capacitor charge from its initial value of Q to its time dependent value q(t), the relation ϕ is zero if the initial charge value is zero

$$\text{Equ 4} \quad q(t)=Q\exp^{-(R/2L)t}\cos\left(\sqrt{\frac{1}{LC}-\frac{R^2}{4L^2}}t+\phi\right) \quad \text{(Young [22])}$$

Since the system was underdamped, it oscillates at a angular frequency ω_0, given by

$$\text{Equ 5} \quad \omega_0=\sqrt{\frac{1}{LC}-\left(\frac{R}{2L}\right)^2} \quad \text{(Young [22])}$$

If equation 4 is differentiated with respect to time, one arrives at equation 6, which gives the temporal profile of the current in the load, while equation 7 gives the 'average peak' current in the load over the one complete period of oscillation

$$\text{Equ 6} \quad i(t)=\frac{V_0}{\omega_0 L}e^{\frac{-R}{2L}t}\sin\omega_0 t \quad [13]) \qquad \text{Equ 7} \quad I_{peak}=\frac{V_0}{\omega_0 L}e^{\frac{-R\pi}{L\omega_0}} \quad [23]$$

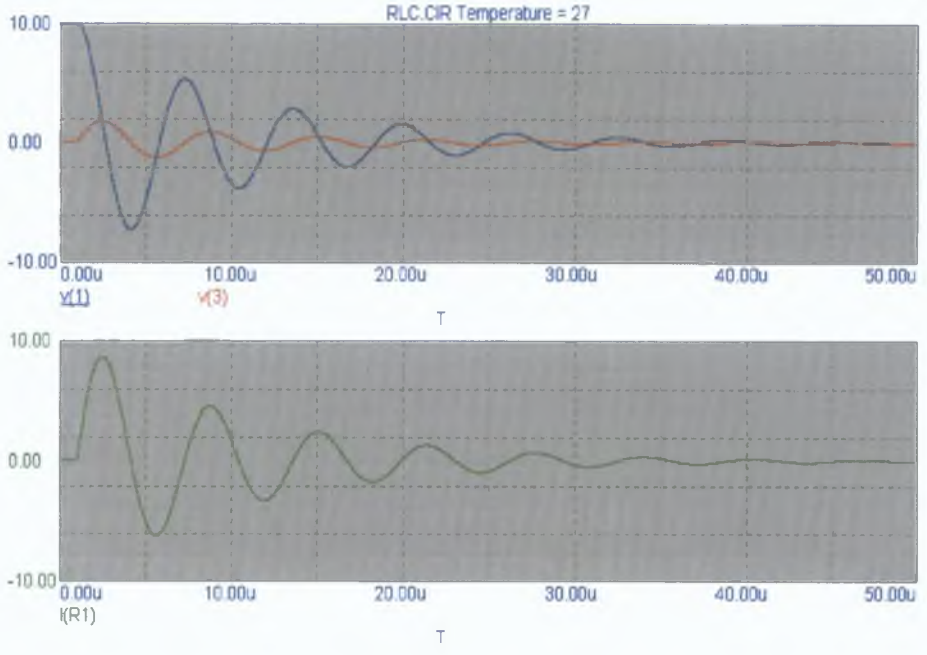

Fig 3.37: Typical waveform for an RCL circuit. In the upper graph, the blue waveform is the profile of the voltage across the capacitor, the red profile is the voltage across the load. The green profile in the lower graph is the current in the load. All units are arbitrary (http://home.san.rr.com/nessengr/ [23]).

3.7.6: Graphical analysis.

For our system settings (L =90mH and C=20μF and R=30Ω), and given equation five, then ω_0=726.4rad/s, and from equation 7, I_{peak} =7.24amps. One can graph the current profile in the coils by plotting I(t) versus time, inputting the correct values for L,R and C. This was done in Origin 5.0, and is displayed below in figure 3.38.

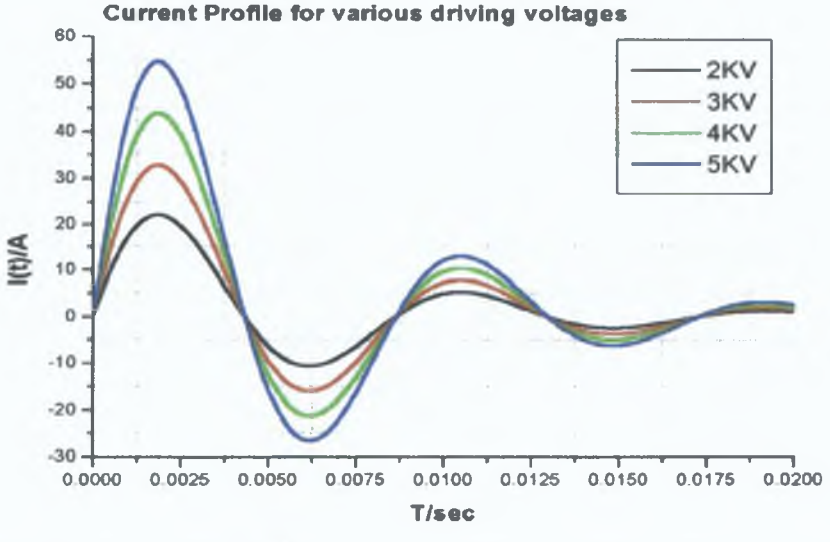

Figure 3.38: Current profile in the coils as a function of time. The profile is plotted for various driving voltages.

The importance of this graph lies in the fact that it demonstrates that the peak achievable current was not simply the driving voltage V divided by the load resistance R (or impedance, Z for a fast system) as given by the ohmic relation V/R=I [22]. If this were so then the peak current should have been 33amps for the 2KV profile. However one can clearly see that in figure 3.38, the peak current in the system for a driving voltage of 2KV does not exceed 25amps. The combination of i^2R losses in the coils and the back *emf* induced in the coil due to the sharply rising current pulse, coupled with the inherent inductance of the coils which prevent the current rising instantaneously, all contributed to system losses.

3.7.7: Energy considerations.

In terms of the energy of the magnetic field, the energy density within the core of a solenoid is given by equation 8:

Equ 8: $u=\frac{B^2}{2\mu}$ J/m^3 (Young [22]) while the total energy supplied by a current I is: Equ 9: $U=\frac{1}{2}LI^2$ J,

(Young [12])

For our system, charged to 2KV, 'μ' had a value of 5.7×10^5 J/m^3, and 'U' was 4.5J (for I =10amps). One might propose that this was in conflict with the energy available from a charged capacitor:

$$\text{Equ 9:} \quad E=\frac{1}{2}CV^2 \text{ J} \quad \text{(Young [22])}$$

However for the purpose of calibration, our system was run at 2KV, and the gate width, or length of time the system was 'turned on' was set at 486μsec. Thus as can be seen from figure 3.39, the peak current did not occur until approximately 1.9msec. In switching off the device at 486μsec, the peak current reached in the solenoid was approximately 10amps, thus giving U a value of 4.5J from equation 9.

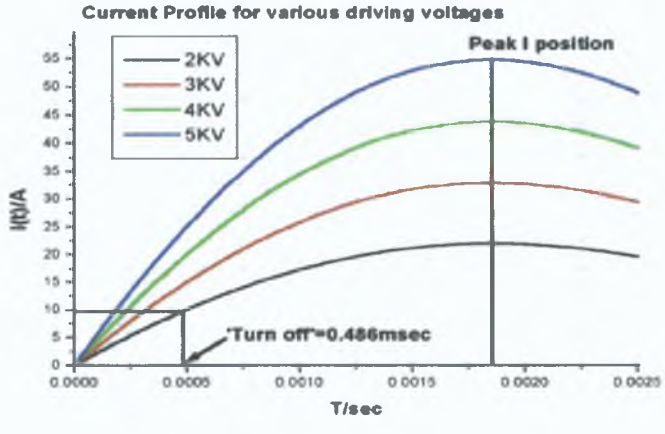

Fig 3.39: Zoom in display of figure 3.38, showing the region where the gate on the FET's is closed, thus setting the current to zero in the coil, at this point the current in the coils had reached a value of ~10amps.
The solenoid could also be treated as an ideal solenoid, characterized by equation 9.1

Equ 9 1 $B_x = \mu_0 INL$ (Young [22])

Here L is the length of the solenoid in meters, n is the number of turns per unit length (per meter) and I is the current in the coil Then if the coils used here (length =0 05m, number turns axially=90, number of layers radially=60, total number of turns 90x65=5850) are scaled to one meter in length, then the number of turns per meter is 1/0 05x5850=117000 Inputting this into equation 9 1, and using I ~10A (approximated current for 2KV divided by load resistance of approximately 300Ω-due to extra turns, with switch off time equal to 486μsec) this gives B~1 4T This is larger then the B-dot measured signal and the B-field analysis using the *Biot-Savart* rule However this approach is an idealization (approximated current and resistance), which ignores the variation in the increasing radius of the turns in the solenoid However it is in good agreement with the first two techniques

3 7 8 Magnetic field analysis and field configuration

With accurate values for the current at the time of turn off', one could then calculate the magnetic field value in the solenoid for that current value This was done using the *Biot-Savart* rule

Equ 10 $B_x = \frac{\mu_0 I a^2}{2(x^2 + a^2)^{3/2}}$, (Young [22])

where a is the radius of a loop of coil, and x is the axial distance from the coil center By summing this process over the entire length of the solenoid, and for each successive layer of wire, the peak magnetic field at the center of the solenoid could be approximated This was done, by writing a software routine in MATLAB(this is described in greater detail in appendix A), which was then compared to the average peak magnetic field, measured via a magnetic flux probe The entire process was repeated for various driving voltages, as displayed in figure 3 40

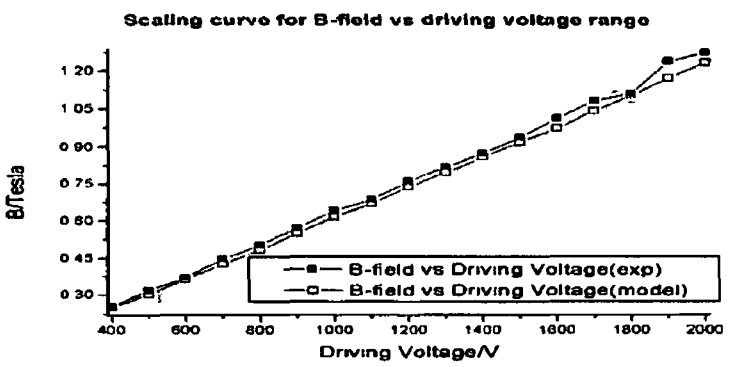

Figure 3 40 Peak average magnetic field at the center of the solenoid for different driving voltage values comparing values from the inductor model with those from magnetic flux measurements

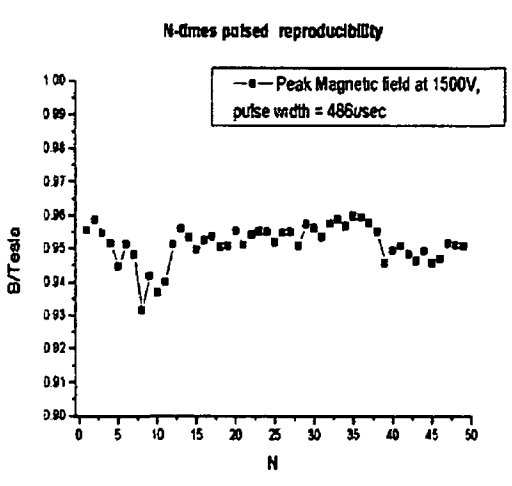

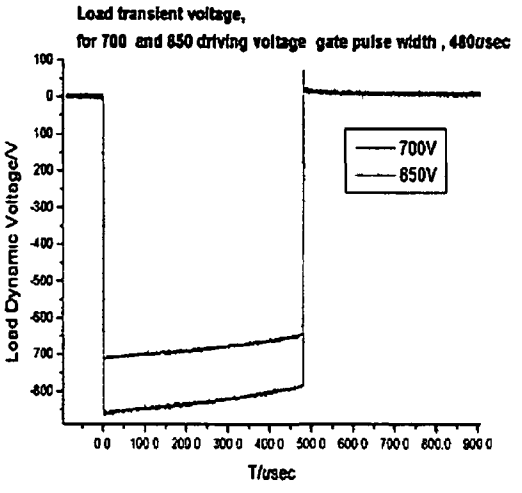

Figure 3 41 (left) Testing the reproducibility of the peak magnetic field at 1500V for 50 traces
Figure 3 42 (right) Voltage profile across the load (coil) for values of 700 and 850V

In order to characterize the system s behaviour, the voltage and pulse width was fixed at 486μsec and fifty B-dot traces were taken, giving the peak magnetic field value over the duration of the test, thus plotting this (fig 3 41), one could see the level of variation of field value With an average value of 0 95T, an average variation of 0 0115T, which gave a 1 15% variation of the averaged value Due to the system configuration, use of a floating ground is an issue If one wanted to probe the system (load, or source-drain channels) one had to employ a high voltage probe using a floating ground (a ground, or zero point which is not connected directly to mains ground) This is generally not a problem until one wishes to capture and save traces on an oscilloscope Connecting a probe to an oscilloscope which is ground to the mains supply will ground the high voltage side of the system, and lead to unacceptable levels of leakage from the high voltage supply to ground Thus to use an oscilloscope, an oscilloscope itself had to be ungrounded at the mains Secondly we did not have a low inductance potential divider, but utilized a −10 probe, and thus we were unable to probe the voltage trace on the load for voltages above 800V, for this would have overloaded the oscilloscope Other issues of importance were the limits on the FET's regarding their ability to deliver a certain current for a limited duration Exceeding this operational limit led to sequential failure of each FET (on a time scale of 500nsec) and thus complete failure of the system This happened on numerous occasions, due to back *emf's* from the coils, which double triggered the driver electronics, which then re-triggered the FET arrays a second time, pushing them beyond their operational limit A careful balance between driving voltage, current limit, pulse width and coil resistance was required to ensure safe and reproducible operation of this system, which in effect is a prototype unit, which the authors are certain is at this time the first of its kind

In order to characterize the coils B field distribution spatially, we employed a magnetic flux probe, placed at various positions Firstly, the probe was placed inside the core of the solenoid and its position varied

from the centre to the edge, moving parallel to the one of the solenoid's axis In this manner the axial B field was mapped, and is displayed in figure 3 43 The same procedure was employed to map the radial component of the B field Here the probe was positioned 8mm outside the solenoid

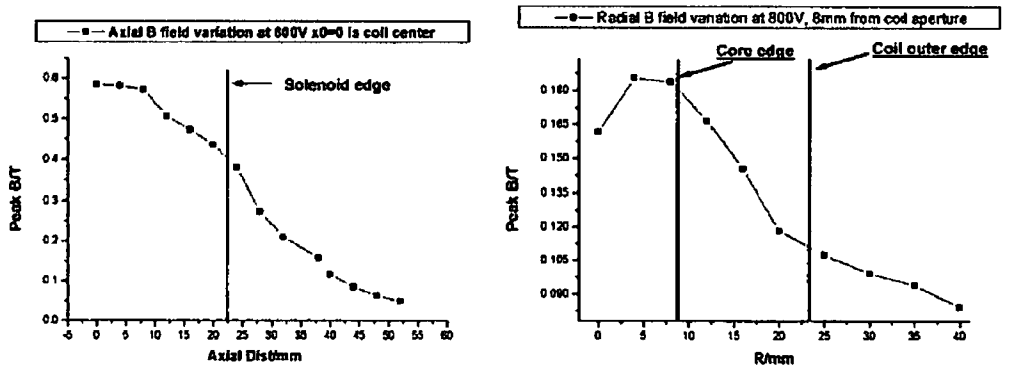

Figure 3 43 (left) Axial variation of the peak B field for a driving voltage of 800V Axial distance=0 is the solenoid's center
Figure 3 44 (right) Radial variation of the peak B field for a driving voltage of 800V Radial distance =0 is the solenoid's center, with the probe placed 8mm from the solenoids face

Beginning at the solenoid's axis (r=0) the probe was moved perpendicular to the solenoid s axis The radial variation of the B field thus mapped is displayed in figure 3 44 From equation 10, the *Biot-Savart* rule indicates that the axial magnetic field inside a solenoid shows a x^2 dependency on the distance from the center of the coils along its axis In order to confirm this, the profile of the B-field was plotted with the required variables from equation 10 in Origin 5 0, and the plot was then normalized to the peak axial field seen in the solenoid by the flux probes (figure 3 43, B_{peak}~0 6T) The two plots were then overlapped for comparison, and are displayed in figure 3 45

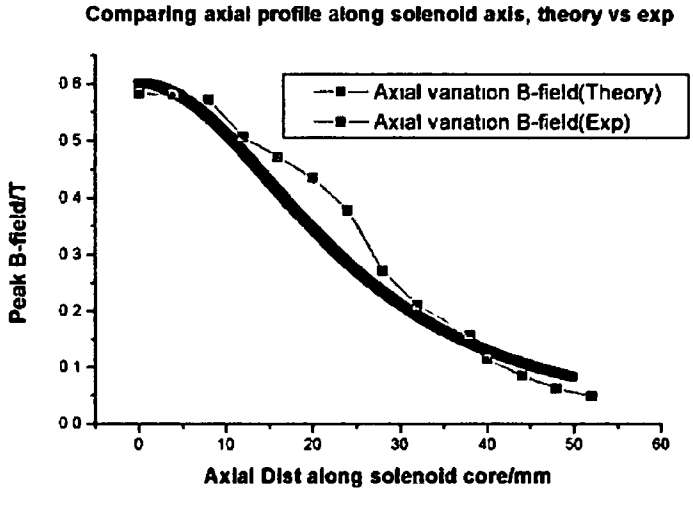

Figure 3 45 Axial variation in the B field from the flux probe, compared with the probe expected by equation 10, which is normalized to the peak B field value from the flux probes at the solenoid center

Figure 3.46 (left): Zoom photograph of the FET array in series with accompanying HV capacitor and resistor components.
Figure 3.47 (right): Photograph of the power supply (lower portion) and capacitor bank (upper portion).

3.7.9: Simplified schematic of the magnetic discharge system.

A schematic of the discharge system (photographed above in the above figures-this is described in greater detail in appendix B, using professional circuit drawing software). The concept is relatively simple.

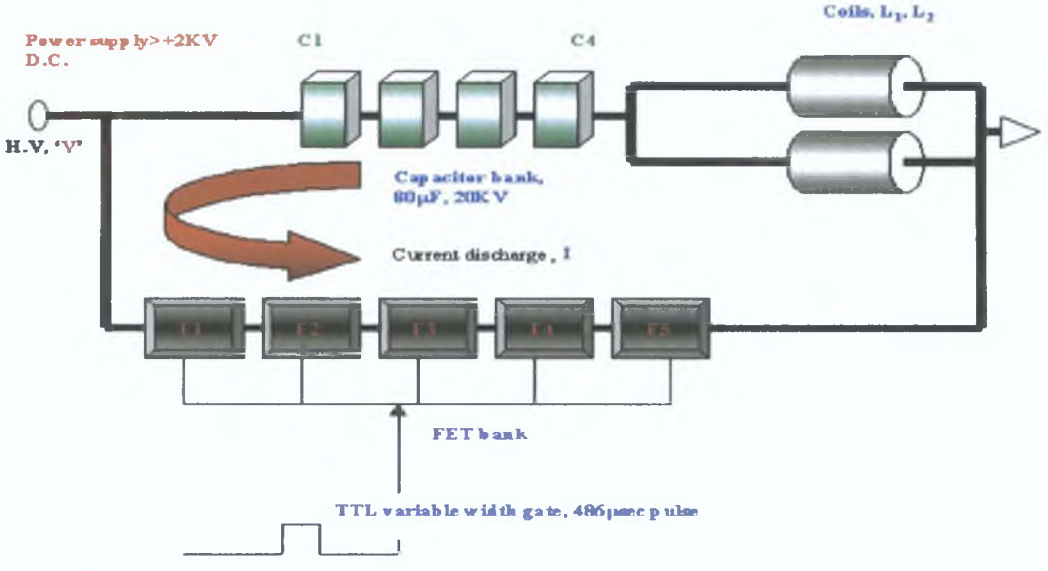

Figure 3.48 is a simplified diagram of the magnetic discharge system. We have omitted the driving electronics (which produce the TTL variable width gate pulse), back *emf* suppression network (across the coils and in series with the HV power supply, just before the capacitor bank), and FET gate synchronization components (placed across each FET to ensure they all switch on together).
The principle is simple. With the high voltage power supply turned on at some voltage V, point C1(left side of the capacitor bank) is charged to voltage V. Point C4 is then at ground (zero) through the coils. When the gate pulse arrives at the FET bank, the FET's close and a short circuit to ground is produced. Thus point C1 jumps to zero. Since the capacitors cannot jump to immediately to zero (due to the inherent discharge time), point C4, which was at zero volts jumps to minus V. This potential difference then drives the current from the capacitor bank in an anti-clockwise direction around the lower portion of the loop, energizing the coils. The current cannot jump immediately to its allowed maximum value, by virtue of the inductance of the coils, and the discharge time of the RCL circuit which this system represents.

3 7 10 Conclusion and comments

The approach used in the construction of this system was of reproducibility, reliability and precision Such characteristics are generally not inherent to other high voltage switching system's such as Thyristors or spark gaps In using banks of high voltage FET's the main assist of this systems configuration is the ability to extend the operating abilities, in terms of current and voltage As previously stated high voltage FET's are limited in terms of the maximum voltage they can hold off before breakdown occurs In this system five FET's are used (figure 3 48), and staggered in series so as to divide the voltage load across them (at 2kV, typically each FET is loaded with ~450V) In this way the entire FET array can hold off a 5kV load (maximum) However each device (FET) is also limited in the current which it can deliver In series the current in all five FET's is the same, thus one is limited in ensuring that the peak current never exceeds the device limited In order to extend the current limited however, one could simply create a second array of FET's, placed in parallel, with the first array The same number of FET's per row would still be required to ensure voltage hold off, but the current which could be delivered would be exactly double what one can achieve from a single row of FET's In fact as other authors have demonstrated (Santamaria and Ness [19]) FET arrays of up to 2400 components are perfectly feasible and reliable One could then have the very high voltage/current load deliverable by spark gaps, but still have the precision and reproducibility of solid state devices Since peak magnetic field intensities scale linearly with the current in the solenoid then doubling the current will double the magnetic field

References

[1]: A. Kiernan, March 1994, PhD thesis, Dublin City University.

[2]: A. Gray, August 1999, PhD thesis, Dublin City University.

[3]: W. Witty, March 1998, PhD thesis, Dublin City University.

[4]: http://www.sciner.com/MCP/MCP.htm

[5]: W. Lochte-Holtgreven, Plasma Diagnostics: AIP press 1996. ISBN 1-56396-388-4

[6]: J. M. Hendron, C. M. O. Mahony, J. Appl. Phys, 81(5), 1 March, 1997.

[7]: I. Weaver, G. W. Martin, Rev Sci Inst, vol 70, no3 March 1999.

[8]: T. N. Hansen, J. Schou, J.G. Lunney, Appl Surf Sci, 138-139 (1999), pp 184-187

[9]: D. Kamke, H. J. Rose, Z. Physik 145, (1956), pp 83.

[10]: B.T. Barnes, S. Eros, J. Appl. Phys. 21 (1950), pp 1275.

[11]: S. Suckewer, C. H. Skinner, H. Milchberg, C. Keane, D. Voorhees, Physical Rev Letts, Vol 55, No 17, 21 October 1985, pp 1753-1756.

[12]: H. Fiedorowicz, M. Szczurek, Inst. Phys. Conf. Ser. No 125: Section 9.

[13]: N. G. Loter, W. Halverson, B. Lax, J. Appl. Phys. 52(8) 1981.

[14]: A. Kasperczuk, Yu. P. Zakharov, Laser and Particle Beams 1999, vol 17, no 3, pp 537-545.

[15]: S. Yu. Gus'Kov, V. B. Rozanov, Laser and Particle Beams 1994, vol 12, no 3, pp 371-377.

[16]: A. F. Semerok, S. V. Fomichev, J. Phys. B: At. Mol. Opt. Phys: 36, 2003, pp 4495-4509.

[17]: R. Chokhawala, S. Sobhani, International Rectifier Corporation, Applications Engineering.

[18]: R. J. Baker, B. P. Johnson, Rev. Sci. Instruments. 64 (6), June 1993.

[19]: G. T. Santamaria, R. M. Ness, Maxwell Laboratories Inc USA.

[20]: Herbert L. Hess, Russel Jacob Baker, IEEE Transactions on Power Electronics, Vol 15, no 5: September 2000.

[21]: R. Serov, M. C. Richardson, P.Burtyn, Rev Sci Instrum, Vol 46, No. 7, July 1975, pp 866.

[22]: Physics 8'th edition, Hugh D. Young, Addison Wesly 52690 (1992).

[23]: http://home.san.rr.com/nessengr/ (engineering homepage)

Chapter Four:

Electrostatic Study of Laser Plasma Plumes

Introduction

This chapter discusses results from the range of experiments performed in the space-time range termed 'far field', using ion and electron probes. Here the laser generated plasma plume was studied for time scales greater then ~600nsec. Plasma plume properties such as electron temperature, electron density, and velocity were compared with ion densities and ion time of flight velocities for various target geometries. The target geometries used included rectangular wedges of fixed height and varying depth with varying fluence, and later fixed depth and varying height at a single fluence. Plume dynamics were studied by measuring the angular distribution of particles in both the vertical and the horizontal. Pronounced collimation of the plume was demonstrated from wedge targets compared to planar targets. Finally plume 'collimation' was studied via angle resolved ion distributions of laser plasma plumes generated between two parallel plates in the vertical plane.

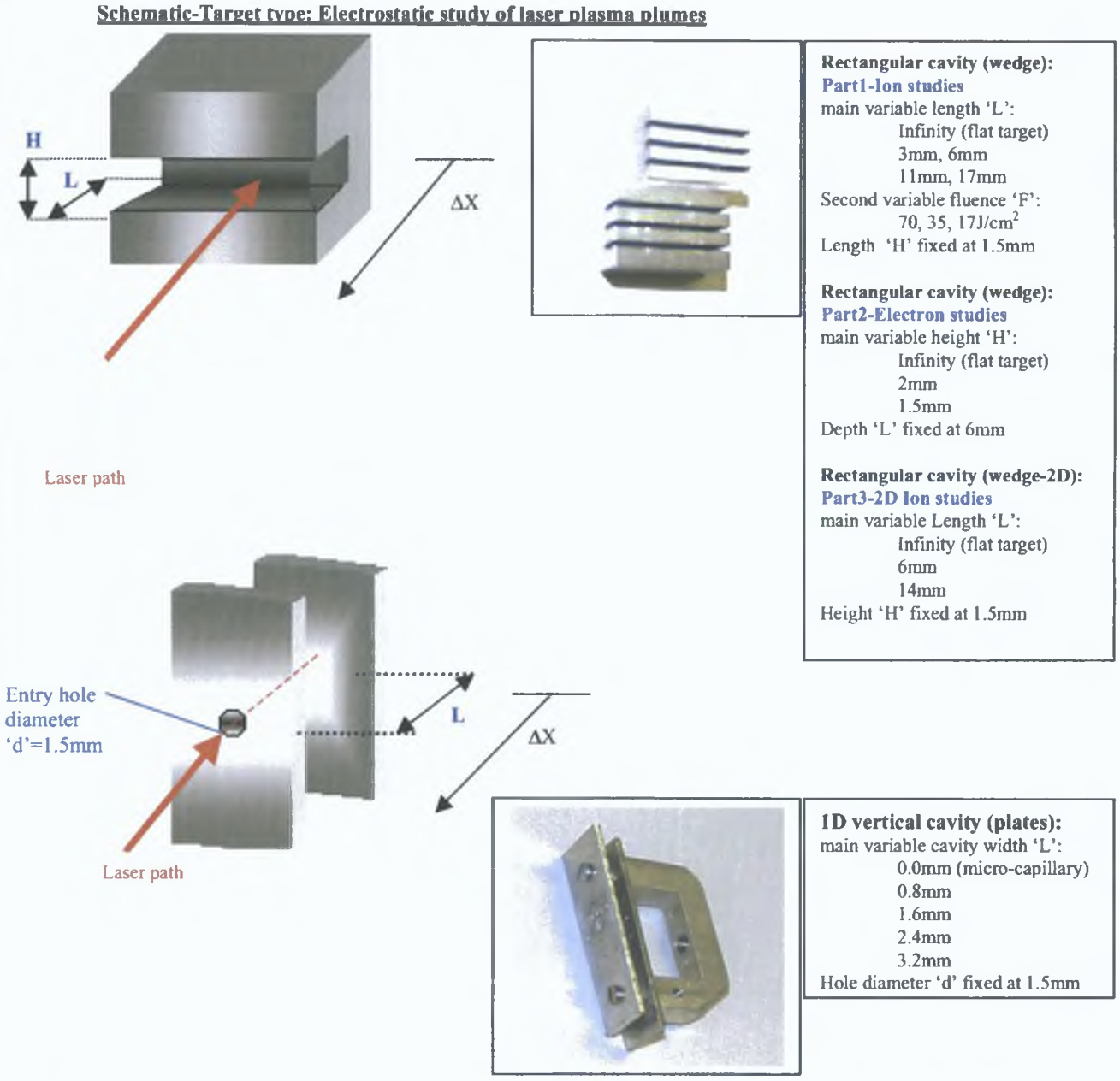

Figure 4.0: Overview of target configurations used in the electrostatic study of laser plasma plumes. The first configuration is the upper type (rectangular wedges). In the first experiments discussed in chapter four, wedges of depth ('L') equal to 3,6,11 and 17mm were used. The height 'H' was kept constant at 1.5mm, while the fluence delivered to the target was varied (from 70, 35 and 17J/cm^2). An array of ion probes was positioned parallel to the target surface to map the angular behavior of the plume under such conditions. Later in order to study electrons, the height ('H') was varied from a planar target to, 2mm, 1.5mm, 1mm wedges. The depth was kept constant at 6mm, and a single fluence was used (70J/cm^2) with a single probe. Lastly in order to study the 2Dimensional nature of the plume and the effects of containment on particle distributions, an array of ion probes in both the horizontal and vertical planes was used. The wedge height 'H' was fixed at 1.5mm, while the depth was varied from 0mm (planar) to 6mm and 14mm.

The third experiment performed involved the target configuration displayed in the lower figure. Here two vertical parallel plates, were orientated normal to the laser path. The laser entered through the hole in the front plate, impinging on the inner surface of the back plate. The distance between the two plates ('L') was varied from 0, 0.8, 1.6, 2.4, to 3.2mm. An array of ion probes, placed in front of the front plate was used to map the angular distribution of particles emerging from the aperture for various plate separations.

Electrostatic study of laser plasma plumes (Far-field)

4 0 Overview

There exists a large body of work, using electrostatic probes to diagnose plasmas, whether from DC plasma of long duration, Z-pinches or laser generated plasmas Generally there are two types of probes Those that sample the ions in a plasma plume, and those that sample the electrons in the plume There are two theories for interpreting the raw data taken from both types of probes Langmuir theory, which can be applied to both ions and electrons, and orbital theory which is more commonly applied to the study of electron signals, but can be equally used to study ions in plumes However, given the constraints of determining the charge of the ions sampled by the probe, Langmuir theory is more usefully applied Langmuir theory requires ion signals to be from singly charged ions, and although the theory is simpler, it is also limited to low fluence studies In this work Langmuir and Orbital theory were applied to study electron signals from high fluence (>50 J/cm^2), high vacuum (10^{-6}mbar) plumes, while Langmuir theory was applied in studying ion signals from mid-high fluence (<18 J/cm^2), and mid vacuum (10^{-3} mbar) plumes

The main strength of electrostatic probes is their spatial resolution, and flexibility If properly mounted they can be moved any point in the plume in order to sample the plume's properties such as density and temperature While they possess very good temporal resolution, this is often limited by the oscilloscope used to record the voltage-time trace Because of the limitations in the theory which allows voltages traces to be converted to useful physical data, probe use is heavily dependent on the fluence used The chief limit is the proximity to the origin, (T_0, X_0) of plasma generation The lower the fluence used, the less energetic the plume, the earlier a stable sheath can form around the probe tip, thus the earlier the probe can sample For the fluences reported here (15-56J/cm^2) and at the pressures used (3.2×10^{-3}mbar, and 5.3×10^{-6}mbar), the spatial limit is approximately 7-8mm from the target surface for ion signal sampling, and 15-20mm for electron signal sampling The temporal limit, of course depends on the flight time of the particles, but is ~600nsec for work reported here One must accept the limitations of certain devices and design experiments around these limitations Here ion probes were employed more extensively because of their ruggedness and ease of analysis Interpretation of electron probe signals is exceptionally difficult under normal circumstances, but at high fluences it becomes mathematically challenging Scientific Systems (www scisys com), a plasma diagnostic company, has successfully produced and sold 'SmartProbe' plasma diagnostic tools, complete with an analysis package for interpreting probe signals Although successful at low fluences, recent reports from research groups (Lunney-TCD, Morrow-Queens) using the device suggest that the analysis package fails at high fluences (>8 J/cm^2) No doubt this is due to the presence of high energy ions which complicate the analysis As a consequence of these limitations, electron probes were utilized less extensively in studying plumes However they do provide a large range of

variables (T_e, V_e, N_e, plasma potential) Data from ion probes, although less extensive, can assist in completing the overall understanding of target geometry effects on plume evolution

4 1 Ion Probe study of plasma parameters from a Horizontally confined plume with varying fluence and cavity depth

4 1 1 Expermental setup

One of the simplest geometric forms of containment is to generate a laser plasma within a rectangular cavity of varying dimensions Here plasma generation was achieved with a Nd YAG Q-switched laser of energy 0 77J at 1 064μm (15nsec FWHM) The laser beam was focused to a spot size of 1200μm using a 20cm plano-convex lens giving an irradiance of ~4 5×10^{9}W/cm^2 The targets were machined from aluminum blocks The targets all had a height of 1 5mm Depth was varied from planar aluminum plate (open target) to 3, 6, 11 and 17mm wedges (figure 4 1) An operating pressure of ~4×10^{-5}mbarr was maintained for all experiments The energy of the laser beam was checked with a power monitor, while the laser was firing at 10Hz Spot diameters were determined from crater diameters on planar aluminum targets after 5 shots, observed under a microscope Eight probes were constructed from 50Ω coaxial cable The core was soldered to a 5mm long 0 2mm diameter tungsten tip, which was surrounded with a two piece ceramic collar, and sealed with araldite The probe was mounted on a rectangular arm which could be positioned away from the target holder, and it was orientated parallel to the target surface, and positioned ~7mm from the laser path and 3 8cm from the target surface, each probe was separated from the next by irregular distances The angular range sampled by the probe array was 7^0, 22 5^0, 32^0, 41^0, 48 4^0, 54^0, 58 4^0, and 62^0 The probes were grounded to the vacuum chamber, and the signals taken through a multi-pin vacuum feed through The bias voltage required to draw positive charges to each probe tip was provided by a biasing capacitor (25μF) The capacitor was biased –28V, this was sufficient to repel all negative charges impinging on the probes when acquiring the saturated ion signal, as the plasma plume streams past it The signals were recorded on a 500Msamples/sec HP oscilloscope, and processed via a GPIB/Labview data acquisition package The fluence to the target was varied by varying the voltage on the flashlamp and amplifier of the laser Values of ~70J/cm^2 (flash lamp ~800V, amplifier ~800V), of ~35J/cm^2 (flash lamp ~700V, amplifier ~700V) and of ~17J/cm^2 (flash lamp ~600V, amplifier ~600V) were used The laser beam was focused onto the back surface of the cavity and the plume expands to fill the cavity, moving away, normal to the target surface By varying the depth of the cavity, the plasma is contained within the cavity for longer periods, thus increasing the time that the plume is in contact with the cavity's inner surfaces

The targets were positioned such that despite the depth of the cavity, the distance from the probe to the target surface was always constant Seven shots were fired to clean the surface, and so avoid anomalous signals from contamination, and three shots were averaged on the oscilloscope

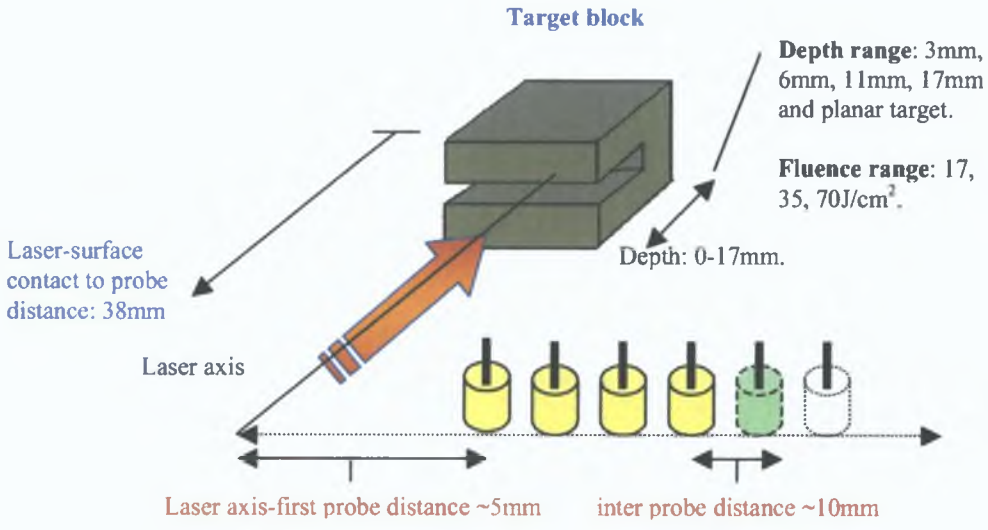

Figure 4.1: Wedge target and probe setup for angle-target depth-fluence resolved plume dynamics study.

4.1.2: General plume trends: Fluence, Depth, and Angle.

In comparing the particle yields from different target configurations, it would be expected that trends for the planar target should display the expected trends. Therefore an important result is the relative independence of the ion yield from laser ablation for the planar target over the fluences used. For F~70, 35 and 17J/cm^2 the peak ion density for the planar target at the probe closest to the laser axis varies from 2.25, 2.42 to 2.35×10^{13} cm^{-3}. As the angle sampled from the laser axis increases, clear differences arise in the ablated yield with fluence. The most recent work on ion yield with varying fluence is by Amoruso [35]. In that work the fluence was varied over the range 3-60 Jcm^{-2} on a aluminum target. A clear saturation of the ion yield occurs ~20 Jcm^{-2}, with a rapid decay in ablated ion yield for lower fluences. Thus we would not expect to see large differences in the ablated ion yield for the high fluences used here on planar targets. A higher fluence on to the target will lead to a more energetic plume, and since laser plasma plumes are highly directional, some differences will be expected in the sampled ion yield for large angles from the laser axis. Indeed as figures 4.1.1-3f show the angle resolved signals for the planar target are almost equal for the probe nearest the laser axis for all fluences used. They do however diverge as the sampled angle increases. However for the wedge targets the trend is different. There is a clear and sustained decrease in the ion yield and peak ion density for each cavity depth over the fluence range studied. This strong drop in signal over the fluence ranges used is most pronounced in the 3 and 6mm cavities, while for the 11 and 17mm cavities the initial decrease in signal (from 70-35 Jcm^{-2}) is small, it is then followed by a moderate increase at 17Jcm^{-2}.

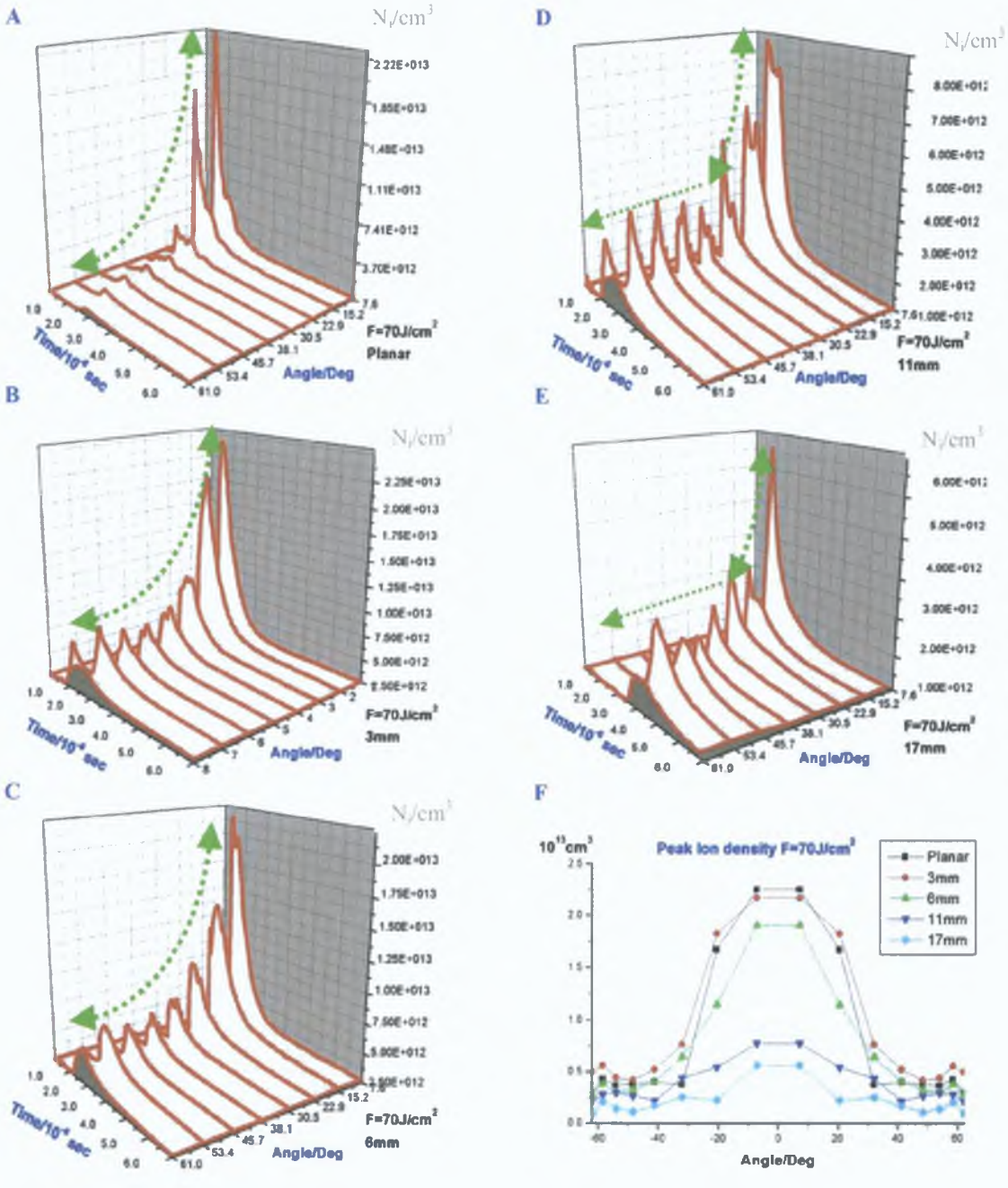

Figure 4.1.1a-4.1.1e: Time-angle-Ni 3D plots for each target studied, for a fluence of 70J/cm^2. The most visible differences between the targets, is the drop in the peak ion density as the cavity depth is increased, and the greater angular spread of the ion signal. The wedge targets all display greater ion density values at large angular ranges, compared with the strong collimation of the ion signal along the laser axis, seen in the planar target. The traces from the wedge targets are also smoother, and more thermalized in their profile.

Figure 4.1.1f (bottom right): Angular dependence of the peak ion density, for all targets at 70J/cm^2. The most notable feature here is the grouping of the profiles. The decay in peak value is clear for increasing cavity depth, but the drop from the 6mm to the 11, and 17mm cavities is large. A probable reason for this is a required minimum time for the plasma to be in contact with a surface for plasma decay into the target to occur. As a consequence of the different distance each probe is from the plasma generation point, each peak in the current trace arrives at increasingly later time delays.

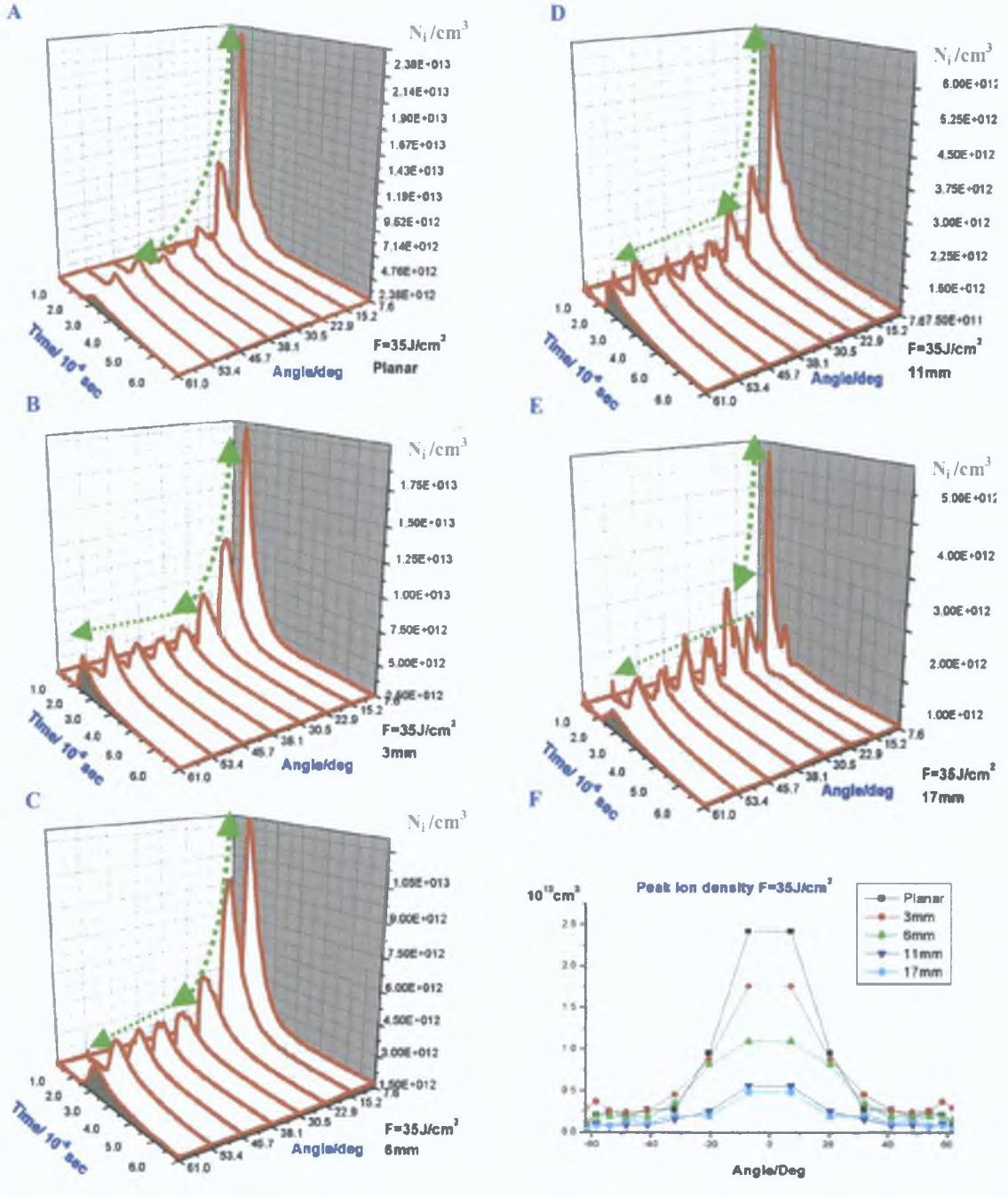

Figure 4.1.2a-4.1.2e: Time-angle-Ni 3D plots for each target studied, for a fluence of 35J/cm^2. As would be expected, decreasing the fluence to the target, produces lower peak ion densities for all wedge targets. The decay in the peak ion density as the cavity depth increases is still present. However while the traces for the planar target are slightly smoother at the lower fluences, the traces for the 17mm cavity are less smooth at lower fluence. Here double peaks emerge in the traces over a large angular range, indicating a shift in the velocity distribution of the plumes particles.

Figure 4.1.2f: Angular dependence of the peak ion density, for all targets at 35J/cm^2. Unlike figure 4.1.1f, the drop in the peak ion density is now more graduated. Grouping exists now at the two deepest cavity depths, 11, and 17mm. The angular profile is also much narrow here, indicating a lower scatter velocity.

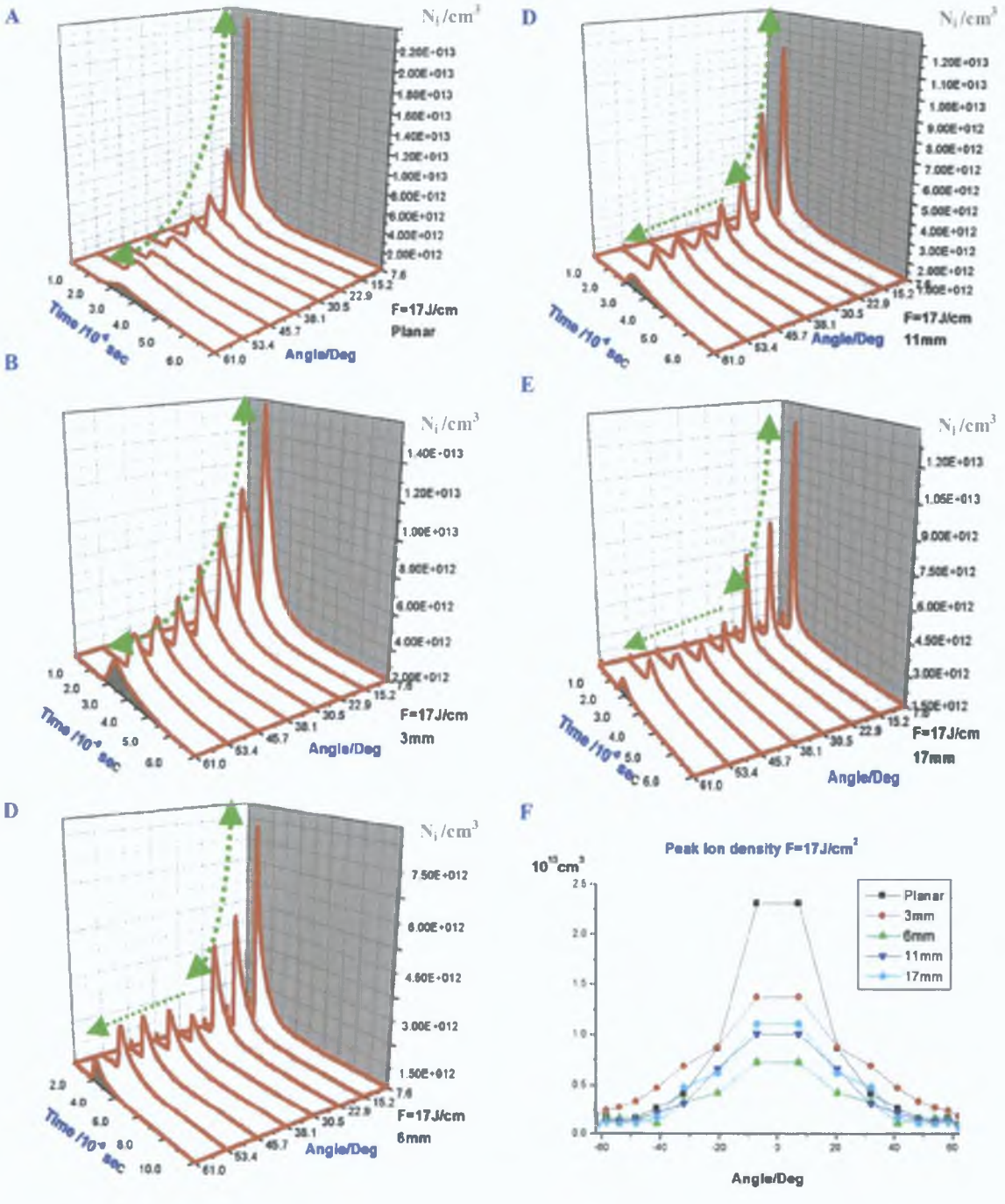

Figure 4.1.3a-4.0.3e: Time-angle-Ni 3D plots for each target studied, for a fluence of 17J/cm^2. At the lowest fluences used, the peak ion density sampled by the probe continues to drop. Unlike the other two fluences studies, at 17J/cm^2 the wedge target show larger values of ion density at larger angles, but only up the 6mm cavity. After this the plume returns to being collimated about the laser axis, as seen for all fluences from the planar target.

Figure 4.1.3f (bottom right): Angular dependence of the peak ion density, for all targets at 17J/cm^2. The angular profiles continue to narrow, however here peak ion density decreases from its peak (planar-3mm-6mm target) and then increases slightly (11mm-17mm target). At lower fluences, plume particles have a lower scatter velocity, and thus both the number of particle hitting the internal surfaces of the cavities and the angles that they do so at is decreased. Minimizing plasma-surface interaction.

At the highest fluence values used (70J/cm^2) the ion traces in the 3D plots are not completely smooth, but display multiple components, this is especially so for the higher fluences of 70 and 35J/cm^2 This is associated with a shift in the velocity distribution of the plume's particles As the plume expands, even in vacuum, some particles will undergo collisions, either with the ambient environment or with layers of the plasma in front and behind a particular region of the plume These collisions represent two distinct regimes within the plume First, particles which do not undergo significant number of collisions, and thus do not suffer from large scatter velocities This component of the plume is not significantly broadened, and moves ahead of the main body of the plume The component of the plume which does undergo a large number of collisions, will display a large scatter velocity and thus the angular distribution of the particles will be larger then that for a collision-less plume Thus in considering figure 4 1 1-3f, which displays the angular profile of the peak ion signal for the main peak for all fluences and all target configurations, there is a substantial narrowing of the angular profile as the fluence decreases The profiles themselves are in good agreement with those studied by Lunney, using Nd Yag laser ablation of various metals, including aluminum at 0 8, and 2 8J/cm^2 A clear trend of decreasing peak ion signal, and narrowing of the angular profile of the ion signal was observed by Lunney for lower fluences (F<5J/cm^2) This behavior is demonstrated here at much higher fluences Thus a less energetic plume is likely to undergo fewer collisions either with a ambient gas medium, or to have fewer scattering collision between discrete layer of the plume itself

The trend of decreasing ion signal for a decrease in the fluence is matched by a decrease in the ion signal, for a fixed fluence, as the depth of the cavity increases Figure 4 1 1-4 1 3a,b,c display a negligible drop in peak ion signal as one decreases the fluence on the planar target from 70-35-17J/cm^2 However the drop for the 3mm target is 21%, and 36%, for the 6mm target it is 45% and 59% as the fluence decreases from the maximum of 70 to the minimum of 17J/cm^2 Thus while lower fluence values do indeed produce lower peak ion signals in the wedge targets, a secondary mechanism, related to plasma confinement within a cavity is augmenting this decay in peak ion signal The most reasonable conclusion is to treat the internal surfaces of the cavities as substrates, through which the plasma loses energy as it moves through the cavity and then expands into vacuum Heat flow is a scalar flux variable, and thus the deeper the cavity the larger the internal area of the confining cavity and hence the larger the surface area that is in contact with the plume, through which the plume bleeds thermal energy and reacts with the target material This would then accelerate the decay of the plume, leading to more rapid formation of neutral particles which the probe cannot sample This would then register as a lower ion single For the highest fluence employed (70J/cm^2), all wedge targets display a larger ion signal at larger angles from the laser axis The most reasonable explanation for this is the target geometry itself For the planar target, the plasma plume is free to expand in all three dimensions However, in the wedge targets, plasma is unable to expand in the vertical plane parallel to the target surface Thus this velocity component of the plasma expansion will contribute to fanning the plume in the horizontal plane, parallel to the cavities plane This will increase the divergence angle of the plume, registering as a larger ion signal at larger angles from the laser axis

4.1.3: Charge and Velocity profiles.

For the fluences employed, TOF velocities and integrated charge sampled from laser plasma plumes show good agreement with those reported by Lunney et al [10, 11, 12] and also Novodvorsky et al [13, 14]. Figures 4.1.4a,b,c display the angular profile of the integrated ion signal

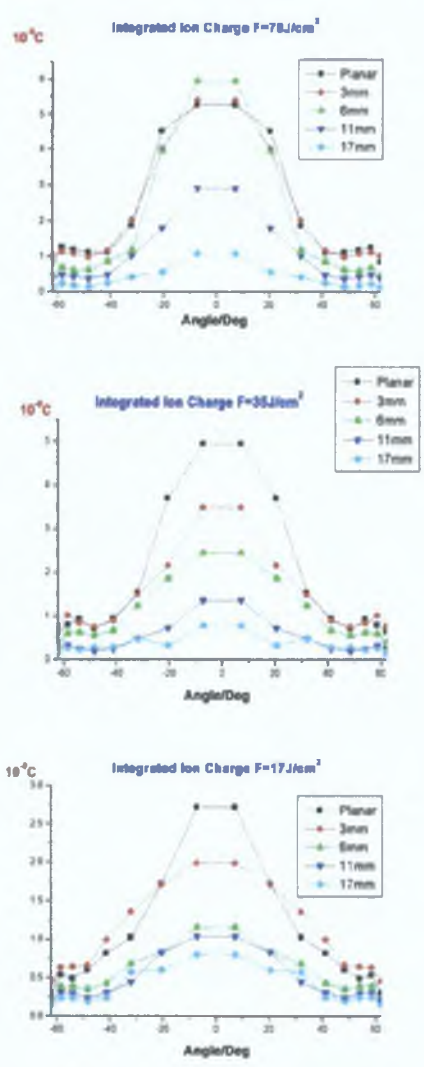

Figure 4.1.4a,b,c (left hand side): Angular profile of the integrated ion signal (or total charge collected from the plasma) for the three fluences studied, for all targets. Mirroring the decrease in the peak ion signals, the total charge collected from each target, decreases as the fluence used increases, and for each fluence value studied, the collected charge decreases as the cavity depth decreases. From studies by Lunney et al [1, 2, 3, 12, 15, 16], the angular profile of both the peak ion signal, the integrated charge and the current signal, does not definitely go to zero within the angles studied by Lunney or in this work. The continuous decrease in peak collected charge is not present at 17J/cm^2, where the peak collected charge decreases until the 6mm cavity, then the rate of decrease slows, followed by a small incremental decrease for the rest of the targets.

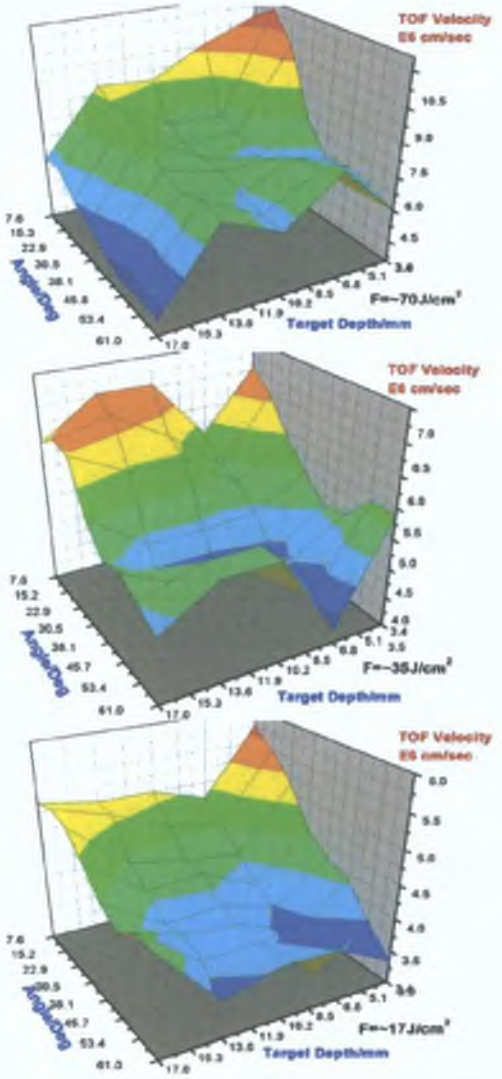

Figure 4.1.5a,b,c (right hand side): Angle and target depth resolved time of flight (TOF) velocities for the three fluence values used. The clear trend is of decreasing peak TOF velocity (determined by the temporal position of the peak in the ion trace, divided by the probe-target distance) as the fluence decreases. Less energy imparted to the target, results in less energy converted to particle kinetic energy. For all fluences and all target depths studied, the TOF velocity decreases, as the angle sampled from the laser axis increases.

from the probe, while figures 4 1 5a,b,c display the TOF velocities for the main peak in all probe traces, plotted against angle and target depth The maximum TOF velocity decreases progressively by ~40% and ~12% [11, 6 5, 5 7E6 cm/sec] as the fluences delivered to the target drops progressively by 50% [70, 35, 17J/cm] However the most striking change is the profile of TOF velocity for probe angle and cavity depth as the fluence changes For the highest fluence value of 70J/cm^2, TOF velocities decrease from the maximum seen in the planar target, at the smallest angle from the laser axis (~7^0) The overall shape of the 3D profile is downward from the 'origin' (smallest angle, zero cavity depth, i e planar target) However as the fluence decreases this trend is no longer as clear The cavities , display larger or equal TOF velocities to the planar target, and this is particularity clear for large angles from the laser axis The targets employed would force the plume to expand in a horizontal fan, parallel to the plane of the cavity, and thus would allow particles sampled by the probe at large angles from the laser axis to have higher kinetic energies then those displayed by the planar target The integrated charge profile for each target and fluence employed displays the same grouping of values as the peak ion signals from figure 4 1 1-3f

In the angle resolved peak ion signals, peak values are clustered at the higher values for the planar, 3mm, and 6mm targets for the highest fluences used (70J/cm) This would infer that for high fluences only significant containment (offered by the 11mm, and 17mm cavities) will affect the peak ion signal This trend is mirrored above in figure 4 1 5a,b,c for the integrated charge signal at the same fluence As the fluence is decreased, the distribution in the peak ion signal and the integrated charge signal from one target to another is more evenly spread Finally at the lowest fluence value employed, both the angle resolved peak ion signal and the integrated charge signal display a grouping of values at the deeper cavities (6mm, 11mm, 17mm) The general conclusion which can be drawn from this is that for a fixed fluence, a minimum degree of containment is required to significantly affect the plume's ion signal, and as the fluence is decreased to lower values, this effect will be seen at smaller cavity depths At still lower fluence, the effect will 'saturate', and not change significantly as the cavity depth is increased beyond a certain value This is not completely unexpected since varying the fluence will result in a saturated effect (particle density, TOF velocity, kinetic energy) at some value (Pappas et al [30]) which depends on the atomic mass of the species undergoing laser ablation However the grouping of both the integrated charge and the peak ion density, combined with the TOF profiles infers, that two competing influences are at work in configuring the plumes properties Firstly, fluence is clearly an important factor in determining the particle density, and the kinetic energy of the ablated particles However, one cannot ignore the large scale interaction of the plume with the internal surfaces of the cavities, which act as substrates The greater the fluence the more energetic the plasma will be, and the greater the population of highly charged species at early timescales Thus high energy particle interaction with the internal surfaces of the cavities is likely to be more important at high fluences High fluences will also result in larger scattering velocities, spreading the plume in the cavities over a large area, thus increasing the surface-area interaction of the plume and cavity internal area Although the plume interaction with the internal volume of the confining cavities

cannot be accurately quantified, it is clear from the particle densities, that for a fixed fluence, lower particle densities are recorded Plume decay into the target volume is the likely cause One might expect that plume collimation would result in the probes recording a larger signal This could be so, however plume decay into the target volume, and resulting formation of neutrals, which the probe cannot register, may mask this effect

For all fluences used in the study of laser plasma plumes, the most notable feature is the shape of the ion traces angular dependence, especially at the smallest angle sampled in the plume, closest to the laser axis The Maxwell-Boltzmann distribution of particles observed, both spatially and temporally in laser plasmas is an attribute which has been verified by many authors with various techniques Geohegan et al [4] combined multiple techniques (absorption and emission spectroscopy, ion probe, and intensified ICCD imaging) in order to study ion distributions of laser plasma yttrium ions in a gas environment An important conclusion of that work was the close similarity of the temporal profile of singly charged ions and neutrals An important concern is that of the probe's inability to sample uncharged particles However Geohegan's work has shown the close relation between neutral and singly excited states in laser plumes Another body of work utilizing absorption in the visible (Whitty and Mosnier [3]) using a Dye laser as a back lighting source, to obtain shadowgrams of lithium laser plasma has demonstrated, that even very early in the plasma history, Maxwell-Boltzmann distributions of plume properties (in Whitty's work intensity variations of Li^0) correctly describe plasma behaviour Both Lunney and Novodvorsky [1, 2, 12, 15, 16, 17, 18] have studied the particle distributions from laser plasmas for various targets, gas pressures, and fluence conditions All of the work reported by both authors demonstrated strong collimation of the plume constituents about the laser axis, which fall rapidly as the angle sampled from the laser axis increases This is clearly evident in the angle vs time vs peak ion density 3D plots for the three fluences reported in figures 4 1 1a,b,c-4 1 3a,bc In these plots the largest ion signal for all fluences and depth values studied is at the angle closest to the laser axis ($\sim 7^0$) The ion signal then decreases as the angle sampled increases However as the plots display, the rate of decrease depends not only on the fluences, but also where, temporally in the time dependent trace one compares the angle resolved values Also it can be clearly seen that the rate of change of peak ion signal depends on the target configuration employed

4 1 4 Plume scattering and particle dynamics

Novodvorsky et al [17, 18] studied the space and time dependency of tantalum and niobium ions from laser plasma plumes using ion probes Using fluences of $2J/cm^2$ at similar pressures and target to probe distances employed here, Novodvorsky measured TOF velocities of $1.9 \times 10^6 cm/sec$ The reported velocities are lower then those seen here, however this is to be expected given the higher fluences used in this work Also, the ion signal displayed a L^{-2} dependency (L being the distance between the probe and the target) in Novodvorsky's studies This was measured for the first tantalum and niobium ion groups, which undergo

few collisions during their flight away from the targets surface Although the probe to target surface distance was not varied here, the length of the confining cavity was Thus plume expansion from the target surface is influenced by the cavities internal surface area, for varying lengths It is clear that greater confinement times (due to the longer time a plume spends in a deeper cavity) leads to lower particle densities In plotting the peak ion signal versus target depth for the three fluences used (taken from figures 4 1 1-3f), the decay profile is not linear, but a smooth decay curve, which exhibits the largest drop from the angles closest to the laser axis The important conclusion here is that lower particle densities from confining targets is due to a non-standard decay mechanism when compared to standard 3D expansion of a laser plasma into vacuum This process is fluence dependent, with the higher fluence ($70J/cm^2$) showing a less pronounced drop in peak particle density than the other two fluences used ($35, 17J/cm^2$) This could be due to either the rapid expansion from the cavities, leading to a shorter confinement time, and hence minimizing the loss mechanism which stems from plasma-surface interaction, or simply that of a more energetic plume containing greater thermal energy at the time of plume exit from the cavities Equally important is the difference in the angular spread of the plume for the fluence and targets investigated

The angular distribution of ablated atoms or ions can be expressed as

$$\text{Equ 1} \quad \frac{F(\theta)}{F(0)} = \cos^{p}\theta + B\cos\theta \qquad \text{(Threstrup et al [16])}$$

where p is an exponent and B is a constant The term $B\cos\theta$ is added for angular profiles which do not have a clearly defined baseline, and p is fluence and target constituent dependent As reported by Threstrup and Lunney [16], p values vary from 8 5(Al) to 19 (Bi) for increasing atomic mass and fixed fluence In the plasma expansion model by Anisimov [14] the angular distribution of the particles in the plume can be expressed in analytical form

$$\text{Equ 1 2} \quad \frac{F(\theta)}{F(0)} = \left(1 + Tan^2\theta\right)^{3/2}\left[1 + \left(\frac{Z_{inf}}{X_{inf}}\right)^2 Tan^2\theta\right]^{-3/2} \qquad \text{(Threstrup et al [16])}$$

where Z_{inf}/X_{inf} (termed the asymptotic expansion ratio) is the ratio of the limiting value of the plume front along the Z axis, normal to the target surface directed into the vacuum and X is the plume front parallel to the target surface Thus the larger the ratio, the more pronounced the forward expansion of the plume away from the target normal The smaller the ratio, the greater the plume's angular spread Fits of the angular distribution for each target and fluence used were made using equation 1 2 Figures 4 16 6a and b display the result of theoretical values and values fitted to the experimental data

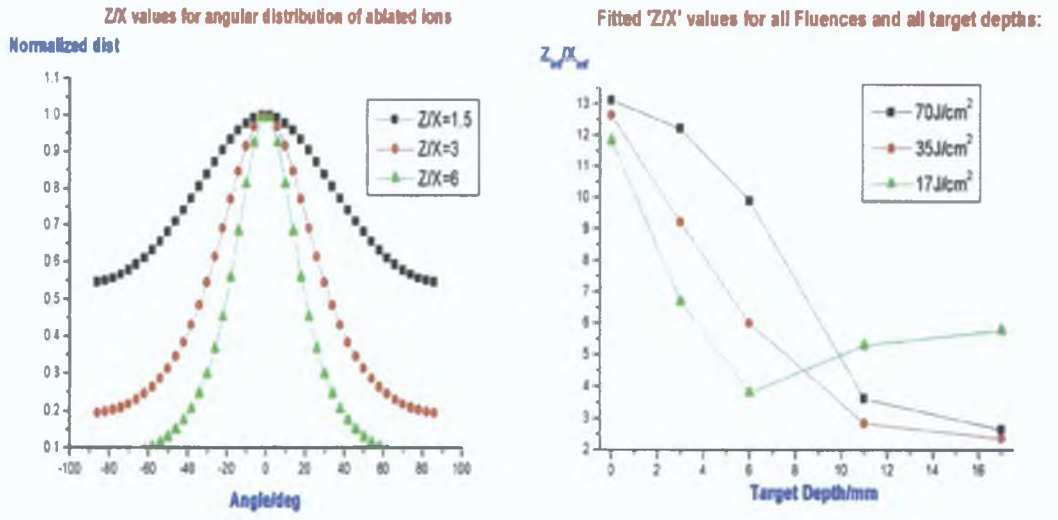

Figure 4.1.6a,b: (left)Theoretical profiles using equation 1.2 for three different ratios of plume normal vs lateral expansion. The lower the ratio of Z/X, the less forward is the expansion of the plume, and thus the larger angular spread of the plume particles. (right) Experimental fit of the raw data for each fluence and target used. A software routine was used to run test values for Z/X from 1.001-25, and then using equation 1.2 to plot the angular distribution of ions. Minimum error between the fitted and the experimental values resulted in the displayed values of Z/X.

As would be expected, for the planar target, decreasing the fluence results in a less collimated plume normal to the target surface, and thus a lower value of Z/X. However the rate of fall of the Z_{inf}/X_{inf} for the fitted data (figure 4.1.6b) is much more pronounced for lower fluences as the wedge depth is increased, but only up to a point. For F=17J/cm^2, it increases after 6mm, and does so only for the lowest fluences value used. This would infer that due to the shape of the cavity, that plume expansion in the forward direction, normal to the target , is matched by fanning of the plume in the horizontal plane over a larger angle. This trend is maintained until the lowest fluence (17J/cm^2) when for the two deepest cavities (11 and 17mm) the value begins to increase over the other two fluences used. Thus the affect of cavity confinement has the same affect as lowering the fluence delivered to the target, or increasing the diameter of the focused laser spot, and thus decreasing the extent of the forward expansion of the ablated species in the plume.

4.1.5: Conclusion.

In summary, utilizing an array of ion probes and varying the fluence delivered to the target surface, the angle resolved particle densities from aluminum laser generated plasma within confining cavities of varying depth were studied. The trend of decreasing peak particle densities with both decreasing fluence and increasing cavity depth was clearly observed. Lower fluence values also displayed flattened, broader angular profiles of both particle density and integrated charge signal from the plume for all target geometries employed close to the laser axis. This is due both to the lower fluence used to generate and heat the plume, but also due to the nature of the target geometry employed. Lower TOF velocities were

observed for increasing cavity depth, a trend which was unexpected given the assumption that a confined plasma should exhibit a higher directed expansion velocity TOF velocities did increase with increasing fluence for all targets employed Lastly, the ratio of the plume extent normal to the target surface versus the plume extent parallel to the target surface scales down with decreasing fluence and increasing cavity depth, displaying a more uniform distribution of particles across a larger angle

4.2: Langmuir and Ion Probe study of electron and ion parameters of plasma plumes from rectangular wedges with varying cavity height.

4.2.0: Introduction.

Having studied the effect on ions of confining plasma expansion to the horizontal plane and varying the fluence delivered to the target, the next logical step would be to evaluate the effects on electrons of such a target geometry. Novodvorsky et al [18] compared ion and electron signals from laser generated tantalum plasma plumes. Substantial differences in the angular and lateral distribution of ions and electrons were reported, thus we would expect to see enhanced differences for plasma electrons contained by a cavity.

4.2.1: Experimental setup.

Plasma generation was achieved with a Nd:YAG Q-switched laser of energy 0.77J at 1.064μm (15nsec FWHM). The laser beam was focused to a spot size of 1200μm using a 20cm plano-convex lens giving an irradiance of ~4.5×10^{9}W/cm^2. The targets were machined from aluminum blocks. The targets all had a depth of 6mm. Height was varied from planar aluminum plate (open target) to 2mm, and 1.0mm wedges. Operating pressure of ~4×10^{-5}mbarr were maintained for all experiments. Fluences on to the target of ~70J/cm^2 were used. The energy of the laser beam was checked with a power monitor, while the laser was firing at 10Hz. Spot diameters were determined from crater diameters on planar aluminum targets after 5 shots, observed under a microscope. The probes were identical to those used in the previous section. Only a single probe was used to study electron signals. The chief difference here is the experimental method which must be followed. The bias voltage on the probe tip is varied over a large range of values. Here a biasing capacitor was biased from –1.2V to +12V, this was sufficient to repel all negative charges impinging on the probe when acquiring the saturated ion signal, and

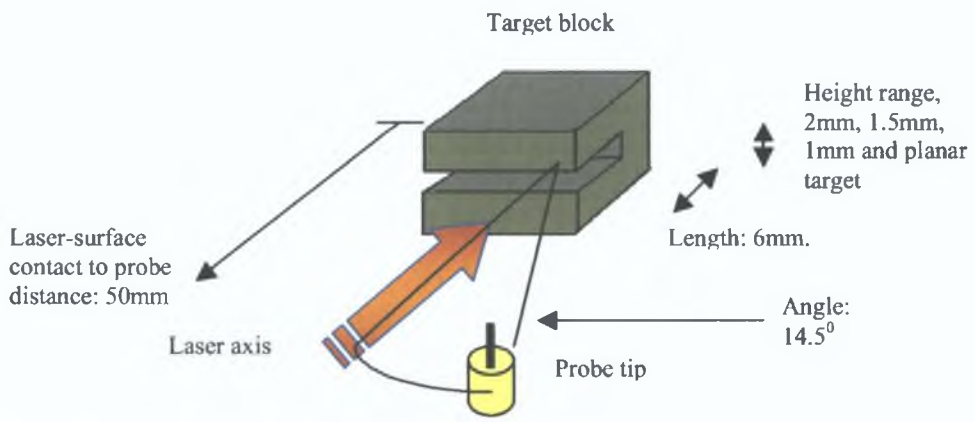

Figure 4.2: Wedge target and probe setup for plume dynamics study.

also to repel all positive charges when acquiring the electron saturation signal as the plasma plume streams past it. The signals were recorded on a 1.2Gsamples/sec oscilloscope, and processed via a GPIB/Labview data acquisition package. The targets were positioned such that despite the depth of the cavity, the distance from the probe to the point where the laser contacted the target surface was always constant. Seven shots were fired to clean the surface, and so avoid anomalous signals from contamination, and three shots were averaged on the oscilloscope, to compensate for signal variation (~10%) from shot to shot.

4.2.2: Data analysis and interpretation overview.

Figure 4.2 (below) shows a typical IV curve for varying bias voltage on a probe. The data below is interpolated in the raw data. This was necessary to ensure smooth slope evolution from one time resolved curve to the next. Otherwise the temporal profile of the electron temperature, when calculated, becomes unstable due to the influence of large negative log values, arising from very small negative signals. The latter was a consistent problem as the signal transits from ion (positive) signal to negative (electron) signal. In order to process these IV curves for data calculation at as many time resolved points as possible, a software package was written in MATLAB 6.0. This imported the 50-60 current traces over the bias range, and formed the IV curves over all temporal values (ignoring very earlier times where the traces are very unstable, due mostly to fast transient plasma, where the stable low velocity plasma has yet to reach the probe).

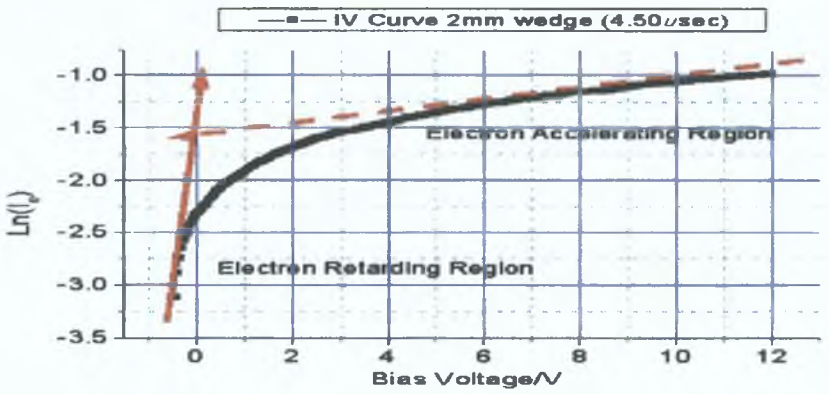

Figure 4.2: IV characteristic for the electron probe, 2mm wedge at 4.50μsec after the laser pulse. The electron retarding region is the linear region to the left of the 'knee' of the curve at the plasma potential (~0.8V), while the electron saturation region is the linear region at the right hand side of the curve. In translating IV-curves to physical data, a good deal of mathematical filtering is required given the problems in interpreting these signals. Firstly the raw data was interpolated, thus increasing the number of points from an average of 65 to 200. This was done for both the ion and the electron signals. Plotting the natural log of the current signal versus the applied voltage gives the standard IV relation. Then the ion saturation signal was subtracted from the electron signal. The former did not saturate as Langmuir theory expects (the lack of saturation in laser plasmas is not new, and is due to the growth in the sheath diameter as the applied voltage is increased (Weaver et al [7]), a similar effect is seen at the electron saturation region). The final operation is that of doubly differentiating the electron signal, which possesses a local maximum at the turning point where the slope of the linear region begins to decrease. A linear fit to this region gives the slope which is related to the electron temperature within the plasma. Extension of this line to intercept a linear fit to the electron saturation region allows one to deduce both the plasma potential and the electron density. The same program was used to plot the square of the electron current versus the applied voltage for Orbital theory calculations.

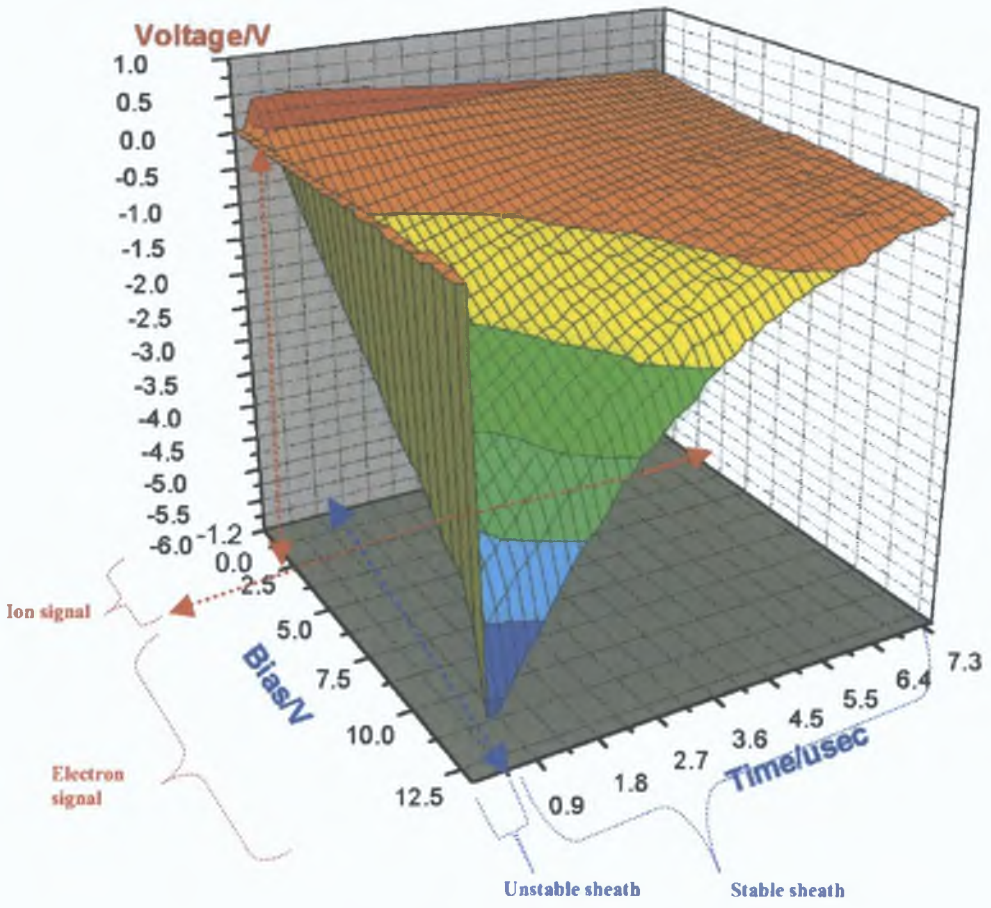

Figure 4.2.1: I-V-T characteristic for the plasma plume, for the planar target. The boundary between stable and unstable sheath is well defined in time, for the planar target it is approximately 950nsec. Although plume signal is resolvable for 100-150nsec earlier than this, calculations with the IV relation for times earlier than ~950nsec are unreliable. As the bias voltage increases, a larger number of electrons are drawn from the probe, and register as an increasing negative signal as a consequence of larger numerical values of negative signal. The earlier time when stable sheath exists will shift back slightly. The I-V-T relations for each plasma plume are unique, and change dramatically for varying fluence and the ablated targets atomic mass, the angle sampled within the plume, and pulse width of the laser beam and the gas pressure which the plume is expanding to.

The general procedure in probe calculations is to form the I versus V relation for a specific time delay after the laser and then begin the mathematical analysis (different for each theory applied). Figure 4.2.1 displays a 3D profile of the plasma plumes response to varying bias voltage, for the complete duration of the plume, as it streams past the probe. The transition from positive ion signal to negative electron signal depends on the fluence of the laser beam. The more energetic the plasma ions the larger the bias voltage range required to map the response of the plume, and the larger the bias voltage required to transit the plume's 3D response profile from positive to negative values (ion to electron). The more energetic the plume, the higher the velocity of the particles. Thus for smooth traces of T_e, and N_e, more points per unit time are needed, and hence the faster oscilloscope used to capture the traces the more accurate the physical properties determined.

Each data trace (T_e, V_e, N_e) has approximately 500-600 points plotted, in reality there are ~8900 points on the oscilloscope trace in total. Approximately 800 points are lost in the time of flight of the plasma, registering as no signal, while the last ~500 points or so are lost due to low signal level which cannot be used with any reliability. Finally, to minimize the computation time, only every 2nd or 3rd time resolved data point was used to produce the time resolved values of T_e, V_e, and N_e. The large number of data points displayed is a large improvement over previous work, (Hendron, Weaver and Lunney [6,7,13]) who plotted no more than 20-40 points per T_e plot for plume signal of duration 10-20μsec.

Automatic linear fitting of both the retarding region and the saturation region allowed electron temperature/ density/velocity, and plasma potential to be automatically calculated. The IV curves were seen to be unstable at both very earlier timescales, where stable sheath growth has yet to develop, and also at very late stages in the plume's lifetime. This is primarily due again to small signals, and resulting shifting of the lower portion of the retarding region, which skews the slope dramatically to larger values.

A number of assumptions are required for analysis of probe data. The theory of flowing plasma plumes registering transient signals was developed by Segall and Koopman [5] who established the use of probes in freely flowing plasma plumes produced by laser ablation. The underlying assumption is that in the bias regions, the desired signal is much larger then the corresponding opposite polarity signal. Thus for negative bias signal the ion saturation signal should be much larger then the electron signal. The current time traces show a strong fast rising peak, representing the leading edge of the plume.

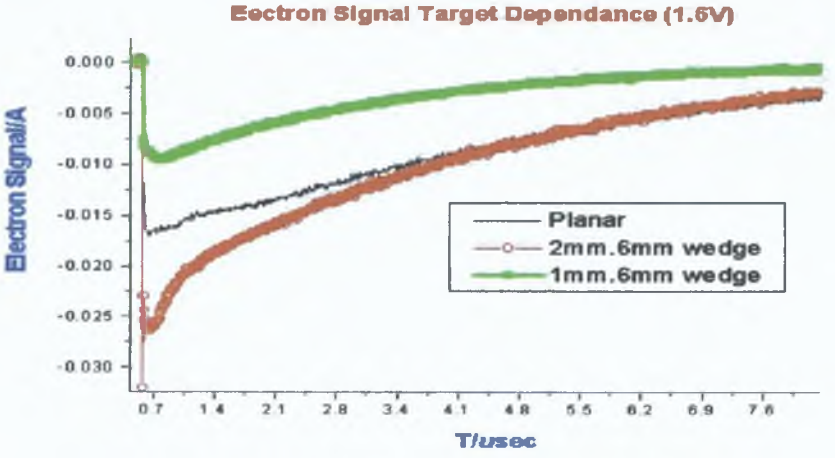

Fig 4.3.1: Electron traces for the three targets studied. One might expect the electron traces to shift in a systematic manner (as the ion trace does below), as the plasma becomes more confined. However since the voltage response of electrons in each plume is different, than the registered electron signal will not necessarily be staggered in a systematic manner at the same voltage, as displayed above. For all acquired traces typically signal variations were of the order of 10% and was compensated for by averaging the signals from three proceeding shots.

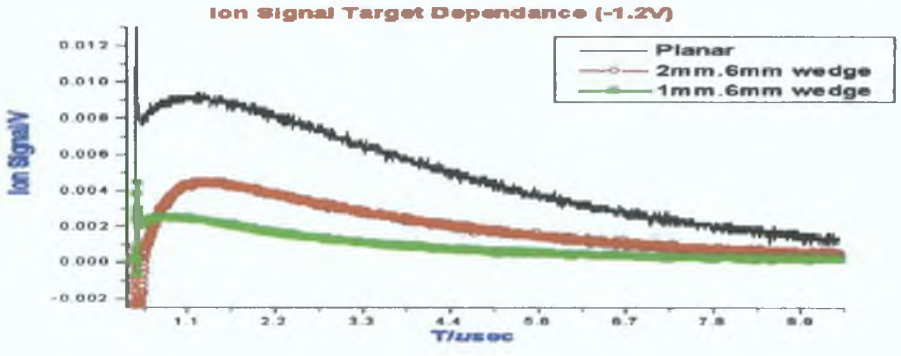

Fig 4.3.2: Ion traces for the three targets studied. There is a small but measurable shifting back of the approximate temporal position of the peak signal for the planar and 2mm case. The shifting back of the 1mm wedge signal is clear.

The fast vertical spike seen in the ion traces is generally attributed to photoelectric emission from the probe surface (figure 4.3.2), either due to radiation from the laser impinging on the surface or radiation from the plasma itself (Hansen et al [1]). A systematic shift of the position of the peak signal can be seen in both electron and ion traces (figure 4.3.1-2). The superior TOF velocity for the wedge targets and the trend observed with decreasing wedge height is a feature also seen at earlier timescales from optical measurements*. In the latter, ion profiles in the visible show shifted emission profiles and higher edge velocities in wedge targets over a planar target, while both TOF and edge velocity scale upwards with decreasing wedge height. This relationship is clearly maintained at much longer timescales as the probe signals show. Despite having left the confining wedge, the collimated plasma maintains its initial higher velocity. However the difference in TOF velocity is small compared to those observed at earlier time scales in the visible*.

4.2.3: Temperature and velocity results.

Probe theories, such as Langmuir theory generally apply to non flowing plasmas, compared to laser plasmas plumes which a have a direct velocity component. Langmuir theory applies to a collision-less sheath condition, however the IV characteristics of a Langmuir probe in a flowing plasma can be shown to approximate those of a static non flowing plasma if the root-mean-square thermal electron velocity V_{rms}, in the vicinity of the probe is at least three times greater than the local flow velocity V_f (Segall et al [5]). The ratio of V_{rms} to V_f for a self-similar adiabatic flow is approximated by R~ $(\tau/s)\sqrt{3kT_e/M_e}$ [7] where τ is the arrival time of the probe signal and s is the target to probe distance. For this work R is ~13.5 for T_e=10000K (wedge targets) and R~12 for T_e=7500K (planar target). Thus the condition is satisfied and Langmuir analysis on flowing plasma plumes can approximate non flowing plasma. In the case of orbital theory, one requirement is that the sheath radius be larger than the probe radius. Here the probe radius was 0.1mm. From Hendron et al [6], the sheath dimension can be written as $S_D \sim 2\lambda_D(eV/kT_e)^{3/4}$, where λ_D is the Debye length. In work reported here, the value of 'S_D' (min) was ~0.5mm at early timescales, and later increasing to ~1mm, with

*Optical measurements of plume parameters, to be presented in chapter 5.

the minimum value corresponding to the peak electron density. Such trends were also observed by Hendron [6]. Figures 4.4.1, 4.4.2 display electron temperatures and velocities for each target. The velocity (thermal velocity) is calculated from the equation 2, chapter three, section 4, and thus is a consequence of higher electron temperatures. However it is in clear agreement with the earlier arrival times of the ion and electron signal traces due to higher TOF velocities (flow velocity). Where visible images* were used to calculate edge velocities from identical targets, peak values ranging from 30, 8.0, 6.0E6 cm/sec (for 1mm, 2mm wedges and planar targets) were calculated. In figure 4.4.2, the electron velocity is a full order of magnitude lower than those from peak optical measurements*, this is not unusual given the differences in the timescales of the two measurements. However despite the large difference, the scaling relationship of greater containment leading to enhanced physical values is maintained (in this case electron temperature).

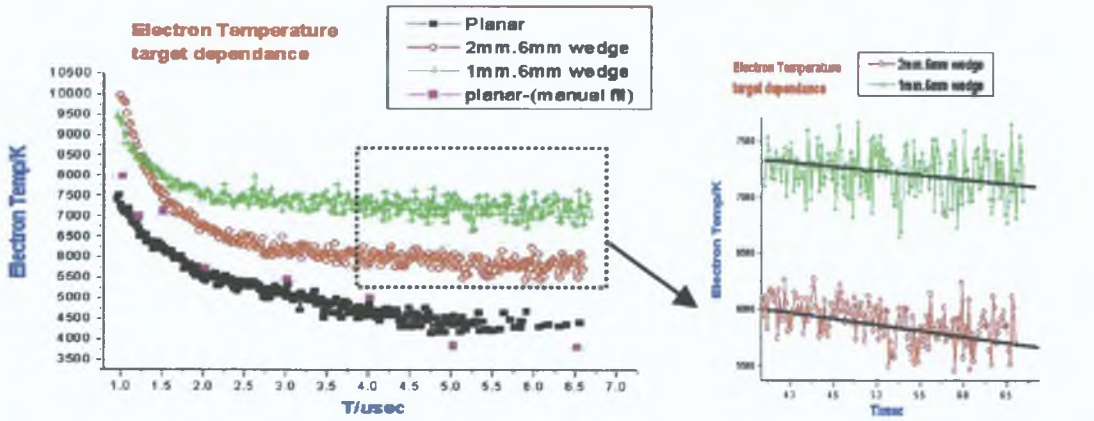

Fig 4.4.1: Time and target resolved Electron temperatures for the three targets, and zoom plot of the later stages of the temperature trace for the 2mm and 1mm wedge profiles, with linear fit to the region inside the dashed box which appears flat (right). As can be seen in the zoomed plot, at later stages the profile becomes increasingly noisy. A number of manual calculations were done for comparison with the automated data.

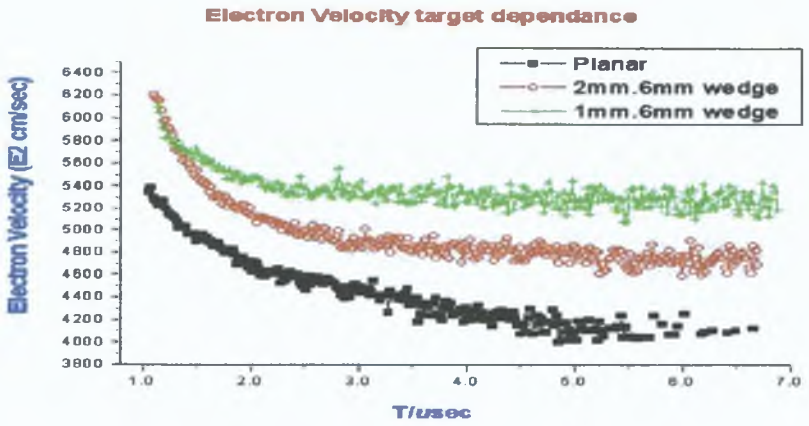

Fig 4.4.2: Time and target resolved Electron velocity. The velocity is calculated from equation 4, chapter 3. The assumption is that particles within the plume exhibit a Maxwellian energy distribution, with their velocity directly related to the temperature of the plume.

*Optical measurements of plume parameters, to be presented in chapter 5.

Notably the 1mm wedge plume displays almost constant temperature at the trailing edge of the signal, and the slope of the temperature decay shows good scaling with the degree of containment (the temperature and velocity profiles for the 2mm and 1mm wedge are in fact not flat, but appear so at this scale). This is not a data or analysis error, intensified gated images* in the visible also show a long extended plume with very uniform intensity along its axis. Secondly the peak temperature of the 1mm wedge plume appears to be slightly lower then the 2mm plume. However spectroscopic measurements* (discussed later) have confirmed superior temperatures for greater containment of the plume. Such superior temperature profiles also arrive earlier, as a consequence of higher kinetic energy of the plume. Thus as discussed above, the temporal limit for stable measurements depends on the plume energy. The 1mm plume electron temperature is indeed higher than the other targets*, however stable IV measurements for the 1mm wedge occur later, after the peak temperature in the 1mm wedge has passed. As a consequence the probe is unable to resolve this superior peak in the temperature profile for the 1mm wedge. (T_e for the 1mm wedge were calculated by the analysis package for t<1μsec, but they were extremely unstable, and were removed)

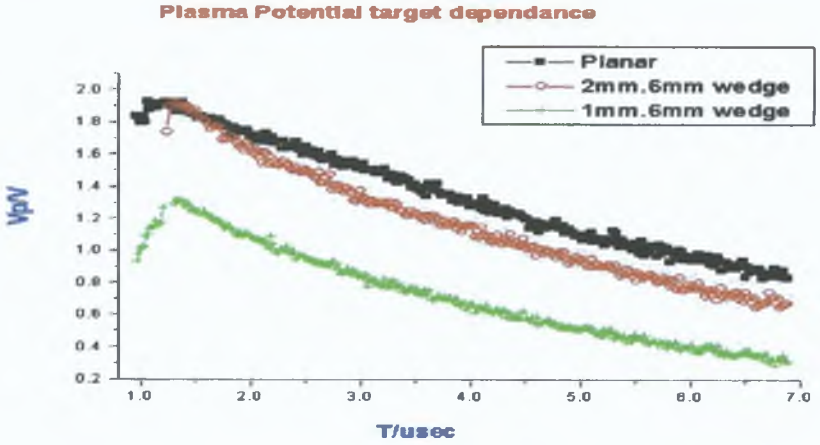

Fig 4.5: Plasma potential, for the three targets. Ideally if T_e values for the 1mm wedge were available for t<μsec (i.e. a clear rising T_e profile in figure 4.4.2), then the V_p profile above would have displayed a sustained rising edge for the 1mm wedge, and clear rising profiles for the other two targets.

The rapid rate of fall of electron temperature from high initial values is a common feature of transient plasma undergoing rapid expansion (Amoruso et al [10]). However, few studies exist for very high fluence plume generation with probes and thus no direct comparison can be inferred with other work. The peak in the plasma potential profile (figure 5) at early timescales partially coincides with the peak of the temperature profiles for all targets. The extent of the rising edge of the plasma potential profile is more pronounced as the extent of containment is increased, i.e. In the wedge target relative to the planar, and as the wedge height decreases. While the peak value of the plasma potential is lower for the wedge targets, its pronounced rising peak, seems to indicate a highly localized region of charge relative to the plasma main body. In visible studies* the authors observed enhanced plume splitting in confining targets for different ion spatial profiles within the wedge. The general understanding of plume splitting is that the source of the multi-component behavior is governed by charge distribution within the plume, with the leading edge

*Optical measurements of plume parameters, to be presented in chapter 5.

composed of energetic ions and electrons in layers, The main body of the plume is mostly thermalized particles undergoing hydrodynamic expansion in a denser region subject to strong recombination [7, 8]. As the delay increases the difference in kinetic energy leads to an increasing separation between the two plume components. Since the targets in this experiment are identical, and assuming that higher velocities and localized charge separation properties, although decaying, are conserved at latter timescales, then the pronounced peaking of the plasma potential in the wedge targets is evidence of earlier charge separation, which results in steep gradients in the plasma potential at later timescales, near the leading edge of the plume.

4.2.4: Electron and ion density results.

Figures 4.6.1-4.6.3, display the electron density (Langmuir theory), the electron density (orbital theory), and the ion density. The good agreement between Orbital and Langmuir theory is evident both in the power values and in the position of the peak as well as the relationship between the three targets (see figure 4.6.1, 4.6.2). The larger numerical value of density from Langmuir theory is not a new trend (Weaver et al [7]). The lower values of electron density from orbital theory are more likely to reflect a realistic rate of capture of electrons relative to their velocity, rather than assuming that all electrons which fall within a certain number of Debye radii from the probe are captured, as Langmuir theory assumes. However the absence of a clearly defined peak for the planar and 2mm wedge raises questions as to the responsiveness of the orbital theory calculations .

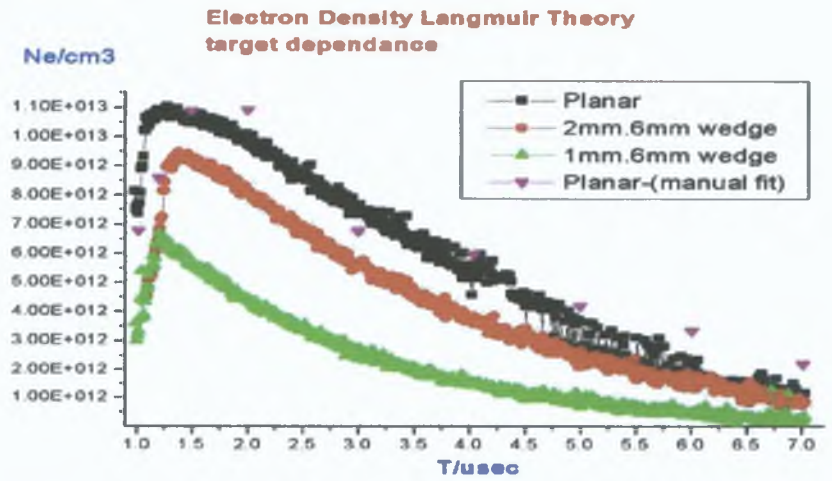

Fig 4.6.1: Electron density, using Langmuir theory for the three targets. All targets display a smooth decay in the electron density from an initial high value. Values of N_e for the planar target were manually calculated for a number of points in order to validate the automated calculations. As can seen from the traces, the fast rising edge of the electron density has fewer points then the falling regions, due to rapid changes at the leading edge of the plume, which is narrow in duration. At the later stages of the plume's history, values of N_e become increasingly noisy, especially in the planar target. The 'sharpness' of the peak N_e for all targets becomes more pronounced ingoing from planar-2mm-1mm wedge. This combined with the profile of the plasma potential indicates that the plume in the 1mm wedge displays a very sharp well defined, and highly localized in time region of high particle density at its leading edge.

*Optical measurements of plume parameters, to be presented in chapter 5.

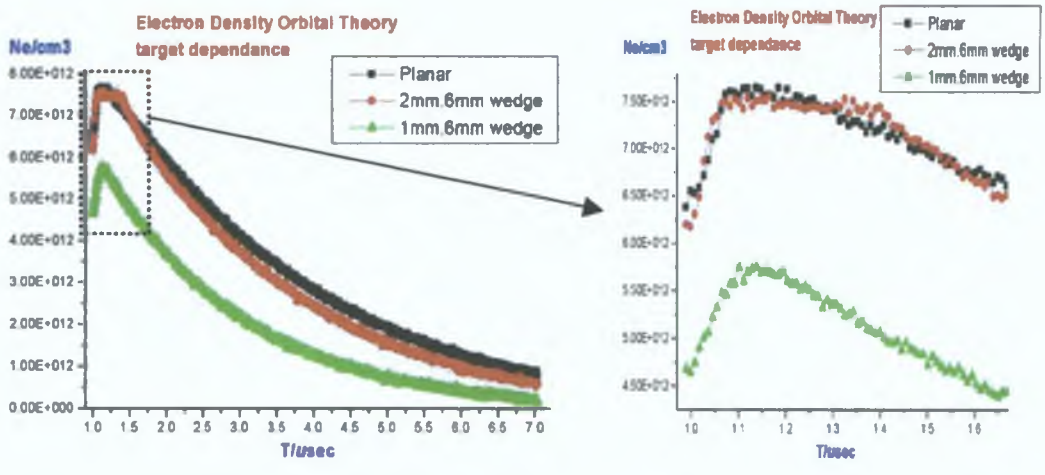

Fig 4.6.2: Electron density, Orbital theory, and expanded region 0-2μsec. Demonstrating that the electron density profile its not completely flat at early timescales. The narrowing of the peak profile in time is still evident for the 1mm wedge target.

Interestingly the 1mm wedge is the only target to show a pronounced peak and rising edge in the density values for figure 4.6.1 and4.6.2 (both theories). For Langmuir theory (figure 4.6.1), the planar and 2mm cavity targets display rounded extended peaks, while the 1mm wedge displays only a sharp well defined peak. While the analysis package used was able to provide electron density values for all targets from Langmuir theory (figure 4.6.1), the early phase values for N_e and T_e, were extremely unstable and had to be removed from the plots. In fact the orbital theory profile of N_e did provide data points at earlier timescales than Langmuir theory, however they were not included as Langmuir theory data point at such early timescales were not reliable. The probable cause for detecting the rising edge in the electron density for one theory (orbital) and not for the other (Langmuir) is the requirement of a stable IV relation for Langmuir theory. One should recall that for Langmuir analysis to function, one must form a stable log(I) versus V plot. Accurate detection of a rising edge in the density or temperature profile of a plume, depends on the relative response of the plasma to the probe's bias voltage. If the plasma flow is turbulent or unstable, or of very high velocity, then stable IV relations will not form at early timescales. However, Orbital theory analysis is less vulnerable to changes in the probe current or turbulent plasma flow, by virtue of the simplicity of plotting I^2 versus V, instead of the Log I versus V relation from Langmuir analysis. The flattened profiles for N_e in figure 4.6.2 for the planar and 2mm wedge were unexpected. Clearly a rounded peak profile in N_e should be present for all targets. However it has been noted that, when the signal from the probe is very small, plots using Log values are far more sensitive to small changes in signal than that of plotting the current or the square of the current from the probe. The most reasonable conclusion is that the flattened regions in figure 4.6.2 for the planar and 2mm wedge were due to insensitivity in the I^2 vs V plots for orbital theory for a limited duration, at early time scales due to very small currents from the plasma. However since no other work has been reported with so many points per time interval in the time dependent Te and Ne traces from probes, it is possible that the flattened N_e profiles are real. This is a

reasonable statement given the smooth profiles of the ion density in figure 4.7. Here the decrease in the particle density is mirrored for ions as seen in figure 4.6.1-2 for electrons. Such a trend for ions is expected given the trends observed in section 1, for cavities of varying depth.

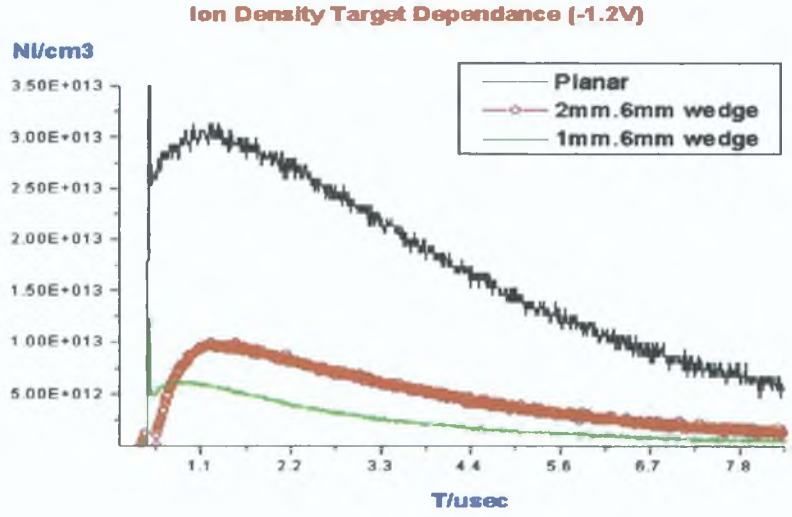

Fig 4.7: Ion density. The clear trend being the decrease in ion density as the degree of containment is increased. There is also a clear shifting back of the peak ion signal, which arrives earlier. The extent of the shift is only very slight for the 2mm wedge , but pronounced for the 1mm wedge. In section 1, laser plasma plume generation in rectangular cavities displayed lower TOF velocities with decreasing depth and fixed height. Here, with cavities of fixed depth, and decreasing height, increases in the TOF velocity of both electrons (figure 4.61-2) and ions (above) is demonstrated.

4.2.5: Theory comparison.

Most authors (Hendron [6], Weaver [7], Lunney [16]) report a t^2 dependence of electron density profiles during the initial rise of the leading edge from a planar target plume, followed by a t^{-3} decay, due to volumetric expansion of the plume. Generally for the timescale of the T_e, N_e profiles (10-20 times the duration of the rising edge), the rising edge will appear linear. However the profiles for electron density here do not. Differences arise between Langmuir theory based densities and Orbital theory based values. The Langmuir and orbital density values, taken from the retarding and accelerating regions, showed a linear rising profile for all targets. The decay profile for the planar target from Langmuir theory is less pronounced its is curvature, yet clear in the orbital theory profile. For both theories, both wedge targets display the standard decay profile. Since the ion density profiles exhibit the standard decay profile seen by others [10, 11] it is assumed that the unusual decay profile of the electron densities in the planar target is due to the high fluences used, leading to unstable flow of plasma about a probe tip. Given such instabilities, the ability of Langmuir's analysis to treat a flowing plume with the same theoretical assumptions as that of a DC plasma is undermined. The sampling of a high energy streaming plume by a probe is a complex interaction, as is plasma plume interaction with surfaces, such as those within the volume of the cavities. However such questions are beyond the brief of this work.

Considering the lower electron density values for both theories, and also the lower ion densities in figure 4 6 3, the general trend is of lower particle density as the plume experiences greater confinement This may seem to be a contradictory statement From optical measurements* where we observed that confining targets produces higher densities at earlier timescales, and within a spatial region close to the target surface However as time progresses and the plume expands inside the cavity, then the large increase in velocity, and the channeling effect of the wedge, allows the forward region of the plume to move away at an enhanced velocity, driven both by higher temperatures, but also larger pressures as a consequence of higher densities at the rear of the plasma, which is still trapped by the cavity This behaviour is also thought to be responsible for the enhanced plume splitting in such targets A Second mechanism, inferred from section 4 1 2, is the influence of the inner cavities surfaces, which act as a substrate Both wedge targets have a larger surface area which is in contact with the plasma, over an extended duration

4 2 6 Conclusion

In summary, utilizing Langmuir and Orbital theory in our analysis to study the spatial and temporal profile of the plasma parameters, the most important trends were of enhanced plasma parameters Changes in the peak value and the time resolved profiles of temperature and velocity were demonstrated with confining targets The lower density for electrons and ions is explained as rapid plasma expansion, with large velocity gradients at early timescales (inside the cavity) leading to enhanced plume extension as seen in optical measurements* A lower density trend with decreasing wedge height seen in the later stages of plume expansion were confirmed with probes at longer timescales For the two wedge targets employed, decreasing the height of the cavity was seen to increase the electron temperature, electron thermal velocity of electrons Decreasing cavity height demonstrated decreasing ion density Differences in the peak values of N_e for both Langmuir and orbital theory and N_i are attributed to the limitation of each theory in interpretation of the IV response of the plume

*Optical measurements of plume parameters to be presented in chapter 5

4.3 Time and angle resolved 2D ion studies of plasma plumes from rectangular wedges of varying depth Horizontal and Vertical behavior

4.3 1 Introduction

Having studied the effect of confining plasma expansion to the horizontal plane, the next logical step would be to evaluate the effects of plasma interaction with the inner surfaces of the cavity This was done, by increasing the depth of the cavity while keeping the height constant Secondly, utilizing only one electron probe at one spatial position, doesn't allow

for the study of how the plume's angular density profile is changing as a consequence of collimation or plume surface interaction In order to quantify the extent of the plume collimation, an array of ion probes was mounted in both vertical and the horizontal directions The experimental setup was similar to that described above

4.3 2 Experimental setup

Plasma generation was achieved with a Nd YAG Q-switched laser of pulse energy 0 77J at 1 064μm (15nsec FWHM) The laser beam was focused to a spot size of 1400μm using a 20cm plano-convex lens giving an irradiance of ~2 5×10^{9}W/cm^2 The targets were machined from aluminum blocks and had a depth of 6mm and 14mm The height was fixed at 1 5mm for the wedge targets

An operating pressure of ~2×10^{-3}mbar was maintained for all experiments, while fluences on to the target of ~50 J/cm^2 were used The energy of the laser beam was checked with a power monitor, while the laser was firing at 0 8Hz, and spot diameters were determined from crater diameters on planar aluminum targets after 5 shots The probes were constructed from 50Ω coaxial cable with the core soldered to a 5mm long 0 4mm diameter tungsten tip This was then surrounded with a two piece ceramic collar, and sealed with araldite The probes were mounted radially on a semi-circular arm which could be positioned away from the target holder, and the probe tip was orientated parallel to the target surface (see figure 4 8) The first probe was positioned 9mm from the laser path and 6 5cm from the target surface when studying the horizontal plume distribution The probe to laser distance was then reduced by 3 5mm while the probe to target distances was kept at 6 5mm for studying the plumes vertical distribution The probes were grounded to the vacuum chamber, and the signal taken through a multi-pin vacuum feed through The bias voltage required to draw positive charges to the probe tip was provided by a biasing capacitor (75μF) The capacitor was biased at -37 5, this was sufficient to repel all negative charges impinging on the probe when acquiring the saturated ion signal, as the plasma plume streams past it The signals were recorded on a 2 5Gsamples/sec oscilloscope, and processed via a GPIB/WaveStar data acquisition package Five shots were fired to clean the surface, and avoid anomalous signals from contamination, and three succeeding shots were averaged on the oscilloscope(typical shot to shot variations were ~10%) The angular positions

of the probes in the horizontal position were 9^0, 19^0, 27^0, 40^0, 58^0, and 76^0. For the vertical array the angles were reduced by 5^0 for each probe. This was required to sufficiently map the vertical distribution in the wedge targets whose plume was highly collimated in the vertical plane. Figure 4.8 shows the experimental setup used. Six probes were mounted radially about the laser axis at increasing angles from the plume's central expansion axis. A seventh probe, mounted on the opposite side of the laser axis, and at the same angular position as the first probe in the array was used to ensure that the plume's ion distribution was indeed symmetrical about the laser axis, as this is a crucial assumption used in the analysis (discussed later).

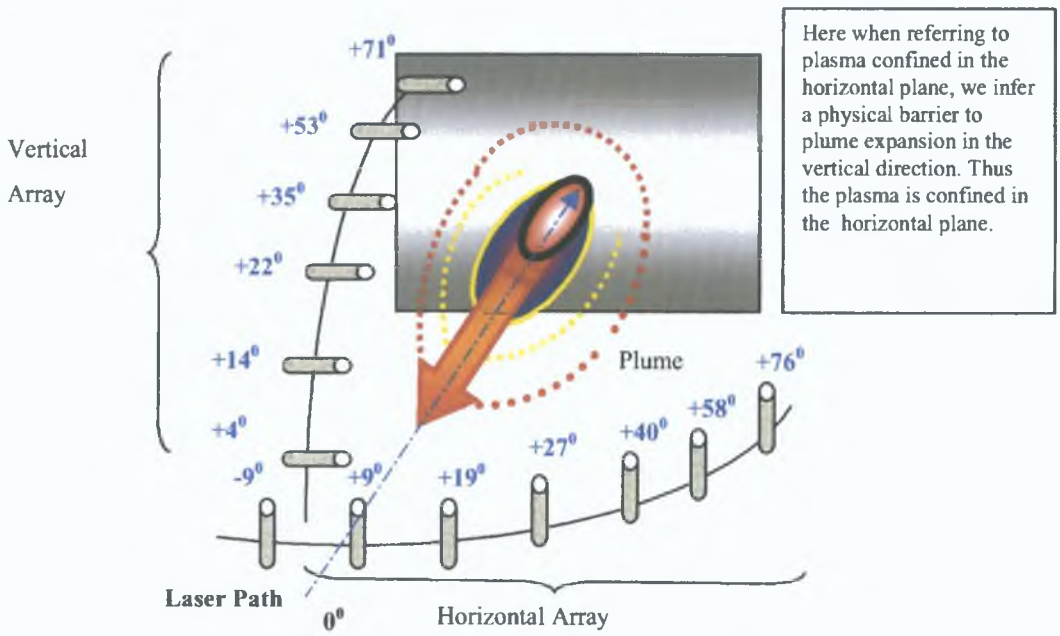

Figure: 4.8 Experimental setup. Two arrays of probes, orientated in a planes of 90^0 to each other, sampled the plumes 2D particle distribution.

Equ.2 $Y=Y_o+\frac{A}{w\sqrt{\frac{\pi}{2}}}\exp\left(\frac{-2(x-x_c)^2}{w^2}\right)$ Gaussian equation for ion angular distribution.

While other authors [12, 13, 15] fitted $A\cos^p\theta$ terms to the angular cross section of the ion distribution, we however do not have a well defined baseline in the angular distribution due to the limited angle sampled, and only have ion traces on one side of the laser axis. Stable fits involving sine or cosine power functions require a large number of points to fit with minimum error. However the ion angular distribution seen here is not unlike that reported in [15, 16]. In most work using ion probes to study plume dynamics, the fluence is low. Thus the traces usually only comprise one mode/velocity group. However when fluences greater than 3-5J/cm^2 are employed [17, 18] then multiple overlapping curves representing plume components with different velocity components are observed. Multiple plume components have been observed by many authors with a range of different diagnostics [17, 18], while the 'plume splitting' aspect of laser ablation has also been modeled (Wood et al [19]). In order to properly resolve the peaks and centers of each

component for a particular trace, the angular distribution for each plume and target was fitted with the above Gaussian function, using the multiple fit algorithm in Origin 5.0.

4.3.3: Analysis.

Figures 4.9 and 4.10 show typical ion probe traces for a planar target, from the vertical array. The multiple components are distinguished by separate curves (colored), whose summation creates the original ion trace (black). The TOF velocity of each group is also displayed. As is expected from laser plasma plumes, the greater the angle from the laser axis sampled, the less distinct the difference in velocity groups. This is demonstrated from figure 4.9, where the first two velocity groups are well separated (at 4^0), yet in figure 4.10. the first two velocity components have merged.

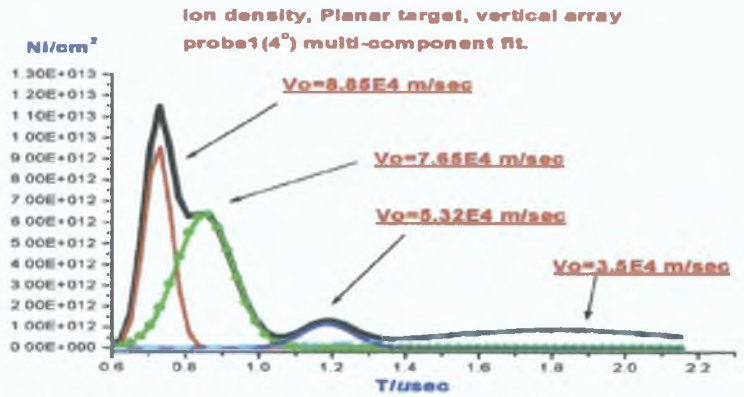

Fig 4.9: Ion trace for planar target, vertical array, probe one (4^0) from the laser axis.

As expected the horizontal and vertical distribution for the planar targets are similar in both their peak ion density, TOF velocity, and the number of velocity groups as well as the angular dependence of the traces in both planes. This is usually a central assumption in plasma models for laser ablation plumes from flat targets.

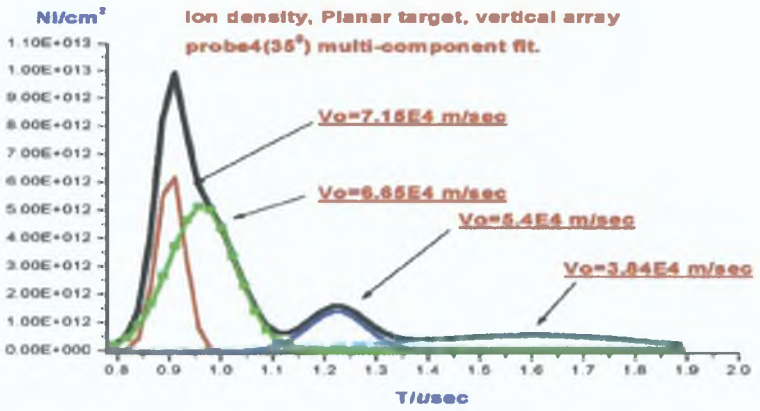

Fig 4.10: Ion trace for planar target, vertical array, probe four (35^0) from the laser axis.

Generally as the angle sampled from the laser axis increases, the number of separate velocity groups sampled in the plume decreases. This is due to the thermalization of the plume's particles which no longer exhibit large differences in velocity. Indeed the highly directed nature of laser plasma plumes is a consequence of rapid forward expansion of the plumes particles. This expansion which is both a 'flow' expansion or bulk motion coupled with secondary forces such as electrostatic acceleration of charged particles due to Knudsen layer formation during the early phases of plasma formation. With either increasing angle (from the laser axis) or increasing distance from the target, plasma density and collision rates decrease rapidly, thus lessening the extent of differences in the velocity distribution of various plume components. However as would be expected the wedge targets show substantial differences in both their bulk distribution of particles spatially within the plume (figure 4.11.1-4.11.2) and also the number of velocity groups observed in each probe trace (figure 4.12.1-12.3, 4.13.1-13.3).

4.3.4: Particle Angular distribution.

If a non standard influence on plume behavior is studied (horizontal confinement), then clearly the greatest difference in plume dynamics will be seen in that plane being directly influenced. To complicate matters further, no models of plasma generation or plume evolution with plasma conductive decay under target confining conditions exist at present, due mainly to the

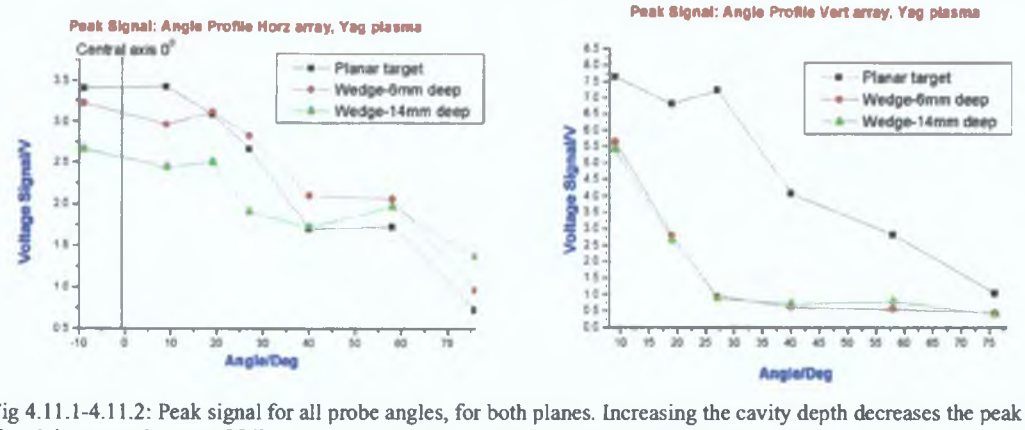

Fig 4.11.1-4.11.2: Peak signal for all probe angles, for both planes. Increasing the cavity depth decreases the peak ion signal, however the rate of fall at large angles is less pronounced for the wedge targets (figure 4.11.1).The sharp cutoff from both wedge targets in the vertical is clear. The similarity of the profile for both wedges in the vertical (figure 4.11.2) indicates that the collimation effect is more strongly dependent upon the cavity height rather than the cavity length.

extremely complicated processes created through plume cooling and decay from contact with a surface, plasma plume deflection from a surface, and multi component plume interaction (in the sense that most models assume that the plume is continuous in the change in velocity/density/temperature from one point to the next, clearly this would not be a valid assumption for plasma generated inside a containing cavity at early timescales where plasma collision with the cavity surfaces could lead to highly complex behaviour).

In considering the temporal behavior of the plume, one can choose to display either the very early timescales (0 5-1 8μsec) involving the leading edge and main peak (fast component) or the trailing edge (2-10μsec) The figures (4 11 1-4 11 2) display the angular dependence of the peak ion signal, showing the lower peak ion signal as one moves away from the laser axis, in both planes of study As will be shown later, the drop in peak ion signal for greater geometric confinement is a recurring trend in plume cavity confinement The rate of fall of the peak ion signal with increasing angular distance from the laser axis is very pronounced for both wedge targets when compared to the planar target in the vertical It is clear that the collimation of a laser plasma plume is much more heavily dependent upon the height of the cavity than the depth, since the difference in the vertical angular profiles for the 6 and 14mm cavities are not significantly different The plumes from the wedge targets display decreasing peak values (especially near the laser axis) We associate this with plasma interaction with the internal area of the cavities, which essentially act as a substrate for plasma to decay onto The effect (plasma decay into the target) would be area and time dependent The internal surface area of the cavities is larger than the planar target, and the length of time the plume spends in the cavity volume increases with cavity depth The peak ion signal for the plume in the horizontal plane has a nearly flat plateau over a relatively large angle (30^0), followed by a shallow decay out to ~60^0 This would indicate that although plasma is being collimated by the wedge target, it is also very uniform in its angular density distribution in the horizontal plane The most probable reason for this, is the high level of collisions occurring within the plumes, while they are within the cavities volume, which reduce the differences in the different group velocities, and produce a more unified streaming plume

The 3D profile of time-angle-densities for each target are displayed in figure 4 12 1-4 13 3 The profiles in the wedge targets in the horizontal (figures 4 12 1-2), display a much smoother decay from the initial peak than a planar trace, which displays a number of multiply grouped velocities just after the main peak An interesting difference is the more pronounced rate of fall of peak ion density with angle It is steeper for the planar than the wedge targets plume, with the 14mm wedge displaying much shallower decay in peak ion density with angle

The smoother decay in both wedge targets from the initial peak is indicative of a higher collisional rate, which lessens the velocity gradients throughout the plume, while the less pronounced signal decay with angle indicates a higher scattering angle of the main ion plume centered on the laser axis Extended tails in TOF traces are usually from low kinetic particle flow overlapping the back front of the electron cloud of the plumes charged part (Ermer et al [22]) This extended 'tail' generally occurs when energy distribution within the plume favours the leading edge Here the majority of particles are charged, and move away with greater velocity than that of the bulk cloud Such trends are inherent in high energy transient systems, such as laser plasmas In the vertical plane, the plume collimation from the wedge targets is dramatic

3D plot Time vs Ion Density vs Angle- probe array(Horz+Vert):

4.12.1

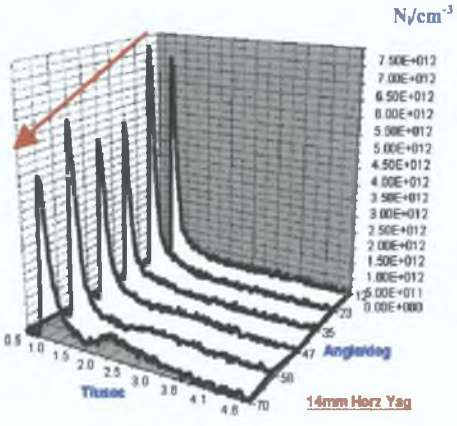

4.13.1

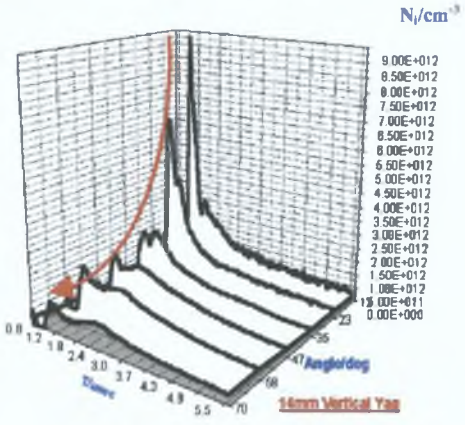

4.12.2

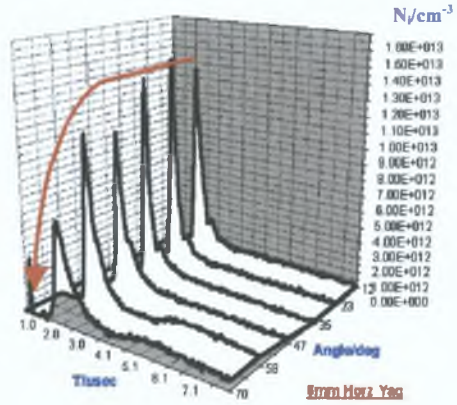

4 13.2

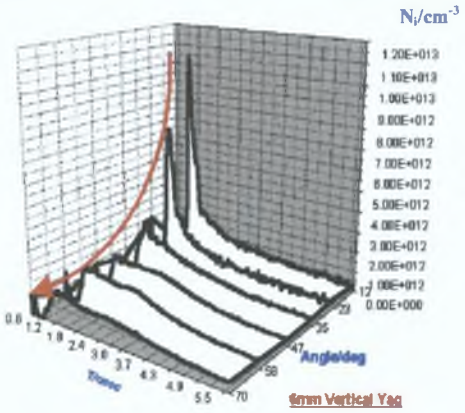

4.12.3

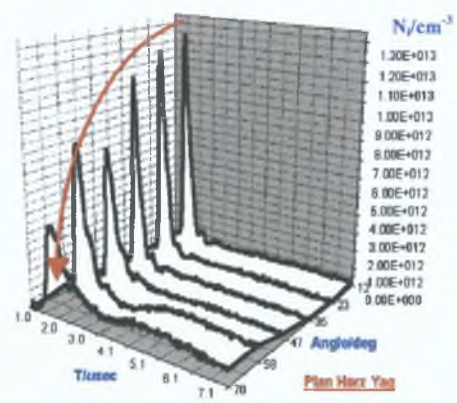

4.13.3

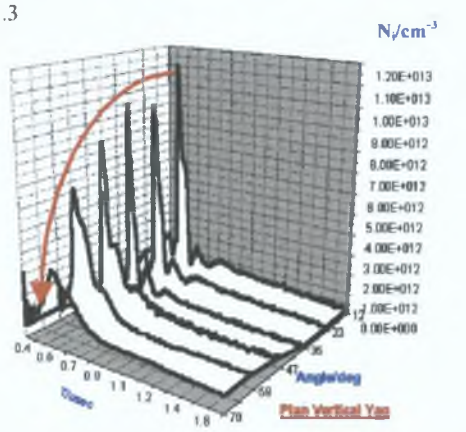

Fig 4.12.1-12.3: Angle-density-time 3D displays of the ion density for the horizontal probe array (left hand side). The continued trend from other work of lower peak particle density with greater geometric confinement is demonstrated here again. Considerable structure is evident not only in the angular dependence but also in the temporal profiles. In all targets the peak density occurs closest to the laser axis, falling steadily with angle for the planar target, and in a less pronounced manner in the wedge targets.

Fig 4.13.1-13.3: Angle-density-time 3D displays of the ion density (Right hand side) for the vertical array of probes. That peak ion density scales down with greater confinement is also evident in the vertical plane. The wedge targets show a more collimated peak density over a smaller angular range while the planar target displays the typical decay profile. For larger angles the wedge cavities no longer display a clearly defined single peak, but show two less well defined components of extended duration.

The rate of fall of ion signal with angle is very pronounced in comparison with the planar target Although the 3D plots have been rescaled to display the main peak more clearly, the duration of the total signal from the wedge targets is approximately 2-4μsec shorter than that from the planar target for the vertical plane The difference in the duration of the signal between the targets increases as the sampling angle is increased, and one moves further away from the laser axis From Anisimov et al [14], 'the forward direction nature of the laser evaporation process has been found to result in an anistropic expansion velocities of the atomic species which are controlled by the plasma dimensions' Thus a plume which is unable to expand vertically will be forced to undergo substantial redistribution of its charged constituents, increasing the ion-electron collision rate

4.3 5 Plume temperature and velocities trends

We have noted higher electron temperatures for plasma plumes from wedge targets of fixed depth and decreasing height in the previous section and thus, assuming a Maxwellian distribution v_e is given by

$$\text{Equ 3} \quad v_e = \left(\frac{8kT_e}{\pi m_e} \right)^{\frac{1}{2}} \quad \text{(Hendron et al [2])}$$

The increase in temperature of electrons translates to a higher electron velocity The large area inside the cavities can lead to both thermonic emission of positive ions and electrons from hot surfaces (Threstrup et al [16]) and also rapid thermal decay at the boundary between the plasma and cavity surfaces However, decay of the plume into the target surface is likely to dominate over any process which might liberate particles from the target surfaces back into the plasma The flux of ions and electrons can be calculated from the Langmuir-Saha and Richardson equations (Lochte-Holtgreven [34]) and both show an exponential increase in the fraction of ionized species with temperature Since an enhanced temperature regime exists at early timescales* for such targets, the effect of plasma collision and decay with the cavity's internal surfaces is likely to be more pronounced for a more highly charged plume This could account for the contradictory trend of lower particle densities from confined plumes In the most probable case, multiple thermal layers will be created horizontally, and as the region of the streaming plume closest to the internal surfaces will thermally decay faster then the plume centered in the cavity, such a process is area dependent The longer the plasma undergoes such a process, the more internal energy a plasma will lose to the target bulk Higher plasma temperatures, will lead to higher thermal ionization, while higher photon energies will lead to higher photo ionization The containing aspect of the cavities will maintain local particle densities for much longer than that of a freely expanding plume This should increase any effect of plasma collision and decay with internal surfaces From the Anisimov model [31], the assumption being that the plasma is axially symmetric, however as one would expect, the further along the cavity the plume propagates the less likely it is that such an assumption can be maintained Indeed the pressure profile from the Anisimov model is given as, Equ 3 1,

*Optical measurements of plume parameters to be presented in chapter 5

$$P(r,t)=\frac{E}{I_2(y)XYZ}\left[\frac{X_oY_oZ_o}{XYZ}\right]^{\gamma-1}\times\left[\psi(x,y,z,t\right]^{\alpha+1}$$ (Anisimov et al [14])

And the density is given by,

Equ 3 2 $$N(r,t)=\frac{M}{I(y)XYZ}\times\left[\psi(x,y,z,t\right]^{\alpha}$$ (Anisimov et al [14])

This gives pressure and density profiles at spatial coordinates x,y,z and at time t Here γ is a constant adiabatic index, I_2 and I_1 are constants related to the gamma function Γ, and $\alpha\sim1/(\gamma-1)$ Such a function displaying the typical shifted Gaussian is usually seen in TOF curves from either ion probes, Faraday cups or spectral intensity of a spatially resolved ion In very energetic plasma plumes the curve from the ion signal is rarely as smooth and simple as the approximations given by the Anisimov model However if the velocity separation between different ion groups in the cloud is small, multiple overlapping ion signals can give a resultant smooth TOF signal (Novodvorsky et al [17]) The number of velocity groups in a trace show a strong dependence on the laser intensity and hence fluence At the high fluences reported here, the temporal separation of the different velocity groups is small due to their high velocity, but clear enough to resolve The full ion traces from both horizontal and vertical arrays are of greater duration than that reported by Novodvorsky et al [17] and P E Dyer, et al [27] The smoothness of the traces for both probe signals in the horizontal and the vertical, becomes more apparent as the cavity depth increases The plume traces near the laser axis show only a short lifetime trailing region, whereas the probes at greater angular range show a large secondary plume, whose amplitude increases with angle This is especially pronounced in probe signal in the horizontal plane

Large scale plume splitting and multi-component plume distribution usually indicates layering of charge and electrostatic acceleration of particles under the influence of dipole model electric fields setup inside the plume(Dreyfus [27]) For laser plasmas, two fluence ranges exist such that free-electron collisions are not as strong a perturbation at the lower range (Dreyfus [27]), and thus do not contribute significantly to collisions at later stages Generally only at high fluence (>12-15J/cm^2 for Al, Amoruso et al [35]) does one observe large scale plume splitting and multiple plume components, due to free particle collisions within the plume's volume Below the threshold fluence, most of the laser energy is expended in ablation and plasma formation, above the fluence threshold, the remaining energy in the pulse is used to heat ionic species to high temperature, giving rise to the characteristic forward expansion of laser plasma plumes The fluence threshold level will clearly depend on when in the laser pulse the plasma density reaches the critical

*Optical measurements of plume parameters to be presented in chapter 5

value (N_c) for which energy delivery to the target surface is attenuated, and instead absorbed at the frontal regions of the plume

4.3 7 Plume 2D angular distribution trends

If the plasma is considered as a body of zero net current flow, then the long range plasma potentials act as an accelerator, whose influence would be volume and density dependent Thus such processes would favour the planar target plasma, given the higher densities seen in both planes for this plume In considering the angular profile of the peak ion signals for each target/wavelength/orientation we fitted a Gaussian cross section using equation 2, to characterize the angular dependence An important assumption is symmetry of the plume properties about the laser axis, which was tested using the seventh probe positioned at -4^0 Figures 4 14 1-4 14 2, display the angular fit to the peak ion signals for the first group velocity for each probe, which is centered about the main peak in the trace This was not repeated for the other group velocities because not only are the number of plume groups different for each target, but the processes involved in shaping the properties of successive groups are many and interdependent The first group is essentially a collision-less, semidetached layer moving ahead of the main plume (Leboeuf et al [25] Wood et al [26])

Considering the horizontal profiles/fits (figure 4 14 1) the most obvious feature is the strong flattening of the angular cross section in comparison to the same plots in figure 4 14 2, which display the angular profile for each target in the vertical plane Usually increasing fluence does allow the width of the plumes forward section to widen due to higher scatter velocity (as seen in section 1 of this chapter), thus allowing a larger deposited area on deposited substrates, however high fluence usually leads to roughness in the film surface (Dyer et al [27]) The 6mm wedge density is higher than the 14mm wedge, a trend seen previously with electron probes and visible emission spectra* The solution to this is to consider the greater coupling between the plasma and the internal area of the cavity Initially confinement of the plume will lead to higher particle densities sampled by the probe, however as the depth of the cavity increases, plasma decay into the target surface will begin to undermine the plumes ability to maintain high enough temperatures required for non-neutrals to exist, this will result in lower signal levels at a probe This trend was also observed in section 1, at high fluence (~70J/cm^2) When the angular profiles were plotted, the initial wedge depth (3mm) wedge displayed little change from that of the planar target, while increasing the wedge depth (6-11-17mm) displayed a large drop in angle resolved peak ion densities The higher the fluence used the deeper the wedge target must be for significant changes to be observed

The penetration depth for laser vaporization increases as the wavelength decreases [28, 29, 30] and as the pulse width decreases However the amount of ablated material is independent of the cavity dimension so long as the cavity height is greater then the laser spot size, otherwise a non-typical coupling of the laser spot to the targets surface will occur However the temperature is likely to be lower due to lower absorption

*Optical measurements of plume parameters to be presented in chapter 5

in the pre-plume (Kim et al [28]) which was also demonstrated by fast ICCD images of plasma generated in wedge targets in the visible*.

4.14.1

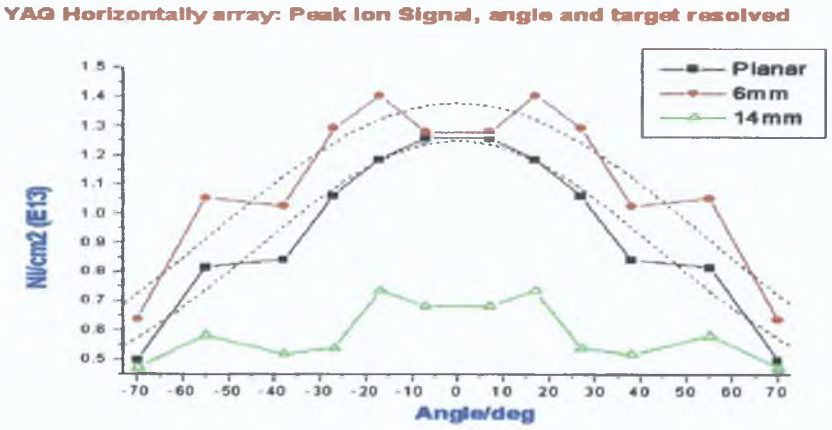

4.14.2

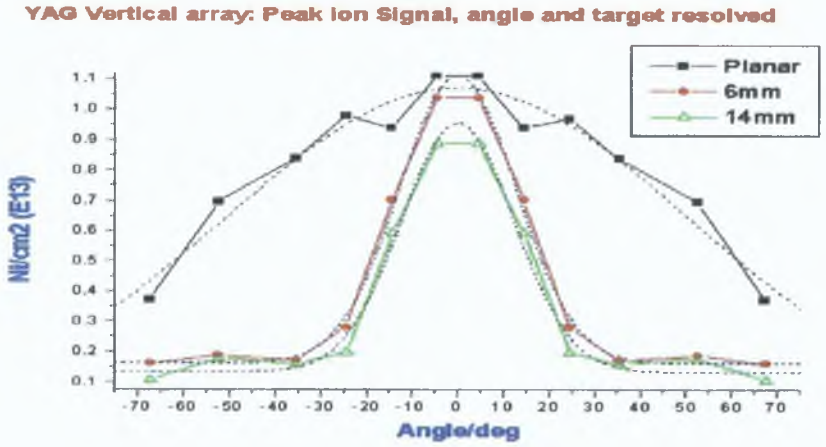

Fig. 4.14.1-4.14.2. Angular distributions of the peak ion density, for each target, for all target plumes, in both the vertical plane and horizontal plane for the first plume group. The dotted lines are the Gaussian fits made to each profile and fitted using equation 2. The angular profiles are similar to those studied by Thestrup and Lunney [16]. The angular profile in this work for the planar target is broader then that observed by Thestrup for aluminum, however the latter used a fluence of 2.5J/cm^2. No fit was made to the 14mm wedge in the horizontal by virtue of the absence of a clear trend in the angle resolved signal, but also due to the absence of a clear baseline..

Notably, for figure 14.4.2, the collimating effect in the vertical plane of plasma generation confined by wedges is not strongly affected by the depth. A strong narrowing of the vertical angular profile is observed in moving from the planar target to the 6mm wedge, but only a small difference exists between the two wedge targets, while all values are slightly lower. The latter aspect is due to greater plasma decay into the larger internal surface area of the 14mm wedge. The higher values of the Ni for figure 4.14.1 in the horizontal was observed in section 1, as a slight increase in the peak value of Ni for 3mm deep wedge targets. Thus such a trend would be expected here. The extent of the increase over the planar target is attributed to collimation of the plume reregistering as a higher measured ion density, which clearly decays

*Optical measurements of plume parameters, to be presented in chapter 5.

rapidly as the cavity depth is increased further (a trend also observed in section 4 1 for all fluences used there)

YAG Horz			YAG Vert		
Target	$w_{1/2}$	Area	Target	$w_{1/2}$	Area
Planar	83	96	Planar	102	141
6mm	109	159	6mm	26	25
14mm	----	----	14mm	24	25

$w_{1/2}$, refers to the half-max width of the curve in degrees, and A is the are under the curve, in arbitrary units

Table 3 Constants fitted with equation 1 to peak profiles from all targets, in both the horizontal and the vertical, w is the half max width A large decrease in the fitted width is present in the wedge targets in the vertical in comparison to the planar target Further increases in wedge depth do not produce further narrowing of the plume to the same degree If a reliable fit could be made to the 14mm target in the horizontal, it would expected that a more broadened plume would be observed as the wedge depth decreases

4.3 7 Particle Velocities, Target and plume trends

In considering table 3, the smaller the half-max width of an angular profile, the greater the extent of plume collimation Thus as can be seen from the half-max width value, the laser plasma is being collimated to a greater extent but as the confinement increases, the bulk signal (the area) is also lower Indeed both numbers scale down as the confinement increases (this is more pronounced in the vertical array) Since the plasma is still free to expand horizontally, we assume that the flattened regions in the wedge targets are in fact due to collimation in the horizontal plane Expansion which normally would occur in three dimensions is now confined Since the wedge targets do not show very large velocity changes at these pressures (~10 ^{3}mbarr), the particles cannot be redirected in the forward direction completely, and thus some portion of the plume which would undergo expansion in the vertical must comprise the wide cross section seen in the wedge targets angular distribution fits

E4m/sec YAG	E4m/sec YAG	E4m/sec YAG
Group1 probe1 (4^{0})	Group2 probe1 (4^{0})	Group3 probe1 (4^{0})
Planar 8 9	Planar 7 7	Planar 5 3
6mm 7 0	6mm 5 9	6mm 4 7
14mm 6 9	14mm 4 5	14mm 3 9
Group1 Probe4 (35^{0})	Group2 Probe4 (35^{0})	Group3 Probe4 (35^{0})
Planar 7 2	Planar 6 6	Planar 5 4
6mm 5 6	6mm 3 7	6mm -------
14mm 6 0	14mm 3 5	14mm ------

Table 4 Group velocities for all targets from the vertical probe array [probe 1 (4^{0}- closest to the laser axis) and probe 4 (35^{0})]

The group velocities scale well relative to the degree of containment(the deeper the cavity the lower the peak velocity, this effect is much more pronounced at small angles) They are a full order of magnitude larger then those reported in (Novodvorsky et al [17]) However the latter used much lower laser energy

(40mJ) compared to ~780mJ used here For all angles studied, and all velocity groups the peak TOF velocity is lower as the degree of containment increases, reinforcing the trend seen in section 4 1 with varying fluence, for a larger number of wedge depths One aspect of the laser plasma plume which usually does not change is the highly directed expansion, back along the laser axis, TOF velocities sampled here should display higher TOF velocities than those at larger angles This is indeed the case as table 4 demonstrates For the first group, velocities near the laser axis (probe 1~4^0) are lower at probe 4 (35^0) for all targets However as the velocity group considered increases, the difference in velocity for 4^0 and 35^0 for all targets is not so large This is clear from figure 4 13 1-3, in the 3D profiles, where all targets exhibit less pronounced secondary peaks as the angle from the laser axis is increased Therefore the component of the plasma most affected by geometric influence (a physical surface) is the fast, frontal region of the plume

4.3 8 Plasma plume target interaction

In considering the group velocities for probe one (4^0) for all targets, and all three velocity groups, the most obvious trend is the decrease in the peak velocity of the plume as the cavity depth is increased (as the degree of confinement is increased) this reinforces trends observed with data from the first section of this chapter, where ion probes displayed lower TOF velocities for cavity targets However one must remember that in section 4 1 the operating pressure was ~10^{-5}mbarr, while here it is ~10^{-3}mbarr, while the probe to target surface distance was also different The fast particles which lead the plume's expansion, and thus have the highest kinetic energies, undergo a large number of collisions with the ambient gas This slows the forward propagation of the plume substantially For cavity confined plumes, this will increase the length of time it takes to exit the cavity volume As stated previously, plasma decay into the cavities internal surface will cause rapid decay of energetic particles into the target This will not only register as a smaller probe signal but will contribute to lowering the internal energy and hence velocity of the plume

Equ 4 $T_e = 2\,88E4 \times A^{1/8}(Z+1)^{-5/8}Z^{3/4}(I\lambda)^{1/2}\tau^{1/4}$ (Novodvorsky et al [17])

where A is the atomic mass of Aluminum (26 98u), Z the average ion charge in the plume, I the laser intensity (W/cm^2), λ the laser wavelength in cm, and τ(c) the pulse duration of the laser beam (Novodvorsky et al [17]) From equation 4 the electron temperature has a square root wavelength dependence In section 4 2 electron probes and wedge targets, displayed electron temperatures peaking at 10000K, 4cm from the aperture of the wedge target, at 1μsec delay after the laser pulse The peak temperature scaled upwards with greater confinement Thus a good estimation for the electron temperature of the plume of the YAG plume is 10600K Collimation of a laser plasma, via a confining target does lead to higher temperatures and higher velocities as was demonstrated in section 2 However the decay of plasma in contact with a surface clearly undermines plasma enhancement The point at which collimation and containment of plumes becomes a disadvantage depends on the internal area of the cavity, and on the

kinetic energy of the plume The latter quantity depends on many factors These include the laser energy and wavelength and the ambient gas pressure

4.3 9 Conclusion

Summarizing the trends seen above, we have observed strong collimation of the plume in the vertical plane due to cavity confinement, and lower angular decay of peak ion signals Multiple velocity groups corresponding to multi-plume component expansion were observed and are attributed to large scale restructuring of charged species within the plume due to the constraints placed on vertical expansion In the horizontal plane, flattened cross sections of ion angular distribution for the first velocity group were observed, leading to a fanning effect as the plasma diverges substantially in the horizontal plane after leaving the cavity The general trend is of lower peak ion densities with greater geometric confinement, i e as the cavity depth increases

The possibility of using wedge target confinement to study superior PLD thin film generation, creating large area film of even thickness, via a larger angular width of even plume density being deposited in the substrate is proposed A definitive conclusion for electron studies for rectangular wedge targets, is the trend of lower electron and ion densities The most probable reason for this is the extension of the plasma plume, as the collimating nature of the targets produces enhanced velocities This point is reinforced given the earlier arrival of the peak ion and peak electron signals for all confining targets The higher electron temperature from the Langmuir probe signals also infer an extended plume, of lower local particle density The term 'local' refers to the assumption that the plasma is not inherently of lower density (the same volume of material is ablated in each case) but is spatially extended, and possessing higher expansion velocities The plume becomes stretched and extended and thus fewer particles exist per mm^3 for the probe to register The ion and electron traces for all targets, display a narrower main peak region followed by a slower moving main body, while confining targets display faster decay of the initial faster plume signal This would indicate a more compact plume, moving at a higher velocity Another possibility is that of plasma decay into the target, and deposition onto the target surface

4 4 Time and angle resolved ion studies of plasma plumes from collimating targets plasma generation between two parallel plates

4 4 1 Introduction

In order to extend our study of the interaction of laser generated plumes with specific target geometries, a laser plume was created via laser ablation of a flat aluminum target The plasma plume was contained between the target surface and a 1 55mm thick flat parallel plate The latter was positioned at different distances from the target surface The laser was delivered to the target surface via a hole in the front plate, and thus the plume interacts with the front plate, and a secondary plume is generated from the expansion of the plume after it passes through the hole in the front plate The second plume was studied with an electrostatic probe, which sampled the plume at various points The most important aspect of this experiment was the comparison to the plume studies described in the previous sections The expansion vector most affected by the targets is different In the earlier studies, plasma expansion parallel to the target surface was constrained However expansion back along the laser axis, normal to the target surface was not In this experiment, forward expansion of the plume is affected, by virtue of the presence of the plate, which is parallel to the target surface As a consequence of this geometry, the expansion vector, normal to the target surface is affected All other expansion vectors are un-affected by geometric influence Experimental conditions were almost identical however there were some differences

4 4 2 Experimental setup

Plasma generation was achieved with a Nd YAG Q-switched laser of energy 0 33J at 1 064μm The laser beam was focused to a spot size of 1600μm using a 24cm plano-convex lens giving an irradiance of ~1×10^{9}W/cm^2 An operating pressure of ~10^{-3}mbarr was maintained for all the experiments The fluence on to the target was ~16/Jcm^2 The electrostatic probe was mounted on a movable arm which could be positioned away from the target holder, and the probe tip was orientated parallel to the target surface The first probe was positioned 9 4mm from the laser path and 40mm from the target surface when studying the plume distribution The probe was grounded to the vacuum chamber, and the signal taken through a single BNC-BNC connector vacuum feed through

The capacitor was biased at –35V, this was sufficient to repel all negative charges impinging on the probe when acquiring the saturated ion signal, as the plasma plume streams past it Five shots were used to clean the target, while three were then averaged The angular positions of the probe in the horizontal position were 11 3^0, 14^0, 16 7^0, 19 3^0, 21 8^0, 24 3^0, 26 6^0, 28 8^0, 30 1^0 The normal distance from the probe tip to the target surface was kept constant at 40mm The probe was translated parallel to the target surface, leading to a maximum angle with the laser path of 30^0 to the target normal

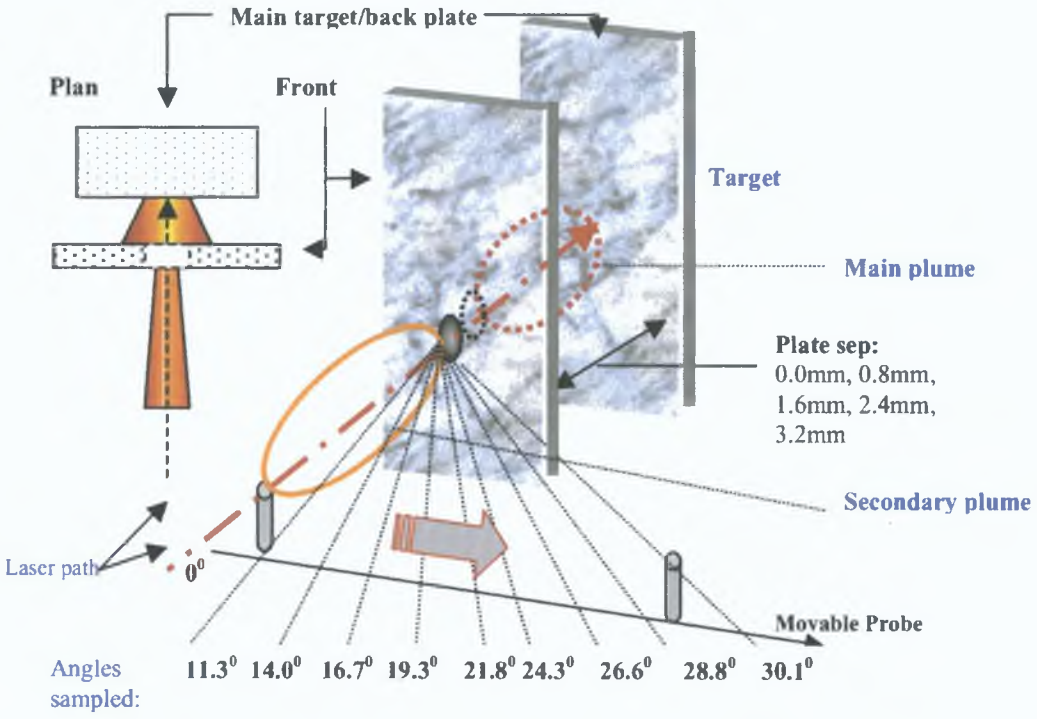

Figure 4.15:(above), experimental setup. The probe was translated parallel to the target surface, and the distance between the plates varied. The distance between the back plate and the probe was constant.

4.4.3: Overview of experimental trends.

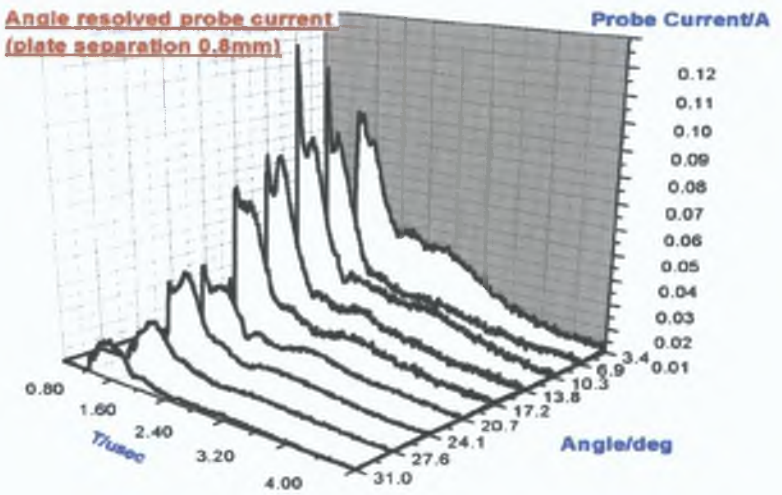

Figure 4.16: (left) 3D time-angle distribution of plume traces. Both the fast component (sharp spike) and the main body of the plume (slow component), show a strong dependence on the distance from the laser path. The integrated charge, peak TOF velocity and width of both components reinforce this trend.

Figure 4.16, displays the ion probe traces for the first probe for all angles sampled, for the second plate separation used (0.8mm). The clear rising edge, which will not always be composed of a single group of particles moving at the same velocity, is still present for the parallel plate arrangement. However it was noted that the duration of this peak, and the entire ion signal was substantially shorter than those seen in

sections 4 1-4 3, for other target configurations It was also observed that for other target geometries, there was a clear separation between the fast main peak and the second slower signal However for the parallel plate geometry, the two signals merge smoothly Secondly, the rapid decrease in the measured particle flux, as the angle from the laser path is increased is also a reoccurring trend in laser ablated plumes This was also demonstrated for the target configurations studied in previous sections and in this section The decay in the peak signal (arising from the fast component in the plume) and the decay in the slower secondary signal with angle is clear The extremely short duration of the signal at large angles when compared to large angle signals from previous sections, demonstrates not only the strong collimation of the plume about the laser axis, but the short duration, of the signal, resulting from a highly localized, high velocity expansion Although other target geometries studied in previous sections displayed enhanced expansion velocities, the duration of the probes signals was still comparable to the signal from planar targets The signal duration in this configuration is the shortest to be seen in this body of work, indicating the plume is physically of shorter scale length, and passes the probe tip over shorter timescale

4 4 4 Plume dynamics

In a two plate target system such as that here, there are three distinct processes occurring Firstly the plume interaction with the inner surface of the front plate, and resulting deposition of plume constituents upon the inner surface Secondly, re-channeling of the plume as it is forced through the hole in the front plate Lastly, the expansion of the second plume from the aperture, which is different to a plume pushing off a flat target In this case the forward force provided to the second plume, other than its own pressure driven expansion is the force of the main plume pushing on the plasma inside the aperture Another aspect of interest is the deflection and sudden decrease in velocity of the main plume between the plates when the main plume collides with the front plate

Considering first the plume collisions with the front plate From fast ICCD imaging of optical work*, it was observed that the plume at the termination of the laser pulse is of approximate dimensions 0 6-0 8mm in height, parallel to the target surface, and extends no more then 0 4mm forward from the target For plate separation of ~0 0mm, the resulting cavity geometry is essentially a capillary, of length equal to the thickness of the front plate (~1 5mm)

For the second plate separation (0 8mm), the cavity width is such that at that point in time when the plume reaches the inner surface of the front plate, the plume expansion in the vertical plume would be relatively small compared to the fast forward expansion The main trend seen here is that for certain cavity widths (~1mm or less), geometric collimation of the plume as it moves through the hole in the front plate alters the velocity distribution of the particles Those particles at the leading edge of the plume (and thus the most energetic constituents of the plume) become increasingly separated from the main body of the plume

*Optical measurements of plume parameters, to be presented in chapter 5

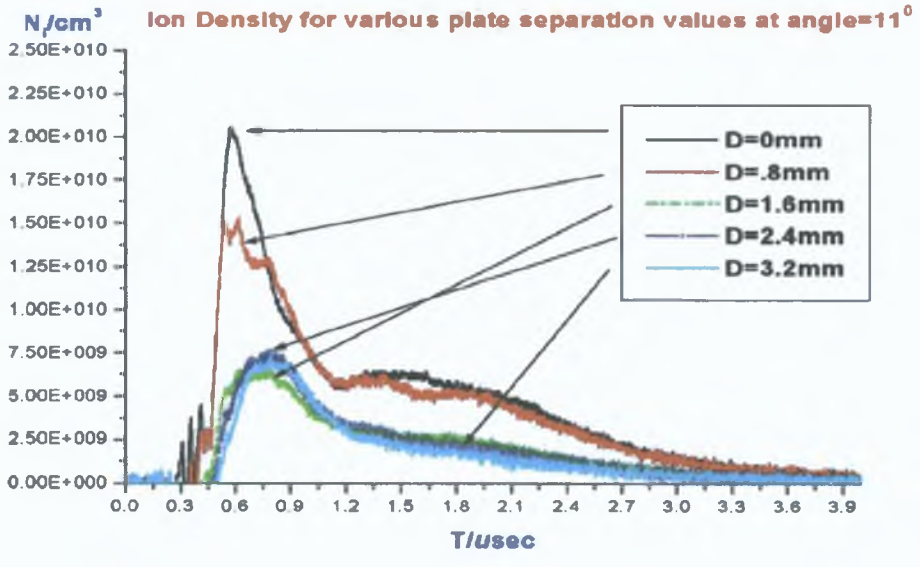

Figure 4.17.1: Voltage traces for the first probe position (11^0) for all plate separation values. The reoccurring theme in this work is the merging of the fast, well defined spike with the slower moving, widened main plume component. The separation of these two distinct components of the plumes velocity distribution decreases as the angles sampled decreases.

This accounts for the absence of a pronounced second peak as the cavity width increases beyond ~1mm (figure4.17.1). Indeed only the first two cavity widths (0mm, 0.8mm) display a pronounced second peak, while increasing the cavity width leads to a smoother trace, indicative of a more continuous, slower moving plume. This would infer that a shift in the velocity distribution of the plumes particles occurs only over a range of particle energies for this particular target-plume interaction. This is due to the fact that the larger cavity separation results in a longer time of flight of the plume before interacting with the front plate, since the plasma density decays rapidly from the plume center then those particles interacting with the front plate will do so at a lower particle densities.

The different traces are similar to those reported previously in (Anisimov et al [31]). In the latter's work, the authors used visible emission spectroscopy and Faraday cup measurements, to study the interaction of a laser plasma plume with a grid (the grid had a transparency of 30%). The ion traces reported there, also display a two component trace, but also an attenuation of both the main peak and the trailing signal. They attributed this to a 'dramatic non-linear transformation of the velocity distribution due to counter streaming particles' (Chrisey et al [32]). One aspect of the laser plasma plume expansion is the strong collimation of the charge distribution. By integrating the total signal over the signal lifetime, the charge collected from the plume by the probe can be measured, and when done for the various parameters provides a useful indication of charge distribution within the streaming plume. This value ranges from a maximum of 100nC for a plate separation of 0.0mm to 6nC for a plate separation of 3.2mm per pulse (figure 4.17.2), with the largest collected charge occurring nearest the laser axis, and falling off steeply as the angle from the target

*Optical measurements of plume parameters, to be presented in chapter 5.

normal sampled increased. These values are comparable to those reported in section 4.1, and to those reported by Lunney at al [12, 13, 15].

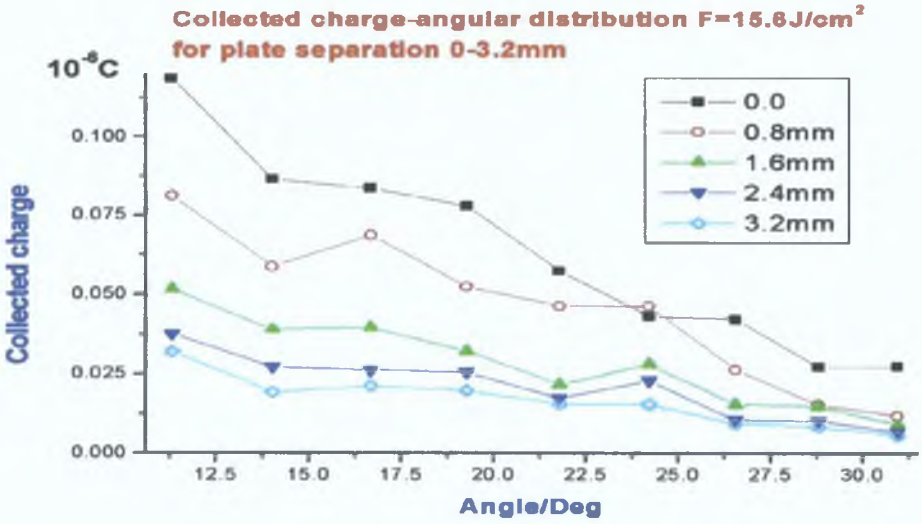

Figure 4.17.2: Collected charge for each probe, for all plate separation values. Integrating the current-time trace. There is a clear grouping of the collected charge for the last three cavity widths relative to the first two. Such a trend was also seen in section 4.1, where angle resolved peak particle densities were clearly grouped for certain cavity depths.

More importantly in Anisimov's work, as the grid was moved closer to the main target surface, the shift in the velocity distribution became greater, with two distinct peaks of equal magnitude. The longer the trailing edge of an ion plume trace, the greater the proportion of the plume particles which have low kinetic energy, in comparison to the high velocity particles which lead a plume's expansion. Thus shifts from a smooth, uniform ion trace to a multi-component trace, is usually indicative of increases in the internal kinetic energy of the plume.

The chief difference between this work and that of Anisimov is the relative volume of plasma which can reach the probe. While the bulk of the plume in Anisimov's work could stream through the grid, only that portion of the plume moving normal to the front plate within the diameter of the aperture will pass through the aperture and register on the probe as a signal. Clearly the closer and earlier to the generation point of the plasma the smaller the dimensions of the plasma will be. Thus the smallest plate separation will allow the largest fraction of the original plume to expand freely in vacuum after the plume has left the aperture of the front plate. Thus it is not unusual that the smaller the plate separation the larger the recorded ion density. An important conclusion here is the difference in the angular profiles of the ions for this target geometry compared to the various wedges employed in previous sections. In the horizontal plane for the wedge targets, the plume underwent angular broadening as a consequence of confinement in that plane. This then leads to lower integrated charge values from each probe for the various plate separations (figure 4.17.2). However here, the plume particles are 'collimated' radially in all planes as they are forced through the aperture on the inner surface of the front plate.

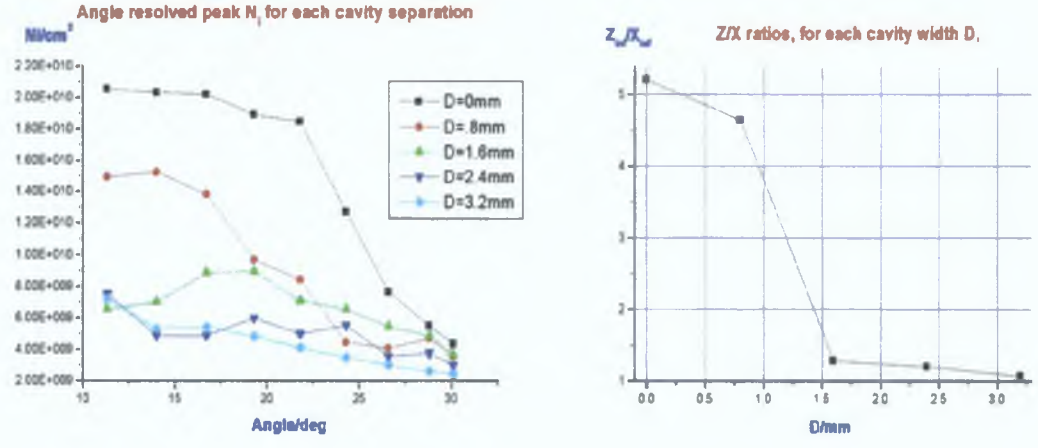

Figure 4.18.1, 4.18.2: (left) Angle resolved peak ion densities for all plate separation values. The smallest plate separation (0mm) displays strong collimation of the initial plasma plume, which registers on the probes as a nearly constant ion density over a relatively large angle (although the angle is small when compared to the angles studied in previous sections). As can be observed, the rate of fall of the ion density with angle, and the peak ion density for each targets drops rapidly from D=0.8mm onwards. Despite the small cavity widths used, when a geometric influence is used to configure the plumes properties, the affect will be greatest if the geometric influence is brought to bear when the plume is at its most energetic, i.e. very early in the plasma history. (Right) Best fit values for Z/X ratios for all targets (fitted from equation 1.2, section 1). As is expected the extent of the forward plume collimation is most pronounced for the smaller cavity separations, where Z/X is large for D=0, 0.8mm but then falls rapidly for larger values of D, mirroring the profile seen in figure 4.18.1 (left).

For fixed fluence previous targets displayed significant changes in the peak ion density recorded and the angular profile of the plume's particles only for certain cavity depths or heights. Equally so here, significant differences in the plumes angular profiles (figure 4.18.1) show large changes for small values of D, and saturated influence at larger values of D, compared to changing the depth of a rectangular wedge in section 4.1 and 4.3, where significant changes in the peak ion density and the angular distribution occur only at moderate to large cavity depths. The chief difference is density, or the density of the plasma when it interacts with the geometric influence. In the above cases, the very small plate separation occurs early on in the plasma history, when the plasmas density is high. In section 1, significant geometric influence occurs only after the plume has filled the rectangular cavity, and emerged from the target's volume.

4.4.5: Ion dynamics and signal angular dependency.

A notable feature generally of laser generated plumes is the peaking of the plume density and the ion flux in the forward direction, normal to the target surface. This distribution of ions occurs not only parallel to the laser axis but also parallel to the target surface, radially out from the expansion vector of the plume. The large difference in the collected charge (figure 4.18) for the first two cavity widths (0.0mm, 0.8mm), compared to the grouping of collected charge values for the other cavity widths (1.6mm, 2.4mm, 3.2mm) indicates that at the fluences reported here, collimation is significant under limited conditions (certain cavity widths). For increasing cavity widths a larger expansion of the plasma plume in 3D space is allowed before the plume collides with the inner surface of the front plate. Therefore, the closer the front plate to the

target surface, the smaller the volume of the plasma as it reaches the front plate Thus the larger the volume of material which will pass through the aperture

Shifts in the velocity distribution are also cavity width dependent Since the target–probe distance is constant, increasing the cavity width effectively lowers the density of the plume which contacts the front plate by virtue of the longer transit time of the plume and expansion driven decreases in particle density, thus effects such as collimation and increases in velocities due to local pressure increases (as the plasma is forced through the aperture) are clearly density dependent High fluence laser ablation signals from electrostatic detectors generally display multiple velocity groups Large electric fields resulting from the high-density plasma, can give rise to strong forward accelerations by way of ambi-polar diffusion (Ermer et al [22]), then ions are accelerated by columbic fields generated by electrons escaping from the plume at high velocity and undergoing relatively few collisions (a Knudsen layer) This has also been proposed by (Pappas et al [33]) In the latter work, the authors argue that strong electrostatic interactions of photoelectrons and the emitted ions result in the formation of a ± charge cloud i e , a tenuous plasma This charge could couple to neutral atoms and molecules sufficiently that electron impact excitation occurs Since the ions and electrons travel together and have greater kinetic energy than the neutrals they should be concentrated at the forward edge of the plume and, given the radial temperature distribution in the plume, the greater proportions of ionized particles should drop dramatically as one moves out from the laser axis Indeed good evidence of this is provided by the relative smoothing of the ion traces as the distance from the laser axis increases With few peaks and velocity groups, the plume displays good thermalization and continuity in particle flux the further out the probe samples

4 4 6 Time of flight velocities trends

Nearer the laser axis, the higher ion flux, and presence of localized electron layering in the plume leads to sharp decreases from the ion peak to negative going signals or 'troughs' in the ion flux signal It is these troughs that allow one to distinguish the different velocity groups, and at high fluence, where the collisional rates between ions and electrons will help to maintain ionization rates, one should expect higher kinetic energies In [30] the authors studied the total positive charge accumulated on a Faraday cup from a KrF laser generated plume as a function of fluence, for MgO in vacuum (10^{-6}mbarr) As the fluence was increased beyond 3J/cm^2, the net charge measured in the plume increases exponentially This net charge provides a moderate potential well for co-moving electrons The authors calculated that a 001% net positive charge over the length of the plasma would provide an electron potential well of ~12eV Electron heating in the plume via collisions should scale with fluence This in turn will drive a broadenmg of the energy distribution of the ions, resulting in the charge localization which is termed 'slow' and 'fast' components The larger the difference in arrival time at the probe of the peaks of such curves, the greater the difference in velocity of the components Equally the narrower the components are in time the more

localized in space these velocity groups are, and the greater the electrostatic potential must be between the charged forward region of the plume and any slower component.

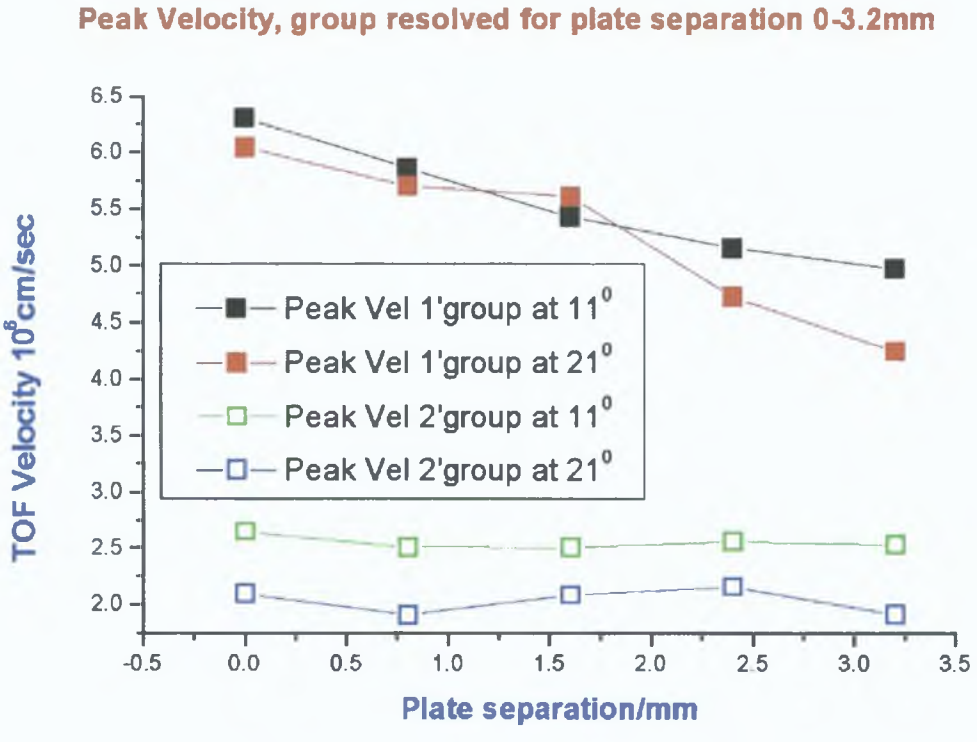

Figure 4.19: Peak TOF velocities for probe positions 11^0 and 21^0, for all plate separations. A unique aspect of this target configuration is the response of the first peak (fast component) against the second peak (main body of the plume) to increasing plate separation. The fast component displays a clear decrease (~linear) for increasing plate separations, while the slower component is relatively unaffected.

The group velocities scale well relative to the degree of containment (increasing plate separation), with the peak TOF velocity scaling down with increasing plate separation. The leading edge of laser plasma plumes is usually highly charged, and moves at higher velocities then the main body of the plume. In moving through the aperture in the front plate the frontal regions of the plasma plume are clearly more affected then the middle or trailing edge of the plume. The decrease in TOF velocity for the first group (located at the frontal regions of the plume) indicated by figure 4.19, and relative lack of responsiveness for the second velocity group (located in the main body of the plume) would infer that the more energetic a plasma plume than the greater the effect of plasma-target surface interaction on plume behavior. From work with electron probes and confining targets in section 4.2, we measured electron temperatures peaking at 8200K, 4cm from the aperture of the confining target, at a 1μsec delay after the laser pulse. The peak temperature scaled upwards with greater confinement. Given the good scaling of the TOF velocity in figure 4.19 and the clearly established trend from section 4.2, that for laser plasma plumes, increased thermal velocity usually goes hand in hand with increased flow velocity, we can assume that if the velocity distribution is indeed

Maxwellian then from equation 4, a higher flow velocity is indicative of a higher temperature within the plume Thus we can assume that collimation of the plume does indeed lead to a higher plume temperatures We have confirmed this with temperature measurements from space and time resolved emission spectroscopy* which showed enhanced temperatures, center of mass velocities and extended line profiles for plasma emerging from an aperture having undergone expansion from a planar surface Interestingly lower peak densities from line widths were also observed Considering figure 4 13 it is clear that the peak TOF velocity distribution displays a nearly linear change in peak value for the various cavity widths, while the second plume component seems to be only partially affected With the exception of simplified modeling of the effect of target geometry on laser-target coupling, no theoretical analysis of plume-surface interaction yet exists, thus no comparison can be made However one clear conclusion is the lower peak ion densities ($Ne \sim 10^{11} cm^3$) reported here compared to section 4 2 ($N_e \sim 10^{12}$-$10^{13} cm^3$) Although the fluence reported there was higher, other conditions were similar The chief difference is the nature of the target (rectangular cavity) Another point of interest is the large difference between the velocity groups reported in section 2 (upwards of four groups per trace) compared to those reported here, where the peak TOF velocities of both groups is within one-quarter order of magnitude of each other, whereas in section 2 the difference is one-half order of magnitude, while the peak velocities themselves are also lower (2 5-6×10^6cm/sec here compared to 8-24×10^6cm/sec reported in section 2

4 4 7 Conclusion

To summarize, we have observed that as the width between the target surface and the front plate is increased that the peak ion density sampled by the probe decreases for the fast component of the plume, but the second slower main body is relatively unaffected TOF velocities show a linear dependence on the cavity width for the main peak and relative insensitivity of the second slower component to collimation In comparison, the angular distribution of the plume out from the laser axis, displays very strong forward concentration of the plumes ions, and a strong fall off in ion signal as the angle from the laser axis is increased The largest change observed in the plasma plumes properties occur when the plate separation values increases from zero to non zero values, corresponding to a change in the geometry of the system, from a micro capillary to a real parallel plate system Further increases in the cavity width display a saturated change in both the peak ion density sampled by the probe but also in the TOF velocity However changes in the TOF velocity are only observed for the main velocity group and not the secondary, slower moving plume component

*Optical measurements of plume parameters, to be presented in chapter 5

4 4 8 Concluding remarks

One trend which emerges from all targets studied, is that of lower peak density for both ions and electrons, when the target area in contact with the plume increases at any stage in the plume evolution The most obvious cause of this is conductive decay of the plasma into the target This can occur via ion collisions with the target surface, depriving the plasma of high energy ions which could maintain plasma temperature through collisions with other particles Secondly, a plasma is usually a highly charged medium, and thus the potential difference between the plasma and the target is a strong loss mechanism for free electrons and low energy ions at the edge of the plume at the plasma target interface Such loss mechanisms are both area and time dependent Thus as the internal area of a cavity increases, not only is conductive decay enhanced, but the time taken for the plume to leave the cavity volume increases Thus any enhancement in velocity and temperature through collimation and containment comes at the price of an enhanced plasma decay rate The most definitive result is for the vertical distribution of the plume's ions from a planar target as compared to a rectangular wedge Strong collimation of the plume was observed resulting in strong narrowing of the plume's cross section in the vertical plane as a consequence of the physical barrier offered by the wedge in lessening plume expansion in one plane

Some interesting trends can now be deduced about the nature of laser plasma plume interaction with surfaces In section 1, it was observed that decreasing the fluence lead to lower peak ion densities and lower TOF velocities However for a fixed fluence, and increasing cavity depth, the trend was repeated Thus containing a laser plasma plume for varying durations (which is effectively forcing a laser plasma plume to interact with a grounded surface) has the same effect as decreasing the fluence delivered to the target In section2, for fixed cavity depths and decreasing cavity height, higher TOF velocities were observed (related to higher temperatures), as well as lower particle densities, for both positively and negatively charged particles Since higher temperatures and velocities scale with increasing fluence, the effect of decreasing cavity height is to mirror that of increasing fluence All metals display a saturation in particle yield beyond some set fluence value However for cavities of decreasing height, the particle yield is in fact lower

Finally, in section 4, plasma plume interaction with a surface normal to its expansion vector, resulted in the funneling of plume through the aperture in the front plate This led to increases in the TOF velocity for the fast plume component, while the slower plume component displayed no change in the TOF velocity for all plate separation values used

References

[1] T N Hansen, J Schou, J G Lunney, Appl Phys A 69, S601-S604, (1999)

[2] B Thestrup, J G Lunney, Appli Surf Sci, 208-209, (2003) 33-38

[3] W Whitty, J-P Mosnier, Appl Surf Sci, 127-129, (1998) 1035-1040

[4] David B Geohegan, A A Puretzky, Appl Phys Lett 67 (2) July (1995)

[5] S B Segall, D W Koopman, Phys Fluids, 16 (1973) 1149

[6] J M Hendron, C M O Mahony, J Appl Phys, 81(5), 1 March, (1997)

[7] I Weaver, G W Martin, Rev Sci Inst, vol 70, no3 March (1999)

[8] R A Al-WAZZAN, J M Hendron, T Morrow, Appl Surf Sci, 96-98, (1996), 170-174

[9] S S Harilal, C V Bindhu, M S Tillack, J Phys D Appl Phys 35(2002) 2935-2938

[10] S Amoruso, X Wang, C Altucci, C de Lisio, Appli Surf Sci, 186, (2002) 358-363

[11] J Wild, P Kudrna, Rev Sci Inst, Vol 72, No2 (2001)

[12] T N Hansen, J Schou, J G Lunney, Appli Surf Sci, 138-139 (1999) 184-187

[13] B Toftmann, J Schou, T N Hansen, J G Lunney, Appl Surf Sci 7386 (2001) 1-5

[14] S I Anisimov, B S Luk'yanchuk, A Luches, Appl Surf Sci 96-98(1996) 24-32

[15] T N Hansen, J Schou, J G lunney, Europhys Letts, 40(4) pp 441-446 (1997)

[16] B Threstrup, B Toftmann, L G Lunney, Appl Surf Sci 197-198(2002) 175-180

[17] O A Novodvorsky, O D Khramova, Optics and Laser in Engineering, 32(2000) 449-457

[18] O A Novodvorsky, C Wenzel, O D Khramova, Optics and Laser in Engineering,36(2001) 303-311

[19] R F Wood, K R Chen, Phys Rev Letts, Vol 7, No 8, 25 August (1997)

[20] G W Martin, L A Doyle, Appl Surf Sci 127-129 (1998) 710-715

[21] Mark A Shannon, Appli Surf Sci 127-129 (1998), 218-228

[22] D R Ermer, S C Langford, J Appl Phys (1997), 81, 1495

[23] Q Y Ying, D T Shaw, Appli Phys Letts, 53 1762(1998)

[24] R W Dreyfus, J Appl Phys 69(3), February (1991)

[25] S S Harilal, C V Bindhu, M S Tillack, J Phys D Appl Phys 35(2002) 2935-2938

[26] J N Leboeuf, K R Chen, Appli Surf Sci, 96-98(1996) 14-23

[27] P E Dyer, J Gonzalo, Appli Surf Sci 109/110 (1997) 345-349

[28] J H Kim, K A Jeon, Mats Sci and Eng, B89, (2002) 70-72

[29] A P McKiernan, J P Mosnier, Appl Surf Sci 197-198(2002), 325-330

[30] D R Ermer, S C Langford, J T Dickinson, Appl Surf Sci 127-129(1998) 977-982

[31] V N Anisimov, M.A Stepanova, Appl Phys Lett, 67, (20), Nov (1995)

[32] *Pulsed Laser Deposition of Thin Films*, D B Chrisey, G K Hubler (Wiley, New York, 1994)

[33] D L Pappas, R W Dreyfus, J Appl Phys 72 (9), 1 Nov 1992

[34] Plasma Diagnostics, Lochte-Holtgreven, AIP press, 1995

[35] S Amoruso, X Wang, Appl Surf Sci 127-129 (1998) 1017-1022

Chapter Five: Space and Time Resolved Visible Emission Spectroscopy and Imaging of Laser Plasma Plumes

Introduction

This chapter discusses results from the range of experiments performed in the space-time range termed 'intermediate field', using space and time resolved visible emission spectroscopy and imaging. Here the laser generated plasma plume was studied for time scales less then 500nsec. The plume properties such as electron temperature and electron density, ionization temperature, and ion edge velocity were compared for various target geometries. The target geometries used included rectangular wedges of fixed depth and varying height, capillaries of fixed length and varying diameters, and vertical parallel plates of varying separation. Plume dynamics were studied using gated ICCD imaging. For confined plumes, enhanced temperatures, densities and emission spectra are demonstrated for all confining targets at early stages after the laser pulse. Other effects such as large increases in the forward extension of the plume, and enhanced edge velocities are also presented. High voltage electric field influence of varying polarity and intensity, on laser generated plasma was also studied. Enhanced electron density, and late stage ion emission was observed. This effect was limited to late stage plasma behaviour and only above certain voltages.

5.0: Overview

As discussed earlier, electrostatic probes are extremely limited by theory, as to the earliest point in the plasma lifetime which they can probe. In order to push the spatial and temporal limit back further to the space-time origin, another form of diagnostics must be employed. As outlined in chapter three, the Chromex visible spectrometer and Andor ICCD are exceptionally versatile. Another positive attribute of visible spectroscopy is the large range of theories which are applicable in translating emission spectra into real physical parameters with which to determine the plasma properties. The chief variable employed is the degree of containment offered by the three target geometries used (figure 5.1.0).

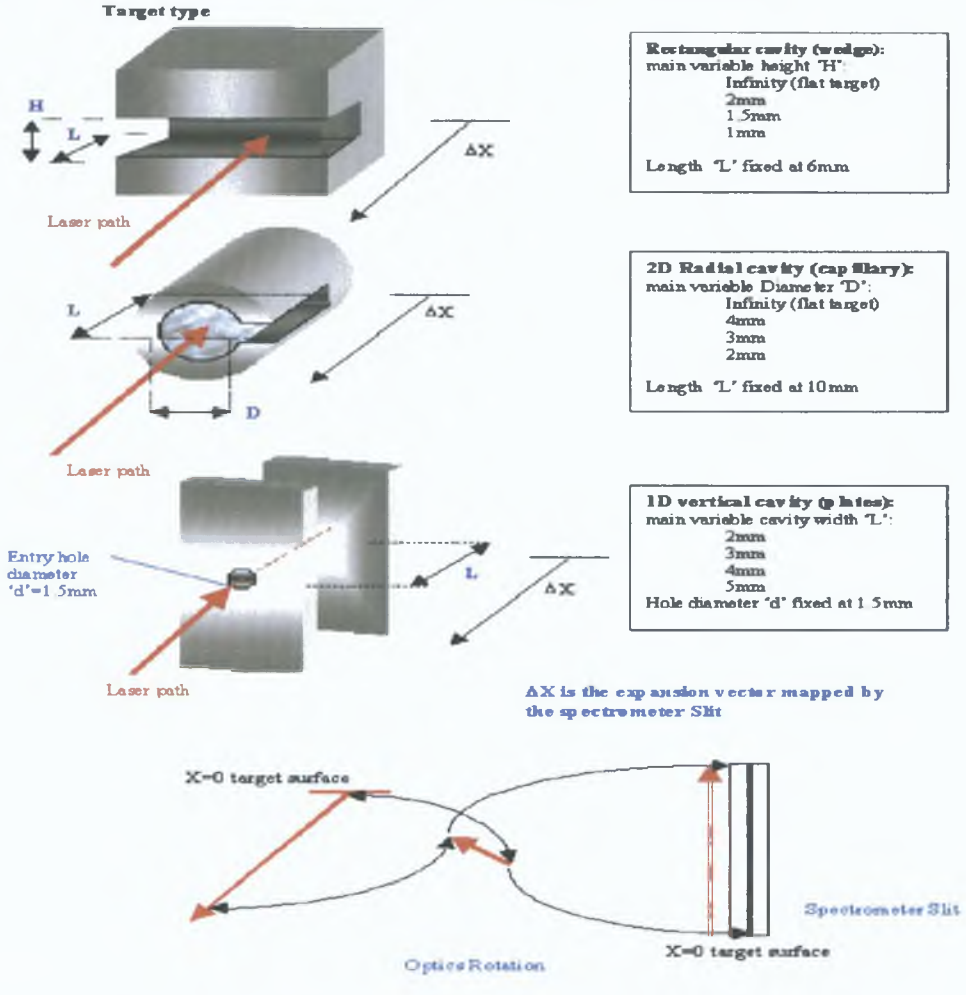

Figure 5.1.0: Schematic overview of the three target configurations employed in this chapter. Each target configuration allowed for varying degrees of containment in different spatial planes. For each target configuration, relative dimensions such as height or diameter were varied in order to study how the plume parameters varied under the influence of varying the volume of the confining influence of each target configuration. Finally using the first target (wedge) high voltage electric field effects were studied by biasing the target.

Each target configuration confined the plasma from different directions. Relative to the plasma, different expansion vectors of the plasma were thus affected by the presence of the internal surfaces of each target. The rectangular wedge target influenced plasma expansion parallel to the target surface in one dimension,

while the expansion vector perpendicular to the target surface was unaffected The capillary target, similar to the rectangular wedge, increased the degree of confinement by effecting expansion vectors parallel to the target surface in two dimensions The third configuration employed, involved retarding the forward expansion of the plasma (normal to the target surface) by generating the plasma between two parallel plates The other expansion vector of the plume, such as those parallel to the target surface, were unaffected Lastly, using a rectangular wedge of fixed dimensions, a variable magnitude and polarity bias electric field was placed on the target to study electric field influence on laser plasma plumes
In this manner, systematic changes in the degree of confinement was studied

5 1 Time and space resolved visible studies of laser plasma generation and dynamics in rectangular cavity's 1-Dimensional horizontal confinement

5 1 1 Experimental Setup

1-Dimensional plasma, confined in the horizontal plane, was achieved by generating the plasma inside a rectangular wedge cut into an aluminum block The wedge height was varied over the range, infinity (planar target) to 1mm separation between the upper and lower plates The wedge targets had a depth of 6mm Clearly there are differences in diagnostic approaches that limit the spatial and temporal range of study To fully understand plasma behaviour under the influence of target configuration multiple diagnostics must be brought to bear In order to study early timescales, space and time resolved visible emission spectroscopy was employed Using the lines emitted within the detectors range, density and temperature profiles for each target were compared at selected times For later timescales, ion probe measurements at selected positions in the plume were used to study the temporal behaviour of the plume Finally Gated visible imaging allowed us to observe the dynamical behaviour over the plume's emission lifetime

Plasma generation was achieved with a Nd Yag Q-switched laser of energy 0 8J at 1 064μm (15nsec FWHM) The laser beam was focused to a spot size of 500μm using a 20cm plano-convex lens giving an irradiance of ~2 5×10^{10}Wcm^{2} The targets were machined from aluminum blocks The targets all had a depth of 6mm Height was varied from planar aluminum plate (open target) to 2mm, 1 5mm and 1 0mm wedges An operating pressure of ~10^{5}mbar was maintained for all experiments The spectrometer and detector system used to study the plume's spectral properties was a Chromex visible spectrometer coupled to an Andor gated visible camera (chapter three, section 3 4) Light from the plasma was coupled to the spectrometer slit via a two lens system and a three-piece prism rotation system (described in more detail in chapter 3, section 3 4 3) The first lens, used to collimate the plasma light was a plano-convex 15cm focal length lens of diameter 5cm, placed 16cm from the plasma The second lens used to focus the plasma image onto the slit was a 10cm focal length lens of diameter 5cm The image formed on the slit was real

and the magnification ratio was ~1:5. Between the two lenses was a rotation prism arrangement. This allowed the plume (moving horizontally away from the target) to be imaged moving up the vertical slit. In this system a single image, gated via the intensifier could be captured over the complete spatial extent of the plume at any time delay chosen. By gating the intensifier with respect to the laser we could study the temporal and spatial behaviour of the plasma in different targets. The bi-dimensional nature of the CCD allowed the spectrometer to project wavelength dispersion along one axis of the CCD, and distance normal from the target surface along the other axis of the CCD. Finally, between the object lens and the prism system a YAG mirror and focusing lens were placed to allow us to bring the laser beam in 90^0 to its usual axis. Combined with rotation of the target, we could focus the beam on the target and have the plasma expand at the spectrometer slit. Thus now, after prism rotation the CCD axis that initially represented distance from the target surface, now represents the vertical extension of the plume. We termed these two setups, 'off axis'(observing the plasma from the side, parallel to the main expansion vector back along the laser axis), and 'on axis', observing the plasma head on, along the main expansion, parallel to the laser axis.

5.1.2: ICCD Spectroscopy parameters.

The gate time on the ICCD when spectra were taken 'off axis' was 25nsec, and when 'on axis' was 17nsec. This was necessary to avoid saturation on the CCD while maintaining the same ICCD settings. Ten shots were accumulated and the background count subtracted from the signal. Each target surface was pre-conditioned with 40 shots of the un-focused laser beam to ensure a clean surface. The slit width on the spectrometer was fixed at 300μm for all experiments. The central wavelength on the spectrometer was fixed at 459nm, the spectral range was thus 447nm to 470nm. The CCD pixel matrix was binned 5×5. Initially it had been intended to use the lines referenced by Gotz et al [1]. Here the authors found three groups of aluminum lines clustered at 360nm, 450nm and 570nm. Our plasma also gave these lines, however for our purposes the lines at 360nm, and 570nm were too short lived in space and time to be of significant use in calculating physical parameters. Thus the four lines over 447-466nm were used. A typical spectrum for this region is displayed below (figure 5.1.1).

Typical emission spectrum, 80nsec, x=2.9mm, planar target.

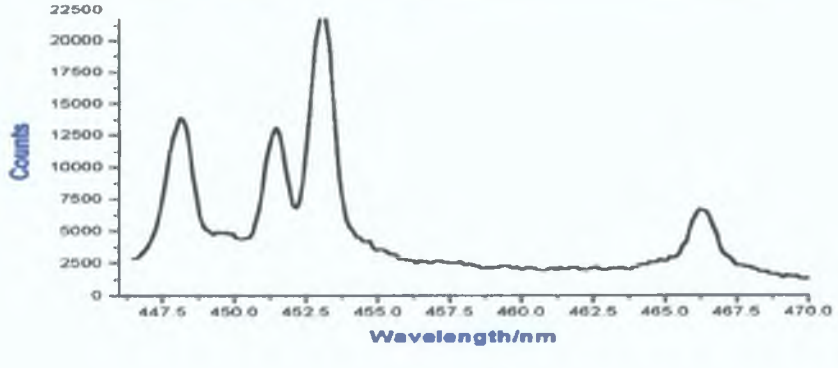

Figure 5 1 1 Typical emission spectrum from a planar target The four lines studied are shown, three Al III on the left side (447-453nm), and the single Al II (466nm) on the far right The total spatial lifetime of the above lines was a maximum of 9 5mm, while the temporal lifetime was 400nsec after the firing of the laser pulse

5 1 3 ICCD Imaging parameters

The Andor ICCD camera, when mounted alone with coupling optics allows the imaging of the plume at selected times The gate in imaging mode was reduced to 11nsec to avoid saturation and increase the temporal resolution to study fast dynamical processes The light from the plasma was further reduced by placing a neutral density filter (0 01% transmission) in front of the camera This was necessary to study the hot compact plume at very earlier timescales (<90nsec) without damaging the CCD array The CCD pixel array was binned 2×2

5 1 4 LTE considerations

Before we proceeded, with the analysis, we assumed that the plasma state is characterized by LTE theory The values of electron density and temperature allows us to check our assumption

$$\text{Equ 1 1} \quad N_e \geq 1\,6 \times 10^{12} \times T(eV)^{1/2} \Delta E(eV)^3 \qquad \text{(Gotz et al [1])}$$

Equation 1 1 gives the minimum density condition for the plasma to be considered to be in LTE ΔE is the largest energy transitions for which the condition holds In our work ΔE is 2 8eV for AL III (447 985nm) The highest temperatures measured (discussed later) were 22500K, this gives a lower limit on the right hand side of equation 1 1 of $5\times10^{13}cm^{3}$ The lowest densities measured using Stark broadening were 2×10^{16} cm^{3}, thus validating our assumption of LTE in the plasma

5 1 5 Electron density and Ionization temperature calculations

In our work the small number of line of the same ionization stage means unacceptable levels of reliability in using the Boltzmann plot method with just three AL III lines present Thus we used the ratios of intensities of successive ion stages of the same element It is important for accuracy that the spectral lines be located in the same spectral window, with no overlapping lines present The two lines chosen were Al III (453 049nm) and Al II (466 186nm) Of the three Al III lines available this line was used because it emerges from the continuum the earliest and showed the greatest spatial extension in the forward direction This allowed us to map the temperature over a large spatial extent for each gated spectrum The main constraint is the presence of the continuum Only when the lines are clearly visible can one safely apply the above procedure For our system the earliest applicable time delay was 60nsec after the laser pulse All spectra before this time were continuum dominated

Ion	ΔE cm^{-1}	E_L cm^{-1}	E_H cm^{-1}	Config	J_i -J_K	Log(gf)	f	A E8 s^{-1}	g_i	g_K
AL III (447.99nm)	22316	167612	189928	4f-5g ($2F^0$-2G)	5/2-7/2	1.0191	1.31	3.35	2	4
AL III (451.3831nm)	24074	143713	167787	4p-4d ($2P^0$-^{2}D)	½-3/2	0.419	1.31	2.15	4	4
AL III (453.0459nm)	22074	143713	165787	4p-4d ($2P^0$-2D)	3/2-5/2	-0.28	1.18	2.552	4	6
AL II (466.186nm)	21439	85481	106920	$3p^2$-3s4p (1D-$1P_0$)	3/2-5/2	-0.285	0.11	5.3	5	3

Table 5.1: Constants for the four lines studied in the visible (NIST databank).

Equ 1.2: $$\frac{I_{ALIII}}{I_{ALII}} = 0.16655 \times T_e^{3/2} \times N_e \exp\left(-\frac{26.78251E4}{T_e}\right)$$

Equation 1.2: Ion to atom ratio equation for AL III (453nm) and AL II (466nm) using equation 8 in chapter two, section 2.1.4. The left hand side is the physical ratio of the intensities of each line in the raw data. Inputting the density, and a range of temperature estimations allows one to generate a calibration curve to match the actual ratio.

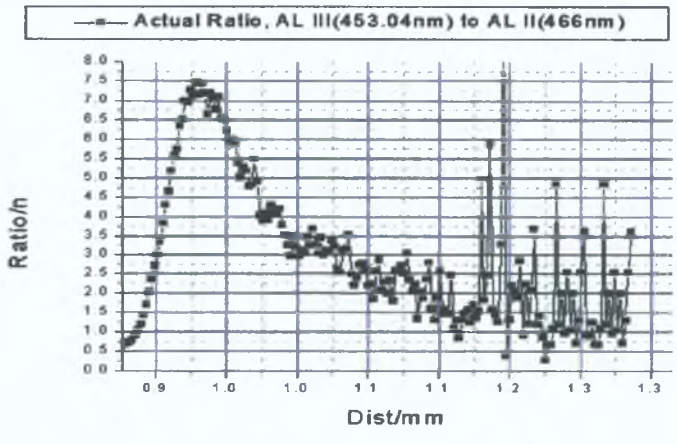

Figure 5.1.2: The actual ratio of the AL III(453.04nm) to AL II(466nm), spatially resolved 60nsec after the laser pulse. The target surface is to the left, and the laser comes from the right. The difference in the physical extension from the target of the two different ion stages leads to increasing instability in the intensity ratio at the leading edge of the plume. Here the more energetic AL III is more extended than the AL II, and moves away from the target faster. At later time delays after the laser pulse, the trailing edge of the ratio becomes unstable, due to the absence of the higher stage (AL III) near the target surface, which has decayed faster than the lower stage (AL II).

For electron densities, calculated from Stark width broadening in the visible, the Al III (453.049nm) line was fitted with a Lorentzian profile, allowing the half-max width of the line to be used in determining the density using the electron impact parameter from Dimitrijevic et al [2].

The most important parameter used in this work is the electron impact parameter, W, for the AL III line at 453nm:

AL III(453.0459nm) [4p-4d($2P^0$-2D)]:

W =1.41A at 10000K, W = 1.22A at 15000K, W = 1.12 A at 20000K. (Dimitrijevic et al [2])

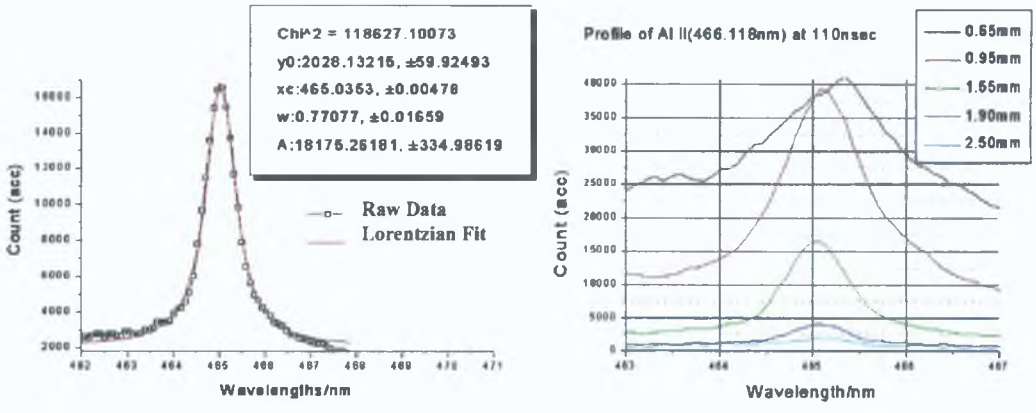

Figure 5.1.3: Lorentzian fit to raw data for AL II visible line (466.18nm) at 200nsec 12.5mm from the target surface. Figure 5.1.4: AL II line profile change with distance from target (same line) at 110nsec.

By combining the density profiles calculated from Stark broadening and the temperature profiles from line intensity ratios, we were able to translate emission spectra into real physical variables. Laser plasmas are characterized by large changes in density throughout the volume, thus spatially varying line widths show measurable changes across the plumes spatial length for a particular time delay, as seen in figure 5.1.4. Although the broadening of lines from the spectrometer was approximated, its component was not subtracted from the line profiles used to determine N_e (see appendix E). The instrument function of the Chromex was Lorentzian, and line fits to used here were also Lorentzian. Thus de-convolution of the instrument function involved direct subtraction of the instrument broadening value from the measured line widths. This was done for one data set (appendix E). The resulting change in the value of the numerator in the electron density is the same for all targets. Thus the trend observed from one target to the next is conserved.

Another important issue is that of the physical extension of the plasma plume in the horizontal plane, and the resulting longer 'line of sight' (cross section) along which light is collected. If all plumes studied were of the same physical shape then this would not be an issue of major concern. However the targets employed here result in a non-standard accumulation of light from a plasma plume, because of the changes in the density profile resulting from target influence (i.e. for rectangular wedge targets, the plume undergoes expansion horizontally, to a greater extent then that of the planar target by virtue of the wedge geometry employed). Since the changes in the distribution of emitted light from different targets has not been characterized (and would be expected to be nontrivial), emission spectra from the different targets have not been compensated for this effect.

5 1 6 Laser target interaction

Plasma ignition depends greatly on the material In metals the leading edge of the pulse penetrates only a short distance into the surface, typically less than one wavelength The heating and ionization of the surface is driven mainly by electric field ionization (10^9-10^{12}Vm $^{-1}$) The initial contact of the laser pulse with the target creates a low temperature high density plume on the surface The criteria for ignition can be considered in terms of the estimated threshold irradiance required for plasma ignition(Liu et al[3], Phipps et al [3 1]) Equ 2

$$\Phi_{thr}(\sqrt{\tau}) \geq B,$$

where τ is the laser pulse duration, and $B \approx 4\times10^5 Ws^{1/2}cm^{-2}$ for τ in the range of 10psec-10nsec (see 5 1 5, next page) In these experiments τ was 16nsec thus giving $\Phi_{thr}(\sqrt{\tau}) \geq 10^8 W/cm^2$ The laser irradiance in this work was greater then $\sim10^{11}W/cm^2$, large enough to establish a high density plasma on the target surface during the laser pulse Initial electrons for plasma formation are probably due to multi-photon ionization of the atomic species in the vapour, fracture ejection of ions and electrons from the surface and continued *inverse bremsstrahlung* at the frontal region of the early plasma for the remainder of the laser

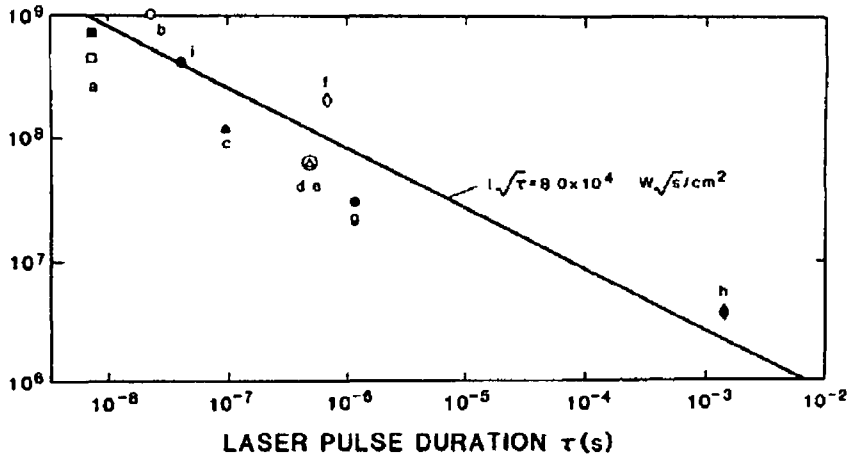

Figure 5 1 5 Threshold irradiance-pulse width dependency for laser plasma ignition (Phipps et al [3 1])

pulse This initial plasma strongly absorbs the trailing edge of the laser pulse, reducing the laser energy reaching the target Absorption of the laser during the pulse by dense plasma layers on the target act as a shield from the trailing edge of the laser pulse, preventing further mass ablation and heating the frontal region of the plume, hence decreasing the plasma density Since collision driven emission during the continuum phase is density dependent, decreasing continuum at early timescales is associated with a lowering of the ablation rate, and a forward expansion of the plume at early timescales infers increasing absorption of the laser in the extended plume Figure 5 2 1 displays the on axis emission spectrum at 10nsec for each target The continuum peak scales upward with decreasing wedge height Figure 5 2 2 shows the off axis emission spectrum at 10nsec (during the trailing edge of the laser pulse for the different targets The decrease in the peak value of the continuum with decreasing wedge height is pronounced It is

proposed that this is due to line of sight summation of light. This statement can only be valid if the spectrometer is seeing a plasma of increasing horizontal extension, back along the laser path.

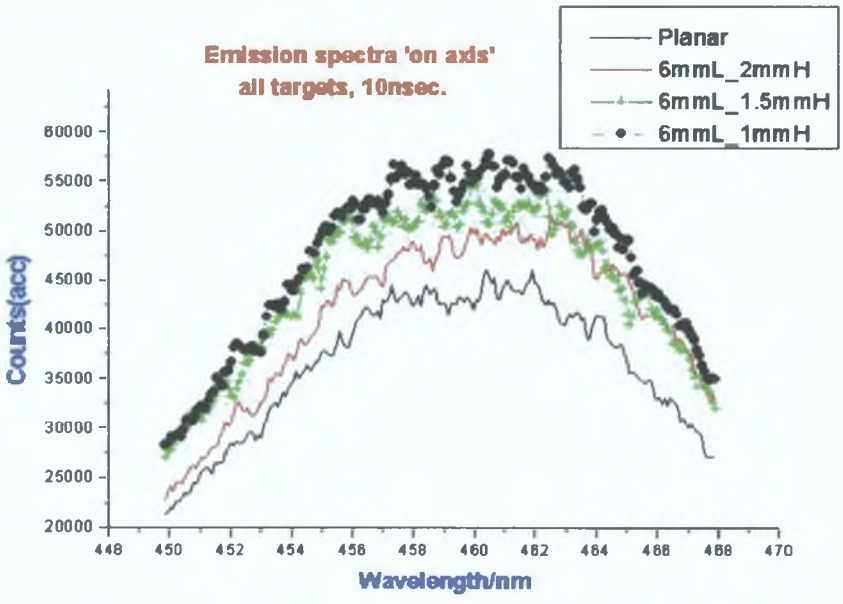

Fig 5.2.1: On axis emission spectra at 10nsec (during trailing edge of the laser pulse). Here the plasma is expanding towards the spectrometer slit. Note the increasing peak continuum count, due to line of sight summation of light on the CCD array. This is a valid statement only if the plasma is increasingly extended along the laser axis as wedge height decreases. (in the graphs , The L after 6mm refers to the wedge length/depth, the H after 2mm, 1.5mm 1.0mm refers to the wedge height/upper–lower plate separation).

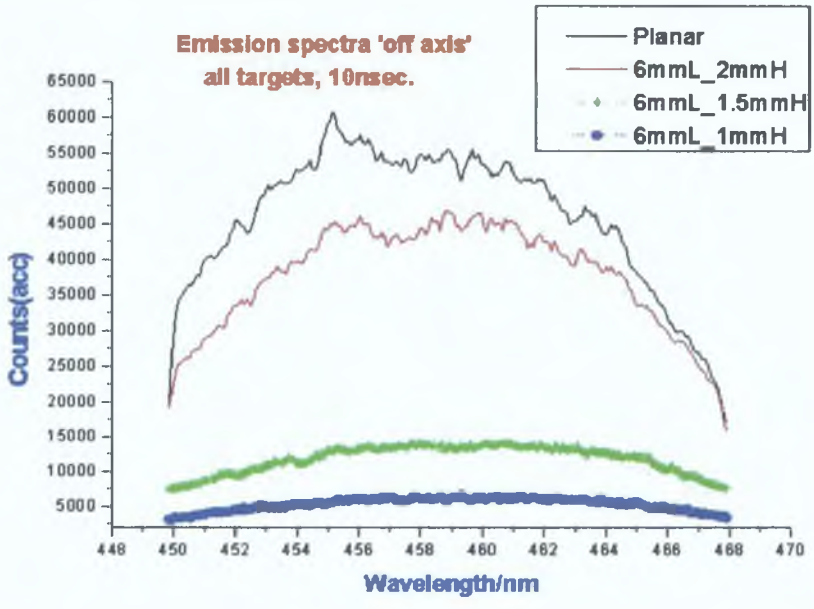

Fig 5.2.2: Off axis spectra at 10nsec, 1.2mm from the target surface. The profile shown for each target is the peak over the spatial extent of each continuum plume for each target. Here the plasma expands away from the target and the spectrometer slit is orientated normal to the targets surface, parallel to the expansion of the plume. The peak continuum values scale downwards as the wedge height is decreased. This is the exact opposite to that of On-axis emission (above). The reason for this is the shifting forward of the position of the peak continuum. As the wedge height is decreased the plasma is channeled forward, resulting in a lower peak continuum value at 1.2mm.

Figures 5 2 3 and 5 2 4 clearly indicate the extension of the AL III (447 99nm and 453 0459nm) with decreasing wedge height at early timescales The peak of each line is shifted forward with respect to the planar target, showing greater forward extension of the plume as the wedge height decreases All wedge targets display greater forward plume extension over the planar target The loss of energy from the target surface to absorption in the frontal regions of the vapor leads to greater heating of the extended plume, and hence higher temperatures, the large difference in the forward extension of the Al III (453 0459nm) line (>80nsec), and the edge of the gated visible images in figures 5 4 1-5 4 4 are clear evidence of increased thermally driven forward velocity The laser energy absorbed by this extended plasma can be expressed as (Liu et al [3]),

$$\text{Equ 3} \quad \Phi_{absorb} = \Phi_0[1-\exp(-\alpha_p L)],$$

where L is the physical thickness and α_p is the absorption coefficient The latter was not calculated here, but from the gated images, a fast, low temperature, plume can be seen moving away from the target at early timescales The physical extension of this vapour plume scales with decreasing wedge height, and matches the trend in decreasing continuum peak emission with decreasing wedge height At early timescales the plasma emission was dominated by continuum which decreased with time This emission was attributed to Bremsstrahlung processes, both collisions of electrons with ions and atoms (free-free emission) and recombination of electrons with ions (free-bound emission) at the leading edge Considering reflection of the laser pulse is dependent on the plasma frequency, given by

Equ 4

$$V_p = 8\,9\times10^3 Ne^{1/2}\ \text{Hz} \qquad \text{(Liu et al [3])}$$

The laser (1 064μm) has a frequency of $2\,828\times10^{14}$Hz If N_e is approx 10^{19} then $V_p = 10^{13}$Hz, thus reflection of the laser pulse is negligible Therefore absorption of the pulse in the extended plume is the more dominant mechanism This is chiefly through *inverse bremsstrahlung*

5 1 7 Early Phase Analysis

The fast decay in continuum emission is due mostly to plume propagation, while long lived low level continuum is due to recombination at longer timescales The early time scales (30nsec-70nsec) show Al II (466 186nm) and AL III (453 0459nm) dominating the spectra The lines are strongly broadened and superimposed on the intense continuum As the continuum decays the spectra are dominated by extended line emission, the three AL III lines being more extended than the AL II line in all targets The difference in spatial extension between the AL III lines as a group and the AL II line becomes more pronounced with decreasing wedge height as the plume expands rapidly forward At later times line emission dominates

from radiative decay of excited species to ground state ions and excited atoms as the plasma cools and expands.

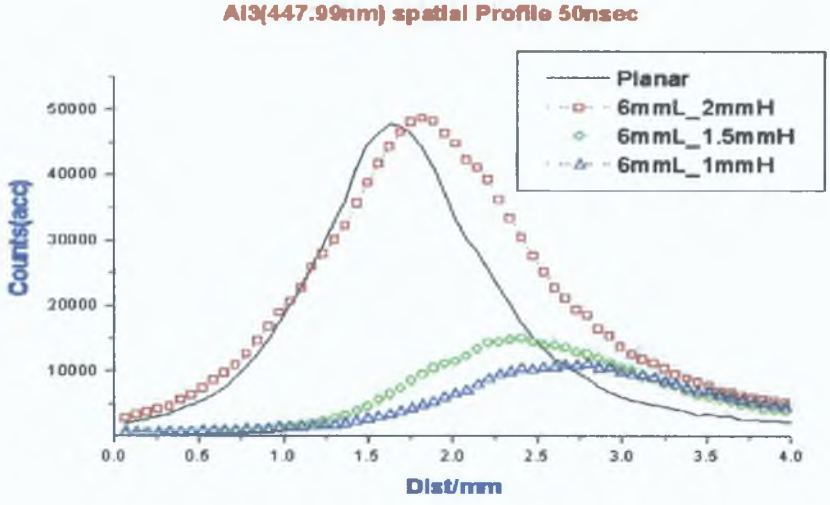

Fig 5.2.3: Off axis spatial profile of AL III (447.99nm) at 50nsec, the profile shown for each target is the peak over the wavelength extent of each line. Note the clear shifting forward of the peak intensity as the wedge height decreases.

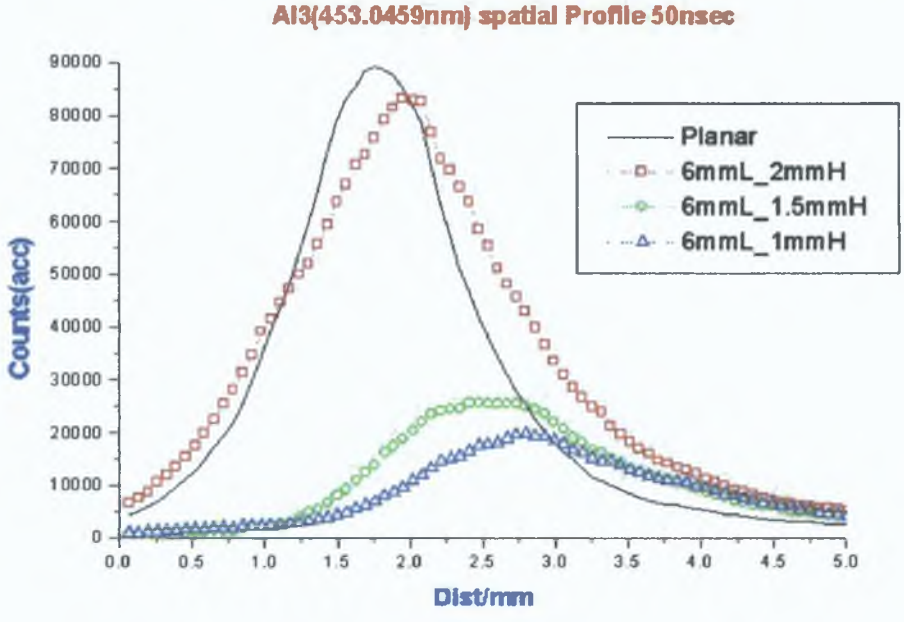

Fig 5.2.4: Off axis profile of AL III (453.0459nm) at 50nsec, the profile shown for each target is the peak intensity over the spatial extent of each line.

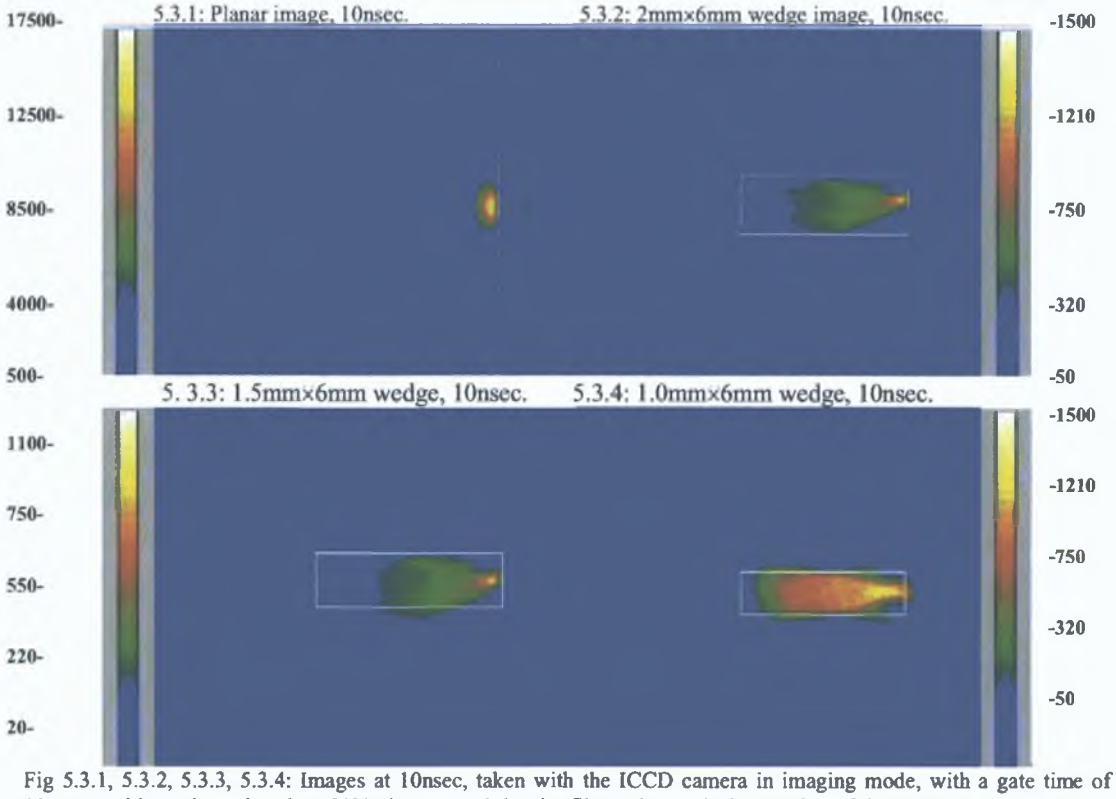

Fig 5.3.1, 5.3.2, 5.3.3, 5.3.4: Images at 10nsec, taken with the ICCD camera in imaging mode, with a gate time of 11nsec, and intensity reduced to .01% via a neutral density filter. The vertical extension of the planar plume is 0.8mm, while the wedge plume heights can be measured with respect to the wedge outline approximated by the white lined rectangle in each image. (The complete set of images for this target group are presented at the end of section 5.1)

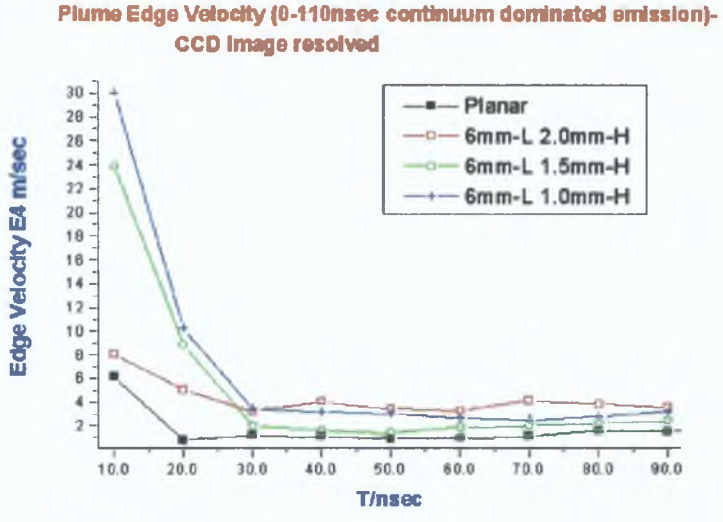

Fig 5.4: Edge velocity of the plasma from each target. The edge velocity of each plume was obtained as the point where the intensity fell to half the peak intensity for that target divided by the delay time on the ICCD. The differences in edge velocity between the targets is very large at the earliest time delay. A five fold increase in the initial velocity, seen as one goes from a planar target to a 1mm high, 6mm deep wedge. This confirms the line, and continuum extension seen in the line profiles, and images.

5 1 8 Analysis 80nsec

Beyond 80-90nsec the continuum has either decayed sufficiently or line emission at the leading edge has become pronounced enough to calculate line widths and temperatures In order to clearly and reliably calculate the line widths and ion/atom ratios required for presenting physical values to diagnose the plasma properties, continuum emission must not be too pronounced and the lines must not be overlapping or have unacceptable signal to noise levels The earliest time when all criteria were meet was 70nsec after the laser pulse As discussed earlier the plume shows a greater spatial extension with decreasing wedge height This difference becomes more pronounced with time Figures 5 5 1-5 5 4, all display the difference in the position of the leading edge of the line In each line profile, the profile is made up of the two regions, the plume in which the continuum is still dominant (left side of the dashed vertical line intersecting the profile) and the extended line emitting region (to the right side of the dashed line) Again the peak continuum value is seen to decrease with decreasing wedge height The physical length of the plume still dominated by continuum increases as the wedge height decreases Initially the lower continuum with decreasing height was attributed to plume extension and resulting laser pulse absorption, lowering the density However as can be seen from images fig 5 3 1-5 3 4, the highly extended plume in the wedges is also brighter, whereas the plasma generated on the planar target is localized completely on the target surface The absorption of the laser beam in this extended plume is likely to enhance large volume photo ionization, at early timescales However as the plume expands rapidly, cooling occurs and the resulting large volume recombination could account for the lower level continuum emission the wedge targets exhibit after the initial hot 20-50nsec period when broad band continuum completely dominates the emission spectrum The AL III lines both show a flattened peak region This is especially pronounced from the 1mm high wedge Initially from Image 5 3 1, (planar target) the vertical diameter of the plasma was calculated to be no greater then 0 8mm Figures 5 5 2 indicates, the strong probability that the plasma in the 1mm high wedge is in direct contact with the upper and lower surfaces of the wedge over the length indicated by the flattened line profiles The AL III (453 014nm) line shows a greater peak 'line emitting' profile (right hand side of the dashed line) in the wedge targets than the planar targets This behaviour is further reinforced by figure 5 7 The peak ionization temperature shows a max of 1000K difference between the planar target and the 1mm wedge Again the wedge targets show a region of constant temperature, which although not perfectly constant, shows very small spatial fluctuations The relatively small differences and almost matching profiles of the planar and 2mm high wedge indicate that only on scales of <1 5mm is the vertical compression of the plume, offered by the other two wedge targets (1 5mm, 1mm high) of significant importance in temperature effects

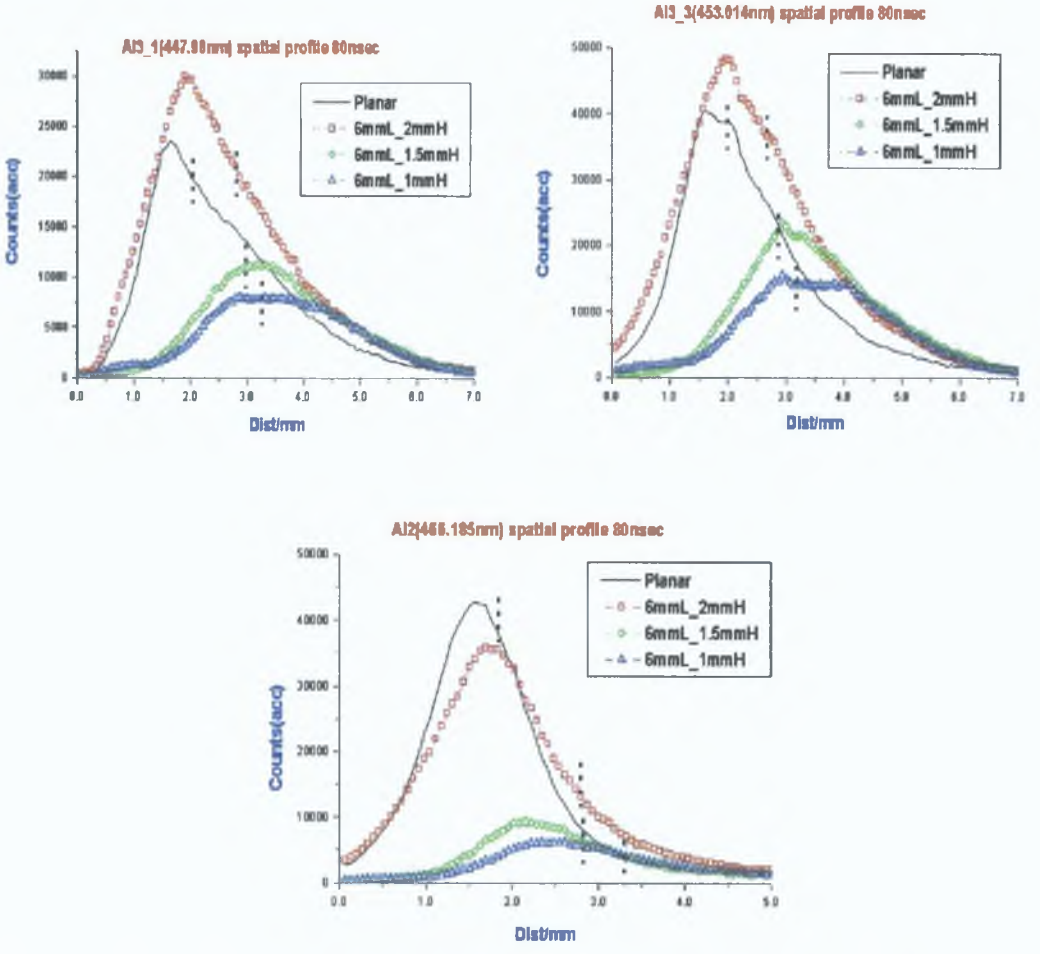

Fig 5.5.1, 5.5.2, 5.5.3: show the spatial profile of the lines AL III (447.985nm), AL III(453.014nm) and the AL II line (466.185nm) at 80nsec delay. The three Al III lines have been designated AL3_1, AL3_2, AL3_3, to describe them independent of wavelength. They refer to the three AL III lines in the spectrum of figure 5.1.1 moving left to right. The legend in each figure indicates the target. Here 'L' is the length of the cavity, and 'H' is the height of the cavity. In each figure, a vertical dashed line represents the division between continuum dominated emission and line dominated emission. The laser beam comes from the right, and the plasma expands from the left. Note that in the profile of AL III (453nm), the 1mm wedge emission profile is nearly flat across an extended region, indicating that the plasma is in direct contact with the inner surfaces of the cavity, and is being channeled along the cavity volume.

Using equation 1.2 at the start of this chapter, the peak intensity ratio of AL III(453)/AL II(466nm) was obtained, and this then allows for the determination of the ionization temperature within the plume. Figure.5.6 displays the spatial profile of the ionization temperature for all four targets at 80nsec. The value of the electron density, required by equation 1.2, was obtained from Stark width of each line for each time delay studied. There is a clear increase in the determined ionization temperature as the degree of containment is increases (i.e. all wedge targets display higher ionization temperature over the planar target). Another important feature of figure 5.6, is the clear extent of the temperature increase over a large scale length from the target surface.

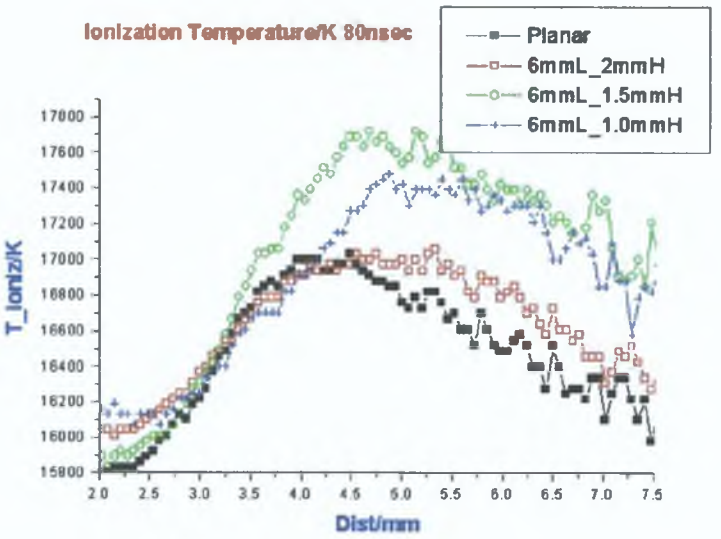

Figure 5.6: Spatial profile of the ionization temperature for all four targets at 80nsec. The leading edge of the profiles becomes increasingly unstable due to the difference in the spatial extension of the two lines used (AL III 453.015nm, AL II 466.185nm). The latter is less extended then the former.

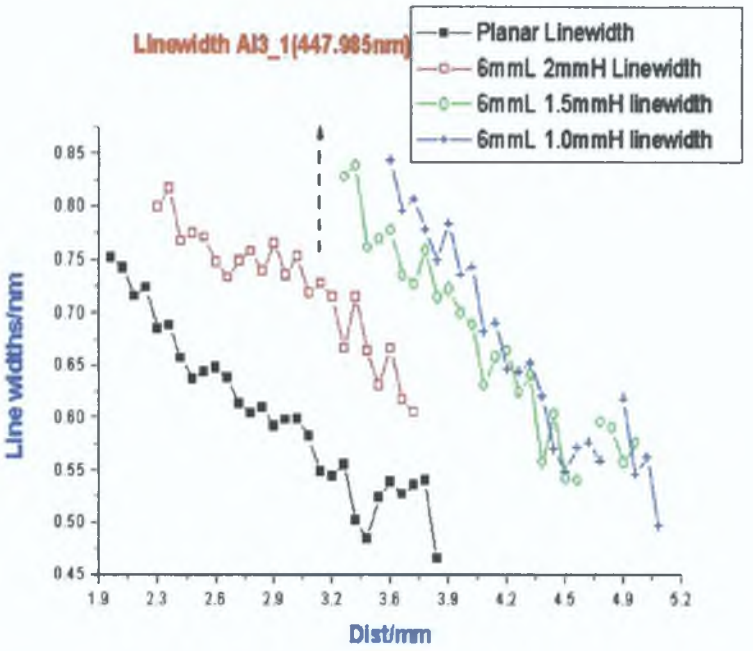

Figure 5.7.1: Spatial profiles of the line width (FWHM) for AL3_1, determined by fitting a Lorentzian line profile to AL III(453nm). Note that although the targets show substantial differences in the position of the peak and its spatial extent, the peak line width for each target is within a small range of values. The approximate decay profile for the line widths is x^{-1}, where x is the distance along a line moving out from the target normal. Such a decay profile has been demonstrated by Liu et al (Liu et al [3]) for early time scales only, later the plasma density profile becomes non-linear.

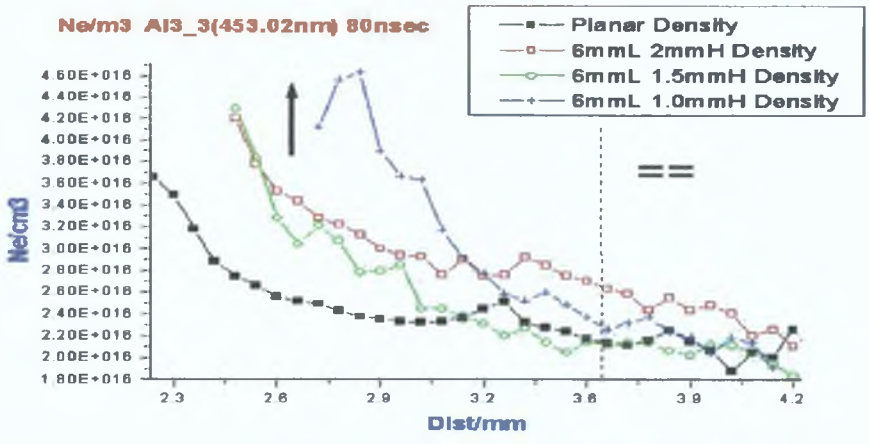

Figure 5.7.2: Spatial profiles of the electron density for AL3_3 (via Stark width broadening of the 453nm line). This was the only line whose electron impact parameter could be determined. The vertical black arrow, indicates that in the spatial region bounded by the target surface to the vertical dashed line (~3.6mm) a clear trend of higher peak electron density and shifting forward of the peak position occurs as the wedge height decreases. The decay profile for the planar target matches that reported by (Liu et al [3]) (using flat targets at different irradiances). Liu reported a $N_e \propto At^{-1}$ decay of electron density in time. The decay profile here is also approximately inverse linear (with distance from the target), but there is a clear flattening of the decay profile for each target at a particular point. The region bounded to the right of the vertical dashed line, displays approximately converging values of electron density for all targets.

Figure 5.7.1, shows, nearer the target surface a clear trend of increasing line width in the AL3_1 line (indicative of increased density). The difference in the peak line width over the four targets is not large, however the extent of the spatial difference over which they appear is large. Again the decreasing wedge height, and resulting higher temperature, and high forward velocity, establishes well resolved lines far ahead of the planar targets lines. Figure 5.7.2 gives a clear indication of higher peak density and greater forward extension with decreasing wedge height. Each target displays peak line and continuum emission at different spatial positions at the same time delay. Figure 5.8, displays the emission spectrum 2.9mm from the target surface. Although the spectra show displays higher continuum levels in the wedge targets, at this spatial point line emission is not substantially greater.

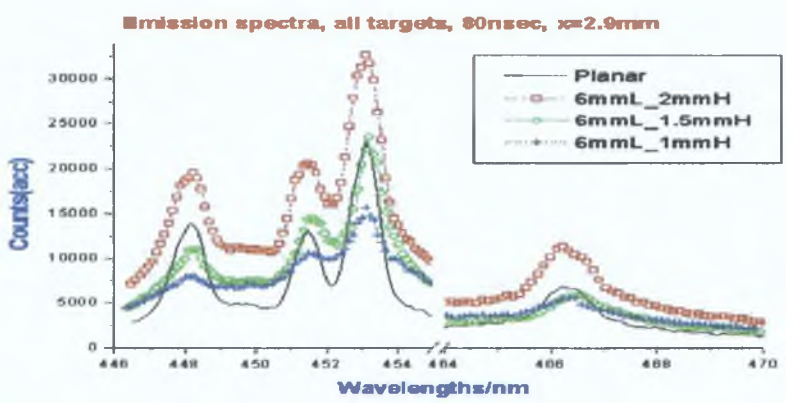

Fig 5.8: Emission spectrum, at 80nsec, at 2.9mm from the target surfaces. The predominance of the 2mm wedge spectrum over the other wedge targets is due to the presence of continuum, which as stated earlier, peaks at different points in the cavity's for each cavity, depending on the height of the latter.

5.1.9: Analysis: 120nsec.

Moving forward 40nsec in our analysis sees the continuing decay of the continuum. The relative change in position of the peak for both AL3_1, AL3_3 lines across the four targets is very different (figure 5.9.1-5.9.3). While the peak of both lines in the planar and 2mm wedge targets shift forward by incremental amounts, the lines for the 1.5mm, and 1mm wedge targets jump by over 2.4mm forward along the laser path. Previously the maximum was shifted back behind the approximate centre of mass of the lines. However now, in the 1.5mm, 1mm wedge targets the peak is now shifted forward of the center of mass. The planar and 2mm wedge show no such shift. The flattened profile from 80nsec in the 1mm wedge is now seen in the 2mm wedge, indicating that the plasma has now contacted the upper and lower surfaces of this target. It displays a rapid extension of line emitting plasma in the forward direction. The three wedge targets now show a second peak at the leading edge. The value of the peak profile scales with decreasing wedge height.

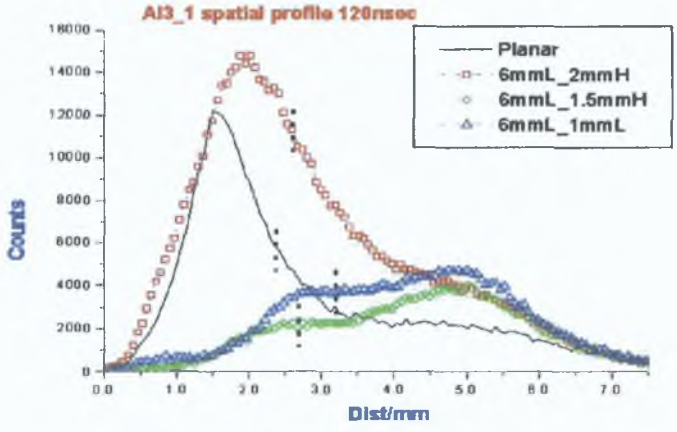

Fig 5.9.1: AL III (447.985nm) spatial emission profile, 120nsec delay.

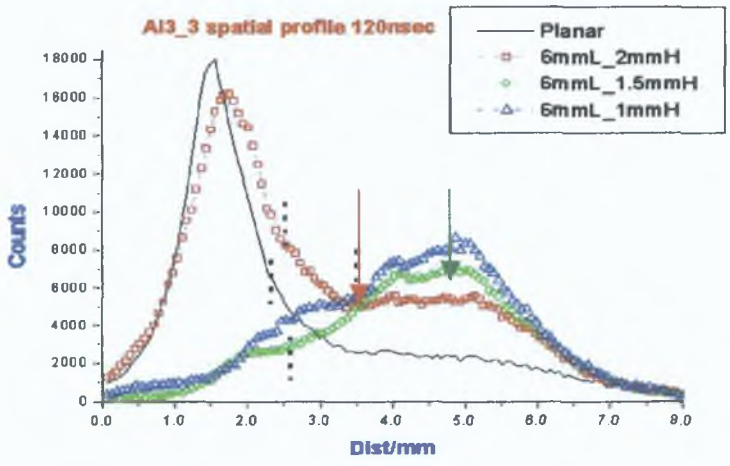

Fig 5.9.2: AL III (453.024nm) spatial emission profile, 120nsec delay.

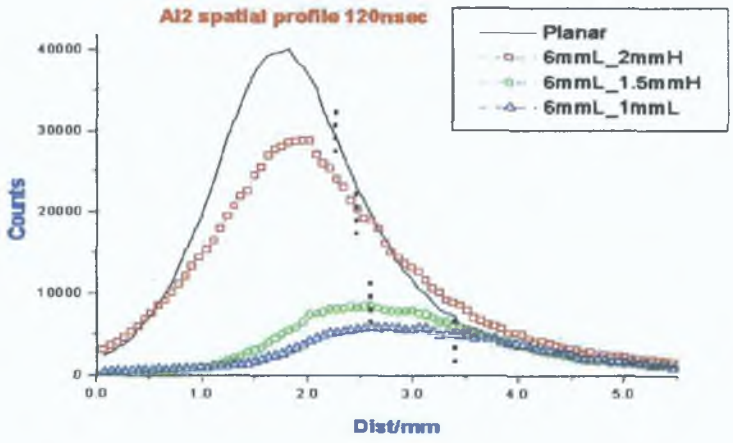

Fig 5.9.3: AL II (466.19nm) spatial emission profile, 120nsec delay.

It is the lowest energy line of the AL III group, AL3_3(453.19nm) that shows the most pronounced difference in spatially resolved emission profiles. While the planar target also displays fast moving line emitting plasma ahead of the continuum dominated peak, which is shifted back towards the target, this line emitting region is of lower intensity than that of the wedge targets.

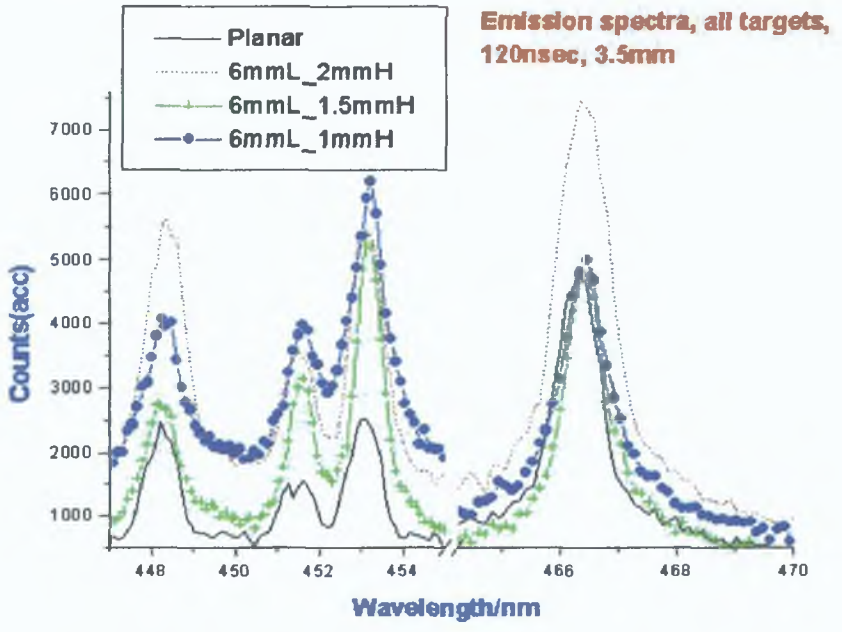

Fig 5.10.1: Emission spectrum, at 120nsec from laser pulse initiation, 3.5mm from the target surfaces. The spectra are taken at the intersection of all wedge targets profiles for AL3_3 (~3.55mm, indicated by the red arrow, figure 5.9.2). It occurs however at the trailing edge of the 1.5mm, 1mm wedge targets for AL3_1.

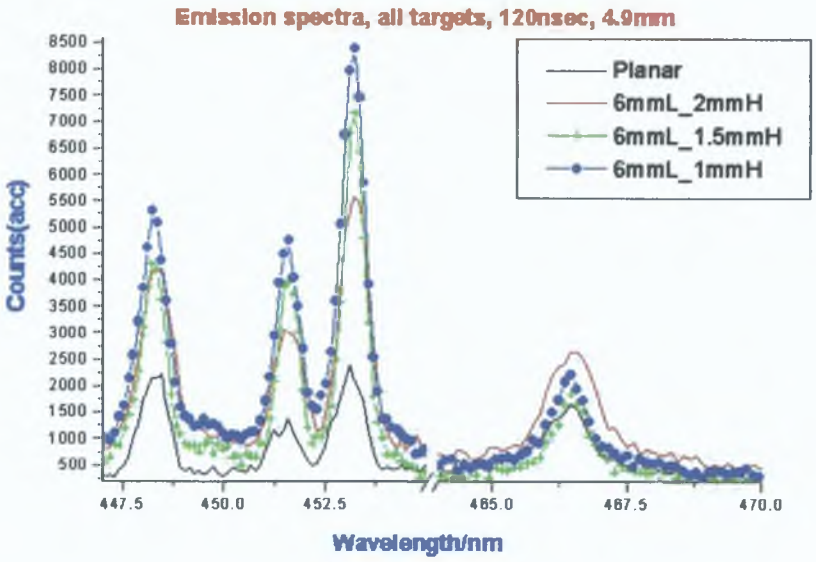

Fig 5.10.2: Emission spectrum, at 120nsec, 4.87mm from the target surfaces, at the leading edge of the second peak in the AL3_3 profiles, indicated by the green arrow in figure 5.9.2.

The most important feature to consider in the spectrum is to compare fig 5.10.1 with fig 5.10.2, specifically with regard to the ratio of intensity of the AL II line with AL3_3 (453nm). Despite being some 1.5mm ahead spatially, the ratio of these two lines in figure 5.10.2 is substantially in favour of the higher stage ion, while the peak count of the Al3_3 line is some 25% higher. This shift is more pronounced as the wedge height decreases.

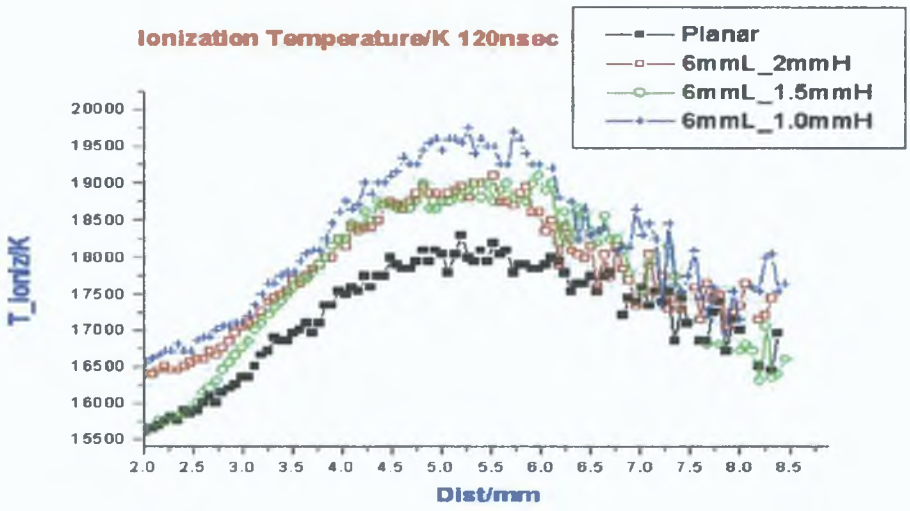

Fig 5.11.1: Ionization temperature profile at 120nsec, spatially resolved for all targets.

Predictably the shift in favor of the higher ion stage at the leading edge of the wedge plumes leads to a large increase in ionization temperature over a spatially extended region. The maximum temperature difference is between the planar target and the 1mm high wedge, some 2000K over a region of 0.7mm (4.9mm to 5.8mm).

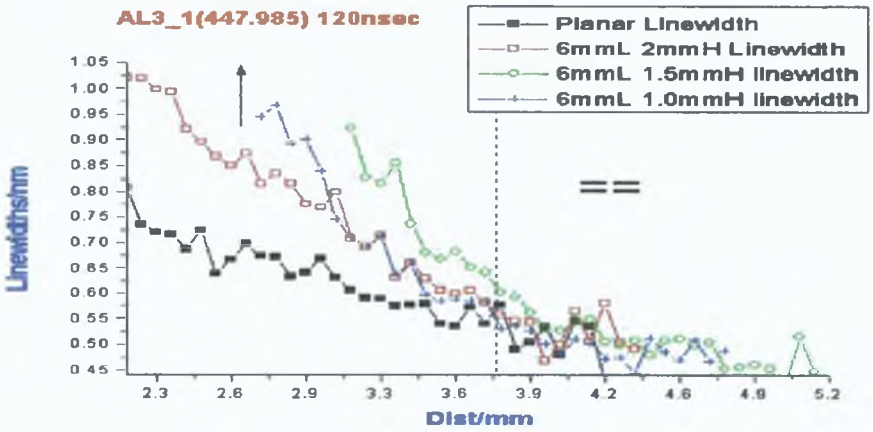

Fig 5.11.2: Line width profile of AL3_1 (447.985nm) at 120nsec. The trend most apparent here is the larger peak line widths for all wedge targets. However at 120nsec, the 1mm wedge displays decaying peak line width, relative to the other wedge targets. All targets display similar values of line width to the right of the vertical dashed line.

Figure 5.11.2 (above) still displays the enhanced forward leading edge line emission from the wedge targets. The difference between the three wedge targets is now less pronounced due to the decrease in edge velocity of the plume (fig.5.4), but all three are now grouped well ahead of the planar target. The line width decreases rapidly at the leading edge, with all targets converging to similar values at 3.8mm. It is precisely at this spatial point that the AL3_3 (453nm) line (fig 5.11.3) shows the increasing line profile, with all wedge targets scaling upwards relative to the planar target. It is at the peak of the profile that the peak temperature is seen (fig: 5.11.1).

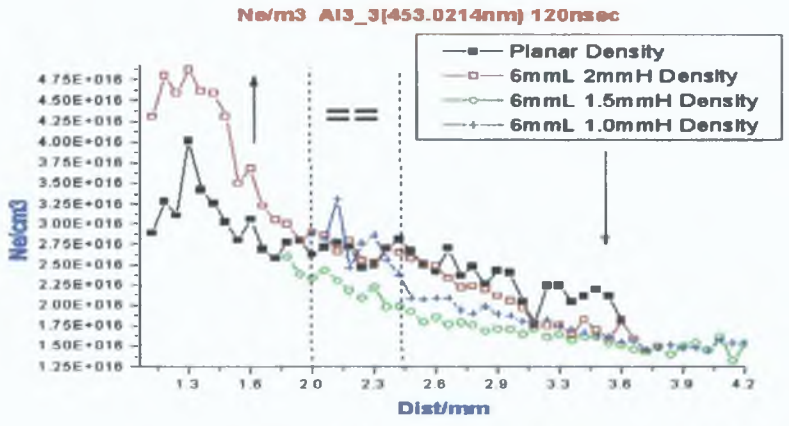

Fig 5.11.3: Density profile of AL3_3 (453.02nm) at 120nsec. At this point in the plasma history, all three decay profiles are visible. Nearer the target surface (left of the first dashed line (0-2mm), with the vertical arrow pointing upwards) the 2mm wedge cavity maintains higher electron densities than the other targets. In the middle region (2-2.5mm) all four targets show similar values of electron density, however from 2.5mm onwards the planar target displays higher values of electron density. Rapid, channeled expansion of the wedge plasmas leads to rapid drops in local particle densities.

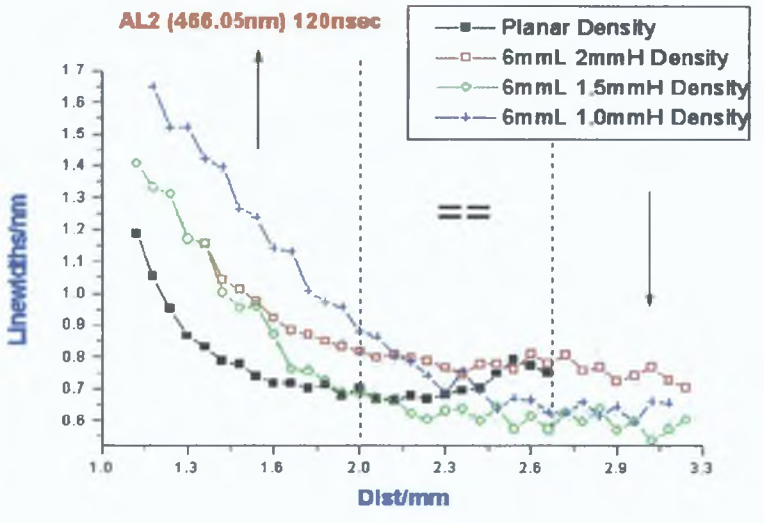

Fig 5.11.4: Line width profile of AL2(466.05nm) at 120nsec. The trend is: 'higher particle density' near the targets surface, followed by 'converging particle densities' at some intermediate spatial point, and finally decreasing particle densities at the leading edge of the plasma, -as the wedge height decreases. All lines exhibit this trend, although at different time delays and over different spatial regions.

Figures 5.11.3, and 5.11.4 display the density from the AL3_3 line and the line width from the ALII line. Only at the trailing edge of the plasma is the increased density with decreasing wedge height still evident in the AL3_3 line. There is a small region where all four targets show similar values of line width related density, however at the leading edge, the line width related density profile is the inverse of that nearer the target surface, namely decreasing density with decreasing wedge height. Similar behaviour is evident in the line width profile of ALII. The width increases with decreasing wedge height, but only near the target surface at the trailing edge of the plasma. Again there is a region where all targets show similar line widths, but at the leading edge the line width profile decreases with wedge height. This is accounted for by considering the collimating effect of the wedge targets and the extended nature of the plume in the wedge which is also evident from the images in figures 5.12.1-5.12.4 (next page). The 2mm and 1.5mm wedges show concentrations of plume on the upper and lower surfaces of the cavity's. The vertical symmetry of the distribution is especially evident in the 1.5mm wedge. The reason such behaviour is not seen in the 1mm wedge is due to the fact that the vertical diameter of the plume at the early timescales (<20nsec) is of the order of 0.8mm (fig.3.1). Thus the plasma in the 1mm wedge does not have sufficient vertical space necessary to split in to two components, as the 2mm and 1.5mm wedges do. Instead if one examines fig 5.12.4 a twisted, rebounding filament of bright plume seems to exist in the 1mm wedge.

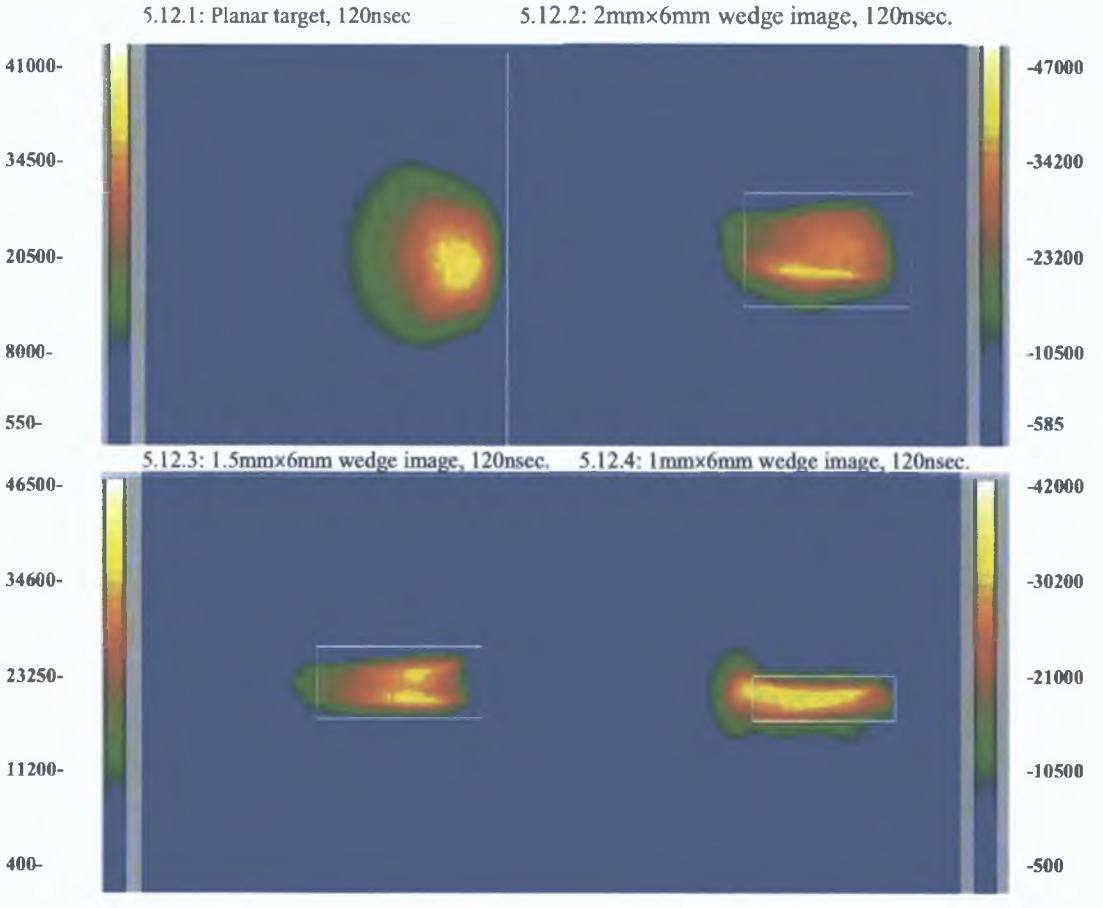

Fig 5.12.1-5.12.4: Images at 120nsec, taken with the ICCD camera in imaging mode, with a gate-time of 11nsec. No filter is present.

It is possible that the enhanced peak profile of the AL3_3 line and AL3_1 lines (and resulting higher ionization temperature) is due to the collision of plasma with the upper and lower surfaces of the cavity. Since the length of each wedge is constant, the difference in height would result in the plasma colliding at a higher temperature and density due to decreased vertical expansion as the wedge height decreases.

5.1.10: Analysis: 160nsec.

This is the last temporal point where significant differences exist between the four targets. From 200nsec onwards the target plumes show rapid convergence in their behaviour. In the line profiles of AL3_3, the 2mm and 1.5mm wedge targets show convergence at their leading edge (fig 5.13.2). Only the 1mm wedge maintains its enhanced profile. There is a clear indication of a two component plume peak from all wedge targets, the position of the secondary peak scaling forward with decreasing wedge height. Figure 5.14.1, the emission spectrum at the peak of the leading edge, displays a shift in the peak scale of the spectrum from each target. In the planar target the AL II line is the most dominant, but as one goes from the planar target to the

1mm wedge the most dominant line becomes the AL3_3 line. This shift is not limited to this line only, but to all the AL III lines.

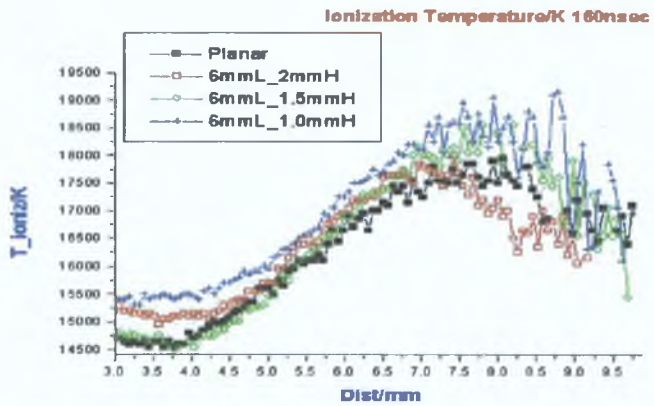

Fig 5.13.1: Spatial profile of the ionization temperature at 160nsec. At this stage in the plasma history, all targets show rapid convergence of plasma temperature profiles.

Despite the large shift in favour of the AL III lines in the spectrum, this is not mirrored by a large shift in temperature (fig 5.13.1). The temperature profiles show convergence at later times, while the leading edge of the temperature profile becomes less continuous. This is a consequence of the difference in the spatial extent of the AL II lines used in the line ratio calculation. In reality the temperature profile cannot be trusted beyond 8.5mm given the lack of extension of the AL II relative to the AL III lines.

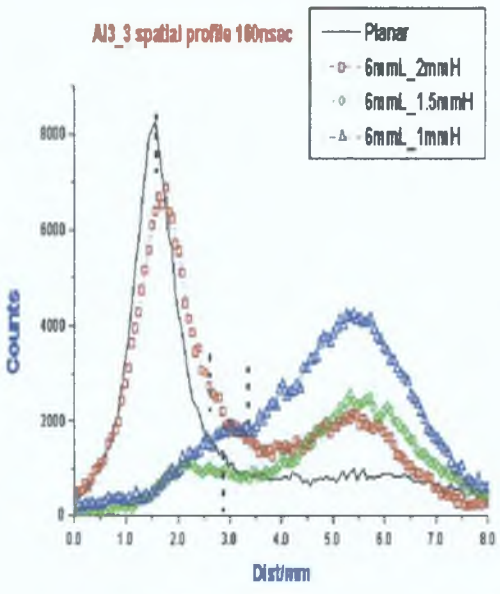

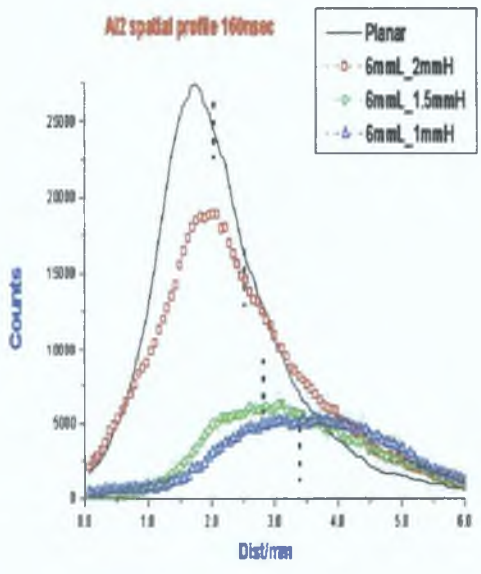

Fig 5.13.2: Spatial profile of the AL III (AL3_3) line at 160nsec. Fig 5.13.3: Spatial profile of the AL II line at 160nsec.

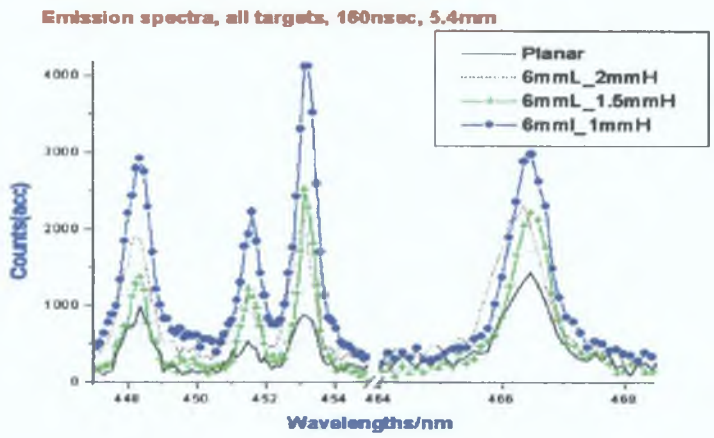

Fig 5.14.1: Emission spectrum at 5.4mm from the target surfaces for all targets. Delay is 160nsec. This spectrum corresponds to the point of peak line intensity for the Al 3_3 profiles (figure 5.13.2). In figure 5.13.2 the wedge targets display superior peak intensity profiles, and this peak is shifted dramatically forward relative to the planar target. The spectrum above demonstrates this. For the planar target the AL II line (466.5nm) displays higher peak intensity then all the AL III lines. However for the wedge targets there is a gradual growth in the AL III lines over the AL II line.

Finally one can see from figure 5.13.2 that the planar target profile also shows a substantial extension forward, however as the value of the profile shows the peak is still shifted back towards the target surface (left hand side), half of which is low level, long lived continuum (indicated by the vertical line through the profiles). Again as with the AL III profiles at 120nsec, the profiles at 160nsec show an almost complete absence of a peak continuum value, this is especially so for the 1.5mm and 1mm wedge targets. Continuum emission is via electron collisions, which itself is density dependent. From this we can infer that the density profile in the wedge targets is very different to that of the planar target. If one considers figure 5.14.2 the 'profile inversion' is now clear for the AL3_3 line, (i.e. reversing the trend of increased density with decreasing wedge height). The planar target shows the largest density, the density decreasing with wedge height.

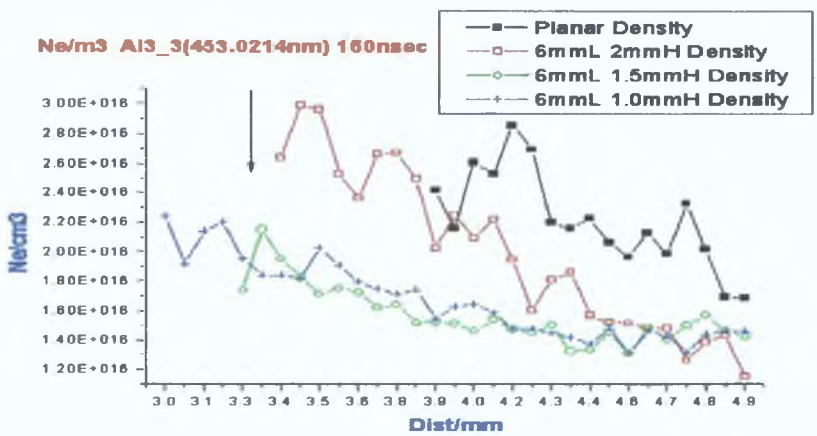

Fig 5.14.2: Spatial profile of density, for the four targets, via the line width of AL3_3 (453nm). The planar target displays higher electron densities then all wedge targets. The trend now is of lower electron density as the wedge height is decreased. This is the complete opposite of the trends which existed at earlier time scales.
The profile inversion exists for different lines at different times.

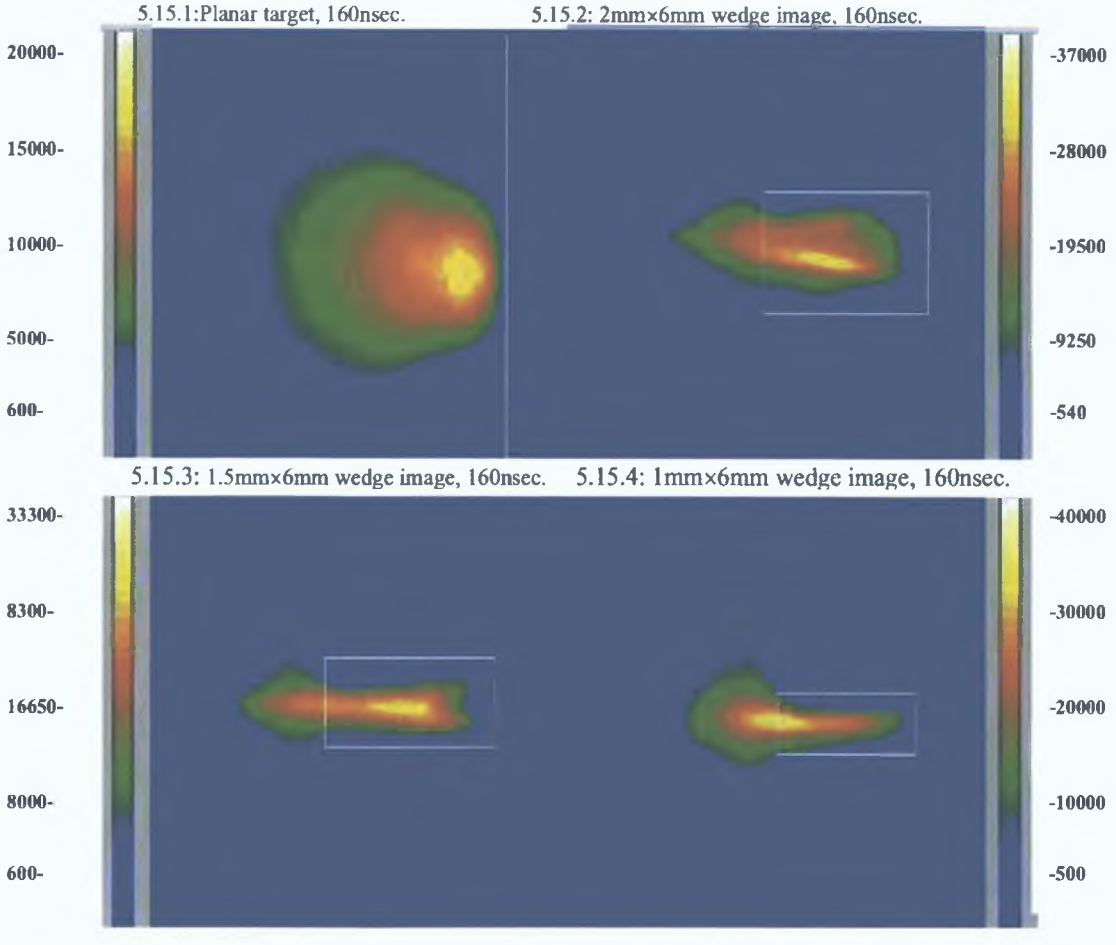

Fig 5.15.1-5.15.4: Images at 160nsec, taken with the ICCD camera in imaging mode, with a gate-time of 11nsec. No filter is present

From this point onwards the AL3_3 line decays rapidly, its density values already showing a lack of smoothness in comparison with earlier timescales. If one considers figure 5.15.1-15.4, we can see a darkened region near the target surface, in the wedge targets, indicating that the plume there has for the most part detached itself from the back surface, this accounts for the lack of continuum in these targets. In the case of the 2mm , and 1.5mm wedges the two 'layers' of plume seen on the upper and lower surfaces at 120nsec have now moved back to the center of the wedge and combined. This combination has produced a new bright region in the wedge center (fig 5.15.3). Given the strong possibility of low level continuum emerging from this region, this may account for the extended low level continuum in the wedge targets profile (fig 5.12.2, fig 5.12.3) which is shifted forward in comparison to the planar target. This low level continuum is also highly extended spatially and is uniformly distributed (fig 5.12.2--1.5mm target).

5.1.11: Analysis: 200nsec.

At this late stage of the plume's expansion, the AL III lines have decayed rapidly and their signal to noise ratio is not good. Thus line widths of these lines are unreliable. The temperature profile, although

calculated is not presented here. It is very noisy, but does show a peak ionization temperature of 15900K for both the 1mm, and 1.5mm wedge targets. The 2mm wedge and planar target have a peak temperatures of 15300K, and 15000K. The peak temperature of the targets are spread over a 0.6mm range from 7.2mm to 8mm, with the planar target trailing the wedge targets.

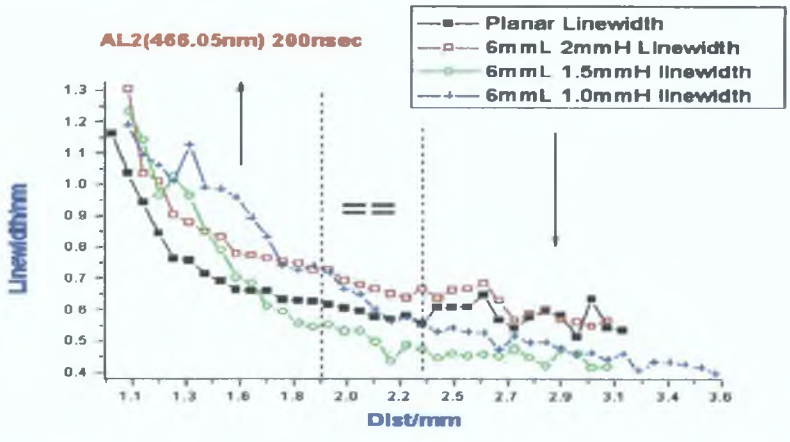

Fig 5.16.1: AL II line width spatial profile at 200nsec. At this late stage in the plasma history, the AL II line now displays a similar three fold trend over its spatial range. Near the target's surface, the wedge targets retain higher particle densities, and converge rapidly over a particular spatial region (1.9-2.4mm), while at the leading edge of the line profiles, the planar targets display superior line width values.

With the AL II line the density profile is still continuous, with the peak line width still increasing with decreasing wedge depth (fig 5.16.1). Again this region is shifted back towards the target. Moving forward towards the leading edge, the line width shows a decreasing profile with decreasing wedge height.

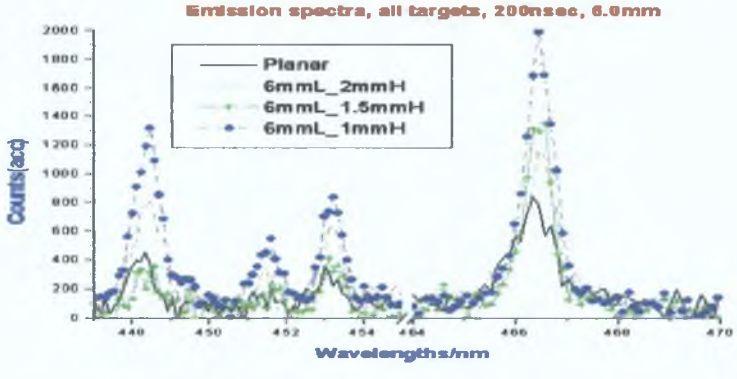

Fig 5.16.2: Spectrum at 200nsec, at x=6mm from the target surface.

Even at this late stage and low signal level of the AL III lines, the wedge targets still retain their superior peak emission value of all lines. This is now especially so for the AL II (466nm) line and the AL3_1(447nm) line. In the final group of images (fig 5.15.1-5.15.3), all plasma plumes have left the target surface and are moving towards the exit of the cavity. The 1.5mm wedge plume is very extended spatially, some brighter plume appears to be moving back into the wedge as well as out of the cavity. The brightest region is highly extended. The 2mm wedge shows a new brighter region centered in the cavity, previously at 160nsec it was the 1.5mm wedge which showed this feature, the plasma in the 2mm wedge had yet to

contact in the center. Now 40nsec later the trailing edge of the two films of plasma that were seen on the upper and lower surfaces are now detaching from the upper and lower surfaces and colliding in the cavity center. Throughout the lifetime of the plasma imaged while the plumes are exiting the wedge targets, the peak region of brightness is the aperture or exit of the wedge. Here the plasma undergoes expansion in the vertical, and appears to curl up and down, along the vertical surfaces of the targets outer face.

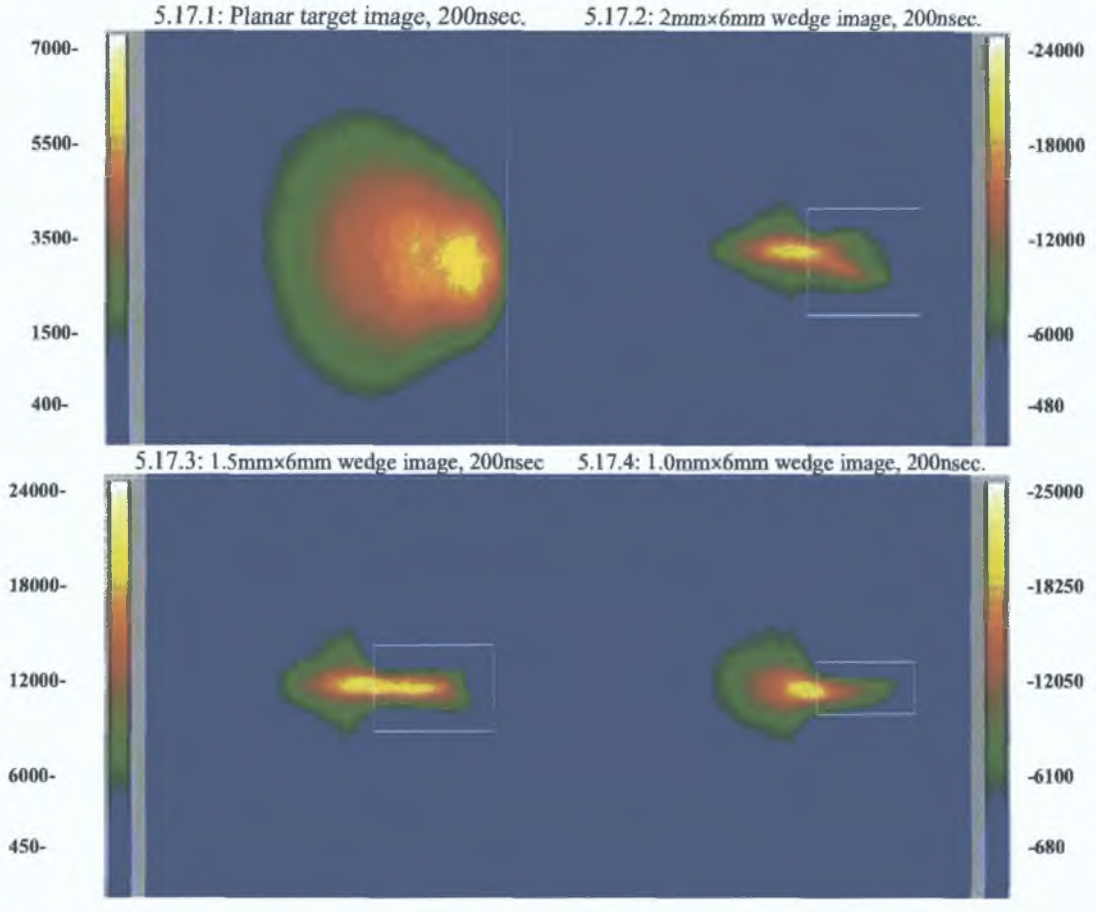

Fig 5.17.1-5.17.4: Images of the of the wedge targets. No filter is present. Time, 200nsec.

This collision of plumes could account for the line width profile of this target, which at the leading edge of the plume shows similar values as the planar target, and higher values than other wedge targets. The localized bright region in the 1mm wedge images, corresponds to a position near the exit of the cavity, the spectra (fig 5.16.3) at that point clearly shows the enhanced line emission, the largest difference being in the peak count of the AL II line. From this time onwards the plumes leave the cavity's and cool and expand rapidly. There is no detectable spectroscopic signal from any of the AL III lines after 330nsec, and the AL II lines decays into background after 390nsec. Images of the plumes are still resolvable up to 400nsec for the planar target and 570nsec for the wedge targets. Beyond 650nsec no photon based signal in the visible range is detectable at the settings used here (i.e. no-gain). A full time history of all plume images is given at the end of this section.

5.1.12: Analysis: >1000nsec.

In order to probe later time delays an ion probe was used to sample the ion signal from each target. The wedge heights used were deliberately different to those reported above. The question as to whether decreasing wedge height leads to lower density at longer timescales requires this to avoid any type of systematic error.

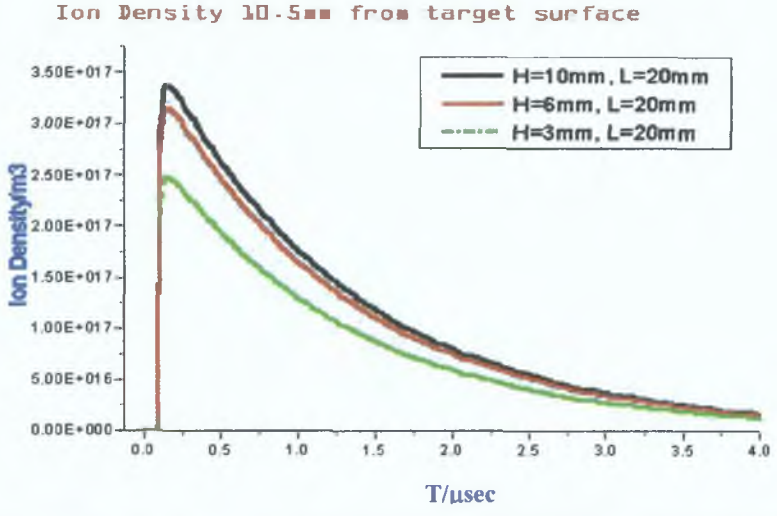

Fig 5.17.5: Ion density trace for three wedge heights, 10mm, 6mm ,3mm. Wedge depth 20mm. Axial distance is 4.5mm.Here 'H' is the height of the wedge, and 'L' is the depth or length of the cavity. The main difference here in comparison to data from chapter four, is that the probe is positioned 4mm from the wedge target block, and the cavity depth (20mm). Thus this depth is the largest employed. The lower peak ion densities are due to the large depth of the cavity (20mm here, compared to 6mm in section 4.2). There is also the possibility of 'shadowing', i.e. that due to the probe's close proximity to the wedge aperture, that the main body of the plume has not expanded greatly parallel to the target surface, and thus most of the plume passes close, but not through the probe tip.

Despite the difference in both timescales and instrument, lower densities at later times, are a feature of wedge targets with decreasing wedge height. The arrival time of the peak of each wedge is 1.3μsec (3mm wedge), 1.4μsec (6mm wedge) and 1.6μsec (10mm wedge). This gives peak velocities of 3.46, 3.21 and 2.81 (10^3) m/sec, thus peak TOF velocity increases with decreasing wedge height.

5.1.13: Conclusion.

In summary, 1-Dimensional horizontal confinement is achieved by generating the plasma inside a rectangular wedge cut into a Aluminum block. Rapid decay of continuum emission is a clear trend at early timescales, and generation of an extended plume, which expands forwards from the wedge back surface was observed. Clearly containing a plasma at early timescales will lead to higher densities near the target surface at early timescales, as the plasma is unable to expand parallel to the target surface. This will also result in forward collimation of the plume. Higher ionization temperatures, and greater forward velocity of the lines are observed as a result of containment, as the plasma is forced to redistribute its internal thermal energy. Usually forward expansion of a plasma is negated by the laser pulse during its duration. This accounts for the lack of low intensity fast plume at early delays. However given the inability of the plasma in the wedge to expand vertically parallel to the target surface, forward expansion is enabled, even during

the laser pulse Thus very large pressure gradients must exist in the plasma The emergence of double peaks in the wedge targets at later timescales (>100nsec), and a shift in favour of higher ion stages in the emission spectrum at these points, seem to indicate a two phase velocity distribution, with a faster, more highly charged plume leading the expansion at the front while a slower secondary component trails behind This is not unlike probe signals at later stages, where one observes a fast main peak, followed by a slower more extended main plume Plume splitting in the vertical dimension was an unexpected aspect of plasma dynamics, as plasma layers build at the upper and lower surfaces of the cavity's , then later leave these surfaces, colliding at the wedge center The most obvious reason for this is to again infer redistribution of plasma particles during the laser pulse The lack of vertical expansion space, and resulting deflection of plasma from the upper and lower surfaces of the cavity's which recombine at later time delays, would be an effect which would increase as the height of the cavity is decreased For selected times, and over a selected spatial region, densities and line widths increase with decreasing wedge height, but decrease at the leading edge of the plume This occurs to a different extent for each of the lines studied Lower peak ion densities and higher peak ion velocities were observed at later timescales (>1000nsec) This latter trend mirrors that seen with electron probes in chapter four Again we infer the 'lower local' density from higher expansion velocities (not lower ablated mass volume), the most credible evidence of this is the ICCD images, which display fast, extended plumes emerging from the cavity's

5 2 Time and space resolved visible studies of laser plasma generation and dynamics in Capillaries 2-Dimensional radial confinement

Having studied 1D containment within a horizontal cavity, we extended this to 2D radial containment within a capillary The main purpose of this is to increase the degree of containment In a capillary the plasma is still free to expand normal to the target surface, however like the wedge targets discussed previously, plasma expansion parallel to the target surface is affected Specifically, in capillaries the expansion parallel to the target surface is allowed only within the diameter of the capillary itself While still using line ratios to calculate ionization temperatures, and line broadening to calculate electron densities, the line-to-continuum temperature technique was also used, for early stage temperature determination This allowed us to probe the plume earlier than the 70-80nsec limit found when using line ratios

5.3 1 Experimental Setup

The capillaries had a section cut from the side wall (1 5mm high 9mm long), along the length of the capillary This facilitated light emission to the spectrometer and minimizes plasma loss from the cavity Although not a perfectly containing cylinder, it was sufficient for 2Dimensional radial containment The experimental setup was identical to the previous experiment, however given the limitations on diagnostics during early timescales another technique was used

5.3 2 LTE Considerations

Although atom to ion ratios are used here, they are only presented for timescales after 80nsec, thus to study temperatures before 80nsec the line-to continuum ratio method was employed Under the assumption of LTE in the plasma, the electron temperature, T_e can be assumed equal to the excitation temperature T_{exc} Thus $T_e=T_{exc}=T$ Again, in the analysis, we assumed that the plasma is in LTE The values of electron density and temperature allow us to check our assumption Returning to equation 1 1,

$$N_e \geq 1\,6 \times 10^{12} \times T(eV)^{1/2} \Delta E(eV)^3 \qquad \text{(Liu et al [3])}$$

This gives the minimum density condition for the plasma to be considered to be in LTE ΔE is the largest energy transitions for which the condition holds In our work ΔE is 2 76eV for AL III (447 9nm) The highest temperatures measured (discussed later) were 60000K (at 20nsec after the laser pulse), this gives a lower limit on the right hand side of equation 3 of $7\,7\times10^{13}cm^{-3}$ The lowest densities measured using Stark broadening were $1\,5\times10^{16}cm^{-3}$, thus validating our assumption of LTE in the plasma for capillary targets In this target configuration, plasma parameters, especially temperature, showed a two phase behaviour At early timescales (<80nsec) values for all targets are seen to decrease very rapidly This occurs as a consequence of high velocity expansion of the dense high temperature plume The second phase, (>80nsec)

shows a less pronounced decrease in physical parameters such aa temperature and edge velocity, but does indicate spatial structure throughout the plume, this is especially so in the confining targets Both densities , and ion spatial profiles, at selected delays indicate both plume splitting and inversion in density profiles (as one goes from the planar target to capillaries of decreasing diameter, trends that existed at early delays are seen to reverse, i e higher densities near the target surface)

5.3 3 Line-to-continuum temperatures

From chapter 2, equation 11, one must chose an emission line, and associated continuum region for inputting into the left hand side of equation 11 We used AL III (453 04nm) here and by taking the center wavelength positions to be the same for both the line and the continuum cases i e $\lambda_l=\lambda_c$, equation 11, chapter 3, is simplified In this case, the peak continuum level is the base line of the Lorentzian fit to the emission line Secondly, for Aluminum, ξ was not accessible from any source Thus its value was calculated by using two lines of the same ionization stage, ALIII at 447 9nm and 453 04nm These were used with equation 11, allowing two equations to be formed with two unknown variables (ξ and T_e) This then gives two simultaneous equations and thus one can solve for ξ The approximated value for ξ found here was ~0 98 This technique was employed by Liu and Mao, for Silicate and Silicon in the visible [3, 5] under similar irradiance levels and laser pulse widths The partition function of AL III ions was calculated via equation 12, chapter 2, at a mean temperature of 28000K (2 41eV) thus giving a degeneracy of 0 13 The values for J_i and E_i were obtained from the NIST databank, Kentucky line list, and NIST ionization levels [4 1, 4 2, 4 3] This technique has been used by Zeng and Russo [5] to study silicate plasma in capillaries

5.3 4 Analysis Phase1 (t<80nsec)

The early phase of plasma generation during the laser pulse is a complex process, The initial plasma generated by the leading edge of the laser usually prevents the trailing edge from reaching the target surface This decreases the particle density in favour of higher temperatures in the absorbing plasma The main mechanism for laser absorption is inverse bremsstrahlung, but also multi-photon ionization The higher temperatures due to laser pulse absorption leads to greater forward extension of the plume and enhanced forward velocity If this process continues, and the irradiance is high, then the bulk vaporization near the target surface decreases, this then lowers the particle density and hence plasma density Laser absorption near the target surface can then increase This balance between pulse absorption near the surface, leading to higher density, and absorption at the frontal region leading to higher temperatures, allows a self regulating regime to exist (Caruso et al [6]) The loss of energy from the target surface to absorption in the frontal regions of the vapour leads to greater heating of the extended plume, and hence higher temperatures and the resulting higher expansion velocities lead to a rapid drop in density in the plume as one moves away from the surface with an inverse dependence (Caruso et al [6]) It is precisely

this relationship of plume absorption and higher temperatures in the frontal region/higher edge velocity/greater forward expansion that we wish to diagnose as a way to understand the dynamics of the plasma in the capillaries for early timescales. Figure 5.18 shows the spatial profile at 458.88nm (a region where no aluminum lines are present at the middle of the spectrometer's spectral window). At 16nsec the laser pulse has terminated, and the plasma begins to move rapidly away from the target surface. This is a well established fact, from both plasma models (Narayan and Singh [11]), Anisimov et al [16]) and from imaging fast imaging studies (Geohegan et al [15]).

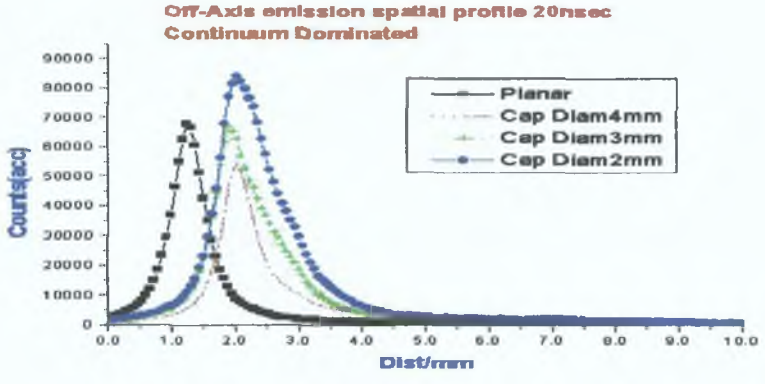

Fig 5.18: Spatially resolved continuum emission at 20nsec.

The notable shifting forward of the plumes leading edge has been a hallmark of all confining targets studied, and is seen to increase as the extent of the confinement increases. The higher peak count is indicative of higher collision rate of ions and electron, from higher localized densities. This would indicate that the absorption of the laser pulse is occurring further from the target surface in the capillaries, or that substantial forward channeling of the plasma is occurring. However as stated, such a process usually occurs due to higher densities at the target surface, resulting in absorption of the beam in the frontal region of the plume via inverse bremsstrahlung.

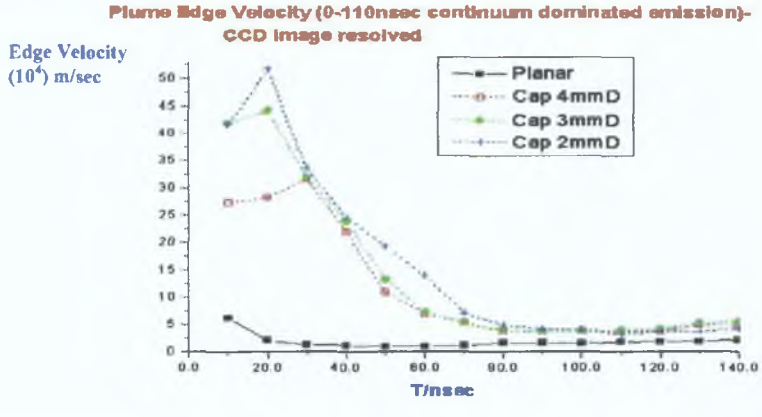

Fig 5.19: Edge velocity of the plume for each target. The edge velocity at any instant is calculated using the motion of the point where the intensity is 50% of the peak intensity.

In our experiment, not only is the peak continuum shifting forward which indicates frontal plume heating and resulting temperature driven expansion, but the spatial extension of the continuum is larger for the capillaries, and its peak value is higher. Observing figure 5.19, the peak edge velocity of the plumes shows a large increase in the confining targets, while their decay profile indicates that they reach their peak velocity later than the planar target. The peak velocity in the capillary targets is higher then that reported previously in section 5.1 with wedge targets, the probable reason for this is the greater channeling of the plasma normal to the target surface. The extent of the spatial extension of the plasmas in the capillary target's continuum could be attributed to either recombination continuum, with the rapid expansion of the plume rapidly lowering the plasma density in the frontal regions, or direct channeling of the plasma via the radial containment offered by the capillary.

5.3.5: Plume extension.

Although gated visible images were taken, these are of limited use, because one can only display a limited region of the plume, allowed by the aperture in the capillary wall. More useful, is to display the spatial profile of emitted light along the central axis of the capillary. Figures 5.20.1-5.20.4. show the light distribution for the four targets for timescales of 0-50nsec. The substantial difference in the extension of each target's plume is evident from very early timescales. The possibility that the capillaries internal surfaces are acting as a plasma light collimator and giving artificially large expansion profiles exists due to scattered visible

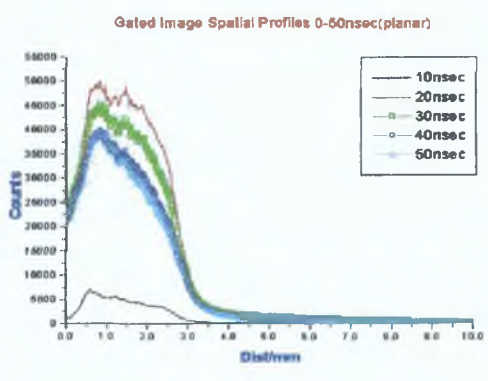

Fig 5.20.1: CCD image emission profile planar target.

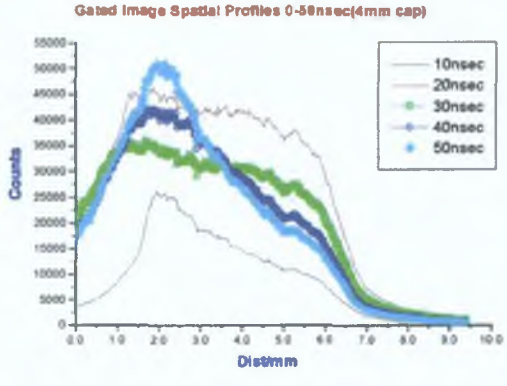

Fig 5.20.2. CCD image emission profile 4mm cap.

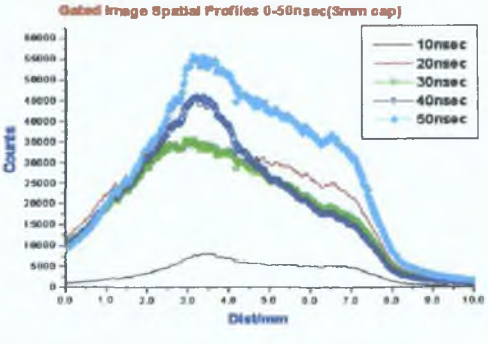

Fig 5.20.3: CCD image emission profile 3mm capillary.

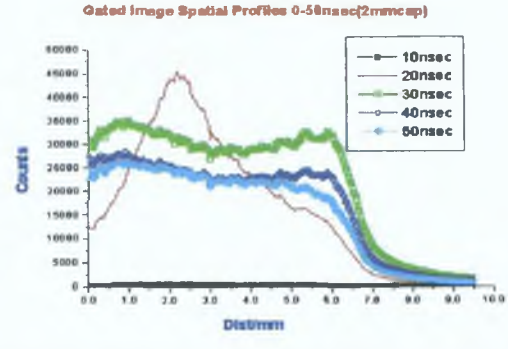

Fig 5.20.4. CCD image emission profile 2mm capillary.

light However the from the internal geometry of the targets, only a small percentage of the reflected light would be directed entirely out through the wall aperture The most important feature is the forward expansion at 10, and 20nsec, during the laser pulse While the planar target shows highly localized emission, the confining targets give unusually structured profiles, extended away from the target surface At later times (30-50nsec), all profiles shift their peak emission back towards the target surface, while the 2mm capillary displays a double peak profile, with a dip, centered at 3 3mm

5.3 6 Earlier phase electron temperatures and velocities

The plasma frequency is density dependent

$$\text{Equ 5} \qquad \omega_p = 8\,9\times10^3 \times \sqrt{N_e}\ (\text{Hz}) \qquad \text{(Liu et al [8])}$$

and the laser frequency is $2\,2\times10^{15}$ Hz

We do not have density values at early timescales If the highest density seen at the earliest timescales (70nsec after the laser firing) is approximately 1×10^{17} cm^3 (presented later), and the bulk number density of aluminum is ~10^{22}cm^3, then a reasonable range of densities at early times could be taken as 10^{18}-10^{20} cm^3 Taking these two values and calculating the resulting plasma frequency, gives $2\,8\times10^9$Hz and $8\,9\times10^{13}$Hz for our two limits Thus despite our liberal estimate for the upper value for the plasma density, it is still below the laser frequency by two orders of magnitude Thus losses due to laser pulse reflection from the plasma are negligible If the dominant mechanism is absorption via inverse bremsstrahlung and the absorption coefficient α_p (cm^{-1}) for the electron–ion inverse bremsstrahlung is

$$\text{Equ 6} \qquad \alpha_p = (3\,69\times10^8)\frac{Z^3 n_i^2}{T^{1/2}\nu^3}\left[1-\exp\left(\frac{h\nu}{kT}\right)\right] \text{(Caruso et al [6])}$$

where Z, N_i and T are the average ion charge state, ion density and temperature of the plasma and v is the frequency of the laser pulse Then for aluminum plasmas in the temperature range of 10eV-14eV, Z=7(approximation) N_i could be approximated at $10^{18\text{-}19}$cm^3 At temperatures of 10eV and upwards, the values in the exponent can be ignored Thus for aluminum, the above equation can be simplified to

$$\text{Equ 7} \qquad \alpha_p = \frac{12\,154}{Te^{3/2}}\ \text{cm}^{-1}$$

Before proceeding, in order to quantify the absorption rate, temperatures at the early timescales involved are required Figures 5 21 1-5 21 4 show the spatially resolved temperature for time delays of 40,50,60,and 70nsec Earlier time scales are too dominated by continuum emission Latter measurements (>80nsec) suffer from poor reliability due to the rapid decay of the continuum relative to the line emission

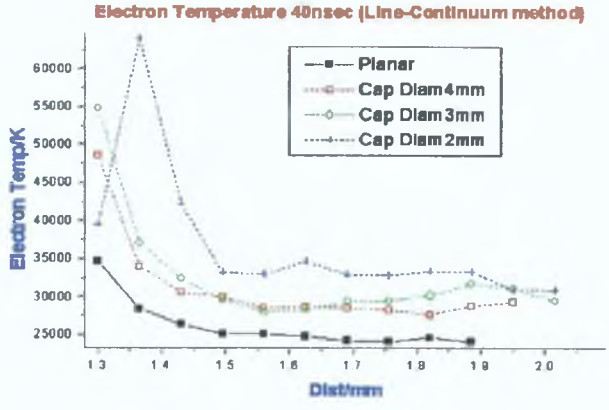

Fig 5.21.1: Temperature spatial profile at 40nsec. The clear trend is of higher peak temperatures, which are shifted forward spatially.

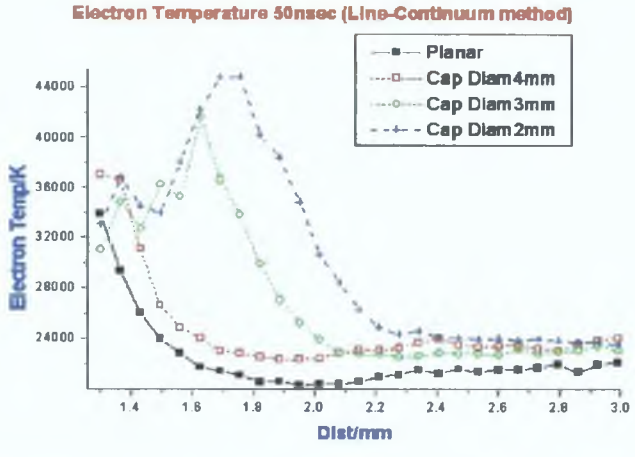

Fig 5.21.2: Temperature spatial profile at 50nsec. At 50nsec the difference in the extent of the forward expansion is pronounced

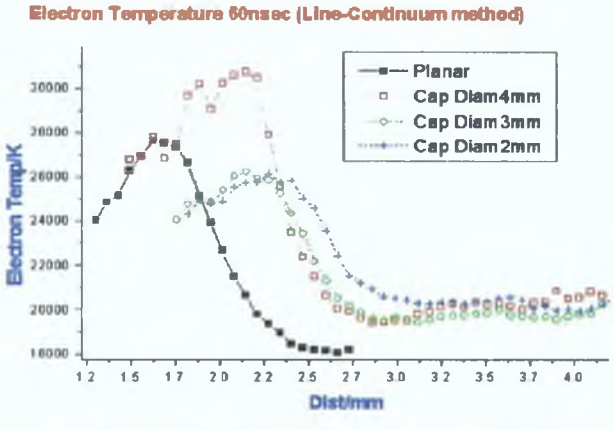

Fig 5.21.3: Temperature spatial profile at 60nsec. With the rapid expansion and forward collimation of the plasma within the capillaries, the local particle density falls rapidly, leading to the rapid decay of continuum, and the subsequent fall in line-to-continuum temperatures.

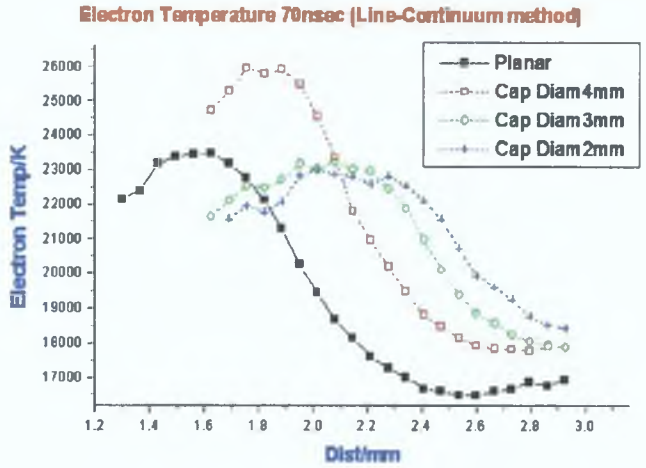

Fig 5.21.4: Temperature spatial profile at 70nsec. At this point one must interpret such measurements with caution. The continuum intensities for all targets have fallen well below the line intensities, thus undermining the responsiveness of the technique.

Given the edge velocities and CCD emission profiles, we expect a large difference in early temperatures. Indeed the four targets show a systematic and pronounced temperature difference from the earliest timescales (40nsec). For all timescales the temperature spatial profile's leading edge value increases as containment via capillary diameter decreases. The frontal regions of the plumes also show large scale extension in the capillaries, at 40nsec. The peak temperatures are grouped close together at 40nsec but spread from 50nsec onwards as thermal energy is rapidly converted to kinetic energy with resulting higher edge velocity. Later, the peak temperatures in the capillaries were seen to decrease for the 2mm, and 3mm targets. This is due to both rapid channeling/expansion of the plume forward, and resulting cooling, leading to the rapid decay in continuum which would result from such an expansion.

From ~90nsec onwards temperatures from line-to-continuum ratios cannot be trusted due to weak continuum signal. To calculate absorption coefficients, temperatures for timescales as early as 20nsec(termination of the laser pulse) are required. Thus by taking the peak temperatures for the four targets from 40-90nsec, and fitting a decay curve, it is possible to extrapolate back to earlier delays (Liu et al [3]). In [3] the authors fitted a linear decay, however while the planar target did show a linear decay, our data for the capillaries simply did not match linear decay. A second order linear decay curve was thus used. Figure 5.22.1 displays the fitted/extrapolated, temporally resolved temperatures for the four targets. Since the processes occurring during the laser pulse are extremely complex, one can not extrapolate back further than the termination of the laser pulse (16nsec).

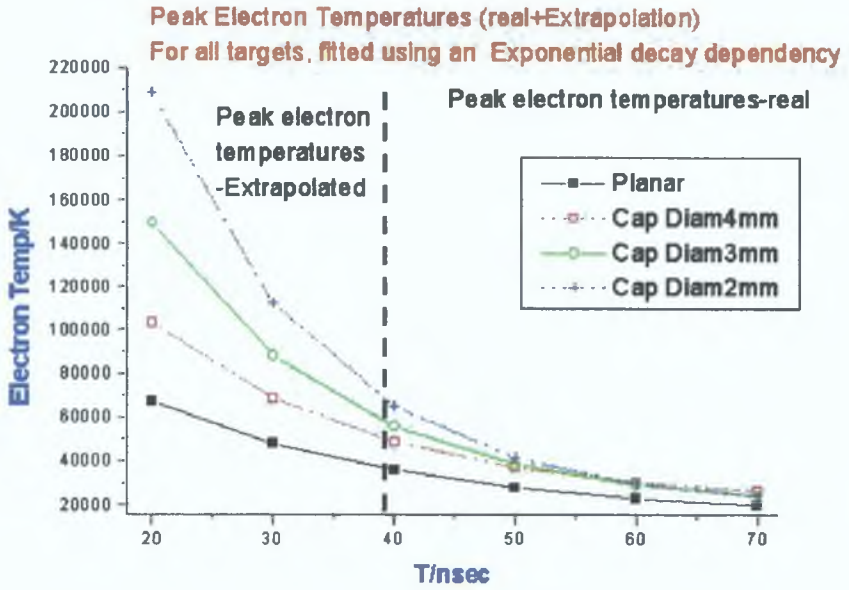

Fig 5.22.1: Temperature versus time, fitted data. The points from 40nsec onwards are real data points, while those for 20 and 30nsec are from the curves fitted to the peak temperatures at earlier timescales. These curves then extrapolated back for 20nsec and 30nsec (left of vertical dashed line). The laser pulse width is ~16nsec. These extrapolated temperatures are in good agreement with XUV Boltzmann and ionization temperatures, from real data from the arrival of the laser pulse (~0nsec), for confining targets (discussed in chapter 6).

Even assuming errors in fitting of 20%(maximum), the temperatures scales well with both time and target capillary diameter. The assumption of large scale laser beam interaction in the frontal regions of the plasma, matching a large increase in the forward extension of the continuum, and large forward expansion in the CCD emission profiles (Fig 5.21.1-5.21.4) propose large temperature increases in capillary targets relative to planar target plasma at early timescales. Figure 5.22.1 is a good indication of this.

5.3.7: Absorption coefficient calculations.

Using these early temperature estimates, and the data from the CCD image profiles to find approximate plume lengths, one can calculate estimates for the absorption length product $\alpha_p l$ (Table.2). This can then be used to calculate the irradiance absorbed during the laser pulse. Since the laser irradiance absorbed by the plasma is given by:

$$\text{Equ.8} \qquad \Phi_{absorb}=\Phi_0[1-\exp(-\alpha_p l)], \qquad \text{(Liu et al [3])}$$

then given a larger absorption coefficient xlength product, resulting in a larger Φ_{absorb}, a greater proportion of the incident beam is converted into thermal energy within the plasma (table 6). We have assumed that the ratio of enhanced electron density from one target to the next, at the same instant as the extrapolated temperatures used to determine α, are approximately the same as the ratio of the enhanced temperatures (from figure 5.22.1), and given the N_e^2 in α, this factor cannot be ignored.

Peak Temperatures/K: **20nsec**	Plume length/mm:**20nsec**	Absorption Coefficients/cm:**20nsec**	Φ_{absorb}:**20nsec**
Planar: **67KK**	Planar: **0.32mm**	Planar: **0.028**	Planar: **0.02 Φ**
4mm capillary: **103KK**	4mm capillary: **0.4mm**	4mm capillary: **0.042**	4mm capillary: **0.041Φ**
3mm capillary: **150KK**	3mm capillary: **0.42mm**	3mm capillary: **0.043**	3mm capillary: **0.042Φ**
2mm capillary: **210KK**	2mm capillary: **0.46mm**	2mm capillary: **0.046**	2mm capillary: **0.045Φ**

Table 6: Peak temperatures (from the extrapolated data (figure 5.22.1), approximated plume lengths (from ICCD image profiles (figure 5.20.1-5.20.4), absorption coefficients (equation 7 -for α calculation using extrapolated T_e and equation 8, for calculation of Φ_{absorb}), and Φ_{absorb} for all targets, after the termination of the laser pulse. Thus for the trailing edge or second half of the laser pulse, the pre-plasma formed by the first half of the laser pulse on the target surface, is absorbing more laser energy in the capillaries then in the planar target, due to greater plume expansion normal to the target surface. This occurs despite lower absorption coefficients for the capillary plasmas, due to higher electron temperatures. It is assumed that N_e scales for each target by the same ratio deduced for the extrapolated temperatures, this is necessary since we do not have early phase N_e values.

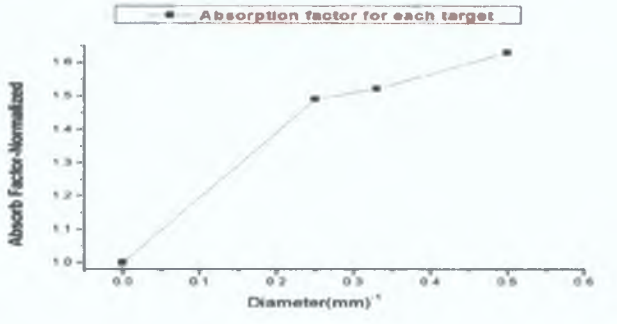

Fig 5.22.2: Normalized absorption factor Φabsorb, versus the inverse of the cavity diameter (normalized to the planar target value of 0.02Φ). Planar target is taken as having diameter equal to infinity. As the degree of containment increases the percentage of the laser beam absorbed by the pre-plasma increases. Note the grouping of the values for the capillaries relative to the planar target.

This may account for the higher peak temperatures in the confining targets from the extrapolated temperatures (20-40nsec), and the experimental temperatures from the data (>40nsec line-continuum method). Thus as the capillary diameter decreases, the pre-plasma formed by the first half of the laser pulse, is being collimated forward away from the target surface. This highly extended plume, is then absorbing the second half of the laser pulse, leading to the high temperatures seen in both the experimental line-to-continuum, and the extrapolated peak temperatures. This explanation is reinforced by figure 5.22.2, which compares the calculated absorption factor for all targets. With respect to the fall off in all temperatures as one moves to the smallest diameter capillary (fig 5.21.3-5.21.4) after 60nsec, one can observe that the experimental temperatures show the 2mm diameter capillary to have a higher temperature then the other capillaries, but that the other capillary profiles are more extended spatially, the rapid expansion leading to lower peak temperatures.

5.3.8: Plasma interaction with target surface.

Finally the question of direct interaction of the plasma with the capillary walls must be addressed. From ICCD images of planar targets in section one, the vertical diameter of the plasma at the termination of the laser pulse was shown to be not more then 0.8mm. Thus at 20nsec, the vertical separation between the

plume edge and the capillary wall (2mm diameter) is greater than 0.4mm on either side. The standoff distance , i.e. the distance from the surface where laser absorption occurs x_l , where this value is small in comparison to the spot diameter d_s is given by,

$$\text{Equ.9} \qquad X_l/\text{cm} = 1365\left[\frac{\delta_t M^{7/16} Z^{5/8}}{(Z+1)^{11/16}}\right] \times(\Phi^{3/4}\lambda^{7/4}\tau^{7/8}) \qquad \text{(Blamer et al [10])}$$

where $\delta_t = 0.071$. λ is 1064nm, M is 27, τ is 16nsec, Z=3, and Φ is 4.0×10^{11}W/cm^2.

When the x_l is calculated, it was much less then the spot diameter. Thus a one-dimensional expansion perpendicular to the target surface occurs within the plasma. Here x_l is 6.8nm. This value is much smaller then the laser spot diameter (500μm), thus $x_l/d_s << 1$; validating the assumption that the plasma expansion is 1-dimensional, occurring perpendicular to the target. The channeling effect seen in the continuum at very early timescales (0-10nsec), where the continuum shifts forward with decreasing capillary diameter, and when the laser pulse has yet to terminate, opens up the possibility that plasma radiation impinging the inner surface of the capillary could either generate a low density layer on the inner surface, or be reflected back to the plasma plume. Balmer and Weber [11], observed three body plasma generation inside a capillary, due to both reflected laser light, and/or reflected plasma radiation. The collision of multiple plasma components under such extreme conditions would enhance both particle densities and ionization rates considerably.

5.3.9: Analysis: Phase2 (t>80nsec): Plasma Density.

With the decay of the continuum one must the use atom-to-ion ratios for ionization temperature measurements. The decay however allows one to use Stark width broadening to calculate plasma densities. Theory and equations for both are discussed in [1, 9, 7] and chapter 2, section 2.1.2, while the electron impact parameter W, required for AL III (453nm) is taken from (Dimitrijevic et al [2]).

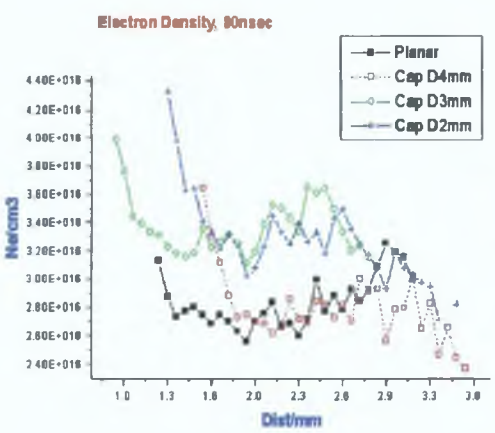

Fig 5.22.2: (80nsec)

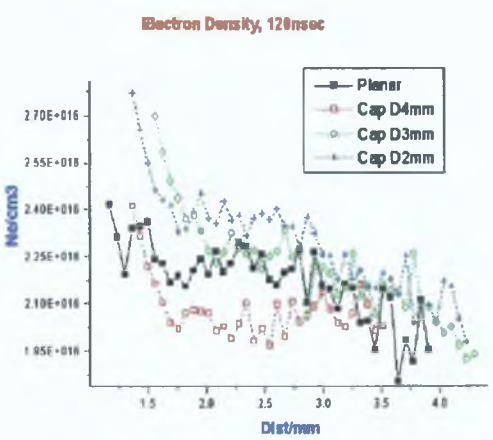

Fig 5.22.3: (120nsec)

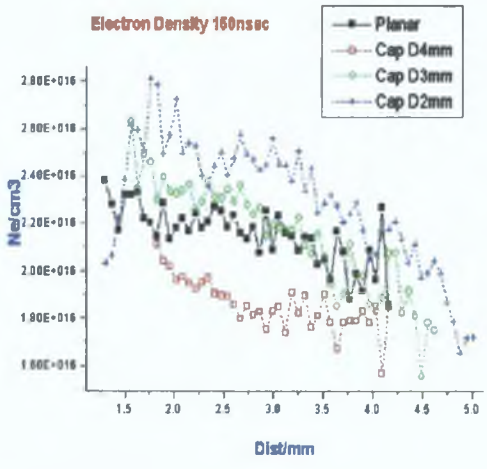

Fig 5.22.4: (160nsec)

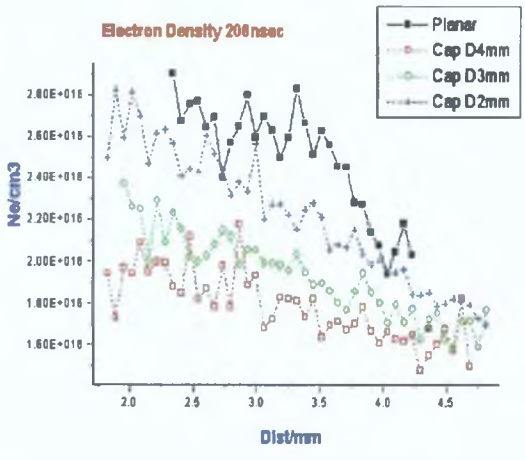

Fig 5.22.5: (200nsec)

Figure 5.22.1-5.22.4: Space and time resolved densities, taken from the line width of AL III(453nm). Note that the density shows a linear decay trend for early timescales(<100nsec), and close to the target. This is in agreement with predictions from the plume expansion model of Narayan and Singh [11]. The density of the planar target (black) can clearly be seen to 'climb' through the other three targets as the time sampled increases. The laser comes from the right, and the plasma expands from the targets surface (left).

Considering the earlier statements about absorption in the forward plume region, the higher peak particle density from 80nsec onwards can be attributed to the confining effect of the capillary. The rapid expansion of the plume in the planar target occurs in all three dimensions. In a capillary after the plume has made contact with the inner walls of the vessel, its expansion is along the capillary axis, thus it is approximately 1Dimensional. Although some plasma will exit through the aperture, this should be a small effect. The first two graphs (80, 120nsec) show that the capillary plasmas lead the planar target spatially, with their density shifted forward.

In section one (wedge targets) it was noted that at early timescales, the confining targets displayed higher densities over their complete spatial range. However as the delay increased, the density profiles of the targets converged spatially, and further out from the target surface, reversed their relative trend to each other. At later timescales, the trend was the inverse of its earlier behaviour. We associated this with very rapid directed expansion of the plume in the confining targets, lowering the local particle density. For the three AL III, and single AL II lines, whose widths were measured in this way, each ion stage showed the before mentioned convergence and inversion at different delays and over different spatial regions. However the trend here with capillaries is that as the delay progresses, the planar target is seen to 'climb up' through the density profiles of the confining targets, eventually peaking above the others at approximately 200nsec. We attribute this to enhanced velocity of the plume as a consequence of the 2D containment offered by the capillary. The significant difference between 1D containment (wedge) and 2D containment, is that in wedge targets the large differences in density between the targets were highly localized spatially. While here the trends occur over the complete spatial distribution of the plume. This behaviour is not unique to AL III (453nm) as figures

5.22.2-5.22.5 show. The AL III line at 447nm, also shows the planar target's continuous increase in density as time proceeds.

5.3.10: Analysis: Phase2 (t>80nsec): Spatial profiles.

In the previous section, we noted the extended nature of the continuum as a consequence of the capillary containment. The initial higher peak velocities, and highly directed expansion of the plume, is maintained also for the ions. Figure 5.8.1-5.8.4 display the spatial profile for each target, at selected time delays.

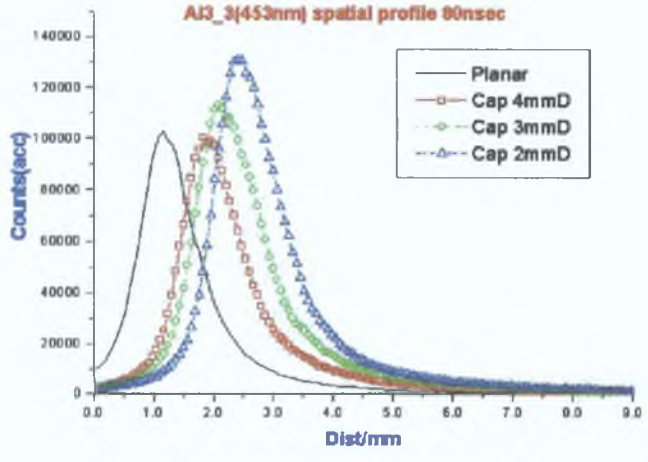

Fig 5.23.1: (80nsec) ALIII (453nm) spatial profile. The peak intensity increases as the capillary diameter decreases, while the position of the peak shifts forward.

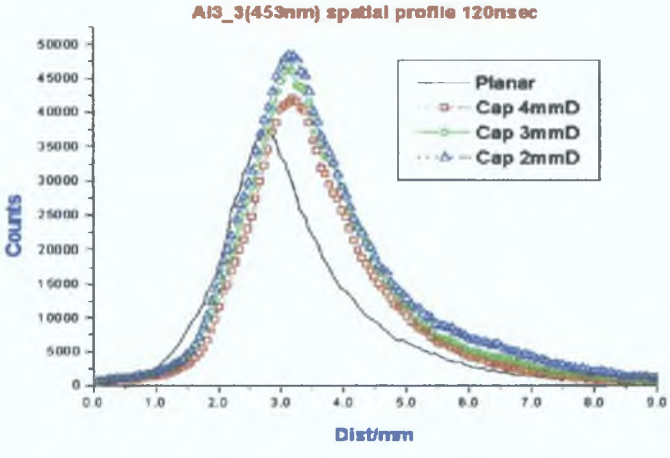

Fig 5.23.2: (120nsec) ALIII (453nm) spatial profile. The peaks now coincide in their spatial location, indicating that the higher peak edge velocities seen in capillary target at early timescales (<60nsec) are no longer present. This reinforces figure 5.19, which shows that 80-100nsec, all edge velocities converge in value.

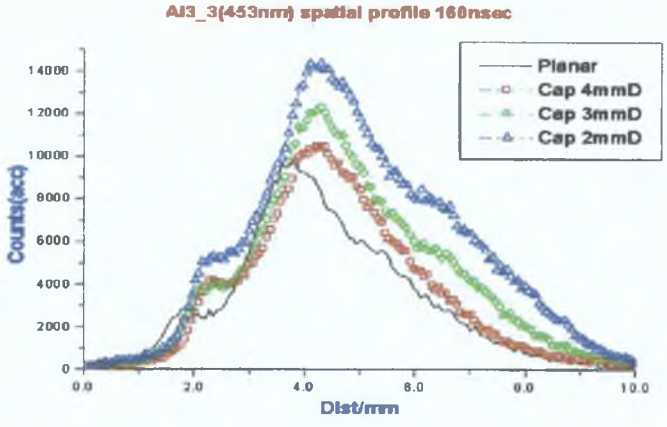

Fig.5.23.3: (160nsec) ALIII (453nm) spatial profile. The peak intensities scales with greater confinement as the capillaries prevent rapid expansion in the vertical plane, which would allow the plasma to cool rapidly. A double structure in the intensity profile begins to emerge.

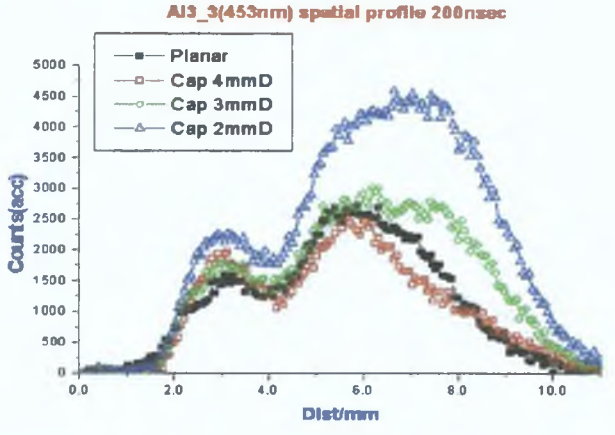

Fig 5.23.4: (200nsec) ALIII (453nm) spatial profile. Timescales after 160nsec show rapid convergence of all physical parameters. However the double peak is now clearly visible.

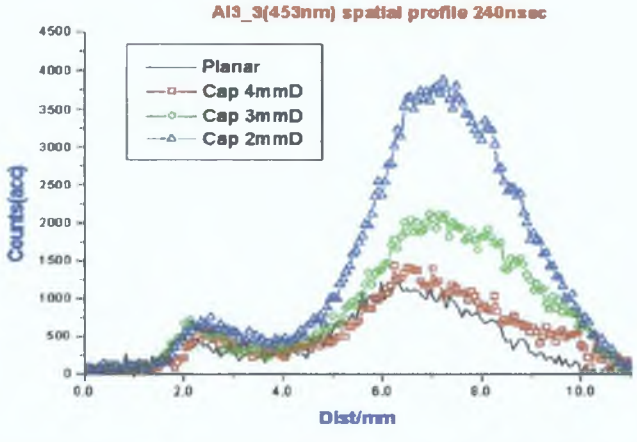

Fig 5.23.5: (240nsec) ALIII (453nm) spatial profile. Although all the plasma from all targets continues to decay, containment offered by the capillaries slows the rate of decay , with the peak intensity of the leading peak scaling with greater confinement.

The higher peak count and greater forward extension at 80nsec is clearly evident. As time proceeds unusual structure emerges in the spatial profiles of the confining targets. Although this is also the case for the planar target, it is greatly enhanced for the capillaries. Such 'plume splitting' has been observed by many authors (Hopp et al [9]), in air, 180mTorr with visible imaging, (Amoruso et al [14]) splitting in air, 150mTorr fast imaging in the visible, [4] in vacuum, utilizing a double laser pulse and electrostatic analyzer for TOF measurements (Anisimov et al [16]). The source of the multi-component behaviour is generally attributed to charge distribution within the plume, with the leading edge composed of energetic ions and electrons in layers, while the main body of the plume is mostly thermalized particles under going hydrodynamic expansion in a denser region subject to strong recombination, hence the brightness of this region's emission profile. As the delay increases the difference in kinetic energy leads to an increasing separation between the two plume components. All four lines show the same behaviour to different degrees. The extent of the plume splitting here is more pronounced than that reported in section one (wedges). A reasonable assumption is that the greater containment and higher temperatures lead to a higher initial expansion velocity and higher collision rate. Geohegan et al [15] proposed that hot/transient electrons, escaping from the main plume at early stages, and not undergoing large scale energy changing collision, and sets up a space charge layer which accelerates a fraction of the ions, creating a two component ion distribution. To reinforce the charge separation/layering idea, one can observe the bulk visible emission from the plasma imaged onto the CCD array, and extract the intensity profile.

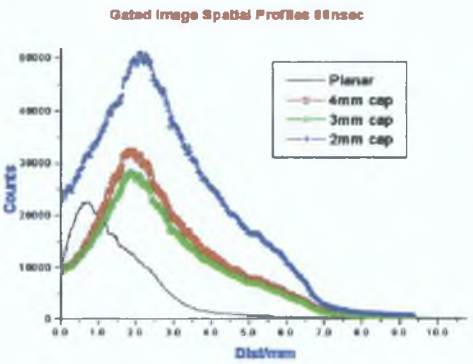

Fig 5.24.1: ICCD image intensity profile(80nsec).

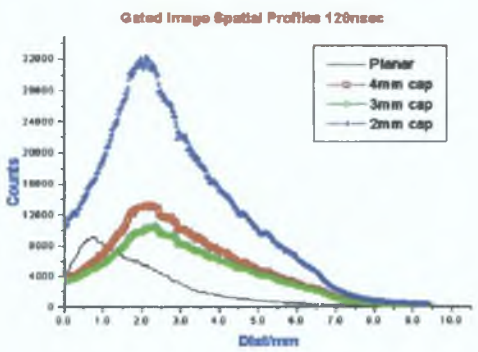

Fig 5.24.2: ICCD image intensity profile (120nsec).

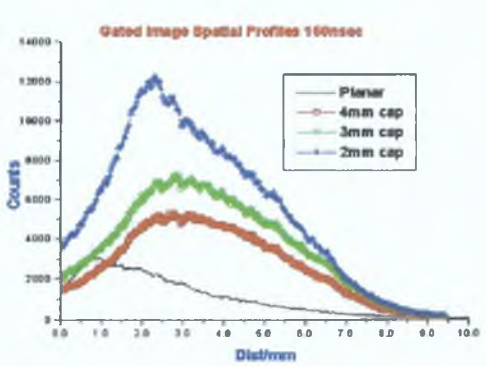

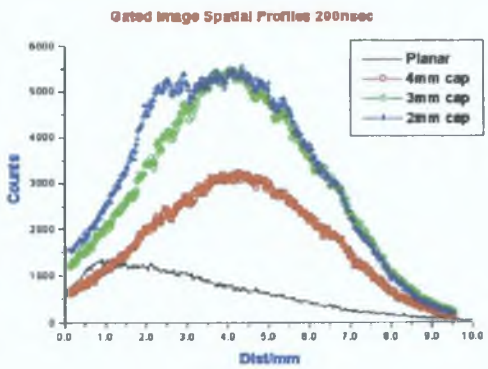

Fig 5.24.3: ICCD image intensity profile (160nsec).

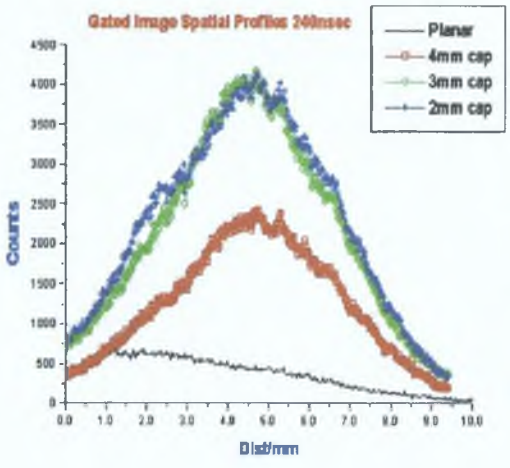

Fig 5.24.4: ICCD image intensity profile (200nsec).

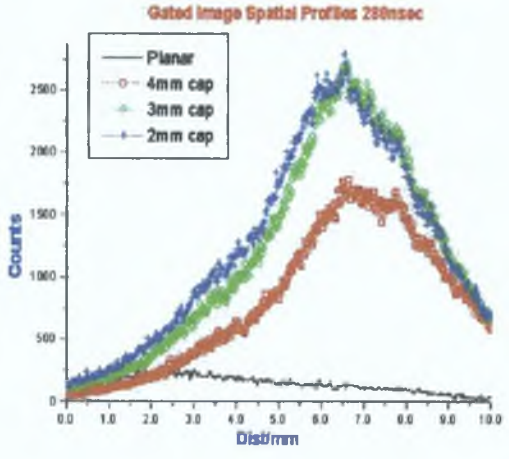

Fig 5.24.5: ICCD image intensity profile (240nsec).

Fig 5.25.6: ICCD image intensity profile (280nsec).

By comparing the spatial profile of the ion stages via the spectrometer against the total light profile one can match the bulk length of the plume, its main emission regions, against the peak emission regions for the ion stages studied. In comparing the emission profile at 80nsec from figures 5.23.1, and 5.24.1, the clearest similarity is the fact that in both graphs, the peak for the three capillary targets are shifted forward relative to the planar target. The peak values also scale in a similar manner. The physical edge of the profiles for the AL III lines is not as extended as the bulk emission profile, while at the trailing edge of the plume there is a clear cutoff, back beyond which there are no AL III lines. The AL III emission stops at 6.5mm, while the bulk emission reaches 8mm from the target surface. Remarkably the AL III profiles at 120nsec all have their peak at the same spatial point, with the planar peak value still lagging behind, this same profile is seen in the bulk emission at 120nsec. At later timescales, the ion profiles exhibit spatial splitting, the bulk emission profiles do not exhibit this but do show a large region of almost constant intensity for the 2mm capillary target at 200nsec. It displays a 'kink' at 240nsec along its trailing edge, while for 280nsec all capillary targets have a linear, downward sloping 'hat' region instead of the smooth Gaussian profile. Finally the most notable feature is the difference in peak bulk emission of the confining targets at later stages, the planar emission has virtually ceased, yet the main body of the plasma in the confining targets continues to move along the capillary axis.

5.3.11: Analysis: Phase2(t>80nsec):Ionization temperatures, emission spectra.

As stated previously, actual values for temperatures beyond 80-90nsec require a method other than the line-to-continuum method. Utilizing the ion-to-atom ratios for AL III(453nm) and AL II (466nm) allows for the spatial profile of ionization temperatures to be calculated at selected time delays. The theory and equations were taken from [2, 17] and chapter 2, section 2.1.4. One limitation found with this approach is the relative position of the two ions used. The higher ion stage, with a higher velocity will cover a specific spatial

region, which the lower stage will not. Thus at early timescales, or when one is dealing with a highly energetic plasma (such

as contained/channeled plume) the ratio becomes unstable due to weak signal from the lower stage (this occurs predominantly at the leading edge, and at early timescales). At later timescales the higher ion stage has left the target surface, thus the trailing edge of its signal is weak. This is evident in figure 5.25.1, where the difference in the spatial extension of the two ion stages leads to increasingly noisy profiles of ionization temperature at the leading edge due to weak AL II signal. Comparing this with figure 5.21.4, the last temperature graph using the line-to-continuum method, the temperatures in the latter run from 23000k upwards, while from figure 5.25.1, they run from 22500K upwards.

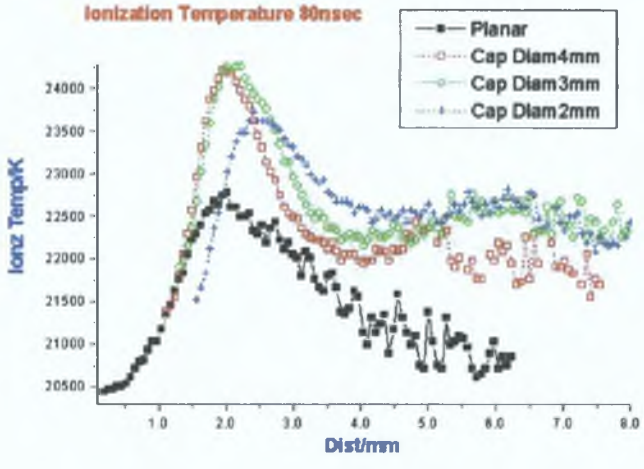

Fig 5.25.1: (80nsec). Ionization temperature for 80nsec for all targets. Recalling figure 5.24.1, which displayed line-to-continuum temperatures for 70nsec. The peak temperature there was decreasing for each capillary, and the planar target had overtaken the capillary targets. However as stated at that stage in the plasma history the low level of continuum undermined the validity of the measurements. Here using atom-to-ion ratios, with good signal strength for both ions used, a more accurate trend is seen. The peak ionization temperature scales upwards as the capillary diameter decreases. The leading edge of the plasma within the capillaries also displays much higher temperatures, extended over a larger spatial range, out from the target surface compared to the planar target.

This is a good indication of the viability of using more then one diagnostic tool to completely map a plasma behaviour. Compared to the very high temperatures, both measured and extrapolated and the rapid rate of temperature decay seen at earlier timescales, the temperatures in figure 5.25.1-5.25.4(next page) show much greater degrees of thermalized equilibrium throughout the plumes.

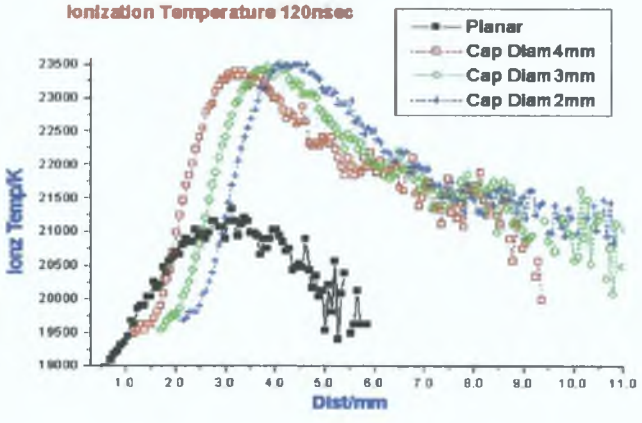

Fig 5.25.2: (120nsec). Ionization temperatures for all targets at 120nsec. Interestingly the three capillary targets do not show large differences in peak temperature, but their peak temperatures scales forward as the capillary diameter decreases.

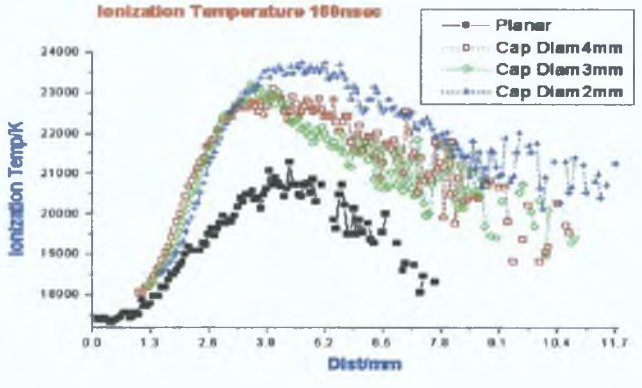

Fig 5.25.3: (160nsec).Ionization temperatures for all targets at 160nsec.

The rate of fall per time resolved graph is very moderate, while from 80nsec onwards the clear trend in the capillary targets is a convergence in temperatures, both in numerical value and spatial profile.

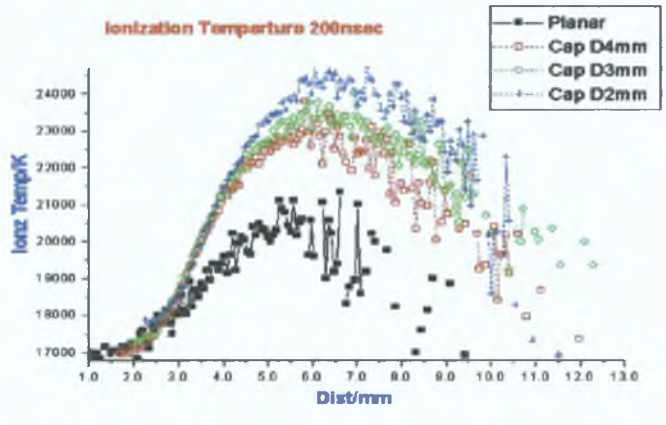

Fig 5.25.3: (200nsec). Ionization temperatures for all targets at 200nsec. One can see, due to weak signal level of one ion stage relative to the other, the intensity ratio becomes increasingly unstable at the leading edge of the plume.

Despite this all capillary targets maintain superior temperature profiles even towards the end of the useful emission lifetime of the lines used (approx 300-350nsec max for the AL III lines, and 350-440nsec for the AL II line). Since the temperatures are calculated from ion ratios, it is useful to look at the emission spectra at selected times, at specific regions spatially. The spatial points chosen correspond to figures 5.23.1-5.23.2 (the AL III spatial profiles), at critical points of interest, i.e. trailing, leading edges, peaks.

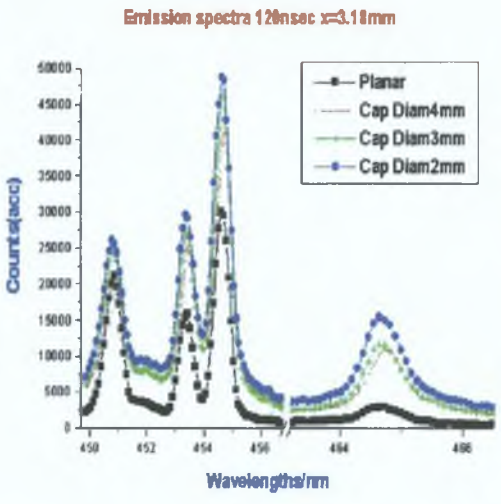

Fig 5.26.1: Emission spectrum (120nsec, x=3.18mm).

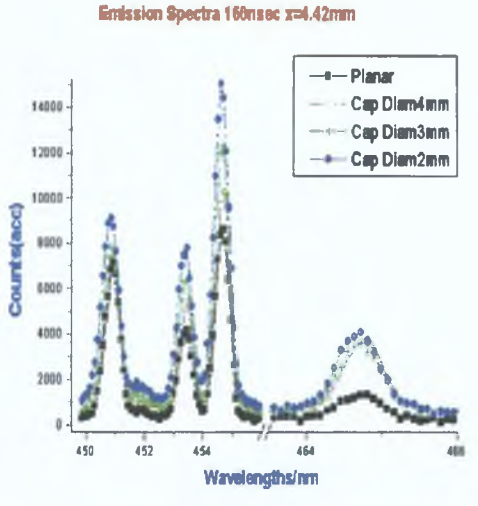

Fig 5.26.2: Emission spectrum (160nsec, x=4.4mm).

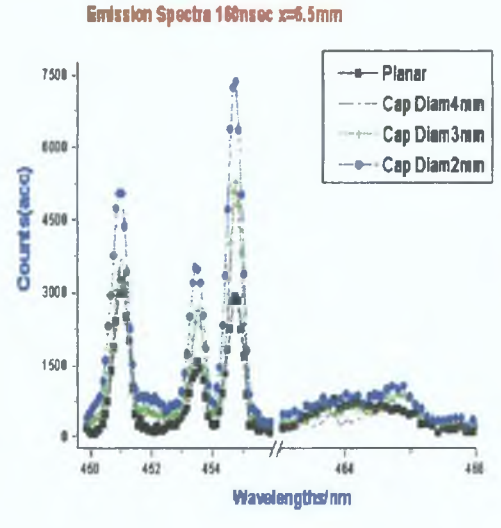

Fig 5.26.3: Emission spectrum (160nsec, x=6.5mm).

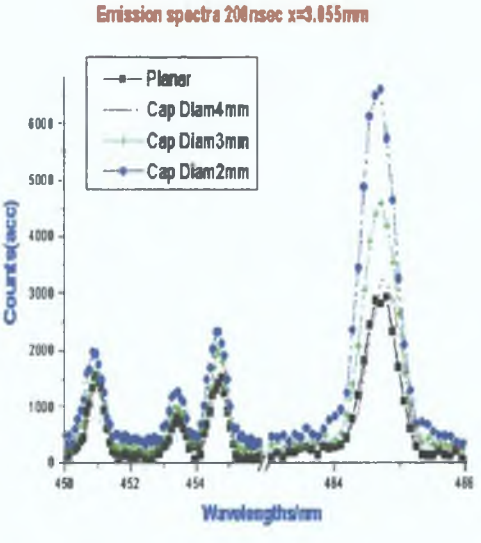

Fig 5.26.4: Emission spectrum (200nsec, x=3.0mm).

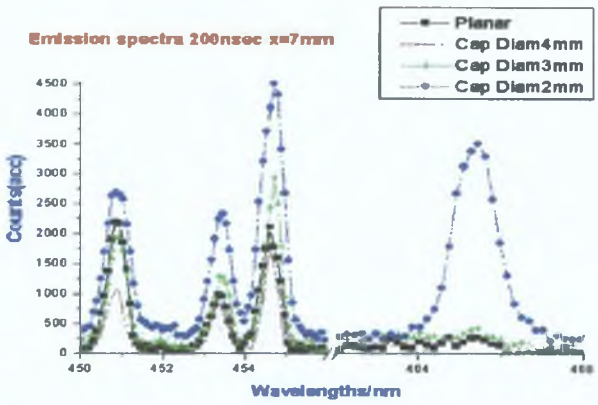

Fig 5.26.5: Emission spectrum (200nsec, x=7mm).

Importantly, in the statement that plume splitting is indeed due to multi-component expansion with separate velocities, and that the leading edge of the second component is mostly highly charged ions, then sampling the spectra at these points should show clearly a higher distribution of higher charge states. In figures 5.23.2, 5.23.3. splitting has yet to occur. The peak emission is centered at 4-5mm from the target, while a leading edge break is seen at approximately 6.5mm. This could represent the first indication of charge separation in the plume. Looking at the spectra at these points (Fig 5.26.2, 5.26.3), the emission in figure 26.2, at the center (4.42mm) shows good AL II emission at 466nm. However at the leading edge (fig 5.26.3, x=6.5mm), Al II emission is almost completely absent, the spectrum is dominated by the AL III stage. This is unusual, since the plasma is thermally energetic enough to sustain such a stage, then the lower stage should also exist in sufficient densities to emit. However if indeed layer charged separation is responsible then this would not be the case. Finally we observe the emission spectrum at a time delay when full plume splitting has occurred, and at the peak of the two components (Fig 5.26.4, 5.26.5), the emission spectrum at the center of the rear peak exhibits a larger peak count for the AL II stage over the AL III stages. Further ahead at the center of the forward component, the ion stage ratio is in favor of AL III over the latter. Interestingly only the 2mm diameter capillary shows good AL II emission at the forward peak (x=7mm), but still maintains its superior AL III peak emission over the lower stage, and over the other targets. It is possible that multiple charge layers could form, the primary electron layer which accelerates the AL 2+ lines is strong enough to pull AL+ ions simultaneously, but also that the subsequent layering of AL 2+ ions, would itself inductively create a second space charge layer in its wake, which could accelerate the lower stage ions via electrostatic repulsion. The relative mass difference between AL 2+ and AL + is negligible, and electrostatic acceleration depends on charge, in this case both the total charge density of the electron layer in front, but also the relative local ion charge. The capillary targets apparently optimize both conditions, as evident by the higher ion stage count, greater extent of plume splitting, and greater forward extension of the plume body.

5.3 12 Conclusion

In summary as the confining effect is increased a number of effects are observed Firstly higher peak temperatures at the termination of the laser pulse, based on higher peak temperatures from line-to-continuum ratios from 40nsec onwards This is attributed to confinement of the hot dense plume, which is unable to decay via rapid expansion, and in which radiative decay is constrained by the capillaries internal volume The confining effect of the capillaries leads to greater forward extension of the plume, which occurs over all timescales due to both the collimating effect of the capillary and also higher temperatures leading to enhanced expansion rates, and spatial structure in the distribution of light of visible light From a simplified analysis based on extrapolated temperatures from the line to continuum technique, greater laser absorption was proposed, which is plume length dependent, was demonstrated within the capillary targets, the percentage of laser absorption scaled with decreasing capillary diameter, due to greater scale length, which arose from forward collimation of the pre-plasma in the capillaries The extent of the laser absorption scales with decreasing capillary diameter and stems from a low density, weakly emitting fast plume which moves away from the target surface at early timescales This fast component is then highly collimated by the capillaries

Higher peak velocities at early timescales were observed and attributed to channeling and enhanced temperatures from confinement coupled with higher peak densities and line widths, close to the target surface and early during the plume's lifetime Rapid drops in densities are attributed to higher plasma expansion velocity over its complete spatial range An effect which emerged at later time scales was of greater 'plume splitting' effects due to charge layering in the plume, causing charge separation spatially into two components in the capillaries The most pronounced difference between plasma contained two dimensionally in capillaries and that with rectangular cavity's relates to the profiles of line width and density The general trend of higher electron density within the rectangular cavity's is maintained only so long as the fast expansion velocity doesn't undermine plasma density Thus the reversal of this trend occurs over a spatial region for different time delays At certain time delays, the density spatial profile within the rectangular cavity's, displays three distinct trends in relation to the four targets However in the capillaries, enhanced density profiles occur over the complete spatial limit of the plume We associate this with the inability of the plume to expand horizontally, as it can in the rectangular cavity's

5 4 Time and space resolved visible studies of laser plasma generation and dynamics in longitudinal cavity's 1-Dimensional longitudinal confinement

In continuing our study of the influence of target configurations on laser plasma generation and plume evolution, we extended our study from 1D horizontal (transverse) confinement (wedges), 2D radial confinement (capillaries), to 1D vertical (longitudinal) confinement The most important effect of this work, was the plasma expansion vector most affected Plasma generation within capillaries or rectangular wedges affects plasma expansion parallel to the target surface However expansion normal to the targets surface is not affected directly In 1-Dimensional longitudinal confinement, two parallel plates are orientated perpendicular to the laser beam path Here the plasma is free to expand parallel to the target surface, but expansion normal to the targets surface is affected by the presence of the front plate To complement electron densities calculated from stark broadening, density sensitive line ratio values for N_e are introduced and compared with N_e values from stark broadening

5 5 1 Experimental Setup

1-Dimensional longitudinal confinement was achieved by generating a laser plasma between two parallel plates, of varying plate separation (similar to that employed in chapter 4 section 4) The laser was delivered to the target via a hole of fixed diameter 1 5mm through the front plate and impinged on the inner surface of the back plate Subsequent plasma generation and rapid expansion allowed the plume to fill the cavity and expand out through the entry aperture, forming a high temperature, high velocity jet Both the plasma within the cavity and the emerging jets properties were studied via space and time resolved visible emission spectroscopy Temperature measurements were taken from the two separate techniques used above for capillary studies The use of line to continuum ratios, whose defining limitation is the requirement of reasonable parity between the continuum intensity and line emission signal created a spatial limit that could be studied The required criteria are only fulfilled over a limited spatial range, usually close to the target surface (<3mm), which infers a limit on the largest time delay after the laser (for power densities on the order of $\sim 10^{11} W/cm^2$, this is approximately 80nsec) In the experiments performed here, this meant that reliable temperature measurement from such a method was limited to regions inside the cavity Ionization temperature measurements using the ratio of two successive ion stages are viable both inside and outside the cavity, although the earliest possible measurements were limited to timescales greater than 70-80nsec The differences in the limit of the above two approaches highlight the two regimes seen in this work First, the generation and rapid expansion of the high temperature, high density plasma, away from the flat target surface Only when the plate separation approaches 2mm approximately does one see substantial differences in the plume emission properties at early timescales In this region (inside the cavity) line widths are seen to increase substantially as the plate separation decreases

5.5.2: Density sensitive line ratio calibration.

Following the approach taken by Tijerina et al [21], density sensitive line ratios were utilized as a means to calculate the electron density using a technique other than Stark broadening. Tijerina published results on this technique, but not for temperatures greater than 20000K for aluminum. Communications with Tijerina's research group, who have the CHIANTI code, and ran the code in order to acquire constants required for the technique, which were not in Tijerina's reported work allowed this technique to be used.

A	B	C	D	T_e
3.9979	1.94918	15.11459	0.55464	10000K
2.92250	0.86603	15.22076	0.55576	15000K
2.56527	0.05049	15.27091	0.55669	20000K
2.0926	0.02351	15.3609	-0.5587	30000K

Table 6.2: Constants required to fit the sigmoid curve (chapter 2, section 2.1.7) to translate the real line ratio to a density value using equation 16 in section 2.1.7. The constants are temperature dependent.

The reliability of this technique has been compared to density calculations in aluminum from Stark broadening by Lenk et al [22], and Kundston et al [23] using laser ablation of aluminum targets and studying several AL II lines to determine the electron density.

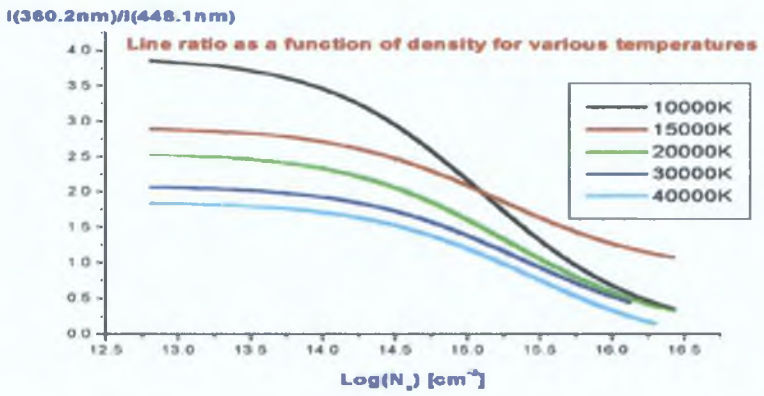

Figure 5.26.6: Calibration curves for density sensitive line ratios using AL III at 360.2nm and 448.1nm. The curves are generated by using the outputted constants from the CHIANTI code developed by the U.S Naval observatory.

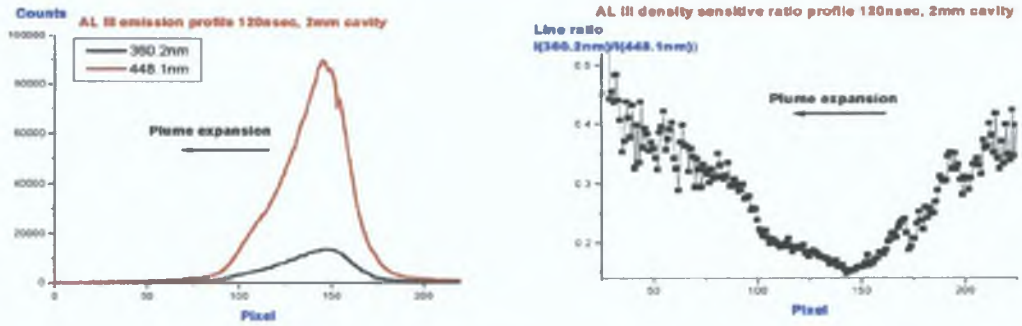

Figure 5.26.7a,b: (left) intensity profile of the two AL III lines used in density sensitive line ratios. (right) ratio of the two lines used. Near the target surface and at the leading edge of the plume, where the line emission is either weak or unstable, the ratio is noisy.

The main advantage of this technique over Stark broadened values, is that the fitting procedure can be automated by software routines, allowing a very large number of points to be resolved. It also does not require knowledge of the instrumental profile, which was not known. The main limitation is the availability of the fitting constants at only certain temperatures. The temperatures used to acquire the fitting constants were taken from ionization temperatures deduced from ion-atom ratios. The latter required that the electron density be known. This parameter was taken from the Stark broadened values. In this manner electron densities calculated from line ratios are directly affected by the electron density values acquired from Stark broadening. Thus one technique is not fully independent of the other. A second concern is that the constants required were available for temperatures of 10, 15, 20, 30000K, and from figure 5.26.6, which uses the constants displayed in table 6.2, the calibration curve is temperature dependent. From ionization temperatures in previous sections, it was clear that temperature differences over a 100nsec timescale did not always drop by a full 10000K. Thus densities from line ratios can be unresponsive in time, due to the absence of a calibration curve at the plasma's exact temperature for any time resolved measurement.

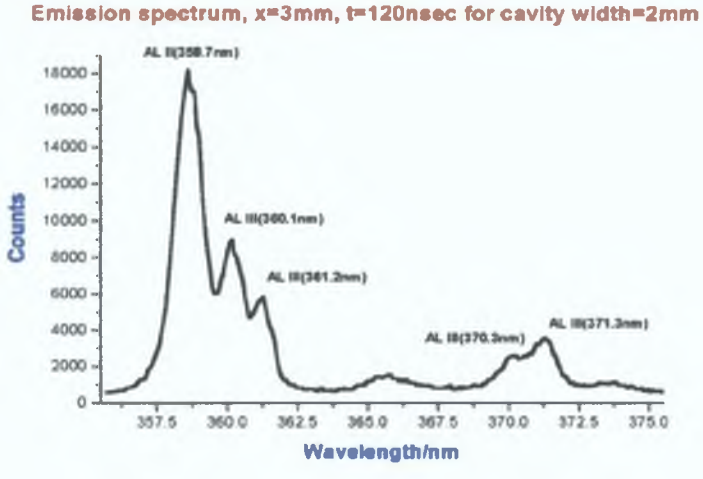

Figure 5.26.7c: Typical emission spectrum for the lines used for density sensitive line ratio. The two AL III lines at 370.2nm and 371.3nm are shorter lived both spatially and temporally then the two on the left hand side of the spectrum.

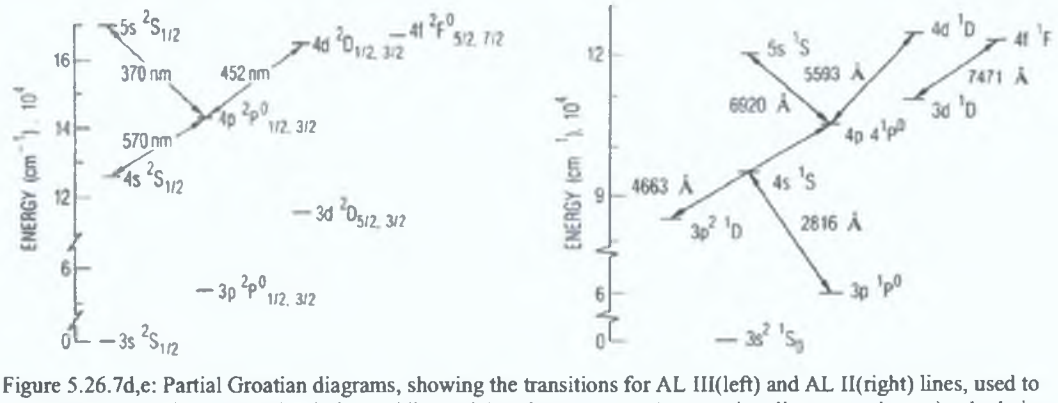

Figure 5.26.7d,e: Partial Groatian diagrams, showing the transitions for AL III(left) and AL II(right) lines, used to calculate electron density (stark widths, and line ratio) and temperature (atom to ion, line to continuum) calculations (Knudtson et al[23]).

5.5.3: Line-to-Continuum temperatures.

Temperatures do not show large increases. Although enhancement is present, it is not as large as the change in density, or as obvious a temperature increase as seen in other target configurations.

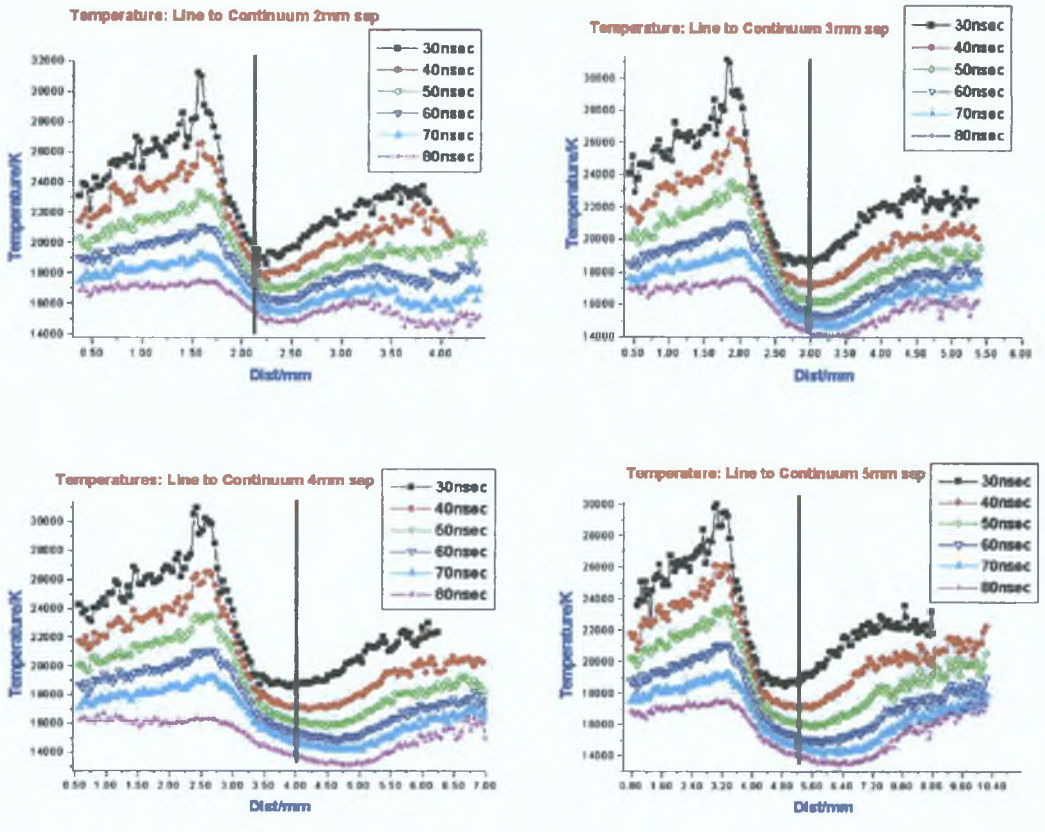

Fig 5.27.1-5.27.4: Line to continuum temperatures for the four plate separations. The peak temperatures for all targets occurs away from the targets surface, with a sharp peak just before or at the inner surface of the front plate. The temperature profile from the target surface to the main peak is linear, compared to temperatures from planar and capillary targets, which were curved, both for the rising edge of the peak and the peak itself. There is a small incremental rise in the peak temperature of the jet outside the cavity (to the right of each graph) as the separation between the plates decreases. The vertical line in each plot is the approximate position of the front plate.

The cause of this is rapid cooling of the energetic plume into the front plate, and the fact that the plasma is free to expand parallel to the target surface. In all values of plate separation, the temperature decay profile is almost identical. The main exception is the numerical difference in temperature and the spatial position of the peak. The differences can be clearly seen in figures 5.27.1-5.27.4. The peak temperature scales upwards as the cavity width is decreased, however the increase is not large, but the position of this peak shifts forward spatially. This indicates that either the plasma is in direct contact with the front plate and is experiencing a retarding pressure, or some form of rebounding plasma particles are impinging on the plasma front. A common feature at later timescales is the nearly flat plateau in temperature in the cavity for all plate separations. The temperature profiles become increasingly noisy as the ratio of continuum to line varies with weakening continuum signal. In reality only the temperatures emerging from the cavity (right of

the black vertical line)from the 2mm plate separation can be trusted. This is due to the low level of continuum relative to the line used for all targets except the 2mm cavity. It displays a second peak moving away from the aperture. The timing and position of this peak correspond well with similar temperatures in the ionization temperature profiles (fig 5.29.1). In such a system there are essentially two plasmas. The initial hot, dense plasma moving away from the target surface, and the emerging jet from the front aperture. In the case of the 2mm and to a lesser extent 3mm cavity's, the expansion velocities of laser plasma (>10^4cm/sec) ensure that the plume which collides with the front plate does so at high density. In such a plume, highly ionized particles will collide with the front plate, dissipating their kinetic energy and could assist in the formation of a low density second plume on the inner surface of the front plate. Images of the early phases of plasma generation and expansion in the cavity's (figure 5.27.5, below) clearly demonstrate the different physical length of the plasma normal to the target surface, dictated by the plate separation.

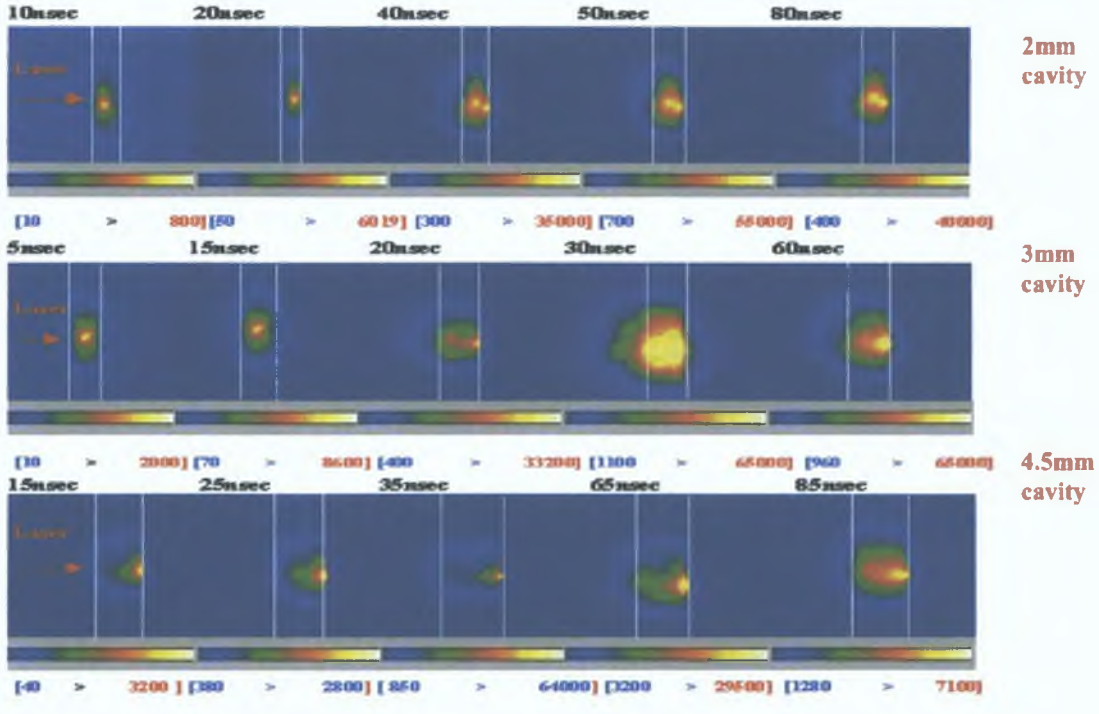

Figure 5.27.5: Time resolved ICCD images of each plate during and just after the termination of the laser pulse. The images are zoomed in images of the raw ICCD data, and focused on the cavity volume only. As the cavity width increases plume extension, normal to the target surface increases.

The extent of this effect would obviously decrease as the plate separation increases and the plume has a larger distance to transit and longer allowed decay time before reaching the front plate. The resulting 'funneling' of such an energetic plume through a narrow diameter aperture will increase the local density in the region of the aperture (fig.5.28.1-5.28.4. next page).

5.5.4: Electron density and plume front plate interaction.

Another important aspect of the plume's interaction with the front plate is the effects on the plumes density (determined via Stark widths of the 453nm line), as particles 'pile' up against the front plate, which is essentially a substrate. This effect can be clearly seen in figures 5.28.1-5.28.4. Secondary peaks in the electron density profile are visible in all plate separations. The slope of this secondary peak is most pronounced in the 2mm cavity.

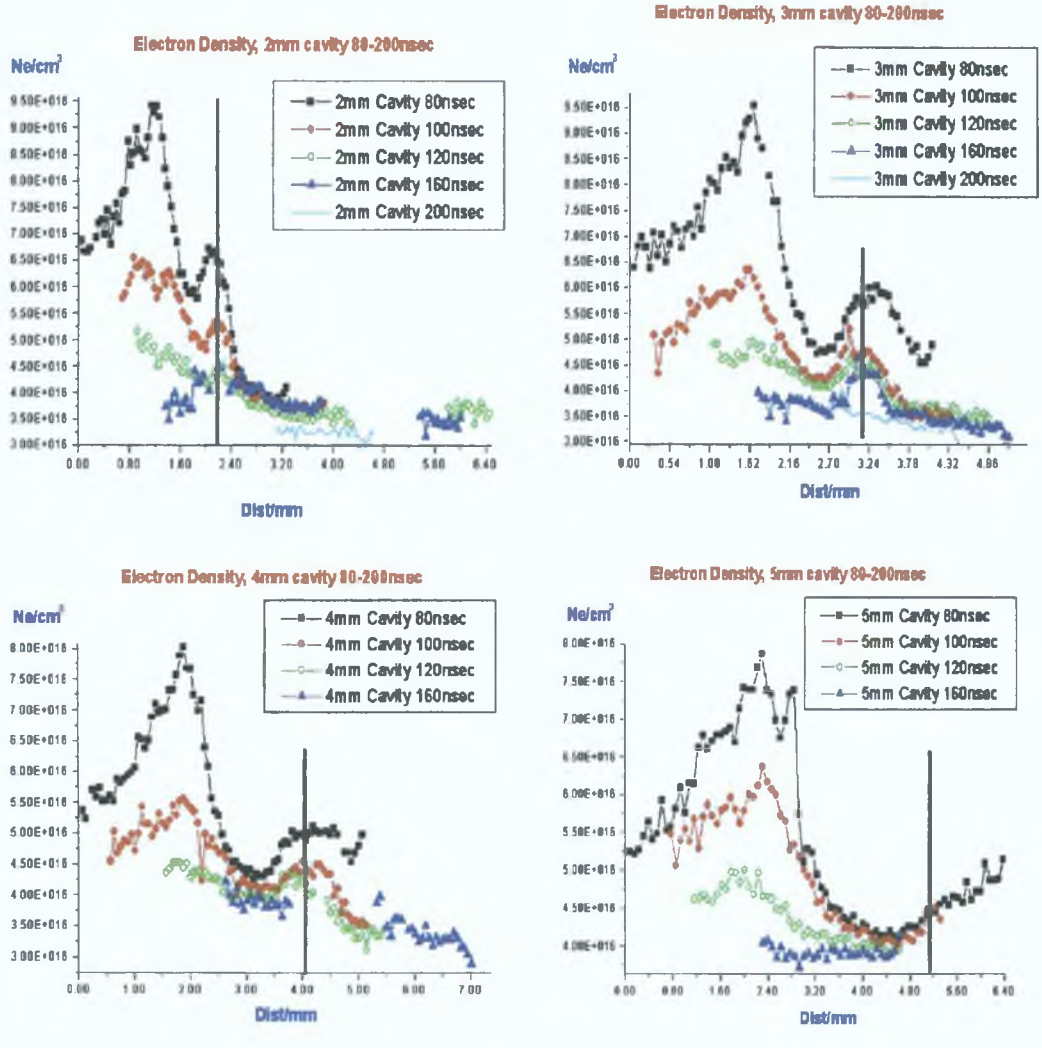

Fig 5.28.1-5.28.4: Time and space resolved density for 80-200nsec range, using Stark broadening of the AL III-453nm line. Peak densities at early times scale upwards as the plate separation decreases. Secondary peaks can be clearly seen at the front plate aperture. The secondary peaks are due to localized 'funneling' of the plume through the aperture. The vertical line in each plot represents the center of the front plate.

The corresponding increase in the collision rate leads to higher temperatures in the front plate's internal cavity (the front plates were 1.8mm in thickness). There are some pronounced differences in the profile of N_e for the line ratio calculations (figures5.28.5-5.28.8). Although the range of values of N_e for both techniques are not dissimilar (1×10^{16} cm^{-3} to 1×10^{17} cm^{-3}), the temporal and spatial profile show marked

differences. The line ratio plots all exhibit lower electron densities for all targets and all time delays than those from Stark broadening (comparing fig 5.28.1-5 with those below).

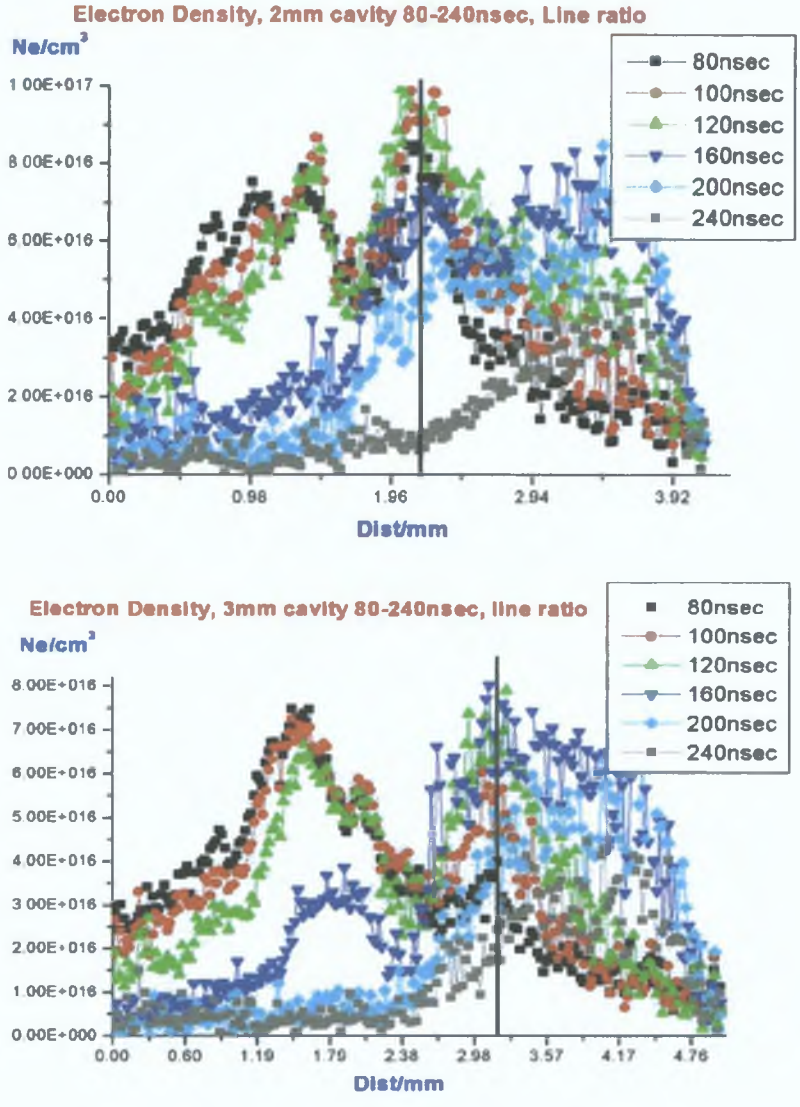

Fig 5.28.5-5.28.6: Time and space resolved density for 80-240nsec range, using the line ratio technique, 2mm and 3mm plate separation. Peak densities at early times scale upwards as the plate separation decreases, mirroring the trend seen in figure 5.28.1-5.28.4 with Stark broadening. Secondary peaks can be clearly seen at the front plate aperture. Two advantages of using line ratios for density calculations over Stark broadening, are the ability to measure densities at earlier and later timescales than would be feasible with Stark broadening, albeit at later timescales the peak signal of the lines becomes less stable, and thus the profile of the density is noisier. A second advantage is the ease of calculation, which can be automated, allowing a much larger number of points to be calculated for the same data batch. The vertical line in each plot represents the center of the front plate.

The difference does exceed ~15%, and thus given the means by which densities are calculated for line ratios, the difference is within the errors of the latter technique, which depends heavily upon the temperature value used to deduce the required parameters for N_e calculation from line ratios. A second difference is the lack of response in time of the line ratio values. All Stark broadened values for N_e display

large drops in the value of N_e with time for all targets. However this is not present in the profiles of Ne for the line ratio plots, which display a small and in some cases an incremental increase is observed. The most probable case of this is the dependency upon temperature of the line ratio technique. Tijerina [21] calculated the constants for the aluminum lines used here for various temperatures, in steps of 10000K from 10000K to 40000K.

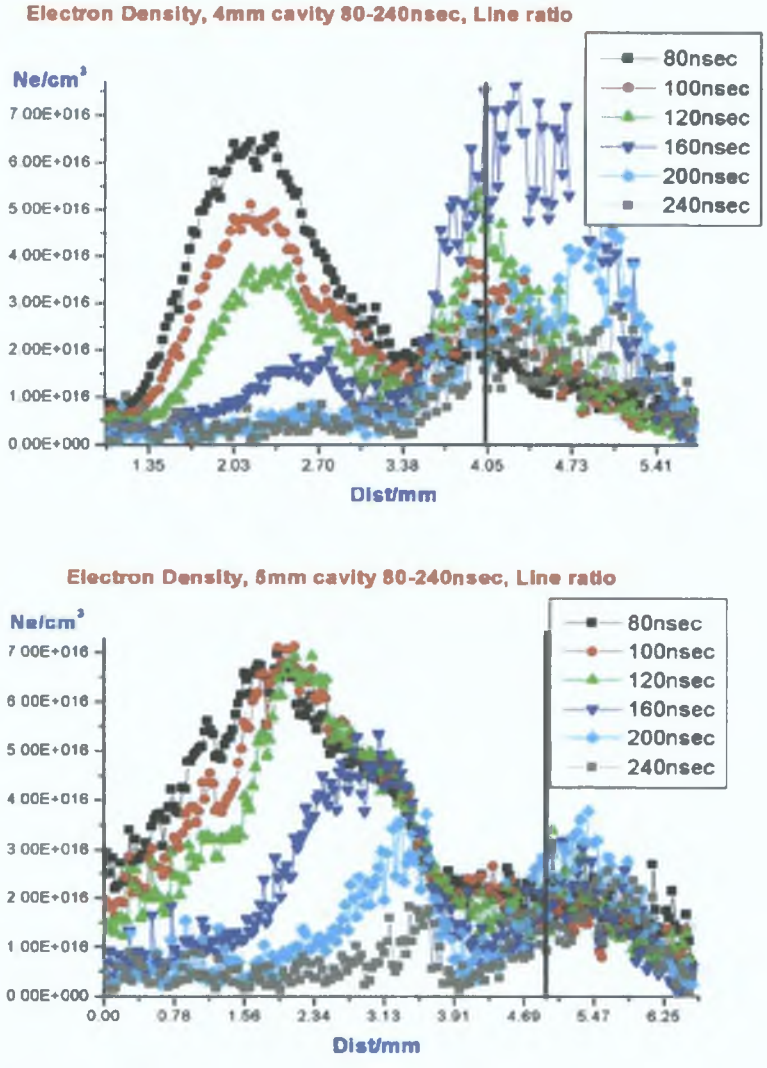

Fig 5.28.7-5.28.8: Time and space resolved density for 80-240nsec range, using the line ratio technique, 4mm, 5mm plate separation.

Laser plasma plumes are characterized by fast plume expansion, leading to rapid drops in temperature. Unless one uses a calibration curve for the exact temperature at every time resolved measurement, translating line ratios to electron densities will be less accurate, and this will manifest as unresponsiveness to actual changes in electron density. N_e values from Stark broadening are a direct measurement of the line width multiplied by the impact parameter (assuming that broadening>>instrument broadening).

We note from fig 5.29.1-5.29.4, that the large temperature increase occurs only after the jet has left the cavity. The second peak is shifted well ahead of the outer surface of the front plate. The temperature inside the cavity continues to decay rapidly, with the rate of decay higher, for the smaller plate separation. Assuming that the plasma is initially isothermal during the laser pulse (Narayan anad Singh [11]), then after the laser pulse termination the expansion becomes adiabatic. The chief difference is the presence of the laser as both a confining and heating influence. Thus in isothermal expansion, temperature gradients of measurable degree cannot form, the energy loss from the plasma being balanced by continued heating from the laser. However rapid expansion allows large thermal gradients to form over the plume's volume. Thus high temperatures are associated with confinement and reheating. The compression experienced by the plume as it is forced through the aperture produces a local increase in plasma density both inside the aperture and in the plume emerging from the aperture. Such a change in particle density would obviously be more pronounced as the initial density of the plasma entering the cavity increases. The resulting compression fuels rapid increases in temperature and the resulting increase in velocity is clear from fig.29.1-29.4.

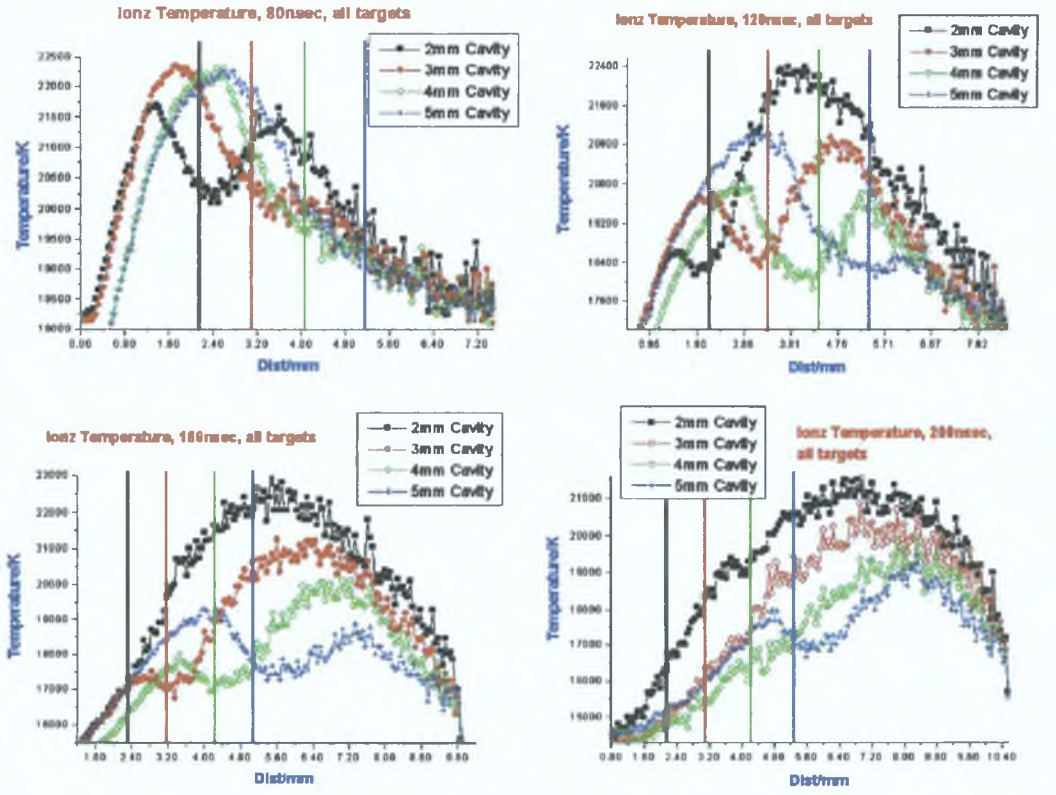

Fig 5.29.1-5.29.4: Time and space resolved ionization temperatures determined from line intensity ratios for 80-200nsec range. The most notable trends are the rapid decrease in plasma temperature in the cavity, and resulting jet emerging from the aperture. The peak temperature and spatial extension of the jet scales with decreasing plate separation. The vertical lines in each plot indicate the position of each front plate for the cavity width used.

The extended nature of the jet emerging from the cavity is also pronounced as is the low rate of temperature decay in the jet at later timescales This is probably due to an 'emitter-feeder' system set up between the plasma still contained between the plates, feeding the jet from the aperture through the front plate The subsequent reheating as the cavity plume is channeled through the aperture, then allows the emerging jet to be spatially extended yet retain a high temperature for long timescales The electron density shows an approximate z^2 dependence, falling off rapidly from a peak shifted near to the target surface However a second peak showing a similar decay profile is evident for all targets The density profile in a plasma at point z and at time t, can be expressed as (Narayan and Singh[11])

Equ 10 $$N_e(x,y,z,t)=\frac{N_T}{2^{1/2}\pi^{1/2}\tau X(t)Y(t)Z(t)}\exp\left[-\frac{x^2}{2X(t)^2}-\frac{y^2}{2Y(t)^2}-\frac{z^2}{2Z(t)^2}\right]$$

where N_T is the density at the center of the laser-irradiated spot (Z=0) at time t According to this equation the electron density should decrease from the target surface However as seen this is not applicable over the entire length of the plume, but only in a limited region after the peak, where a linear decay is seen This seems to imply that for that region the plasma expansion is indeed one dimensional, which is in agreement with predictions given by Narayan and Singh [11]

The unusual rising edge of the electron density profile is a unique feature of this target configuration It has been observed for other target configurations (Wedges and Capillaries) Another unusual feature of this target configuration is the high electron density inside the cavity at early timescales In section 5 1 (wedge targets) and section 5 2 (capillary targets) enhanced confinement gave densities peaking at $4\ 6E10^{16}cm^{3}$ compared to planar targets, where densities did not exceed $1\ 5E10^{16}cm^{3}$ The extent of the containment in the above was much greater then that reported here However despite this, peak electron densities here are nearly twice that of previous experiments

5 5 5 Expansion dynamics

Despite the larger dimensions and the ability of the plume to expand through the aperture, electron densities peak here at nearly $9\ 5E10^{16}cm^{3}$, twice those reported earlier Thus since the defining difference between section 5 1 and 5 2 is the expansion vector of the plasma which is being affected, we can conclude that retarding the plasma expansion vector parallel to the laser axis has a greater influence on localized plasma densities than that of vectors parallel to the target surface (i e laterally) Since the temperatures both inside the cavity and outside in the jet are lower than those reported in the preceding two sections, then clearly the bulk of the ablated mass is directed forward, back along the laser axis The plasma is still free however to decay via expansion parallel to the target surface, and through conductive decay into the target surface Thus containing a plasma inside a cavity (capillary or rectangular wedge) constrains the plasma during the initial hot phase, and thus is more effective in generating high temperatures, which no doubt lead to high expansion velocities which are highly

collimated, thus leading to rapid decay of densities. This argument is further reinforced by the increase in the jet temperature after expansion through the aperture, the densities in the jet are not as enhanced as those in the cavity, yet the temperature difference is pronounced. Again radial confinement is more conducive to high temperatures, but not higher densities. Effectively the aperture and front plate act as a micro-capillary.

5.5.5: Velocity profiles.

The velocity profiles for the different targets (determined by following the intensity half max count in the ICCD images) show good trend evolution from one cavity separation to the next. A rapid second order decay is followed by a less pronounced linear decay, with the emergence of a second peak in both the 4mm and 5mm cavity's. A proposed explanation for this is the dynamic relationship between the forward velocity of the expanding plume, and expansion into tenuous, low density medium

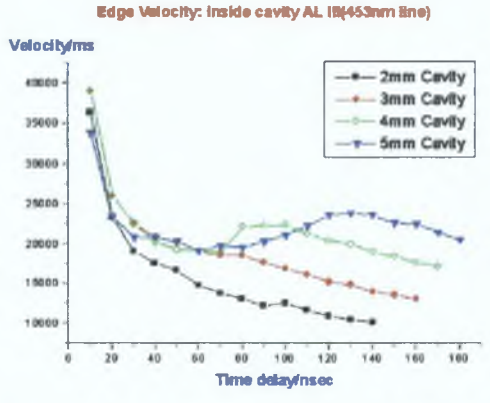

Fig. 5.30.1: Center of intensity velocity for the plasma inside the cavity(between the plates).

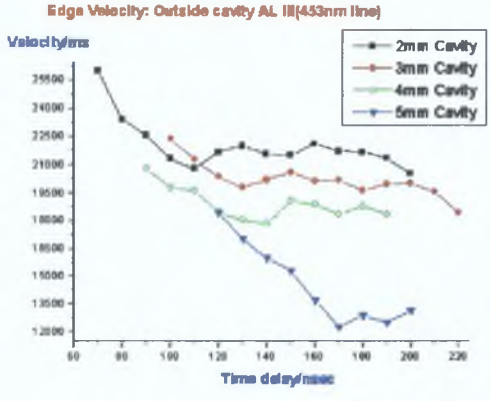

Fig. 5.30.2: Center of intensity velocity for the cavity jet outside (emerging from the hole in the plate).

which could form ahead of the main plume as a consequence of fast blow off gas becoming trapped in the cavity and acting as temporary gas medium into which the main plume must expand. The smaller the plate separation the more pronounced such an effect would be. The effect of channeling plasma through an aperture allows the higher temperature plume to expand at an enhanced rate (fig. 5.30.2). The higher velocity is maintained for longer durations, and as seen from figure 5.31, the enhanced intensity profile matches the ionization temperature profile for that time delay.

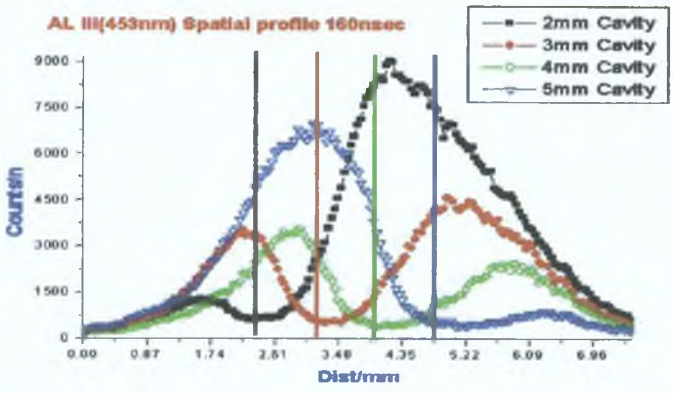

Fig 5.31: Spatial resolved intensity profile for AL III (453nm) at 160nsec. The vertical lines are the center of the front plates for each target. The plume moves from left to right.

While the leading edge of the intensity profile for each target does not show significant differences , the trailing edge of the jet emission is more pronounced for smaller cavity depth. Curiously the emission intensities for each target's jet show close convergence at the aperture of each front plate (all ~700 counts). The enhanced temperatures are seen only after the jet has left the cavity and aperture. After 200nsec the fast jet from all four targets displays rapid convergence of temperature and decreasing intensity. The 2mm cavity jet maintains its greater spatial extension until approximately 320nsec, when emission from the AL III lines becomes too weak to resolve clearly above the background signal

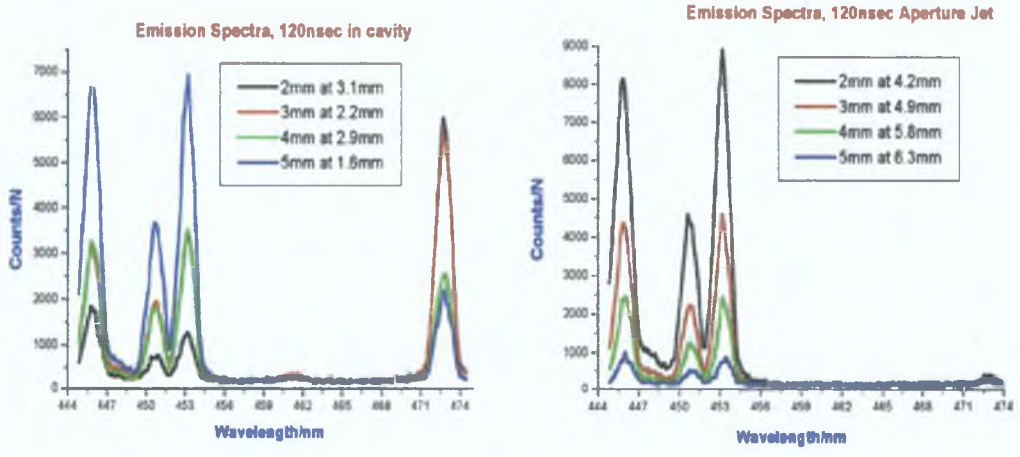

Fig 5.32.1: Emission spectra for all targets at the peak of the AL33 (453nm) line spatial profile within the cavity(left)
Fig 5.32.2: Emission spectra for all targets at the peak of the AL33(453nm) spatial profile in the jet(right) at 120nsec for each target. The peak intensity occurs at different spatial points for each target. Note the reversal of intensities within the cavity, where emission is dominated by the AL II line and for the jet AL III dominates. As the cavity width decreases, the jet is increasingly dominated by the higher ion stages.

5.5.7: Plume dynamics imaging.

Figure 5.33.1-15 (next page) display the IICD images of laser plasma plume generation between two parallel plates, for plate separation values of 2, 3, 4.5mm. The two most notable differences in the

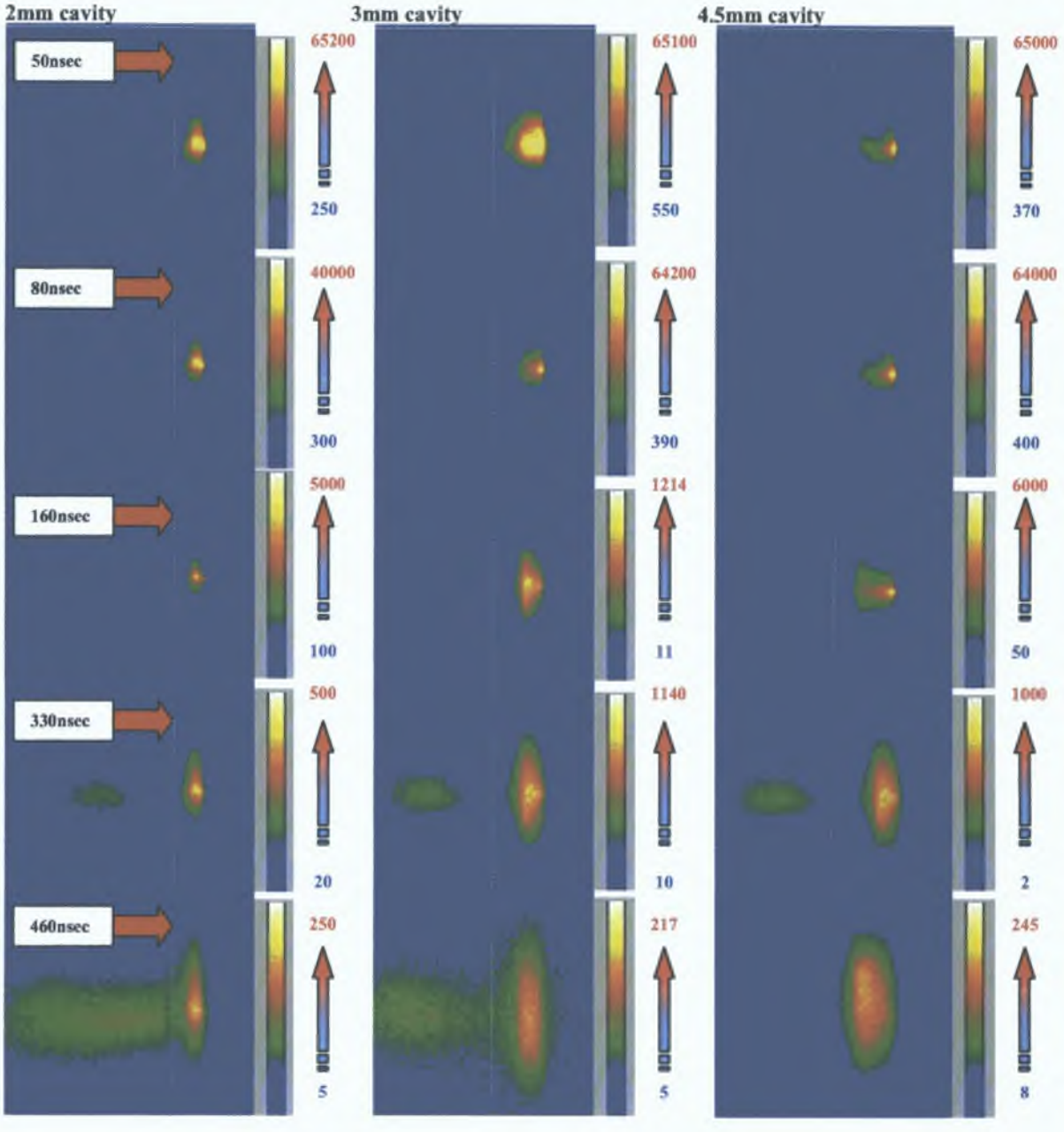

Figure 5.33.1 (top left)-5.33.15 (bottom right): ICCD images of the plasma plume for various time delays for plate separation values of 2mm, 3mm, and 4.5mm. These values, were deliberately different from the values used in the spectroscopic work, in order to ensure that any trends seen in the spectra, should be mirrored in the images, and should also be a continuous trend, and not specific to certain plate separation values. The most striking aspects are at later time delays, were the jet has completely separated from the front plate and the dynamics is analogous to gas puff generation. The expansion of the plasma along the vertical plane, along the inner surface of the front plate is clear in the 3mm cavity at 160nsec. Obviously this effect occurs at different time delays for each target. (the white vertical dashed line represents the approximate center of the front plate for each cavity width)

plumes occurs later in the plume's history, where all plate separation values display a detached, spatially localized plasma plume, leaving the aperture at the front plate and moving away (330nsec). The emission lifetime of this detached jet is largest for the 2mm cavity.

The emission spectra for 120nsec after the laser pulse, both within the cavity and for the aperture jet, give good indication of the temperature within the two different plumes without the need to perform temperature calculations In the jet, the spectra is completely dominated by AL III, and completely lacking in AL II photons The higher kinetic energy of the more highly charged ions, and subsequent re-heating of the plumes as it is forced through the aperture gives the AL III a superior TOF velocity The ratio of AL III to AL II inside the cavity, would indicate that as the cavity width is increased, the temperature at selected times within the cavity increases However in reality a more probable answer is the rapid channeling of plasma through the aperture, which as the cavity width decreases, will channel plasma of higher density and temperature initially The further away the front plate is from the target surface the lower the particle density will be when it does contact the inner surface of the front plate, and thus if temperature increases seen in the second jet occur due to re-collimation, then this process will be density dependent

5.5 8 Equilibrium considerations

In the analysis, we assumed that the plasma is in LTE, thus a Maxwellian distribution of the free electrons is required LTE conditions require that the collision excitation and de-excitation processes predominate over radiative processes, i e that the electron number density is sufficiently high The values of electron density and temperature allows us to check our assumption, again using equation 1 1,

$$N_e \geq 1\,6 \times 10^{12} \times T(eV)^{1/2} \Delta E(eV)^3 \quad \text{(Gotz et al [1])}$$

Here ΔE is the largest energy transitions for which this condition holds In this work ΔE is 2 7668eV for AL III (447 985nm) The highest temperatures measured were 33000K, this gives a lower limit on the right hand side of equation 2 of $6\,2\times10^{13}cm^3$ The lowest densities measured using Stark broadening were $9\,4\times10^{16}$ cm ^{3}, thus validating our assumption of LTE in the plasma

5.5 9 Conclusion

Generation of laser plasma within the vertical, formed by two parallel plates, resulted in enhanced peak electron density values, and a lower rate of decay in electron density both spatially and in time The cavity plasma was seen to collide with the front plate and localized regions of high electron density were seen to form in and around the aperture of the front plate Subsequent generation of high temperature plasma jets, emerging from the aperture were seen, with enhanced peak temperature, velocity and spatial extension as a consequence of decreasing plate separation and enhancement of plume parameters as it was channeled through the aperture It was concluded that one dimensional confinement along the laser axis enhances electron densities, but not plasma temperature significantly within the cavity's While 1Dimensional horizontal (wedges) and 2Dimensional radial confinement (capillaries) enhances electron temperature and

expansion velocity normal to the targets surface, but not electron density to the same extent The virtual absence of enhanced temperatures within the parallel plates geometries are even more apparent when compared with the temperature increases within capillaries and rectangular wedges (20-35%)

5 6 Time and space resolved visible emission spectroscopy of laser plasma generation and dynamics in Horizontal cavity's with high voltage electric field influence 1-Dimensional Horizontal geometric and electrostatic confinement

Having studied 1D containment within a horizontal cavity, 2D radial containment within a capillary, and 1D vertical confinement between parallel plates, we sought to introduce a new variable, namely the presence of an electric field We consider such a variable a 'non-standard' influence on laser plasma generation and evolution, given the relatively limited work done using electric fields The target employed was a rectangular cavity, of height 1 5mm, and depth 14mm The target, isolated from all other metal surfaces in the vacuum chamber was charged with a bias voltage ranging from -9KV to +9KV Following the analysis used in previous sections, line ratios were employed to calculate ionization temperatures, and stark broadening to calculate electron densities

5 7 1 Experimental Setup

The experimental setup was identical to the previous experiments in the visible, however the target block was isolated from the chamber and main target holder by sandwiching it between sheets of Perspex, which can hold off 20KV per mm The target was biased using two industrial high voltage "GRIFFON" D C power supplies Each delivered a maximum of 5KV each The power supplies were stacked in series, thus providing a maximum of 10KV The bias voltages used were ±2, 3, 4, 6, and 9KV The gate, or sample time on the ICCD was set at 30nsec, and the plasma generation and evolution was studied for a maximum of 300nsec after the firing of the laser pulse The ICCD was delayed in steps of 10nsec, and in this way the time and space resolved behaviour of the plasma under the influence of varying electric field intensities was studied No gain was used on the intensifier, and the pixels were binned 10 by 10

5 7 2 Geometry and field considerations

Little research has been done in the area of electric field interaction with laser generated plasmas With the exception of work by Williamson [19], who studied laser KrF ablation of titanium at a fluence of 4Jcm^{2}, and then influenced the plasma plume by placing a fine copper mesh placed 14mm from and parallel to the target surface A bias on the mesh was varied over a range of ±200V, while the target was grounded Williamson observed an 8 fold increase in the LIF signal from the plasma as the bias voltage was increased from 0 to +200V Only a small change in the plasma was observed for negative voltages This study was time integrated, and at low fluence The only other reported work with electric fields is by Varro et al [19] In this work, the authors used a configuration similar to Williamson, with a plate, positioned 10mm from the target surface (Au, which was grounded) A -20KV DC bias voltage was then placed across the gap A 10^{12}Wcm^{2} ps laser beam was then delivered at grazing incidence to the target A low temperature plasma

was then generated on the target surface, the electric field influences pushed photo ionized electrons back to the

target surface. The result was a short burst of XUV radiation of duration equal to the laser pulse duration , from the target surface, which was not present without the bias voltage, or even with a positive voltage. Although there are some theoretical treatments of electric field influence on laser plasmas, they remain few in number, and as yet unproven. In this work, we adopt the same approach as Williamson [18] and Varro [19], with one main difference, the geometry of the target is not planar but a wedge cavity of depth 14mm, and height 1.5mm. Secondly, in this work, the target is charged up and the ground plane is in front of the main target block (Figure 5.4).

Schematic of target and approximated field configuration:

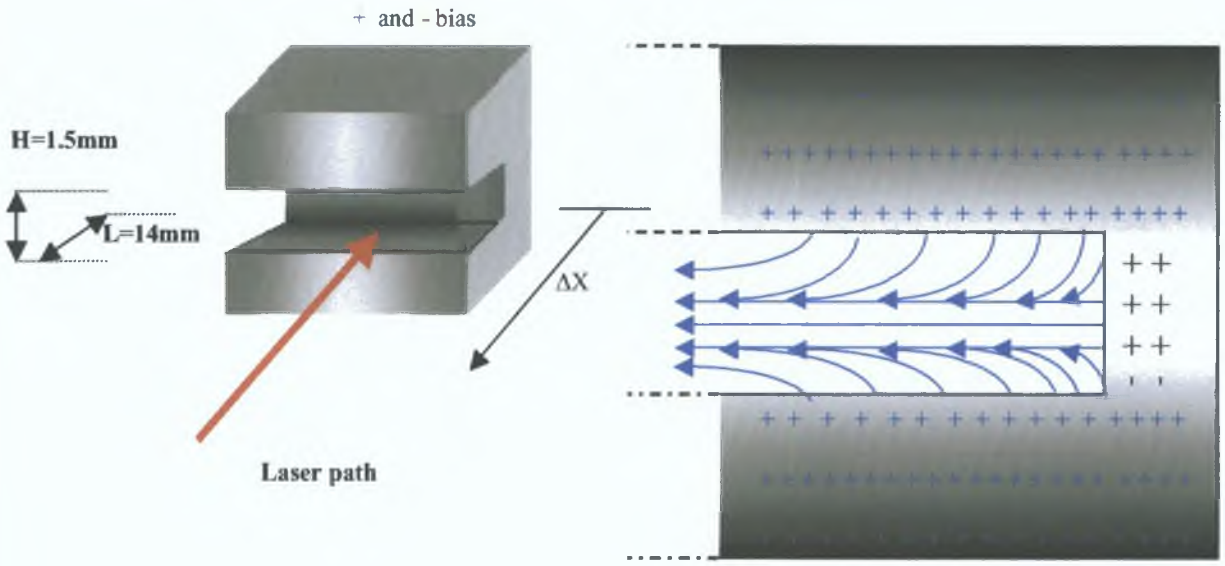

Side view: Cavity internal field configuration (approximation)

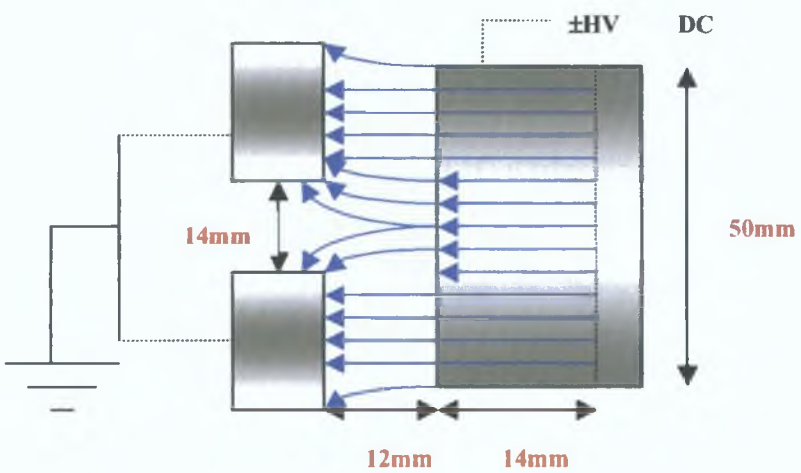

Top view Cavity internal field configuration (approximation)

Figure 5 4 Schematic overview of target configuration and field lines (approximation) For negative bias voltages, the field lines are directed from the ground point, to the target block For positive bias voltages, the field lines are directed away from the target to the ground point. Where the field lines are highly compressed and close together, the electric field flux per unit area of space is high

symmetry for simplified analysis A good example of this is the assumed symmetry of plasma plume expansion from a flat surface However as we have shown in the previous sections, geometric effects upon plasma parameters are not simple or trivial Equally so, it would be expected that geometry would configure the electric field lines from a charged body in a complex manner Utilizing a software package,'Equipotential3D' which is available commercially from [20], the electric field intensity and energy density distribution throughout the internal volume of the cavity was calculated The only inputs required by the 'Equipotential3D' software were the proportions of the surfaces, and the approximate surface charge density per m^2 This quantity was first determined

In calculating the surface charge density per m^2, a number of approximations were made Firstly the approximate capacitance of the target was calculated From Young [21], the capacitance of a simplified parallel plate capacitor is given by equation 11

$$\text{Equ 11} \quad C = \varepsilon_0 \frac{A}{d} = \frac{Q}{V}$$

Here, Q is the charge on the target, V is the bias voltage, A is the surface area of each plate, and d is the distance between each plate ε_0 is the permittivity of the dielectric (8.85×10^{-12}F/m) The value of ε_0 in vacuum differs from air by less then 6% For this simplified calculation we ignored the cavity's internal volume and consider only the area on the front of the target block, facing the grounding plane This gives $Q\sim14\times10^{-11}$ C for a bias voltage of 9KV The surface charge density is given by equation 12

$$\text{Equ 12} \quad \rho = \frac{Q}{A_{Sn}}$$

A_{Sn} is the area of the n'th surface, and from Young [21], charge is distributed uniformly across the targets surface Thus summing the entire surface area of the target block gives $A_{Sn}\sim0.00386m^2$, and from equation 2, $\rho=0.03626\ \mu Cm^{-2}$ Since the electric field intensity is related to the charge density, given by

$$\text{Equ 13} \quad E_{\perp} = \frac{\rho_0}{\varepsilon_0}$$

Then $E_{\perp}$ here is $\sim0.4\times10^{4}\ Vm^{-1}$ This value for the electric field strength is an approximation, namely for a single surface Clearly the internal geometry of the cavity will affect the field distribution To perform such calculations manually would be exceptionally challenging However the use of software packages makes analysis of field distributions by target configurations less burdensome, and the 2Dimensional nature of the software's calculations allow one to observe the electric field distribution within the cavity Figures 5 5a,b,c are the programs output for three input voltages (giving three charge values and hence three charge

density values). The numerical value over the field lines are the electric field intensities (in units of 10^4 Vm). The unbroken linear green lines represent the outlines of the cavity.

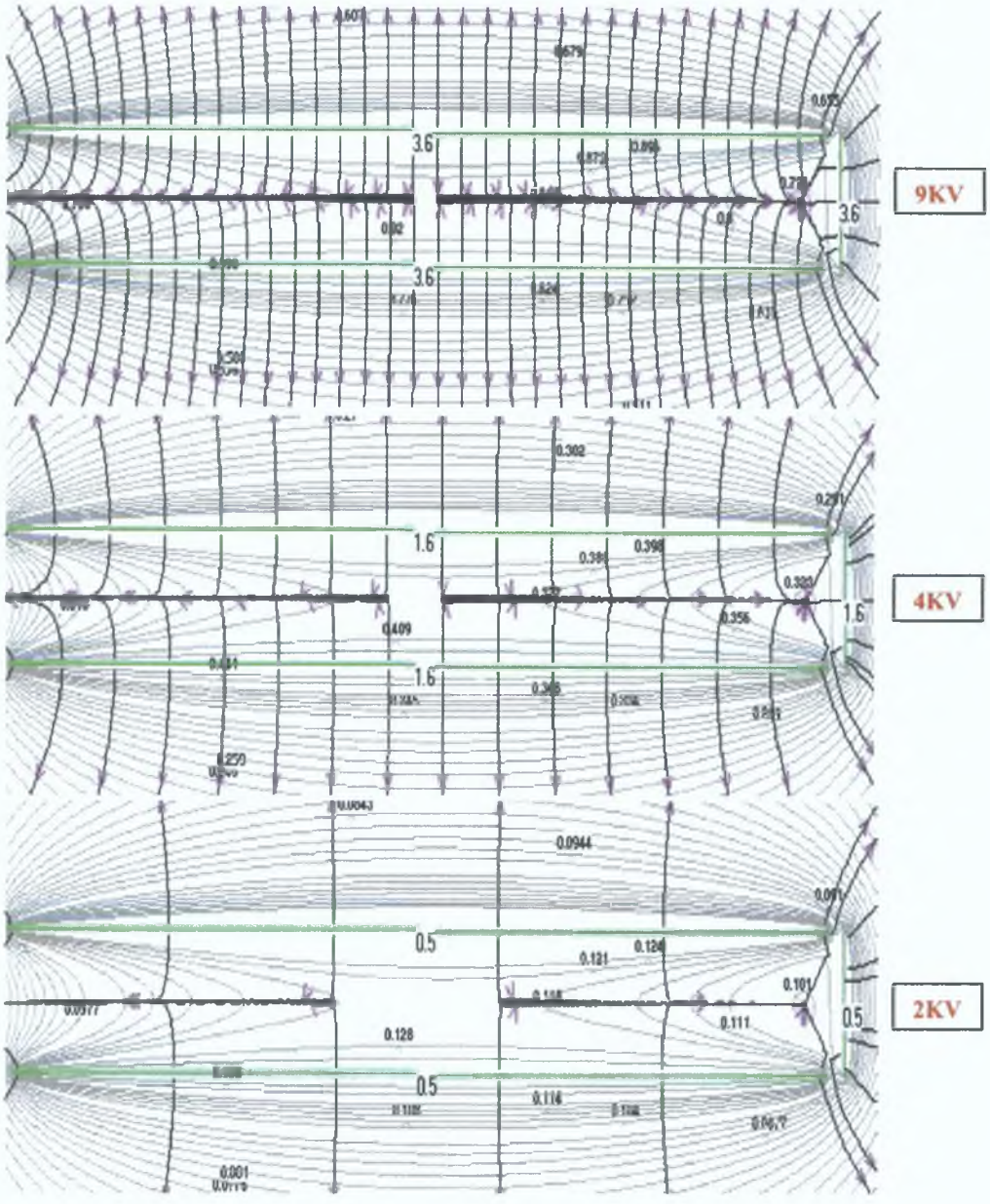

Figure 5.5a,b,c: Electric field intensities and configurations within the cavity for different bias voltages. Top: 9KV, middle, 4KV, bottom: 2KV. The configuration of the field lines are modeled in 'equipotenial3D'[21]. The solid green lines are the outline of the internal surfaces of the cavity. The numerical values on each graph represent the field intensity at that point (in units of approximately 10^4 V/m). The field lines are also color coded, darkened lines indicate weak field intensities. Thus observing the above three graphs, all display compressed, darkened field lines at the center of the cavity, parallel to the plane of the cavity. Here field intensities are low, due both to lower field intensities at lower bias voltages and due to cancellations of opposing field lines at that point. In the 2KV case, a dark blue region runs along the cavity. Here the field lines are weak, compared to the 9KV case, where a similar region of low field intensity exists, but as the color code shows, light blue, the field at the center here is stronger. The numerical values confirm this. In laser plasma experiments performed here, the laser beam entered from the left, and was focused onto the vertical surface, to the right, indicated by the large numerical value.

The clear trend is that as the bias voltage is increased, not only does the charge density increase on each surface, but the field lines are closer together. For all bias voltages, a null region occurs in the central region, parallel to the plane of the cavity, where the field intensity is low. This is due to cancellation of field lines from opposite faces. The size of this 'null' region decreases for higher bias voltages. The field lines point away from the surfaces, but for a negatively charged target the lines would face into the target surfaces. From Young [21], the energy residing in the electric field is given by:

$$\text{Equ 14: } u = 0.5\varepsilon_0 E^2 \quad J/m^3$$

The value of u is also calculated by 'Equipotential3d'. Figure 5.6a,b,c display a false color images of the u for three values of the bias voltage used.

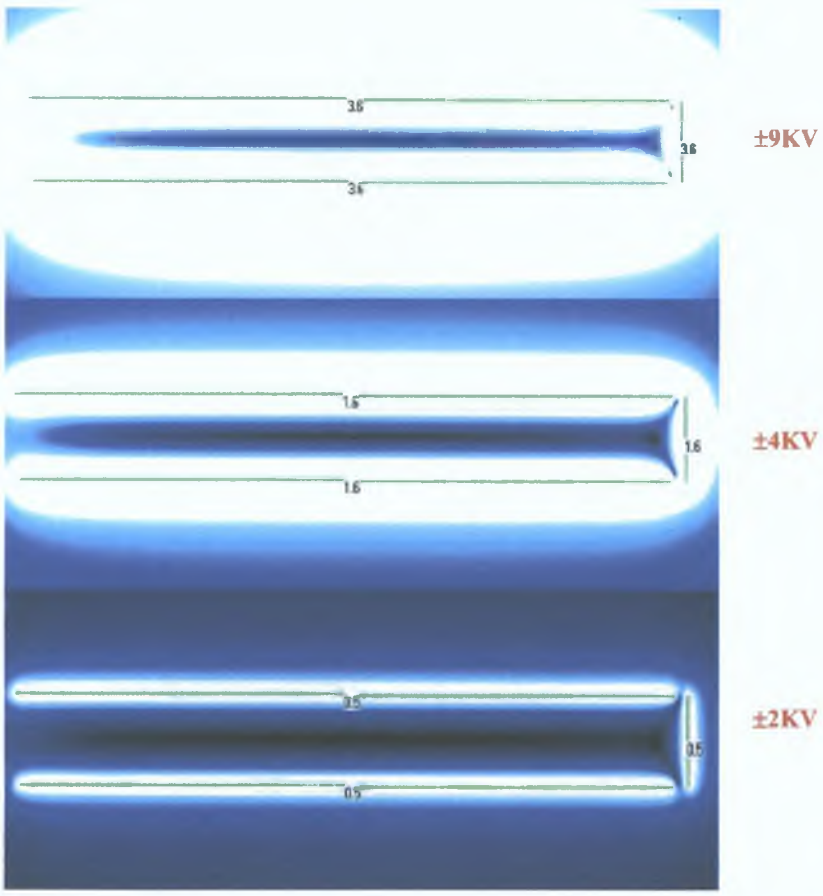

Figure 5.6a,b,c: False color images of the energy density within the volume of the cavity as a consequence of the electric field, with darkened regions indicating near zero field levels. The numerical values assigned to each case indicates the normalized (relative to the 9KV case) charge density on each surface of the cavity. Since the energy density is proportional to the square of the electric field, the rate of fall of energy density as one moves away from the cavity's surfaces is higher than that of the field intensity itself. Thus at that centre of each cavity, a large well defined darkened region exists, where either the field intensity is zero or extremely low, due to oppositely directed field lines canceling each other out. The higher the bias voltage applied, the higher the electric intensity at each point, and the smaller the region of zero field energy at the cavity's center. Thus at some very high value, we would expect the entire cavity to be filled with a non-zero value for the energy density. In laser plasma experiments performed here, the laser beam entered from the left, and was focused onto the vertical surface, to the right, indicated by the numerical value.

The energy density within the cavity's is substantially different from that of a planar target, where the electric field intensity and the energy density fall off rapidly as the distance from the target surface increases. The overall picture given by the field analysis will assist in the analysis of plasma parameters such as plasma electron density and ionization temperature.

5.7.4: Electron density analysis.

Using Stark width broadening of the same line (AL III, 453nm) as was employed in previous sections, the electron density was calculated for each bias voltage used, for two time delays after the laser, over the length of the plasma at each time resolved event.

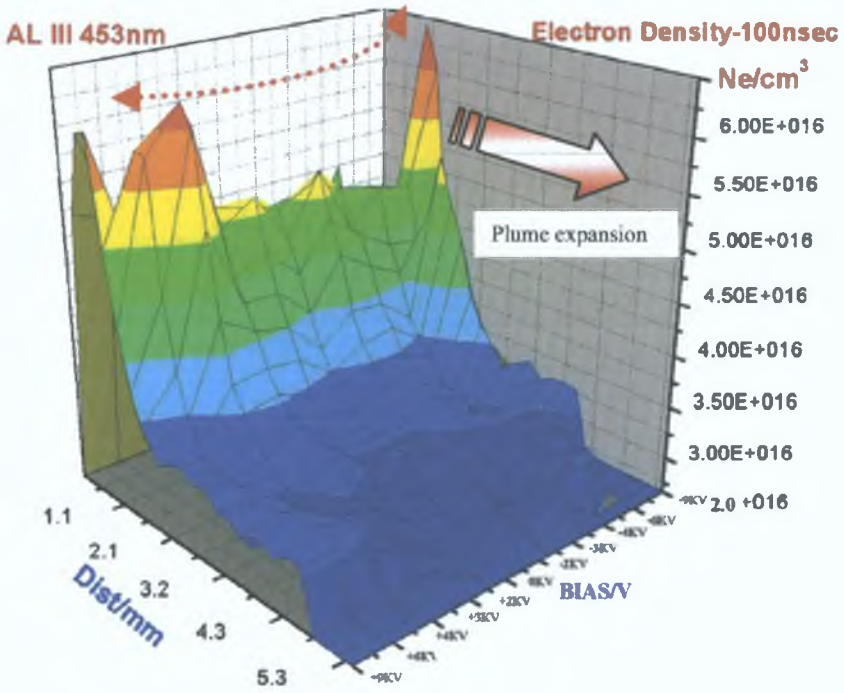

Figure 5.7: Electron density at 100nsec time delay. Space and bias voltage resolved. At this early stage in the plasma expansion, only moderate differences are visible for different voltages, and these differences occur at high voltages. Distance from the back surface of the cavity is labeled 'Dist/mm'.

Laser plasma plumes are characterized by high particle density and highly ionized charged states. Such a system will exhibit a very high internal electric and magnetic field, which will shield the plume from the influence of external electric and magnetic fields. Although field influence during early phases of the plumes history are possible as Varro et al [19] have shown, they do require very large electric field intensities. Even in the work reported by Varro the laser beam was incident on the target surface at an grazing angle, which would greatly reduce the power density of the laser beam and hence the density of the plasma. However the chief problem with work of this kind is to balance the need for the plasma density to fall sufficiently for field influence. The longer the delay after the laser pulse, the weaker the plasma signal, This then has a detrimental affect on the viability of plasma diagnostics (such as measuring line widths)

which become more unstable as the plasma signal becomes weaker. By using higher voltages, the earliest time when significant field influence is observed will be shifted back in time, closer to the laser pulse termination. However, very high voltages (>20KV) are required for good signal change from the plasma for early time scales.

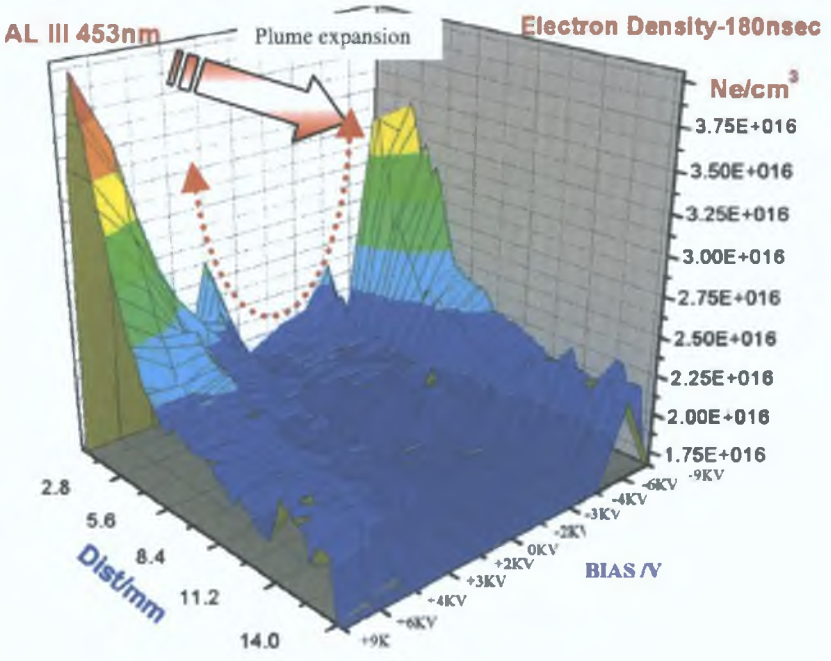

Figure 5.8: Electron density at 180nsec time delay. Space and bias voltage resolved. At this late stage of plasma history, the plasma density has dropped enough for significant field effects to be observable. The concave nature of the density profile for the various bias voltages is especially pronounced.

In calculating the electron density at a later time delay (180nsec, figure5.8), comparing the plasma density in the cavity for 0KV bias for 100nsec and 180nsec, the peak value falls from ~6×10^{16}cm^{-3} to ~2×10^{16} cm^{-3}. However for the largest bias values used (±9KV) the peak electron density drops from ~5×10^{16}cm^{-3} (at 100nsec, figure 5.7) to ~4×10^{16}cm^{-3} (figure 5.8). The rate of fall of peak electron density for both polarities of high voltage bias is far less than that of the unbiased cavity. The second notable feature is the extended nature of the electron density profile in figure 5.8 for both bias polarities. There is a clear trend of greater forward extension of the plume, and higher density values at the forward region for increasing bias voltages. The peak electron density for the positive bias is approximately 17% higher than that of the negative bias. The position of the peak electron density is also shifted slightly back for positive bias voltages when compared to the unbiased case. Another important feature of figure 5.8, is the relative absence of change in N_e until ~±5KV. From 0KV to ~±5KV, the peak electron density does not change, however values of N_e are resolvable for increasingly larger distances in the forward direction. Above ~±5KV there is a large and sustained increase in the peak value of N_e, and the overall value (space resolved). Both the forward and back regions of the plume display enhanced electron densities for high bias voltages, the positive bias displaying slight enhancement over the negative bias. This is not unique, as

Williamson [19] observed similar changes in the LIF signal from a titanium plasma, with enhanced emission from positive and negative bias, the positive bias enhancement being 10-12% more than that of the negative bias enhancement relative to the unbiased signal Using ICCD images, Williamson also observed a shifting forward of the plasma's peak emission point for negative bias voltages, but observed no shift for positive bias voltages

There are two possible reasons for enhanced electron densities First, where a particle is repelled by the field, being of like polarity (i e electrons repelled from the cavity's internal surfaces by a negative bias), the electric field will act as a buffer against plasma decay into the target surfaces, which act as substrates In observing the electric field energy density plots (figure 5 6a,b,c) it can be clearly seen that at the center of the cavity for each bias used, a large darkened region exists, where the particles will 'collect' or reside in being repelled by the charged surfaces This 'null' region of electric energy, could essentially emulate a cavity of lesser height From section 5 1, it was observed that higher electron densities and greater forward expansion of the plasma plumes was demonstrated when the height of the cavity was decreased Thus it is possible that the greater the bias voltage applied, the greater the repulsion of like charged particles from the surfaces Coupled with the compression of the plume's particles in a region of lesser height then that of the cavity itself However for each bias polarity, particles of opposite charge will be attracted to the cavity's inner surfaces Thus for a positive bias, electrons will be attracted to the cavity's inner surfaces, and ions repelled Given the ratio of the mass of an electron ($9\ 1\times10^{-31}$Kg) to that of the a doubly charged aluminum ion ($44\ 8\times10^{-27}$Kg), it is reasonable to propose that unless the bias voltage is exceptionally high, the plasma ions are not strongly influenced by the electric field for either polarities, and this would be especially so given that average velocities for Al III ion in such cavity's is approximately of the order of ~5×10^{5}cm/sec at the time delays studied here (section 5 1) Therefore the enhancement of the electron density for positive bias voltages must be explained It is highly possible given the particle densities, and the rapid motion of the plume away from the back surface, that electrons are undergoing collisions with other particles as they are deflected towards the upper and lower surfaces of the cavity The length of the cavity and relative uniformity of the energy density of the field along the cavity could result in an extended length over which such particle deflections and collisions can occur

5 7 5 Ionization temperatures

Utilizing the same technique and lines as those used in section 5 1, ionization temperatures were calculated for a range of time delays after the laser pulse, for all bias voltages used, over as large a spatial range as the lines extension would allow The same trend as that seen in the density profiles emerges Although ionization temperatures were calculated for the time range of 80nsec to 240nsec, only at ~120nsec does any observable difference between the bias voltage resolved profiles become visible (figure 5 9) even here, the chief difference is the slight shifting forward of the position of the peak in the ionization temperature for

the unbiased case, whereas for both polarities, the peak is further back. There is a negligible difference in the peak temperature itself.

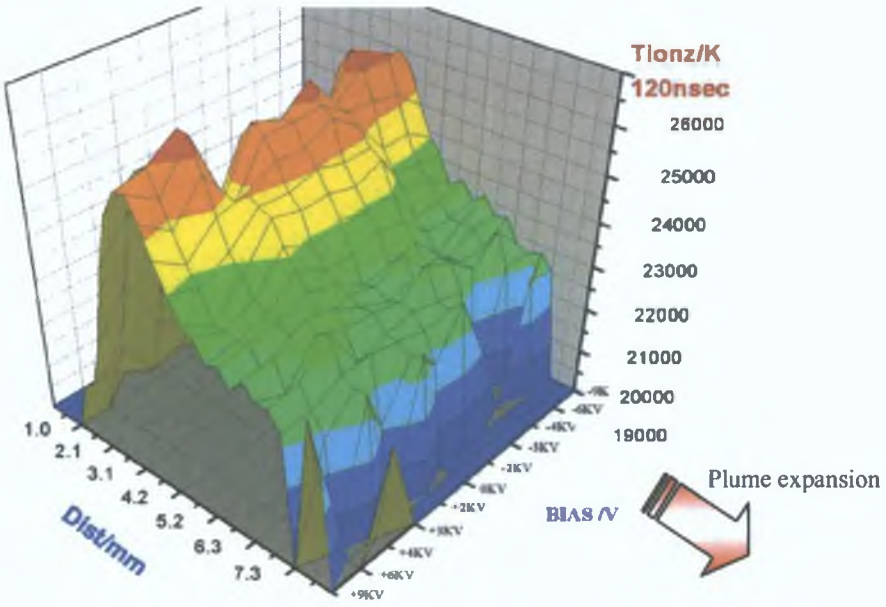

Figure 5.9: Ionization temperatures for a delay of 120nsec after the laser pulse, for all bias voltages used. Ionization temperatures were calculated for time delays of 80,100,120,160,180 and 240nsec after the laser pulse. No discernible differences were observed for time scales of less then 120nsec.

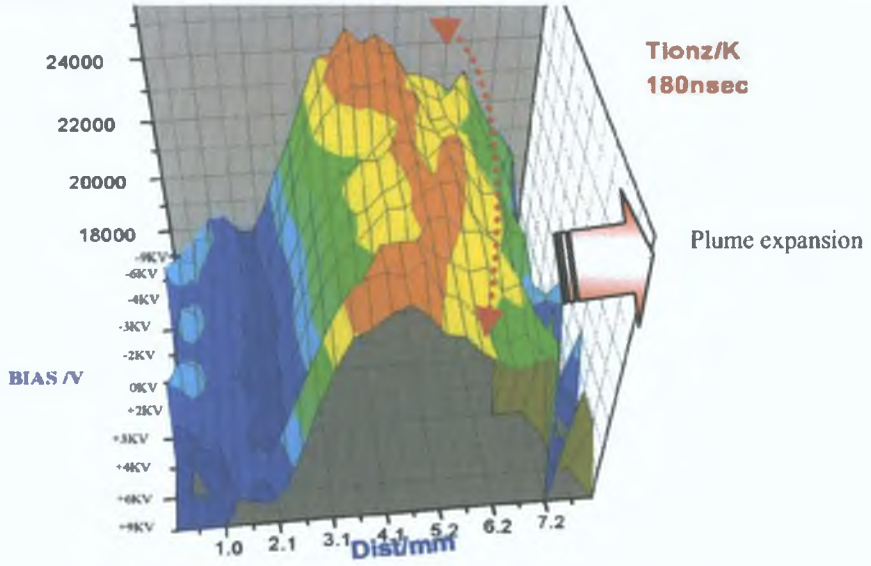

Figure 5.10: Ionization temperatures for a delay of 180nsec after the laser pulse, for all bias voltages used. Although a small difference (<1000K) exists for ionization profile for the unbiased versus the high voltage (±9KV) case, the most notable difference is the shifting back of the position of the peak ionization temperature for both polarities.

For ionization temperatures at 180nsec, clearly visible trends begin to emerge, with the peak ionization temperature for both polarities being ~1000K larger at the maximum voltages used (±9KV). The shifting back of the peak ionization temperature relative to the unbiased target is now clear, and the extent of the retardation of the profile is greater for the positive voltage than for the corresponding negative value. Even

given these differences, the extent of the influence of the bias voltage for figure 5.10, is not as dramatic as that seen for electron density for the same time delay (figure 5.8). Although unexpected this is not a new aspect of this work. In the previous sections, plasma plumes generated between parallel plates, displayed substantial increases in electron density, but negligible changes in electron temperature, while plasma plume generated in rectangular wedges and capillaries displays medium increases in electron density and large increases in temperature.

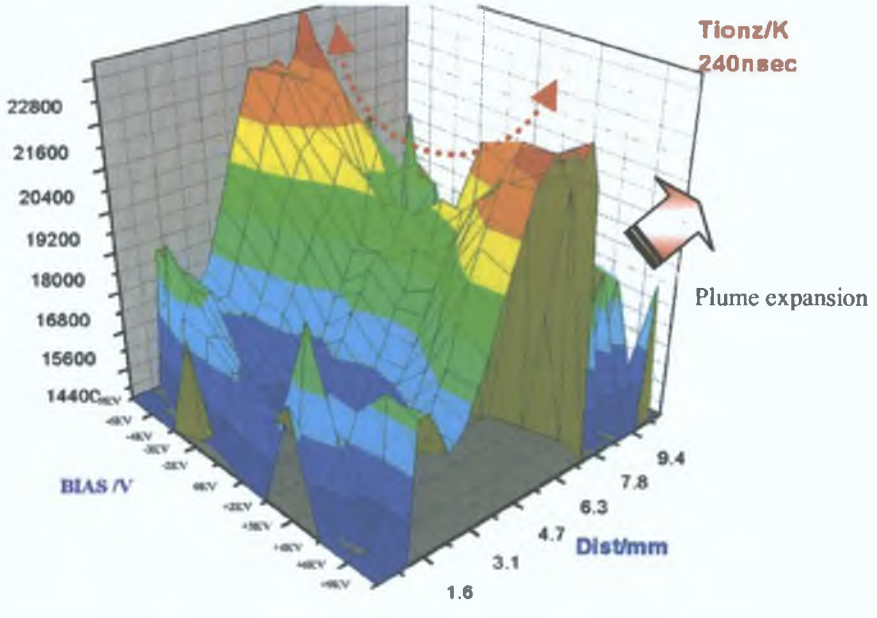

Figure 5.11: Ionization temperatures for a delay of 240nsec after the laser pulse, for all bias voltages used. At this late stage in the plasma history, clear differences in the profile of the ionization temperature emerge. For both polarities, the peak value increases for increasing bias voltage.

The latest time resolved measurement of ionization temperature was at 240nsec. Here (figure 5.11) differences of ~3500K (maximum) were observed over the complete bias range studied, with the peak of the temperature profile for the positive bias still shifted slightly back relative to that of the position of the peak for the negative bias. The leading edge of this late delay temperature profile is noisy, due to weak signals from the AL II line, which is not as spatially extended as the AL III line. Calculations at later time delays were not viable given the weak signal levels of both ions.

5.7.6: Emission profiles.

The final variable considered here is the spatial profile of the peak emission intensity of the AL III (453nm) line for various time delays after the laser pulse (figure 5.12a,b,c). It is not surprising that the profile mirrors that of both the electron density and the ionization temperature, with no observable difference in the emission intensities before a certain time delay. In the case of emission intensities this is ~160nsec, where the maximum negative bias voltage (-9KV) displays a 20% increase in the peak emission intensity. All other bias values display a small but observable increase in intensity, but relative to the unbiased target

the differences do not exceed ~10%. There is a slight curvature of the profiles front, with the unbiased target leading the biased cases for all bias voltages and for both polarities.

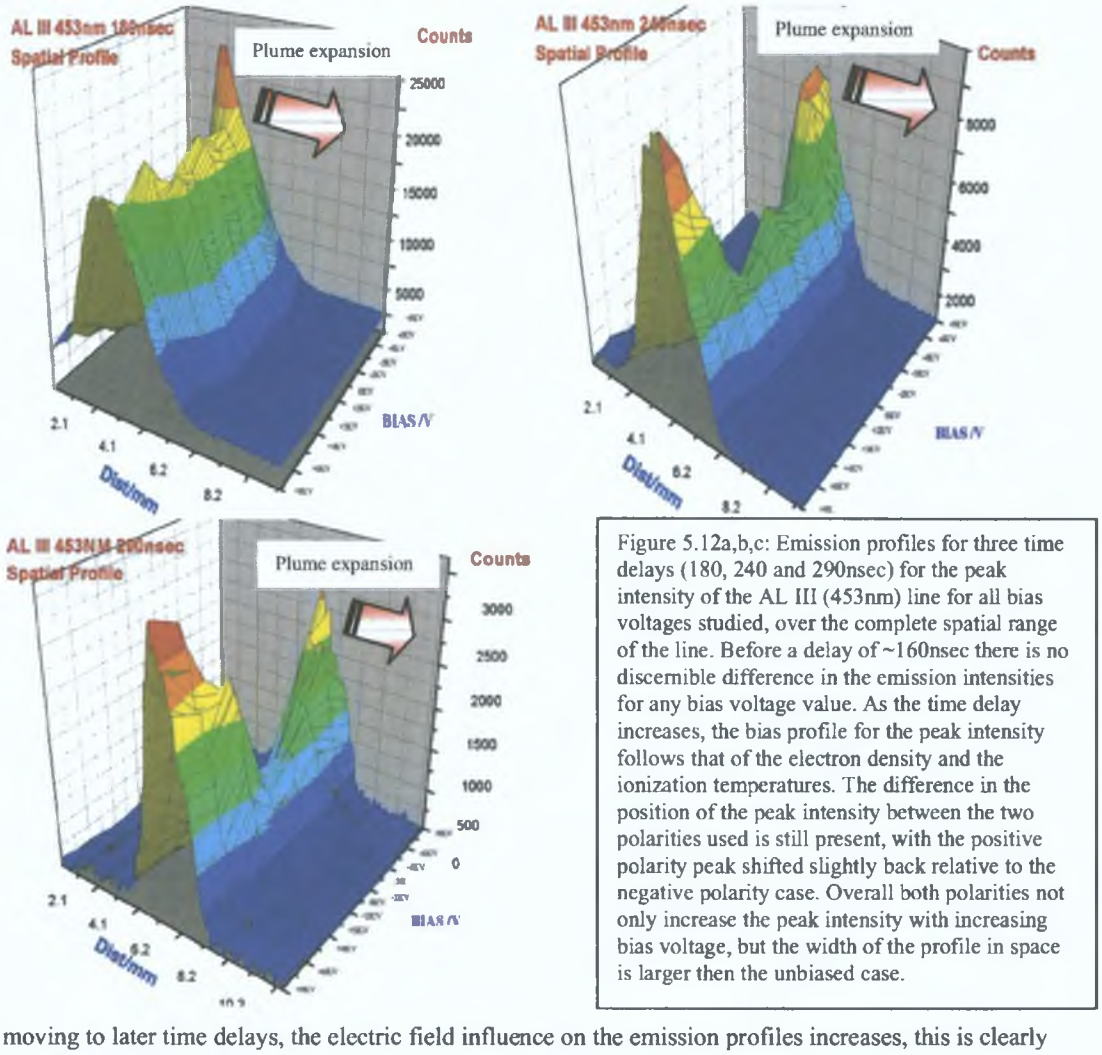

Figure 5.12a,b,c: Emission profiles for three time delays (180, 240 and 290nsec) for the peak intensity of the AL III (453nm) line for all bias voltages studied, over the complete spatial range of the line. Before a delay of ~160nsec there is no discernible difference in the emission intensities for any bias voltage value. As the time delay increases, the bias profile for the peak intensity follows that of the electron density and the ionization temperatures. The difference in the position of the peak intensity between the two polarities used is still present, with the positive polarity peak shifted slightly back relative to the negative polarity case. Overall both polarities not only increase the peak intensity with increasing bias voltage, but the width of the profile in space is larger then the unbiased case.

In moving to later time delays, the electric field influence on the emission profiles increases, this is clearly present from 240nsec onwards. The peak profile of the line is not only larger, but is also broadened by the bias voltage for both polarities, with the positive bias showing greater enhancement then the negative. This is also seen in the electron density profiles, and was also reported by Williamson [18]. Plume particles also respond to positive bias voltages more readily than negative bias voltages, as indicated by figure 5.12c, where the large increases in emission intensity occur after +3KV, while the increases for the negative bias is less sharp, and almost linear in appearance. This fact was also reported by Williamson in studying the LIF intensity profile of titanium ions.

5.7.7: Particle-field interaction analysis.

Williamson [18] attempted to analysis plume particle interaction with the electric field in his experiments by considering the velocity changes occurring due to the electric field force on a charged particle. A similar analysis was attempted here, however the geometry in this work is radically different from the standard planar target and parallel charged plate. As a consequence a number of assumptions must be made in the analysis. A diagrammatical overview of the analysis is shown in figure 5.13.

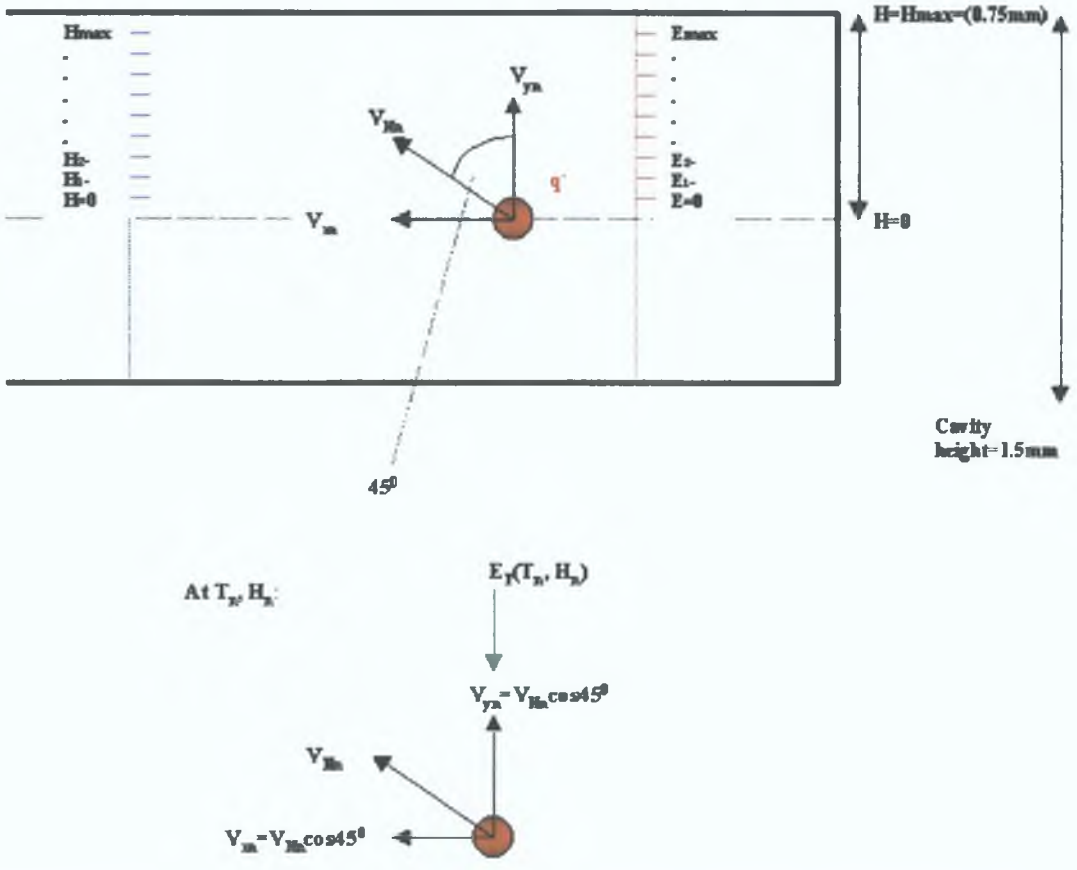

Figure 5.13: Schematic of the analysis of the electric field influence on a charged particle, of charge q, moving with velocity V_{Hn} at an angle of 45^0 to the plane of the cavity, with resolved velocity components parallel and perpendicular to the cavity plane (V_{Xn}, V_{Yn}). Here we assume that the normal field component at the centre of the cavity at height H=0, is negligible, due to field cancellation from opposing surfaces. As the particle moves upwards towards the upper surface, for each height H_n the field intensity E_n varies, as does the force on the charged particle E_{Fn}, thus each iteration of the upward velocity component V_{Yn} at some H_n combined with the downward force on the particle from electric force E_{Fn} will produce a gradient in the particle's upward velocity, which will be reduced as the particle approaches the upper surface. The rate of decrease in the particle's upward velocity, and the velocity at the point and time of impact with the upper surface, will all depend upon the particles initial velocity, and the rate of increase of electric field intensity. The latter depends upon the bias voltage and the cavity dimensions. The particle's velocity component parallel to the plane of the cavity V_{Xn} will be unaffected by the electric field, due to the field lines emerging perpendicular to the surfaces from which they originate. To simply the analysis the force on the particle from the vertical back surface, whose field lines run parallel to the cavity's plane, are ignored. This is a valid assumption given the profile of the energy density from figure 5.6a,b,c which clearly indicates that the field influence from the back surface is highly localized, and does not extend forward greatly along the cavity. It can be seen from the electron density plots (figure 5.7-8) that significant field influence for the bias values used here does not occur until later timescales (>140nsec). At such times, the

plume particles, moving at approximately 10^4m/sec will travel a distance of ~1.5mm along the cavity, away from the back surface.

In the analysis, a range of velocities could be considered, and all particles were assumed to be moving at a angle of 45^0 to the plane of the cavity. The force on a charged particle of mass m, charge e, and in the vicinity of an electric field E, is given by:

Equ 15: F=-eE [Young 20]

Thus if the particle velocity is known at some initial time T_1, and the particle is at H=0 (center of the cavity) moving upwards towards the upper (or lower surface) of the cavity, then the force on the particle could be calculated, and the change in the particle's velocity for each height H_n under the influence of a field E_n can be known. In this way a range of velocities for different bias voltages (and hence different electric field intensities) could be studied and the effect of the field related to the observed results. Firstly the electric field distribution must be numerically calculated at each height H_n.

5.7.8: Cavity-field profile.

In order to calculate the electric field distribution within the cavity, the approach followed by Young [20] is employed. In that analysis, a charged particle is positioned at distance x from a rod, of length 2a, with charge Q distributed uniformly along its length (figure 5.14).

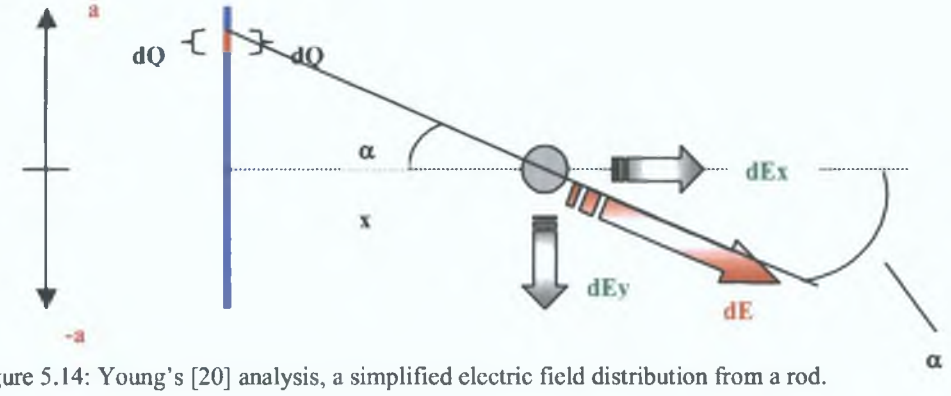

Figure 5.14: Young's [20] analysis, a simplified electric field distribution from a rod.

Young divided the rod into infinitesimal sections of length dy, with corresponding charge dQ. For uniform charge distribution the ratio of dQ to Q is equal to the ratio of dy to 2a, the total length. Thus:

$$\text{Equ 16: } \frac{dQ}{Q} = \frac{dy}{2a}$$

and rearranging this gives,

$$\text{Equ 17: } dQ = \frac{Qdy}{2a}$$

The distance r from this section to the charge is $(x^2+r^2)^{1/2}$, dE at this point is given by:

Equ 18: $dE=\frac{Q}{4\pi\varepsilon_0}\frac{dy}{2a(x^2+r^2)}$

If this field is vector resolved then :

Equ 19a,b: $dE_x=dE\cos\alpha$ $dE_y=dE\sin\alpha$

$\sin\alpha=\frac{y}{\sqrt{y^2+x^2}}$ and $\cos\alpha=\frac{x}{\sqrt{y^2+x^2}}$, so that substituting these into the equation 18, gives:

Equ 20a.b: $dE_x=\frac{Q}{4\pi\varepsilon_0}\frac{xdy}{2a(x^2+y^2)^{3/2}}$ and $dE_y=\frac{Q}{4\pi\varepsilon_0}\frac{ydy}{2a(x^2+y^2)^{3/2}}$

To find the total field components E_x and E_y, one must integrate over the range a to –a. After this operation E_x and E_y are described by:

Equ 21a,b: $E_x=\frac{Q}{4\pi\varepsilon_0}\frac{1}{x(x^2+y^2)^{1/2}}$ and $E_y=0$.

Due to the symmetry, E_y summed over the length of the rod is zero. If this analysis is to be applied to the cavity case, then firstly x becomes H (height from the center of the cavity), and 2a becomes L, the length of the cavity. Secondly, upon rotating Young's rod 90^0 to represent a finite strip of the cavity's inner surface (figure5.15), the entire calculation must then be done twice, to represent both the strip on the lower surface and the upper surface. The field distribution from both surfaces must then be added, and should cancel at H=0, at the cavity center.

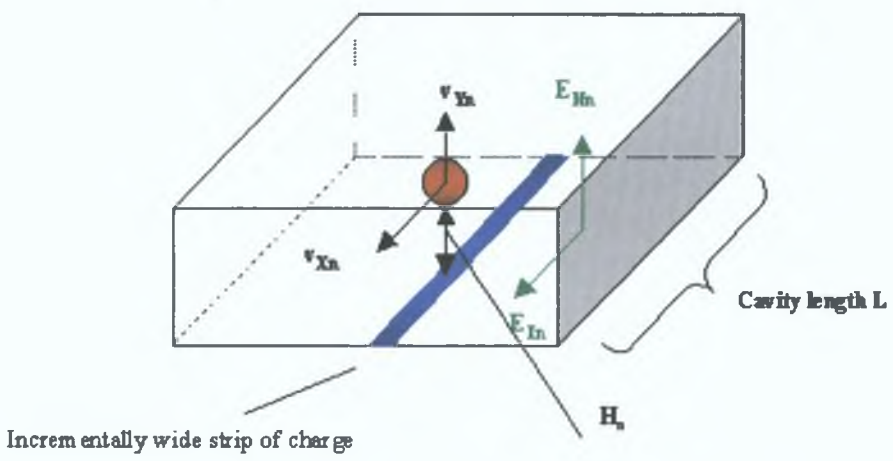

Figure 5.15: Following Young's [20] analysis, a simplified electric field distribution within the cavity's volume is considered. The electric field influence or field lines not emanating from the incremental narrow strip of inner cavity surface were ignored (i.e. the field lines to the left and right of the particle's trajectory parallel to the charge strip are ignored, only those field lines from the strip are considered). The electric field is resolved into two components parallel and perpendicular to the surface. We consider only the influence of field components normal to the cavity surface.

Using equation 21a, the Electric field distribution within a cavity was calculated for various bias voltages, by writing a routine in MATLAB 6.0. The field for each surface (upper and lower surfaces in the cavity) was calculated and then the profiles for each surface were summed. The E field distribution was thus mapped over the cavity's height (figure 5.17a,b).

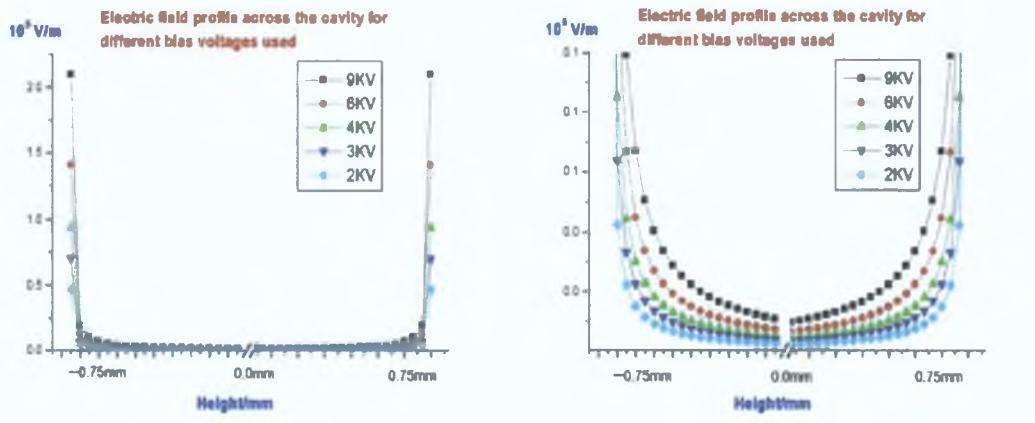

Figure 5.16a,b: Electric field distribution in the cavity, for various bias voltages (left-full scales, right-rescaled to lower values). Height =0 represents the center of the cavity. With the particles equidistant from the upper and lower surfaces within the cavity, and moving parallel to the two inner surfaces.

As can be seen from the above figures, the electric field intensity falls rapidly as the distance from the source surface is increased, and as figure 5.16b displays, field cancellation at the cavity's center gives negligible or very small values for the field intensity. As the distance to the source surface decreases the differences in the E-field for the various bias voltages increases dramatically, this is due to the inverse square dependence in equation 21.

5.7.9: Velocity profile response.

In considering the interaction of an energetic particle with a retarding field, the most important variable is the particle's velocity. Since the effect of the field is to act as a retarding force, then the higher the initial velocity of the particle, the longer it will take the field to significantly influence the particle. Equally if the duration of the influence is fixed then, the extent of the velocity reduction from the field will be lesser, as figure 5.17 demonstrates. Here the charged particle (an electron) experiences a retarding force

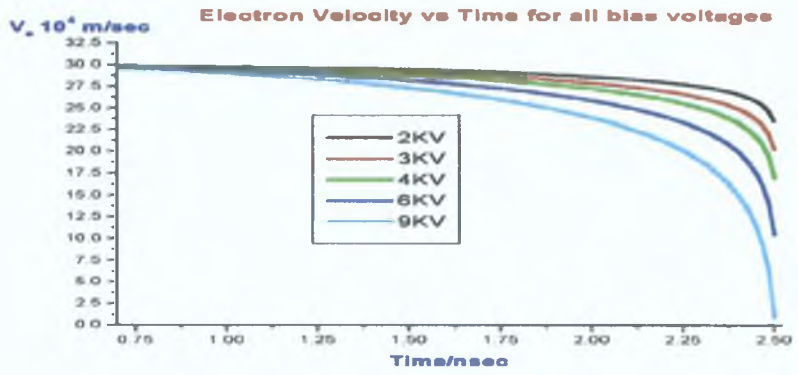

Figure 5.17: Velocity profile of an electron launched at 30×10^4m/sec, and exposed to the field influence for a limited duration. The greater the field strength, the greater the extent of the velocity reduction.
from a negative bias field, and thus the particles slows.

As the bias voltage is increased the electric field intensity at each point in the cavity increases. Secondly, given the inverse squared dependence of the field intensity from the source, the closer the particle is to the source the greater the retarding force, and the more rapidly the particle will decelerate under this force. At some point for a fixed velocity and bias voltage, the particle will undergo velocity reversal and begin to move away from the source and be accelerated by the now repulsive force of the negative field. For a range of velocities at a fixed field intensity, the fastest particles will both show the smallest drop in velocity, but will also reach the source surface more rapidly, and thus will experience the very high intensity field near the source surface. This can be clearly seen in figure 5.18. Here a range of velocities were inputted into the analysis routine for a fixed bias voltage (9KV). While the slowest moving particles (1×10^4m/sec) took the longest to reach a region of high field intensity, they also under went a reversal of velocity further from the source surface (inner surface of the cavity). The greater the velocity of the particle, the sooner it reached a high field region and began to experience a retarding force, but the longer it took for that force to reduce the particles velocity to zero, in some cases the particle's velocity was high enough to over come the retarding force, and it still reached the inner surfaces of the cavity. This can be seen in figure 5.18, where for particle's velocities greater then 35×10^4m/sec at 9KV, the particle reached the cavity's surfaces despite the retarding force (this explains the sudden termination of the velocity traces in these cases for V_e=75, 50, 35×10^4 m/sec, compared to lower velocities).

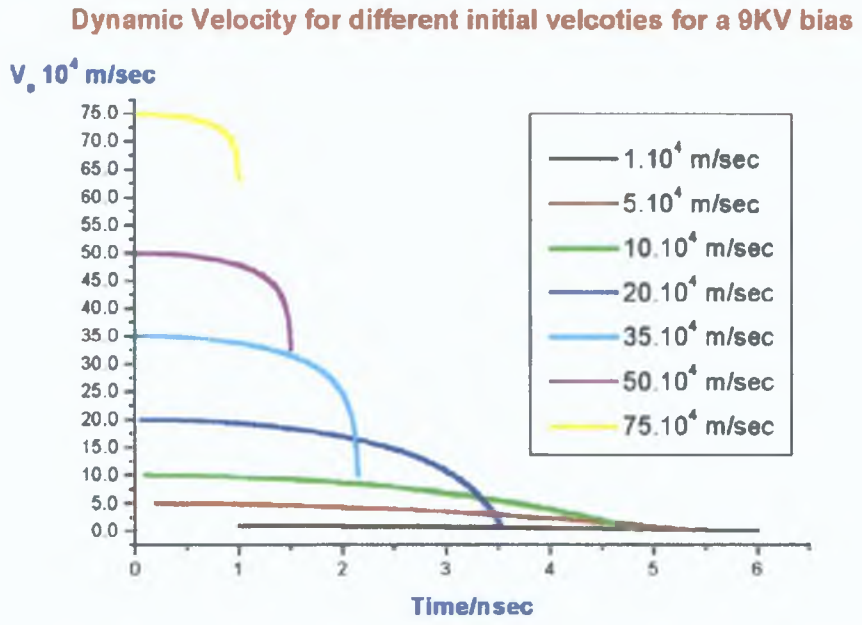

Figure 5.18: The higher the initial velocity the more rapid the velocity decay, but some particles still overcome the retarding field (75-35×10^{4}m/sec). For each velocity displayed, the flight time from cavity center to upper surface, moving at 45^0 to the plane of the cavity dictated the 'run' time of these calculations. This explains the cutoff of the higher velocities (75-20×10^{4}m/sec), which reach the upper surface with non-zero velocity.

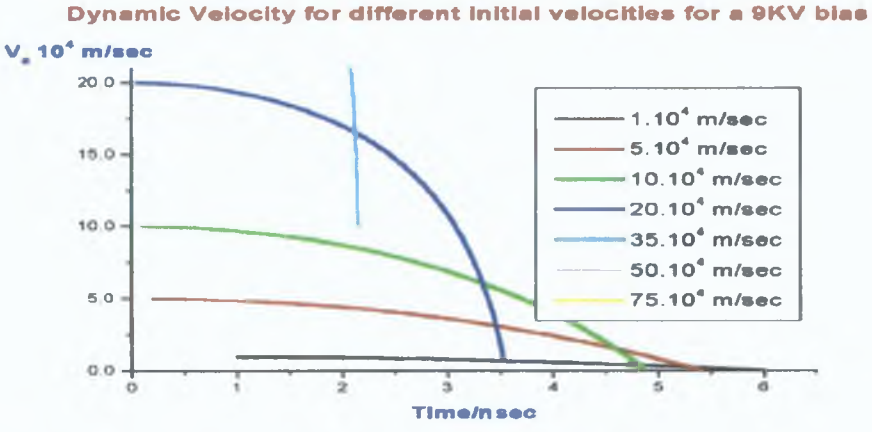

Figure 5.19: A rescaled figure of figure 5.19 for velocities below 20×10^{4}m/sec.

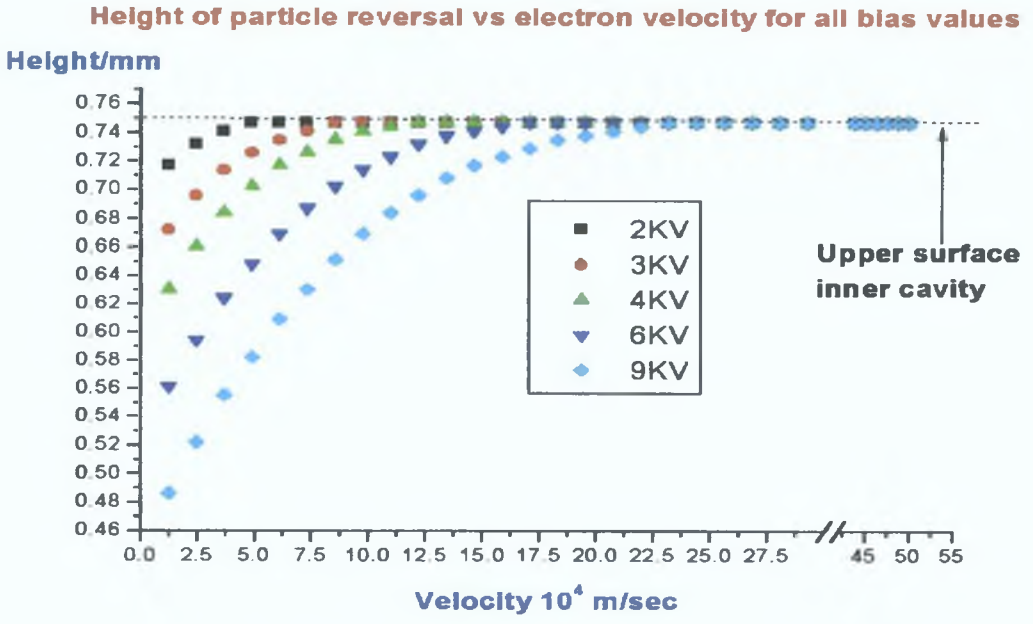

Figure 5.20: For each velocity value and each bias voltage value a particle will under velocity reversal at some height H, from the center of the cavity. The upper surface is 0.75mm from the cavity center. Choosing a bias voltage (i.e. 2KV), a range of velocities were inputted into the analysis. The point of zero velocity (or velocity reversal) was determined. If the particle reached the upper surface with non-zero positive velocity then the field had failed to halt its motion. This height of zero velocity was then plotted against the initial velocity. In the 2KV case, only particles of velocity less then 5×10^4m/sec are repelled and experience velocity reversal. All other particles reach the upper cavity surface with non-zero positive velocity. As the bias voltage is increased, a larger proportion of particles begin to experience a sufficient reduction in velocity which leads to velocity reversal, and they are repelled by the charged inner surface. For high field intensities a large proportion of the particles are either dramatically slowed before they reach the inner surface, or they are repelled from the surface completely. In either case, electron densities in the plasma could be maintained at higher values for a greater duration than that of the no field case, where particles are free to impinge on the cavity surface and decay into the target. Since this mechanism exists all along the cavity (which is 14mm long), then as the plasma decays with time and velocities within the plume shift to lower ranges, such a process would become even more pronounced. This would also explain why, at early time scales no change in the plasma conditions are seen. Simply the electron velocity is too high.

Figure 5.20, clearly infers greater velocity change due to a fixed bias voltage as the velocity range shifts to lower values. Even if the concept of a reversal of velocity in a plasma is questionable, the consequences for the local electron density within the plume cannot be ignored. Lower particle velocities near the surface of the inner surfaces of the cavity will lead to a less steep electron density gradient as one moves from the centre of the cavity to the surfaces. Such a state will also reduce the rate of decay of the plasma's internal energy into the target volume. Since plasma decay into surfaces has been a recurring aspect of cavity contained laser plasma studies in this work, then any process which offsets this decay is important. Indeed for all laser plasma studies in the visible in this chapter, geometric confinement has demonstrated enhanced electron densities due to the plasma's inability to expand 3Dimensionally, however this came at the cost of faster decay of the plume at later timescales. The strength and stability of the electron density values from

figure 5 8, and the intensity profiles from figure 5 12c all demonstrate superior values and lifetimes as the containing effect of the electric field offsets plasma decay within the cavity

The next logical question to arise is the effect upon electrons when a positive bias is applied We infer the same explanation as Williamson [19], in that accelerating electrons across the volume of the plasma will enhance collisions within the plume, and assist in maintaining the populations of ions within the plasma Clearly this effect will also increase as the bias voltage is increased, with collision velocities increasing with the applied electric field It is possible that the same mechanism could be applied to ions, However given the mass difference between ions and electrons it is more reasonable to infer that electrostatic acceleration and de-acceleration is more dominant a process for electrons than ions Although the extent of the force felt by a particle will depend upon the particle's charge, and given that the electron density is taken from the line width of the AL III line, the question remains as to whether the larger force experienced by the ion due to its charge can offset the increased mass, which the field must overcome if significant influence is to seen in the plasma's behaviour Clearly we have ignored the field effects parallel to the cavity plane Such field components would effectively accelerate or de-accelerate a charged particle (affecting its velocity component parallel to the cavity) Although such an effect would exist, further analysis beyond the simplistic model given above is beyond the scope of this work

5 7 10 Conclusion

The space and time dependent electron density, ionization temperature and emission profiles for ions in the visible range 453nm-464nm were studied, for laser generated aluminum plasmas inside rectangular cavity's charged with various bias voltages, ranging from -9KV to 9KV Substantial enhancement of the electron density was observed for increasing bias voltages of both polarities, but only for late timescales in the plasmas history (>120nsec) This was attributed to particle containment by the electric field which repelled like charged particles and enhanced collisions by oppositely charged particles which are accelerated towards the field source Calculation of ionization temperatures displays enhancement, which is also only significant at later timescales, and the extent of the enhancement is not as large as that in the electron density The emission profile of the AL III (453nm) line is enhanced and broadened strongly for large bias voltages in comparison with the unbiased target Small but observable differences in the position of the peak emission profile and ionization temperature profile were observed for bias targets over the unbiased case, with peaks shifting back as the bias increases This is similar to that observed by Williamson at much lower fluence and bias voltage

Finally attempts were made to characterize the behaviour of electrons with various velocities inside the cavity's for the different bias voltages applied The general trends which emerged from this analysis are of greater influence of the electric field for particles of lower velocity, with either significant decreases in velocity or full reversal of the particles trajectory towards the inner surfaces of the cavity if the applied bias is high enough to repel the charged particle A well defined velocity range was observed to not undergo significant changes in particle trajectory for a particle value of the bias as the kinetic energy of the electrons

was too high to be influenced by the field at the intensities used No attempts were made to analysis the effects upon ions of electric fields, as the ion mass is significantly higher than that of electrons

5 7 11 Concluding remarks

Given the differences seen in containing a plasma in a manner which does not inhibit the forward expansion of the plume (wedges and capillaries), one must ask what exactly is enhancing the temperature within the capillaries and rectangular cavity's (1Dimensional confinement in the horizontal and 2Dimensional radial confinement), but not the parallel plates (1Dimensional confinement in the vertical) Collision of plasma with the front plate is essentially plasma deposition with a substrate, thus plasma temperatures should show a small and highly localized temperature increase in the vicinity of the front plate as particles compact and 'pile up' at the plate surface, this should lead to a higher collisional rate, and indeed a sharp peak in the temperature is seen in figures 5 27 1-5 27 4 Yet the temperature increases here are negligible in comparison to the 5000-8000K differences seen in the other confining cavity's The most obvious source of enhancement are particle collisions within the plume This could be achieved either through maintaining a high electron density and sufficiently high temperatures for highly ionized ions to exist, or through the collision of plasmas of varying volume and degree of ionization Within both the capillaries and the rectangular wedge, both of the above exist Superior electron densities exist in both capillaries and the rectangular wedge as do higher ionization and electron temperatures

ICCD images of plasma dynamics within the rectangular cavity's display multiple plasma components undergoing deflection and collision within the cavity volume While particle collisions are probably enhanced when the plasma collides with the front plate in the parallel plate geometries, and indeed small temperature increases are observed at the front plate surface, however by default, the most energetic component of the plasma will still exit through the aperture (the most energetic ions move almost exactly along the laser path normal to the target surface), while the plume within the cavity is still free to expand parallel to the plane of the two parallel plates as can be seen from the ICCD images The relatively large contact area between the plasma and the front plate will invariably allow for rapid conductive decay into the target surface However in the capillary and wedge targets, the most energetic components (within the plume center) are not in direct contact with the inner surfaces of the cavity's, but are buffered by plasma layers which will be in contact with the inner surfaces

Thus although plasma surface interaction will cause plume decay, this process will be slowed by the temperature gradients which will exist in capillaries and the rectangular wedge targets Over all one could say that the energy flux between the plasma and any surface will be maximized in the parallel plate geometry and minimized in capillaries and the rectangular wedge targets The effect of plasma–surface interaction is seen to be affected by the presence of a high intensity electric field, generated by a bias placed on the target Here particles (electrons) could undergo significant shifts in their velocity distribution

such that localized values of electron density are maintained at a high value, with this value and the spatial extent of the electron density profile increasing as the bias increases For sufficiently high electric field intensities ,and lower electron particle velocities, particle repulsion form the targets inner surfaces is possible

References

[1]: S Gotze, S Ellwi Z Andreic. Phy Letts A: 299 (2002) 571-576.

[2]: MS Dimitrijevic, Z Djuric, AA Mihajlov. J Phys D: AppL Physics 27(1994) 247-252.

[3]: H. C. Liu, X. L. Mao. Spectrochima Acta Part B(1999), 1607-1624.

[3.1]: C. R. Phipps. R. W. Dreyfus, Laser Ionization Mass Analysis, ISBN 0-473-53673-3, Wiley & Sons (1993).

[4.1]: http://physics.nist.gov/cgi-bin/AtData/main_asd (Nist).

[4.2]: http://www.pa.uky.edu/~peter/atomic/ (atomic line list v2.04).

[4.3]: http://physics.nist.gov/PhysRefData/ASD1/archive/GS_IE/A1_gs_ic.html

[5]: X. Zeng, S. S. Mao, R. E. Russo, Spectrochima Acta Part B: 58, (2003), 687-877.

[6]: A. Caruso, R. Gratton, Plasma Phys. 10, 867, (1968).

[7]: Lochte-Holtgreven, Plasma Diagnostics, AIP Press.

[8]: H. C. Liu, X. L. Mao, J. H. Yoo, Spectrochima Acta Part B : 54, (1999), 1607-1624.

[9]: B. Hopp, N. Kresz, Cs. Vass, Z. Toth, T. Smausz, F. Ignacz, Appl Surf Sci, 186 (2002) 298-302.

[10]: J E Blamer, R Weber. Laser and Particle Beams: vol8 no1-2, pg327-337.

[11]: R. K. Sing, J. Naranyan, Phys. Rev. B 41, 8843 (1990).

[12]: R. A. Al-WAZZAN, J. M. Hendron, T. Morrow, Appl Surf Sci, 96-98, (1996), 170-174.

[13]: S. S. Harilal, C. V. Bindhu, M. S. Tillack, J. Phys D: Appl. Phys. 35(2002) 2935-2938.

[14]: S. Amoruso, X. Wang, C. Altuci, C. de Lisio, Appl Surf Sci, 186, (2002) 358-363.

[15]: D. B. Geohegan, A. A. Puretzky, Appl. Phys. Lett. 67(2), 10 July (1995).

[16]: S. I. Anisimov, B. S. Luk'yanchuk, A. Luches, Appl Surf Sci 96-98(1996) 24-32.

[17]: Mohamed Abbas Khater. Ph.D. Thesis, DCU, Dec 2001 Ch6, pg175.

[18]: T. P. Williamson. Ph.D. Thesis, QUB, Sept 2001.

[19]: S. Varro, Gy. Farkas, F. Ehlotzy, Optics Communications 172 (1999) 47-53.

[21]: www.electrostatics3D.com

[20]: Young's Physics, 5'th Ed, Wiley Press (1996).

[21]: E. Perez-Tijerina, J. Bohigas, R. Machorro, J. Appl. Phys. Vol 90, No 7, October 2001.

[22]: A. Lenk, G. Granse, Appl Surf Sci 96-98, 195(1996).

[23]: J. T. Knudtson, W. B. Green, J. Appl. Phys. 61 4771 (1987.)

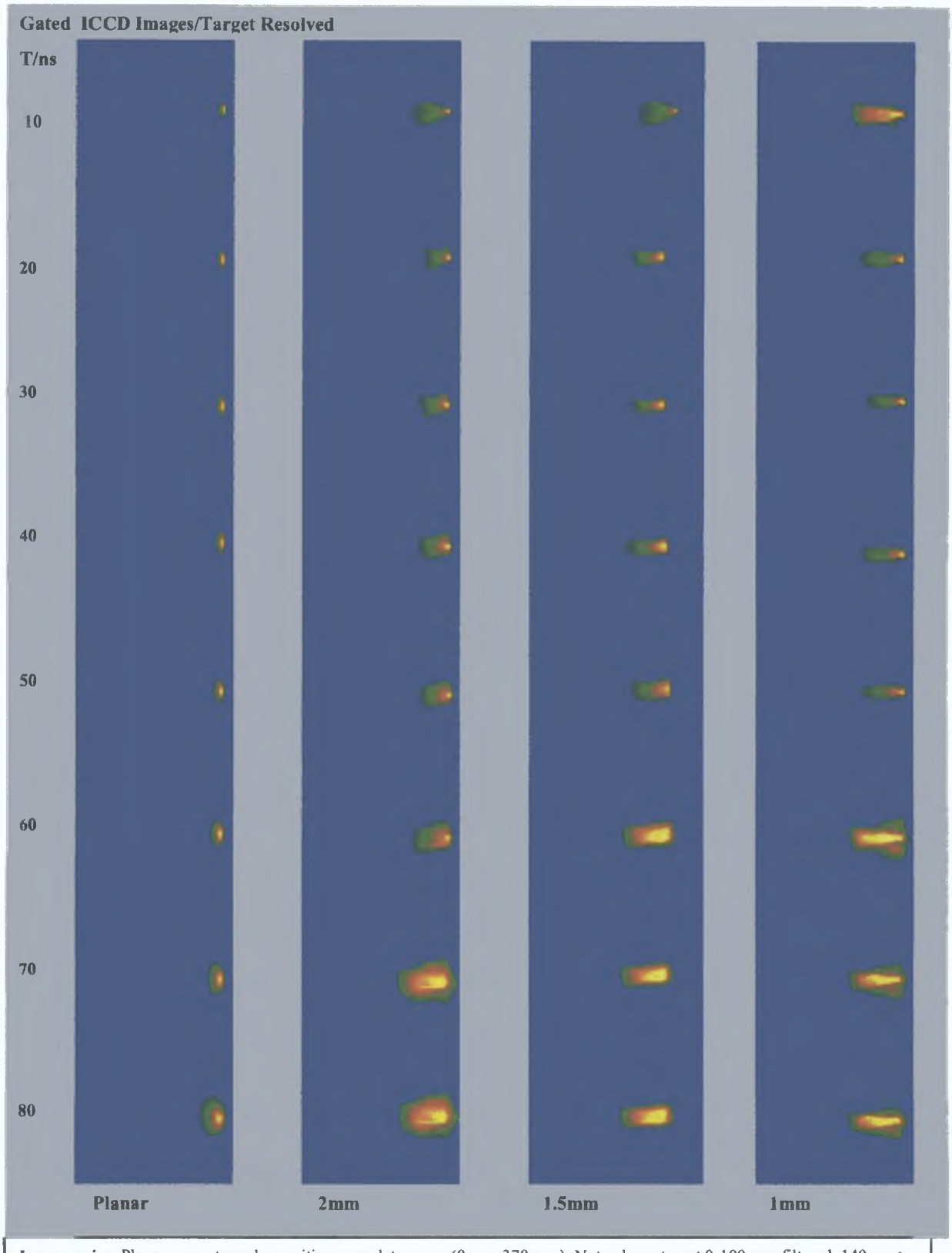

Image series: Planar vs. rectangular cavities, complete range (0nsec-370nsec). Note planar target 0-100nsec filtered, 140nsec> without filter. 2mm cavity 0-60nsec filtered, >60nsec unfiltered. 1.5mm cavity 0-50nsec filtered, >50nsec unfiltered. 1mm cavity, 0-50nsec filtered, >50nsec unfiltered.

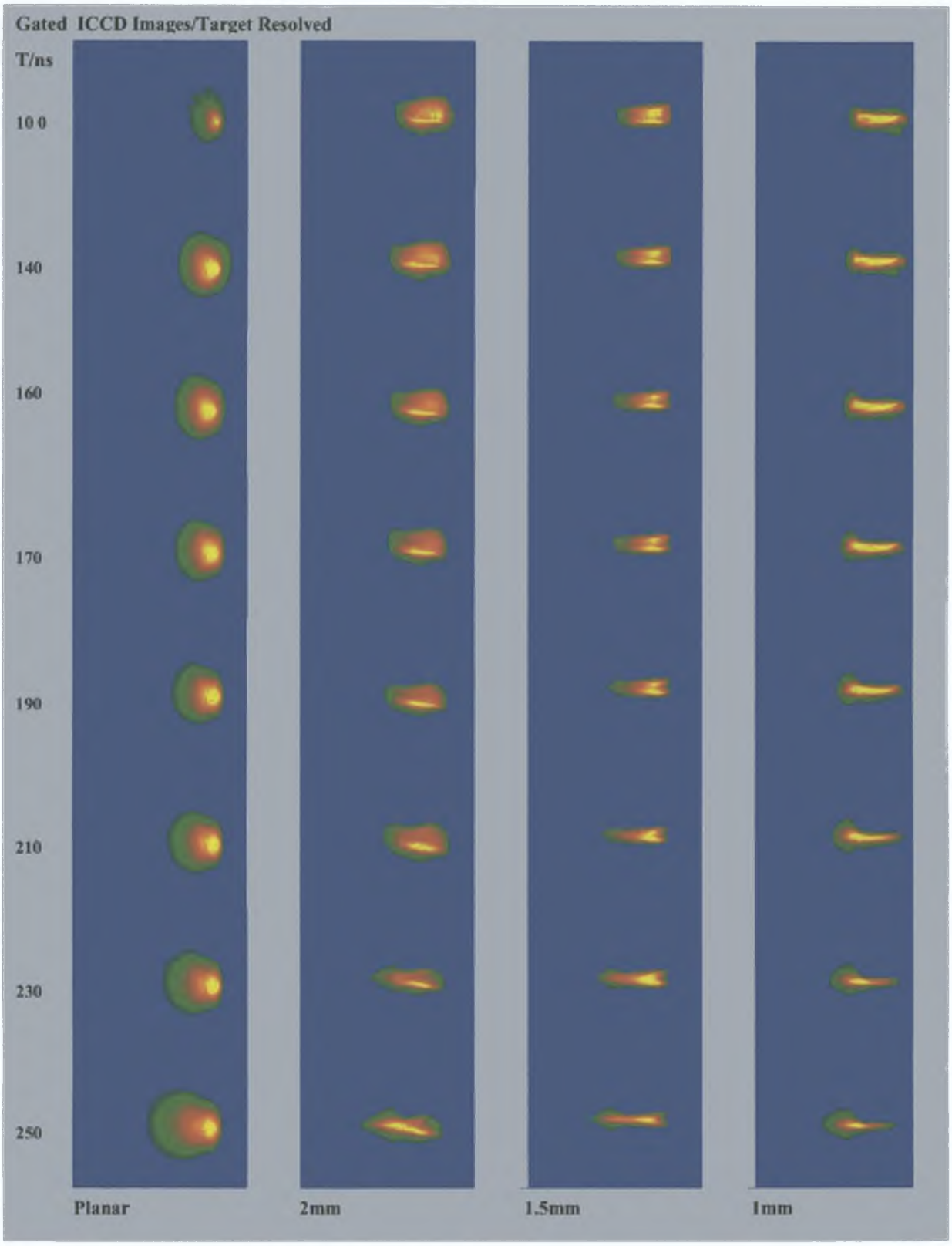
Gated ICCD Images/Target Resolved
T/ns
100
140
160
170
190
210
230
250
Planar
2mm
1.5mm
1mm

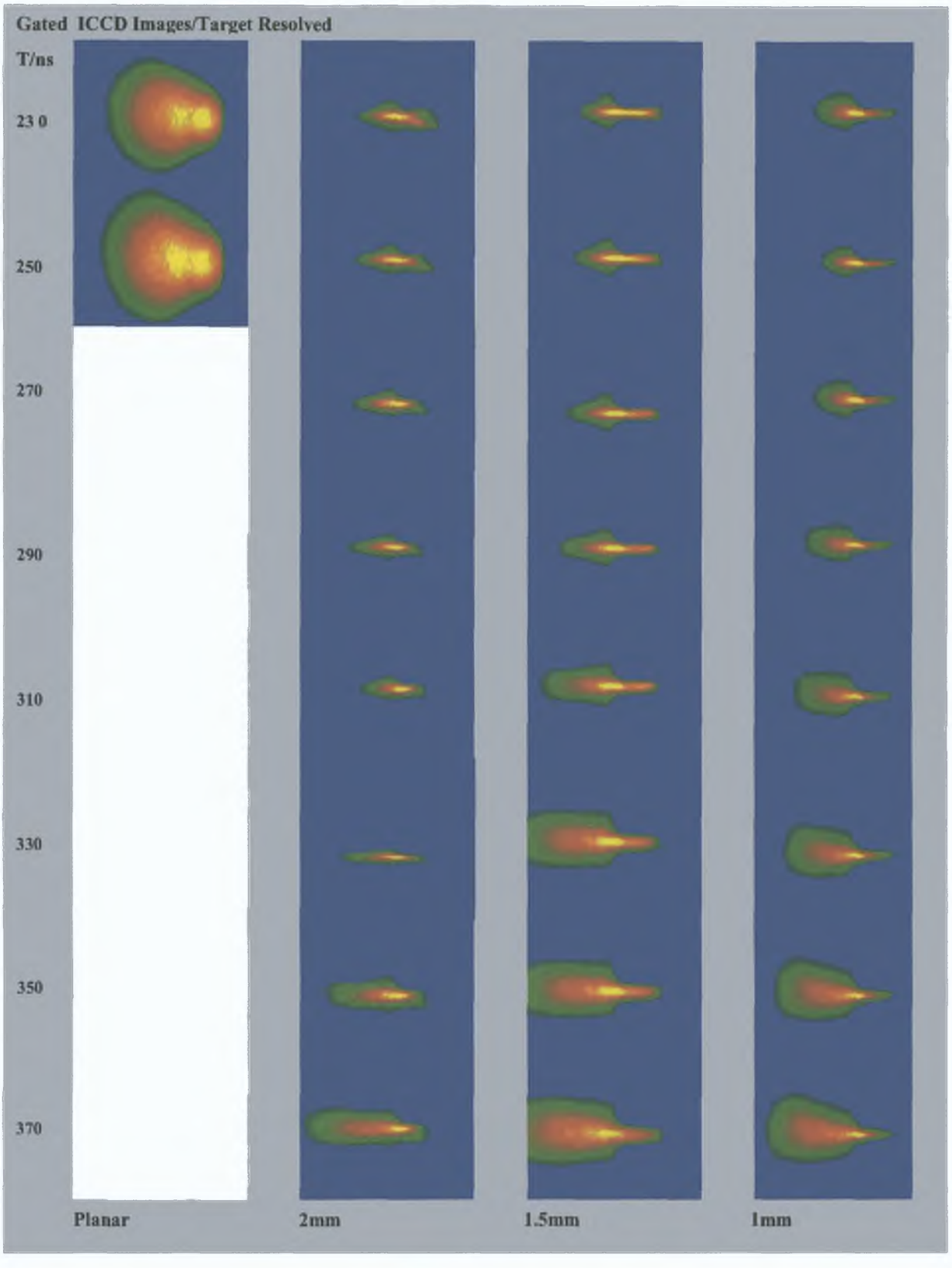
Gated ICCD Images/Target Resolved
T/ns
23 0
250
270
290
310
330
350
370
Planar
2mm
1.5mm
1mm

Chapter Six: Space and Time Resolved EUV Emission Spectroscopy of Laser Plasma Plumes

Introduction

This chapter discusses results from the range of experiments performed in the space-time range termed 'near field', using space and time resolved EUV emission spectroscopy. Here the laser generated plasma plume was studied for time scales less then 40nsec after the laser pulse. The plume's properties such as electron temperature and line width, ionization temperature, and ion space-time profiles were compared for flat and wedge targets. Double beam experiments were performed, where one laser creates a laser plasma, and another heats this plasma. This was done for planar and wedge targets to study the effects of plasma confinement on the laser-plasma coupling process. For confined plumes, enhanced temperatures, densities and emission spectra are demonstrated at early stages during and after the laser pulse. Other effects such as large increases in the forward extension of the plume, and enhanced edge velocities are also presented. Plasma re-heating by secondary laser beams demonstrated higher re-heated intensities for contained plasma than re-heated plasma from a planar target.

6 0 Overview Space and time resolved EUV studies (Near field)

In general the spectrum from a laser produced plasma consists of lines and continuum The latter arises from bremsstrahlung and or recombination radiation The contribution of the different components depends heavily on the atomic number of the target material, the power density of the laser used, and the spectral region under study The higher the atomic number of the sample the greater the contribution of continuum emission from high density collisions during early stage emission Indeed for high Z targets, continuum emission predominates and at short wavelengths, emission from the plasma is completely continuum dominated (Carroll et al[1]) Early stage (<50nsec) emission from laser plasma is dominated by continuum emission due to high densities, and moving to shorter wavelengths allows for the study of processes during the laser pulse Having seen large scale enhancements in visible continuum emission from confining targets, the next logical step was to push the space-time envelope back further However in order to probe higher energy regimes, shorter wavelength/higher energy photons had to be used Utilizing the 2 2m EUV grazing incidence spectrometer allowed the emission properties of aluminum ions in the regions below 33nm to be studied The space time domain covered by EUV emission was approximately 60nsec after the arrival of the laser pulse, and spatially the EUV emission range was approximately 1 8-2 0mm from the target surface This is almost precisely the space-time range which is off limits to visible spectroscopy due to the domination of continuum emission

6 1 EUV space-time diagnostic study

6 1 1 Experimental setup

Laser ablation was achieved via a Nd YAG laser (λ_l=1 06μm, τ_{pulse}=15nsec, E=0 78J) focused onto a planar aluminum target via a 20cm Plano-convex lens The resulting irradiance was calculated at ~0 5×10^{11}W/cm^2 with a 350μm spot size An operating pressure of ~5 0×10^{-5}mbar was maintained for all experiments The MCP detector was equipped with a gating unit (Kentech high voltage pulsar) which allowed the system to be time resolved with a sampling width of 12-14nsec By moving the bulk target and focusing lens with respect to the spectrometer slit the spatial distribution of species throughout the plume could be sampled The target was moved in steps of 0 15mm with respect to the slit and the time step was 3nsec The total spatial region studied was from the target surface to 1 8mm from the surface The EUV signal lasted a maximum of 45nsec, depending on the position being sampled The signals were shot averaged for 8 shots and the spectral regions studied were 51 5-45 92eV, 44 6-39 8eV, and 41 32-37 5eV This was required to acquire sufficient number of lines to form Boltzmann plots for AL VI and AL VIII lines, which were spread across the above spectral regions Secondly these regions all have lines for which the spectroscopic constants are all reliably known Figures 6 1 1-6 1 3 displays typical emission spectra for the regions sampled We were unable to locate any electron impact parameter for the lines studied here, thus density determination from line widths was limited to observing the relative change in the FWHM of the lines studied and interpreting this as a reliable indication of

density throughout the plume. This was done for Al VI (243A), Al VII (240A), and Al VIII(250A). These were chosen due to their strong signal, good separation from other lines and extended lifetime compared to other lines for the same stages.

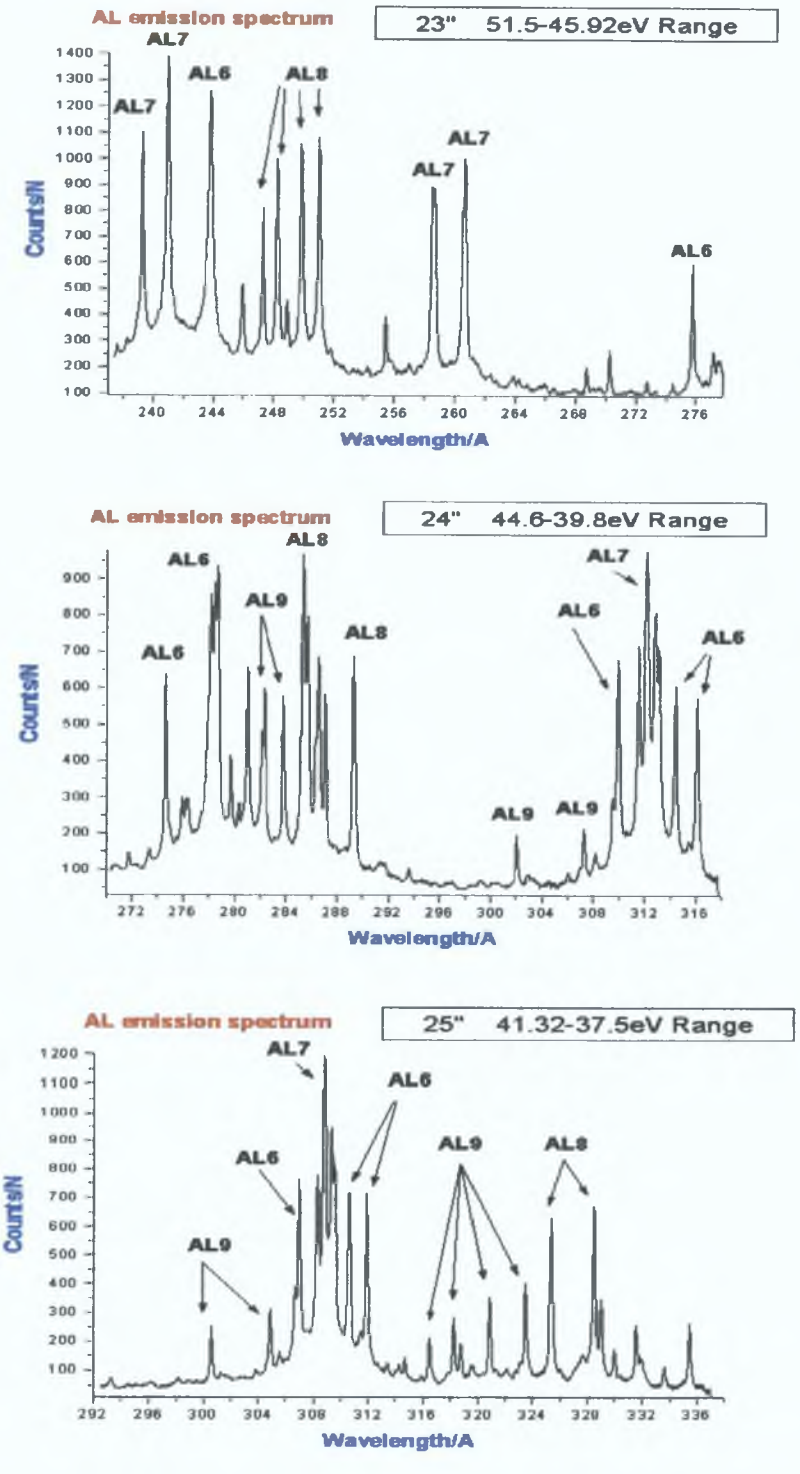

Figure 6.1.1, 6.1.2, 6.1.3: Sample spectra for the three spectral ranges studied (not from the same space time coordinates).

6.1.2: Diagnostic techniques.

In order to determine the temperature we utilized the two most reliable techniques available. Namely Boltzmann plots, which require no knowledge of the density, and ion to atom line intensity ratios which do require a value for the density. The lines chosen for the Boltzmann plots were AL VI and AL VIII. There were sufficient numbers of lines for each ion stage to justify Boltzmann plots of both ion stages. A detailed description of applying the theory to temperature calculations is given in (Khater [15]). However briefly, plotting $Ln(I\lambda^3/gf)$ (I is the area under the line λ is the wavelength of the lines, g and f are spectroscopic constants for the transition, λ^3/gf in the plots is a constant for each line represented by C), versus the upper energy of the transition, and fitting a straight line yields the electron temperature. The most useful aspect of this technique is its independence from electron density, and the range of conditions under which it can be applied. The greater the number of lines sampled the better is the stability of the plot.

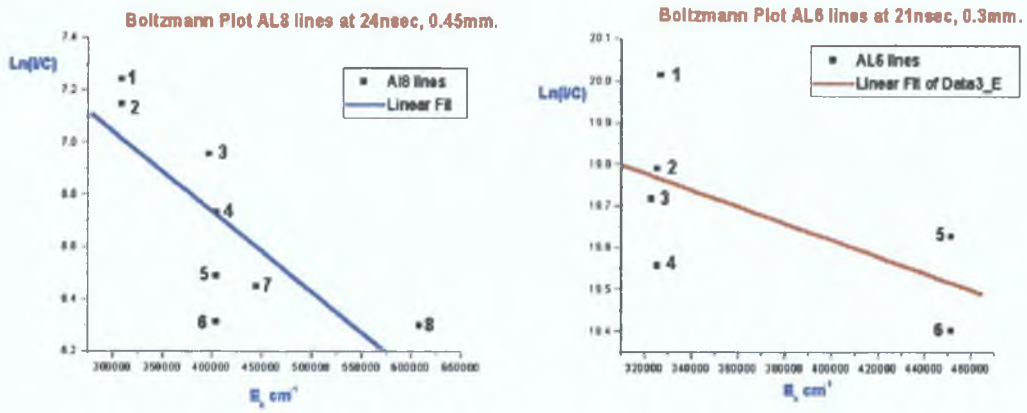

Figure 6.1.4, 6.1.5: Boltzmann plots for the various Aluminum lines in the EUV (left plot AL VIII, right plot AL VI region) used to calculated electron temperatures for space and time resolved emission studies. Given the large errors for such a fit, temperatures extracted from the above should be interpreted with caution.

Ionization stage	Wavelength (A)	gf value	Energy levels cm^{-1}
1: AL VIII	325.31	0.093254	309110-1710
2: AL VIII	328.20	0.1210598	309110-4420
3: AL VIII	285.467	0.953015	397020-46720
4: AL VIII	247.401	0.11015	404200-0
5: AL VIII	248.45	0.33426	404200-1710
6: AL VIII	250.139	0.53456	404200-44200
7: AL VIII	251.347	0.653105	444570-46720
8: AL VIII	289.12	0.6834	608100-262180

Table 7: Constants for Boltzmann plot with AL VIII lines in the EUV region.

One important issue was the variation in the EUV detectors response across its length (chapter 3, section 3.3.7). In the above Boltzmann plots, where the same line can be seen at two different detector settings, the maximum difference in the intensity of this line was ~17%. Thus in using lines from three different detector settings, one should compensate for the variation in detector sensitivity. However it was found that the ~17% in signal translated into only a ~0.15 (maximum) difference in the natural log of $I\lambda^3/gf$ for various lines. Since this

would not make a large difference to the Boltzmann plots, and since the variation across the detector is not constant at 17% it was decided not to adjust the spectra, and to thus perform the calculations with the raw data.

Ionization stage	Wavelength (A)	gf value	Energy levels cm^{-1}
1: AL VI	312.237	0.2558	323002-2732
2: AL VI	307.249	0.258821	325469-0
3: AL VI	310.907	0.20417	325469-3829
4: AL VI	308.563	0.20417	326815-2732
5: AL VI	242.766	0.6412	451396-41167
6: AL VI	275.343	0.1227	451396-88213

Table 8: Constants for Boltzmann plot with AL VI lines in the EUV region.

Although ideally one should attempt to map as many lines as is physically possible over as large a range as possible, in order to form stable Boltzmann plots, in reality this is not feasible, especially in the EUV. Here one must translate the target and focusing lens such that the spectrometer slit samples a different region of the plume. For each sample point one must then take time resolved spectra, and then for three different detector settings. Lastly as is discussed later, if one wishes to compare different targets, this procedure becomes extremely laborious with the total number of spectra which need to be analyzed reaching some 550 for each target. Ideally, one should fit a line function to the emission lines of study (i.e. a Lorentzian or Gaussian function). However given the large number of lines to be processed (for AL VIII for three detector settings, at 12 spatial points for 15 time resolved events for eight lines, =4320 lines, and six lines for AL VI=3240 lines) it was not feasible to fit manually such a large number of lines in Origin. Attempts were made to write software in MATLAB 6.0, to fit Lorentzian and Gaussian functions to lines in an automated manner for a large number of lines. While this approach was successful, given the large number of variables required for successful line function fit, the limits of the program resulted in unacceptable iteration time. It was also found that, for a handful of lines fitted manually in Origin, that MATLAB was overestimating the line width for Lorentzian fits and under estimating the line width for Gaussian fits (by ~22%). Thus a mathematically simpler method of calculating the curve area was required. It was decided to use the mid-point approximation formula to approximate the area under the lines, as displayed in figure 6.1.6.

Equ: 1.0 $$\int_a^b f(x)dx \approx \left(\frac{b-a}{n}\right)[y_0 + y_1 + \cdots y_{n-1}]$$ (Anton, [14])

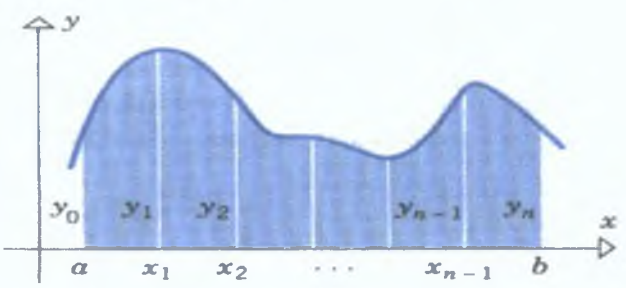

Figure 6.1.6: Mid-point approximation to irregular curve [14].

The main difference in applying a line function, such as a Lorentzian and area approximation, is the absence of a base line in the approximation. However, as pointed out by Khatar [15], the relative intensities and gf values for the measured spectral lines, as opposed to the absolute values, will not affect the calculated temperature, and will only result in a change in the intercept. Taking the Boltzmann plot from figure 6.1.4, AL VII, at 24nsec, at 0.45mm, and recalculating the area under each spectral line using Origin 6.0, then fitting a Lorentzian function and then re-plotting the Ln(I/C) values gives figure 6.1.7.

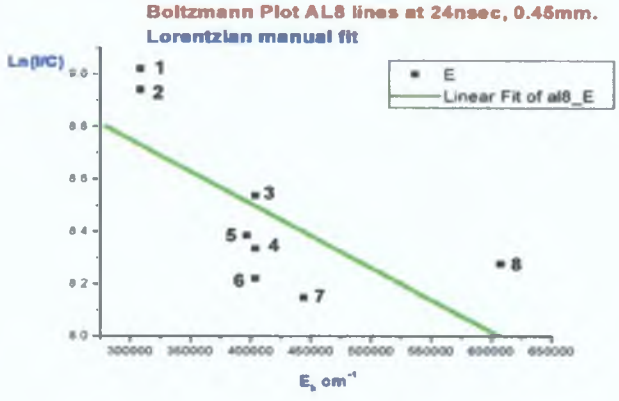

Figure 6.1.7: Manual fit of the lines in Origin 6.0, using the Lorentzian line function. Clearly the vertical scale is different due to different integrated areas, yet the linear fit is similar regarding the proximity of each point, and the slope value calculated. Again, given the grouping of points, the Boltzmann plots are very sensitive to changes in a single points value (i.e. point 8).

When one compares the automatic fitting and the tested linear fit (in Origin, figure 6.1.4), the position of the fitted line relative to the points for both the automatic fitting (figure 6.1.5), and the manual fit (figure 6.1.7) are not dissimilar. Secondly the slopes calculated are ~20% of each other (computer slope~7.06×10^{-6}, T_e~141600K, Manual slope ~5.72×10^{-6}, T_e~174800K). Although a 20% error is relatively large, one must recognize that applying spectroscopic techniques to diagnose plasma under such extreme conditions will lead to difficulties in data interpretation and theory reliability. The larger the number of lines used in a Boltzmann plot the more reliable the calculated slope and the less vulnerable the plots are to sudden shifts in the position of one point. However for the EUV range in aluminum, increasing the number of lines studied would have involved a large increase in the volume of collected data, and an even larger amount of data processing would have been required (especially given the need to map a large space-time envelope for two separate targets). Therefore, one should interpret the space and time resolved temperatures from Boltzmann plots with caution. The approach adopted should be to compare theoretical values for electron density and temperature (Dreyfus equation 1.1-1.2), ionization temperatures from atom-ion intensity ratios and Boltzmann plots with the understanding that in order to quantify a physical system, which by nature is extreme, more than one approach should be adopted.

6.1.3: Theoretical plasma parameters.

The second technique, ion-to-atom is much simpler to apply, and can operate at very low signal levels. However its chief weakness is the requirement of inputting a value for electron density. Here in the EUV, the absence of an electron impact parameter, forced us to use a substitute value. The analytical model of self-regulating laser

ablation of Phipps and Dreyfus gives the flowing expressions for electron temperature and density at the end of the laser pulse:

Equ 1.1: $T_e=2.98\times10^4\frac{m_{ion}^{1/8}Z^{3/4}}{(Z+1)^{5/8}}(I_p\lambda\tau_{pulse}{}^{1/2})^{1/2}(K)$ (Phipps et al[3])

Equ 1.2: $N_e=3.59\times10^{11}\frac{m_{ion}^{5/6}}{Z_{1/8}(Z+1)^{9/16}}\frac{I_p^{1/3}}{\lambda^{3/4}\tau_{pulse}^{3/8}}(cm^{-3})$ (Phipps et al[3])

m_{ion} is the mass of the ion in atomic mass units, λ is the laser wavelength in cm, τ is the duration of the laser pulse in sec. Thus for I_p ~$0.5\times10^{11}Wcm^{-2}$) and Z=6, these expressions give values of T_e ~14eV (185000K) and Ne~$3.6\times10^{19}cm^{-3}$. As will be shown later, the value given by Dreyfus, is in good agreement with temperatures calculated from Boltzmann plots. Taking the density from above, and simplifying the analysis by assuming a homogenous density which various by more then one half order of magnitude across the volume of the plasma at any one time instant studied (i.e. that from the centre to the edge of the plasma the variation in N_e is less then $0.5\times10^{19}cm^{-3}$), we can then apply the ion-to-atom ratio to calculate ionization temperatures (Atwee et al[5]). Given the large number of lines available, the above ratio was calculated for many different pairs of ions. Those presented here are: Al V III/Al VII (285A/309A), Al VIII/Al VII (250A/239), Al VII/Al VI (239A/243A), and Al XI/Al VIII (284A/285A).

6.1.4: Ionization equations for the EUV.

Below are the equations for the line ratio equations for lines in the EUV region used here. Multiple line ratios allow one to study the relative reliability of using this technique, and the different response for different pairs of ions.

Equ 2.1-2.11: The simplified equations below are taken from chapter five, section 5.1.5. However here using the constants from tables 7 and 8, the equations have been simplified to their most relevant variables (ionization temperature, numerical multiplier and the intensity of the two lines used).

$$\frac{I_{AlVIII}}{I_{ALVII}}=5.4717\times10^{-4}\times T_e^{3/2}\exp\left(-\frac{28.4483E5}{T_e}\right)$$ **Al8/Al7** [285.467/309.023]

$$\frac{I_{ALVIII}}{I_{ALVII}}=8.17898\times10^{-4}\times T_e^{3/2}\exp\left(-\frac{28.386E5}{T_e}\right)$$ **Al8/Al7** [289.12/309.023]

$$\frac{I_{ALVII}}{I_{ALVI}}=9.02722\times10^{-4}\times T_e^{3/2}\exp\left(-\frac{39.403E5}{T_e}\right)$$ **Al7/Al6** [309.0233/307.249]

$$\frac{I_{ALVII}}{I_{ALVI}}=9.5931\times10^{-4}\times T_e^{3/2}\exp\left(-\frac{22.161E5}{T_e}\right)$$ **Al7/Al6** [309.023/312.237]

$$\frac{I_{ALVIII}}{I_{ALVII}} = 4.83\times10^{-4} \times T_e^{3/2} \exp\left(-\frac{26.9202E5}{T_e}\right)$$ **Al8/Al7** [250.139/240.77]

$$\frac{I_{ALVIII}}{I_{ALVII}} = 2.135\times10^{-4} \times T_e^{3/2} \exp\left(-\frac{26.964E5}{T_e}\right)$$ **Al8/Al7** [250.139/239.03]

$$\frac{I_{ALVII}}{I_{ALVI}} = 8.1505\times10^{-4} \times T_e^{3/2} \exp\left(-\frac{29.4915E5}{T_e}\right)$$ **Al7/Al6** [240.77/243.766]

$$\frac{I_{ALVII}}{I_{ALVI}} = 4.8877\times10^{-4} \times T_e^{3/2} \exp\left(-\frac{22.5349E5}{T_e}\right)$$ **Al7/Al6** [239.03/243.766]

$$\frac{I_{ALIX}}{I_{ALXIII}} = 2.969\times10^{-4} \times T_e^{3/2} \exp\left(-\frac{32.467E5}{T_e}\right)$$ **Al9/Al8** [284.015/285.467]

$$\frac{I_{ALIX}}{I_{ALVIII}} = 13.35910^{-4} \times T_e^{3/2} \exp\left(-\frac{35.2296E5}{T_e}\right)$$ **Al9/Al8** [321.027/325.31]

$$\frac{I_{ALIX}}{I_{ALVIII}} = .47066\times10^{-4} \times T_e^{3/2} \exp\left(-\frac{34.89E5}{T_e}\right)$$ **Al9/Al8** [305.045/285.407]

ionization energies (Taken from the NIST data base, required when used as lower stage in the ratio)

Al VI 190.549ev

Al VII 241.833ev

Al VIII 284.745ev

We observed that ionization temperatures calculated from the intensity ratio of pairs of ions of the different charge gave small but acceptable differences in temperature, however as the ion stages used increase in degree of ionization, the peak temperature also increases. For example the peak ionization temperature from the ratio of Al VII to Al VI was seen to peak at 210000K (18eV), while the peak value for the ratio of Al IX to Al VIII was 260000K (22eV). Equally so, differences in temperature exist for the two Boltzmann plots used. In the analysis, we assumed that the plasma is in LTE (complete space-time plots of T_{ionz} for the various ratios are given later, fig 6.6.1-4, page 256).

6.1.5: Equilibrium and density considerations.

The values of electron density and temperature allows us to check our assumption. LTE is said to exist if the time between collisions of the particles in the plasma is small compared with the duration over which the plasma undergoes significant change. Thus when the electron collisions are the major processes of de-excitation, the system is said to be in LTE (Voevdin et al[4]).

Equ.3 $N_e \geq 1.6 \times 10^{12} \times T^{1/2} \Delta E^3$

Equation 3 gives the minimum density condition for the plasma to be considered to be in LTE ΔE is the largest energy transitions for which the condition holds In our work ΔE is 75 41eV for AL VIII (289 12nm) The highest temperatures measured (discussed later) were in the range 250000K-290000K, this gives a lower limit on the right hand side of equation 5 of $1\ 4\times10^{19}cm^{-3}$ Although we have estimated the electron density from equation 1 2, and simplified the analysis by not taking into account the obvious variation in the numerator for N_e over the plasma volume, the good agreement between Phipps and Dreyfus temperature (equation 1 1), and all temperature profiles calculated here, reinforce our assumption of LTE, or at least close convergence of plasma conditions to those associated with LTE

6 1 6 Laser-surface interaction

When the electromagnetic field of the incoming laser pulse contacts the target surface it penetrates into the bulk material by only a fraction of a wavelength However the electric field is sufficiently intense to ensure conduction and vaporization of the surface to occur The r m s electric field strength E in Vm^{-1} is given by $E=19\ 4\phi^{1/2}$ so that for $\phi=10^{16}$-10^{22} Wm^{-2} E ranges from 2×10^{9} to 2×10^{12} Vm^{-1} Thus the net effect of this transient interaction is the generation of a thin plasma layer close to the target surface The 'pre-plasma' is relatively cool and of low density The extent of this pre-plasma generation depends heavily on the wavelength and the pulse duration of the beam The initial contact of the laser pulse with the target creates a low temperature high density plume on the surface As the laser pulse continues to arrive at the target the electrons in the pre-plasma begin to absorb the incoming laser energy and increase their kinetic energy substantially The increase in electron energy leads to enhanced collisional ionization and thus higher electron densities Thus the rate of photon absorption by electrons and the resulting increase in electron densities increases until Ne approaches a critical value At this point reflection from the front surface and high level absorption at the front of the plume dominates This lowers the amount of energy reaching the target surface, resulting in a decrease in plasma generation The large increase in kinetic energy of the particles at the frontal regions of the plume leads to rapid expansion The electron density thus decreases, and the laser pulse can again reach the target surface This changing processes continues until termination of the laser pulse The density, temperature, and dimensions of the plasma adjust in a such a manner to ensure that the plasma absorbs the same amount of laser energy to maintain a self-regulating regime This assumption is valid in laser produced plasmas where the thermalization time τ_{ei} is significantly less than the plasma expansion time, resulting in the establishment of a uniform temperature in the plasma The thermalization time of energy exchange between electron and ions during collision can be estimated from the relation (Harilal et al[5]),

Equ 4 $$\tau_{ei}=\frac{252MT_e^{3/2}}{\ln(\Lambda)n_e}$$ where Equ 5 $$\Lambda=\frac{3(kT)^{3/2}}{4(\pi m_e)^{1/2}e^3}$$

and ln(Λ) is the Coulomb logarithm, which involves dynamical information about the ion-electron collisions and for laser produced plasmas takes a value ranging from 5 to 10, and M is the atomic weight. With $n_e=5\times10^{19}$ cm^{-3} and $T_e=180000K$, the relaxation time is on the order of ~0.4nsec, which is much smaller than the plasma expansion time or the laser pulse (16nsec).

6.1.7: Laser absorption mechanisms.

The two dominant mechanisms responsible for plasma absorption at the laser irradiance levels used in this work are inverse bremsstrahlung and photo-ionization. Inverse bremsstrahlung absorption α_{ib} via free electrons is approximated by:

Equ 6: $\alpha_{ib}(cm^{-1})=1.37\times10^{-35}\lambda^3 n_e^2 T_e^{1/2}$ (Gamely et al[7])

where λ is the wavelength of the laser in μm. Laser absorption due to inverse bremsstrahlung increases exponentially from low irradiances (<10GW cm^{-2}) to higher values (>15GWcm^{-2}) and saturates at higher values (65GWcm^{-2}). Given the N_e^2 and $T_e^{1/2}$ dependency in equation 6, it is not unexpected that continuum emission exists predominantly during and just after the laser pulse, peaking at approximately near the peak of the laser (figure 6.2, determined by averaging a 5nm window of continuum values centered at 22.5nm).

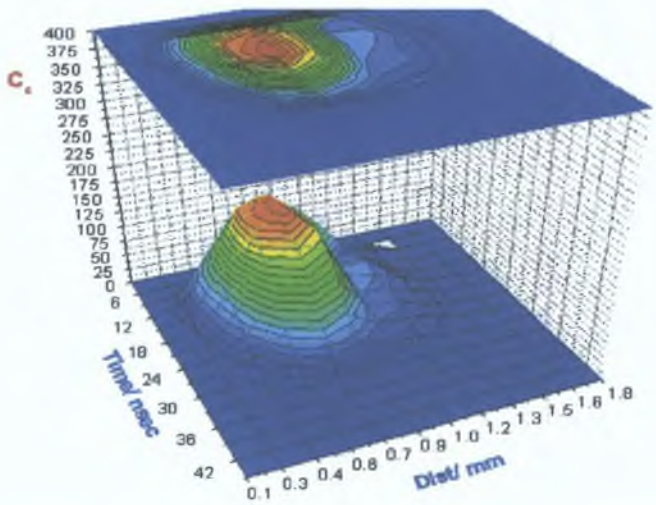

Figure 6.2: Continuum Coefficient (C_C) space time profile at 22.5nm. Significant EUV continuum emission is highly localized spatially and peaks near or just after the peak of the laser pulse.

Continuum emission, especially at short wavelengths, is indicative of high electron density and temperature, and at EUV wavelengths, is highly localized in time during the laser pulse, and spatially near the target surface, as figure 6.2 shows. The other important mechanism, absorption via photo-ionization can be estimated from Kramer's formula:

Equ 7: $$\alpha_{ib}=\sum_n 7.9\times10^{18}\left(\frac{E_n}{h\nu_l}\right)^3\left(\frac{1}{E_n}\right)^{1/2}N_n$$ (Gamely et al[7])

where E_n and N_n are the ionization energy and number density of the excited state n, h is Planck's constant, ν_l is the laser frequency (2.828×10^{14}Hz), I is the ionization potential of the ground state atom. The absorption coefficient of photo-ionization is obtained by summing up all the excited states for which ionization energies are smaller than the laser photon energy. Since excitation potentials of atomic transitions in aluminum are much greater than the photon energy of the pump beam used (1.171eV), direct photo-ionization by the absorption of the laser photon is ruled out. The only possibility for this type of ionization to occur is by simultaneous absorption of a number of photons. The ionization rate in case of photo-ionization is given by:

$$\text{Equ 8:} \quad W_n=\omega_0 n_e^{3/2}\left(\frac{\xi_{0s}}{I_i}\right)^p \quad \text{(Gamely et al[7])}$$

where $p=I_i/\omega_0\hbar$ is the number of photons absorbed and ξ_{0s} is the electron oscillation energy which is given by $\xi_{0s}=0.093\lambda^2 I(eV)$, where I is the power density used for the ablation (Wcm^{-2}). During the initial stages of the laser pulse, low electron and ion densities and large numbers of neutral atoms are present. Free-Free transitions involving neutral atoms may provide another absorption mechanism. When the ion density increases slightly, free-free transitions take over and become the dominant mechanism for laser absorption. The absorption coefficient is given by equation 9 (in terms of the ion density) and equation 6 (in terms of the electron density):

$$\text{Equ 9:} \quad \alpha_{ib}=3.69\times10^{8}\left(\frac{Z^3 n_i^{\,2}}{T^{1/2}\nu^3}\right)\left[1-\exp\left(\frac{-h\nu}{kT}\right)\right] \quad \text{(Atwee et al[5])}$$

Here X, n_i, v, and T are the average charge, ion density and frequency of the laser, and temperature of the plasma. The laser energy is highly absorbed if $\alpha_{ib}X$ is large, where X is the dimension perpendicular to the target of the expanding plasma. With the absorption coefficient having a n_i^2 dependence, the plasma absorbs the laser energy only close to the target surface, where the density is high. This can clearly be seen in the space time plot of line width for various lines below.

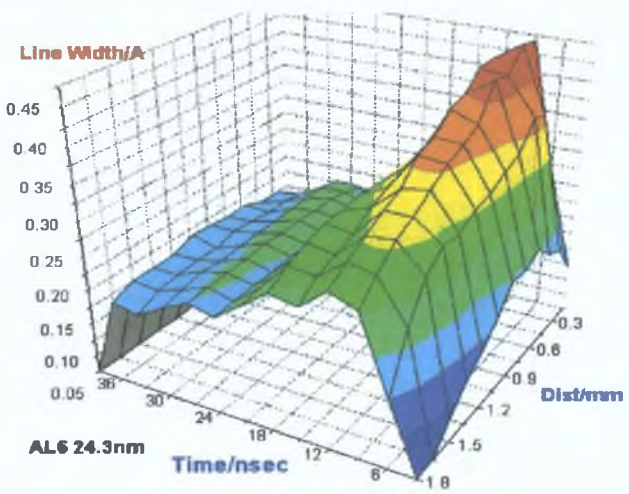

Figure 6.3.1: Space time profile of Lorentzian line width for Line width profile for AL 6 (24.3nm).

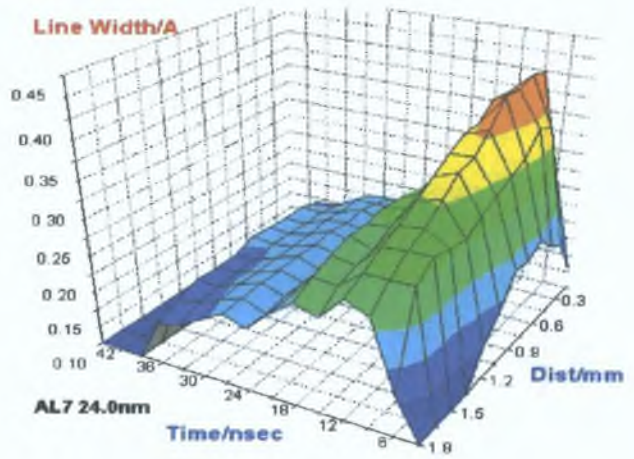

Figure 6.3.2: Space time profile of Lorentzian line width for AL7 (24.0nm).

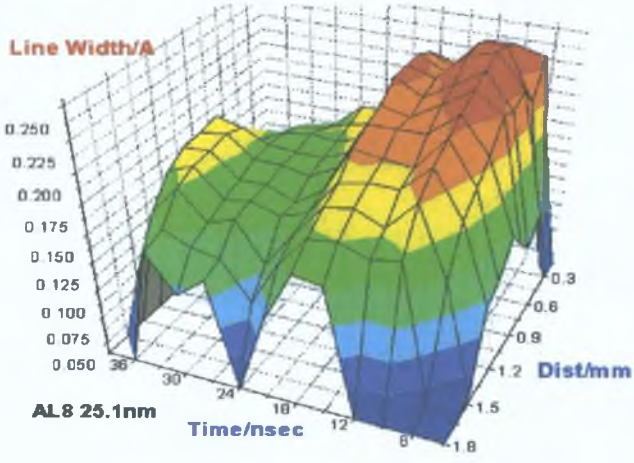

Figure 6.3.3: Space time profile of Lorentzian line width for AL8 (25.1nm).

The Line width has a clearly defined peak close to the target surface for all three ion stages. However the decay profile is not consistent with that from the Anisimov model, which gives a $(XYZ)^{-1}$ profile for density and a $(XYZ)^{-(\gamma-1)}$ profile for temperature. The peak line width from both the 3D plots for line width and the above profile at 6nsec, clearly indicate that the peak density occurs away from the target surface, and during the peak of the laser pulse. The forward nature of the line width profile after the main peak does indicate frontal heating of the plasma during the laser pulse. If an electron impact parameter (W) was available for these lines then one could infer a value for the electron density in the plume at the peak of the laser pulse and compare this to the critical density for aluminum plasmas. A 'W' value would also make ionization temperatures from atom-ion ratios in the EUV more accurate (as the theory for atom-ion ratios requires a value of N_e) it would then allow other temperature measurements, such as Boltzmann plots (which are independent of N_e) to be more accurately compared. Despite the absence of N_e values, interpretation of the line width profiles does allow some trends to be deduced. The line width profile at 9nsec in figure 6.4 (above), does not go to zero at large values of distance from the target surface.

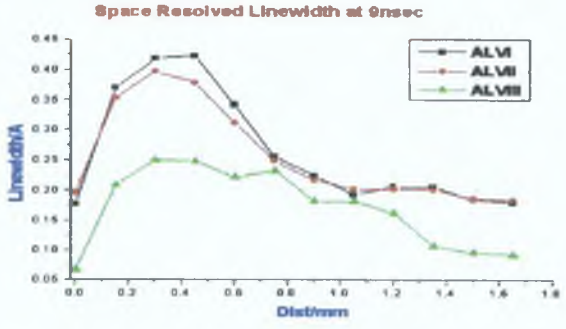

Figure 6.4: Line width spatial profile at 9nsec (peak of the laser) for three ion stages.

This can not be due to instrument limited broadening, as this has been determined to ~0.05A (chapter 3, section 3.3.6), far lower than the above values for the line width. The absence of a strong decreasing slope in the line width would infer laser pulse absorption. This would lower the density at the target surface as the beam reaching the target is attenuated via absorption from free electrons.

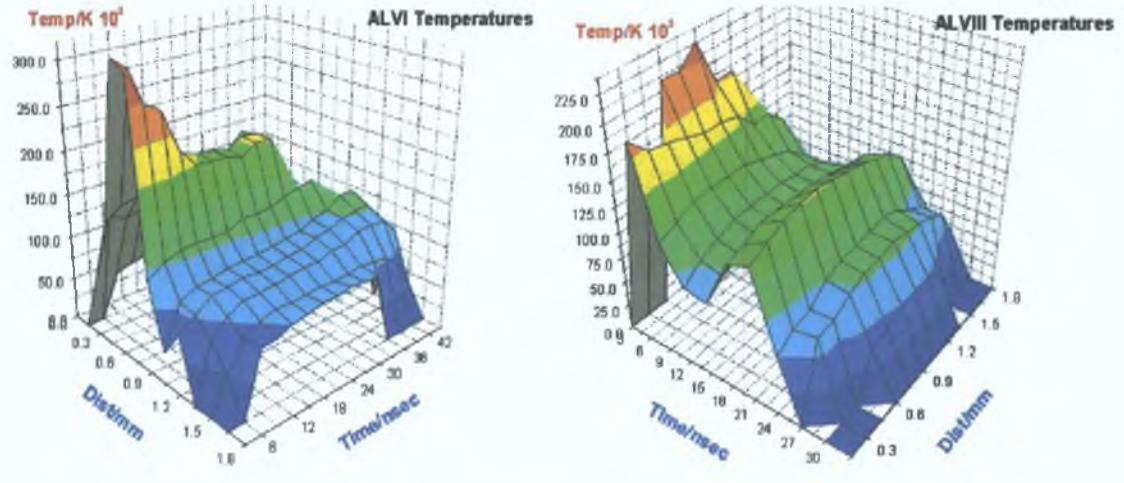

Figure 6.5.1, 6.5.2: Electron temperatures for AL VI and AL VIII (via Boltzmann plots)

Considering the Boltzmann temperature plots for AL VIII, ALVI (figures 6.5.1, 6.5.2) one can clearly see that the peak temperatures reside close to the target surface, during the peak of the laser pulse. Thus if inverse bremsstrahlung is to predominate it would do so relatively deep inside the plasma, during the laser pulse. The enhanced kinetic energy of the ions near the front of the plasma would lead to higher expansion velocities and lead to the more extended lower density region seen in figure 6.4, which one must recall displays the spatial profile of line widths at 9nsec (peak of the laser pulse).

6.1.8: Plume dynamics.

From [2] the standoff distance , i.e. the distance from the surface where laser absorption occurs is x_l. Where this value is small in comparison to the spot diameter d_s a one dimensional expansion of the plasma occurs , where $\delta_t = 0.071$. λ is 1064nm, M is 27, τ is 16nsec, Z=9, and Φ is 5×10^{10}W/cm^2.

Equ.10: $X_l/\text{cm} = 1365\left[\frac{\delta_l M^{7/16} Z^{5/8}}{(Z+1)^{11/16}}\right] \times (\Phi^{3/4} \lambda^{7/4} \tau^{7/8})$ (Liu et al[2])

When the x_l is calculated, if it is much less then the spot diameter then a one-dimensional expansion perpendicular to the target surface occurs within the plasma. Here x_l is 10.2nm. This value is much smaller then the laser spot diameter (350μm), thus $x_l/d_s \ll 1$; validating the assumption that the plasma expansion is 1-dimensional.

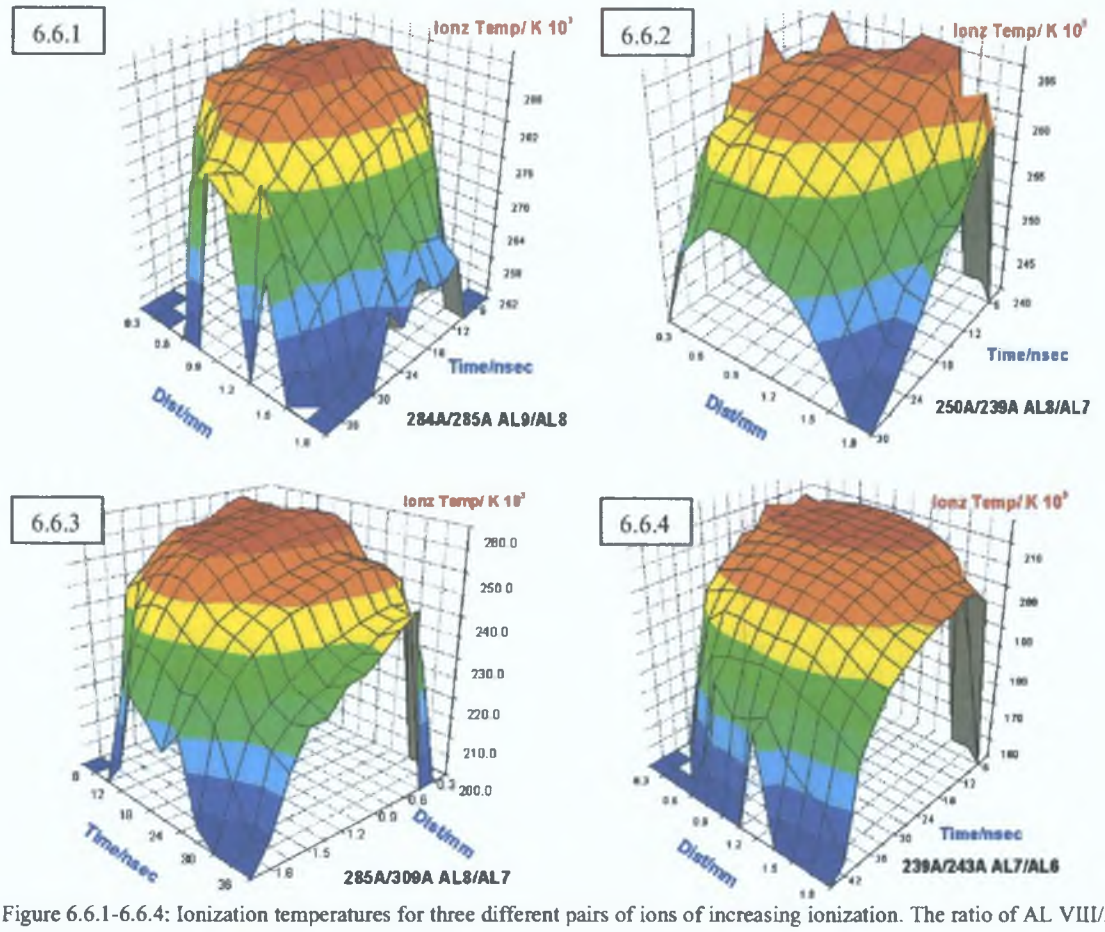

Figure 6.6.1-6.6.4: Ionization temperatures for three different pairs of ions of increasing ionization. The ratio of AL VIII/AL VII is shown for two separate pairs, giving slightly different peak temperatures.

Thus the expansion of the plume parallel to the target surface is negligible, thus reinforcing the proposed heating of the frontal plume as a reason for the extended nature of the line width profile in figure 6.4. Observing figure 6.6.1-6.6.4, the most pronounced difference is the relative sensitivity of the space time plots as the ionization levels increase. The ratio of AL VII/AL VI (fig 6.6.4) is almost constant over a large area, bounded by the duration of the laser pulse in time, and extending for 1mm from the target surface. Upon termination of the laser pulse the ionization temperature for this pair drops rapidly. In fact all plots display this behavior for a limited space time region. The trend is that of constant temperature for a larger space time region as the ionization stage of the pair decreases, the constant region also extending out further from the space time origin. The slope of the decay is also most dramatic for the higher ion stages. One might argue that this is a

consequence of the higher stages decaying faster as the plume expands and cools If the energy difference in the upper levels between the line pairs is calculated (ALIX/ALVIII-4 69eV, ALVIII/ALVII-9 4eV, ALVIII/ALVII-1 38eV and ALVII/ALVI-3 6294eV) and then the ionization energy of the lower stage is included (ALVIII-284eV, ALVII-241eV, ALVI-190eV) to give the total energy difference between the ion pairs which is (used in equation 8, chapter 3, section 2 1 4) then equal to 279eV-ALIX/ALVIII, 232eV-ALVIII/ALVII, AL VIII/ALVII-138eV and 193 6eV-ALVII/ALVI Thus as a consequence of the ionization energy of the lower ion stage, the energy difference is larger for ALIX/ALVIII and lowest for ALVII/ALVI The larger the values of ΔE in the exponential term of equation 3 (chapter 3, sec 2 1 4) the steeper the temperature dependent curve (which represent the expected atom-to-ion ratio) and as a consequence the more responsive the calculated ionization temperatures will be to small changes in the intensity ratio of both lines

Thus ultimately to ensure the best possible response curve in converting intensity ratios to usable temperatures the highest ionization stages should be employed However since such high ion stages would be relatively short lived both spatially and temporally, this would severely limit their applicability Thus ionization temperatures, although involving two ionization stages are a reasonable indication of the relative conditions seen by each ion stage in the plasma The termination of the laser pulse marks the beginning of rapid temperature decay for all ion pairs However spatially the rapid decay occurs further back as the upper ion stage increases For AL IX/AL VIII, 0 5mm from the target surface, for AL VIII/AL VII, 0 65mm and for AL VII/AL VI the distance is approximately 1mm

6 1 9 Temperature trends

The Boltzmann plots for AL VI display a highly localized temperature peak bounded by the laser pulse (figure 6 5 1), and defined within a region 0 4-0 9mm from the target surface The decay profile in time matchs that seen by [9], and the space time plot shows two distinct regions Firstly, a high temperature region, bounded by the duration of the laser pulse, and showing a non-linear fast decay profile, and a second region, of lower temperature, decaying slowly This is in conflict with ionization temperatures, but direct comparison cannot be made given that the latter involves two separate ion stages The Boltzmann plot temperatures for AL VIII displays (figure 6 5 2) an unusual space time profile Again the peak temperature is bounded by the laser pulse and close to the target, however the increase seen at 21nsec over the complete spatial region is unexpected The secondary increase in the space time plot is both smooth and of lower peak value than the primary peak We noted that figure 6 3 3, displaying the line width of AL VIII is not as smooth as that of AL VI or AL VII There is no well defined peak, and the decay profile is not a smooth curve, but an extended main peak followed by a plateau region and finally a sharp decrease in the line width Thus the line width profile and ionization temperature profile in space and time for AL VIII are not dissimilar The same similar decay profile is seen for the line widths and Boltzmann plot temperatures for AL VI The peak line width and peak electron temperature both occur at the same space time point, and decay in the same manner In [9] the authors studied the temporal decay of a Boron laser plasma in the X-EUV Their studies indicate that plasma expands isothermally within the duration of the laser pulse, however it expands adiabatically after the laser pulse During this expansion the thermal energy is converted into kinetic energy and expansion occurs along side a rapid decrease in

temperature Indeed such a rapid expansion would lower the local density greatly and this is observed from figure 6 3 1-6 3 3, where the line width of the three lines studied is seen to decay sharply after the laser pulse

6 1 10 Conclusion

In summary we have used space and time resolved EUV spectroscopy to map the properties of highly charged ions in a aluminum laser plasma, at early stage of laser plasma generation and expansion, where continuum dominated UV/VIS spectroscopy is unusable The ionization temperatures and Boltzmann plot electron temperatures of similar values numerically with Phipps and Dreyfus model of self regulating laser ablation and plasma formation (equations 1 1, 1 2) The temporal profile of temperature, and line widths related to density are in good agreement with other authors [10, 11] We have observed a region of almost constant temperature in space and time for various line ratios, the area of which increases as the ion stages in the ratio calculation decreases This is associated with lower responsiveness of the intensity ratio calibration curve due to smaller energy differences between the upper level energies of the associated lines and the lower ionization energy of the lower stages Peak line widths are seen to peak away from the target surface and occur at a point localized within 0 3mm of the surface The peak line width shifts back in space and time for higher ion stages The reliability of spectroscopic techniques during and just after the laser pulse is questionable, given the insensitivity of intensity ratios, and the small number of lines available for Boltzmann plots However the space-time profile of both experimental techniques is not in question, i e a decay profile which displays peak temperatures at or near the space-time envelope covered by the laser pulse, and temperatures which decay as the space time coordinate increases The median peak temperature inferred by both experimental techniques is approximately 260000K The temperature at the termination of the laser pulse, as given by equation 1 1 (Dreyfus) is 185000K, and the peak temperatures at this time from the data are 200000K (AL VI Boltzmann plot), and 155000K (AL VIII Boltzmann plot), while ionization temperatures averaged for all ratios gives T_e~240000K at the end of the laser pulse Thus to conclude, one could state that although diagnostic techniques in the EUV, and at early timescales are difficult, they can provide a upper limit on the peak temperatures within the plasma

Initially this body of work was undertaken to characterize the response and viability of the gating unit for the EUV detector, and then secondly to attempt to expand the data available for interpretation of laser plasma generation, i e other than visible emission spectra and probes We attempted to employ various diagnostic techniques in this spectral range and to test their applicability in the EUV The lack of responsiveness and sensitivity of ion ratios at early timescales for lower ionization stages limits their use in the EUV during the laser pulse and for this system, up to two laser pulses widths after the pulse arrival onto the target Line width measurements, as an indication of plasma density, are stable even during the laser pulse However the absence of an impact parameter in the EUV is a major obstacle to early phase electron density measurements To conclude, early phase plasma diagnostics in the EUV range are feasible, but should be considered with a degree of openness and caution

6 2 Overview

In chapter five, enhanced plasma parameters in the visible were observed for plasma confined within a rectangular cavity The earliest point in the plasma lifetime when lines emerged from the continuum was 50-70nsec Thus meaningful measurements earlier than ~60nsec were unobtainable In utilizing grazing incidence EUV spectroscopy, comparisons could be made during this early phase between EUV emission from planar targets and EUV emission from confining targets This then extended the space time envelope back to the arrival of the laser pulse at the target Secondly in studying the EUV emission from wedge targets, the enhancement trends seen in the visible could be confirmed for earlier time scales

6.3 Enhanced EUV emission from laser generated aluminum plasma in confining cavities

6.3 1 Experimental setup

The experimental conditions used are identical to those reported above, however 5 shots were averaged instead of 8, this was due to the limited area within the cavities Secondly this study focused on the 24" range (44 6-39 8eV) only Figure 6 7 displays a typical spectrum for the regions sampled In attempting to study space and time resolved behaviour, we found that the effects of interest occur across a range of spatial regions, but at selected times only This is an aspect of target configuration influence on plasma dynamics that is well established in the visible, but not the EUV Our studies focused on AL VIII (289 12A) This line was chosen due to its strong signal, good separation from other lines and extended lifetime compared to other lines for the same stage The target used (other than the planar target), was also of aluminum The cavity was machined from a block, and was rectangular in shape, 1 2mm in height and 3 5mm in depth The main impetus for studying emission at such short wavelengths is to extend the study of target configuration effects on plasma generation and evolution The only means available for very early studies (<50nsec) of plasma behaviour is short wavelength spectroscopy Secondly, early stage studies are by default both spatially limited and occur during the laser pulse, thus both imaging and electrostatic diagnostics are useless under such constraints VUV and Visible emission spectroscopy are continuum dominated in the spatial temporal range studied here Thus one is forced to use grazing incidence emission spectroscopy, which when time resolved can provide information on plasma dynamics from 'first-light' EUV signal up to 50nsec after the arrival of the laser pulse

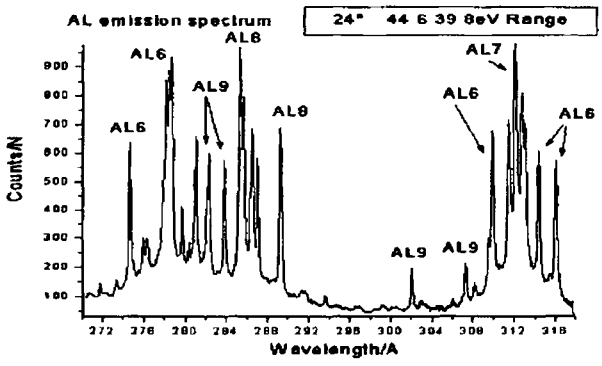

Figure 6 7 Sample spectra for the spectral range studied.

Regarding diagnosing plume dynamics within the cavity, as stated in section 6.1.4, we have found that line ratios when used for temperature determination, are somewhat insensitive under such extreme conditions, however their peak values for temperature are not in conflict with the model by Dreyfus and Phipps.

6.3.2: Early phase emission.

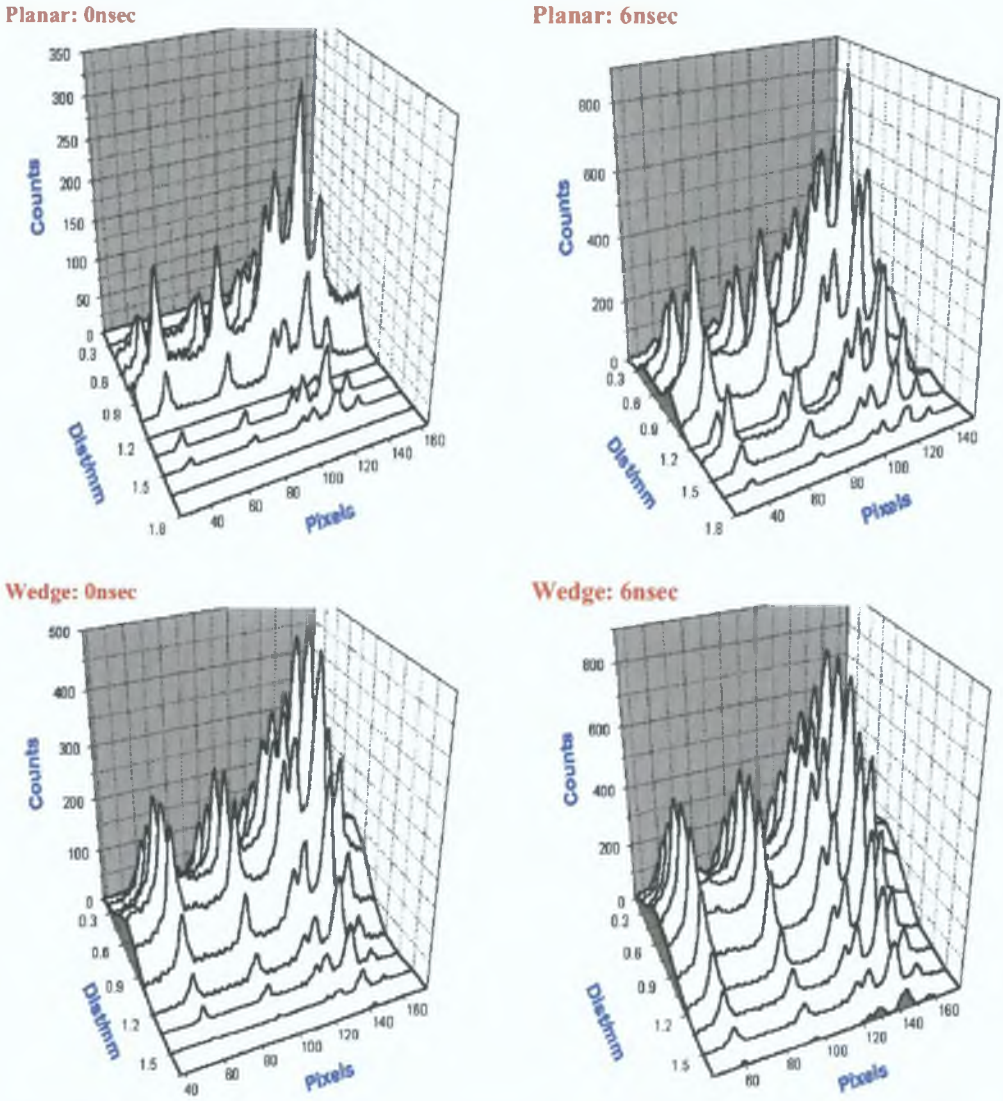

Figure 6.8.1-6.8.4: Space and wavelength resolved spectra at 0nsec (first signal) and 6nsec for both planar and wedge targets. The extent of the continuum in the wedge relative to the planar is pronounced, especially at 0nsec, as is the forward extension from the back surface. Previously this had been observed in the visible. Plasma generated within the cavity had displayed a spatially enhanced peak value of the continuum, while the spatial width (extent of forward extension) and the position of the peak continuum were dramatically shifted forward in comparison to the planar target.

Its clear from figures 6.8.1-6.8.4, that not only is the continuum enhanced considerably in the wedger, but is shifted forward and more spatially extended at early timescales. This can only be accounted for via absorption of the laser pulse in the low temperature plume which forms at the onset of the laser pulse. From section 5.1.2, visible

imaging of laser plasma generation in rectangular cavities (wedges) displayed, a collimated, low intensity plume within the cavity moving away from the target surface during the laser pulse (15nsec long) The peak intensity in the cavity is distributed over a much larger range spatially This would indicate that the absorption of the laser pulse is occurring further from the target surface in the wedge However as stated, such a process usually occurs due to higher densities at the target surface, resulting in absorption of the beam in the frontal region of the plume via inverse bremsstrahlung As can be seen from the spectra at 0 65mm (figure 6 9 13) the plasma is substantially enhanced over that of the planar target The relative difference in the peak count of the AL IX lines grouped at 284A relative to the AL VIII at 285A indicates a highly excited and energetic plume, and such high charge states would indicate a high collisional rate within the plasma Later timescales show both plasmas converging in their spectral properties (figure 6 9 5-6 9 7-profiles and 6 9 14-15-spectra) In trying to understand how the cavity causes such unusual differences in both line and continuum emission, we must consider the differences in spectral line emission first From studying EUV emission from flat targets (section 6 1) it was already found that peak lines and continuum emission occurs well away from the target surface, and this was so for a flat target Thus under ordinary conditions the pre-plasma formed at the leading edge of the laser pulse, is absorbing the main body of the laser energy and is doing so relatively far away from the surface, as indicated by the position of the peak continuum from visible studies (section 5 1) This pre-plasma is relatively cool and of low density However considering the difference in the spectra at 0 15mm at 3nsec, the wedge target displays enhanced line emission but relatively little continuum emission Thus the pre-plasma formed within the cavity is already displaying significant differences in line emission intensity Given the ion profiles at 3nsec, we can see that the pre-plasma is extended well ahead of the target surface The peak ion profile for both targets displays the peak emission at similar distances, yet the spectra at these points, especially at the peak have radically different continuum levels High level continuum, being indicative of large numbers of free electrons under going collisions, and subsequently causing ionization enhancement is clearly seen in the spectra from the wedge plasma at 0 65mm at 3-6nsec

6 3 3 Spectra and ion Profiles

Considering figures 6 9 1-15 This is especially clear in the peak intensity of AL IX lines at 284A, 300A and 305A Spectral emission at 0 65mm after the laser pulse (~12nsec) still displays the enhanced wedge emission for both continuum and lines, but the differences are less stark than those at early timescales, during the laser pulse Indeed further out (1 35mm at 21nsec) the spectra clearly show the wedge plasma emission decaying rapidly below that of the planar spectra Both the termination of the laser pulse, leading to rapid expansion, and the collimating effect of the wedge all contribute to a faster rate of thermal decay of the plasma in the cavity (as is evident from the ion profiles) The role of conductive decay into the target (the wedge having a much larger surface area) cannot be ignored, even at such early timescales Given the extent of the pre-plume extension, self-focusing of the laser beam in the plasma cannot be ignored This is due to density gradients seen by the beam as it penetrates the plasma edge Hora (Hora, 1981 [12]) derived the laser power threshold for non-linear force self focusing of a laser beam in a plasma,

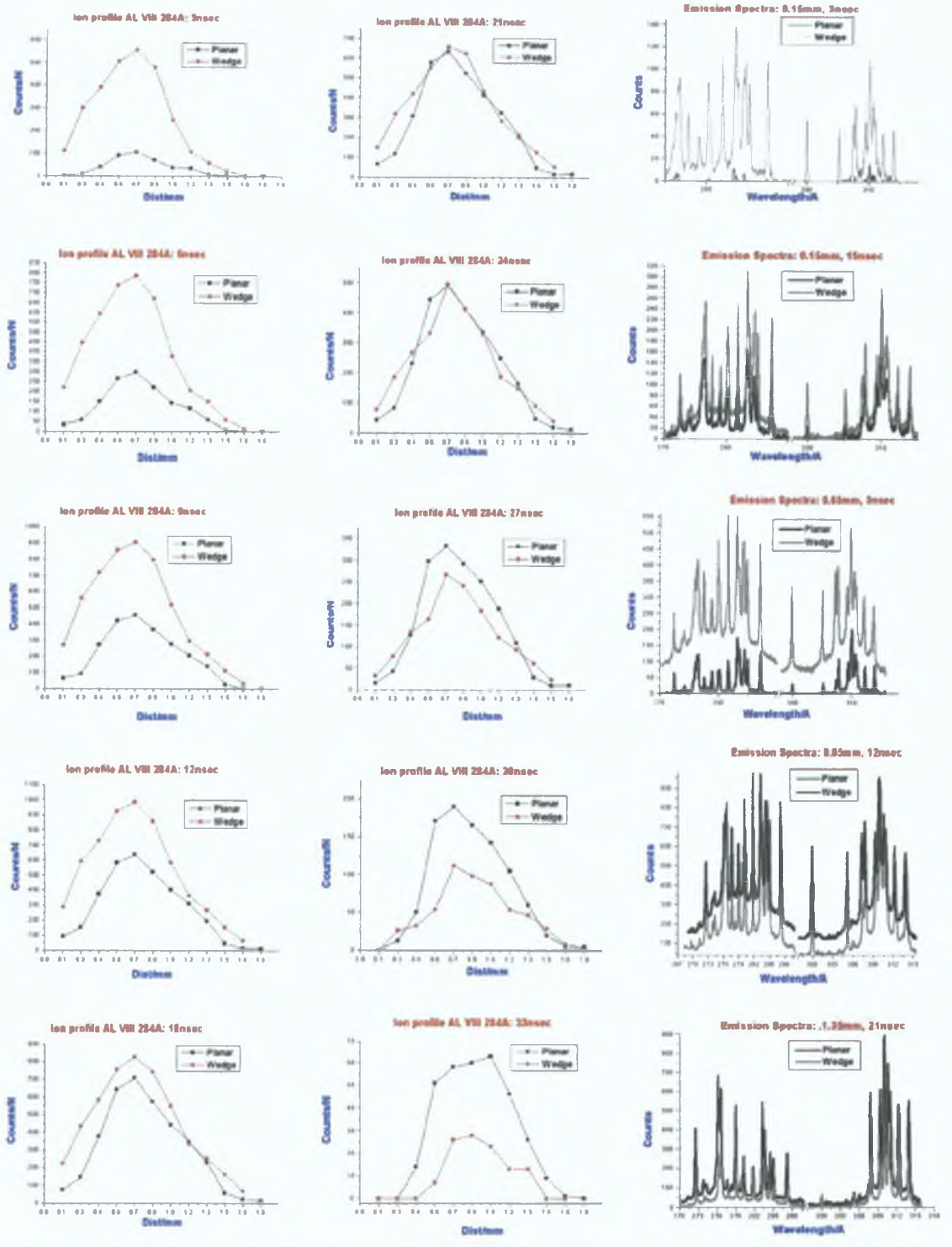

Figure 6.9.1-6.9.15: Peak intensity space resolved ion profiles of AL VIII (284.12A) for selected delays after 'first signal'. The most pronounced trend is the large scale enhancement of the ion profile at early timescales and close to the target surface where the effects of cavity containment are more pronounced. As seen in earlier work, enhanced temperatures and the collimating effect of the cavity, gives the line profile of the contained plasma substantial enhancement over the planar profile. However eventually the planar profile overtakes the cavity plasma, this process is dominant after the laser pulse, when the cavity plasma is free to expand, and no longer has the benefit of energy input via photo-ionization.

Equ 11 $P \geq 1.46\times10^{6}T^{5/4}$ for $\omega_p \leq \omega$, and $T \geq 10eV$
$P \geq 1.15\times10^{4}T$ for $\omega_p << \omega$,

P is the laser power in watts, T is the plasma temperature in eV ω_p is the plasma frequency and can be calculated from

Equ 12 $\omega_p = 8.9\times10^{3} \times \sqrt{N_e}$ (Hz)

The laser frequency is 2.1×10^{15} Hz However we do not have density values at early timescales Thus if the highest density seen at the earliest timescales (in the EUV range) is approximately 1×10^{19} cm^{-3}, and the bulk number density of aluminum is $6.0\times10^{22}cm^{-3}$, then a reasonable range of densities at early times could be taken as 10^{19}-10^{20} cm^{-3} Taking these two values and calculating the resulting plasma frequency, gives 2.8×10^{13}Hz-8.9×10^{13}Hz If these values are inputted into equation 11 with a average temperature of 18eV, the the right hand side of equation 11 ($\omega_p \leq \omega$,) for gives 8, and $2\times10^{11}W/cm^2$ Thus despite our liberal estimate for the upper value for the plasma density, it is still below the laser frequency by two orders of magnitude If $I\sim0.5\times10^{11}W/cm^2$ then in the EUV range, self focusing during the laser pulse due to density gradients in the plasma is possible However it is on the threshold of the required condition If the same calculations are done with T~5eV, and $N_e\sim10^{17}cm^{-3}$ (from visible emission studies), then for the case of $\omega_p << \omega$ ($\omega = 2.8\times10^{12}$Hz), the right hand side of equation 11 for the second case gives 5.7×10^{4} This is clearly much lower then the power density used in any of the experiments reported in both chapter 5 (visible emission studies) and chapter 6 (EUV emission studies) The assumption here is that the self focusing is occurring at an increasingly large distance from the target surface, due to the forward extension of the plasma

6.3.4 Laser-plasma interaction

For plasma laser beam interactions, much higher laser light intensities are produced when self focusing occurs than those produced from the beam divergence and focal properties of lenses This would cause a sharp increase in the power density seen by the plasma, and could account for the massive difference in continuum levels at 0.65mm at 3nsec in the spectra from the two targets Indeed the best evidence of this is the fact that the emission spectra for both targets at 15nsec aren't dissimilar at 0.15mm, yet are very different at 0.65mm Clearly any enhanced absorption by a pre-plasma would cut off laser heating of that pre-plasma back near the target surface This appears to be the case here The rapid decay of the emission profile from the wedge target at later timescales, is driven by a rapid decrease in plasma density itself fueled by a higher edge velocity

More recently we have become aware of work using femtosecond lasers focused inside micro-rectangular grooves (Nishakawa et al [13]) The authors studied the temporal emission from aluminum cavities in the 4-10nm soft x-ray region, studying the emission spectrum at 45^0 degrees off angle to the target surface Here the authors observed a 9.1 times (max) enhancement and a 5.4 (min) times enhancement of the peak x-ray emission intensity (depending on the dimensions of the cavity) This is in good agreement with the peak intensity enhancement seen at 3nsec for AL VIII (5.56) in the wedge cavity The authors in Nishakawa et al [13] propose

that plasma collisions with the side walls of the cavity are responsible for the enhanced emission, in which two separate components were observed A fast x-ray spike and a smoother longer emission profile The first emission spike is driven by laser ablation and heating of the target, while the second is collision driven Since this later component was of 2nsec duration and separated from the fast initial spike, there are good grounds for attributing the enhanced emission seen in this work to both collisional processes in the cavity, but as proposed by us, plasma density gradient effects during the ablation duration, and subsequent effect on the expansion of the plasma Here it is likely that we are unable to distinguish the EUV emission from the laser plasma generation and the EUV emission from plasma collision with the inner surfaces Not only is our gate time much larger than that quoted in (Nishakawa et al [13]), but the duration of our laser is substantially longer Thus one would expect to observe the enhanced emission from plasma collisions to be included in the bulk EUV emission from the plasma itself If we take the distance from the target surface to x=0 65mm, where the difference between the wedge spectra and the planar spectra are the largest, and then average an arrival time for ions at that point of approximately 10nsec, then the average velocity for aluminum ions would be $0\ 4\times10^5$m/sec This would give such ions an average kinetic energy of 0 21KeV However equivalent emission intensities from the planar target do not occur until 20nsec at that point (0 65mm) This gives an ion energy of approximately $0\ 19\times10^5$m/sec, and a kinetic energy of 0 051KeV Lastly the authors of (Nishakawa et al [13]) observed a systematic increase in the duration and peak value of emission from the second component as the depth of the cavity was increased, while no second component was observed for depths less then 135μsec Thus clearly there is a required minimum confinement distance from the target surface in order to observe enhanced emission properties from laser plasmas The most reasonable cause of this is the assumption that fast particles or plasma components, projected out normal to the target surface, are undergoing collisions with plasma components and particles rebounding from the cavities internal surfaces Unless a cavity is of a certain minimum depth, then most of the plasma plume (especially at early timescales, when the plasma is of limited volume) will simply expand normal to the target surface, undergoing few or no collisions with internal surfaces Indeed, most plasma models assume a 1-dimensional expansion during the early phases of plasma history

6.3 5 Conclusion

To summarize the data trends here, we have studied space and time resolved EUV emission from Aluminum laser plasma for different target configurations Reinforcing earlier work in the visible range, we have observed enhanced line and continuum emission at early time scales, leading to enhanced forward expansion of the cavity confined plasma Peak continuum and line emission is seen to shift forward in the cavity, and is assumed to be due to either plasma interaction with the cavity's inner surface or absorption and self focusing of the laser pulse in a fast low temperature plume collimated forward by the cavity The enhanced velocity and collimation leads to faster decay of the confined plasma, and mirrors inversion behaviour seen in the visible region at later timescales in similar targets The enhancement factor is in good agreement with that of (Nishakawa et al [13]), taking into account the difference in power density, target dimensions and sampling time of the EUV detector used here

6 4 Overview

Having studied the effects of target geometry on laser plasma generation and evolution, the question arose as to what affect target geometry has on other processes A prime example is the coupling of a second laser pulse to a pre-existing plasma The different plasma gradient profile for a contained plasma would no doubt effect not only the percentage of laser energy absorbed, but also over what scale length within the main plume the second beam would be absorbed If the time delay between the plasma generating laser and the re-heating laser is varied, then the two systems should respond differently, as laser heating of the pre-plasma is affected by the different rate of change of process within the plasma, the latter is affected by the influence of the confining target

6 5 Second stage EUV enhanced emission Studies of the effect of confinement on laser heating of a laser generated pre-plasma with variable time delay

6.5 1 Experimental setup

We employed a rectangular aluminum cavity of depth 3 5mm, and vertical width 1 2mm Using time resolved EUV emission spectroscopy in the 24-31nm range, laser generated plasma from such a cavity and a planar bulk target is studied, the experimental setup was identical to that described above (section 6 1 1) A second laser was then used to heat the pre-plasma, and the time delay between the two lasers was varied In order to cancel out the enhanced EUV emission when a plasma is generated inside such a cavity, all spectra of the plasma heated by the second laser are normalized to the pre-plasma, for each target Thus enhancement seen due to laser coupling with a pre-plasma can be studied, and secondary enhancement of this process inside a cavity can be compared to planar targets The basic interaction model is that the pre-pulse laser forms a layer of evaporated target material, which is highly ionized This layer then undergoes reheating to higher temperatures upon arrival of the second pulse, while causing further ablation of the main target surface The extent of this second ablation depends greatly on the scale length of the plume at the arrival of the second beam, and also the density gradients encountered by the second beam, which will configure where and to what extent the second beam is absorbed Clearly if the influence of the confining cavity is seen by the plasma at an early stage in its evolution, then the effect will be to shape the density gradients of the plasma, which heavily affect radiation absorption, i e absorption of a second beam Indeed having seen enhanced emission both spatially and for a limited temporal range (section 6 3) within confining cavities one would expect that any trends seen in planar targets with respect to delaying the second laser pulse, should be substantially different inside a cavity, irrespective of its geometry In Nishakawa et al [13] the authors performed a similar experiment utilizing femtosecond lasers, and much smaller cavities The proposed source of the 9 5 times enhancement for lines emitted by the contained plasma (also aluminum) was collision of the hot plasma after the termination of the laser pulse with the upper and lower faces of the cavity They extrapolated the leading edge of a spherical plasma at 45^0 and estimated the time taken for collision to occur between the plasma edge and the inner walls of the cavity This estimated time was in good agreement with the observed XUV (7nm) spike, relative to the less intense XUV signal of nanosecond duration

6.5.2: Power density effects.

Clearly collisionally driven ionization is heavily dependent on the free electron density and on the average ionization state in the plasma, both of which are dependent on the power density of the laser used. One undesirable aspect of aligning two laser beam on to the same spot size by the means employed here, is the smearing of the focused spot, forming a horizontal ellipse, thus lowering the power density. Here two Nd:Yag lasers each of duration 15nsec, and wavelength 1.064μm, were focused onto the same spot via two 18cm plano-convex lenses.

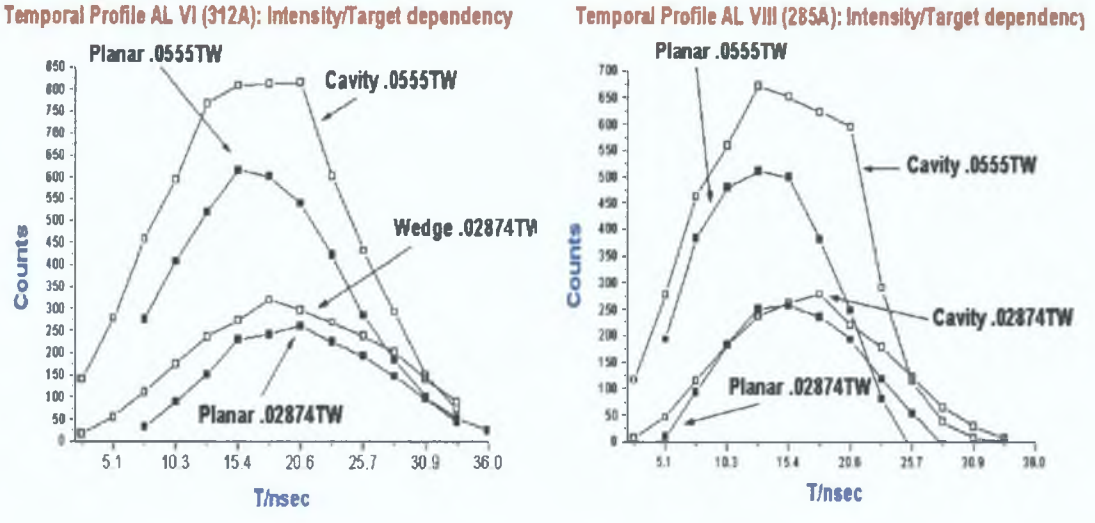

Figure 6.10.1, 6.10.2: Temporal profile of AL VI (31.2nm), and AL VIII (28.412nm), for both targets and both lasers. As previously stated in section 6.3 comparing both of these targets at I~0.5TW, a five fold increase in line intensity of a confined plasma was seen at early timescales, but highly localized spatially. The enhancement is still present at the lower power densities (I~0.055TW for the heating laser , lower due to spot 'smearing'), but is greatly reduced, and reduced further for the lower energy laser (YAG ~0.44J, giving I~0.0287TW for the plasma generating laser). In the above graphs 'T/nsec', is time from the arrival of the laser pulse at the target, measured via a photo detector.

The crater on the target was elliptical in shape (in the horizontal, of minor diameter ~1.1mm). The first laser, used to generate the pre-plasma (E=0.44J), gave I~0.028TW, and for the heating laser (E=0.78J), I~0.055TW. These intensities are substantially lower then those reported in similar work in section two 6.3, there enhancement factors of up to 5.5 in the peak emission intensities of lines were seen from the two targets discussed (I_p>0.05TW). Thus in the pre-plasma emission spectra we expected to see far less enhancement than reported before, as figures 6.10.1 and 6.10.2 display. Indeed as we will show, plasma emission intensity, enhanced via containment is heavily dependent on the power density. In plasma with a longer scale length, heat conductivity is lower and a higher temperature remains for a longer duration. Hence both the collisional and the recombination rates decrease as the plume scale length increases. Increasing the separation between the lasers pulses, results in a longer duration EUV pulse. This is clearly evident in the differences between the spectra emitted from both targets at 18nsec. Here the base (pre-plasma) emission spectra is displayed with that of the reheated plasma spectra for the three time delays (figure 6.11.1-6.11.4, next page).

The planar target shows enhanced emission over the pre-plasma spectra for all time delays, however clearly the larger the time delay the less pronounced the enhancement. However the reheated spectra from the wedge target shows large enhancement on the wedge pre-plasma spectra, and all time delays are convergent, with only a slight fall off in peak intensity of the emitted species and continuum, as the time delay increases. The dependence of the EUV emission on the laser wavelength, pulse duration and energy may be related to the time-dependent electron density (N_e) and temperature (T_e) profiles.

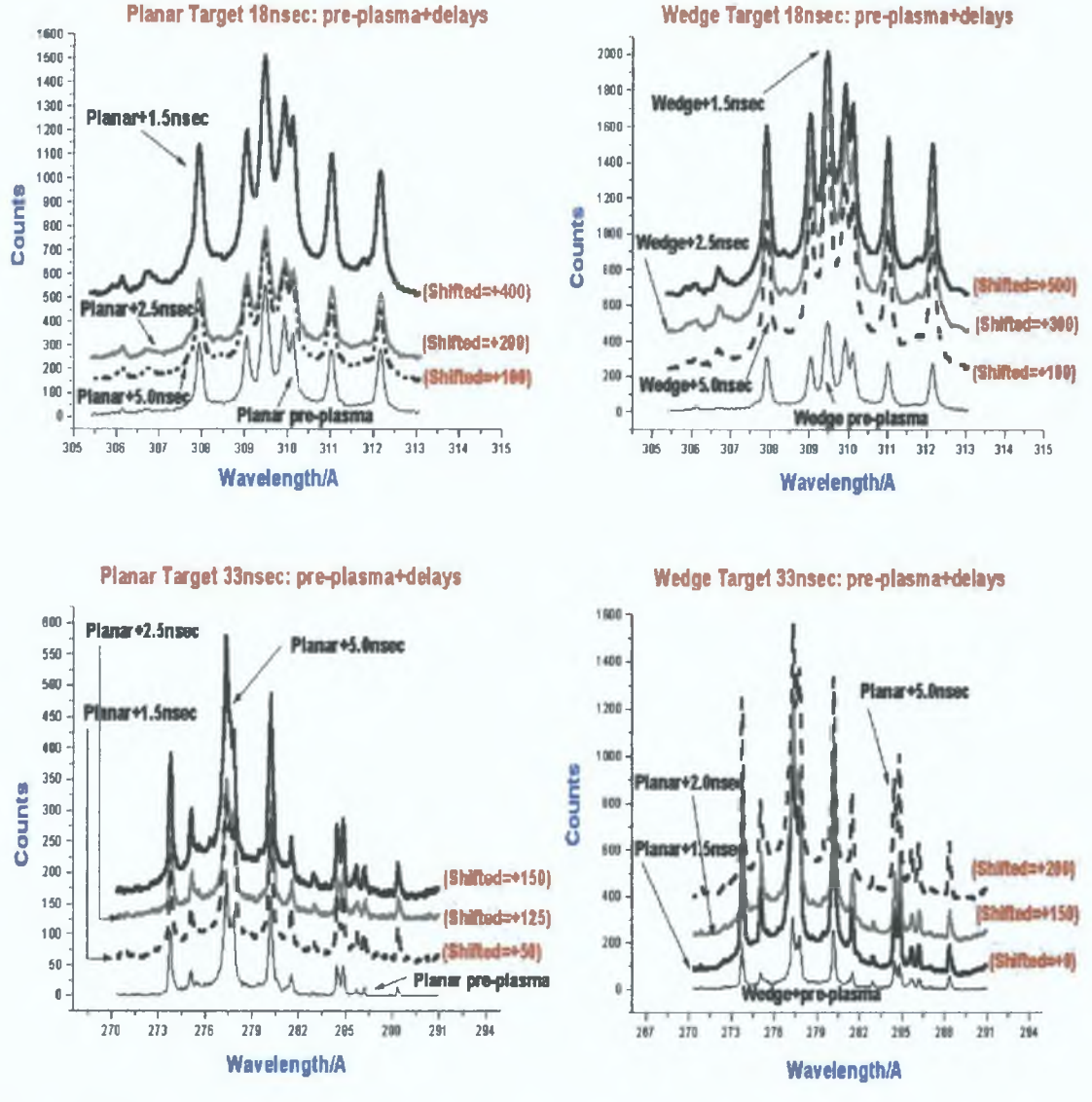

Figure 6.11.1-6.11.4: EUV emission spectra for both targets, with pre-plasma spectra and delayed re-heated emission spectra, for two wavelength ranges. The spectra are shifted for clarity. Here, 'planar pre-plasma' refers to the spectrum from the generating laser (I_p~.028TW), while 'planar +1.5nsec', refers to the spectra from the re-heated plasma with the delay between the lasers equal to 1.5nsec. The most pronounced differences are the relative value of the continuum baseline. For both the pre-plasma spectra and the re-heated plasma spectra in the cavity, it is superior. As the inter-laser delay increases, the increase in intensity for the planar target falls steeply from its initial peak (1.5nsec inter-laser delay). However for the wedge targets the increase in intensity is very stable over the complete set of inter-laser delays used. This is clearly seen in figure 6.12.1, and 6.12.2.

6 5 3 Laser and plasma interaction

In the case where the laser undergoes direct interaction with the target bulk, higher electron densities are generated, thus interaction of a second beam usually occurs at the frontal region of the pre-plasma, where densities tend to be lower Another aspect of plasma behavior is the oscillation of charge particles in an electric field of the heating laser Defining the plasma frequency, w_p, for case of electron oscillation

Equ 13 $$w_p = \left(\frac{n_e e^2}{m_e \varepsilon_0} \right)^{1/2} = 56\,4 n_e^{1/2}$$ (Hora [12])

then clearly optimum transfer of energy from the heating laser to the pre-plasma occurs when the laser frequency matches that of the plasma (for N_e~0 5×10^{19} cm^{-3}, w_p~2 5×10^{13}Hz), if the laser frequency is 2 84×10^{14}Hz, then considering the forward collimation of the plasma even during the laser pulse as a consequence of confinement, excitation of the plasma's forward region by the intense electric field of the heating laser is a good candidate for understanding the superior emission from cavities with reheating from a second laser The fact that such enhancement is seen only in the forward regions (from the previous section) and not at the targets surface reinforces this proposal The r m s electric field E, is related to the irradiance ϕ(Wm^{-2}) by

Equ 14 $$\overline{E}_{rms} = 19\,4\phi^{1/2}\ (\mathrm{V\ cm^{-1}})$$ (Hora [12])

In this work the irradiance used was of the order 10^{14} Wm^{-2} , thus $\overline{E}_{rms}$ has a corresponding value of ~10^{7}Vcm^{-1} If we accept that excitation of the pre-plasma by the electric field of the heating laser plays an important role in enhancement, then the success of this enhancement depend heavily on the density of free electrons in the pre-plasma This scales directly with the power density of the incoming beam. Spectra from both the planar and the wedge target for both laser intensities reported here (lower as a result of beam smearing) but also from previous work on such targets with a highly focused beam display continuum and line emitting intensities which scale with higher power density

6 5 4 Temperature, irradiance and radiation trends

Although the wedge target maintains enhanced continuum and line intensities for all power densities reported (0 02-0 05TW/cm^2), the extent of the enhancement is clearly reduced as the power density is lowered Thus given estimates of the peak electron density from the analytical model of self-regulating laser ablation of Phipps and Dreyfus (N_e~0 364×10^{20} cm^{-3}), it is highly reasonable to assume that lower electron densities exist at the leading edge of the plasma, especially in the wedge target's pre-plasma, at the reduced power densities reported here Thus a good mechanism for accounting for the superior enhancement in the cavity upon re-heating the pre-plasma with a second beam is electric field excitation from the second laser pulse within the frontal region of the plume In fact as the time delay increases between both lasers, the wedge target actually displays increased intensity profiles over a very large temporal lifetime, while the planar target, displays decreasing enhancement for increasing inter-laser delay, and steep decay in line profile intensities Obviously laser absorption would play an important role in photo-ionization driven excitation of the pre-plasma The absorption coefficient is scale length dependent

Equ.15 $\Phi_{absorb} = \Phi[1-\exp(-\alpha_{ib}L)]$, (Liu et al[2])

which immediately favours the cavity plasma. Indeed we proposed that enhanced emission from such cavities (section 5.1 in the visible and section 6.3 in the EUV) was due not only to higher electron densities but also superior absorption of the trailing edge of the main laser beam. Therefore absorption of the pulse in the extended plume is the more dominant mechanism for direct plasma generation, but is also dominant for pre-plasma heating. This is chiefly through *Inverse Bremsstrahlung*. If the dominant mechanism is absorption via inverse bremsstrahlung and the absorption coefficient α_{ib} (cm^{-1}) for the electron–ion inverse bremsstrahlung is given by equation 11, page 7, then for aluminum plasmas in the temperature range of 10eV-14eV, Z=7(approximation). N_i could be approximated at $10^{18\text{-}19}cm^{-3}$, possibly this figure could be upwards of a full order of magnitude lower at the leading edge. At temperatures of 10eV and upwards, the values in the exponent can be ignored. Given the extent of the pre-plume extension, self focusing of the laser beam in the plasma cannot be ignored. This is due to density gradients seen by the beam as it penetrates the plasma edge. Hora derived the laser power threshold for non-linear force self focusing of a laser beam in a plasma, as equation 11. The plasma frequency (2.5×10^{13}Hz from above) is based on the assumption of constant electron density throughout the volume of the plasma. Clearly this is not valid, and the density gradient in the cavity is likely to be very different to that from a planar target. Lens focused laser beams are not limited by the diffraction limit, but mostly by aberrations in minimizing the diameter of the beam. The question then arises as to what optimizes self focusing of the beam within the plasma itself, and do the density gradients and enhanced intensities seen in cavities, affect strongly the absorption of a second beam at a laser frequency of 2.2×10^{14} Hz. From classical optics, the greater the gradient of refractive index per infinitely thin slab of medium, the greater the refraction. Indeed studies have demonstrated refraction and self-focusing at MW power levels (Hora et al [12]). Space and time resolved visible studies (section 5.1) on rectangular cavities demonstrated much higher densities gradients spatially in the cavities for the first 80nsec, with the peak electron density observed well ahead of the planar target's peak density. Thus self focusing during the laser pulse due to density gradients in the plasma is possible. As a consequence, secondary heating via another beam, which will undergo much greater self-focusing contained in a rectangular cavity than that of a planar target, can possibly account for the difference between the spectra observed from the re-heated pre-plasma from both targets.

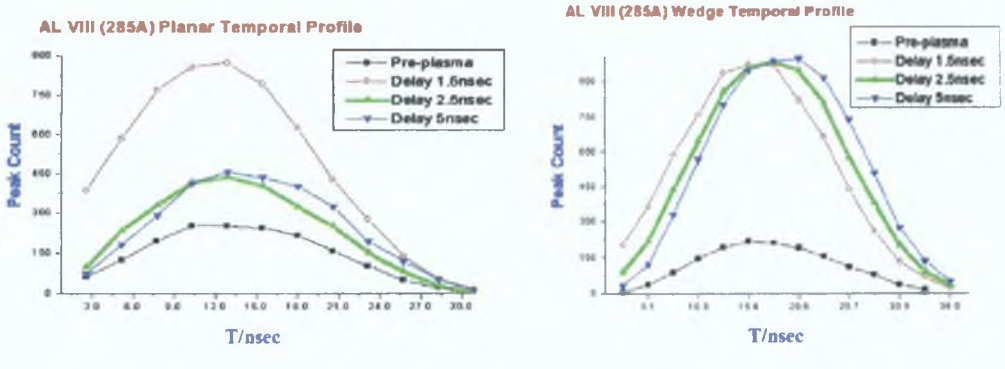

Figure 6.12.1, 6.12.2: Temporal profile of AL VIII(28.5nm) for both targets for pre-plasma and re-heated intensity counts.

6.5.5: Normalized enhanced emission.

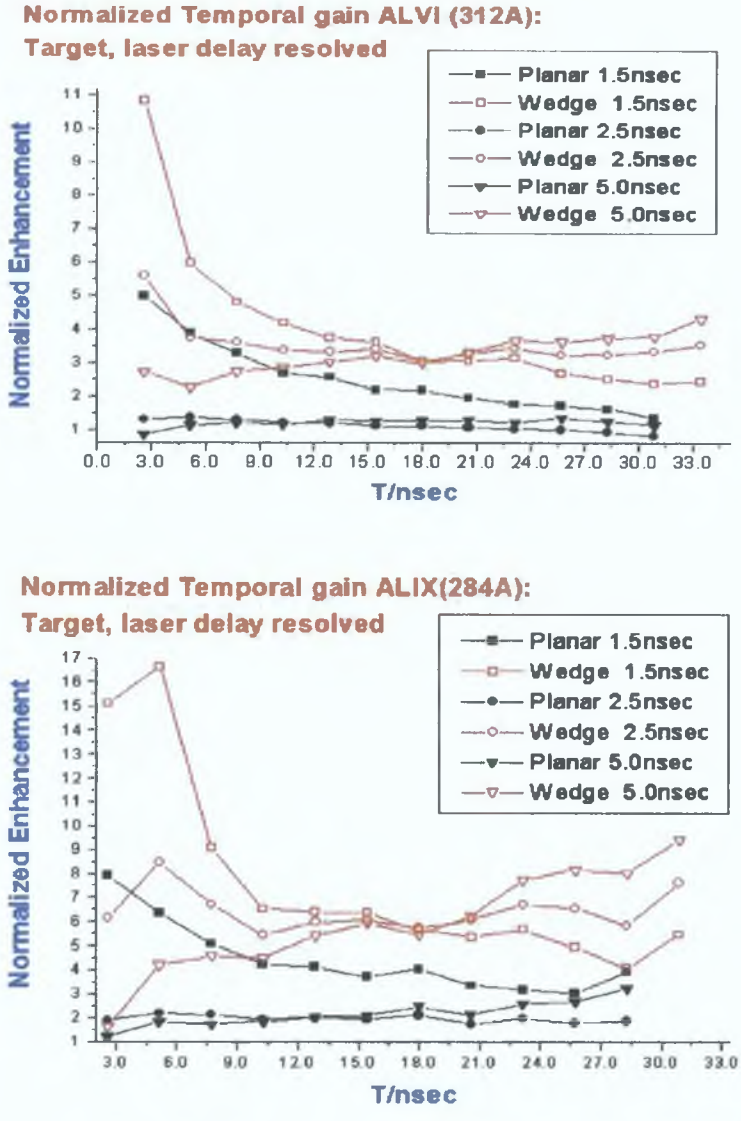

Figure 6.13.1, 6.13.2: Temporal profile of AL IV(31.2nm) and AL IX(28.4nm) lines for both targets for pre-plasma and re-heated plasma for different inter laser delays. Here, we took the emission profile in time of the two ions displayed, and used the emission profile for the pre-plasma as the base line, to which the delayed re-heated emission profiles were normalized by dividing the pre-plasma time profile into the delayed re-heated profiles. This was done for both targets. Thus the differences observed are independent of the enhancement one would see from the pre-plasma being generated in the cavity, and thus the differences for the three time delays, are a direct indication of enhanced coupling processes for laser heating of the pre-plasma in rectangular cavities.

One can clearly see that gain for each time delay in the cavities is greatly superior to that of the planar target for both ions, the gain being higher for the higher ionization stage. Another unusual feature is the clear convergence of the gain factor for all time delays in the cavity target for both ions. In both cases its occurs at 18nsec, just after the termination of the laser pulse (15nsec). The gain factor increases after the convergence point, simply because the cavity affords the plasma a longer period of enhancement in terms of offsetting radiative decay and cooling as the plasma expands, the greater the time delay of the second laser after the pre-plasma, the more pronounced the upward slope of the gain factor, but this occurs only at later times, thus re-heating is effecting the pre-plasma for a longer period after the arrival of the pre-plasma laser pulse by virtue of the pre-plasma being contained.

The assumption here is that the self focusing is occurring at an increasingly large distance from the target surface, due to the forward extension of the plasma. For plasma laser beam interactions, much higher laser light intensities are produced than those produced from the beam divergence and focal properties of lenses, this would cause a sharp increase in the power density seen by the absorbing plasma.

One final question of interest is that of plasma collision with the inner surfaces of the cavity. In (Nishakawa et al [13]), secondary XUV signals of nanosecond duration were observed and later accounted for by femotsecond generated plasma colliding with the internal walls of the cavity, which was also a rectangular in shape.

In section two, we observed large scale enhancement in space and time resolved EUV emission from the cavities discussed here. The enhancement occurred over a range of 0.7-1.05mm from the back surface of the cavity where the laser impinges the target. Along this length, the peak EUV emission of highly charged ions is seen to be nearly constant. This region is the approximate centre of a projected line from the center of the back wall, up at 45^0 to the upper and lower surfaces of the cavity. Collision driven enhancement, if it occurs should be seen here. This is approximately the range spatially where the spectra from the cavity displays much higher peak line and continuum emission over a planar plasma. Figure 6.13.1, and 6.13.2 are the best indication of enhanced laser coupling to a pre-plasma in a cavity over a planar target. The gain factor is in good agreement with that reported by (Nishakawa et al [13]) for enhanced line emission in Aluminum rectangular cavities (peak gain factor 9.6) in the 7-10nm range for femotsecond laser ablation. Murphy et al [13] observed a 3.5 gain factor in heating a nanosecond generated pre-plasma with a picosecond laser pulse. The gain profile for the time delays employed displayed a peak (inter-laser delay 10nsec), followed by a smooth decay in the gain factor, the target being planar. Trends seen there do not conflict with those seen here.

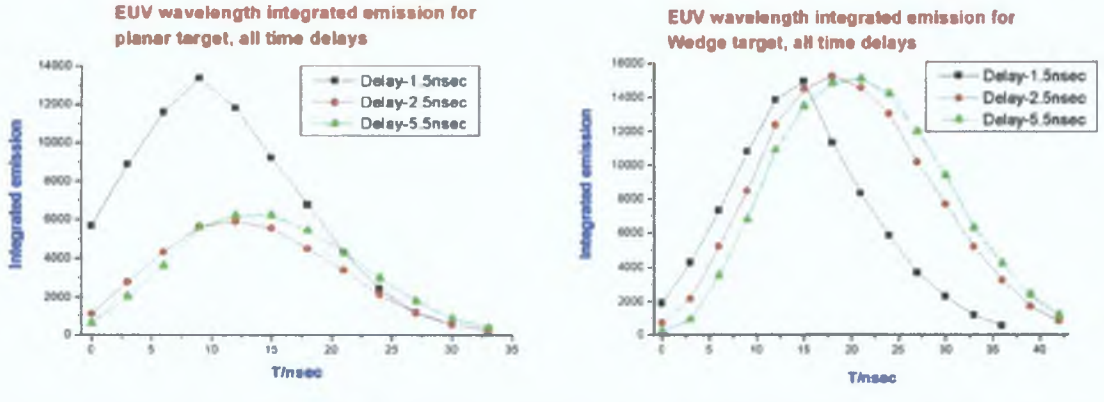

Figure 6.14.1, 6.14.2: time resolved wavelength integrated EUV emission values for both targets. Here the EUV spectra were integrated, summing all EUV bulk signal received by the detector. Note the rapid fall in peak signal in the planar target after the first delay, compared to the wedge target which is nearly constant for all time delays. This trend exactly mirrors those in figures 6.12.1, and 6.12.2, where the temporal profile of detected ions displays the same trends as the bulk signal.

If one considers that at the point of study (x=0.65mm) the wedge target displays substantial enhancement over the planar target, then it not surprising that other processes, such as secondary beam heating, ion profile and bulk EUV signal also exhibit enhancement at this point. The most important feature here however is the relative lack of change of the bulk integrated signal from the wedge target for the three different time delays. While the

planar target drops by over 50%, for both the ion temporal profiles and the bulk EUV signal, the wedge target maintains the superior ion and bulk EUV profile, thus since plasma radiative and collisional processes are most density dependent then the logical conclusion is that a cavity confined EUV scale plasma is very homogenous, in comparison with a freely expanding plasma An important application of this is the ability to prolong plasma lifetimes for enhanced photo-absorption studies where in the absence of good absorbing cross sections for strong absorption relative to background signal, one could employ long duration backlighting sources Here good absorption signal summing with the scale length of the absorbing plumes would be replaced with absorption time scales with the duration of the pump signal While this approach would not be suitable for spatial scanning of an absorbing plume, it would be feasible where such a plume is contained either geometrically or magnetically or by a gaseous medium, and the plumes overall length is small, in terms of presenting a large cross section to the pumping beam or back lighting source

6 5 6 Conclusion

In summary, we have studied the effects of generating a pre-plasma and heating this pre-plasma by a second laser pulse, with varying time delays This system was studied for both planar targets and rectangular cavities Base enhancement of plasma generation in cavities was seen to decrease as the power density of the laser generating the pre-plasma decreased This trend was reinforced when comparing enhancement in such targets at higher power densities Secondly by normalizing emission profiles for two ionization stages for each target, we observed a large gain factor during early stage emission for reheating of the pre-plasma with a second laser and for the cavity this factor converged for all time delays after the termination of the pre-plasma laser pulse The cavity target displayed superior gain factors for both ionization stages studied and for all time delays between pre-plasma and heating laser

6 5 7 Concluding comments

This thus completes our attempt to push the space-time limit of diagnostics back to the space-time origin, and to investigate whether enhancement of plasma parameters, such as temperature and density seen in the visible, is a trend which exists at even earlier timescales The general picture which emerges is of plasma generation, geometrically confined, being substantially different from plasma expanding from a planar target The inhibited expansion, leading to higher local particle densities probably drives collision based ionization, and enhances laser absorption in the leading regions of a plume, which itself drives rapid expansion of the plasma, even during the laser pulse It is not clear to what extent enhanced temperatures owe their origin to enhanced laser absorption or to particle collisions due to enhanced density arising from containment Indeed high particle densities near the target surface tend to lead to beam attenuation and reduced ablation rates, which will then drive laser absorption further out from the target surface, where the particle density is lower However as seen from ICCD images and EUV particle profiles, this will fuel rapid expansion of the leading edge of the plume, driving the particle density into a rapid decay across the front half of the plume This balance between ablation and beam attenuation by low density plasma is probably accelerated in time by confining cavities Cavities collimate the fast blow off particles seen in ICCD images and other fast framing devices, and this would play a

crucial role in deciding where exactly the trailing edge of the beam is absorbed (or indeed a second laser beam) If indeed particle profiles in the visible indicate a substantial shifting forward of plume constituents (especially visible continuum emission) at early timescales, then one can infer that density gradients in cavities at early times decay less sharply as one moves away from the target surface, then beam heating of this low density extended plume is likely to occur not at a precise point, but over an extended scale length A crucial element in diagnosing plasma behaviour under an influence such as target geometry is the reliability of temperature and density techniques It is not sufficient to simply observe emission and absorption spectra and attempt to infer physical mechanisms to describe plasma history Since interaction of a hot, high density plasma plume with a geometrically irregular target and the resulting 'macroscopic' change which occurs to the density profiles, microscopic and atomic process can then be inferred to understand and explain the observed effects It is definitely a case of bulk dynamics first (plasma-target interaction), macroscopic dynamics second (temperature and density profiles), and atomic processes leading to the observed spectra, last

References

[1] P K Carroll, E T Kennedy, G O'Sullivan, Opt Lett 2, 72, (1978)

[2] H C Liu, X L Mao, R E Russo, Spectrochima Acta Part B54 (1999), 1607-1624

[3] C R Phipps, R W Dreyfus Laser Ionization Mass Analysis, Chemical Analysis Series, Vol 124,Wiley, New York, (1993)

[4] A A Voevdin, J S Zabinski J Appl Phys, 78, 4123 (1995)

[5] T Atwee, S S Harilal, H-J Kunze, J Appl Phys D,34 (2001), 1213-1218

[6] J J Chang, B E Warner Appl Phys Lett 69, 473 (1996)

[7] E G Gamely, Laser Par Beams 12, 185 (1994)

[8] R H Singh, J Narayan J Appl Phys 68 233 (1990)

[9] T Atwee, S S Harilal, H-J Kunze J PhysD Appl Phys, 34 (2001) 1213-1218

[10] H Hora, Physics of Laser Driven Plasma (1981), Wiley &Sons

[11] T Nishikawa, H Nakano, N Uesugi, Inst Phys Conf Proc No 159, 539-542, (1998)

[12] H Hora, Plasma at High Temperature and Density, Applications and Implications of Laser-Plasma Interactions (1991)

[13] A Murphy, J S Hirsch, J T Costello, SPIE Proceedings, pp 4876 (2003)

[14] Calculus, Howard Anton, 4'th edition 1992 Wiley and Sons

[15] M A Khater, PhD Thesis, December 2001, Dublin City University

Conclusion

Introduction

This chapter summarizes the most important aspects of the present work, including the hardware development and new equipment commissioning and application of theories relevant to each diagnostic tool used to interpret raw data.

A summary of the broader conclusions derived from the study of laser plasma plume generation with varying target configurations is also given.

An outline of possible avenues of future investigation into configuring laser plasma plumes is discussed, and other diagnostic techniques which can augment existing tools are outlined.

Summary

In the present work, the effects of multi-variable target conditioning upon laser generated plasma plumes have been investigated In order to fully diagnose the effect of such variables upon plasma behaviour, the plume has been studied over as large a space-time range of plasma history as was feasible by employing multiple diagnostic tools

These diagnostics required the development of new hardware and techniques in order to properly apply the new diagnostic tools

The target material, aluminum was chosen primarily because of the ease of machining various target geometries and because of the large body of work already existing on the studying of aluminum laser plasma plumes

In order to achieve the required goals, numerous hardware developments were undertaken Firstly, a new multi-purpose vacuum target chamber was designed with the main goal of flexibility in utilizing all diagnostics tools employed Since the requirements of one diagnostic technique were generally in conflict with others, the design had to include the requirements of each diagnostic technique in its design, i e mounts, range of motion, precision and reproducibility of positioning The system was also configured to allow continuous upgrades for future work

The use of probe techniques required the development of a chamber and power supply unit capable of holding and biasing many probes in order to study laser plasma plumes at many spatial points Automated software acquisition and signal processing were instigated in order to ensure efficient processing of large volumes of data and to increase the number of time resolved points which were translated into a physical parameter Both ion and electron probes were utilized, and a number of theories were applied in translating the raw data to physical parameters

In employing space and time resolved visible emission spectroscopy, a Chromex visible gated spectrometer and Andor ICCD were commissioned and their final configurations were optimized for rapid data acquisition and to allow full spatial sampling of a laser plasma plume's emission spectrum The need to fully diagnose the plume's temperature and density led to the application of numerous techniques in raw data interpretation over a large space-time range of the plume's visible emission history For each technique employed (N_e from Stark broadening and line ratios, T_e from Boltzmann and line-to-continuum techniques and T_{ion} from line intensity ratios) automated data processing was employed in order to ensure that a large volume of both space and time resolved data was available for interpretation Substantial effort was also employed in both the vacuum chamber's design and the format of the experiments in order to perform experiments in the visible range to study the effect of high voltage electric fields on the temporal and spatial evolution of laser plasma plumes

In utilizing space and time resolved EUV emission spectroscopy, a high speed gating detector unit was commissioned Since time resolved measurements had not been feasible up to this point, the temporal response of the plasma and the optimum operating parameters for time resolved experiments in the EUV had to be determined Techniques applied in the visible range for interpreting spectra and translating raw data into physical parameters were employed and the viability of such techniques was studied

Finally, although not employed in actual experiments, a precision high current magnetic pulse generator was designed and tested It had been intended to study the effect of magnetic field influence of laser plasma in both the visible and EUV ranges The vacuum chamber was designed to facilitate from its inception the installation of the magnetic coils, and the required high voltage, high current delivery required for such a system The success of the device is thus seen as a hardware development aspect of this project which will augment future work for CLPR

Conclusions

The following conclusions were drawn from this work

Langmuir probe measurements

Langmuir probes were utilized for very long timescales and by virtue of plume expansion, at moderate distances from the target surface (>30mm)
Laser plasma plumes are characterized by high TOF velocity, and high particle flux It was initially believed that confinement of a laser plasma plume would lead to a higher particle density However for all target geometries employed, and for plume sampling both in the vertical and horizontal planes, lower particle densities were observed The greater the degree of confinement (the larger the internal volume of the cavity, irrespective of its configuration) the lower was the peak particle density The temperature response of the plume was the reverse of its density response Higher confinement led to higher electron temperatures Sampling the plume's spatial distribution in 2Dimensions clearly identified the collimating properties of different target configurations
The first target configuration employed, of rectangular wedges with varying depth demonstrated a recurring property (assuming fixed fluence) of decreasing particle density as the internal volume of the cavity increases (through varying depth of the cavity) The increasing depth corresponds to an increase in the total surface area, and the length of time the plasma is in contact with such surfaces The rate of decay of the plume's particle flux depends on the fluence used For high fluence only cavities of sufficient depth have a significant effect on the spatial distribution of the plume and its peak particle densities However as the fluence is decreased, observable effects become apparent for smaller cavity depths

For the particle distributions in the horizontal plane from rectangular cavities of varying height or depth a common feature is the fanning effect the cavity has on the angular distribution of the plume particles, resulting in a very large angular region of small variations in peak particle density In contrast, the vertical distribution of particles from rectangular cavities, displays substantial collimation of the plume as a consequence of the target influence

For the other target configuration employed, that of parallel plates, the most striking effect is the relative independence of the TOF velocity of the slower main component on the cavity width Contrasted against this is the linear dependence of the TOF velocity of the fast component of the plume on the cavity width (plate separation)

Space and time resolved visible studies

The trends observed through the visible spectral range diagnostics, reinforced those seen with probe studies The most obvious conclusion is the lack of increased temperatures (either electron or ionization temperatures) for plasma generated between two parallel plates compared to the large (~30%) and sustained increase in temperatures from both rectangular cavities and capillaries However the parallel plate system demonstrated the largest increase in electron density (70%) for all target configurations reported here Individually all targets displayed unique behaviour For the rectangular cavities a decrease in the cavity height was followed by an increase in temperature (approximately 5000K increase over the planar target) and density (especially at the early phase, t<100nsec) The enhanced temperatures and velocities which drive a rapid expansion of the plume in the cavity leads to a rapid drop in electron density after ~150nsec This drop in density is most pronounced at the plume's frontal region, where the highest particle velocities are to be found The above trends were also seen in the capillary targets, where the extent of the enhanced temperatures and densities were ~25% higher then those observed in the rectangular wedge targets This is attributed to the greater degree of containment offered by the capillaries The rapidly decaying plume emerging from the confining targets, exhibiting lower particle densities, then register at the probes as decreasing N_e and N_i with greater confinement This trend is the exact inverse seen in the early stages of visible emission history

Space and time resolved EUV studies

Extending the study of target influence to shorter wavelengths, resulted in the extension of the space-time limit back to the origin (laser arrival on the target surface) This then allowed for the confirmation of trends seen in the visible Indeed laser plasma generation in rectangular cavities display substantially enhanced emission properties over those from a planar target Although we were unable to deduce densities or temperatures from EUV spectra from cavity plasmas (due to the absence of electron impact, 'W' values), the space time profile of the peak intensity of various lines for both a planar target and a wedge target were

similar to that observed in the visible Cavity plasmas in the EUV demonstrated large increases in peak emission intensity, but only for a limited duration and only over a discrete spatial region The cavity plasma then decayed rapidly and was overtaken by the emission from the planar target This is exactly the trend observed in the visible Again, the confining effect of the cavity leads to higher expansion velocities and a more rapid decay in the plume's temperature and density

Alongside the physical influence on the plasma from the cavity, the effect of the cavity on the plume's N_e profile led to enhanced reheating effects from a second laser beam The extent of the reheating was a second enhancement mechanism observed in cavity plasmas over a plasma from a planar target The reheating effect was observed to be more stable for a larger range of inter-laser time delays for the cavity plasma than that of the planar plasma, which demonstrated reheating enhancement which peaked at a specific inter-laser time delay

In all experiments performed, the importance of multiple techniques for physical parameter determination was reinforced when the difference in various techniques was not insignificant i e N_e values from Langmuir versus Orbital theory, T_e values from ion ratios, line-to-continuum, and Boltzmann plots, and N_e values from Stark widths versus density sensitive line ratios

Since each theory or technique is most reliable at different phases in the plasma history, one must employ not only different diagnostic tools, but also different theories for raw data translation if a reliable and complete overview of a particular influence is to be studied

The trends extracted from target effects on plume density values demonstrates the importance of not drawing unwarranted general conclusions from observing a limited region of the plumes history

Future work

Future work which could extend that reported here could take form of three distinct paths

Firstly there exists a large range of other diagnostic techniques which could be employed to augment the study of laser plasma plumes Each has a different temporal range over which it would be employed Lenk et al [1], employed taking the electrical signal of the target during the laser pulse and for 1-2 laser pulse widths after the termination of the laser pulse itself This technique allows for the calculation of electron temperatures at extremely early phases in the plasma history, and being an electrical measurement it doesn't require a plethora of theoretical assumptions or corrections, as is frequently the case with spectroscopic techniques The technique utilizes high kinetic energy electrons escaping from the plasma, which act as a source of potential between the target-plasma system and some grounded point By measuring the current in the target via a set of low inductance resistors, one can build up a time dependent

IV relation for the plasma Assuming a Maxwellian energy distribution for the plasma electrons, the target current is given by

$$I_i = I_0 \exp^{-e(U0+UT)/kTe}$$

I_0 is a constant, Te is the electron temperature, U0 is the plasma work function and UT is the induced target voltage Plotting U-ln(I) for a single time resolved event should give a straight line graph with the slope equal to $1/kT_e$

A second approach is to utilize the charged nature of plume constituents to effectively study discrete signals from the plume The retarding field analyzer has been employed by many authors for plasmas generated by various means [2-5] Again this is an electronic measurement and is exceptionally diverse in the ranges of conditions under which it can function Effectively the technique is identical to an ion probe, however by design one can select which ions one wishes to study by biasing the multiple grids at increasing voltages to reject all but the most energetic particles (figure A) More importantly since particles of undesired polarity can be rejected (i e electrons are rejected via the first grid which is negatively charged), such a technique can operate at much higher fluences than either ion or electron probes, and thus by default (for laser plasmas) be employed much closer to the plasma origin (i e the target, and thus will sample the plume at a very early point in its history) With good design these devices can be extremely small thus this would not only increase the spatial accuracy but would allow the device to be mounted on a movable mount, effectively allowing a large range of positions within the plume to be studied

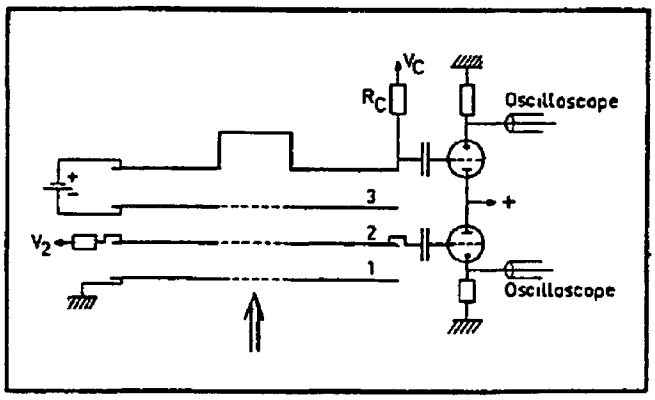

Figure A Schematic of the retarding field analyzer used by Demtroder and Jantz [2]

Another interesting technique is to sample the magnetic field generated from the plasma Such magnetic signals are by nature very short lived (<50nsec) and highly localized They are typically present only for the very early phase of the plasma history, and again electrical measurements are relatively easy to employ By minimizing the diameter of the loop, the spatial resolution is increased If a 2D array of such sensors was placed behind the target (assumed planar and thin, i e not greater then 5mm) then the space and time resolved magnetic field generated from the plasma could be sampled With interpretation one can deduce

the average current following in the plume under very extreme conditions, this can then be related to the electron density

This technique, combined with the other discussed above, and integrated with ion and electron probes represent a multi-faceted approach to non-optical based measurements of laser plasma plumes, over a very large space-time range They are inherently faster then any optical measurement, by virtue of the limitation of existing gating units for photon based detectors (typically the faster photon based detectors are ~nanosecond scale devices, picosecond EUV and x-ray detectors are available but are very expensive)

All of the above represent device or detector development, another avenue for future experiments would be to employ field influences such as magnetic and electric fields The number of studies using magnetic fields are too numerous to state here (see chapter 3, section 3 7) but such a variable represents a highly complex and hence interesting aspect of plasma behaviour The main challenge is to generate a sufficiently intense magnetic field so as to produce a measurable and useful difference in the plasmas behaviour

To date there is only a handful of reports on electric field influence on laser plasma plumes The absence of work in this area (with the exception of laser plasma ion sources) and the large envelope of variables (field geometry , intensity DC or pulsed, polarity) mean that such any effort directed at studying electric field influence upon laser plasmas would yield a worthwhile dividend

The importance of fusion work and its dependence on magnetic containment would warrant developing expertise in magnetic field generation and influence for any research group Secondly the coming deployment of large scale plasma propulsion systems which employ field influences to accelerate the plasma, will no doubt mean the direct application of research done by laboratories presently to future propulsion projects Indeed expertise and capability in such an area, especially for high field intensities would represent a specialist aspect of a laboratory's capabilities

Finally, regarding the continuation of work reported here, a number of aspects of plasma-surface interaction could be investigated One means of studying such an effect would be to use a rectangular wedge target with upper and lower surfaces of a different material than that of the ablated target surface Comparing the emission intensities, ionization temperatures, electron temperature and electron densities of aluminum plumes when the upper and lower surfaces are ceramic as compared to metallic (in order to study heat conduction effects) would assist in formulating the main mechanism responsible for lower plume particle densities from confining targets Another interesting effect would be to study re-heating of a laser plasma plume by a second laser, with the latter focused a few millimeters from the target surface in order to couple to the expanding plume With varying inter-laser time delays an array of probes could study the large increase in the particle's kinetic energy as a consequence of re-heating by the second laser This system could be repeated for various target configurations, which should influence the absorption of the second laser pulse and hence affect the reheated plumes particle distribution Such an experiment could

also be done in the visible range, to extend and compare those trends observed in the EUV with secondary beam re-heating of plasma plumes The influence of different wavelengths, and pulse durations of the re-heating laser could also be studied in both the far-field (with probes), inter-mediate field (visible spectroscopy) and near field (EUV)

If very early phase diagnostics (magnetic probe arrays, and target signal sampling) were included, then a similar approach to multi-composite targets and plume reheating could be undertaken as was pursued in this work

References

[1] A Lenk, TH Witke, G Granse, Appl Surf Sci 96-98 (1996) 195-198

[2] W Demtroder, W Jantz, Plasma Physics, Vol 12, pp 691-703 (1970)

[3] S Amoruso, M Armenante, V Berardi, R Bruzzese, G Pica, R Velotta, Appli Surf Sci, 106 (1996) 507-512

[4] Y Sakamoto, S Miyoshi, Fusion Eng and Des, 34-35 (1997) 543-546

[5] Y Yuan, J Bansky, J Engemann, A Brockhaus, Surf and Coatings Tech 74-75 (1995) 534-538

[6] A V Kabashin, W Marine, P I Nikitin, M Sentis, Appl Surf Sci, 96-98 (1996), 139-143

[6] J A Stamper, J M Dawson, Physical Rev Letts, Vol 26, No 17, April (1971), 1012-1015

[7] R Serov, M C Richardson, Appl Phys Letts, Vol 28, No 3, 1 Feb (1976), 115-118

Appendix A-list of files

Filename	Package/format
Binned m	MATLAB 6 0
Cont_ratio m	MATLAB 6 0
Cont_ratio2 m	MATLAB 6 0
Density_ratio m	MATLAB 6 0
Density_raio2 m	MATLAB 6 0
Efield m	MATLAB 6 0
Efield2 m	MATLAB 6 0
Ion_import m	MATLAB 6 0
Ion_import2 m	MATLAB 6 0
Ion_import3 m	MATLAB 6 0
Ionz_ratio m	MATLAB 6 0
Ionz_rartio2 m	MATLAB 6 0
Magfield m	MATLAB 6 0
Pulse m	MATLAB 6 0
XUV1 M	MATLAB 6 0
XUV2 M	MATLAB 6 0
XUV3 M	MATLAB 6 0
XIV4 M	MATLAB 6 0
Spectra2_GO m	MATLAB 6 0
Spectra3_LO m	MATLAB 6 0
Spectra4_LO m	MATLAB 6 0
Spectra5 m	MATLAB 6 0
TEST C	C++
Ion C	C++
Optical_model m	MATLAB 6 0
Calibration m	MATLAB 6 0
Main54501a vi	LABVIEW 5 0
Scope_init vi	LABVIEW 5 0

Appendix A: Software and Programs

```
%%%%%%%%%%%%%binned.m%%%%%%%%%%%%%%%%%%%%%%%
format long;
filename3='2mm_t20.asc';
raw1=[];
raw2=[];
raw1=dlmread(filename3,' ');
[n,m]=size(raw1);
ccc=1;
ddd=1;
for ii=1:2:n;
     ddd=1;
    for jj=1:2:m;

        raw2(ccc,ddd)=raw1(ii,jj)+raw1(ii,jj+1)+raw1(ii+1,jj)+raw1(ii+1,jj+1);
        ddd=ddd+1;
    end
    ccc=ccc+1;
end
r_file1='B';
r_file2=strcat(r_file1,filename3);
fid=fopen(r_file2,'wt');
[m,n]=size(raw2);
for m5=1:1:m;
   for n5=1:1:n;
      count=fprintf(fid,'%.8f ', raw2(m5,n5));
   end
  fprintf(fid,'\n');
end
fclose(fid);
clear r_file1 r_file2 count m5 n5;

%%%%%%%%%%%%%%%%%%cont_ratio.m%%%%%%%%%%%%%%%%%%%%%%%%%%%%%
%%%%%%%%%%%%%%%%%%%continuum to line ratio program.%%%%%%

format long;
raw=[];
final=[];
values=[];
filename3='5mmt5.asc';
raw=dlmread(filename3,' ');
[n,m]=size(raw);
cont_cent=74;   %col entry of cont center
line_cent=74;   %col entry of line center
d_start=50;     %%col in array to start
d_stop=211;     %%col in array to stop
x_start=50;
x_stop=84;
average_cont=0;
ref_C=0;
iii=1;
for ii=d_start:1:d_stop;
        values(:,1)=[raw(x_start:x_stop,1)];
        values(:,2)=[raw(x_start:x_stop,ii)];
        %ref_C=min(values(:,2));
        ref_C=raw(100,ii);
```

```
      line_area=sum(values(:,2))-ref_C*34;
      dx=(values(34,1)-values(1,1))/34;
      line_e=line_area*dx;
      cont_area=(ref_C*34)/dx;
      cont_data(iii,1)=iii;
      cont_data(iii,2)=abs(line_e/cont_area);
      cont_data(iii,3)=ii;
       iii=iii+1;
      clear values ref_C line_area dx line_e cont_area;
end
temp=[1000:10:120000];
[n,m]=size(temp);
for jj=1:1:m;
cal_ratio(jj)=(.1013655/temp(jj))*exp(9.151E4/temp(jj))*(1/.13216)*(.5*(1-exp(-3.567E4/temp(jj)))+exp(-
3.567E4/temp(jj)))^-1;
end
[n2,m2]=size(cont_data);
for jjj=1:1:n2;
   [tempval]=find(cal_ratio<cont_data(jjj,2));
   final(jjj,1)=d_start;
   if size(tempval)==0;
      entry=' ';
   else
   row=tempval(1);
   entry=temp(row);
   end
   final(jjj,2)=entry;
   d_start=d_start+1;
   clear entry row tempval;
   end

%%%%%%%%%%cont_ratio2.m%%%%%%%%
r_file1='R-';
r_file2=strcat(r_file1,filename3);
fid=fopen(r_file2,'wt');
[m,n]=size(final);
for m5=1:1:m;
  for n5=1:1:n;
    count=fprintf(fid,'%.8f ', final(m5,n5));
  end
 fprintf(fid,'\n');
end
fclose(fid);
clear r_file1 r_file2 count m5 n5;


%%%%%%%%%%%%%%%%%%%%density_ratio.m.%%%%%%%density sensitive line ration in the VIS
%%%%%%
write=1;
format long;
raw1=[];
raw2=[];
final=[];
filename1='2mm_t8.asc';
filename2='2mmb_t8.asc';
raw1=dlmread(filename1,' ');
```

```
[n1,m1]=size(raw1);

raw2=dlmread(filename2,' ');
[n2,m2]=size(raw2);
profile1(1:m2-1)=raw1(74,2:m1);
profile2(1:m2-1)=raw2(57,2:m1);
for ii=1:1:m2-1;
ratio(ii)=(profile2(ii)/profile1(ii));
end
start=1*10^14;
stop=5*10^17;
Ne=[start:(stop-start)/8000:stop];
[t,y]=size(Ne);
for jj=1:1:y;
R(jj)=2.56727+((.05049-2.56727)/(1+exp(-(log10(Ne(jj))-15.27091)/0.55669)));  %20KK
R(jj)=2.0926+((.02351-2.0926)/(1+exp(-(log10(Ne(jj))-15.3609)/0.5587)));     %30KK
R(jj)=-.2174+((1.8601+.2174)/(1+exp(-(log10(Ne(jj))-15.422)/0.5612)));       %40KK
End
 for kk=1:1:m2-1;
   [temp1]=find(R(:)>ratio(kk));
   value=max(temp1);
   if length(temp1)==0;
      entry=1;
   else
   entry=Ne(value);
   end
   final(kk,2)=entry;
   final(kk,1)=kk;
   clear value entry temp1;
end
%clear raw1 raw2 profile1 profile2 R Ne;
if write==1;
r_file1='R-';
r_file2=strcat(r_file1,filename2);
fid=fopen(r_file2,'wt');
[m,n]=size(final);
for m5=1:1:m;
  for n5=1:1:n;
    count=fprintf(fid,'%f', final(m5,n5));
    end
 fprintf(fid,'\n');
end
fclose(fid);
clear r_file1 r_file2 count m5 n5;
end
```

%%%%%%%%%%Efield.m%%%%%%%%%%

```
write=1;
cavity_l=14^10-3;
height=[0.0005*10^-3:0.005*10^-3:1.5*10^-3];
Q=3.08*10^-11;
l=length(height);
for rr=1:1:l;
Eprofile(rr)=(Q*9*10^9)*(      1/(    height(l+1-rr)* (    (height(l+1-rr)*10-3)^2+14*10-3^2   )^.5    ));
end
Eprofile2(1:rr)=fliplr(Eprofile);
```

```
Eprofile3=(abs(Eprofile-Eprofile2));

Eprofile4=Eprofile3(150:300);
clear x;
Vyn(1)=75*10^4;
time=.005*10^-3/Vyn(1);
m=9.1*0^-31;
 for tt=2:1:rr*0.5;
   Ayn(tt)=(-1.6*10^-19*Eprofile4(tt))*.1098*10^+31;
   Vyn(tt)=Vyn(tt-1)+Ayn(tt)*time;
   Tyn(tt)=time*tt;
   stats(tt,1)=time*tt*10^9;
   stats(tt,2)=Vyn(tt);
end

%%%%%%%%%%%%%%%%%%%%%%%%%%%%%%%%%%%%%%%%%%%%%%%%
if write==1;
r_file1='2KV-';
r_file2=strcat(r_file1,'EF');
fid=fopen(r_file2,'wt');
xxx=[Eprofile3]';
[m,n]=size(xxx);
for m5=1:1:m;
  for n5=1:1:n;
    count=fprintf(fid,'%.8f ', xxx(m5,n5));
  end
  fprintf(fid,'\n');
end
fclose(fid);
clear r_file1 r_file2 count m5 n5;
end
%%%%%%%%%%Efield2.m%%%%%%%%%%%%%%%
write=1;
cavity_l=14^10-3;
ds=3*10^-6;
height=[0.005*10^-3:ds:1.5*10^-3];
Q=3.08*10^-11;
l=length(height);
for rr=1:1:l;
Eprofile(rr)=(Q*9*10^9)*(1/(height(l+1-rr)*((height(l+1-rr)*10-3)^2+14*10-3^2   )^.5));
end
Eprofile2(1:rr)=fliplr(Eprofile);
Eprofile3=(abs(Eprofile-Eprofile2));
Eprofile4=Eprofile3(l*.5:l);
Vrange=[10*10^4:1*10^4:50*10^4];
m=9.1*0^-31;
for jj=1:1:length(Vrange);
Vyn(1)=Vrange(jj);
time=(ds)/Vyn(1);
for tt=2:1:rr*0.5;
   Ayn(tt)=(-1.6*10^-19*Eprofile4(tt))*.1098*10^+31;
   Vyn(tt)=Vyn(tt-1)+Ayn(tt)*time;
end
[u]=find(Vyn(:)>0);
point=max(u);
stats(jj,1)=u(point)*ds;
```

```
stats(jj,2)=u(point);

clear u point Vyn Avy time;
end
clear Eprofile Eprofile2 Eprofile3 Eprofile4;
%%%%%%%%%%%%%%%%%%%%%%%%%%%%%%%%%%%%%%%%%%%%%%%%%
if write==1;
r_file1='2kv';
r_file2=strcat(r_file1,'bias');
fid=fopen(r_file2,'wt');
[m,n]=size(stats);
for m5=1:1:m;
   for n5=1:1:n;
      count=fprintf(fid,'%.8f ', stats(m5,n5));
   end
  fprintf(fid,'\n');
end
fclose(fid);
clear r_file1 r_file2 count m5 n5;
end
%%%%%%%%%%%%%%%%%%%ion_import.m%%%%%%file reading from
ptobes%%%%%%%%%%%%%%%%%%%%%

char name_array1=[];
s1='EAL6p1_';             %%%%first string in names, first matrix group
s2='.txt';               %%  data type, .txt, or .dat or .asci
no_files=81;             %%no of files to read in from eacg group, each group must have same number of files
file_next=[11:1:91];%'1';         %%number, stepper to designate difference, must increase sequentially
for ii=1:1:no_files;
convert=file_next(ii);
add=num2str(convert);
add2=strcat(s1,add);
add3=strcat(add2,s2);
name_array1(ii,:)=add3;
clear add add2 add3;
end
%%%%%%%%%%%%%%%%%%%%%%%%%%%%%%%%%%%%%%%%%%%%%%%
%%%%%%%%division section, read in two files at a time.
format long;
%name_array1=['vbp1.txt';'vbp2.txt';'vbp3.txt';'vbp4.txt';'vbp5.txt';'vbp6.txt';'vbp7.txt';'vbp8.txt';'vbp9.txt'];
name_array1=['vbp10.txt'];
for jj=1:1:1;
char name1=name_array1;
raw=dlmread(name_array1(jj,:),'\t');
[n,m]=size(raw);
maxp=max(raw(:,2));
[x,y]=find(raw(:,2)==max(raw(:,2)));
values(jj,1)=jj;
values(jj,2)=raw(x(1),1);
values(jj,3)=maxp;
clear x y maxp raw name1;
end
%%%%%%%%%%%%%%%%%%%%%%%%%%%%%%%%%%%%%%%%%%%%%%
%%%%%%%%%%%%%Ionz_ratio.m%%%%%%%%%%%%
%first col is temp
%second is actual values RHS of eq for each temp try
```

```
%third col is actual line ratio LHS of eq
format long;
no_targets=6; %no of columns relative to number of lines
raw=[];
final=[];
filename3='tion4mm.dat';
raw=dlmread(filename3,' ');
[n,m]=size(raw);
for ii=2:1:no_targets+1;
    for jj=1:1:n;
    [temp1,temp2]=find(raw(:,ii)<raw(jj,ii+no_targets));
    final(jj,1)=jj;
    if size(temp1)==0;
        entry=1;
    else
    row=max(temp1);
    entry=raw(row,1);
    end
    final(jj,ii)=entry;
    clear entry;
    end
end
%%%%%%%%%%%%%Ionz_ratio2.m%%%%%%%%%%%%
r_file1='R-';
r_file2=strcat(r_file1,filename3);
fid=fopen(r_file2,'wt');
[m,n]=size(final);
for m5=1:1:m;
   for n5=1:1:n;
      count=fprintf(fid,'%.8f ', final(m5,n5));
   end
  fprintf(fid,'\n');
end
fclose(fid);
clear r_file1 r_file2 count m5 n5;
%%%%%%%%%%%%%Ionz_ratio3.m%%%%%%%%%%%%

%cols are ratios for lines al33, al2 in visible (453nm, 466nm)
write=1;
format long;
no_targets=11; %no of columns relative to number of lines
calib=[];
raw=[];
final=[];
filename3='vbtion24.dat';
raw=dlmread(filename3,' ');
[n,m]=size(raw);
Ne=[3.5E16 3.1E16 2.2E16 1.4E16 0.6E16 0.5E16 0.6E16 1.4E16 2.2E16 3.1E16 3.5E16];
temp=[15000:20:35000];
for ii=1:1:no_targets;
for hh=1:1:1000;
calib(hh)=(4.83E15/Ne(ii))*(temp(hh)^1.5)*exp(-26.925*1E4/temp(hh));
end
for jj=1:1:n;
    [temp1]=find(calib(:)<raw(jj,ii));
  if size(temp1)==0;
```

```
        entry=1;
    else
    row=max(temp1);
    entry=temp(row);
    end
    final(jj,ii)=entry;
    clear entry temp1;
    end
clear calib;
end
clear raw;
if write==1;

r_file1='R-';
r_file2=strcat(r_file1,filename3);
fid=fopen(r_file2,'wt');
[m,n]=size(final);
for m5=1:1:m;
   for n5=1:1:n;
      count=fprintf(fid,'%.8f ', final(m5,n5));
   end
  fprintf(fid,'\n');
end
fclose(fid);
clear r_file1 r_file2 count m5 n5;
end
%%%%%%%%%%%%%%%%%%%%Langmuir1.m%%%file read in%%%%%%%%%%
char name_arraya=[];
char name_arrayb=[];
s1='ALP1plan_';              %%%%first string in names, first matrix group
s2='.txt';              %%  data type, .txt, or .dat or .asci
no_files=52;            %%no of files to read in from each group, each group must have same number of files
for ii=1:1:9;
    convert=ii;
add=num2str(ii);
add2=strcat(s1,add);
add3=strcat(add2,s2);
name_arraya(ii,:)=add3;
clear add add2 add3;
end
ddd=1;
%%%%%%%%%%%%%%%%%%%%%%%%%%%%%%%%%%%%%%%%%%%%%%
for iii=11:1:no_files;
convert=iii;
add4=num2str(convert);
add5=strcat(s1,add4);
add6=strcat(add5,s2);
name_arrayb(ddd,:)=add6;
ddd=ddd+1;
clear add4 add5 add6;
end

%%%%%%%%%%%%%%%%%%%%%Langmuir2m%%%form 3D data matrix%%%%
values=[];
vbias(1:47)=[-1.2:.2:8];
vbias(48:52)=[8.5 9 10 11 12];
```

```
final=[];
for jj=1:1:9;
name1=name_arraya(jj,:);
raw=dlmread(name1,' ');
[n,m]=size(raw);
values(:,jj)=raw(2000:10000,2);
clear raw name1;
end
%clear name_arraya;
raw=dlmread('ALP1plan_10.txt',' ');
values(:,10)=raw(2000:10000,2);
time=raw(2000:10000,1);
clear raw;
jjj=1;
for jj=11:1:no_files;
name1=name_arrayb(jjj,:);
raw=dlmread(name1,' ');
[n,m]=size(raw);
values(:,jj)=raw(2000:10000,2);
clear raw name1;
jjj=jjj+1;
end
%clear name_arrayb;

%%%%%%%%%%%%%%%%%%%%Langmuir3.m%%calculations%%%%
Me=9.1*10^-31;
A=.1727; %probe area in cm2
e=1.6*10^-19;
k=1.38*10^-23;
start=100;
stop=6500;
ccc=1;
for kk=start:10:stop;
   vbias(1:47)=[-1.2:.2:8];
   vbias(48:52)=[8.5 9 10 11 12];
   final(ccc,1)=time(kk);
  %data_int(:,1)=[vbias(1):.05:vbias(52)]';
  %data_int(:,2)=interp1(vbias,values(kk,:),data_int(:,1),'spline');
  data(:,1)=[vbias]';
  data(:,2)=[values(kk,:)]';
  [x,y]=find(data(:,2)<0);
  cutoff1=x(1);
  data2a=data(cutoff1:no_files,1);
  data2b=log(abs(data(cutoff1:no_files,2)/50));
  [a,b]=find(data2b>-12);
  [a2,b2]=polyfit(data2a(a(1):a(1)+6),data2b(a(1):a(1)+6),1);
  final(ccc,2)=e/(k*a2(1));     %Tc/K
  final(ccc,3)=(((8*k*final(ccc,2))/(3.14*Me))^.5)/100;  %vel cm/sec
  [o,p]=size(data2a);
  [a3,b3]=polyfit(data2a(o-10:o),data2b(o-10:o),1);
  x2=(a2(2)-a3(2))/(a3(1)-a2(1));
  y2=a2(1)*x2+a2(2);
  final(ccc,4)=exp(y2);
  final(ccc,5)=(final(ccc,4)/(e*A))*(2*3.14*Me/(k*final(ccc,2)))^.5; %%ne in cm3
  for lll=1:1:o;
  temp(lll)=exp(data2b(lll))^2;
```

```
  end
[a4,b4]=polyfit(data2a(o-20:o),[temp(o-20:o)]',1);
  final(ccc,6)=((Me*9.8596*a4(1))/(2*(A^2)*e^3))^.5;  %%ne orbital theory in cm3.
  final(ccc,7)=x2;      %plasma poten V
  final(ccc,8)=69*(final(ccc,2)/(final(ccc,5)*10^6))^.5; %debye length.
  clear data a2 b2 a b data2a data2b data_int data cutoff x2 y2 a3 b3 a4 b4;
  ccc=ccc+1;
end
%%%%%%%%%%%%%%%%%%%%%%Langmuir4.m%%write file%%%%
write_name='ALp15MM.txt';
r_file1='R-';
r_file2=strcat(r_file1,write_name);
fid=fopen(r_file2,'wt');
[m,n]=size(final);
for m5=1:1:m;
  for n5=1:1:n;
    count=fprintf(fid,'%5.8f ', final(m5,n5));
  end
 fprintf(fid,'\n');
end
fclose(fid);
clear r_file1 r_file2 count m5 n5;
disp('FINISHED');

%%%%%%%%%%%%%%%%%%%%%%magfield.m%%%%%%
c=20*10^-6;  %capacitance
v=2*10^3;   %driving voltage
rcoil=60;   %coil resistance
Icoil=10.11;%v/rcoil: %dc current approx
fl=.055;       %former length in m
fd=.05;       %former diameter in m
intfd=.016;      %core diameter in m
wireth=.0004;      %thickness of wire in m
turnsl=fl/wireth;       %number of turns axially
turnsr=(fd-intfd)/wireth; %number of turns radially
radii=[intfd/2:wireth:fd];
lengths=[0:wireth:fl];
for ir=1:1:turnsr;
   for il=1:1:turnsl;
b(ir,il)=((12.56*10^-7)*Icoil*(radii(ir))^2)/(2*(lengths(il)^2+radii(ir)^2)^1.5);
   end
end
btotal=sum(b(:,:));
bfinal=sum(btotal)
%%%%%%%%%%%%%%%%%%%%%%pulse.m%%%%%%
v=2*10^3;
c=8*10^-6;
q=c*v;
t=483*10^-6;
inst_c=82;%q/t;
wire_diam=.002;  %wire diameter in m
former_l=.055;    %former length in m
former_r=.02;   %former radius in m
first_c=.012;    %diameter from inside first turn in m.
no_l=former_l/wire_diam;     %no of turns longditually;
no_r=former_r/wire_diam;  %no of turns radially;
```

```
b=4*3.12*10^-7*inst_c*no_l/2;  %%b field no divided by radius
edge=round(no_r)
invert=[];
for ii=1:1:edge;
  invert(ii)=1/(first_c*.5+ii*wire_diam);
end
scaler=sum(invert);
final_b=scaler*b   %%%peak b field at center of former for all layers
x=[0:.001:former_l];
avg_r=[first_c:.003:no_r*wire_diam];
row=1;
for kk=1:1:length(avg_r);
   for jj=1:1:length(x);
     n(row,jj)=((x(jj)/avg_r(kk))^2+1)^1.5;
end
row=row+1;
end
n_final=[];
for pp=1:1:length(x);
n_final(pp)=sum(n(:,pp));
end
for ll=1:1:length(x);
final_bx(ll)=final_b/n_final(ll);
end
%%%%%%%%%%%%%XUV.1%%%%%%%%%%%%%%%%%%3D peak form%%%%%%%%%
char name_arraya=[];
char name_arrayb=[];
profile=[];
s1='wx';            %%%%first string in names, first matrix group
s2='.dat';           %%  data type, .txt, or .dat or .asci
wc=751;
xn=11;           %%number of space resolved points
tn=14;           %%number of time resolved points
for ii=1:1:xn;
 clear add2;
 add=num2str(ii);
 add2=strcat(s1,add);
 clear add;
  for jj=1:1:tn;
  add3=num2str(jj);
 add4=strcat(add2,'t');
 add5=strcat(add4,add3);
 add6=strcat(add5,s2);
clear add3 add4 add5;
raw=dlmread(add6);
value=max(raw(wc-2:wc+2));
profile(ii,jj)=value;
clear value add6 raw;
end
 end
write_name='.txt';
r_file1='Wal9-284';
r_file2=strcat(r_file1,write_name);
fid=fopen(r_file2,'wt');
[m,n]=size(profile);
```

```
for m5=1:1:m;
   for n5=1:1:n;
      count=fprintf(fid,'%5.8f ', profile(m5,n5));
    end
  fprintf(fid,'\n');
end
fclose(fid);
clear r_file1 r_file2 count m5 n5 n m;
disp('FINISHED');
clear all;
%%%%%%%%%%%%XUV2.m%%%%%%%%%%%%Ionization ratio%%%

format long;
a=0;
b=0;
div1='Pal9-284.txt';
div2='Pal8-285.txt';
raw=dlmread(div1);
raw2=dlmread(div2);
temprange=[120000:100:400000];
[t]=length(temprange);
for cc=1:1:t;
values(cc)=(2.969E-4)*(temprange(cc)^1.5)*exp(-32.4678E5/temprange(cc));
end
ratio=[];
ratio2=[];
[mm,nn]=size(raw2);
for kk=1:1:mm
    for tt=1:1:nn-1;
        a=raw(kk,tt);
        b=raw2(kk,tt);
        ratio(kk,tt)=(a/b);
 [temp1]=find(values<ratio(kk,tt));
if size(temp1)==0;
            entry=1;
          else
             entry=temprange(max(temp1));
          end
ratio2(kk,tt)=entry;
        clear entry;
    end
end

s5='.txt';
s6='TP';
s7='ratio';
r_file1='284-285';
r_file2=strcat(s6,r_file1);
r_file2a=strcat(r_file2,s5);
r_file3=strcat(s7,r_file1);
r_file3a=strcat(r_file3,s5);
%%%%%%%%%%%%%%%%%%%%%%%%%%%%%%%%%%%%%%%%%%
fid=fopen(r_file2a,'wt');
[m,n]=size(ratio2);
for m5=1:1:m;
   for n5=1:1:n;
```

```
      count=fprintf(fid,'%5.5f ', ratio2(m5,n5));
      end
  fprintf(fid,'\n');
end
fclose(fid);
clear r_file2 r_file2a count m5 n5 m n;
disp('FINISHED');
%%%%%%%%%%%%%%%%%%%%%%%%%%%%%%%%%%%%%%%%%%%%%%%%%%%%%%%%%%
id=fopen(r_file3a,'wt');
[m,n]=size(ratio);
for m5=1:1:m;
   for n5=1:1:n;
      count=fprintf(fid,'%5.5f ', ratio(m5,n5));
   end
  fprintf(fid,'\n');
end
fclose(fid);
clear r_file1 r_file3 r_file3a count m5 n5;
disp('FINISHED');
%%%%%%%AL8 Boltzmann plots%%%%%%%%%%%%XUV%%%%%%%%%%%%%%%
save=1;
raw4=[];
raw4a=[];
raw4b=[];
data2=[];
s='23x12t';               %%%%first string in names, first matrix group
sa='24x12t';
sb='25x12t';
s1='x1';
s2='.dat';               %%  data type, .txt, or .dat or .asci
xt=15;             %%number of time resolved points
for ii=1:1:xt;
  add4=num2str(ii);
  add5=strcat(s,add4);
  add6=strcat(add5,s2);
  add5a=strcat(sa,add4);
  add6a=strcat(add5a,s2);
  add5b=strcat(sb,add4);
  add6b=strcat(add5b,s2);
  raw4=dlmread(add6);
  raw4a=dlmread(add6a);
  raw4b=dlmread(add6b);

w=[32.531 32.82 28.5467 25.0139 24.7401 24.845 25.1347 28.912];
gf=[.093254 .1210598 .953015 .53456 .11015 .33426 .53456 .6834];
E=[309110 309110 397020 404200 404200 404200 444570 608100];
l(7)=(sum(raw4b(253:287))*21)/21;
l(8)=(sum(raw4b(199:214))*2*15)/15;
l(5)=(sum(raw4a(701:719))*2*18)/18;
l(3)=(sum(raw4(697:724))*27)/27;
l(1)=(sum(raw4(763:788))*15)/15;
l(2)=(sum(raw4(742:763))*21)/21;
l(4)=(sum(raw4(670:697))*27)/27;
l(6)=(sum(raw4a(604:630))*26)/26;
%l(5)=l(6);
for yy=1:1:8
```

```
data(yy,1)=log((l(yy)*w(yy)^3)/gf(yy));
data(yy,2)=E(yy);
end
slope=polyfit(data(:,2),data(:,1),1);
temp(ii)=(slope(1)*-1)^-1;
%clear slope l data raw rawa rawb add4 add5 add6 add4a add5a add6a add4b add5b add6b;
end
if save==1;
s3='.txt';
write_name=strcat(s1,s3);
r_file1='TAl8Bltz-';
r_file2=strcat(r_file1,write_name);
fid=fopen(r_file2,'wt');
[m,n]=size(temp);
  for n5=1:1:n;
    count=fprintf(fid,'%5.8f ', temp(n5));
     fprintf(fid,'\n');
  end
 fclose(fid);
clear r_file1 r_file2 count m5 n5 n m;
disp('FINISHED');
end

%%%%%%%AL6 Boltzmann plots%%%%%%%%%XUV%%%%%%%%%
save=1;
raw4=[];
raw4a=[];
s='23x2t';            %%%%first string in names, first matrix group
sa='24x2t';
s1='x2';              %%write line
s2='.dat';            %% data type, .txt, or .dat or .asci
xt=15;              %%number of time resolved points
for ii=1:1:xt;
 ii=14;
 add4=num2str(ii);
 add5=strcat(s,add4);
 add6=strcat(add5,s2);
 add5a=strcat(sa,add4);
 add6a=strcat(add5a,s2);
  raw4=dlmread(add6);
 raw4a=dlmread(add6a);
w=[31.2237 31.0907 30.7249 30.8563 24.3766 27.5343];
gf=[.2558 .20417 .258821 .199986 .6412 .1227];
E=[323002 325469 325469 326815 451396 451396];
l(1)=sum(raw4a(23:53));
l(2)=sum(raw4a(61:89));
l(3)=sum(raw4a(161:172))*2;
l(4)=sum(raw4a(137:153))*2;
l(5)=sum(raw4(844:887));
l(6)=sum(raw4a(923:930));
for yy=1:1:6;
data(yy,1)=log((l(yy)*w(yy)^2)/gf(yy));
end
data(1,2)=E(1);
data(2,2)=E(2);
data(3,2)=E(3);
```

```
data(4,2)=E(4);
data(5,2)=E(5);
data(6,2)=E(6);
slope=polyfit(data(:,2),data(:,1),1);
temp(ii)=(slope(1)*-1)^-1;
clear slope l data raw rawa  add4 add5  add4a add5a add6a a add5b;
end
if save==1;
s3='.txt';
write_name=strcat(s1,s3);
r_file1='Al6Bltz-';
r_file2=strcat(r_file1,write_name);
fid=fopen(r_file2,'wt');
[m,n]=size(temp);
  for n5=1:1:n;
    count=fprintf(fid,'%5.8f ', temp(n5));
     fprintf(fid,'\n');
  end
fclose(fid);
clear r_file1 r_file2 count m5 n5 n m;
disp('FINISHED');
end
%%%Spectra3_GO.m%%minimize error fit to iterate the range of w-half-gaussian %%%%each
variable is varied separately.
format long;
w_test_temp=[];
w_test_range_temp=[];
w_test_peak_temp=[];
w_test=[];
w_diff=[];
w_diff2=[];
count_r=[];
wave_r=[];
w_best_fit=[];
w_test_range=[];
w_diff_center=[];
w_diff2_center=[];
final_fit=[];
point_step=1;
for line_step=line_start:1:line_stop;
wave_lside=array_2(point_step,5);
wave_rside=array_2(point_step,6);
line_step
w0=array_2(point_step,2);  %%central peak frequency raw_data
count_r_raw=array_main(wave_lside:wave_rside,line_step);
wave_r_raw=array_main(wave_lside:wave_rside,1);  %%range of wavelengths that the line exist over
w_length=length(wave_r_raw);
%%%%%%%%%%%%%%%%%%%%%%%%%%%%%%%%%%%%%%%%%%%%%%%%%%%%%%%%%%%%%%%%%%%%%%%%%%%%%%interpo
late raw data
wave_r=wave_r_raw(1):.01:wave_r_raw(w_length);
count_r=interp1(wave_r_raw,count_r_raw,wave_r,'cubic');
[new_peak1,new_peak2]=max(count_r);
w0=wave_r(new_peak2);
%%%%%%%%%%%%%%%%%%%%%%%%%%%%%%%%%%%%%%%%%%%%%%%%%%%%%%%%%%%%%%%%%%%%%%%%%%%%%%%%%%
w_0=length(count_r);
w_1=length(wave_r);
```

```
area=sum(count_r_raw)*(wave_r_raw(w_length)-wave_r_raw(1))/w_length;
wave_half_r=(.25:(wave_r(1)-wave_r(w_l))/-200:(wave_r(1)-wave_r(w_l))*-1.5);     %%range of half
widths  that the line exist over
w_l2=length(wave_half_r);
for  width4=1:1:w_l2;
for width5_temp=1:1:w_l;
    w_test_temp(width5_temp)=(area/(wave_half_r(width4)*1.2529964))*exp((-2*(wave_r(width5_temp)-
w0)^2)/wave_half_r(width4)^2);
 end  y_base=abs(min(count_r_raw))+abs(min(w_test_temp));
   [t_w1,t_w2]=max(w_test_temp-y_base);
   for width5=1:1:w_l;
   w_test(width5)=new_peak1*((w_test_temp(width5)-y_base)/t_w1);
  end
for width6=1:1:w_l;
   w_diff(width6)=(sqrt((w_test(width6)-count_r(width6))^2))^2;
 end
   w_diff2(width4)=sum(w_diff);
end
[w_b1,w_b2]=min(w_diff2);
w_best(point_step)=wave_half_r(w_b2);
%%%%%%%%%%%%%%%%%%%%%%%%%%%%%%%%%now have optimized width-halfmax
wavelength best guess%%%%%
%%change the central wavelengths to check lineshift%%%%
 w0_range=[w0-.12:.01:w0+.12];
 %w0_range=454.932;
w_l3=length(w0_range);
for width8=1:1:w_l3;
   for width9_temp=1:1:w_l;
       w_test_range_temp(width9_temp)=(area/(w_best(point_step)*1.2529964))*exp((-
2*(wave_r(width9_temp)-w0_range(width8))^2/(w_best(point_step))^2));
    end
    y_base2=abs(min(count_r_raw))+abs(min(w_test_range_temp));
[t_c1,t_c2]=max(w_test_range_temp-y_base2);
for width9=1:1:w_l;
w_test_range(width9)=(new_peak1)*((w_test_range_temp(width9)-y_base2)/t_c1);
  end
for width10=1:1:w_l;
   w_diff_center(width10)=(sqrt((w_test_range(width10)-count_r(width10))^2))^2;
   end
   w_diff2_center(width8)=sum(w_diff_center);
   [w_c1,w_c2]=min(w_diff2_center);
   w_best_center(point_step)=w0_range(w_c2);
end
%%%%now have optimized center wavelength best guess
%%%%%%%%%%%%%%%%%%%%%%%%%%%%%%%%%%%%%%%%%%%%%%%%%%
%%%%%%%%%%%%%final alogrithm to best guess peak value%%%
%w0_peak=[array_2(point_step,1)-250:100:array_2(point_step,1)+2000];
w0_peak=new_peak1;%[new_peak1-200:20:new_peak1+100];
w_l4=length(w0_peak);
for width12_temp=1:1:w_l;
w_test_peak_temp(width12_temp)=(area/(w_best(point_step)*1.2529964))*exp((-
2*(wave_r(width12_temp)-w_best_center(point_step))^2/(w_best(point_step))^2));
  end
  y_base3=abs(min(count_r_raw))+abs(min(w_test_peak_temp));
  [t_d1,t_d2]=max(w_test_peak_temp);
```

```
 for width11=1:1:w_l4;
 for width12=1:1:w_l;
   w_test_peak(width12)=(w0_peak(width11))*(w_test_peak_temp(width12)-y_base3)/t_d1;
 end
  for width13=1:1:w_l;
  w_peak(width13)=(sqrt((w_test_peak(width13)-count_r(width13))^2))^2;
  end
  w_peak2(width11)=sum(w_peak);
  [w_d1,w_d2]=min(w_peak2);
  w_best_peak(point_step)=w0_peak(w_d2);
end
%%%%now have optimized center peak value%%%%%best guess
%%%%%%%%%%%%%%%%%%%%%%%%%%%%%%%%%%%%%%%%%%%%%%%%%%%
%%%%%%%%
w_best_fit(1:601,1)=[(wave_r(1):(wave_r(1)-wave_r(w_l))/-600:wave_r(w_l))]';
for width7_temp=1:1:601;
 w_best_fit_temp(width7_temp)=(area/(w_best(point_step)*1.2529964))*exp(-
2*(w_best_fit(width7_temp)-w_best_center(point_step))^2/(w_best(point_step))^2);
end
 y_base4=abs(min(count_r_raw))+abs(min(w_best_fit_temp));
[w_f1,w_f2]=max(w_best_fit_temp-y_base4);
for width7=1:1:601;
  w_best_fit(width7,2)=((w_best_fit_temp(width7)-y_base4)/w_f1)*w_best_peak(point_step);
end
%%%%%%%%%%%%%%%%%%%%%%%%%%%%%%%%%%%%%%%%%%%%%%%%%%%
%%%%%
%w_best_center(point_step)
[b_d1,b_d2]=max(w_best_fit(:,2));
final_fit(point_step,1)=w_best_fit(b_d2,2);    %%%peak value best fit
final_fit(point_step,2)=w_best_fit(b_d2,1);    %%%wave center best fit

final_fit(point_step,3)=w_best(point_step);   %%%halfmax wave best fit
final_fit(point_step,4)=((w_best_fit(601,1)-w_best_fit(1,1))*sum(w_best_fit(:,2)))/601;   %%%integrated
%%area under line best fit
point_step=point_step+1;
%figure;
%plot(wave_r,count_r,'*b');
%hold on;
%plot(w_best_fit(:,1),w_best_fit(:,2));
%plot(wave_r_raw,count_r_raw,'r*')
%hold off;
clear wave_r wave_l count_r wave_r wave_half_r w_test w_diff w_diff2 w0_range w_best_fit_temp
w_test_temp;
clear w_test_range w_diff_center w_diff2_center w0_peak w_test_peak w_peak w_peak2 w_peak_fit
count_r_raw wave_r_raw;
end
clear w_best w_best_center w_best_peak;%
%%%%%%%%%%%%%%%%%%%%%%%%%%%%%%%%%%%%%%%%%%%%%%%%%%%
%%%%%
%%%Spectra3_LO.m%%minimize error fit to iterate the range of w-half-Lorentzian %%%%each
variable is varied separately.
format long;
w_test_temp=[];
w_test_range_temp=[];
w_test_peak_temp=[];
```

```
w_test=[];
w_diff=[];
w_diff2=[];
count_r=[];
wave_r=[];
w_best_fit=[];
w_test_range=[];
w_diff_center=[];
w_diff2_center=[];
final_fit=[];
print_command=2;
point_step=1;
for line_step=line_start:1:line_stop;
wave_lside=array_2(point_step,5);
wave_rside=array_2(point_step,6);
line_step
w0=array_2(point_step,2);  %%central peak frequency raw_data
count_r_raw=array_main(wave_lside:wave_rside,line_step);
wave_r_raw=array_main(wave_lside:wave_rside,1);  %%range of wavelengths that the line exist over
w_length=length(wave_r_raw);
%%%%%%%%%%%%%%%%%%%%%%%%%%%%%%%%%%%%%%%%%%%%%%%%%%%%%%%%%%%%%%%%%%%%%%%%%%%%%%%%%%%%%%%%%%%%%%%%interpo
late raw data
wave_r=wave_r_raw(1):.01:wave_r_raw(w_length);
count_r=interp1(wave_r_raw,count_r_raw,wave_r,'cubic');
[new_peak1,new_peak2]=max(count_r);
w0=wave_r(new_peak2);
%%%%%%%%%%%%%%%%%%%%%%%%%%%%%%%%%%%%%%%%%%%%%%%%%%%%%%%%%%%%%%%%%%%%%%%%%%%%%%%%%%%%%%%%%%%%%%%%%%%
w_0=length(count_r);
w_l=length(wave_r);
area=sum(count_r_raw)*(wave_r_raw(w_length)-wave_r_raw(1))/w_length;
wave_half_r=(.25:(wave_r(1)-wave_r(w_l))/-200:(wave_r(1)-wave_r(w_l))*-1.5);     %%range of half
widths  that the line exist over
w_l2=length(wave_half_r);
for  width4=1:1:w_l2;
 for width5_temp=1:1:w_l;
   w_test_temp(width5_temp)=(2*area/3.14)*(wave_half_r(width4)/(4*(wave_r(width5_temp)-
w0)^2+(wave_half_r(width4))^2));
 end
   if min(count_r_raw)>min(w_test_temp);
     y_base=min(count_r_raw)-min(w_test_temp);
  elseif min(count_r_raw)<min(w_test_temp);
       y_base=(min(w_test_temp)-min(count_r_raw))*-1;
   end
 [t_w1,t_w2]=max(w_test_temp+y_base);
  for width5=1:1:w_l;
   w_test(width5)=new_peak1*(w_test_temp(width5)/t_w1)+y_base;
  end
for width6=1:1:w_l;
   w_diff(width6)=(sqrt((w_test(width6)-count_r(width6))^2))^2;
  end
  w_diff2(width4)=sum(w_diff);
end
[w_b1,w_b2]=min(w_diff2);
w_best(point_step)=wave_half_r(w_b2);
%%%%%%%%%%%%%%%%%%%%%%%%%%%%%%%%%%%%%%%%%%%%%%%%%%%%%%%%%%%%%%%%%%%%%%%%%%%%%%%%%%%%%%%%%%%%%%%%now have optimized width-halfmax
wavelength%%%%%best guess
```

```
%%change the central wavelengths to check lineshift%%%%
 w0_range=[w0-.12:.01:w0+.12];
 %w0_range=454.903;
w_l3=length(w0_range);
for width8=1:1:w_l3;
   for width9_temp=1:1:w_l;
       w_test_range_temp(width9_temp)=(2*area/3.14)*(w_best(point_step)/(4*(wave_r(width9_temp)-
w0_range(width8))^2+(w_best(point_step))^2));
    end
    if (count_r_raw(1)+count_r_raw(w_length))*.5>min(w_test_range_temp);
          y_base2=(count_r_raw(1)+count_r_raw(w_length))*.5-min(w_test_range_temp);

   elseif (count_r_raw(1)+count_r_raw(w_length))*.5<min(w_test_range_temp);
          y_base2=(min(w_test_range_temp)-(count_r_raw(1)+count_r_raw(w_length))*.5   )*-1;
    end
    [t_c1,t_c2]=max(w_test_range_temp+y_base2);
  for width9=1:1:w_l;
     w_test_range(width9)=(new_peak1)*(w_test_range_temp(width9)/t_c1)+y_base2;
  end
   for width10=1:1:w_l;
   w_diff_center(width10)=(sqrt((w_test_range(width10)-count_r(width10))^2))^2;
   end
   w_diff2_center(width8)=sum(w_diff_center);
   [w_c1,w_c2]=min(w_diff2_center);
   w_best_center(point_step)=w0_range(w_c2);
end  %%%%now have optimized center wavelength%%%%%best guess
%%%%%%%%%%%%%%%%%%%%%%%%%%%%%%%%%%%%%%%%%%%%%%%%%%%%
%%%%%%%%%%%%%final alogrithm to best guess peak value%%%
%w0_peak=[array_2(point_step,1)-250:100:array_2(point_step,1)+2000];
w0_peak=new_peak1;%[new_peak1-200:20:new_peak1+100];
w_l4=length(w0_peak);
    for width12_temp=1:1:w_l;
     w_test_peak_temp(width12_temp)=(2*area/3.14)*(w_best(point_step)/(4*(wave_r(width12_temp)-
w_best_center(point_step))^2+(w_best(point_step))^2));
  end
    if (count_r_raw(1)+count_r_raw(w_length))*.5>min(w_test_peak_temp);
          y_base3=(count_r_raw(1)+count_r_raw(w_length))*.5-min(w_test_peak_temp);
elseif (count_r_raw(1)+count_r_raw(w_length))*.5<min(w_test_peak_temp);
          y_base3=(min(w_test_peak_temp)-(count_r_raw(1)+count_r_raw(w_length))*.5   )*-1;
    end
  [t_d1,t_d2]=max(w_test_peak_temp+y_base3);
 for width11=1:1:w_l4;
 for width12=1:1:w_l;
    w_test_peak(width12)=(w0_peak(width11))*(w_test_peak_temp(width12)/t_d1)+y_base3;
 end
   for width13=1:1:w_l;
   w_peak(width13)=(sqrt((w_test_peak(width13)-count_r(width13))^2))^2;
   end
   w_peak2(width11)=sum(w_peak);
   [w_d1,w_d2]=min(w_peak2);
   w_best_peak(point_step)=w0_peak(w_d2);
end
%%%%now have optimized center peak value%%%%%best guess
%%%%%%%%%%%%%%%%%%%%%%%%%%%%%%%%%%%%%%%%%%%%%%%%%%%%
%%%%%%%%
```

```
w_best_fit(1:601,1)=[(wave_r(1):(wave_r(1)-wave_r(w_l))/-600:wave_r(w_l))]';
for width7_temp=1:1:601;
  w_best_fit_temp(width7_temp)=(2*area/3.14)*(w_best(point_step)/(4*(w_best_fit(width7_temp)-
w_best_center(point_step))^2+(w_best(point_step))^2));
end
    if (count_r_raw(1)+count_r_raw(w_length))*.5>min(w_best_fit_temp);
        y_base4=(count_r_raw(1)+count_r_raw(w_length))*.5-min(w_best_fit_temp);
   elseif (count_r_raw(1)+count_r_raw(w_length))*.5<min(w_best_fit_temp);
        y_base4=(min(w_best_fit_temp)-(count_r_raw(1)+count_r_raw(w_length))*.5   )*-1;
    end
[w_f1,w_f2]=max(w_best_fit_temp+y_base4);
for width7=1:1:601;
  w_best_fit(width7,2)=(w_best_fit_temp(width7)/w_f1)*w_best_peak(point_step)+y_base4;
end
%%%%%%%%%%%%%%%%%%%%%%%%%%%%%%%%%%%%%%%%%%%%%%%%%%%
%%%%%
%w_best_center(point_step)
[b_d1,b_d2]=max(w_best_fit(:,2));
final_fit(point_step,1)=w_best_fit(b_d2,2);   %%%peak value best fit
final_fit(point_step,2)=w_best_fit(b_d2,1);   %%%wave center best fit
final_fit(point_step,3)=w_best(point_step);   %%%halfmax wave best fit
final_fit(point_step,4)=((w_best_fit(601,1)-w_best_fit(1,1))*sum(w_best_fit(:,2)))/601;   %%%integrated
area under line best fit
final_fit(point_step,5)=line_start+point_step;    %%%index on cdd array
point_step=point_step+1;
if print_command==1;
figure;
plot(wave_r,count_r,'*b');
hold on;
plot(w_best_fit(:,1),w_best_fit(:,2));
plot(wave_r_raw,count_r_raw,'r*')
hold off;
end
%%%%%%%%%%%%%%%%%%%%%%%%%%%%%%%%%%%%%%%%%%%%%%%%%%%
%%%%%%
clear wave_r wave_l count_r wave_r wave_half_r w_test w_diff w_diff2 w0_range w_best_fit_temp
w_test_temp;
clear w_test_range w_diff_center w_diff2_center w0_peak w_test_peak w_peak w_peak2 w_peak_fit
count_r_raw wave_r_raw;
%%%%%%%%%%%%%%%%%%%%%%%%%%%%%%%%%%%%%%%%%%%%%%%%%%%
%%%%%%
end
clear w_best w_best_center w_best_peak;%

%%%%%minimize error fit to iterate the range of w-half-Lorentzian %%%%multi-variable program
which iterates all possible values simultaneously%%%%5
format long;
w_test_temp=[];
w_test_range_temp=[];
w_test_peak_temp=[];
w_test=[];
w_diff=[];
w_diff2=[];
count_r=[];
wave_r=[];
```

```
w_best_fit=[];
w_test_range=[];
w_diff_center=[];
w_diff2_center=[];
final_fit=[];
print_command=1;
point_step=1;
for line_step=line_start:1:line_stop;
wave_lside=array_2(point_step,5);
wave_rside=array_2(point_step,6);
line_step
w0=array_2(point_step,2);  %%central peak frequency raw_data
count_r_raw=array_main(wave_lside:wave_rside,line_step);
wave_r_raw=array_main(wave_lside:wave_rside,1);  %%range of wavelengths that the line exist over
w_length=length(wave_r_raw);
%%%%%%%%%%%%%%%%%%%%%%%%%%%%%%%%%%%%%%%%%%%%%%%%%%%%%interpolate raw data
wave_r=wave_r_raw(1):.01:wave_r_raw(w_length);
count_r=interp1(wave_r_raw,count_r_raw,wave_r,'cubic');
[new_peak1,new_peak2]=max(count_r);
w0=wave_r(new_peak2);
%%%%%%%%%%%%%%%%%%%%%%%%%%%%%%%%%%%%%%%%%%%%%%%%%%%%%
w_0=length(count_r);
w_l=length(wave_r);
wave_half_r=(.25:(wave_r(1)-wave_r(w_l))/-200:(wave_r(1)-wave_r(w_l))*-1.5);     %%range of half widths  that the line exist over
w_l2=length(wave_half_r);
y_baseA=min(count_r);
count_r_temp(1:w_l)=count_r(1:w_l)-y_baseA;
area=sum(count_r_temp)*(wave_r(w_l)-wave_r(1))/w_l;
for  width4=1:1:w_l2;
for width5_temp=1:1:w_l;
    w_test_temp(width5_temp)=(2*area/3.14)*(wave_half_r(width4)/(4*(wave_r(width5_temp)-w0)^2+(wave_half_r(width4))^2));
 end
 low1=min(w_test_temp);
  low2=min(count_r_temp);
  y_baseB=low2-low1;
  w_test(1:w_l)=w_test_temp(1:w_l);
for width6=1:1:w_l;
   w_diff(width6)=(sqrt((w_test(width6)-count_r_temp(width6))^2))^2;
 end
   w_diff2(width4)=sum(w_diff);
end
[w_b1,w_b2]=min(w_diff2);
w_best(point_step)=wave_half_r(w_b2);
w_best_fit(1:601,1)=[(wave_r(1):(wave_r(1)-wave_r(w_l))/-600:wave_r(w_l))]';
for width7_temp=1:1:601;
  w_best_fit_temp(width7_temp)=(2*area/3.14)*(w_best(point_step)/(4*(w_best_fit(width7_temp)-w0)^2+(w_best(point_step))^2));
end
low7=min(w_best_fit_temp(:,2));
low8=min(count_r);
y_base4=low8-low7;
w_best_fit(1:601,2)=[w_best_fit_temp(1:601)]'+y_base4;
```

```
%%%%%%%%%%%%%%%%%%%%%%%%%%%%%%%%%%%%%%%%%%%%%%%%%%
%%%%%
%w_best_center(point_step)
 [b_d1,b_d2]=max(w_best_fit(:,2));
final_fit(point_step,1)=w_best_fit(b_d2,2);    %%%peak value best fit
final_fit(point_step,2)=w_best_fit(b_d2,1);    %%%wave center best fit
 final_fit(point_step,3)=w_best(point_step);   %%%halfmax wave best fit
final_fit(point_step,4)=area;%((w_best_fit(601,1)-w_best_fit(1,1))*sum(w_best_fit(:,2)))/601;
%%%integrated area under line best fit
final_fit(point_step,5)=line_start+point_step;    %%%index on cdd array
point_step=point_step+1;
if print_command==2;
figure;
plot(wave_r,count_r,'*b');
hold on;
plot(w_best_fit(:,1),w_best_fit(:,2));
plot(wave_r_raw,count_r_raw,'r*')
hold off;
end
%%%%%%%%%%%%%%%%%%%%%%%%%%%%%%%%%%%%%%%%%%%%%%%%%%
%%%%%%
clear wave_r wave_l count_r wave_r wave_half_r w_test w_diff w_diff2  w_best_fit_temp w_test_temp;
clear   area count_r_raw wave_r_raw;
%%%%%%%%%%%%%%%%%%%%%%%%%%%%%%%%%%%%%%%%%%%%%%%%%%
%%%%%%
end
clear w_best w_best_center;
```

```
////////////////////////////////////////Langmuir1.C/////////////////////////////////////////////////////////
#include <stdlib.h>
#include <stdio.h>
#include <string.h>
#include <conio.h>
#include <math.h>
#define delta_vb  59/*no of files with diff bias V same probe*/
#define real_value 25/*number of temporal values to be saved*/
#define first   75/* point in time amongest waveform to start entries*/
#define width 2   /*out put from lab view*/
#define length 500  /*length of waveform*/
#define tmax 5*pow10(-6);   /*far right in oscilliscope window*/
#define tmin 0;      /*initial time in oscilliscope window*/
void main()
{
FILE *fp, *stream;  /*fp is a pointer to a file for readin, stream is for file write*/
int number, i, k, k2, k3, k4, k5, k6, k7, k9, nline, nline2;
int nline3, nline4, nline5, nline6, nline7, nline8, nline9, nline10;
int v_counter, v_counter2, counter, level, stepper, extraline, ref_position;
int trst, vsvb, vsvb2, vsvb3, vsvb4, sign_test, ref_position2;
int slope_change, end_value, test_val2, test_val3;
int dvc, sub_delta_vb, refer, entry, sub_first;
////////////////////////////////////////////////
int write=1;  /*set to 0 for no write, set to 1 for write*/
////////////////////////////////////////////////
char string[delta_vb][15], filestepper[7], type[5];
char  pathpc1[50], pathpc2[40];
char lp_fnames[delta_vb][40];              /*final array of file names and paths*/
```

```
char *str1 = "\123_",
char *str2 = " txt",
char *str3 = "a \\",
char *str4 = "\"  ",
float axy1, bxy2, bx2a, bx2b,
float by2a, by2b, ay1a, ay1b, ax1a, ax1b,
float cxy2, cx2a, cx2b, cy2a, cy2b,
float c1, c2, aslope, bslope, xcc, ycc, A, A1, B, B1, A2, B2,
float buffer[1000],
float main_array[real_value][width][delta_vb],   /*main array where all waveforms are read into*/
float temp_main_array[length][width],   /*main array where all waveforms are read into for a set vbias*/
float v_initial, diff_value, adjust_val,
float v_stepper, min_vb, sheath, e_perm,
float v_actual,
float v_values[delta_vb],
float IV_form[delta_vb][2],
float lnIV_form[delta_vb][2],
float DIDV[delta_vb][2],
float vslope[delta_vb-1][3],
float FINAL_vplasma[real_value][11],
float vb_diff[delta_vb-1],
float temp, temp2, temp3, temp4, temp5, temp6,
float temp7, temp8, temp9, temp10, temp11, temp12, temp13, temp14, temp15, temp16, temp18,
float temp17, sheath_r,
float e=1 6*pow10(-19),
float boltzmann=1 38*pow10(-23),
float pie=3 141592654,
float Me=9 11*pow10(-31),
float Te, No, Ne, Ne_acc, Ve, debye_L,
float Ap= 1727,   /*area of probe in cm squared*/
float VB=15 0,
float ref_voltage,
sub_delta_vb=delta_vb,
sub_first=first,
end_value=real_value,
temp13=tmax,
temp14=tmin,
k3=0,   /*used to write data to files*/
nline=0,
vsvb=0,
vsvb2=0,
vsvb3=0,
nline3=0,
temp7=0 0,
temp4=0 0,
slope_change=1,
v_initial=0 0,
v_stepper=0 10,
////////////////////////////////////////////////
stepper=1,     /*value to allow stepping through time values*/
////////////////////////////////////////////////
clrscr(),
i=0,
for (i=0, i<sub_delta_vb, i++)     /*first loop to increment the number after the file name main*/
{
number=i+1,
```

```
/*printf("\n %d", i),*/
strcpy(*(string+i), str1),
strcpy(type, str2),
/*itoa(int,string,numbertype(e g  decimal=10))*/
itoa(number, filestepper, 10),
strcat(*(string+i), filestepper),
strcat(*(string+i), type),
/*printf("\n %s %d", *(string+i), i),  /*string containd the file names and type*/
}
////////////////////////////////////////////////////
////////////////////////////////////////////////////
for (k=0,k<sub_delta_vb,k++)        /*second loop to place a \ and " in file name string for fp=fopen*/
{
/*printf("\n %d", k),*/
refer=0,
nline=0,   //line stepper for file read-in//
entry=0,
strcpy(pathpc1,str3),
strcpy(pathpc2,str4),
strcat(pathpc1, *(string+k)),
/*printf("\n %s %d", pathpc1, k),*/
strcpy(*(lp_fnames+k), pathpc1),
/*printf("\n  %s", *(lp_fnames+k)),*/
fp = fopen(pathpc1,"r"),    /*open command and read*/
/*printf("\n %s", pathpc1),     /*(final array of annotated paths*/
while(fgets(buffer, 1000, fp)!=NULL )
{
sscanf(buffer, "%f %f", &temp_main_array[nline][1], &temp_main_array[nline][0]),
/*printf("\n % 10f % 10f", temp_main_array[nline][1], temp_main_array[nline][0]),*/
nline++,
}
/*printf("\n % 10f % 10f", temp_main_array[499][1], temp_main_array[499][0]),*/
fclose(fp),
free(pathpc1),
free(pathpc2),
entry=sub_first,
do{
main_array[refer][0][k]=temp_main_array[entry][0],
main_array[refer][1][k]=temp_main_array[entry][1],
/*printf("\n % 10f % 10f", temp_main_array[entry][0], temp_main_array[entry][1]),*/
entry+=stepper,
/*entry+=50,/*,  this can be used to get every n entry*/
refer++,
} while(refer<end_value),
free(temp_main_array),
free(buffer),
}
free(filestepper),
free(string),
free(type),
free(lp_fnames),
/*printf("\n %f %f", main_array[0][0][0], main_array[0][0][1]),*/
////////////////////////////////////////////////////
/*v_values[0]=-1 0,
v_values[1]=- 9,
v_values[2]=- 8,
```

```
v_values[3]=- 7,
v_values[4]=- 6,
v_values[5]=- 5,
v_values[0]=- 3,  */
v_values[0]=- 25,
v_values[1]=- 2,
v_values[2]=- 15,
v_values[3]=-0 1,
v_values[4]=-0 05,
v_counter2=5,
for(v_counter=0,v_counter<46,v_counter++)
{
v_actual=v_initial+v_stepper*v_counter,
v_values[v_counter2]=v_actual,
/*printf("%f %d\n", v_values[v_counter], v_counter2),*/
v_counter2++,
v_actual=0 0,
}
/*printf("\n%f %d\n", v_values[45], v_counter2),*/
v_values[51]=5 0,
v_values[52]=5 5,
v_values[53]=6 0,
v_values[54]=6 5,
v_values[55]=7 0,
v_values[56]=7 5,
v_values[57]=8 0,
v_values[58]=9,
/*printf("\n%f %d\n", v_values[56], v_counter2),   */
////////////////////////////////////////////////////
trst=0,    /*time stepper*/
do{
temp7=0 0,
vsvb=0,
do{
/*printf("\n % 8f %d", temp7, vsvb),*/
temp7=main_array[trst][0][vsvb],
/*printf("\n % 8f %d", temp7, vsvb),*/
IV_form[vsvb][0]=temp7,
IV_form[vsvb][1]=v_values[vsvb],
/*printf("\n %f %f", IV_form[vsvb][0], IV_form[vsvb][1]),*/
vsvb++,
}while(vsvb<sub_delta_vb),
/*printf("\n %f %f", IV_form[0][0], IV_form[0][1]),*/
/*printf("\n %f", main_array[0][0][0]),*/
////////////////////////////////////
vsvb2=0,
nline5=0,
nline8=0,
do{
if(IV_form[vsvb2][0]<0 && IV_form[vsvb2+1][0]<0
  &&IV_form[vsvb2+2][0]<0 && IV_form[vsvb2+3][0]<0
  &&IV_form[vsvb2+4][0]<0 && IV_form[vsvb2+5][0]<0)
  sign_test=2,
else(sign_test=0, vsvb2++, nline5++),
}while(sign_test<1),
printf("\n %d %f %f %f", nline5, IV_form[nline5][0], IV_form[nline5][1], IV_form[nline5+1][0]),
```

```
////////////////////////////////////
temp18=0 0,          /*approx ion sat current*/
/*temp18=(sqrt(pow(IV_form[nline5-1][0], 2))+sqrt(pow(IV_form[nline5-2][0],
2))+sqrt(pow(IV_form[nline5-3][0], 2)))/3,*/
ref_voltage=-3 0*pow10(-8),
ref_position=0,
/*for(nline10=nline5,nline10<5+nline5,nline10++){
  if(IV_form[nline10][0]>ref_voltage)
  ref_position=nline10,
  }
/*printf("\n %d", ref_position),*/
if(ref_position==0)
ref_position2=0,
else(ref_position2=ref_position-nline5+1),
////////////////////////////////////
temp11=0,
temp12=0,
test_val3=nline5,
/*printf("\n %d", ref_position2),*/
/*printf("\n %f %f", IV_form[nline5][0], IV_form[nline5][1]),*/
temp11=sqrt(pow(log(sqrt(pow(IV_form[nline5+ref_position2][0], 2))), 2)),
for(nline8=ref_position2+nline5+1,nline8<10+nline5,nline8++){
 temp12=sqrt(pow(log(sqrt(pow(IV_form[nline8][0], 2))), 2)),
if(temp11<=temp12){
   temp11=temp12,
   test_val3=nline8,
 }
    /*printf("\n%d %f %f %d", nline8, temp11, temp12, test_val3),*/
}
/*printf("\n %d %d %f %f", nline8, test_val3, IV_form[test_val3][0], IV_form[test_val3][1]),*/
////////////////////////////////////
vsvb3=0,
temp6=0,
nline7=test_val3,
nline6=nline7,
/*printf("\n %d", nline6),*/
do{
temp6=IV_form[nlme6][0]-temp18,
lnIV_form[vsvb3][0]=log(sqrt(pow(temp6, 2))),
lnIV_form[vsvb3][1]=IV_form[nline6][1],
/*printf("\n %d %f %f\n", vsvb3, lnIV_form[vsvb3][0], lnIV_form[vsvb3][1]),*/
vsvb3++,
nline6++,
}while(vsvb3<sub_delta_vb-nline7),
/*printf("\n %d", vsvb3),
printf("\n %f %f", lnIV_form[0][0], lnIV_form[0][1]),
printf("\n %f %f", lnIV_form[1][0], lnIV_form[1][1]),*/
////////////////////////////////////////////
dvc=0,
do
{
DIDV[dvc][0]=lnIV_form[dvc+1][0]-lnIV_form[dvc][0],
DIDV[dvc][1]=lnIV_form[dvc+1][1]-lnIV_form[dvc][1],
vslope[dvc][1]=lnIV_form[dvc][1],
vslope[dvc][2]=lnIV_form[dvc+1][1],
temp9=DIDV[dvc][0],
```

```
temp10=DIDV[dvc][1],
vslope[dvc][0]=temp9/temp10,

dvc++,
}while(dvc<sub_delta_vb-nline7-1),
////////////////////////////////////
/*printf("\n %f", vslope[0][0]),
printf("\n %f", vslope[1][0]),
printf("\n %f", vslope[2][0]),
printf("\n %f", vslope[3][0]),
printf("\n %f", vslope[4][0]),
printf("\n %f", vslope[5][0]),*/
////////////////////////////////////
nline3=0,
while(slope_change==1)
{
if(vslope[nline3][0]>=vslope[nline3+1][0]
  &&vslope[nline3][0]>=vslope[nline3+2][0]
  &&vslope[nline3][0]>=vslope[nline3+3][0]
  &&vslope[nline3][0]>=vslope[nline3+4][0]
  &&vslope[nline3][0]>=vslope[nline3+5][0]
  &&vslope[nline3][0]>=vslope[nline3+6][0]
  &&vslope[nline3][0]>=vslope[nline3+7][0]
  &&vslope[nline3][0]>=vslope[nline3+8][0])
/*note limit to number of allowed statments is*/
 slope_change=0,
else nline3++,
 }
/*printf("\n %d", nline3),*/
////////////////////////////////////////////
if(nline3==0)
extraline=5,
else if(nline3==1)
extraline=4,
else if(nline3==2)
extraline=3,
else if(nline3==3)
extraline=2,
else if(nline3>3)
extraline=1,
/*printf("\n %d", extraline),*/
////////////////////////////////////////////
ax1a=0,
ax1b=0,
ay1a=0,
ay1b=0,
axy1=0,
k5=0,
do{
ax1a+=lnIV_form[k5][1],
ax1b+=pow(lnIV_form[k5][1], 2),
ay1a+=lnIV_form[k5][0],
ay1b+=pow(lnIV_form[k5][0], 2),
axy1+=lnIV_form[k5][1]*lnIV_form[k5][0],
/*printf("\n%f %f %f %f %f %d", ax1a, ax1b, ay1a, ay1b, axy1, nlme3),*/
k5++,
```

```
}while(k5<nline3+extraline),


/*printf("\n %f %f", lnIV_form[0][1], lnIV_form[0][0]),*/
A=(((nline3+extraline)*axy1)-(ax1a*ay1a))/((ax1b)*(nline3+extraline)-pow(ax1a, 2)),
B=((ax1b*ay1a)-(axy1*ax1a))/((ax1b*(nline3+extraline))-pow(ax1a, 2)),
printf("\n %f %f", A, B),
//////////////////////////////////////////
bx2a=0,
bx2b=0,
by2a=0,
by2b=0,
bxy2=0,
k6=0,
do{
bx2a+=lnIV_form[sub_delta_vb-k6-1-nline7][1],
bx2b+=pow(lnIV_form[sub_delta_vb-k6-1-nline7][1], 2),
by2a+=lnIV_form[sub_delta_vb-k6-1-nline7][0],
by2b+=pow(lnIV_form[sub_delta_vb-k6-1-nline7][0], 2),
bxy2+=lnIV_form[sub_delta_vb-k6-1-nline7][1]*lnIV_form[sub_delta_vb-k6-1-nline7][0],
/*printf("\n %f %f %f %f %f", bx2a, by2b, by2a, by2b, bxy2),*/
k6++,
}while(k6<10),
A1=(((10)*bxy2)-(bx2a*by2a))/(((bx2b)*(10))-pow(bx2a, 2)),
B1=((bx2b*by2a)-(bxy2*bx2a))/((bx2b*10)-pow(bx2a, 2)),
printf("\n %f %f ", A1, B1),
//////////////////////////////////////////
cx2a=0,
cx2b=0,
cy2a=0,
cy2b=0,
cxy2=0,
k7=0,
do{
cx2a+=IV_form[sub_delta_vb-k7-1][1],
cx2b+=pow(IV_form[sub_delta_vb-k7-1][1], 2),
cy2a+=pow(IV_form[sub_delta_vb-k7-1][0], 2),
cy2b+=pow(IV_form[sub_delta_vb-k7-1][0], 4),
cxy2+=IV_form[sub_delta_vb-k7-1][1]*pow(IV_form[sub_delta_vb-k7-1][0], 2),
k7++,
}while(k7<10),
/*printf("\n %f %f %f %f %f" , cx2a, cx2b, cy2a, cy2b, cxy2),*/
FINAL_vplasma[trst][9]=A2,
A2=(((10)*cxy2)-(cx2a*cy2a))/(((cx2b)*(10))-pow(cx2a, 2)),
B2=((cx2b*cy2a)-(cxy2*cx2a))/((cx2b*10)-pow(cx2a, 2)),
/*printf("\n % 9f % 9f", A2, B2),*/
//////////////////////////////////////////
aslope=A,
bslope=A1,
c1=B,
c2=B1,
xcc=(c2-c1)/(aslope-bslope),   /*intercept of both lines x*/
ycc=(-aslope*c2+c1*bslope)/(bslope-aslope),   /*intercept of both lines y*/
/*printf("\n%f %f", xcc, ycc),*/
//////////////////////////////////////////////////////
FINAL_vplasma[trst][0]=xcc,                    /*x-intercept */
```

```
FINAL_vplasma[trst][1]=ycc,

////////////////////////////////////////////////////////////////////////////
////////////////////////////////////////////////////////////////////////////
FINAL_vplasma[trst][2]=A,   /*slope of log I vs V*/
/*printf("\n %f %f ", A, FINAL_vplasma[trst][2]),*/
for(counter=0,counter<sub_delta_vb-nlme7,counter++)
{
 vb_diff[counter]=sqrt(pow((xcc-lnIV_form[counter][1]), 2)),
 }
/*printf("\n %f %f %f %f %f", vb_diff[0], vb_diff[1], vb_diff[2], vb_diff[3], vb_diff[4]),*/
/*printf("\n %f %f %f %f %f", vb_diff[5], vb_diff[6], vb_diff[7], vb_diff[8], vb_diff[9]),  */
diff_value=0,
nline4=0,
do
{
  if(vb_diff[nline4]>vb_diff[nline4+1])
  nline4++,
  else if(vb_diff[nline4]<vb_diff[nline4+1])
  diff_value=1,
  } while(diff_value!=1),
/*printf("\n %d", nline4),*/
FINAL_vplasma[trst][3]=lnIV_form[nline4][0],  /*electron sat current*/
/*printf("\n %f", lnIV_form[nline4][0]),*/
////////////////////////////////////////////////////////
Te=(e/(FINAL_vplasma[trst][2]*boltzmann)),
/*printf("\n %f", Te),*/
temp4=0 0,
FINAL_vplasma[trst][4]=Te,
Ve=(sqrt((8*boltzmann*Te)/(pie*Me)))/100,     /*in cm/sec*/
/*printf("\n%f %f %f %f", Te, Ve, temp4, A2),*/
FINAL_vplasma[trst][5]=Ve,
temp4=exp(FINAL_vplasma[trst][3]),
debye_L=0 0,
Ne=(temp4*4 0)/(Ap*e*Ve),
FINAL_vplasma[trst][6]=Ne,
/*printf("\n %f %f", Ne, A2),*/
temp17=((Me*pow(pie, 2)*A2)/(2*pow(Ap, 2)*pow(e, 3))),
/*printf("\n %f %f", temp15, temp16),*/
Ne_acc=sqrt(temp17),
/*printf("\n %f %f", Ne, FINAL_vplasma[trst][6]),*/
FINAL_vplasma[trst][8]=Ne_acc,
debye_L=69*( sqrt (Te/(Ne*pow10(6)) ) )*pow10(6),
FINAL_vplasma[trst][9]=debye_L,
sheath_r=(e*VB)/(boltzmann*Te),
FINAL_vplasma[trst][10]=2*debye_L*(pow( 75, sheath_r)),
printf("\n%f %f %f %f %f %f %f", Te, Ne, Ne_acc, xcc, debye_L, sheath_r, temp4),
free(IV_form),
free(lnIV_form),
free(vslope),
free(vb_diff),
free(DIDV),
trst++,
}while(trst<end_value),
free(v_values),
free(main_array),
```

```
/*end of loop for selecting time values*/
////////////////////////////////////////////////////
/*sets up matrix time, containing all time values used in program*/
for(k4=0,k4<end_value,k4++)
{
FINAL_vplasma[k4][7]=((temp13*(sub_first-1+(k4*stepper)))+temp14)/(5*pow10(2)),
/*printf("\n % 9f", FINAL_vplasma[k4][7]),*/
}
////////////////////////////////////////////////////
k3=0,
if(write==1)
{ stream = fopen("2R txt", "w+"),
/* write some data to the file */
  do{
  fprintf(stream, "% 8f %f %f %f %f %f %f %f % 5f\n", FINAL_vplasma[k3][7]
,FINAL_vplasma[k3][0], FINAL_vplasma[k3][1], FINAL_vplasma[k3][2],
  FINAL_vplasma[k3][3], FINAL_vplasma[k3][4], FINAL_vplasma[k3][5], FINAL_vplasma[k3][6],
FINAL_vplasma[k3][8], FINAL_vplasma[k3][9], FINAL_vplasma[trst][10]),
  k3++,
   } while(k3<end_value),
  /* close the file */
  fclose(stream),
 }
free(FINAL_vplasma),
}
////////////////////////////////////////////ION C////////////////////////////////////////////////
#include <stdio h>
#include <string h>
#include <conio h>
#include <math h>
#define delta_vb 21    /*no of files with diff bias V same probe*/
#define real_value 1/*number of temporal values to be saved*/
#define first 201/* point in time amongest waveform to start entries*/
#define width 2   /*out put from lab view*/
#define length 500  /*length of waveform*/
void main()
{
FILE *fp, *stream,  /*fp is a pointer to a file for readin, stream is for file write*/
int number, i, k, k2, k3, k4, k5, k6, nline,
int v_counter, stepper,
int trst, vsvb,
int end_value,
int dvc, sub_delta_vb, refer, entry, sub_first,
////////////////////////////////////////////
int write=1,  /*set to 0 for no write, set to 1 for write*/
////////////////////////////////////////////
char string[delta_vb][12], filestepper[7], type[5],
char  pathpc1[30], pathpc2[10],
char lp_fnames[delta_vb][30],              /*final array of file names and paths*/
char *str1 = "\ion",
char *str2 = " txt",
char *str3 = "a \\",
char *str4 = "\"  ",
float axy1, ay1a, ay1b, ax1a, ax1b,
float  A, B,
float buffer[1000],
```

```
float main_array[real_value][width][delta_vb],  /*main array where all waveforms are read into*/
float temp_main_array[length][width],  /*main array where all waveforms are read mto for a set vbias*/
float v_initial, diff_value,
float v_stepper,
float v_actual,
float v_values[delta_vb],
float IV_form[delta_vb][2],
float lnIV_form[delta_vb][2],
float DIDV[delta_vb-1][2],
float vslope[delta_vb][3],
float FINAL_ion[real_value][2],
float temp7, temp6,
float ion_C=1 6*pow10(-19),
float pie=3 141592654,
float m_ion=4 4867*pow10(-27),
float Ap= 1727,/*area of probe in cm squared*/
sub_delta_vb=delta_vb,
sub_first=first,
end_value=real_value,
k3=0,
nline=0,
v_initial=-5,
v_stepper=-2,
////////////////////////////////////////////////
stepper=1,     /*value to allow stepping through time values*/
////////////////////////////////////////////////
clrscr(),
for (i=0, i<sub_delta_vb, i++)     /*first loop to increment the number after the file name main*/
{
number=i+1,
strcpy(*(string+i), str1),
strcpy(type, str2),
//itoa(int,string,numbertype(e g  decimal=10))
itoa(number, filestepper, 10),
strcat(*(string+i), filestepper),
strcat(*(string+i), type),
/*printf("\n %s", *(string+i)),  /*string containd the file names and type*/
}
////////////////////////////////////////////////////
////////////////////////////////////////////////////
for (k=0,k<sub_delta_vb,k++)       /*second loop to place a \ and " in file name string for fp=fopen*/
{
refer=0,
nline=0,  //line stepper for file read-in//
strcpy(pathpc1,str3),
strcpy(pathpc2,str4),
strcat(pathpc1, *(string+k)),
strcpy(*(lp_fnames+k),pathpc1),
/*printf("\n fullpath is  %s", *(lp_fnames+k)), */
fp = fopen(pathpc1,"r"),   /*open command and read*/
/*printf("\n fullpath is  %s", pathpc1),    /*(final array of annotated paths*/
while(fgets(buffer, 1000, fp)!=NULL ){
sscanf(buffer, "%f %f", &temp_main_array[nline][1], &temp_main_array[nline][0]),
/*printf("\n % 10f % 10f", temp_main_array[nline][1], temp_main_array[nline][0]),*/
nline++,
}
```

```
/*printf("\n % 7f % 7f", temp_main_array[499][1], temp_main_array[nline][0]),*/
/*printf("\n % 10f % 10f", main_array[0][1][k], main_array[0][0][k]),*/
fclose(fp),
entry=sub_first,
do{
main_array[refer][0][k]=temp_main_array[entry][0],
main_array[refer][1][k]=temp_main_array[entry][1],
/*printf("\n % 10f % 10f", main_array[refer][1][k], main_array[refer][0][k]),*/
entry+=stepper,
/*entry+=50,/*, this can be used to get every n entry*/
refer++,
} while(refer<end_value),
free(temp_main_array),
/*printf("\n % 10f % 10f", main_array[1][0][k], main_array[1][1][k]),*/
free(buffer),
}
free(pathpc1),
free(pathpc2),
free(filestepper),
free(string),
free(type),
free(lp_fnames),
////////////////////////////////////////////////////////
v_values[0]=v_initial,
for(v_counter=1,v_counter<sub_delta_vb,v_counter++)
{
v_actual=v_initial+v_stepper,
v_initial=v_actual,
v_values[v_counter]=v_actual,
/*printf("%f %d\n", v_values[v_counter], v_counter),*/
}
/*printf("%f\n", v_values[0]),*/
////////////////////////////////////////////////////////
trst=0,    /*time stepper*/
do{
vsvb=0,
do{                /*form the IV curve for the probe at time trst*/
temp7=main_array[trst][0][vsvb],
IV_form[vsvb][0]=sqrt(pow(temp7, 2)),
IV_form[vsvb][1]=v_values[vsvb],
temp6=IV_form[vsvb][0],
lnIV_form[vsvb][0]=pow((temp6), 2),
lnIV_form[vsvb][1]=v_values[vsvb],
/*printf("\n %f %f %f %d", temp7, IV_form[vsvb][0], lnIV_form[vsvb][0], vsvb),*/
vsvb++,
}while(vsvb<sub_delta_vb),
////////////////////////////////////////////////////////
for(dvc=0,dvc<sub_delta_vb-1,dvc++)
{
DIDV[dvc][0]=lnIV_form[dvc+1][0]-lnIV_form[dvc][0],
DIDV[dvc][1]=lnIV_form[dvc+1][1]-lnIV_form[dvc][1],
vslope[dvc][1]=lnIV_form[dvc][1],
vslope[dvc][2]=lnIV_form[dvc+1][1],
vslope[dvc][0]=DIDV[dvc][0]/DIDV[dvc][1],
}
////////////////////////////////////////////
```

```
/*method of least squares, for the line fit*/
//////////////////////////////////////////
ax1a=0,
ax1b=0,
ay1a=0,
ay1b=0,
axy1=0,
for(k5=0,k5<sub_delta_vb,k5++)
{
ax1a+=lnIV_form[k5][1],
ax1b+=pow(lnIV_form[k5][1], 2),
ay1a+=lnIV_form[k5][0],
ay1b+=pow(lnIV_form[k5][0], 2),
axy1+=lnIV_form[k5][1]*lnIV_form[k5][0],
}
A=(((sub_delta_vb)*axy1)-(ax1a*ay1a))/((ax1b)*(sub_delta_vb)-pow(ax1a, 2)),
B=((ax1b*ay1a)-(axy1*ax1a))/((ax1b*(sub_delta_vb))-pow(ax1a, 2)),
/*printf("\n%f %f %f %f %f %f %f", ax1a, ax1b, ay1a, ay1b, axy1, A, B),*/
printf("\n %f", A),
//////////////////////////////////////////
FINAL_ion[trst][0]=sqrt((m_ion*-4*pie*A)/(3*pow(Ap, 2)*pow(ion_C, 3))),
printf("\n % 12f", FINAL_ion[trst][0]),
//////////////////////////////////////////
free(IV_form),
free(lnIV_form),
free(vslope),
free(DIDV),
trst++,
}while(trst<end_value),
//////////////////////////////////////////
/*end of time loop*/
free(v_values),
free(main_array),
/*end of loop for selecting time values*/
//////////////////////////////////////////////////////
/*sets up matrix time, containing all time values used in program*/
for(k4=0,k4<end_value,k4++)
{
FINAL_ion[k4][1]=(5*pow10(-6))*((sub_first-1+k4*stepper)/(5*pow10(2))),
/*printf("\n % 9f", FINAL_vplasma[k4][1]),*/
}
//////////////////////////////////////////////////////
if(write==1)
{ stream = fopen("ionR txt", "w+"),
/* write some data to the file */
  do{
  fprintf(stream, "% 8f % 8f \n",FINAL_ion[k3][0], FINAL_ion[k3][1]),
  k3++,
   } while(k3<end_value),
  /* close the file */
  fclose(stream),
 }
free(FINAL_ion),
 }
```

Appendix B List of figures, Graphs and photos

Introduction

Chapter One

Chapter Two

Chapter Three

Chapter Four

Chapter Five

Chapter Six

Tables

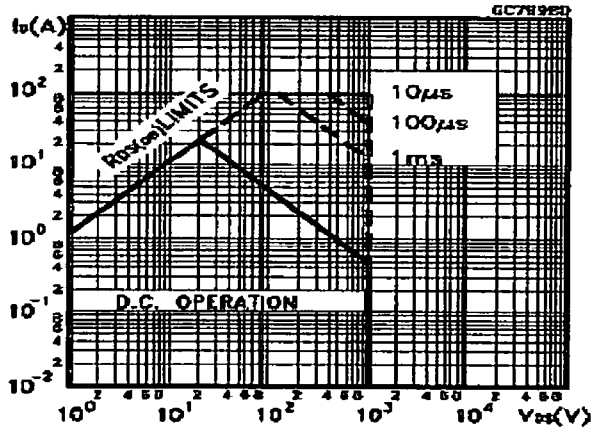

Current versus voltage for FET array device pulse width dependence

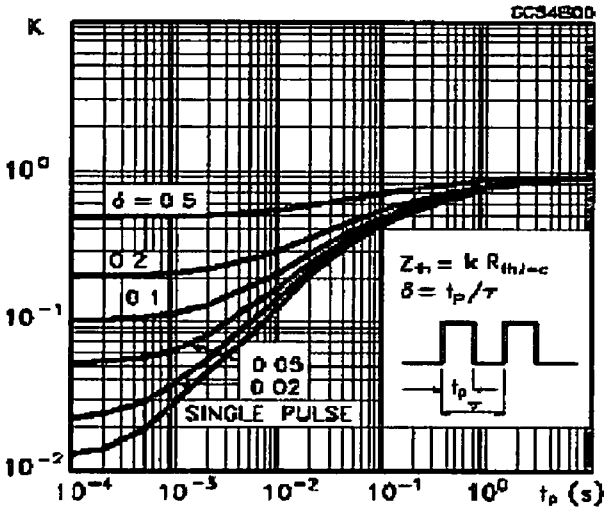

Rep rate for variable pulse width

TOP LEFT

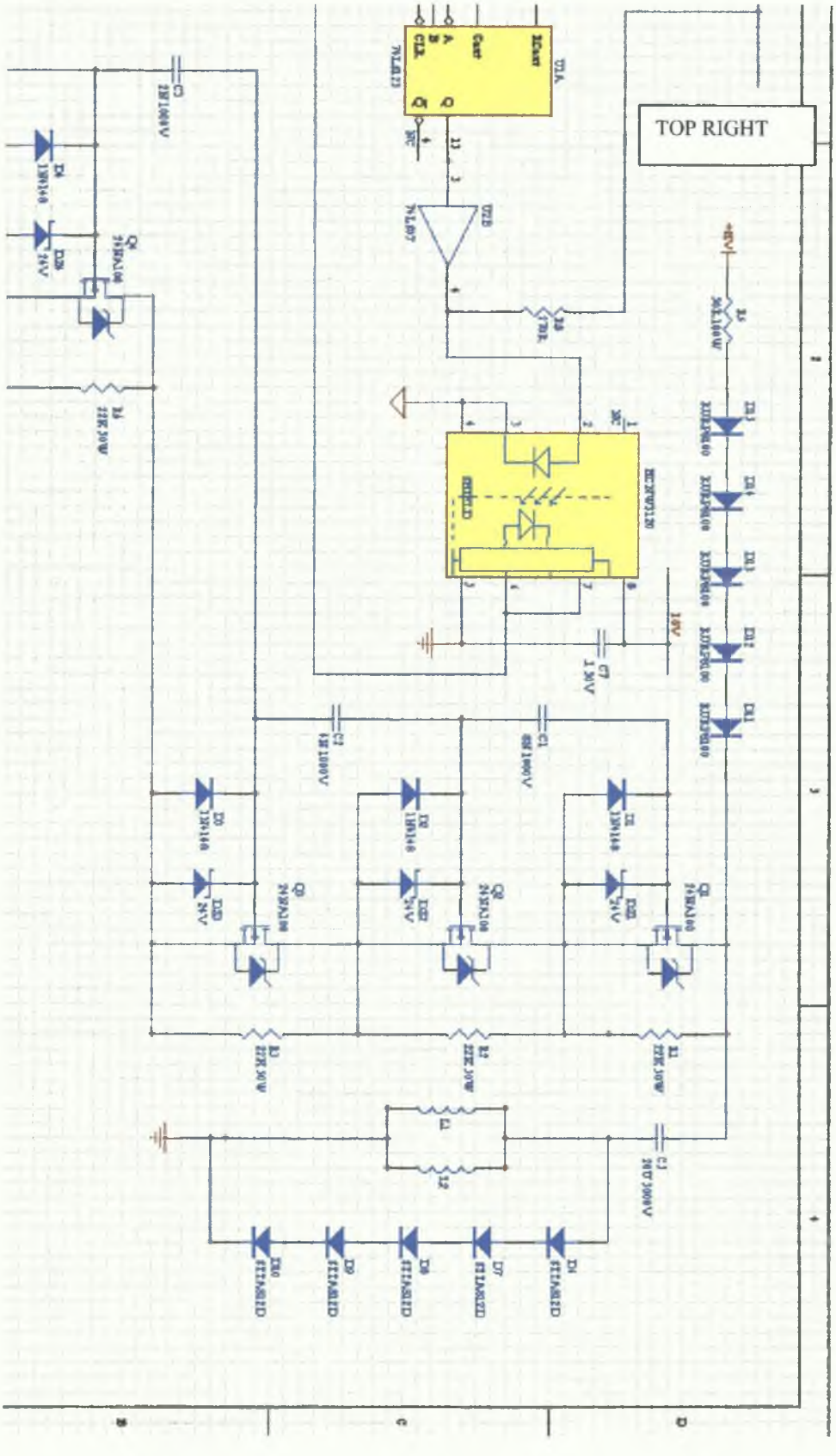
TOP RIGHT

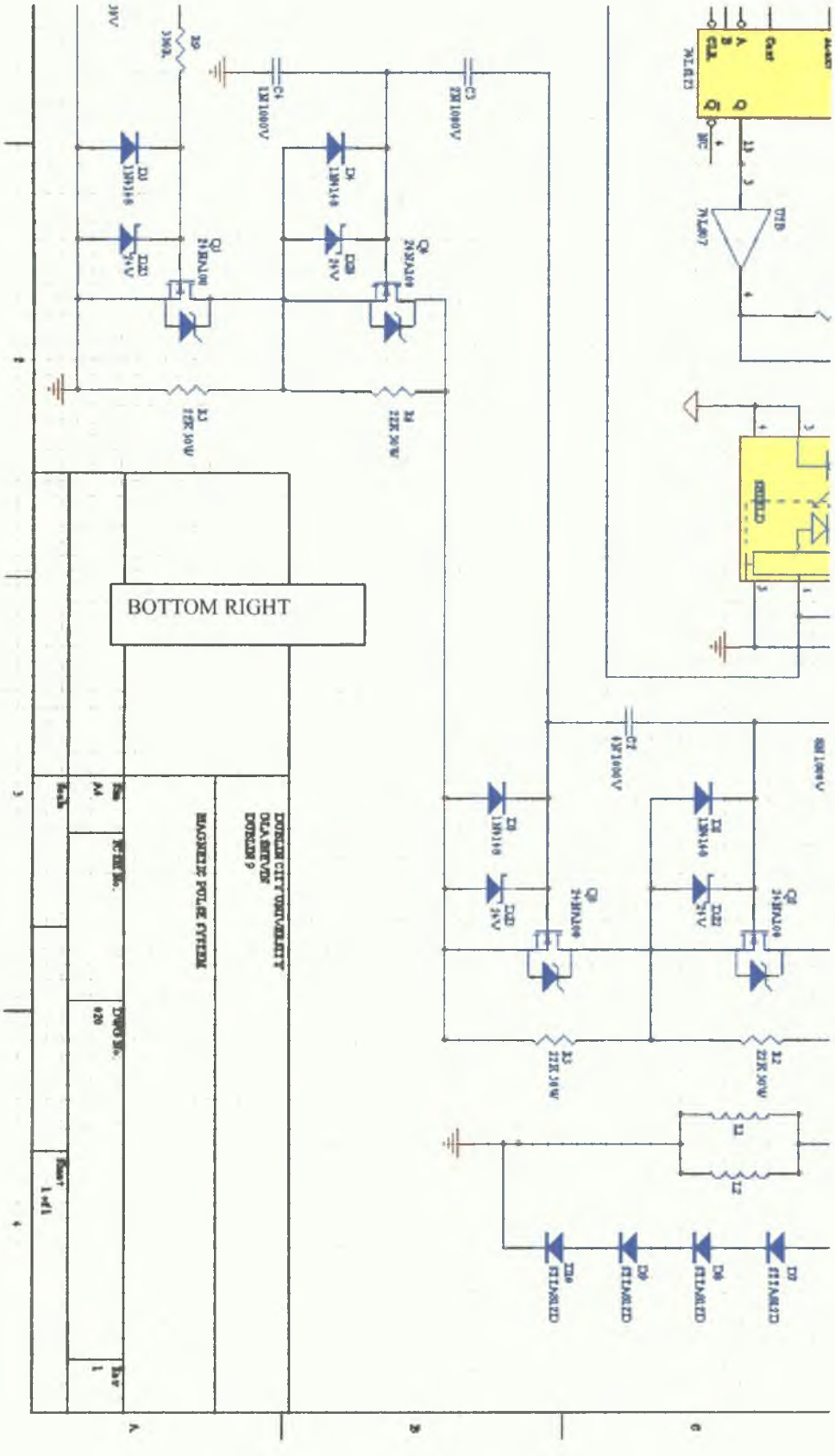
BOTTOM RIGHT

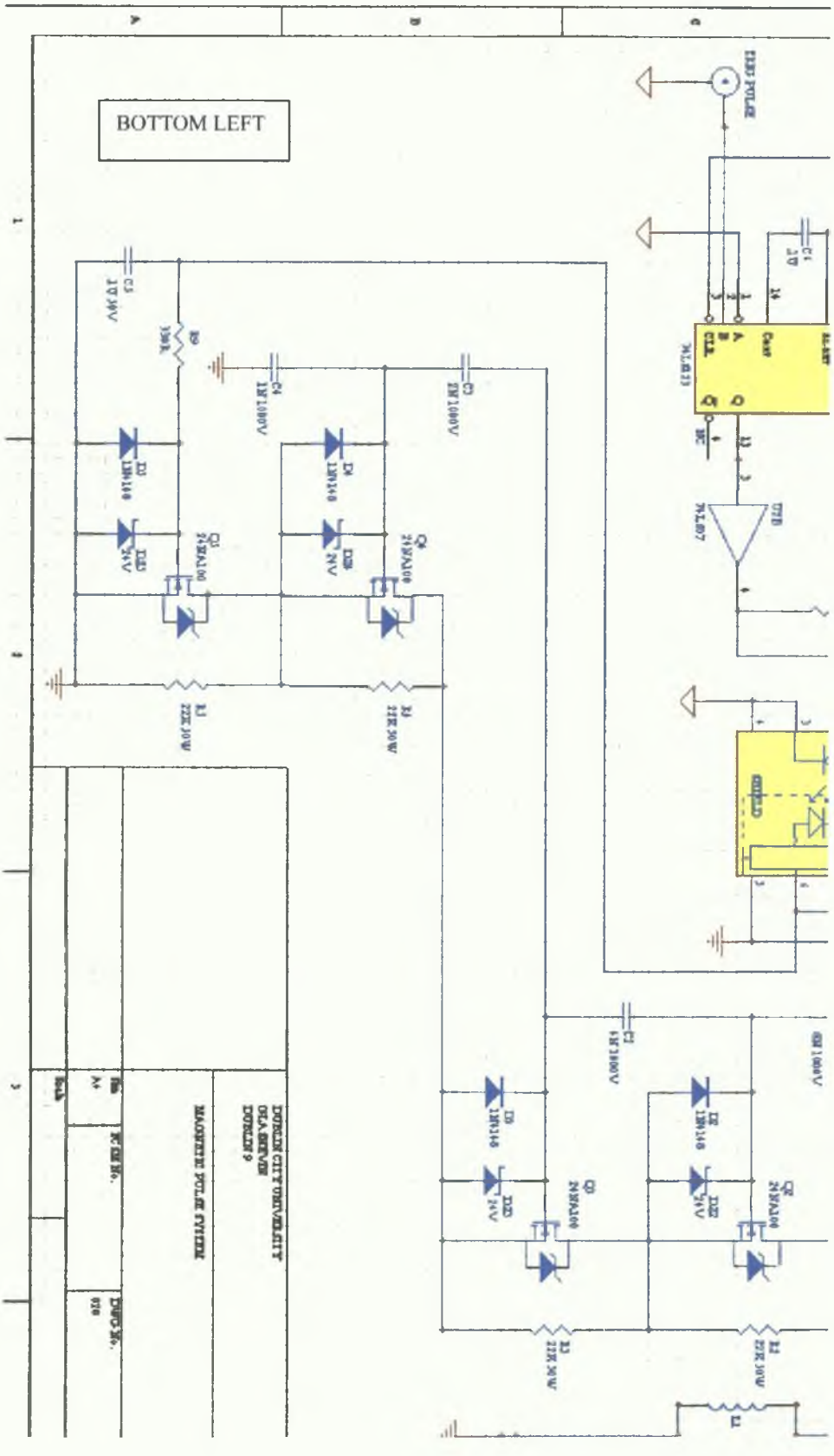
BOTTOM LEFT

Appendix D Equations and constant determination
Continuum correction factor determination

$$\text{Equ 1}\quad \frac{\varepsilon_l}{\varepsilon_c} = C_r \frac{A_{21} g}{U_t} \frac{\lambda_c^{\,2}}{\lambda_l T_e} \exp\left(\frac{E_t - E_2 - \Delta E_t}{kT_e}\right) \times \left[\xi\left(1 - \exp\frac{-hc}{\lambda kT_e}\right) + G\left(\exp\frac{-hc}{\lambda kT_e}\right)\right]^{-1}$$

Using two AL III lines in the same spectral window, and under the assumption that ξ is identical for each line Using ALIII at 447 9nm and 453 04nm and inputting the required variables for the above equation, two equations with unknown variables (ξ and T_e) can be formed

	447nm	453nm
C_r	2×10^{5} (sK)	-------
A_{21}	$3\,35\times10^{-8}$	$2\,55\times10^{-8}$
g_k	4	6
λ_c	453nm	453nm
λ_L	447nm	453nm
U	0 3	--------
E_i	189928	165787
E_0	167612	143713
ΔE	22316	22074

For the above equation G, the Gaunt factor is assumed to be one by Cramers rule, which emerges from the analysis by Biberman et al [] in approximating formulas for hydrogen like ions The exponential function associated with G above, is approximately zero for high temperatures or long wavelengths, and thus the term 1-exp(*) term associated with ξ is equal to one Therefore the entire denominator in the above equation is reduced to ξ

When the above values are inserted the following equations result

For the 447nm line

$$\text{Equ 2}\quad \xi\left(\frac{0\,2}{0\,0236}\right) = \frac{1}{T_e}\exp\left(\frac{5\,6\times10^{4}}{T_e}\right)$$

and for the 453nm line

$$\text{Equ 3}\quad \xi\left(\frac{0\,31}{0\,1066}\right) = \frac{1}{T_e}\exp\left(\frac{9\,18\times10^{4}}{T_e}\right)$$

isolating the term $1/T_e$ in one expression and substituting this into the other equation, ξ can be isolated as a function of the temperature

$$\text{Equ 4}\quad \xi = \sqrt{\frac{1}{23\,8}\exp\left(\frac{14\,8\times10^{4}}{T_e}\right)}$$

The range of allowed values for ξ from the analysis by Biberman [1] and Schuler [2] is from 0.5 to 4.0. ξ should be a weak function of temperature, and from Locke-Holtgreven [3] the profile of ξ is not smooth with wavelength and is highly irregular over a large wavelength range.

In plotting equation 4, we observe the change in the value of ξ for the inputted temperature range. The minimum temperature allowed is 25000K, limited by the analysis of Biderman in setting the upper limit of ξ to 4. The maximum temperature inputted here was 185000k, as this is the temperature of the aluminum laser plasma plume at the determination of the laser pulse [4], however as the profile displays, the value of ξ quickly reaches a level of ~0.6 after 50000K. The average value of ξ is thus 0.98 for AL III in the visible of the temperature range studied.

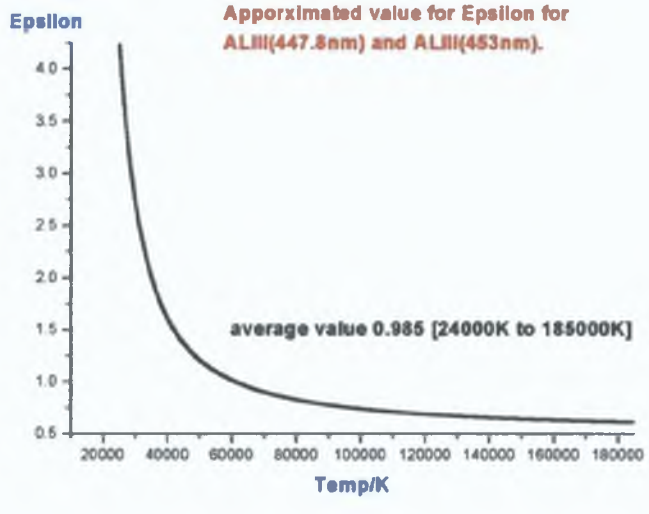

Figure 1: Profile of ξ for the temperature range considered for the visible lines studied (AL III 447.8, 453nm).

electron ion collision frequency

$$\nu_{ei} = 2\times10^{-6}\,\frac{Zn_e Ln\Lambda}{T_{eV}^{3/2}}\ \text{sec}^{-1}$$

electron electron collision frequency

$$\nu_{ee} = 5\times10^{-6}\,\frac{n_e Ln\Lambda}{T_{eV}^{3/2}}\ \text{sec}^{-1}$$

ion ion collision frequency

$$\nu_{ei} = Z^4\left(\frac{m}{M}\right)^{1/2}\left(\frac{T_e}{T_i}\right)^{3/2}\nu_{ee}$$

collision mean free path

$$\lambda_{ee} \approx \lambda_{ii} = 3.4\times10^{13}\,\frac{T_{eV}^2}{nLn\Lambda}\ \text{cm}$$

Plasma frequency

$f_p = 9000\sqrt{n}$ sec^{-1} (n in cm^{-3})

Debye length

$\lambda_D = 740(T_{eV}/n)^{1/2}$ cm (n in cm^{-3})

Plasma parameter

$\Lambda = 4\pi n\lambda_D^3/3$ (n inn cm^{-3}, λ_D in cm)

Coulombic electron-ion mean free path

$$\tau_{eiE} = \frac{2^{5/2}Am_p(kT_e)^2}{\pi^{3/2}m_e Zn_e e^4 Ln\Lambda}\ \text{cm}$$ (A =27 for Al T in eV, m_e, m_p in grams, e=4.85×10^{-10} ergs K, Z is average charge)

Three body recombination per unit time

$$\tau_{ei3BR} = 5.85\times10^{19} T_e^{4.5}/N_e^{2} \text{ /sec} \qquad (T \text{ in K, } N_e \text{ in cm}^{-3})$$

(all input variables such as Te and Ne are taken from the experimental data for the planar targets only)

	EUV	VIS	PROBE
V_{ei} /sec	6.0×10^{12}	1.9×10^{12}	7.5×10^{6}
V_{ee} /sec	1.6×10^{15}	4.0×10^{13}	20.0×10^{6}
V_{ii} /sec	2.8×10^{16}	1.2×10^{12}	0.46×10^{6}
λ_D /μm	1.0	20.0	250
f_p /Hz	7.0×10^{10}	1.3×10^{10}	5.6×10^{7}
$\lambda_{ee}\approx\lambda_{ii}$ /μm	0.65	17.0	1500
$\ln\Lambda$	11.77	20.7	16.8
τ_{eiE} /nm	743600	15.91	2.03
τ_{ei3BR} /nsec	58.5	1.46	0.749

References

[1] Biderman L>M, G E Norman, Opt I Spektroskopiya 8 (1960) 230

[2] D Schluter, Z Astrophys, 61 (1964) 67

[3] Locht-Holtgreven, AIP press, Plasma Diagnostics 1995

[4] C R Phipps, R W Dreyfus Laser Ionization Mass Analysis, Chemical Analysis Series, Vol 124,Wiley, New York, 1993

Appendix E: Chromex instrument function

In order to estimate the value of the FWHM of a line which is broadened by the visible Chromex spectrometer, the emission from a Cd discharge lamp was focused onto the spectrometers slit, and the width of the FWHM of the line measured on the ICCD. The line used was CDI at 441.5nm (figure 2).

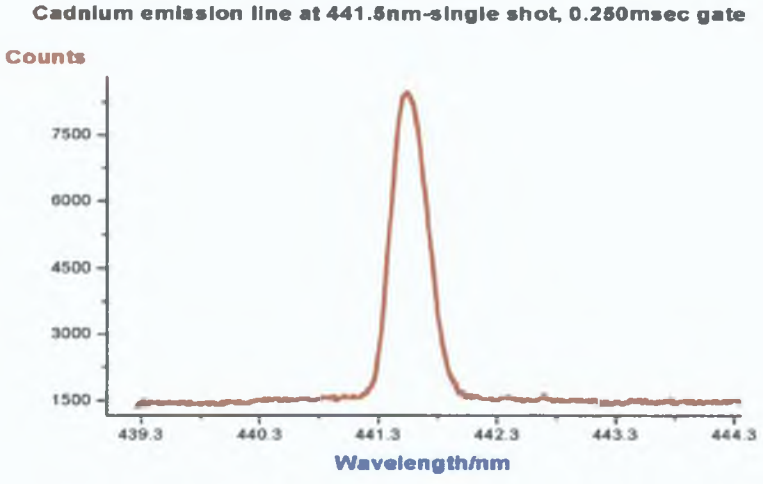

Figure 2: Emission line from Cd I at 441.5nm.

Assuming that the influence of the slit is the chief determiner of the width of an infinitely narrow line after it has passed through the spectrometer, then varying the slit width should reduce the width of the observed line, to some minimum (figure 3). Further reductions in the slit width do not reduce the FWHM of the observed line any further. Thus one assumes that the observed FWHM at some minimum slit width is a good approximation of the broadening introduced by the instrument.

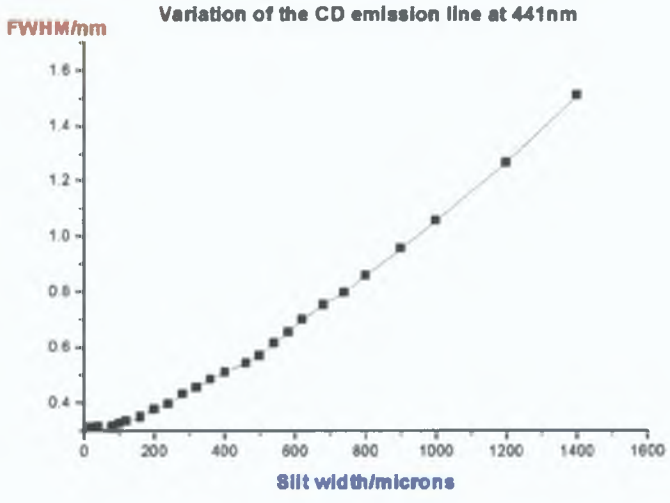

Figure 3: Variation of the FWHM of the Cd line with slit width. The fit used to determine the FWHM was Lorentzian.

Since the instrument profile was observed to be Lorentzian, and the line function used to determine the FWHM of each line was also Lorentzian (chapter 4), then to correct the observed width of the studied emission line, one must subtract the line width introduced by the instrument (here taken to be ~0.3nm, from figure 2, and from the minimum line width measured throughout all visible studies using the Chromex spectrometer) from the measured line width (minimum ~0.4nm, maximum ~1.3nm ---from chapter 4). Then if one is to convert the line width to electron density values, a linear product of a 'W' values (electron impact value) is used to deduce N_e. Thus a smaller FWHM, results in a smaller value for N_e.

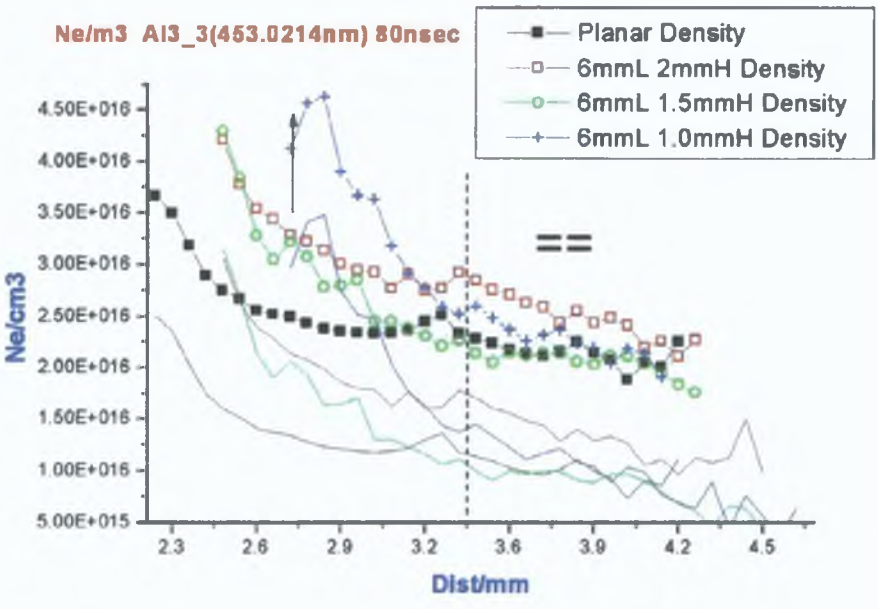

Figure 4: Shifted profiles of N_e from chapter 5, section 5.1.8. All profile shift down by the same amount, which only affects the numerator significantly (~20%). The trend from one target to the next remains the same.

The density profiles displayed in this work have not be shifted to compensate the instrument function because of the large body of data presented in this work, but also because of the chief motivation for this work. To produce a broad overview of target effects, and to display the trends in plasma parameters as a particular variable is changes i.e. capillary diameter.

Since the instrument profile was observed to be Lorentzian, and the line function used to determine the FWHM of each line was also Lorentzian (chapter 4), then to correct the observed width of the studied emission line, one must subtract the line width introduced by the instrument (here taken to be ~0.3nm, from figure 2, and from the minimum line width measured throughout all visible studies using the Chromex spectrometer) from the measured line width (minimum ~0.4nm, maximum ~1.3nm ---from chapter 4). Then if one is to convert the line width to electron density values, a linear product of a 'W' values (electron impact value) is used to deduce N_e. Thus a smaller FWHM, results in a smaller value for N_e.

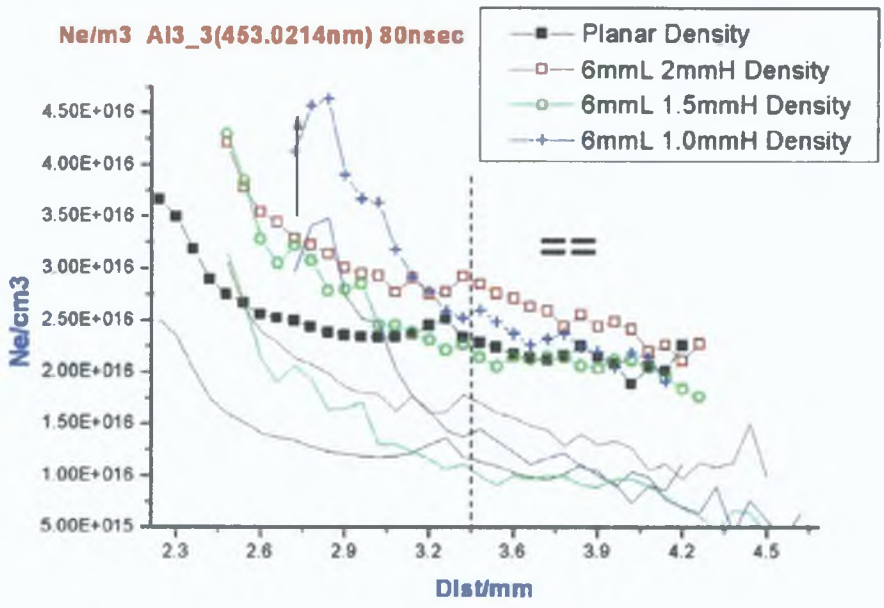

Figure 4: Shifted profiles of N_e from chapter 5, section 5.1.8. All profile shift down by the same amount, which only affects the numerator significantly (~20%). The trend from one target to the next remains the same.

The density profiles displayed in this work have not be shifted to compensate the instrument function because of the large body of data presented in this work, but also because of the chief motivation for this work. To produce a broad overview of target effects, and to display the trends in plasma parameters as a particular variable is changes i.e. capillary diameter.